EXPERIMENTAL INVESTIGATION OF WATER, SNOW AND GRANULAR ICE EFFECTS ON ICE FAILURE PROCESSES AND IMPACT LOADS

by

© Regina Sopper, B.Eng., M.Sc.

A dissertation submitted to the School of Graduate Studies

in partial fulfillment of the requirements for the degree of

Doctor of Philosophy

Faculty of Engineering and Applied Science

Memorial University of Newfoundland

May 2016

St. John's Newfoundland and Labrador Canada

Abstract

A large series of laboratory ice crushing experiments was performed to investigate the effects of external boundary condition and indenter contact geometry on ice load magnitude under crushing conditions. Four boundary conditions were considered: dry cases, submerged cases, and cases with the presence of snow and granular ice material on the indenter surface. Indenter geometries were a flat plate, wedge shaped indenter, (reverse) conical indenter, and spherical indenter. These were impacted with artificially produced ice specimens of conical shape with 20° and 30° cone angles. All indenter – ice combinations were tested in dry and submerged environments at 1 mm/s and 100 mm/s indentation rates. Additional tests with the flat indentation plate were conducted at 10 mm/s impact velocity and a subset of scenarios with snow and granular ice material was evaluated.

The tests were performed using a material testing system (MTS) machine located inside a cold room at an ambient temperature of - 7°C. Data acquisition comprised time, vertical force, and displacement. In several tests with the flat plate and wedge shaped indenter, supplementary information on local pressure patterns and contact area were obtained using tactile pressure sensors. All tests were recorded with a high speed video camera and still photos were taken before and after each test. Thin sections were taken of some specimens as well.

Ice loads were found to strongly depend on contact condition, interrelated with pre-existing confinement and indentation rate. Submergence yielded higher forces, especially

at the high indentation rate. This was very evident for the flat indentation plate and spherical indenter, and with restrictions for the wedge shaped indenter. No indication was found for the conical indenter. For the conical indenter it was concluded that the structural restriction due to the indenter geometry was dominating. The working surface for the water to act was not sufficient to influence the failure processes and associated ice loads. The presence of snow and granular ice significantly increased the forces at the low indentation rate (with the flat indentation plate) that were higher compared to submerged cases and far above the dry contact condition.

Contact area measurements revealed a correlation of higher forces with a concurrent increase in actual contact area that depended on the respective boundary condition. In submergence, ice debris constitution was changed; ice extrusion, as well as crack development and propagation were impeded. Snow and granular ice seemed to provide additional material sources for establishing larger contact areas. The dry contact condition generally had the smallest real contact area, as well as the lowest forces. The comparison of nominal and measured contact areas revealed distinct deviations. The incorporation of those differences in contact process pressures-area relationships indicated that the overall process pressure was not substantially affected by the increased loads.

Acknowledgements

This research was only made possible through the infinite support and encouragement of several great people. I would like to express my deepest gratitude and appreciation to all those who contributed to this project.

First of all, my special thanks go to my supervisor Dr. Claude Daley who gave me the opportunity to immerse myself into cold environments and Arctic science studies, for his financial support, guidance, and confidence in my abilities.

Dr. Bruce Colbourne for always keeping an open door, his endless patience and inspiration in countless constructive conversations. Most especially for bringing me back on course when needed.

Dr. Stephen Bruneau for his infinite support, patience in many invaluable discussions, and encouragement to be master of myself. His creativity and inspiration always opened my eyes to new perspectives.

Many thanks also go to the irreplaceable team of technicians in the laboratory facilities at Memorial University of Newfoundland: Mr. Craig Mitchell for his unlimited support and expertise during the physical experiments, and for his friendship. Mr. Matthew Curtis and all other technologist who provided assistance in the laboratory. Thanks also go Dr. Ian Jordaan for sharing his equipment. I would also like to express my gratitude to Mr. Brian O'Rourke and all work term students who willingly suffered in the cold room without complaints: Jacob Paul Harris, Emily Gerard Antle, Timothy Luke Purdy, Tony Caines, Yuna Zhang.

Furthermore, I would like to thank Mr. David Snook, Mr. William Bidgood and their teams at Technical Services. The rapid fabrication of the test setup, instant repair works, constructive ideas, and continuous support during the experiments are very much appreciated.

I would also like to express my thanks to Dr. Markus Bruehl, Mr. Joris Brouwer and Mr. Henry Piehl for their immensely quick and qualified assistance in programming the

analysis code where needed. Without their help I would probably still be struggling with the implementations of Fast Fourier Transform and differential integrals.

Many thanks also go to my friends Mr. Jordan Gasior and Mr. Dan Oldford. To Dr. Bruce Quinton for his support in handling the MTS machine, his advice on technical matters and his insight on being a Ph.D. candidate. Special thanks also go to Dr. Adedoyin Odukoya for never letting rise doubt but creating confidence that this project was possible to be finished within the anticipated time frame. I drew energy and motivation from our many priceless conversations.

This research was funded by STePS^2 project (Sustainable Technology for Polar Ships and Structures) and I would like to thank all the project partners, as well as NSERC CREATE for financial support received during my program.

Moreover, I would like to thank St. John's, a city I truly fell in love with, and all people of Newfoundland; your friendliness, kindness and generosity still amazes me every day.

Last but not least, my infinite gratitude goes to my parents and my brother. No words quantify their support, believe, trust, and encouragement throughout my life. I thank you for understanding, patience and endless conversations. There were never limits to the height you believed I could reach. Without you I would not be at this significant junction of my life.

Table of Contents

Abstract ii
Acknowledgements iv
Table of Contents vi
List of Tables xiii
List of Figures xv
List of Symbols, Nomenclature and Abbreviations xxxii
List of Appendices xxxiv

Chapter 1 Introduction 1
1.1 The Problem 3
1.2 Objectives 7
1.3 Scope of Work 8
1.4 Original Contributions 8

Chapter 2 Literature Review 10
2.1 Introduction 10
2.2 Ice Properties and Ice Mechanics 11
2.2.1 Ice Types - Sea Ice and Glacial Ice 11
2.2.2 Ice Strength Dependencies - Strain Rate and Temperature 12
2.2.3 Local Ice Failure Mechanisms 15
2.2.4 Ice Extrusion 16
2.2.5 Ice Friction 18
2.2.6 Ice Failure and Microstructural Analysis 21
2.3 Experimental Data 25
2.3.1 Tests Using Different Indenter Shapes – Confinement Aspects 25
2.3.1.1 Field Tests 25
2.3.1.2 Laboratory Tests 26
2.3.2 Tests in Dry Divergent Ambient Conditions 28
2.4 Pressure-Area Relationships 31
2.4.1 Spatial Pressure Distribution 32

2.4.2 Nominal Process Pressure-Area Curve 32
2.5 Pressure Sensing Technologies 35
2.5.1 Chemical Pressure Measurement Film 35
2.5.2 Tekscan I-Scan® Sensors 36
2.5.3 Impact Module 38
2.6 Summary 39

Chapter 3 Methodology and Execution of Physical Experiments 42
3.1 Introduction 42
3.2 Experimental Setup, Test Parameter and Test Scenarios 43
3.2.1 Experimental Setup 43
3.2.2 Ice Holder 44
3.2.3 Ambient Temperature 44
3.2.4 Ice Specimens 45
3.2.5 Indenter 47
3.2.5.1 Flat Plate 48
3.2.5.2 10° Wedge (Concave) 48
3.2.5.3 10° Conical Indenter (Concave) 49
3.2.5.4 Half Hemi Sphere (Convex) 50
3.2.6 Indentation Rates 51
3.2.7 Environmental Testing Conditions 51
3.2.7.1 Dry 52
3.2.7.2 Submerged 52
3.2.7.3 Snow 53
3.2.7.4 Granular Ice (Chips) 54
3.3 Test Scenarios and Test Nomenclature 55
3.3.1 Test Scenarios 55
3.3.2 Test Overview 56
3.3.3 Test Nomenclature 57
3.4 Data Acquisition 58
3.4.1 Material Testing System (MTS) 58
3.4.2 High Speed Camera (HSC) 59
3.4.3 Still Photos 59

3.4.4 Microstructural Observations (Thin Section Procedure) 59
3.4.5 Tactile Pressure Sensors 62
3.5 Boundary Conditions 64
3.5.1 Ice Holders 64
3.5.2 Ice Properties and Ice Age 64
3.5.3 Submergence of Specimen Mounting Steel Plate 65
3.5.4 Test Setup Compliance 66
3.5.5 Buoyancy and Drag in Submerged Tests 66
3.5.6 Container Walls 66
3.5.7 Indenter Surface Roughness 67
3.5.8 Cone Tip Accuracy 68

Chapter 4 Analytical Procedures 69
4.1 Geometry Relations and Contact Area Definitions 69
4.1.1 Ice Sample Geometry 69
4.1.2 Nominal Contact Area for the Flat Indentation Plate 69
4.1.3 Effect of Cone Tip Offset 70
4.1.4 Nominal Contact Areas for Other Indenter Shapes 71
4.1.5 Comparison of Projected Contact Area for a 30° Cone and Different Indenter Shapes (Flat, Wedge, Conical) 73
4.1.6 Maximum Displacement 74
4.2 Spectral Analysis (FFT) 75
4.3 Analysis Procedure for Force vs. Displacement Histories 76
4.4 Contact Area and Spatial Pressure Pattern (Tactile Pressure Sensors) . 77
4.5 Microstructural Observations (Raw Samples, Ice Age) 79
4.6 Multiple Regression Analysis 80

Chapter 5 Analytical Results and Interpretation 83
5.1 Flat Indentation Plate 84
5.1.1 Test Overview 84
5.1.2 Measured Force and Nominal Process Pressure 87
5.1.2.1 Indentation Rate: 1 mm/s 87
5.1.2.2 Indentation Rate: 10 mm/s 91
5.1.2.3 Indentation Rate: 100 mm/s 95

5.1.3 Local Pressure Pattern and Contact Area (Tactile Pressure Sensors) 99
5.1.3.1 Indentation Rate: 1 mm/s 100
5.1.3.2 Indentation Rate: 100 mm/s 105
5.1.4 General and Microstructural Observations 110
5.1.4.1 General Observations – During Testing: Ice Debris Formation, Ice Extrusion and Crack Propagation (HSC) 110
5.1.4.2 General Observations – After Test Completion: Contact Area and Surface (Still Photos) 114
5.1.4.3 Microstructural Observations 118
5.1.5 Multiple Regression Analysis 119
5.1.6 Summary and Discussion 124
5.1.6.1 Force 124
5.1.6.2 Nominal Process Pressure 126
5.1.6.3 Ice Failure and Local Pressure Pattern 127
5.1.6.4 Contact Area 128
5.1.6.5 Contact Pressure (Adjusted Nominal Process Pressure) 130
5.1.6.6 Discussion 135
5.2 Wedge Indenter 137
5.2.1 Test Overview 137
5.2.2 Measured Force and Nominal Process Pressure 138
5.2.2.1 Indentation Rate: 1 mm/s 138
5.2.2.2 Indentation Rate: 100 mm/s 140
5.2.3 Local Pressure Pattern and Contact Area (Tactile Pressure Sensors) 142
5.2.3.1 Indentation Rate: 1 mm/s 142
5.2.3.2 Indentation Rate: 100 mm/s 146
5.2.4 General and Microstructural Observations 150
5.2.4.1 General Observations – During Testing: Ice Debris Formation, Ice Extrusion and Crack Propagation (HSC) 150
5.2.4.2 General Observations - After Test Completion: Contact Area and Surface (Still Photos) 151
5.2.4.3 Microstructural Observations 154
5.2.5 Multiple Regression Analysis 155

5.2.6 Summary and Discussion 158
5.2.6.1 Force 158
5.2.6.2 Nominal Process Pressure 158
5.2.6.3 Local Pressure Pattern and Contact Area 158
5.2.6.4 Contact Pressure (Adjusted Nominal Process Pressure) 159
5.2.6.5 Discussion 161
5.3 Conical Indenter 164
5.3.1 Test Overview 164
5.3.2 Measured Force and Nominal Process Pressure 165
5.3.2.1 Indentation Rate: 1 mm/s 165
5.3.2.2 Indentation Rate: 100 mm/s 167
5.3.3 General and Microstructural Observations 169
5.3.3.1 General Observations – During Testing: Ice Debris Formation, Ice Extrusion and Crack Propagation (HSC) 169
5.3.3.2 General Observations - After Test Completion: Contact Area and Surface (Still Photos) 170
5.3.3.3 Microstructural Observations 172
5.3.4 Multiple Regression Analysis 173
5.3.5 Summary and Discussion 175
5.4 Spherical Indenter 177
5.4.1 Test Overview 177
5.4.2 Measured Force and Nominal Process Pressure 178
5.4.2.1 Indentation Rate: 1 mm/s 178
5.4.2.2 Indentation Rate: 100 mm/s 180
5.4.3 General and Microstructural Observations 182
5.4.3.1 General Observations – During Testing: Ice Debris Formation, Ice Extrusion and Crack Propagation (HSC) 182
5.4.3.2 General Observations - After Test Completion: Contact Area and Surface (Still Photos) 184
5.4.3.3 Microstructural Observations 186
5.4.4 Multiple Regression Analysis 187
5.4.5 Summary and Discussion 189

Chapter 6 Theoretical Implications 191
6.1 Effect of Indentation Rate and Contact Condition 191
6.1.1 Flat Plate 191
6.1.1.1 20° Ice Specimens 191
6.1.1.2 30° Ice Specimens 194
6.1.2 Wedge 197
6.1.3 Conical indenter 199
6.1.4 Spherical Indenter 199
6.1.5 Summary 201
6.2 Effect of Indenter Shape 201
6.3 Effect of Contact Condition 207
6.3.1 Submergence at High Indentation Rate 208
6.3.1.1 Influence of Indenter and Ice Geometry 209
6.3.1.2 Effect on Ice Debris Constitution (IDC) 210
6.3.1.3 Effect on Crack Development and Propagation (CDP) 212
6.3.1.4 Hydrodynamic Confinement Zone (HDC) 213
6.3.1.5 Pressure Spreading Effect (PSE) – at Grain Boundaries 215
6.3.1.6 Ice Friction 216
6.3.1.7 Implications for Ice-Structure Interactions with other Geometries 217
6.3.1.8 Summary of Submergence Effects at High Indentation Rate 218
6.3.2 Snow and Granular Ice at Low Indentation Rate 218
6.3.2.1 Confinement Effect – Impeded Ice Extrusion 219
6.3.2.2 Recrystallization 220
6.3.2.3 Local Pressure Spreading Effect 220
6.3.2.4 Summary of Snow and Granular Ice at Low Indentation Rate 222
6.4 Pressure-Area Effect 222
6.5 Other Influences 225
6.5.1 Water Level 225
6.5.2 Water Temperature 226
6.5.3 Mounting Steel Plate 226
6.5.4 Ice Age 226

6.5.5 Indentation Rate Variations 227
6.5.6 Malfunction of Tactile Pressure Sensors 227
6.6 Implications for Numerical Simulations 228

Chapter 7 Summary, Conclusions and Recommendations 230
7.1 Summary 230
7.2 Conclusions 232
7.3 Recommendations 235

References 238
Appendices 245

List of Tables

Table 3.1: Overview of tests performed with the flat indentation plate. 56

Table 3.2: Overview of tests performed with the wedge shaped indenter. 57

Table 3.3: Overview of tests performed with the conical indenter. 57

Table 3.4: Overview of tests performed with the spherical indenter. 57

Table 4.1: Overview of maximum achieved and considered displacements depending on indenter shape and ice cone angle. 74

Table 4.2: Overview of in the analysis considered area ranges and associated displacements depending on the respective indenter and ice cone angle.....77

Table 5.1: Overview of 71 tests performed with the flat indentation plate. 85

Table 5.2: Flat plate, 1 mm/s, 20° ice cones, all conditions: comparison of the nominal contact area with individual contact area measurements from the tactile pressure sensors.....103

Table 5.3: Flat plate, 1 mm/s, 30° ice cones, all conditions: comparison of the nominal contact area with individual contact area measurements from the tactile pressure sensors.....105

Table 5.4: Flat plate, 100 mm/s, 20° ice cones, dry and submerged conditions: comparison of the nominal contact area with individual contact area measurements from the tactile pressure sensors. 108

Table 5.5: Flat plate, 100 mm/s, 30° ice cones, three contact conditions: comparison of the nominal contact area with individual contact area measurements from the tactile pressure sensors. 109

Table 5.6: P-Values for factors and factor interactions of regression models at significance level α=0.15 for the flat indentation plate. 120

Table 5.7: Model lack of fit, R^2, R^2 adjusted and R^2 predicted of linear regression models at significance level α=0.15 for the flat indentation plate 121

Table 5.8: Overview of 8 tests performed with the wedge shaped indenter. 137

Table 5.9: Wedge, 1 mm/s, 30° ice cones, dry and submerged conditions: comparison of the nominal contact area with individual contact area measurements from the tactile pressure sensors. 146

Table 5.10: Wedge, 100 mm/s, 30° ice cones, dry and submerged conditions: comparison of the nominal contact area with individual contact area measurements from the tactile pressure sensors. 149

Table 5.11: Overview of 12 tests performed with the conical indenter. 164

Table 5.12: Overview of 10 tests performed with the spherical indenter. 177

Table 6.1: Identification of the submergence effect depending on indenter geometry and indentation rate. 207

Table 6.2: Identification of the influence of snow and granular ice on the flat indentation plate depending on indentation rate and ice cone angle. 207

List of Figures

Figure 1.1: Overview of research areas on ice mechanics and ice loads for ships and offshore structures. 6

Figure 2.1: Influence of strain rate on uniaxial compressive ice strength (Source: U. S. Army Corps of Engineers, 2006). 13

Figure 2.2: Uniaxial compressive strength for iceberg ice at -10°C (Source: Jones, 2007). 14

Figure 2.3: Local processes during ice failing against a vertical structure (Source: Jordaan, 2001). 15

Figure 2.4: Friction coefficient dependence on temperature (left) and on velocity with increased drag caused by melt water (right). (Source: Kietzig et al., 2010). .. 20

Figure 2.5: Internal ice friction dependent on the temperature (Source: Cole, 2001). 20

Figure 2.6: Pressure-Area data compiled by Sanderson (1988) showing a decreasing pressure trend with increasing area. 32

Figure 2.7: Pressure distribution using Chemical Pressure Measurement Film with different resolutions (Source: Kim, 2014). 35

Figure 2.8: Examples of pressure distributions using Tekscan I-Scan® (Source: Wells et al., 2010). 36

Figure 2.9: (Left) Image showing contact area during impact taken with the high speed camera inside the Impact Module. (Right) The resulting pressure distribution. (Source: Sopper et al., 2015b). 39

Figure 2.10: Concept sketch indicating during ice-structure collisions (dry contact) occurring processes that would be affected by other external boundary conditions. 41

Figure 3.1: Experimental setup showing the aluminum container attached to the piston of the MTS machine and an ice sample mounted to the steel plate on the stationary crosshead. 44

Figure 3.2: (Left) Ice holder - aluminum bucket setup to grow ice specimen. (Right) Ice holder with unprocessed cylindrical specimen. 46

Figure 3.3: Ice shaping apparatus to machine conical ice specimen. 47

Figure 3.4: Image of flat indentation plate.....48

Figure 3.5: 10° Wedge shaped indenter: drawing with dimensions (side view). 49

Figure 3.6: 10° Wedge shaped indenter: still photo (isometric view). 49

Figure 3.7: 10° Conical indenter (reverse cone). (Left) Top view with diameters indicated. (Right) Image of isometric view. 50

Figure 3.8: Spherical indenter. (Left) Side view of sphere with dimensions. (Right) Image displaying the spherical indenter mounted to an aluminum plate.....51

Figure 3.9: Overview of test scenarios. (Left) Flat plate; top to bottom for dry, submerged, and snow and granular ice contact conditions. (Middle) Wedge or conical indenter and (Right) spherical indenter; top for dry and below for submerged conditions.....55

Figure 3.10: Picture showing an ice specimen with a warm wire winded around for detaching it from the mold. 60

Figure 3.11: Image of manually operated microtome to machine thin ice sections. 61

Figure 3.12: Thin section of test T52_01_S_LS_Sp_20. (Left) Between cross polarized filters for examining the crystal structure. (Right) With side light to reveal fractures. 62

Figure 3.13: Tekscan I-Scan® model 5101 overall dimensions and specifications (Source: Tekscan, 2003). 63

Figure 4.1: Ice specimen dimensions dependent on different cone angles; (Left) 20° angle. (Right) 30°angle. 69

Figure 4.2: Comparison of contact area for a 20° and 30° cone with the flat indentation plate. 70

Figure 4.3: Comparison of projected and tangent contact area for a 20° cone and the spherical indenter for a displacement up to 34 mm. 72

Figure 4.4: Contact area between a 30° cone and different indenter shapes (flat, wedge, conical). 73

Figure 4.5: Image of a pressure pattern of submerged test S T92-01 at 100 mm/s with the flat indentation plate and with 20° ice cone angle (penetration depth approx. 11 mm). Left from the pink line is the damaged sensor section. 78

Figure 4.6: Images of vertical and horizontal thin sections between a cross-polarized filter of raw samples (Left) young: 2-3 weeks, (Right) old: 95 days. The images show the crystal structure of the parent (intact) ice. Cracks evident in the vertical thin sections were introduced during shaping with the microtome.... 80

Figure 5.1: Still photos of the test setup for dry (top left), submerged (top right), snow (bottom left) and granular ice (bottom right) contact conditions with the flat indentation plate and 30° ice cone angle. 84

Figure 5.2: Flat plate, 1 mm/s, 20° ice specimens: force vs. displacement for all contact conditions. The shaded areas enclose all dry tests (5) in green and submerged tests (4) in blue. 88

Figure 5.3: Flat plate, 1 mm/s, 20° ice specimens: nominal pressure-area curves for all contact conditions. The shaded areas enclose all dry tests (5) in green and submerged tests (4) in blue. 89

Figure 5.4: Flat plate, 1 mm/s, 30° ice specimens: force vs. displacement for all contact conditions. The shaded areas enclose all dry tests (4) in green and submerged tests (6) in blue. 90

Figure 5.5: Flat plate, 1 mm/s, 30° ice specimens: nominal pressure-area curves for all contact conditions. The shaded areas enclose all dry tests (4) in green and submerged tests (6) in blue. 91

Figure 5.6: Flat plate, 10 mm/s, 20° ice specimens: force vs. displacement for all contact conditions. The shaded areas enclose all dry tests (4) in green and submerged tests (3) in blue. 92

Figure 5.7: Flat plate, 10 mm/s, 20° ice specimens: nominal pressure-area curves for all contact conditions. The shaded areas enclose all dry tests (4) in green and submerged tests (3) in blue. 93

Figure 5.8: Flat plate, 10 mm/s, 30° ice specimens: force vs. displacement for all contact conditions. The shaded areas enclose all dry tests (2) in green and submerged tests (3) in blue. 94

Figure 5.9: Flat plate, 10 mm/s, 30° ice specimens: nominal pressure-area curves for all contact conditions. The shaded areas enclose all dry tests (2) in green and submerged tests (3) in blue. 95

Figure 5.10: Flat plate, 100 mm/s, 20° ice specimens: force vs. displacement for all contact conditions. The shaded areas enclose all dry tests (6) in green and submerged tests (4) in blue. 96

Figure 5.11: Flat plate, 100 mm/s, 20° ice specimens: nominal pressure-area curves for all contact conditions. The shaded areas enclose all dry tests (6) in green and submerged tests (4) in blue. 97

Figure 5.12: Flat plate, 100 mm/s, 30° ice specimens: force vs. displacement for all contact conditions. The shaded areas enclose all dry tests (5, excluding D T09-04) in green and submerged tests (6) in blue.....98

Figure 5.13: Flat plate, 100 mm/s, 30° ice specimens: nominal pressure-area curves for all contact conditions. The shaded areas enclose all dry tests (5, excluding D T09-04) in green and submerged tests (6) in blue.....99

Figure 5.14: Flat plate, 1 mm/s, 30° ice cones: pressure patterns in approx. 37.65 mm penetration depth for all contact conditions. (Top) left: dry T73-01, right: submerged T93-02; (Bottom) left: snow T80-08, right: granular ice T98-01 (the granular ice case is for one sensor (half contact area) only).....101

Figure 5.15: Flat plate, 1 mm/s, 20° ice specimen angle, all contact conditions: contact area vs. displacement from pressure sensor measurements. Note that all curves display the doubled contact area of one pressure sensor measurement. 102

Figure 5.16: Flat plate, 1 mm/s, 30° ice specimen angle, all contact conditions: contact area vs. displacement from pressure sensor measurements. Note that all curves display the doubled contact area of one pressure sensor measurement. 104

Figure 5.17: Flat plate, 100 mm/s, 20° ice cones: pressure patterns in approx. 23 mm penetration depth in dry (left, D T76-04) and submerged (right, S T92-01) contact conditions. The images show a clearly larger contact area in the case of submergence. 106

Figure 5.18: Flat indentation plate, 100 mm/s, 30° ice cones: pressure patterns in approx. 40 mm penetration depth in dry (left, D T77-05) and submerged (right, S T95-04) contact conditions. 106

Figure 5.19: Flat plate, 100 mm/s, 20° ice specimen angle, dry and submerged contact conditions: contact area vs. displacement from pressure sensor measurements. Note that the contact area of the submerged test is corrected by 284 mm^2 to eliminate the offset that was caused by a defective sensor column. 108

Figure 5.20: Flat plate, 100 mm/s, 30° ice specimen angle, three contact conditions: contact area vs. displacement from pressure sensor measurements. Note that the contact area of the submerged test was corrected by 284 mm2 to eliminate the offset that was caused by a broken sensor column.....109

Figure 5.21: Flat plate, 100 mm/s, 30° ice specimen angle, three contact conditions: change in ratio between nominal and measured contact areas with displacement.....110

Figure 5.22: Flat plate, 1 mm/s, 20° ice specimens, dry (left, D T35-01) and submerged (right, S T94-03) contact conditions, approx. 15.6 mm penetration depth. Snap shots of HSC footage. Cracks and ice fragments are clearly visible in the dry environment. Ice debris is considerably less distinguishable in the submergence case. 111

Figure 5.23: Flat plate, 100 mm/s, 30° ice specimen, dry D T77-05. HSC footage. (Top) approx. 18.9 mm penetration depth; cracks occurred and penetrated the entire ice specimen. (Bottom) approx. 35.1 mm; large ice fragments break off and are freely extruded. 112

Figure 5.24: Flat plate, 100 mm/s, 30° ice specimen, submerged S T31-03. HSC footage. (Top) approx. 7.4 mm penetration depth; the impact affects the specimen localized at the cone tip. (Middle) approx. 20.4 mm; larger cracks occur, but the ice spalls remain in place. (Bottom) approx. 34.8 mm; cracks occurred and water intruded, visible in terms of the shaded areas. 113

Figure 5.25: Flat plate, 1 mm/s, 20° ice specimens: images of samples after testing for each contact condition; on the left of indented surfaces, on the right with lighting applied from the back. 115

Figure 5.26: Flat plate, 100 mm/s, 20° ice specimens: images of samples after testing for each contact condition; on the left of indented surfaces, on the right with lighting applied from the back. 117

Figure 5.27: Flat plate, 100 mm/s, 20 ° ice samples: thin sections of dry (left) and submerged (right) conditions. The images show the sections between a cross-polarized filter on the left, and with side lighting applied on the right. 119

Figure 5.28: Overview of main effects on the means of the four responses for the flat indentation plate (α=0.15, stepwise selection of model terms, no data transformation). 122

Figure 5.29: Overview of factor interactions for the four responses for the flat indentation plate (α=0.15, stepwise selection of model terms, no data transformation). 124

Figure 5.30: Flat plate, 1 mm/s, 20° ice specimens: contact pressure-area curves for all contact conditions. The adjustment (multiplication) factors were 1.48 for dry, 0.94 for submerged, 0.65 for snow and 0.80 for granular ice. 132

Figure 5.31: Flat plate, 1 mm/s, 30° ice specimens: contact pressure-area curves for all contact conditions. The adjustment (multiplication) factors were 1.56 for dry, 1.37 for submerged, 0.87 for snow and 0.79 for granular ice. 132

Figure 5.32: Flat plate, 100 mm/s, 20° ice specimens: contact pressure-area curves for dry and submerged contact conditions. The adjustment (multiplication) factors were 2.58 for dry, 1.15 for submerged. The curves of snow and the granular ice tests are left out because no adjustment factor could be established. 133

Figure 5.33: Flat plate, 100 mm/s, 30° ice specimens: contact pressure-area curves for dry, submerged and snow contact conditions. The adjustment (multiplication) factors were 2.23 for dry, 2.20 for submerged, 2.25 for snow. The curves of the granular ice tests are left out because no adjustment factor could be established. 134

Figure 5.34: Still photos of the test setup for dry (left) and submerged (right) contact conditions with the wedge shaped indenter and 30° ice cone angle. 137

Figure 5.35: Wedge, 1 mm/s, 30° ice specimens: force vs. displacement for dry and submerged contact conditions. The shaded areas enclose all dry tests (2) in green and submerged tests (2) in blue. 139

Figure 5.36: Wedge, 1 mm/s, 30° ice specimens: nominal pressure-area curves for all contact conditions. The shaded areas enclose all dry tests (2) in green and submerged tests (2) in blue. 140

Figure 5.37: Wedge, 100 mm/s, 30° ice specimens: force vs. displacement for dry and submerged contact conditions. The shaded areas enclose all dry tests (2) in green and submerged tests (2) in blue. 141

Figure 5.38: Wedge, 100 mm/s, 30° ice specimens: nominal pressure-area curves for all contact conditions. The shaded areas enclose all dry tests (2) in green and submerged tests (2) in blue. 142

Figure 5.39: Wedge, 1 mm/s, 30° ice cones: pressure patterns in approx. 30 mm penetration depth for dry (left) and submerged (right) contact conditions. (Left) dry tests D T65-01 (top) and D T67-01 (bottom); (Right) submerged tests S T69-03 (top) and S T71-05 (bottom). 143

Figure 5.40: Wedge, 1 mm/s, 30° ice specimen angle, dry and submerged contact conditions: contact area vs. displacement from pressure sensor measurements. 144

Figure 5.41: Wedge, 1 mm/s, 30° ice specimen angle, dry and submerged contact conditions: change in ratio between nominal and measured contact areas with displacement. 145

Figure 5.42: Wedge, 100 mm/s, 30° ice cones: pressure patterns in approx. 18 mm penetration depth for dry (left) and submerged (right) contact conditions. (Left) dry tests D T66-02 (top) and D T68-02 (bottom); (Right) submerged tests S T70-04 (top) and S T72-06 (bottom). 147

Figure 5.43: Wedge, 100 mm/s, 30° ice specimen angle, dry and submerged contact conditions: contact area vs. displacement from pressure sensor measurements. 148

Figure 5.44: Wedge, 100 mm/s, 30° ice specimen angle, dry and submerged contact conditions: change in ratio between nominal and measured contact areas with displacement.....149

Figure 5.45: Wedge, 1 mm/s, 30° ice specimen, dry (left, T67-01) and submerged (right, T 69-03) contact conditions, approx. 14.9 mm penetration depth. Still photos of HSC footage showing the different ice debris development in dry and submerged environments. 150

Figure 5.46: Wedge, 100 mm/s, 30° ice specimen, dry (left, T66-02) and submerged (right, T 70-04) contact conditions, approx. 14.9 mm penetration depth. Snap shots of HSC footage. 151

Figure 5.47: Wedge, 1 mm/s, 30° ice specimens: images of ice samples after testing in dry (top) and submerged (bottom) contact conditions; on the left of indented surfaces, on the right with lighting applied from the back.....152

Figure 5.48: Wedge, 100 mm/s, 30° ice specimens: images of ice samples after testing in dry (top) and submerged (bottom) contact conditions; on the left of indented surfaces, on the right with lighting applied from the back.....153

Figure 5.49: Wedge, 1 mm/s and 100 mm/s, 30° ice specimens: images of vertical cross-sections showing the effect of indentation rate (1 mm/s, 100 mm/s) and contact condition (dry, submerged). In the dry condition, the samples are penetrated by cracks. In submergence cases, the samples were affected in less depth and have no cracks and fractures.....154

Figure 5.50: Wedge, 100 mm/s, 30° ice cones: Thin sections of tests in dry (left) and submerged (right) conditions. The images show the sections between a cross-polarized filter on the left and with side lighting applied on the right.....155

Figure 5.51: Overview of main effects on the means of the four responses for the wedge shaped indenter.....156

Figure 5.52: Overview of the effect of indentation rate and contact condition interaction on the means of the four responses of the wedge shaped indenter. 157

Figure 5.53: Wedge, 1 mm/s, 30° ice specimens: contact pressure-area curves for all contact conditions. The adjustment factors were 2.28 and 1.69 for the dry, and 2.09 and 1.50 for the submerged tests.....160

Figure 5.54: Wedge, 100 mm/s, 30° ice specimens: contact pressure-area curves for all contact conditions. The adjustment factors were 3.73 and 3.60 for the dry, and 1.51 and 1.76 for the submerged tests.....161

Figure 5.55: Still photos of the test setup for dry (left) and submerged (right) contact conditions with the conical indenter and 30° ice cone angle. 164

Figure 5.56: Conical indenter, 1 mm/s, 30° ice specimens: force vs. displacement for dry and submerged contact conditions. The shaded areas enclose all dry tests (3, excluding D T43-01) in green and submerged tests (3) in blue.....166

Figure 5.57: Conical indenter, 1 mm/s, 30° ice specimens: nominal pressure-area curves for all contact conditions. The shaded areas enclose all dry tests (3, excluding D T43-01) in green and submerged tests (3) in blue. 167

Figure 5.58: Conical indenter, 100 mm/s, 30° ice specimens: force vs. displacement for dry and submerged contact conditions. The shaded areas enclose all dry tests (3) in green and submerged tests (2) in blue. 168

Figure 5.59: Conical indenter, 100 mm/s, 30° ice specimens: nominal pressure-area curves for all contact conditions. The shaded areas enclose all dry tests (3) in green and submerged tests (2) in blue. 169

Figure 5.60: Conical indenter, 1 mm/s, 30° ice specimens, dry (left, D T46-04) and submerged (right, S T56-01) contact conditions, approx. 19.3 mm penetration depth. Still photos of HSC footage showing distinct fractures and ice spalls in the dry environment. The submerged sample seems to be fairly intact. 170

Figure 5.61: Conical indenter, 100 mm/s, 30° ice specimens, dry (left, D T61-03) and submerged (right, S T63-05) contact conditions, approx. 19.4 mm penetration depth. Still photos of HSC footage showing significant ice debris formation in the dry testing environment, but considerably less in submergence. 170

Figure 5.62: Conical indenter, 1 mm/s, 30° ice specimens: images of ice samples after testing in dry (top) and submerged (bottom) contact conditions; on the left of indented surfaces, on the right with lighting applied from the back. 171

Figure 5.63: Conical indenter, 100 mm/s, 30° ice specimens: images of ice samples after testing in dry (top) and submerged (bottom) contact conditions; on the left of indented surfaces, on the right with lighting applied from the back. 172

Figure 5.64: Conical indenter, 100 mm/s, 30° ice cones: thin sections tests in dry (left) and submerged (right) conditions. The images show the sections between a cross-polarized filter on the left and with side lighting applied on the right.173

Figure 5.65: Overview of main effects on the means of the four responses for the conical indenter.....174

Figure 5.66: Overview of the effect of indentation rate and contact condition interaction on the means of the four responses of the conical indenter. 175

Figure 5.67: Still photos of the test setup for dry (left) and submerged (right) contact conditions with the spherical indenter and 20° ice cone angle. 177

Figure 5.68: Sphere, 1 mm/s, 20° ice specimens: force vs. displacement for dry and submerged contact conditions. The shaded areas enclose all dry tests (3) in green and submerged tests (2) in blue.....179

Figure 5.69: Sphere, 1 mm/s, 20° ice specimens: nominal pressure-area curves for all contact conditions. The shaded areas enclose all dry tests (3) in green and submerged tests (2) in blue. 180

Figure 5.70: Sphere, 100 mm/s, 20° ice specimens: force vs. displacement for dry and submerged contact conditions. The shaded areas enclose all dry tests (3) in green and submerged tests (2) in blue.....181

Figure 5.71: Sphere, 100 mm/s, 20° ice specimens: nominal pressure-area curves for all contact conditions. The shaded areas enclose the dry tests (3) in green and submerged tests (2) in blue. 182

Figure 5.72: Sphere, 1 mm/s, 20° ice specimens, dry (left, D T50-03) and submerged (right, S T52-01) contact conditions, approx. 19.3 mm penetration depth. Still

photos of HSC footage. In the dry contact condition (left), crushed ice is extruded and ice spalls break off. In submergence, the ice debris mostly consists of ice flakes and only later ice spalls are formed that float to the water surface. 183

Figure 5.73: Sphere, 100 mm/s, 20° ice specimens, dry (left, D T51-04) and submerged (right, S T53-02) contact conditions, approx. 19.3 mm penetration depth. Snap shots of HSC footage. In the dry contact condition (left), crushed ice is waterfall-like extruded. In submergence, ice spall formation is reduced and the ice debris appears cloud-like. 184

Figure 5.74: Sphere, 100 mm/s, 20° ice specimens: images of ice samples after testing in dry (top) and submerged (bottom) contact conditions; on the left of indented surfaces, on the right with lighting applied from the back.....185

Figure 5.75: Close-ups of surface contact areas of dry tests with the spherical indenter at 1 mm/s (left, D T59-01) and 100 mm/s (right, D T49-02) indentation rates. The images display rate-typical contact areas, i.e. a circular shape for low speed tests, and a branch-like pattern for high speed tests.....185

Figure 5.76: Sphere, 100 mm/s, 20° ice cones: thin sections of tests in dry (left) and submerged (right) conditions. The figure shows the sections of the specimens between a cross-polarized filter on the left and with side lighting on the right. 186

Figure 5.77: Overview of main effects on the means of the four responses for the spherical indenter. 187

Figure 5.78: Overview of the effect of indentation rate and contact condition interaction on the means of the four responses of the spherical indenter. 188

Figure 6.1: Flat plate, 20° ice specimens, dry: force vs. displacement for 1 mm/s (5), 10 mm/s (4) and 100 mm/s (6). 192

Figure 6.2: Flat plate, 20° ice specimens, submergence: force vs. displacement for 1 mm/s (4), 10 mm/s (3) and 100 mm/s (4). 192

Figure 6.3: Flat plate, 20° ice specimens, snow: force vs. displacement for 1 mm/s (2) and 100 mm/s (2). 193

Figure 6.4: Flat plate, 20° ice specimens, granular ice: force vs. displacement for 1 mm/s (2), 10 mm/s (1) and 100 mm/s (2). 194

Figure 6.5: Flat plate, 30° ice specimens, dry: force vs. displacement for 1 mm/s (4), 10 mm/s (2) and 100 mm/s (5). 195

Figure 6.6: Flat plate, 30° ice specimens, submergence: force vs. displacement for 1 mm/s (6), 10 mm/s (3) and 100 mm/s (6). 195

Figure 6.7: Flat plate, 30° ice specimens, snow: force vs. displacement for 1 mm/s (2) and 100 mm/s (2). 196

Figure 6.8: Flat plate, 30° ice specimens, granular ice: force vs. displacement for 1 mm/s (2), 10 mm/s (1) and 100 mm/s (2). 197

Figure 6.9: Wedge, 30° ice specimens, dry: force vs. displacement for 1 mm/s (2) and 100 mm/s (2). 198

Figure 6.10: Wedge, 30° ice specimens, submerged: force vs. displacement for 1 mm/s (2) and 100 mm/s (2). 198

Figure 6.11: Sphere, 20° ice specimens, dry: force vs. displacement for 1 mm/s (3) and 100 mm/s (3). 200

Figure 6.12: Sphere, 20° ice specimens, submerged: force vs. displacement for 1 mm/s (2) and 100 mm/s (2). 200

Figure 6.13: Sphere, 20° ice specimens, dry: force vs. nominal area for 1 mm/s (3) and 100 mm/s (3). 204

Figure 6.14: Flat plate, 30° ice specimens, dry: force vs. nominal contact area up to 2000 mm^2 for 1 mm/s (4), 10 mm/s (2) and 100 mm/s (5). 204

Figure 6.15: Sphere, 20° ice specimen, submerged: force vs. nominal area for 1 mm/s (3) and 100 mm/s (3). 205

Figure 6.16: Flat plate, 30° ice specimens, submerged: force vs. nominal contact area up to 2000 mm^2 for 1 mm/s (4), 10 mm/s (2) and 100 mm/s (5). 205

Figure 6.17: Extrusion angle θ dependend on indenter-ice geometry combination. On the left, for the flat indentation plate and 20° (top) and 30° (bottom) ice specimen angle. On the right for the spherical indenter and a 20° ice cone. 206

Figure 6.18: Concept sketch indicating processes and components at the ice-structure interface during ice crushing. The blue areas represent three different effects of the water: hydrodynamic confinement (HDC), effect on ice debris constitution (IDC), and pressure spreading effect (PSE). The purple area is mostly affected by PSE and IDC. Green color indicates the influence on crack development and propagation (CDP).....208

Figure 6.19: Flat plate, 100 mm/s, 20° ice specimens, dry (top, D T76-04) and submerged (bottom, S T92-01), approx. 14.4 mm penetration depth. HSC footage. The

photos show the different development and extrusion of ice debris due to contact conditions. Compared to the dry condition (top), both are clearly altered by the surrounding water (bottom). Also clearance angle θ between ice specimen and indentation plate is indicated. 211

Figure 6.20: Visualization of contact area (C) and hydrodynamic confinement zone (HDC) ratios to explain the varying importance of the submergence effect depending on ice specimen penetration depth (δ). 215

Figure 6.21: Visualization of contact area (C) and hydrodynamic confinement zone (HDC) for an ice floe. The working surface of the water (submergence effect) would linearly change in an ice-structure interaction that would cause the ice floe to expand sideways. 217

Figure 6.22: Flat plate, 1 mm/s, ice specimen angles 20° (left) and 30° (right), granular ice condition: pressure distribution at peak pressure. Only small isolated high pressure zones can be recognized. Pressures are locally low but the overall load is increased, as is the contact area. 221

Figure 6.23: Flat plate, 1 mm/s, both ice specimen angles: peak pressures in (Left) the dry contact condition for 20° (top) and 30° (bottom) ice specimens. (Right) pressure patterns for 30° specimens in submergence (top) and with snow (bottom). Images consistently show large areas of local high pressures that dinminish with distance to the center contact area. 221

List of Symbols, Nomenclature and Abbreviations

A_{nom}	Nominal contact area during impact
D_{nom}	Nominal cone diameter
F_F	Frictional force
F_N	Normal force
ABS	American Bureau of Shipping
BV	Bureau Veritas
C	Contact area
CDP	Crack development and propagation
Con	Conical indenter
DNV-GL	Det Norske Veritas – Germanischer Lloyd
D	Dry
EER	Escape, evacuation and rescue
F	Flat indentation plate
FFT	Fast Fourier Transform
h	Lubricated layer thickness
HSC	High speed camera
HDC	Hydrodynamic confinement zone
HPZ	High pressure zone
HS	High speed
IDC	Ice debris constitution
LPZ	Low pressure zone
LS	Low speed
LVDT	Linear variable displacement transducer
MS	Medium speed
MTS	Material testing system
NSR	Northern Sea Route
NWP	Northwest Passage

P	Pressure
PC	Polar class
PSE	Pressure spreading effect
R	Surface roughness, coefficients of determination
S	Submerged
Sp	Spherical indenter
T	Temperature
W	Wedge shaped indenter
α	Ice specimen angle
δ	Penetration depth
θ	Angle between ice cone and indenter, extrusion angle
μ	Friction coefficient

List of Appendices

Appendix A : Projected and Tangent Contact Area Derivations 246
Appendix A1 : Wedge Shaped Indenter 247
Appendix A2 : Conical Indenter 251
Appendix A3 : Spherical Indenter 253
Appendix B : Flat Indentation Plate 256
Appendix B1 : Spectral Analysis (FFT) 257
Appendix B2 : Plots for 1 mm/s Indentation Rate 264
Appendix B3 : Plots for 10 mm/s Indentation Rate 266
Appendix B4 : Plots for 100 mm/s Indentation Rate 268
Appendix B5 : Pressure Patterns (Tactile Pressure Sensors) 270
Appendix B6 : General Observations: 10 mm/s, 20° Ice Cone Angle 297
Appendix B7 : Microstructural Observations (Thin Sections) 298
Appendix B8 : Multiple Regression Analysis 301
Appendix C : Wedge Indenter 306
Appendix C1 : Spectral Analysis (FFT) 307
Appendix C2 : Plots for 1 mm/s Indentation Rate 310
Appendix C3 : Plots for 100 mm/s Indentation Rate 311
Appendix C4 : Pressure Patterns (Tactile Pressure Sensors) 312
Appendix C5 : Microstructural Observations 321
Appendix C6 : Multiple Regression Analysis 322
Appendix D : Conical Indenter 326
Appendix D1 : Spectral Analysis (FFT) 327
Appendix D2 : Plots for 1 mm/s Indentation Rate 330
Appendix D3 : Plots for 100 mm/s Indentation Rate 331
Appendix D4 : General Observations 332
Appendix D5 : Microstructural Observations 335
Appendix D6 : Multiple Regression Analysis 338
Appendix D7 : Effect of Indentation Rate 342

Appendix E : Spherical Indenter 343
Appendix E1 : Spectral Analysis (FFT) 344
Appendix E2 : Plots for 1 mm/s Indentation Rate 346
Appendix E3 : Plots for 100 mm/s Indentation Rate 347
Appendix E4 : General Observations 348
Appendix E5 : Microstructural Observations 349
Appendix E6 : Multiple Regression Analysis 351
Appendix F : Tactile Pressure Sensors 355
Appendix G : Effect of Cone Tip Offset 362

Chapter 1 Introduction

Growing demand for natural resources requires expanding resource exploitation, even when accessibility is extremely difficult. In the Arctic, where harsh marine operating conditions prevail, there are many known reserves that have not yet been accessed. It is believed that more resources worthy of exploitation have yet to be discovered. A 2008 study by the United States Geological Survey (U.S.G.S., 2009) estimates that out of the world's undiscovered resources, 30% of the undiscovered gas and 13 % of undiscovered oil are located in the Arctic in water depths less than 500 m (Gautier et al., 2009). Other studies also speak of vast known and unknown resources of oil and gas that may be technically accessible (Houseknecht et al., 2012b).

In view of technological developments and the declining extent of sea ice, the resources are becoming more easily accessible. A general recession of sea ice, despite some annual fluctuations, is observed in several studies (NSIDC, 2014; ACIA, 2005). This also increases expectations of a progressive opening of the Northwest Passage (NWP) and the Northern Sea Route (NSR) for ship transits. In the long term, this could imply that vessels (PC6) travel through the North and possibly take the NWP by the mid-century (Smith and Stephenson, 2013). During this period, the NSR could have opened up so far as to allow open-water vessel traffic.

Recent studies by Pizzolato et al. (2014) or the Northern Sea Route Information Office (www.arctic-lio.com/nsr_transits) report a significant increase in activities in the Arctic concurrent with more frequent passages of the NSR. The rising ship traffic is not limited to commercial ships but includes passenger ships with researchers and tourists onboard.

Cruise ships travel as far as 78° North to the Norwegian archipelago Svalbard. In most cases, those ships do not meet any ice class requirement and were not designed to operate in Arctic waters. This presents a significant problem regarding strategies for escape, evacuation, and rescue (EER).

All activities in Arctic waters involve considerable risks and pose hazards for humans and equipment due to the remote location and harsh environmental conditions. With growing ship traffic and exploitation, the probability of ship-ice or ice-structure collisions, in general, increases. Moreover, with the recession of first-year ice, the mobility of multi-year ice increases, allowing it reach lower altitudes (Pizzolato et al., 2014; ACIA, 2005; Mariport Group Ltd., 2007), and ice-structure collisions become more likely.

A study by the National Research Council of Canada (Kubat and Timco, 2003) reported 125 incidents (from damage up to the sinking of the ship) in the Canadian Arctic covering a period of 25 years (starting from 1978). Seventy percent of the ship damage originated from ice collisions in the presence of, or directly with, multi-year ice. Three ships sank.

The number and severity of accidents show the need for strategies to prevent and mitigate those risks. This requires a comprehensive approach. Intense efforts have been applied in the establishment of systems to identify multi-year ice well in advance to allow ship captains time to react and avoid collisions with hazardous ice features (e.g. Johnston and Timco, 2008), but the reliable prediction of prevailing ice conditions is still a challenge (Kubat et al., 2006). Consequently, if an ice collision cannot be avoided, the structure has to be resistant enough to withstand the impact. In the design of arctic marine structures, ice forces are often the driving factor and classification societies such as Det Norske

Veritas – Germanischer Lloyd (DNV-GL), Bureau Veritas (BV) or the American Bureau of Shipping (ABS) provide guidelines for ice design loads. Those guidelines are to ensure a safe and economic design of ships and offshore structures based on the state of knowledge, preferably derived from the field. However, the available field data is limited due to the laborious and costly work required to gather field data. This makes laboratory tests indispensable. In addition to generally lower costs, laboratory tests have other advantages such as a higher number of repetitions and better controllability of boundary conditions that allows the study of specific factors. Laboratory tests are common in ice research and in the investigation of ice-structure collisions. Nevertheless, ice-related research remains a challenging undertaking. Ice material properties do not compare to any other material and show substantial randomness. Ice behavior depends on various factors such as indentation rate, temperature, grain size, crystal orientation, and salinity. This emphasizes the need for reliable procedures to generate reproducible ice specimens with consistent properties. A standardized practise mitigates apparent randomness and leads to good test repeatability thus reinforcing trust in the results.

1.1 The Problem

Icebergs still pose a significant risk of causing damage to marine structures. In 2000, Hill (2000) introduced an iceberg database with information on environmental conditions and damage severity at the time of the incidents available data. The database comprises 670 events between 1810 and 2004 involving fishing boats, passenger ships, tankers, bulk carriers, and freighters. In just above a quarter of the events recorded, the vessel sunk or had to be abandoned. Generally, sea ice was found to positively affect the persistence of

icebergs due to subdued wave action and lower water temperatures. As a result, in years of heavy sea ice that pose higher risks for ice-structure collisions in general, iceberg impacts also become more likely. The numbers of accidents and severe damage reveal the need for suitable measures to prevent risks and damage.

Figure 1.1 displays an overview of the various fields in ice related research. There are two broad categories, numerical simulations and physical experiments, and both are equally essential. Numerical simulations always require physical data input to start with and for validation of results. This makes physical experimentation the crucial element. More importantly, it still is the main basis for design requirements from classification societies (e.g. ABS, DNV-GL, BV) and in design standards (ISO 19906). Physical experiments can be divided into field and laboratory with numerous subcategories depending on the main objective (e.g. ship performance, microstructural analysis, etc.). Since field experiments are rather cost intensive and elaborate, laboratory tests play a significant role and provide a good alternative for disclosing fundamental relations. This involves, for instance, investigations of i) ice impacts, ii) ship or offshore platform performance, and iii) the ice's microstructure. Microstructural analysis aims at developing a better understanding of the processes during ice breaking or ice crushing on a microstructural level (i.e. cracks, influence on grain size, and the depth to which the ice is affected). The second category focuses on the assessment of a ship's performance while it is travelling through level ice or on the effect of floating ice hitting and piling up on an offshore platform. Ice impacts particularly deal with ice loads on ships and offshore structures that are caused by ice floes or large ice features like icebergs. In this category, substantial research has been

done on a variety of aspects, such as indentation rate and different ice geometry and/or indenter shape. The shape of the impacted surface implies different levels of confinement. Typically more confinement results in higher ice loads imposing more severe risks for any offshore structure. Considerably less information is available on the effect of different environments or contact conditions on the magnitude of ice loads. For example, the event of an iceberg-structure collision is most likely to occur underwater. Notwithstanding, most of the tests for investigating ice loads have been done in a dry environment but only a very few considered water. If water was added, generally higher ice loads were observed compared to the dry case (Varsta, 1983; Kim et al., 2011). Despite this observation, very limited research has been done that considered the effect of water or that directly compared dry, submerged, or other contact conditions to examine how this was affecting ice loads. This information is essential during the development or revision of design requirements for a safe and economic design of ships and offshore structures. The establishment of the necessary knowledgebase requires some fundamental work. This study makes a first move to elucidate basic processes and interrelations between contact conditions and other parameters that influence the magnitude of ice loads.

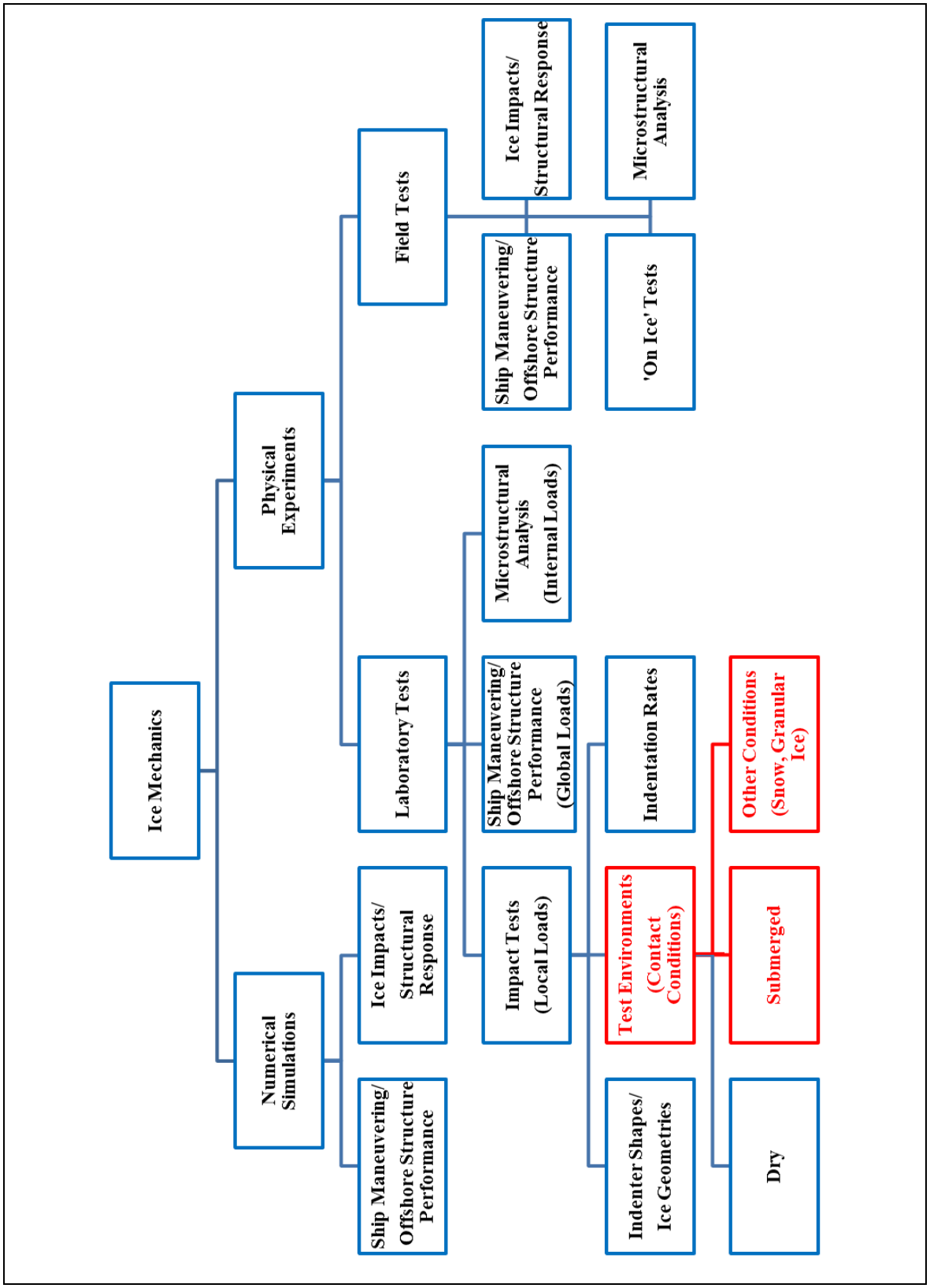

Figure 1.1: Overview of research areas on ice mechanics and ice loads for ships and offshore structures.

1.2 Objectives

The main objective of this research is to examine the circumstances in the boundary area of the contact zone that lead to different ice load magnitudes. The aim is to further elucidate processes during ice-structure interactions and contribute to the general understanding of ice loads. This is essential to assess the implications that different contact conditions have on the structure experiencing the loads and whether this aspect needs to be considered in the future design of ships and offshore structures. This is investigated by a series of laboratory tests that took place in the thermodynamics laboratory at Memorial University of Newfoundland in St. John's, Canada. The effects of factors, such as indenter shape, indentation rate and in particular of contact boundary condition on the magnitude of ice loads are investigated. Thereby the following aspects are addressed:

- How does submergence or other contact boundary conditions affect the magnitude of ice loads?
- Does the effect of submergence differ for different indentation surface geometries or at different indentation rates?
- Does water induce a confining effect, similar to confinement originating from the shape of the impacted surface?
- What may be the primary underlying physical processes in the case of submergence that would lead to different ice loads?
- Is the difference in ice loads due to different shapes, indentation rates or submergence significant enough to be mandated in present design requirements?

1.3 Scope of Work

The objective of this study is to investigate ice-structure interactions on differently shaped surfaces in dry and submerged conditions. The basis is data derived from a set of laboratory ice crushing experiments. The tests took place in a cold room at an ambient temperature of around -7°C, using a hydraulic material testing system (MTS) machine. Laboratory manufactured ice specimens of conical shape were impacted with four types of aluminum indenters: a flat plate, wedge shaped indenter (concave), conical indenter (concave) and spherical indenter (convex) (for images refer to section 3.2.5). These shapes represent geometries that can be found on ship hulls and offshore structures. The primary focus was on the relative load difference in dry and submerged conditions. Additional exploratory tests involved snow and granular ice on the indenter surface around the contact area. The main tests with the flat indenter were performed at three impact speeds (1 mm/s, 10 mm/s, 100 mm/s) to account for the variability in ice strength and ice failure due to indentation rate. Testing with other indenter shapes involved 1 mm/s and 100 mm/s impact velocities.

The results of these tests are presented in the form of force-displacement histories, average nominal process pressure-area curves, as well as by general and microstructural observations; information on local pressure pattern, contact area, and implications on the nominal process pressure are provided and discussed where applicable.

1.4 Original Contributions

Fundamental work is essential to enhance our understanding of ice-structure interactions and the arising ice loads. This is the basis for modelling ice impacts and to extrapolate ice

design loads. Other researchers (Varsta, 1983; Kim et al., 2011) have reported that the presence of water in ice-structure interactions significantly affected ice loads- a quite common circumstance in nature. All past literature on this subject matter reported higher forces when water was present compared to a dry contact surface. Although this was noticed, the phenomenon itself has not been studied in detail. The reasons for the increase are not explained. Only a few publications exist that specifically addresses the matter of submergence.

This study is a first step to elucidate the reasons for the observed effect of submergence. The objective is to quantify differences in ice loads and to offer phenomenological explanations for the observed ice loads. In additional scenarios the effect of snow and granular ice on the indented surface are investigated with the same objectives. The outcome will enhance the knowledge on ice loads and will support the endeavor to further improve and optimize ice design loads for in the Arctic operating ships and offshore platforms.

Chapter 2 Literature Review

2.1 Introduction

Ice or Arctic engineering is a relatively young field of engineering. In recent years, research efforts have been intensified to investigate the properties of ice and processes during ice and structure interactions. Generally, it can be divided into two main types of loads relevant in the design of marine structures: global and local loads. Global loads refer to the overall forces that are subjected on a structure. This concerns the general structure stability and its capability to withstand loads. Exceeding the global resistance leads to the failure of an entire structure or the system that holds it in place. On the other hand, local loads can lead to local failure such as denting or fracture of single structural members. Consequently, local loads govern the design of structural elements, e.g. ship plating or stiffener spacing. Ice features can cause severe local damage on ships and offshore structures operating in the Arctic. Generally, the design process for ice load utilizes a pressure area relationship that embodies ice strength and the apparent randomness in the ice failure.

Ice does not react uniformly. It is sensitive to external factors and the reaction strongly depends on its material constitution. This makes it challenging to quantify loads during ice-structure interactions. This is reflected in a study by Timco and Croasdale (2006). Twenty-one specialists were asked to predict ice loads for level and first-year ice on vertical structures as well as for interactions of old ice with structures. The agreement between predictions was acceptable for scenarios involving young ice, which was explained by better availability of data for this ice type. On the other hand, estimates

significantly differed when it came to the interaction of multi-year ice features with structures. The study clearly showed the demand for a more data to enhance the assessment of ice loads especially due to multi-year ice.

2.2 Ice Properties and Ice Mechanics

2.2.1 Ice Types - Sea Ice and Glacial Ice

In general, ice relevant for interactions with marine structures can be differentiated between two categories, sea ice and glacial ice. Glacial ice is formed on land by compression and sintering of snow over thousands of years and is free of salt inclusions. When parts of a glacier break away into the ocean, icebergs or ice islands are formed. Drifting with ocean currents icebergs pose major risks for any type of marine structure. Sea ice, on the other hand, develops in the ocean. Its growth is initiated by impurities or single ice crystals with further accumulation of ice particles. In favorable circumstances, at low water and air temperatures, low wind speeds and limited wave action, ice crystals build up to a continuous sheet of level ice. In the first season, when the ice is just developed, it is referred to as first-year ice. If the ice survives one summer's melt it becomes second-year ice and multi-year ice, when it endured more than two summers. The latter is also summarized in the term "old ice". Over the seasons impurities such as brine pockets, air bubbles and other particles are ejected due to physical processes. Due to the latter physical processes and the larger thicknesses of multi-year ice, it is considerably stronger compared to first-year ice. It is often comparable to glacial ice in strength and other properties. Mechanical processes, such as ridging and rafting can lead to ice pile up and can create large ice features such as ice ridges with built up ice strength. More

detailed explanations of underlying processes, different stages in ice growth, and ice formations due to mechanical alterations (e.g. ice ridges, ice rafting, ice rubbles) can be found in various literature (e.g. Michel, 1978; Sanderson, 1988; Palmer and Croasdale, 2013). A comprehensive summary of the current state of knowledge concerning sea ice properties is also given in Timco and Weeks (2010). Although the data refers mainly to the Canadian Arctic, it is a well-established source of information on general ice growth, associated influences and on the current engineering practices to determine ice properties.

2.2.2 Ice Strength Dependencies - Strain Rate and Temperature

Measured ice strength depends on a variety of parameters such as indentation rate, temperature during the impact, and several other factors. The influence of impact speed on ice failure behavior was investigated by Yen et al. (1970). Spheres were dropped on ice and cracks were found to occur more likely at higher impact velocities, where the ice failed in a brittle mode. At lower impact speeds, the ice had time to elastically and elasto-plastically deform; its response was ductile and it did not fracture.

Most studies show increasing ice strength for increasing strain rates between 10^{-8} s^{-1} up to about 10^{-4} s^{-1}. In that range, ice is commonly observed to creep and fail in a ductile manner. This is followed by a transition zone, where the ice fails in a mixed mode of ductile and brittle behavior. From strain rates of around 10^{-2} s^{-1} and above, ice failure is generally brittle and eventually becomes strain rate independent. This relationship is displayed in Figure 2.1 that is a compilation of different data sources for uniaxial strength and indentation strength vs. strain rate on a logarithmic scale.

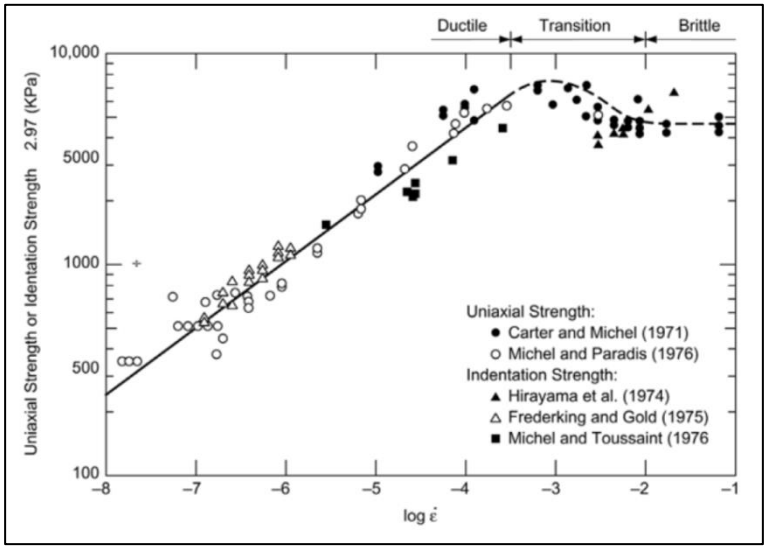

Figure 2.1: Influence of strain rate on uniaxial compressive ice strength (Source: U. S. Army Corps of Engineers, 2006).

Jones (1997) focused on ice strength at indentation rates close to what was expected for ice impacting a propeller. The uniaxial compression tests were done for indentation rates of up to 10^1 s^{-1} with freshwater and saline ice at -11°C temperature. The results showed a trend of a peak stress at 10^{-2} s^{-1} rate and constant or increasing ice strength at higher strain rates. Similar result was found by Shazly et al. (2009) for ice cylinders composed of single crystals and polycrystalline ice. The lowest strain rate was about 90 mm/s, which is high compared to most other studies. And yet, increasing the rate from 90 mm/s up to a rate of 1250 mm/s revealed a rising trend in ice strength. Higher ice strength was also observed at a lower temperature of -30°C compared to -10°C, but boundary conditions were not found to have an effect at high rates.

Another study by Jones et al. (2003) on iceberg ice, reports ice strength of around 10 MPa at a temperature of about -10°C and a strain rate of 10^1 s^{-1}. Ralph et al. (2008) established temperature profiles from icebergs on the Grand Banks of Newfoundland in 2001. The

profiles covered temperatures from -15.4°C at 60 cm depth inside to 0°C on the surface, where the ice was exposed to air and water. Jones (2007) compared that data to other studies. Measurements of icebergs from different regions showed temperatures in a similar range with 0°C on the berg's surface down to -20°C in depths up to 12 m towards the ice core. Uniaxial compressive ice strength was determined to be approximately 5 MPa at 0°C on the ice surface, and to 8.5 MPa at -20°C in depths of 10-20 m into the core. It once more revealed the significant influence of temperature on ice strength. Furthermore, the compiled data exhibited an overall tendency of rising compressive strength from strain rates between 10^{-8} s^{-1} up to around 10^{-3} s^{-1} (Figure 2.2). At this point, the highest strength measured was just above 10 MPa. Above this pressure, the compressive strength slightly decreased until about a strain rate of 10^{-1} s^{-1} and began to ascend again.

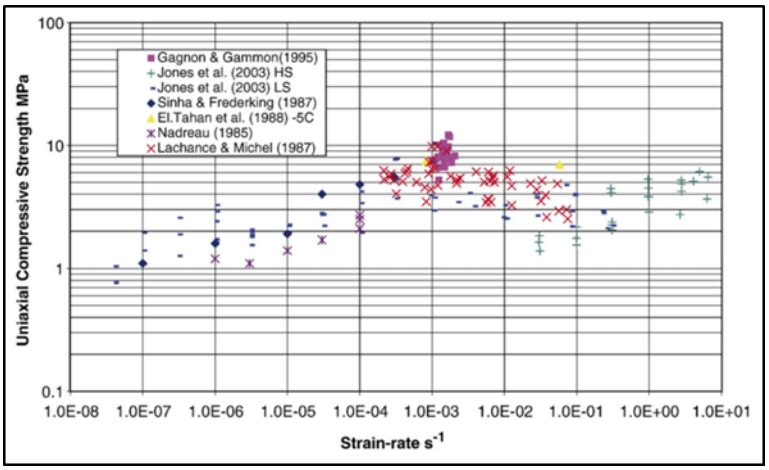

Figure 2.2: Uniaxial compressive strength for iceberg ice at -10°C (Source: Jones, 2007).

Obviously, ice reacts differently depending on indentation rate and temperature. The focus of many studies has been to more precisely describe underlying processes and to create an understanding of what causes these variations. In this respect, the mechanisms leading to ice failure and the associated effects on the ice microstructure are closely investigated.

2.2.3 Local Ice Failure Mechanisms

The chaotic behavior of ice (or any other material) failure presents a major problem. During a crushing event, various processes occur on macro- and microstructural scales. The sketch by Jordaan (2001) in Figure 2.3 shows the main components. While the ice fails against the structure, cracks develop and the ice is broken up into smaller pieces. As the event proceeds, comminution and pulverization continue and ice debris and rubble are extruded. The contact area is comprised of zones of high pressure (HPZs), where most of the force is transmitted, and are surrounded by low pressure zones (LPZs). High impact speeds are characterized by multiple HPZs that quickly shift throughout the event.

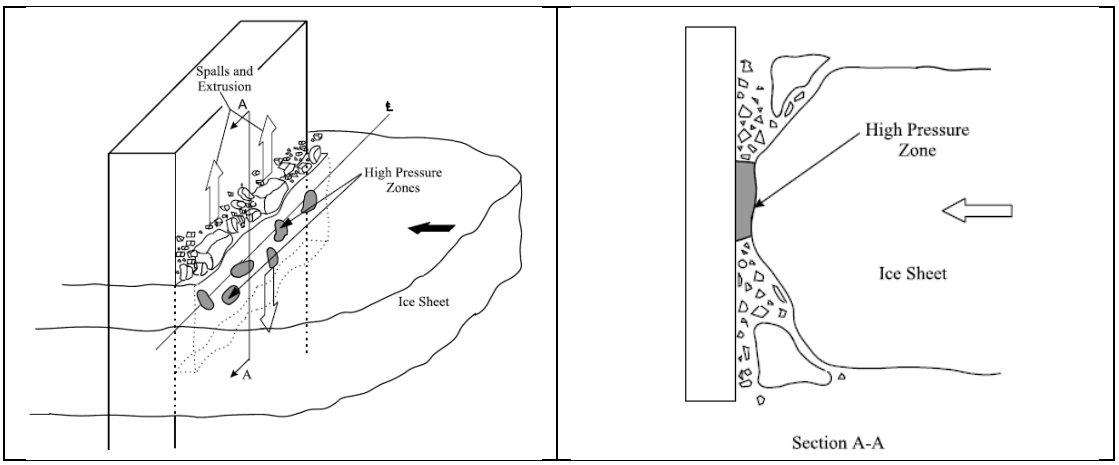

Figure 2.3: Local processes during ice failing against a vertical structure (Source: Jordaan, 2001).

Numerous analytical and numerical approaches exist to describe the ice failure mechanism. Daley's (1991, 1992) method provided for an ice edge failing against a rigid indenter, with cracks forming at the ice edge (central contact region) and advancing to the open surface. A failure criterion served to define the crack formation. The accumulation of cracks evoked successive levels of spalling from the parent ice separating ice flakes that were termed as the actual failure events. The main contact area would thereby shift within the centre region and the overall pressure would decrease with increasing area. The model was based on several simplifying assumptions, e.g. ice extrusion and pulverization, as well as crack curvature from the contact surface to the ice edge were neglected.

Kujala (1994) further developed Daley's approach by introducing cracks with curvature to account for radial stresses in impacted ice wedges. He also noticed that it required less force to initiate curved flakes, and this was more pronounced for larger ice wedge angles.

This model was further extended to any type of ice failure not just flaking events (Daley et al., 1998). Different discrete processes during ice-structure interactions were recognized, such as micro- and macro-crack formation, extrusion of flakes and comminution. These processes were not sequential but followed a hierarchy of events. The most likely occurring failure mechanism depended on ice properties, boundary conditions, and previous ice failure.

2.2.4 Ice Extrusion

Ice extrusion and its implications has been the subject of numerous studies. For example, in medium-scale indentation tests at Pond Inlet and Hobson's Choice, Kennedy et al. (1994) found that ice extrusion was an ice failure governing process. A common

laboratory approach is to study ice extrusion from a point of view, where the ice is already crushed and to focus on its flow and the pressures that it causes.

In a study by Tuhkuri and Riska (1990), crushed ice was filled between two plates consisting of steel and ice. By moving the plates towards each other (1 and 10 mm/s), the crushed ice was forced to extrude sideways. The outcome distinctly varied for similar test scenarios, but a rough ice surface in combination with the low rate seemed to impede ice extrusion and to lead to pressure build up earlier than in other cases. The second part of the study comprised crushing tests with wedge shaped ice samples. Those were observed to involve two processes, ice crushing and ice extrusion; which for the latter part seemed to be similar to the ice extrusion tests. Furthermore, for the crushing wedges the average pressure was noted to have been constant.

Another experimental study by Spencer et al. (1992) aimed to separate the effects of ice extrusion, compaction and flow. A similar setup was used as the one described above. In the center of the platens, where the crushed ice material was the most confined and pressures were the highest, the formation of a cohesive material was observed. That phase change, also referred to as ice fusion, was also reported by Singh et al. (1995). They noticed ice being stuck to the plate over an area that increased with increasing loads. Furthermore, ice deformation was seen without ice being extruded, and generally higher loads were obtained for lower test velocities.

Most studies found that the extruded ice behaves differently dependent on the applied pressure. It was suggested (e.g. Singh and Jordaan, 1996) that its properties would be best described by a Mohr-Coloumb criterion at low pressures, but the material was similar to a

viscous fluid at higher pressures. Also Daley et al. (1996) discussed the importance of ice extrusion on ice loads. The presence of snow or ice debris, respectively, would change the pressure distribution (compared to the situation without ice debris). The pulverized ice carries a considerable part of the load and impedes subsequent crack formation, due to confining effects.

Despite common studies on ice extrusion, less information is available on how the presence of an existing snow or granular ice (crushed ice) layer would affect ice loads during an ice-structure collision; a likely circumstance in nature.

2.2.5 Ice Friction

Ice friction also plays a role in the transmission of ice forces to a structure. It is of special concern for icebreakers and of importance in ice clearing processes, also for other ice going ships. For example, much of the energy of an ice breaking ship is needed to overcome the frictional resistance between ship hull and ice, in order to get moving and induce crushing or flexural failure. Ice friction can act between ice and a structure, but also internally between ice grains. The simplest case is dry friction as it is expressed in Eq. (2.1).

$$F_F = \mu F_N \tag{2.1}$$

where F_F is the frictional force, F_N is the normal force and μ is the coefficient of friction. This is probably not the case in ice-structure contact, where water might be present due to various reasons either environmental (marine water) or originating from ice mechanics (pressure melting). Kietzig et al. (2010) explain the basic principles influencing ice friction for the contact between ice and sliders. Besides dry friction, three other types of

friction are considered: boundary friction, hydrodynamic, and mixed friction. Either type is most likely to occur for different ratios between melting temperature T_m and temperature in the contact zone T, as well as for a certain ratio between surface roughness R and the thickness h of a lubricated layer. The theory of boundary friction implies a lubricating layer that is significantly smaller than the surface roughness ($h \ll R$), while $T < T_m$. In that case, the friction coefficient is less compared to the dry case. With rising temperature, the thickness of the lubricating layer increases causing adhesive effects due to capillary bonding between the ice and the other surface. This circumstance is considered to increase the frictional resistance due to emerging drag effects. This occurs when $T > T_m$ but the lubricated layer is still smaller than the surface asperities. Hydrodynamic friction is defined to be prevalent when $T > T_m$ and $h > R$. The thickness of the lubricating layer is larger than the surface roughness and carries the entire load preventing actual contact between slider and ice. Figure 2.4 from Kietzig et al. (2010) shows the dependence of the friction coefficient on temperature (left) and velocity (right). Although summarized data in these plots was derived for different boundary conditions (normal force, temperature, contact area, velocity), it displays similar trends. The friction coefficient is lowest between -2°C and -7°C, and increases with lower and higher temperatures. Figure 2.4 right shows the velocity dependency for the hydrodynamic friction regime, where drag forces dominate over other friction mitigating effects.

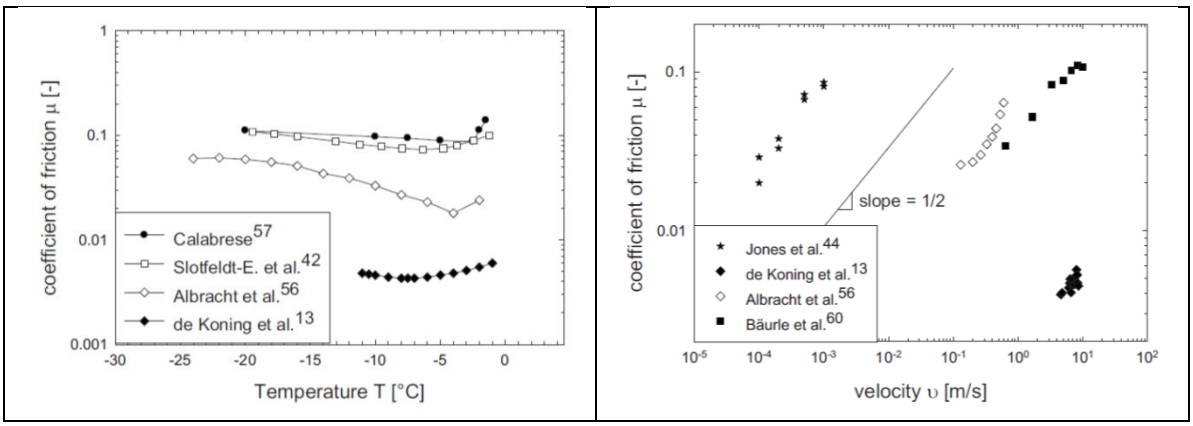

Figure 2.4: Friction coefficient dependence on temperature (left) and on velocity with increased drag caused by melt water (right). (Source: Kietzig et al., 2010).

Cole (2001) thoroughly examined effects, such as temperature and grain size on internal ice friction. The conditions at the grain boundaries were identified to play an important role especially in view of polycrystalline ice such as iceberg ice. However, Figure 2.5 reveals that the internal friction peaks in a certain temperature range which is fairly independent of ice type but it decreases at lower temperatures; contrary to the surface friction (Figure 2.4, left).

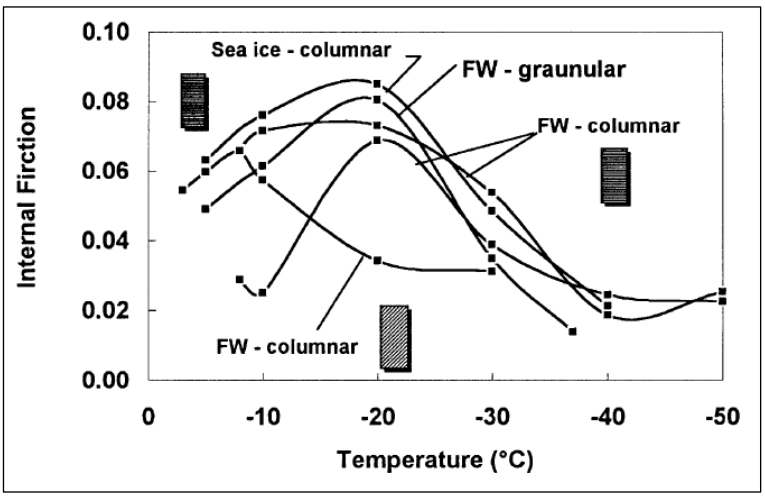

Figure 2.5: Internal ice friction dependent on the temperature (Source: Cole, 2001).

This agrees with what was found in a laboratory ice on ice experiments by Schulson and Fortt (2012). For polycrystalline ice with 1 to 8 mm grains, the kinetic friction coefficient did not depend on the grain size or type. For warm ice (close to -10°C), an increase in frictional resistance was noticed for increasing velocity below approximately 0.01 mm/s. Above this velocity, a decrease in friction with increasing velocity was reported. Surface roughness had a slight effect on the friction coefficient.

In general, a different surface condition will likely affect the external friction. This was proven in field tests by Pritchard et al. (2012). Ice blocks of different mass were pulled over sea ice. A layer of snow led to increased frictional resistance especially for lighter ice blocks.

2.2.6 Ice Failure and Microstructural Analysis

Microstructural analysis is used to gain insight into the change in the ice crystal structure due to a crushing event. The microstructure reflects the ice's response when it is impacted and helps to comprehend the ice internal processes. This information allows the improvement of numerical simulations of ice-structure interactions and ice load determinations.

Stone et al. (1997) identified two major mechanisms governing brittle ice failure, micro crack formation and shear-damage processes. Deformation behavior, crack formation, and changes in the ice microstructure were compared in uniaxial and triaxial tests for initially undamaged and damaged ice. In triaxial tests, the ambient pressure mostly prevented crack formation. This was observed in the ice microstructure showing alternations that were ascribed to recrystallization and void formation. The latter phenomenon appeared to

be more distinct at higher indentation rate with higher axial strains. Overall, higher strain rates were achieved in triaxial than in uniaxial tests. Strains were also higher for previously triaxially damaged ice, compared to initially intact or uniaxially damaged ice. The results suggested that the confinement applied through the overall pressure closed small cracks and impeded new crack formation. In uniaxial conditions with unimpeded crack development, damage was mainly caused by micro cracks. Triaxial tests by Melanson et al. (1999) and Meglis et al. (1999) led to similar conclusions. The findings indicated recrystallization as the dominating process at low strain rates, while micro-cracking was prevailing at higher strain rates.

Muggeridge and Jordaan (1999) analysed data from a series of iceberg impacts tests on the Labrador coast in 1995. Thin sections taken from an iceberg (approximately 500 t) in close vicinity to the centre of the impact, showed the microstructure had substantially changed and consisted of mostly small grains that encompassed some larger grains. In a region of approximately 80 mm depth from the impacted surface towards the iceberg's core, the ice was relatively intact (large grains). The margin between the upper layer, where most of the microstructural change occurred, and the lower layer, where the ice was mostly intact, was not as distinct as at some distance to the centre of the impact. Further away the fine sized grain layer was thinner, but a clearly visible line of very fine grained ice separated both layers. Muggeridge and Jordaan (1999) explained this by means of confining pressures. In proximity to the impacted zone a higher confining pressure exists due to the surrounding ice that prevents ice extrusion and stimulates recrystallization. At this point there is one large high pressure zone, where most of the

load is transmitted. At some distance to the centre, ice fracture prevails; ice pulverization due to mechanical processes is more likely and ice debris is more easily extruded to the free surface (low confining pressure). This agrees with earlier studies that report high pressure zones surrounded by areas of lower pressure and that there are associated differences in the grain structure. The results correlated with observations of changes in microstructure in laboratory tests under different confining pressures, where recrystallization was ascribed to be the prevalent process (Melanson et al., 1999; Meglis et al., 1999; Stone et al., 1997).

Jordaan (2001) offers a comprehensive discussion of the processes during ice impacts and offers a probabilistic approach to estimate design ice loads. The apparent randomness in ice loads was found to be more distinct at higher indentation rates as a result of higher stress concentrations that cause mainly spalling events. Most of the forces were transmitted in local high pressure zones (HPZs), comparable to triaxial stress states. The significant shear in HPZs causes the ice microstructure to substantially change, leading to the characteristic smaller grain sizes. The comparatively soft ice originating from microcracking, dynamic recrystallization, and pressure melting, is overall termed “damaged ice”. Zones of high pressure quickly shift and are surrounded by low pressure zones (LPZs). Fracture is considered to be the dominating process in LPZs that are usually closer to a free surface. The lower confining pressures in these regions facilitate crushed and pulverized ice extrusion. Jordaan (2001) found that the theory of HPZs was scale independent, an important conclusion in terms of the transferability of findings of small-scale laboratory experiments to ice load predictions at full scale.

Browne et al. (2013) did a study focusing on high pressure zones in the context of confined cylindrical ice specimen, where ice fracture was impeded. Two differently sized spheres were used in a compliant and rigid test setup. It was found that for one indentation rate, a testing temperature of -5°C led to a damaged layer with significant recrystallization, whereas microfracture prevailed at -15°C.

Parsons (1993) assessed the damage to columnar freshwater ice when impacted with a four sided pyramidal indenter at -15°C. Loads ranging from 88 N to 1189 N were slowly applied to prevent dynamic effects. Microcracking was found to dominate in the direct contact region. Furthermore, radial cracks and overall crack lengths were observed that were between two times the grain size (1 mm) up to more than 10 times the length with higher loads.

A comprehensive analysis of ice failure processes was also done by Schulson (2001). He explored the brittle failure of columnar and granular ice under biaxial and triaxial states of stress and for different prevailing loading directions. His work was based on experimental data as well as on data from Arctic sea ice and other geomaterials (e.g. rocks). The examination of the different data sources suggested similarities of failure mechanisms of ice and of other brittle or semi-brittle materials. It was concluded that the mechanisms involved may be scale independent; similar to what was stated by Jordaan (2001).

2.3 Experimental Data

2.3.1 Tests Using Different Indenter Shapes – Confinement Aspects

2.3.1.1 Field Tests

The influence of different indenter shapes has been focus of various tests. Frederking et al. (1990) describe the results of indentation tests with a flat circular indenter (0.8 m^2), a rectangular indenter (0.375 m^2), and a spherical indenter (0.8 m^2) on Hobsons's Choice Ice Island. For the tests, a long channel was dug into the multi-year sea ice. Indentation rates ranged from 0.3 to 100 mm/s and creep deformation, ice crushing, as well a mixture of both was observed. In spite of different compliant test setups and shapes of the flat indenters, both contact areas were rectangular; the contact area of the spherical indenter was circular. The pressure distribution was found to be non-uniform and pressures in the centre of the contact area were three times the average pressure.

Other field experiments at Hobson's Choice involved flexible and rigid indenters, flat and wedge shaped, of different sizes, and with varying ice geometries (Masterson et al., 1993). Flat indenters were crushed against wedge or pyramidal shaped ice, wedge shaped indenters against flat ice surfaces, both at indentation rates of 100 mm/s and 400 mm/s. Overall, tests with flat rigid indenter had pressures building up with increasing penetration depths, slightly above those when indenter and ice geometries were reversed. For the latter combination the trend of the pressure-area curve was opposite and overall decreased with increasing contact area.

Kennedy et al. (1994) published data derived from medium-scale tests with half hemispheres of different diameters and radii of curvature. All force histories displayed

oscillations in a sawtooth-like pattern, varying with indentation rate. Also Pond Inlet data (Baffin Island in 1984) showed high oscillation frequencies at fast indentation rates (starting at 100 mm/s) that were generally lower at slower impact velocities. Structural response (vibration) was observed at 25 Hz for a sphere with 3.0 m^2, but at 50 Hz for the half hemisphere with 1.0 m^2, although in some tests it was at 25 Hz and 32 Hz respectively. Data derived from comparable tests at lower indentation rate (about 19 mm/s) on Hobson's Choice Ice Island in 1989 also revealed the sawtooth pattern, which was slightly less pronounced.

2.3.1.2 Laboratory Tests

Based on small indentation tests (spheres with diameters of less than 10 cm), Jordaan et al. (1988) presented an approach to describe failure of a flat ice block against a rigid spherical indenter in terms of a set of analytical equations. Ice pulverization was observed to be associated with a loss of shear stiffness. In accordance with field indentation tests, an oscillating "sawtooth" like force pattern at high indentation rates was noticed. This was explained by suddenly occurring spalling events that were followed by the removal of the ice debris and subsequent building up of forces. A viscous material model was proposed, consisting of a layer of crushed ice with a presumed constant thickness. Frictional forces on the indenter surface were ignored. With assumed values for ice viscosity and crushed ice layer thickness, reasonable agreement between calculated loads and experimental measurements was achieved.

In a laboratory study, Tukhuri (1995) investigated the influence of different angles (90°, 120°, 180°) of small wedge shaped (elongated) ice blocks, made out of freshwater. A

strong correlation between the first recorded peak load and wedge angle was reported. Also ice extrusion was noticeably impeded for cases with less clearance between ice and indenter. In those cases, the formed ice flakes contributed to further ice damage by increasing the confinement, leading the tests to be comparable to experiments with initial larger surface areas.

Other small-scale laboratory tests with spherical indenters were done by Wells et al. (2011). A 20 mm diameter spherical indenter was used to impact unconfined ice blocks. The observed ice failure and pressure distributions were very similar to those found in medium and full-scale trials. Ice failure at low indentation rate tests (0.2 mm/s) was ductile and characterized by ice recrystallization leading to permanent deformation. A combination of ductile failure and isolated ice crushing was observed at the medium rate (2-5 mm/s) associated with loads drops, falling pressures, and minor variations in contact area. Brittle failure and fracture were prevalent at high indentation rates (8-10 mm/s) and resulted in the formation of local ice spalls and in ice crushing. Fracture was observed to depend on existing ice flaws and would therefore be a scale dependent process.

Kim et al. (2012) performed spherical indentation tests with ice blocks that were unconfined and with blocks that were laterally confined by aluminum plates. The varied parameters were indenter diameter (5.0 mm and 12.7 mm), grain size (< 6 mm) of the indented ice block, test speed (0.05 mm/s, 0.51 mm/s, 2.8 mm/s, 5.08 mm/s), and testing temperature (-10°C and -40°C). The ice failure regime, dependent on indentation rate, was found to be similar to that reported by Wells et al. (2011). For lateral confined ice blocks, Kim et al. (2012) observed less ice splitting and higher forces. The larger indenter

led to higher vertical forces but the indenter size did not significantly affect the average pressure.

Kim (2014) studied the effect of differently shaped indenters in laboratory experiments at 1 mm/s and 100 mm/s indentation rates. Specimens were ice cylinders and cones with different angles. A wedge shaped indenter with a large angle experienced lower loads than a flat plate or a smaller wedge angle (which were very similar). On the other hand, for a conical shaped indenter, forces were found to be significantly higher (on average 2.68 times) than those of the flat plate.

All the laboratory studies cited above refer to results obtained in dry testing environments. Very little information on the influence of geometry is available if the contact condition was other than dry (i.e. wet or submerged). In some studies, it was noticed that water led to increased ice loads and pressures.

2.3.2 Tests in Dry Divergent Ambient Conditions

Studies on impacts with ice sheets naturally involve water. In many cases, those tests are done with pressure panel instrumented ships to assess the pressures the ship hull experiences when impacted by ice. For instance, Masterson and Frederking (1993) examined local pressures and forces on icebreakers that rammed ice floes. The average pressure trend decreased with overall increasing area, independent of speed within the tested range (0.26 – 2.1 m/s). Although geometries and ice types were different, the data was in good agreement with results from dry indentation tests at Pond Inlet (iceberg ice, spherical indenters).

In 2001, the Canadian Coast Guard Ship Terry Fox was equipped with strain gauges and 178 ice impacts with bergy bits (up to 20,000 t) were accomplished. The results were published in Ritch et al. (2008) showing a trend of decreasing average pressure with increasing area. When high loads occurred, it was observed that a substantial part of the load was transferred through the adjacent area that would consist of crushed ice. A theoretical link was established between load magnitude and the contact area that it is transferred over. That area grows with the increasing amount of crushed ice; successively further impeding ice extrusion (in a way a self-reinforcing process). Load magnitude and activated area were also found to closely correlate with maximum pressure.

While it is a given fact in such field test programs for ice-structure interactions to occur underwater, or at least partially underwater, ice strength information is most often derived from laboratory dry tests.

Elsewhere there is very limited literature available that directly compares ice loads in wet and dry environments, although many reports and papers cover ice failure processes and associated loads during ice-structure interactions. Earlier field and laboratory experiments done by Varsta (1983) focused on ice loads on ship hulls. He proposed that average ice pressures on ice edges were transmitted by two layers. One was a viscous layer of water and crushed ice, and another one of uncrushed ice. As part of this study dry and wet crushing tests were performed. These involved ice blocks that were indented with rough and smooth plates at 45° angle at a maximum indentation rate of 130 mm/s. The ice was naturally grown in the Baltic and cut into shape. For wet tests the ice blocks were sprayed with water to create a liquid layer. Despite this being far from submergence, the peak

pressures in wet tests were clearly above those of the dry tests. Meanwhile, the average pressures for both conditions followed a similar decreasing trend with increasing penetration.

A more recent study was done by Kim et al. (2011). A small series of 17 experiments was conducted in dry, wetted, and submerged conditions, at two indentation rates (10 mm/s, 100 mm/s), and air temperatures (-5°C, -10°C). The water temperature was 0°C. The ice was artificially made and the conical specimens were 10 cm in diameter with an overall height of 22 mm at the 22° angle. The crushing depths ranged between 12 mm and 20 mm using a flat indenter. Although these tests were limited in scope, generally higher loads were found for the wetted and submerged cases, and impact speed and temperature were of major importance. The lower temperature resulted in higher loads in the dry environment, but in particular at the lower indentation rate (10 mm/s).

Preliminary test results to the present study were published in Sopper et al. (2015a). The effect of submergence on ice crushing loads was examined in thirty three small scale indentation tests in dry and submerged conditions. In accordance with other studies (Varsta, 1983; Kim et al., 2011), generally higher forces were obtained in submerged tests. Furthermore, the difference between the dry and submerged conditions was more pronounced at the high indentation rate. In contrast Kim et al. (2011) reported the effect of the indentation rate was similar for both conditions; generally higher loads were observed at the low indentation rate independent from the environmental condition.

2.4 Pressure-Area Relationships

Pressure-area relationships are a common method to determine design ice loads in maritime structure design. Varsta (1983) conducted a study on the penetration of large ice blocks (Baltic Sea ice). His results showed decreasing pressure with advancing penetration. The most cited and debated pressure-area relationship was developed by Sanderson (1988). He analyzed data from various field and laboratory tests involving different types of ice (freshwater ice, first-year and multi-year ice) at different scales. Sanderson found that the average pressure decreased with increasing contact area (Figure 2.6). This relation can be expresses according to Eq. (2.2).

$$P = C \cdot A^{-ex} \tag{2.2}$$

Where P is the pressure in MPa, C is the pressure referring to one unit area (1 m^2), A is the contact area, and with the negative exponent ex ranging between 0.1 and 1.0.

Sanderson's curve neglected some important aspects that were addressed by Timco and Sudom (2013). They proposed that the ice-strength (ice type, ice temperature, ice salinity, and ice density), ice failure mode, aspect ratio of ice-structure interaction, and indentation rate influence the pressure-area curve and therefore need to be considered. Furthermore, Sanderson did not consider the presence and magnitude of local high pressure zones, an important consideration since local pressure peaks can lead to local structure failure, while the average pressure would not impose any risk for the stability of the global structure.

Generally in the literature, it is distinguished between two pressure-area relations: spatial-pressure area and process-pressure area. Both will be further explained in the following section.

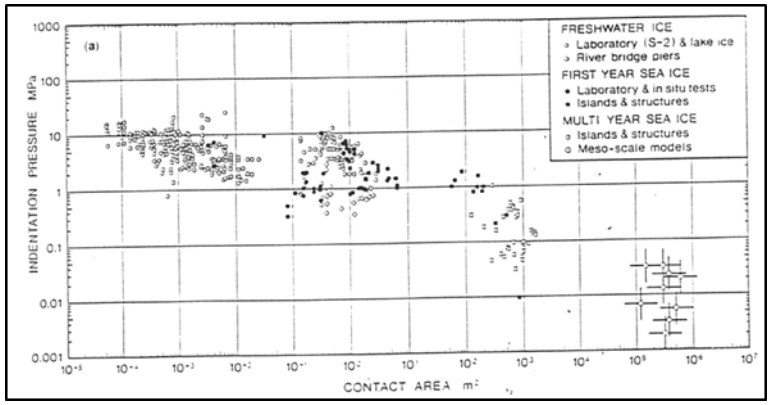

Figure 2.6: Pressure-Area data compiled by Sanderson (1988) showing a decreasing pressure trend with increasing area.

2.4.1 Spatial Pressure Distribution

The spatial pressure distribution describes pressure variation in space at one instant in time; thereby several peak pressures within an area can exist. With this relation, the pressure for a given percentage of the nominal contact area can be determined and used to dimension the local structure.

2.4.2 Nominal Process Pressure-Area Curve

The nominal process-pressure refers to the time varying average pressure over a nominal contact area as a crushing event proceeds, and as force and contact area change. The nominal contact area is the theoretical intersection of ice feature and indenter. It does not account for the area loss due to spalling or the spatial pressure distribution, or area gain due to other effects. In the literature, it is most commonly referred to the nominal process pressure to characterize the time varying load that is experienced by the structure during a

crushing event. The basis of today's ice design loads often is a pressure vs. area curve where also the nominal area changes in time.

The process pressure is the focus of many studies. Frederking (1998) summarized data from various field indentation tests in nominal process pressure area plots. Data from the M.V. Arctic, ramming thick multi-year ice flows, and data from hydraulic indentation tests at Pond Inlet, both showed decreasing average pressures with increasing area. On the other hand, results from hydraulic indentation tests at Hobson's Choice and from Louis St. Laurent did not follow that trend. In contrast, the average pressure of the Louis St. Laurent first rose to a maximum before decreasing later on.

The latter is in support of the point that was made by Daley (2004, 2007). Based on a detailed examination of spatial and process pressure area-relationships, Daley maintained that there was hardly any premise for the process pressure to decrease. The available data that would lead to such conclusion was usually not collected through independent measurements of pressure, but based on nominal contact area and nominal force. At the same time a decreasing process pressure would not preclude rising pressures within the spatial pressure distribution.

Masterson et al. (2007) emphasized the relevance of a more precise examination of actual measured data and current design loads. Based on Molipaq data, it was shown that present design equations over predicted loads on small areas of approximately 1 m^2 by more than a third, while loads for contact areas of about 10 m^2 were underestimated by 33 %. The evaluation of a several field data sources (Molipaq, Pond Inlet, Gulf flat jack, Hobson's Choice 1989) revealed a decrease in average pressure with increasing contact area, but

that was based on a purely empirical pressure-area relationship. Masterson et al. (2007) also pointed out that ice loads substantially varied dependent on the Arctic region.

Palmer et al. (2009) addressed the circumstance of the area over which a force is measured not necessarily being equivalent to the area that “controls” the force; that can be considerably smaller.

These studies and opinions on the progress of the process pressure or pressures, in general, display today’s challenge in determining realistic ice loads. Daley (2004, 2007), Masterson et al. (2007), Palmer et al. (2009), as well as many other studies, reveal a lack of available information and the effect that extrapolation or different assumptions can have. The lack of consensus emphasizes the importance of clearly identifying the area that the loads are related to, and that substantially influences the development of the pressure that a structure must reliably withstand. It also indicates that the design of an optimized maritime structure requires a more specific approach, where also other factors such as the area of operation (Masterson et al., 2007) and several other aspects (see Timco and Sudom, 2013) need to be taken into account.

2.5 Pressure Sensing Technologies

Understanding ice pressures can be augmented by technologies that allow insight into actual pressure and contact area during an ice impact. The following sections provide examples of three pressure sensing technologies that are available and have been used in research on ice-structure interactions.

2.5.1 Chemical Pressure Measurement Film

Chemical pressure measurement films are used for a variety of industry applications such in the determination of the contact between two metal or steel parts of engines. In studies by Ulan-Kvitberg (2012), Kim et al. (2012), Kim and Daley (2013) and Kim (2014) Fujifilm Prescale® was used to visualize ice pressures and contact area. Several film options are available covering different pressure ranges. Figure 2.7 shows examples of pressure distributions for different pressure film resolution sensitivities.

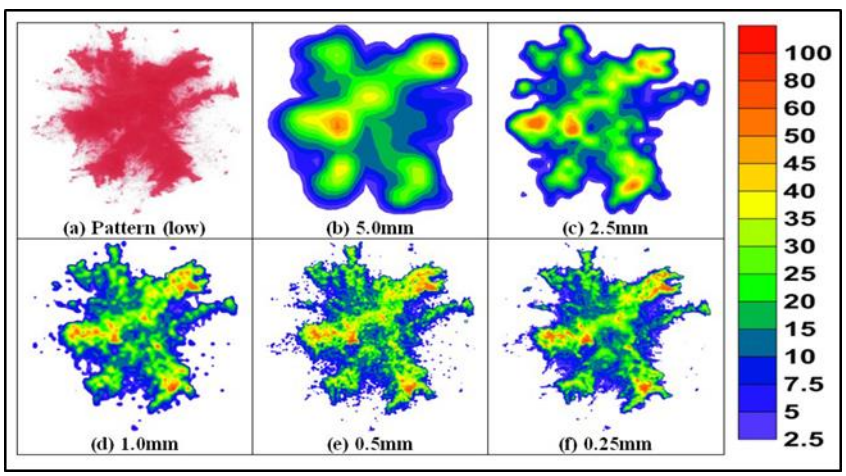

Figure 2.7: Pressure distribution using Chemical Pressure Measurement Film with different resolutions (Source: Kim, 2014).

An advantage of the pressure measurement films is that size and shape can be easily adapted. A disadvantage of this technology is that the result only displays the spatial pressure distribution at one instant in time, but it does not provide information on the process pressure.

2.5.2 Tekscan I-Scan® Sensors

Tactile pressure sensors have been used in numerous laboratory tests for investigating local ice pressures. In small scale laboratory tests by Wells et al. (2010) and Browne et al. (2013) the sensors were placed directly on the ice specimen surface and impacted with spherical indenters. The development of high and low pressure zones could be observed, and the data was generally in good agreement with recordings from the material testing system (MTS). Ice spalling events, evident in the form of load drops in the MTS data were well reflected by sudden area losses captured by the sensors. Figure 2.8 shows the pressure distributions of two tests, where a sphere impacted ice blocks at 2 mm/s indentation rate. Both pressure patterns show zones of higher pressure (indicated by light colors) surrounded by lower pressure (blue colors).

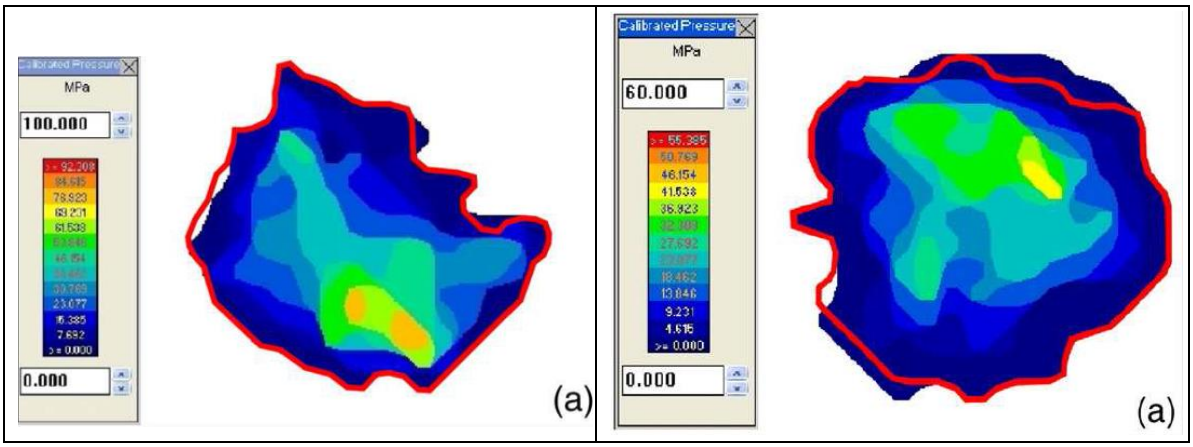

Figure 2.8: Examples of pressure distributions using Tekscan I-Scan® (Source: Wells et al., 2010).

In another type of experiment, ship models were instrumented with tactile pressure sensors to measure loads exerted by ice sheets (Izumiyama et al., 2007). The comparison of data from the model tests with full-scale observations for a ship bow showed that at both scales the force was transmitted by un-continuous line loads ("broken-line-like loads"). Force-time histories of the pressure sensors had load peaks, intermittent with periods of very low loads that agreed with full-scale measurements for a ship frame. A similar study was done by Kujala and Arughadhoss (2012), where line loads on differently shaped model ship hulls were examined. Also in that case, the laboratory data was found to correlate well with field data.

Tactile pressure sensors are used in numerous application fields and various issues are associated with their application. Sumiya et al. (1998) tested the sensitivity and dynamic response time of F-Scan sensors for the by a foot applied pressure of a walking person. In the tests, the sensors were covered with felt of different thicknesses. The consequence was a significantly decreased sensitivity and a slow reaction time (0.32 s). It was also noted that there may have been an effect of the change in temperature when a person walked. The Tekscan sensor model was different from previously mentioned ice studies (I-Scan), but the basic sensor principles (constitution and functioning) are the same. Thus the conclusions are relevant to the application in ice research: tactile pressure sensors are temperature sensitive and have a rather limited dynamic response time compared to other data acquisition systems.

The implication in view of ice-structure interactions is that fracture and spalling events cannot be captured in every detail. Many studies also refer to problems with calibrating

the sensors and inaccurate measurements for many different reasons. By comparing Figure 2.7 and Figure 2.8 it can be interpreted that the spatial resolutions of the tactile pressure sensors corresponds to a fairly coarse resolution (5.0 mm) of the pressure measurement film. However, tactile pressure sensors enable continuous measurements during a test, and allow observing contact area and pressure with the proceeding event. Studies such as by Wells et al. (2010), Browne et al. (2013), Izumiyama et al. (2007), and Kujala and Arughadhoss (2012) demonstrated the capability of the sensors to provide good reference pressures and an insight into pressure pattern developments.

2.5.3 Impact Module

The Impact Module, developed at the National Research Council Canada, offers the possibility to measure real time area and contact pressure distribution. The Impact Module is described in detail in Gagnon (2008). It consists of an acrylic block embedded with 9 strain-gauges, resting on four flat-jack load-cells to measure impact loads. On the surface of the acrylic block are acrylic strips that are slightly curved in section so when pressure is applied, the strips flatten against the acrylic block. A high speed camera is mounted behind the acrylic block. The images obtained during a test sequentially show the degree of flattening seen in the acrylic strips and this is used to determine the pressure distribution. An example is given in Figure 2.9; the image on the left displays the contact area that appears as the pressure strips flatten against the acrylic block. The images were translated into pressure distributions (right of Figure 2.9) using a specifically developed software routine.

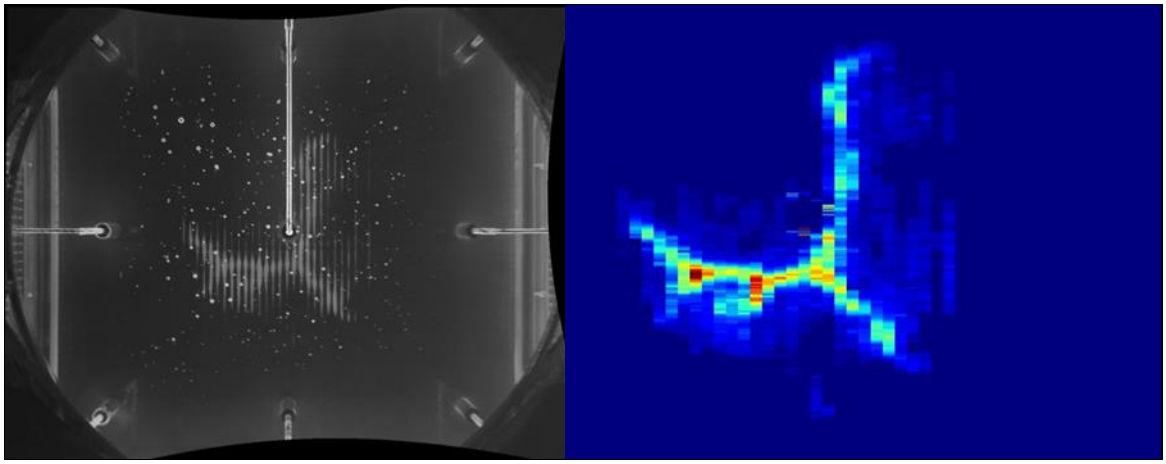

Figure 2.9: (Left) Image showing contact area during impact taken with the high speed camera inside the Impact Module. (Right) The resulting pressure distribution. (Source: Sopper et al., 2015b).

The results of several tests with 1 m diameter ice cones colliding with the Impact Module (Gagnon et al., 2009; Gudimetla et al., 2012; Sopper et al., 2015b) proved its quick response time to spalling events. The images showed real-time contact areas during the crushing event; a feature that makes the Impact Module preferable to various alternative technologies with longer reaction times, especially considering the extremely fast fracture and spalling events during ice breaking.

2.6 Summary

This chapter provides an overview of the current state of ice related research. Many studies focus on the determination of ice strength and local ice failure mechanisms; some investigate processes such as ice extrusion and ice friction. The examination of ice crystal structure offers valuable information on the reaction of the ice during an impact and provides evidence on prevailing failure mechanisms. Significant differences in ice load magnitudes were found to be dependent on indentation rate and on the degree of confinement that the impacted structure supplied. Although a dry contact surface rarely

occurs in nature, most studies are based on a dry ice-structure contact surface. This is despite the increased ice loads that have been observed when water was present. The objective of this study is the evaluation of the effects of submergence and other external boundary conditions on ice crushing load magnitude, which has not been addressed in detail to date. These boundary conditions are examined for different indentation rates to account for the ice failure behavior that changes with impact velocity. The concept sketch in Figure 2.10 displays some of the mechanisms occurring during ice failure against a flat surface. It pictures the dry case, where crack and ice spall development and progression are unrestricted, and the originating (dry) ice debris is freely extruded. It is postulated that these processes would be affected if the impact takes place under water or if granular ice material was present at the ice-structure interface. The influence of environmental boundary conditions would also depend on other aspects, such as restraints resulting from the indenter geometry. In order to prove this hypothesis, several indenter shapes are employed representing different degrees of structural confinement. The findings of this study help to enhance the understanding of the processes occurring during ice failure and identify the factors that influence ice loads. This contributes to better ice failure modelling and consequently more accurate ice load determinations in future design of ships and offshore structures.

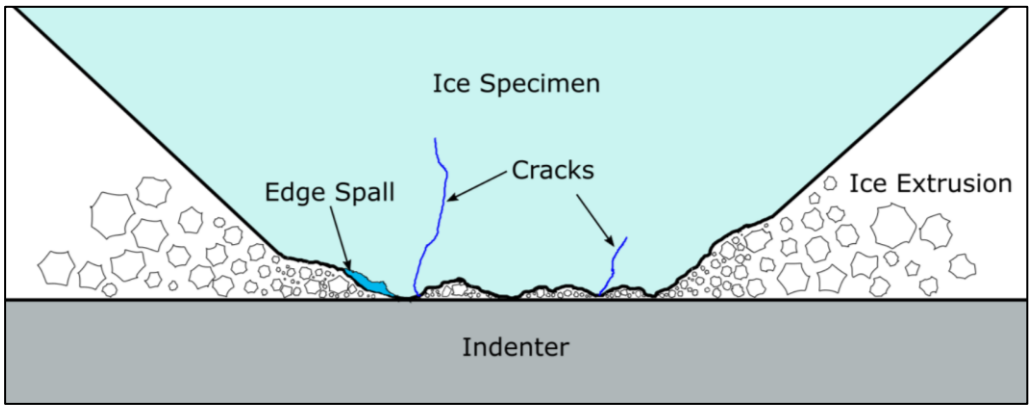

Figure 2.10: Concept sketch indicating during ice-structure collisions (dry contact) occurring processes that would be affected by other external boundary conditions.

Chapter 3 Methodology and Execution of Physical Experiments

3.1 Introduction

Ice design loads are commonly derived from dry laboratory or field tests but neglect other environmental boundaries. It can be assumed that most ice-structure interactions in nature involve water or other granular ice material (snow, ice chips from previous crushing). To date, these circumstances and their effects on ice loads have not been addressed in detail. In order to further the understanding of the influence and significance of environmental boundaries, attention needs to be paid to the processes and mechanisms involved in ice failure.

For this study, a total of 101 laboratory tests were carried out. The experiments took place in the thermodynamics laboratory at Memorial University of Newfoundland. The following factors were varied:

- Ice specimen geometry: test samples were conical ice specimen with two different angles to examine the effect for differently pointed ice features;
- Indenter shape: representing different geometries that can be found on ship hulls or offshore structures, constituting varying degrees of structural confinement;
- External boundary conditions: dry and submerged conditions as well as two additional environments, snow and granular ice;
- Indentation rate: all indenters were employed with 1 and 100 mm/s, one (the flat plate) in addition with 10 mm/s. The impact speed was varied to account for rate dependent differences in ice failure.

The variation of these parameters indicates the significance of single factors or factor combinations. For instance, it helps to evaluate whether the restriction from the fluid or from the structural confinement is prevailing, or if the significance of the influence of external boundary conditions is speed dependent.

3.2 Experimental Setup, Test Parameter and Test Scenarios

3.2.1 Experimental Setup

The tests took place in a refrigerated chamber (cold room) using a 500 kN closed-loop controlled material testing system (MTS), a compressive loading machine. All tests were performed inside a watertight aluminum container that enabled the testing in different environmental conditions (Figure 3.1). The internal dimensions of the container were 40 cm x 40 cm by 37 cm height. It provided a clear distance of 7 cm inside the container on either side of the ice sample ensuring that the ice specimens, or fluid behaviour, were not affected by the side walls. Visual observations were facilitated by 24.8 cm x 31.1 cm openings covered with 1.25 cm thick acrylic panels on all four sides. The container was attached to the piston that moves upwards towards the fixed crosshead of the MTS machine. At the crosshead a steel plate was screwed into the load cell by a 5 cm diameter threaded bolt. Ice specimens were attached to that plate by fastening the flange of the ice holder with four bolts to the plate.

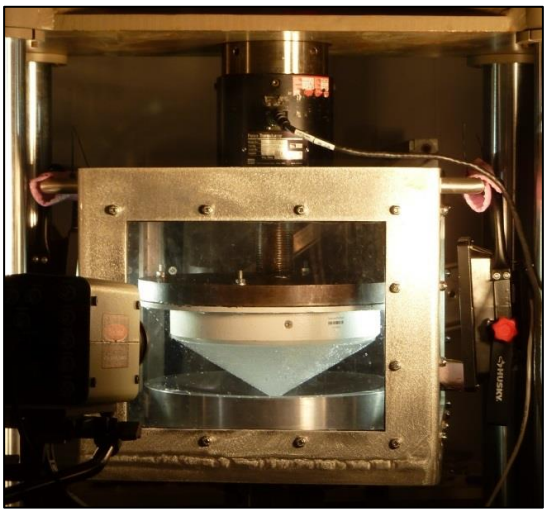

Figure 3.1: Experimental setup showing the aluminum container attached to the piston of the MTS machine and an ice sample mounted to the steel plate on the stationary crosshead.

3.2.2 Ice Holder

The ice specimens were grown in ice holders consisting of 25 cm diameter by 5 cm tall steel rings. Flanges were welded around the rings at the bottom of the ice holders to facilitate an attachment to the MTS machine. Each steel ring had four small bolts screwed radially through, located 90° apart from each other and protruding inside the holder. These bolts prevented the ice grown inside from slipping out of the holder.

3.2.3 Ambient Temperature

The ambient air temperature inside the cold room was maintained at -7°C. As the ice specimens were stored inside the cold room for at least 24h prior to testing, this was also the temperature of the ice. Earlier cited studies on icebergs found fairly constant temperature of iceberg cores due to the insulation characteristics of ice. From the surface up to a few meters depth into the iceberg core the temperature mostly ranged between

0°C and -10°C (Jones, 2007). This was used to guide the testing temperature as it indicates an iceberg-structure collision would be within that range.

Another aspect in defining the testing temperature originated from physical implications, as a smaller temperature gradient between the ice and surrounding water was believed to mitigate the risk of thermal stresses in the ice; as well as practical considerations, as an ambient temperature of -7°C was expected to permit a longer time frame for conducting tests before the water would become slushy and freeze.

3.2.4 Ice Specimens

Ice samples were 20° and 30° cones with a base diameter of 25 cm. The cone shape was preferred to other shapes since it provided very stable initial boundaries and a good repeatability of the tests. The ice specimens were laboratory produced following the procedure as described in Bruneau et al. (2012). The method was developed to generate ice with a crushing strength equivalent to that of multi-year sea ice or glacial ice. Therefore water was distilled, deionized and deaerated to minimize flaws originating from ion or air bubble inclusions. The water was chilled to a temperature of about 2°C. Generic available ice cubes were crushed into small chips. In order to ensure fairly constant ice properties and to avoid major flaws the ice seeds were manually sieved to exclude grain sizes above 10 mm.

The ice holders were covered with aluminum buckets (Figure 3.2 left). Insulation was wrapped around the sides of the buckets before they were placed upside down in a specially manufactured and insulated lid for a standard freezer set at -20°C. The ice chips were poured into the buckets and consolidated by stirring. The purified water was added

and the set-up covered with insulated lids. The insulation around the buckets and the orientation in the freezer caused the ice to freeze up from the bottom of the suspended assembly which was from the top of the specimen to the bottom with the flange. This procedure forced the ice to grow in one direction thus pushing out air and impurities.

After three days the cylindrical samples were well frozen and removed for shaping (Figure 3.2 right). In the first step the back side (flange side) of the samples were melted using a steel plate to obtain a flush surface. Subsequently the samples were stored for at least 24 hours inside the cold room to adjust to the testing temperature.

Figure 3.2: (Left) Ice holder - aluminum bucket setup to grow ice specimen. (Right) Ice holder with unprocessed cylindrical specimen.

The final step involved shaping the specimens into cones. The samples were attached by the flange to a rotary table. A planer blade that was mounted on a crossbar was lowered into the ice while the table was turning thereby gradually machining the initial ice cylinder into cone shape (Figure 3.3). The planer blade was adjustable allowing for cone angles.

Figure 3.3: Ice shaping apparatus to machine conical ice specimen.

This method guaranteed consistent sample properties. For 37 samples the weight including the ice holder (approximately 4.1 kg) before and after the test was recorded, and an average ice density was determined to 928 kg/m^3.

3.2.5 Indenter

The common indenter material was aluminum to ensure resistance to corrosion, while being exposed to water in submerged tests. The surface roughness was generally about 0.4 µm or less. The indenter shape was varied to account for different sections of ships and offshore structures, each supplying another degree of geometrical restriction and inducing variations in ice failure and ice extrusion.

3.2.5.1 Flat Plate

The flat plate had a base area of 35 cm x 35 cm and a thickness of 2.5 cm (Figure 3.4). It represented vertical sections on a ship hull or an offshore platform. Tests involved 20° and 30° ice specimens.

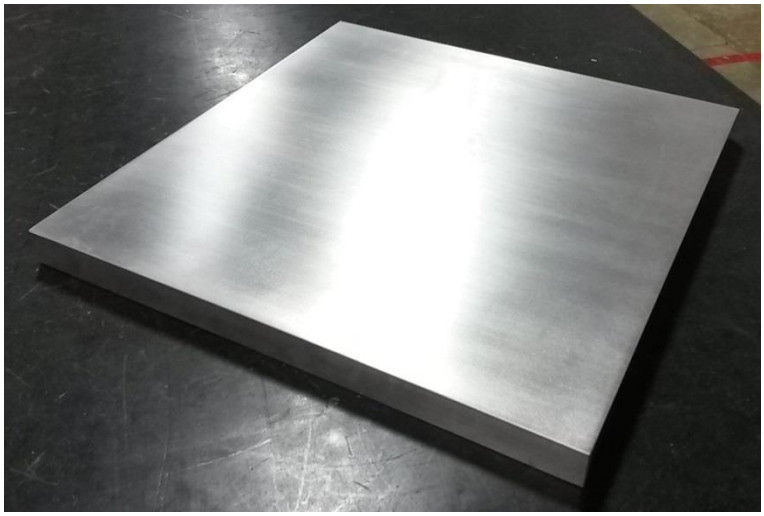

Figure 3.4: Image of flat indentation plate.

3.2.5.2 10° Wedge (Concave)

Figure 3.5 displays the geometrical dimension of the wedge shaped indenter from a side perspective. The base area was 35 cm x 35 cm with a height of 5 cm. The angle of 10° refers to the angle enclosed between a horizontal line drawn from the middle of the indenter (trough) and the sloped surface. From the isometric view in Figure 3.6 one can observe the “one-directional” confinement that the wedge provided, similar to locations on ships where two components connect, e.g. where a pod is attached to the ship hull or at the pod itself. Such geometries can be found also on offshore platforms, e.g. in transition areas from pontoons to the horizontal platform. Tests were done with 30° ice specimens.

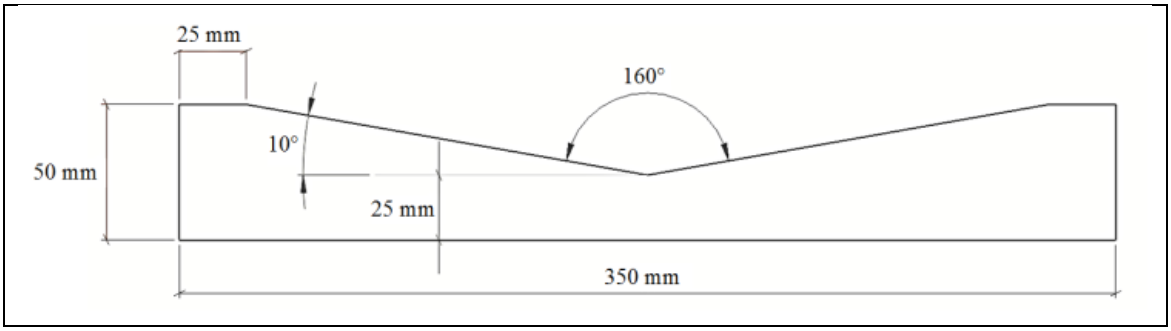

Figure 3.5: 10° Wedge shaped indenter: drawing with dimensions (side view).

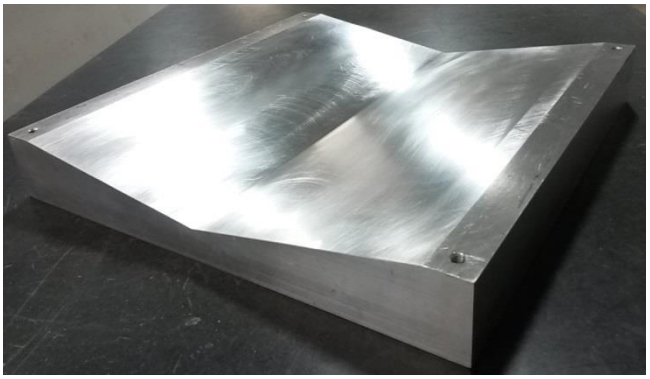

Figure 3.6: 10° Wedge shaped indenter: still photo (isometric view).

3.2.5.3 10° Conical Indenter (Concave)

The 10° conical indenter or reverse cone (Figure 3.7) had an external diameter of 34 cm and a height of 5 cm. This profile represented a permanently deformed area of a structure due to a former incident. In contrast to the wedge, this shape provided “omnidirectional” confinement, i.e. ice extrusion was equally impeded to all sides. This shape was tested with 30°cones only.

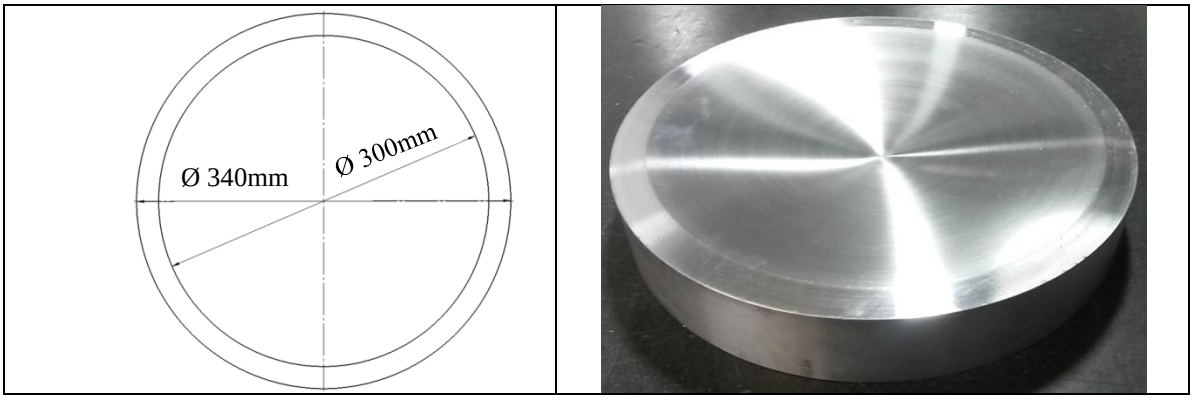

Figure 3.7: 10° Conical indenter (reverse cone). (Left) Top view with diameters indicated. (Right) Image of isometric view.

3.2.5.4 Half Hemi Sphere (Convex)

The convex indenter was a 5 cm diameter half hemi sphere machined from a 7 cm diameter round aluminum bar (Figure 3.8). The shoulder of 1 cm around the hemi sphere is assumed to have had no influence on the experimental results, since the ice crushed only at the top of the indenter. The sphere was mounted by a 5 cm diameter threaded bolt in the center of a flat plate. Its geometry is a simplified analogous to the rounded structure of a propulsion unit. Testing involved only the blunter ice cone specimens with 20° angle. Impacts with more pointed ice geometries are unlikely, particularly under water, where currents and turbulences would cause the ice feature to deflect.

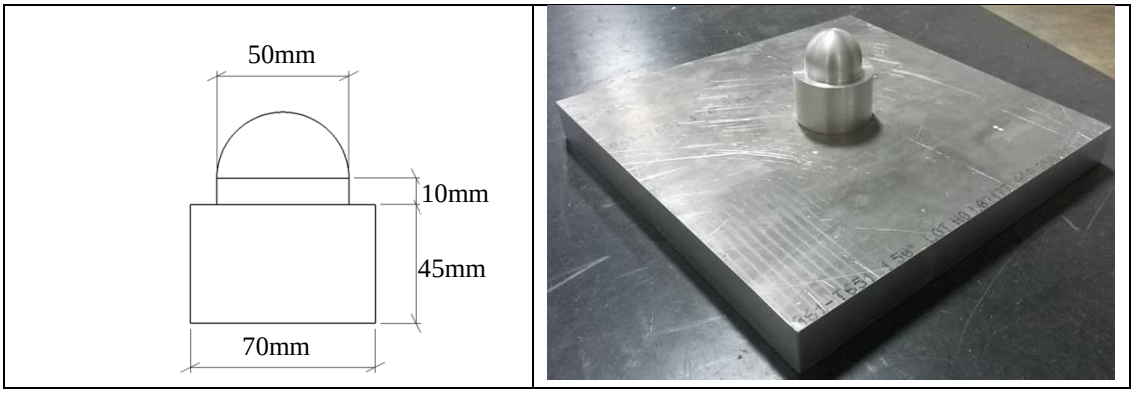

Figure 3.8: Spherical indenter. (Left) Side view of sphere with dimensions. (Right) Image displaying the spherical indenter mounted to an aluminum plate.

3.2.6 Indentation Rates

To account for various types of ice failure and their effects on ice loads tests were performed at several indentation rates. The maximum impact velocity was limited to 100 mm/s by the capacity of the testing apparatus, and all tests were performed with displacement control. Tests with the flat indentation plate were performed in dry and submerged condition at 1 mm/s, 10 mm/s, and 100 mm/s. Tests in other environments and with other indenters were conducted at 1 mm/s and 100 mm/s to capture extreme differences and limit the number of tests.

3.2.7 Environmental Testing Conditions

The core of this research was to investigate ice load differences in dry and submerged conditions by performing a series of laboratory experiments. Tests in submergence imitate ice-structure interactions as they commonly occur in nature. These tests are the first intensely investigated case to best of my knowledge. In addition, several tests with layers of snow and granular ice on the indenter surface (flat plate only) were conducted. This served to get an initial impression, but it also allowed comparing the significance of

the external boundary conditions. The relevance of these materials is not just given due to ice comminution that takes place during a crushing event, but also in view of a realistic environmental scenario, where snow or granular ice material is likely present at the ice-structure interface (e.g. on an ice floe).

3.2.7.1 Dry

In dry tests each ice specimen was positioned just above the indenter surface. The tests were performed using the respective indentation rate from the start until the maximum anticipated displacement was reached. Data acquisition occurred over that time frame. In later tests, the procedure was changed to leave a gap of approximately 5 mm between cone tip and the indenter. This was to account for the reaction time of the MTS machine, while it accelerated to the anticipated rate and to ensure that all data from the beginning of the impact was captured.

3.2.7.2 Submerged

For submerged tests, salt water was favored over fresh water for several reasons. Water with salinities between 26 ppt and 36 ppt has a freezing point ranging from -1.4°C to -2.0°C. This enabled testing at low water temperatures and was believed to mitigate the introduction of thermal stresses based on temperature differences between ice specimen and water. Moreover, it extended the time span for testing before the water would become slushy or eventually freeze. The water temperature was 2°C to 4°C at the time it was filled into the aluminum container.

For each test, water temperature and salinity were monitored using a traceable salinity meter by Fisher Science Education®. The measurements were taken before the cone was positioned and was presumably slightly lower at the time testing took place.

After each test, floating ice and slush were removed using a dip net. Due to the exposure to the cold room temperature of -7°C and ice crushing, the water temperature quickly decreased with proceeding tests. When the temperature was low and development of ice particles and slush were noticed, a part of the water (approximately 4 l) was replaced with salt water at room temperature.

The water level was measured before each test and the ice specimen was positioned with the cone tip just above the water. In order to generate comparable initial conditions (i.e. a similar exposure of the ice specimen to the water), the ice specimens were first moved at 10 mm/s through the water before it was switched to the test speed (or remained constant). The final indentation rate was set to commence at a distance of approximately 5 mm before first contact was expected and the data acquisition system of the material testing system (MTS) was simultaneously triggered. This was to compensate for tolerances in water level and positioning, for a possible delay between data triggering and recording, as well as to ensure that the impact occurred at the anticipated test velocity. In later tests, data acquisition also comprised the sample moving through the water.

3.2.7.3 Snow

Snow of less than 1 mm grain size was obtained from the ice cone shaping process. During shaping, the redundant material of the initial cylindrical ice sample was expelled in the form of dry snow. The snow condition primarily involved the flat plate. The

material was loosely filled into the aluminum container up to a layer thickness of about 20 mm.

The tests were performed by positioning the ice specimen just above the snow. Indentation rates were 1 mm/s and 100 mm/s. In early tests, the procedure was the same as for the submerged tests, including a switch of the indentation rate just before the impact was anticipated. Data acquisition comprised the time from the change of the indentation rate until the end of the test. In some cases, this caused difficulties in the determination of the first impact when rate change (associated with deviations in force) and first contact occurred nearly at the same time. In later tests, the respective indentation rate was applied from the beginning and maintained until the anticipated penetration depth was achieved. Data was recorded throughout. After each test, the entire snow material was replaced by fresh snow to ensure no larger debris remained that could affect the results.

3.2.7.4 Granular Ice (Chips)

The granular ice material consisted of the same generic available ice used for the ice samples. It contained all grain sizes from snow up to more than 10 mm, but the particular distribution was not determined. In analogy to the snow condition, it was only deployed with the flat plate and a layer was loosely filled into the container to an approximate depth of 20 mm. The cone tip was positioned just above the granular ice. The respective indentation rate (1 mm/s, 100 mm/s) was applied from the beginning of the test and the data acquisition system was triggered simultaneously.

3.3 Test Scenarios and Test Nomenclature

3.3.1 Test Scenarios

A scenario can be defined as a specific combination of cone angle, indenter geometry, indentation rate, and contact condition. The scenarios are shown in Figure 3.9; in the left column, from the top to the bottom are tests with the flat plate for dry, submerged, and conditions involving snow or granular ice; the column in the middle contains dry and submerged conditions for the wedge or conical indenter, respectively; the column on the right displays the two testing conditions for the spherical indenter. The basic or reference tests with the most repetitions involved the flat indentation plate in dry and submerged condition with a total of 53 tests (19 at 1 mm/s, 12 at 10 mm/s, 22 at 100 mm/s).

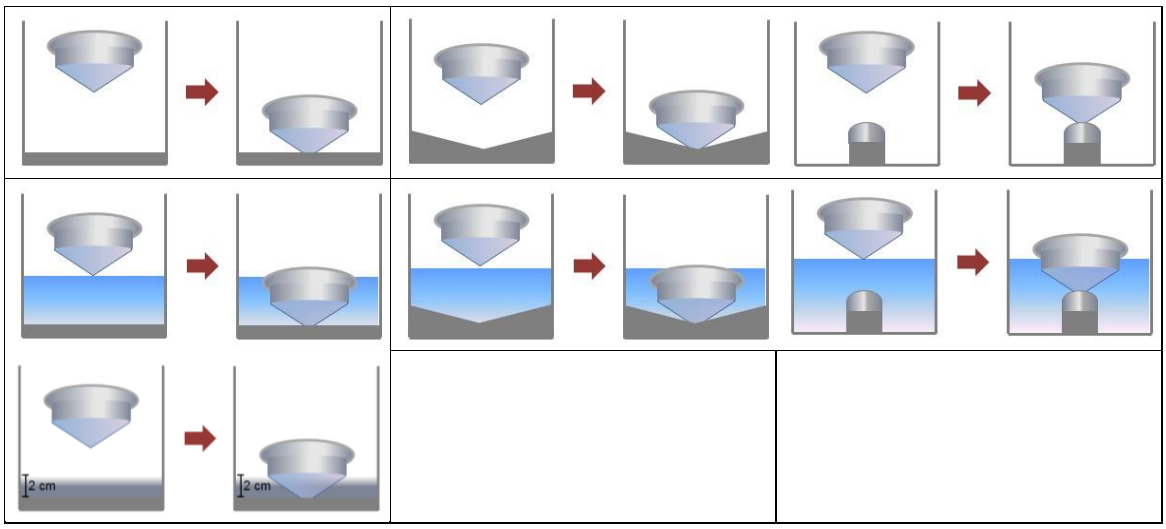

Figure 3.9: Overview of test scenarios. (Left) Flat plate; top to bottom for dry, submerged, and snow and granular ice contact conditions. (Middle) Wedge or conical indenter and (Right) spherical indenter; top for dry and below for submerged conditions.

3.3.2 Test Overview

In total 101 tests were performed. Table 3.1 to Table 3.4 below summarize the test quantity separately for each indenter. More detailed information is provided in the result section at the beginning of each chapter of the individual indenter.

Table 3.1: Overview of tests performed with the flat indentation plate.

Indenter	**Condition**	**Indentation Rate [mm/s]**	**Cone Angle [°]**	**No. of Tests**
Flat Plate	Dry	1	20	5
			30	4
		10	20	4
			30	2
		100	20	6
			30	6*
	Submerged	1	20	4
			30	6
		10	20	3
			30	3
		100	20	4
			30	6
	Snow	1	20	2
			30	2
		100	20	2
			30	2
	Granular Ice	1	20	2
			30	2
		10	20	1
			30	1
		100	20	2
			30	2
				Σ 71

* One test was excluded from the analysis.

Table 3.2: Overview of tests performed with the wedge shaped indenter.

Indenter	Condition	Indentation Rate [mm/s]	Cone Angle [°]	No. of Tests
Wedge	Dry	1	30	2
		100		2
	Submerged	1		2
		100		2
				Σ 8

Table 3.3: Overview of tests performed with the conical indenter.

Indenter	Condition	Indentation Rate [mm/s]	Cone Angle [°]	No. of Tests
Conical	Dry	1	30	4*
		100		3
	Submerged	1		3
		100		2
				Σ 12

***** One test was excluded from the analysis.

Table 3.4: Overview of tests performed with the spherical indenter.

Indenter	Condition	Indentation Rate [mm/s]	Cone Angle [°]	No. of Tests
Sphere	Dry	1	20	3
		100		3
	Submerged	1		2
		100		2
				Σ 10

3.3.3 Test Nomenclature

A test nomenclature was established to distinguish the tests. It comprised test specific parameters and started with the test day in the format of YYYY-MM-DD. This was followed by the overall sequential number that was indicated with prefix “T”. The two

consecutive numbers specified the test order on a particular day. The condition was indicated by either “D” for dry, “S” for submerged, and “Chips” or “Snow”, respectively. The next two letters represented the indentation rate, “HS” for high speed (100 mm/s), “MS” for medium speed (10 mm/s), and “LS” for low speed (1 mm/s). The next letter(s) specified the indenter with “F” for the flat indentation plate, “Sp” for spherical indenter, “W” for wedge shaped indenter and “Con” for conical indenter. The last two digits were either 20 or 30 for the respective ice specimen angle.

For example 2014-11-03_T09_04_D_HS_F_30 identifies a test that was performed on November 3rd, 2014. It was the ninth test in the program and the fourth test on that particular day. The test was done with a dry contact surface at 100 mm/s, with the flat plate and a 30° ice specimen.

3.4 Data Acquisition

3.4.1 Material Testing System (MTS)

The main data source was the MTS machine. Tests were executed via displacement control and the collected data comprised time, force, and vertical displacement, all saved in *.dat files.

Axial forces were recorded by a MTS 661.23E-01 series high capacity force transducer, located at the crosshead of the MTS machine. The load cell is capable of measuring tension and compression forces up to 500 kN.

The piston was a Series 244.41 hydraulic actuator with a force rating of 500 kN. Its displacement was recorded with an internal linear variable displacement transducer (LVDT).

The sampling rate was generally set to 2048 Hz in low indentation rate tests (1 mm/s), and to 4096 Hz in medium and high indentation rate tests (10 mm/s, 100 mm/s).

3.4.2 High Speed Camera (HSC)

All tests were recorded using a black and white high speed camera that was positioned inside the cold room. Although the data sources were not synchronized, the videos facilitated the correlation of visual observations to force-histories from the MTS machine and to pressure patterns from tactile pressure sensors. Low indentation tests were recorded with up to 300 frames per second (fps) and high speed test with up to 1000 fps depending on test scenario.

3.4.3 Still Photos

Still photos of the samples were taken before and after each test to monitor sample constitution and the test run in general.

3.4.4 Microstructural Observations (Thin Section Procedure)

In order to gain insight into the effect of different test scenarios on the ice microstructure, thin sections of 31 tested ice specimens were taken some time after the tests. First the ice samples needed to be detached from the ice holder. The four bolts keeping the specimen in the ice holder were removed and a square piece of insulation with a circular opening in the middle was placed around the steel ring. In a small gap between ice holder and

insulation a heated rubber coated wire was placed around the steel ring (Figure 3.10) to melt the ice.

Figure 3.10: Picture showing an ice specimen with a warm wire winded around for detaching it from the mold.

After a few minutes, the ice was soft enough to slide out of the steel ring when moderate pressure was applied. Next, using a band saw the sample was vertically cut into a slice of 7-8 mm thickness that contained the center area where the ice was impacted. Smaller thicknesses most often resulted in the ice sample breaking. Then, a rectangular section with the impacted area was cut and attached with some water drops to a small glass plate. Subsequently, using a manually operated microtome (Figure 3.11) the free surface of the ice slab was machined down so that asperities caused by the coarse blade of the bandsaw were removed. Using a cutter knife the ice was disengaged from the glass plate. In many cases, this step resulted in fracture of the ice. If still acceptable, it was flipped and attached with water along the entire perimeter to another small glass plate. This side of

the ice slab was machined down to a thickness of 1 mm or less. The ice was prone to breakage in general but it sometimes contained significant cracks that resulted in repeated fracture of the ice slab. In those cases, the ice was not flipped and it was impossible to machine it down to the desired thickness.

Figure 3.11: Image of manually operated microtome to machine thin ice sections.

For the examination of the crystal structure, the thin section was placed between two cross- polarized filters (Figure 3.12, left). Normally, no light is transmitted when the two filters are perpendicular but because the ice crystals alter the polarization, each crystal takes on a color depending on its orientation. Gray colors indicate a vertical orientation of the c-axis, while other colors represent horizontal orientation. Fractures are best visible by applying light from the side (Figure 3.12, right).

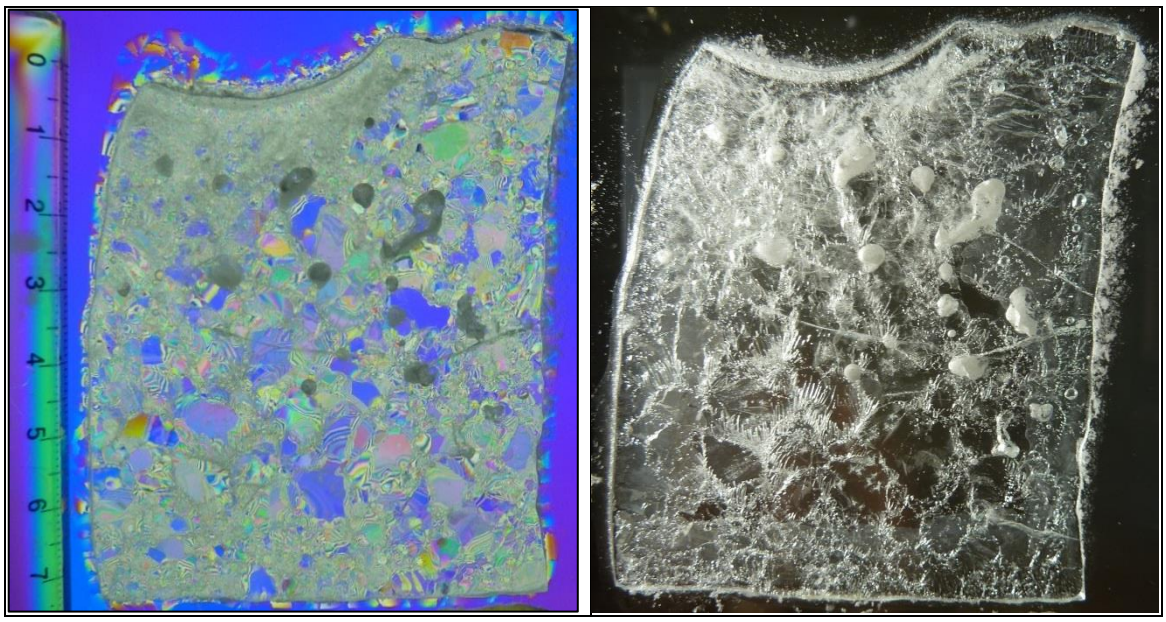

Figure 3.12: Thin section of test T52_01_S_LS_Sp_20. (Left) Between cross polarized filters for examining the crystal structure. (Right) With side light to reveal fractures.

3.4.5 Tactile Pressure Sensors

In order to receive insight into pressure patterns and contact area during an ice impact Tekscan I-Scan® sensors model 5101 were incorporated in 25 tests with the flat indentation plate, as well as in all 8 tests with the wedge. Dimensions and specifications of the models used are displayed in Figure 3.13. The matrix area for a single sensor is 111.8 mm x 111.8 mm with a total number of 1936 sensels (sensing pixels). The sensors were rated for pressures up to 5000 psi (34.47 MPa) with a physical turn-on threshold of approximately 0.41 MPa (60 PSI). The information from the pressure sensors were received by USB handles that transmitted the information at a maximum rate of 100 Hz to a laptop outside the cold room. Special software (Tekscan I-scan Version 7.5, Serial # 33954) was used to process the sensor outputs. A software addition (named Map 5101D) allowed the interconnection of two individual pressure sensors into one large

sensing area. For more information on general considerations, preparation setup and procedure, and on encountered challenges, refer to Appendix F.

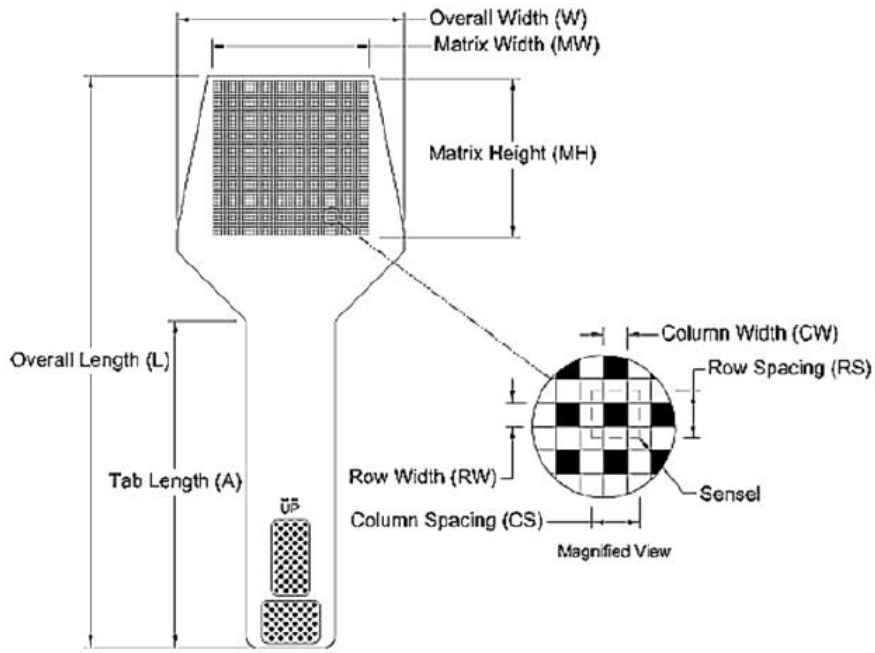

Overall Length L	Overall Width W	Tab Length A	Matrix Width MW	Matrix Height MH	Columns			Rows			Total No. of Sensels	Resolution Sensel Density
					CW	Pitch CS	Qty.	RW	Pitch RS	Qty.		
(in.) 13.39	(in.) 5.86	(in.) 6.59	(in.) 4.40	(in.) 4.40	(in.) 0.050	(in.) 0.100	44	(in.) 0.050	(in.) 0.100	44	1936	(sensel per in.^{2}) 100.0
(mm) 340.1	(mm) 148.8	(mm) 167.4	(mm) 111.8	(mm) 111.8	(mm) 1.3	(mm) 2.5	44	(mm) 1.3	(mm) 2.5	44	1936	(sensel per cm^2) 15.5

Figure 3.13: Tekscan I-Scan® model 5101 overall dimensions and specifications (Source: Tekscan, 2003).

3.5 Boundary Conditions

3.5.1 Ice Holders

All ice specimens were held in identical fabricated ice holders as described in section 3.2.2. The containment effect of these holders relevant to the present study was previously examined (Dillenburg, 2012). Compared to unconstrained ice samples, the ice holder facilitated a more continuous load build up in the ductile failure regime. It furthermore mitigated the amplitude of sudden load drops for both ductile and brittle ice failure. Consequently, the ice holder has some effect but it is consistent throughout all the tests and thus should not influence the comparability of the test results.

3.5.2 Ice Properties and Ice Age

One of the main concerns in experimental ice studies is to ensure consistent ice properties. A standardized procedure for generating and processing the ice specimens was followed. Each step (ice chipping, water preparation, mixing, processing, etc.) was monitored, date and general observations were kept in a log book. The general intention was to test within a short time period after the samples were produced.

In the second test period (March/ April 2015) failure of the hydraulic pump of the material testing system (MTS) caused a major delay in the test schedule. At that time more than 20 ice specimens were ready for testing. Those were moved back into deep freezers at -20°C and were packed into plastic bags to mitigate sublimation or evaporation of water. It was anticipated that this would not significantly alter the ice properties, but it was still an uncertainty. In order to account for this circumstance, each ice specimen's age was determined and was as part of the analysis evaluated. The ice age was defined as the

time between the day when the ice chips and water were mixed in the freezer and the day the sample was tested. Most (81) “young” ice specimens were between 4 and 25 days old; “old” ice specimens (20) were 91 up to 105 days. To further verify that the ice had not substantially changed, a randomly selected old ice raw sample was used for thin sectioning. The examination of the crystal structure did not indicate any changes and reinforced the trust that the ice properties were unaltered. When testing resumed, the ice age was still noted.

3.5.3 Submergence of Specimen Mounting Steel Plate

At advanced displacements, the steel plate was submerged, which could lead to a sudden additional resistance measured by the MTS machine. This was more likely at high impact velocity (100 mm/s) and was thus verified for all submerged high speed tests with the flat indentation plate. High speed camera (HSC) recordings were used to determine when the steel plate hit the water. The penetration that was covered up to that point was compared to the MTS data to examine whether any force deflection occurred in that region. In some tests, there seemed to be a slight force increase around these instants. However, it could not be determined if this originated from the steel plate or coincidentally emerged from unknown factors. In some tests, a distinct ice fracture event was observed in the HSC videos, close to the time when the steel plate was submerged. Other force-histories did not display any noticeably difference. Overall, there is not enough evidence to conclude that the force measurements were affected by the steel plate hitting the water.

3.5.4 Test Setup Compliance

The ice specimen mounting plate was attached to an approximately 15 cm long and 5 cm diameter steel bolt that screwed into the load cell of the MTS machine. One concern was to preserve the equipment and to ensure that no part of the MTS machine, especially not the load cell, came in contact with salt water. This required a longer bolt than preferred and likely introduced some compliance into the test setup.

3.5.5 Buoyancy and Drag in Submerged Tests

In submerged tests, static and dynamic buoyancy forces develop due to the ice mass travelling through the water. This was verified assuming the worst scenario of a 20° ice cone moving at an average speed of 92.9 mm/s and being entirely submerged. The rough calculation resulted in a static buoyancy force of 7.49 N, and a dynamic buoyancy force of 0.11 N, 0.22 N, and 0.33 N (for dynamic drag coefficients of 0.5, 1.0, and 1.5); negligible in view of general force fluctuations recorded by the MTS machine, as well as in view of ice load variations.

3.5.6 Container Walls

In dimensioning the aluminum container to perform the tests, two main considerations played an important role. First, the entire test setup had to fit into the available MTS machine. Second, the intention was to have a manageable setup (two people were able to lift it), that was also flexible enough to accommodate quick installations and adjustments (e.g. indenter change, pressure sensor installation).This limited the clear distance inside the container to 40 cm, and left approximately 7 cm free space between the container

walls and the ice samples. The extent to which this may have influenced the tests was not further investigated or quantified. This restriction was the same in all tests.

3.5.7 Indenter Surface Roughness

The effect of three different rough plates (smooth: 0.13 µm, medium: 0.47 µm, rough: 500 µm) at various indentation rates was examined by Dragt (2013). The tests were done in similar (dry) testing conditions (conical ice specimens, 4-10 mm ice seeds, flat plate, -10° C), covering a speed range from 0.01 mm/s to 100 mm/s. Average peak force and crushing energy differed due to roughness and speed combination, but the surface roughness did not affect overall trends originating from indentation rate. Furthermore, for 1 mm/s, 10 mm/s, and 100 mm/s indentation rates, force vs. displacement histories of smooth, and medium rough plates did not noticeably differ; neither in magnitude, nor in overall progress. The roughness of indenters used in this study was 0.4 µm or less, but did not vary much between the indenters. Therefore, roughness is not considered to have induced any different ice failure or to have led to different load magnitudes. In tests involving the pressure sensors, the surface comprised a sheet of Mylar that served to protect the sensors (see Appendix F). This effect was not quantified and based on Dragt's results it is not expected to have a considerable effect.

3.5.8 Cone Tip Accuracy

In some tests, it was noticed that the ice cone tip was not perfectly pointed. The influence that this distortion may have had on the force measurements was not further investigated. Small variations in point of initial contact cause deviations in calculated nominal pressures for small penetration depth. The implication of this circumstance on the analytical work is discussed in section 4.1.3.

Chapter 4 Analytical Procedures

4.1 Geometry Relations and Contact Area Definitions

4.1.1 Ice Sample Geometry

Figure 4.1 shows the overall dimensions of the ice specimens based on cone angles α of 20° and 30° (only the part above the ice holder is shown). Based on a 250 mm diameter, the cone heights with 45.5 mm and 72.2 mm constrained the maximum penetration stroke in all tests.

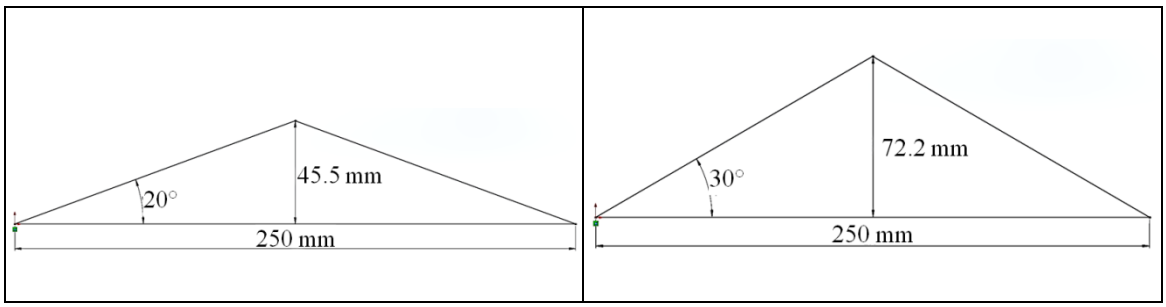

Figure 4.1: Ice specimen dimensions dependent on different cone angles; (Left) 20° angle. (Right) 30°angle.

4.1.2 Nominal Contact Area for the Flat Indentation Plate

For a known displacement δ, the nominal contact area dependent on ice cone angle can be determined. Figure 4.2 displays the different paces that the nominal areas of 20° and 30° ice cones increase. These areas are the basis used to derive the nominal average pressures by relating the measured forces to the nominal contact area, calculated as a function of the measured displacement.

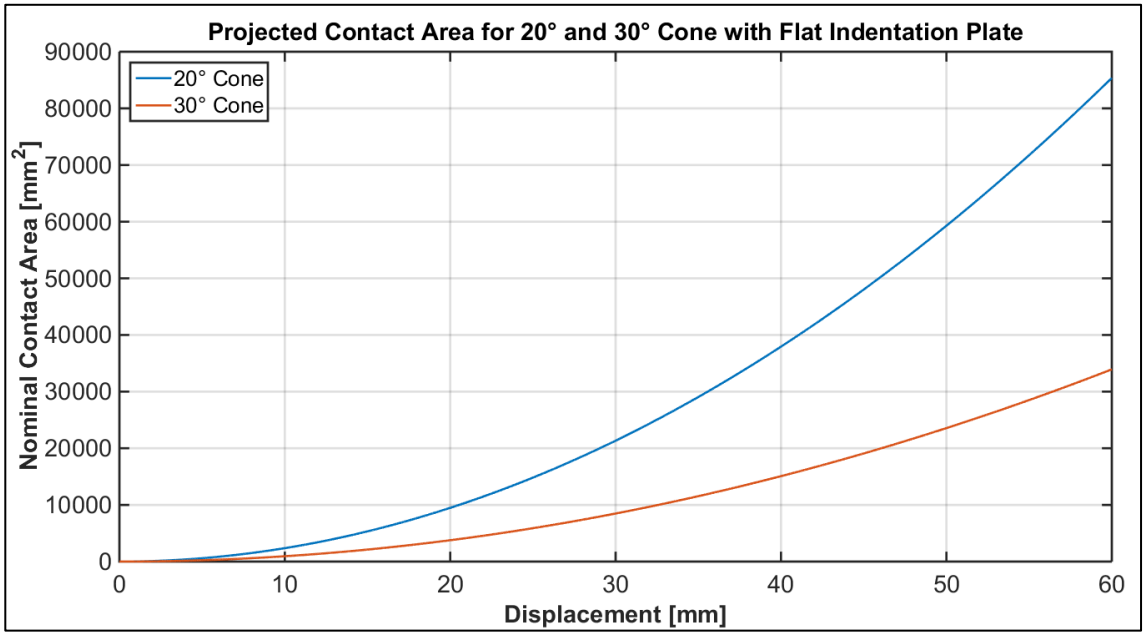

Figure 4.2: Comparison of contact area for a 20° and 30° cone with the flat indentation plate.

4.1.3 Effect of Cone Tip Offset

For a perfectly pointed ice cone tip the area at zero displacement ($\delta_0 = 0$; just before the impact occurs) equals zero ($A_{\delta_0} = 0$). This would be the ideal case, but sometimes a cone tip was slightly blunt or truncated generating an initial area. To examine how this would influence the nominal process pressure, four initial areas at zero displacement δ_0 were assumed for four representative tests. The nominal process pressures were compared for varying nominal area ranges. The entire investigation is included in Appendix G. At this point, it is should be mentioned that a cone tip offset, even though small, affects the calculation of nominal process pressure, particularly for small areas. It was concluded that for areas above 1000 mm^2 (3.2 cm x 3.2 cm) the error was within an acceptable range and this was set as the minimum limit for average process pressure evaluations in later

analysis (except for the spherical indenter). Furthermore, the code that was written to analyze the data allowed accounting for a cone tip offset by including an offset value $\Delta\delta$.

4.1.4 Nominal Contact Areas for Other Indenter Shapes

Apart from the flat indentation plate, for the three other indenter shapes two nominal contact areas are conceivable: projected and tangent. The tangent contact area is the area that forms on the indenter's surface. The projected contact area is the vertical projection of the ice-indenter interface on a horizontal plane and generally smaller than the former.

From a design perspective using the latter is the more conservative approach, leading to higher nominal average pressures. Examining the problem from the ice mechanics perspective, it is likely that forces are mainly perpendicularly transmitted to a structure. This would be better reflected by the projected contact area. Common practice in most studies that work with average process pressures, based on a nominal contact area, is to relate forces to the projected area. This approach was also chosen in the present study. The difference between both areas is negligible for the wedge shaped and conical indenters (less than 2% for the wedge; also see figures in Appendix A1 (wedge) and Appendix A2 (conical indenter) that display the respective progresses over displacement). The appendices also contain the derivations of the area equations.

For the spherical indenter (Appendix A3) there is significant difference between both contact areas (Figure 4.3). Due to the sphere's curvature the tangent contact area (green) on the indenter surface increases rapidly compared with the projected area (red). Furthermore, at $\delta = 34.099\,mm$ displacement the sphere is entirely enclosed by the ice (calculation provided in Appendix A3). As a consequence the maximum displacement

considered in the analysis is set to 30 mm. This is associated with a nominal (projected) contact area of approximately 1914 mm^2. Due to the fact that the contact area for the half-hemisphere is substantially smaller compared to all other indenters, the minimum nominal area margin was changed to 100 mm^2 (instead of 1000 mm^2).

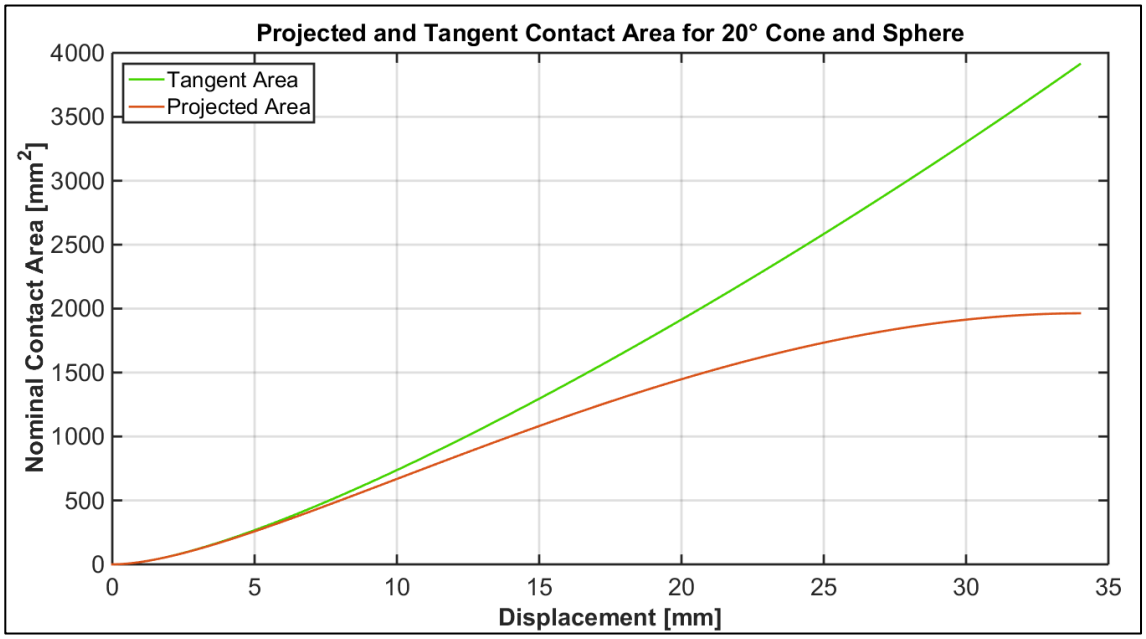

Figure 4.3: Comparison of projected and tangent contact area for a 20° cone and the spherical indenter for a displacement up to 34 mm.

A more individual approach was chosen by Jordaan et al. (1988), who assumed a layer of crushed ice with constant thickness to calculate pressures and forces on a spherical indenter. This requires information on the ice microstructure (thin sections) of each specific test. The main objective of the present research is to get an overall idea of force differences due to different contact conditions, but not to develop an analytical set of equations to replicate forces and pressures. Therefore the more generalized method using the projected area is preferred, as it was also used in past studies (e.g. Kim et al., 2012).

4.1.5 Comparison of Projected Contact Area for a 30° Cone and Different Indenter Shapes (Flat, Wedge, Conical)

The 30° ice specimens were used with the flat plate, the wedge, and the conical indenter. Figure 4.4 shows the increase in nominal (projected) contact areas with penetration depth for each shape. The flat plate (yellow) has the least slope; this is followed by the wedge (red), but the steepest incline has the conical indenter (blue). The contact areas are shown for a displacement up to 60 mm. Only in the scenarios involving the flat plate was this displacement achieved. Tests with the wedge and the conical indenters were limited to 35 mm displacement.

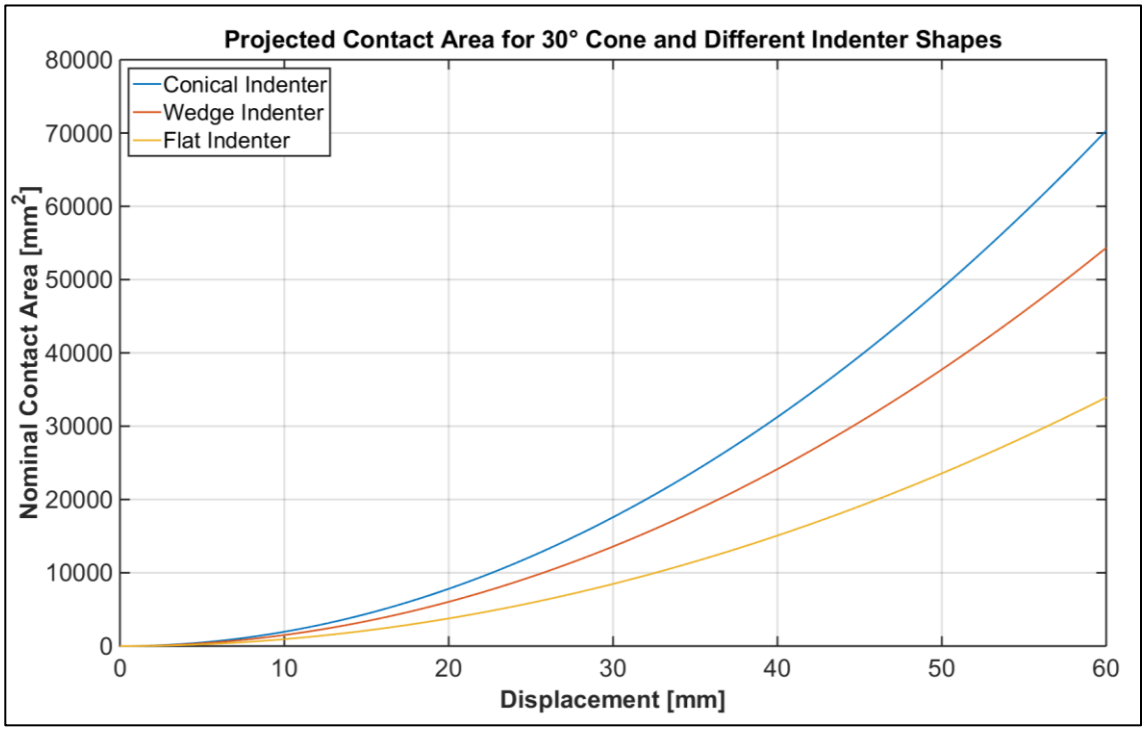

Figure 4.4: Contact area between a 30° cone and different indenter shapes (flat, wedge, conical).

4.1.6 Maximum Displacement

Indenter and ice specimen geometry governed the penetration stroke in all tests. Generally, the analysis did not extend to the maximum achieved displacement, but the data was cut sometime before the test ended. This accounted for tolerance in the positioning of the test sample as well as to exclude possible effects of the MTS machine decelerating. Displacements achieved and considered for analysis and dependent on the ice cone angle-indenter combination are provided in Table 4.1.

The maximum considered displacement was not always accomplished for practical reasons. This mainly concerns tests with snow and granular ice, as these cases involved uncertainties in determining the exact material layer thicknesses and less penetration depth was accepted to prevent a collision of ice holder with the indenter.

Table 4.1: Overview of maximum achieved and considered displacements depending on indenter shape and ice cone angle.

Indenter	**Cone Angle** [°]	**Maximum Displacement [mm]**	
		Achieved (Target)	**Considered for Analysis***
Flat Plate	20	40	35
	30	65	60
Wedge, Conical	30	40	35
Sphere	20	45	30

* In some cases the maximums were not achieved to prevent equipment damage and in these cases the available data was used for analysis.

4.2 Spectral Analysis (FFT)

In general, tests with the flat indentation plate at high (100 mm/s) and medium (10 mm/s) rates were sampled at 4096 Hz, low speed tests (1 mm/s) at 2048 Hz. Other indenters at all impact speeds were recorded at 4096 Hz.

All the data were analyzed with Fast Fourier Transform (FFT) to expose interferences that may have originated from resonances of the experimental set-up, or from noise of the data acquisition system. It also allowed some insight into the structural response during an impact and on disparities depending on the contact condition. Details and several examples are provided in the Appendix of each individual indenter. At this point, it should be mentioned that none of the tests exhibited a dominant frequency. For the flat indentation plate, wedge and conical indenter, variations in the Fourier spectra, particularly at the high indentation rate, indicated some distortions; possibly caused by external effects (in several tests the connection plug of the cable to the load cells was loose) or compliance in the test setup. As a consequence, all the data of these indentation shapes were processed with a low pass filter at 200 Hz. This removed most distortions and preserved the original force histories. The resulting signals still contained a range of frequencies relevant to practical structures, which are commonly considered not to exceed about 100 Hz. Higher frequencies are filtered in the ship hull or offshore structure.

The Fourier spectra of the tests with the spherical indenter did not exhibit comparable distortions, but were characterized by large variations in general. This was attributed to the shape associated with a distinctly different structural response. For that reason and

because the application of a low pass filter significantly altered the force history, the unfiltered data was analyzed.

4.3 Analysis Procedure for Force vs. Displacement Histories

The data was analyzed using a dedicated code that was written in Matlab® R2014b. The code was developed as part of this study to process time, displacement, and force data obtained from the MTS machine (*.dat files). Among other parameters, main user input comprised the determination of first impact by means of the raw force-time history for each test. That instant was identified being the point when the force started to deflect. Forces before that point were averaged and served as a tare value to normalize the subsequent force history. Time and displacement were normalized to this point. Based on the displacement, a nominal contact area was calculated depending on the respective indenter shape. The normalized force was set in relation to the nominal contact area to determine the nominal average process pressure. Other optional user inputs included a cone tip offset and a data filter in the frequency domain (low pass filter).

Table 4.2 provides an overview of areas and correlating displacements as used for analyzing the average nominal process pressure. For previously explained reasons (section 4.1.3), the minimum margin was set to 1000 mm^2 area, except for the sphere where it was 100 mm^2. The maximum area was predetermined by the upper considered displacement (Table 4.1) or the limit of the available data.

Table 4.2: Overview of in the analysis considered area ranges and associated displacements depending on the respective indenter and ice cone angle.

Indenter	**Cone Angle** [°]	**Displacement [mm]**		**Area [mm^2]**	
		Minimum	**Maximum**	**Minimum**	**Maximum**
Flat Plate	20	6.5	35.0	1000	29051
	30	10.3	60.0	1000	33929
Wedge	30	8.1	35.0	1000	18490
Conical	30	7.2	35.0	1000	23930
Sphere	20	2.7	30.0	100	1914

4.4 Contact Area and Spatial Pressure Pattern (Tactile Pressure Sensors)

Outputs from the tactile pressor sensor included contact area in units of mm^2, as well as force and contact pressure in raw units. The evaluation of the measurements was impeded, and sometimes impossible, because sensor damage occurred at some points in the test program; in particular in submergence or with granular ice on the indented surface. The damage was evident in form of a pink vertical line in the readings (Figure 4.5), indicating the saturation of that sensel column. This resulted in constant initial offsets in contact area (284 mm^2) and raw force (11220) in subsequent tests. For the affected tests, reasonable results were obtained by subtracting the initial offset values from the histories of area and raw force. For the contact pressure, on the other hand, this approach was not feasible. In addition, some issues were encountered in the sensor preparation and data processing (for more details see Appendix F). On these grounds, raw force and pressure were not further evaluated. The measurements only serve for the qualitative comparison of contact area and pressure patterns of the different test scenarios among each other.

It can be expected that the measurements of the tactile pressure sensors for contact area and raw force are slightly underestimating for two reasons. First, a small gap remained in between the two facing sensors, where no information was obtained. Secondly, the pressure sensors were not large enough to cover the entire contact area at advanced penetration depths.

One of the two handles that transmit the information from the pressure sensors to the data acquisition system was also damaged during the latter part of the testing. As a consequence, for the flat indentation plate, tests in the granular ice environment were only recorded with one pressure sensor (right hand side).

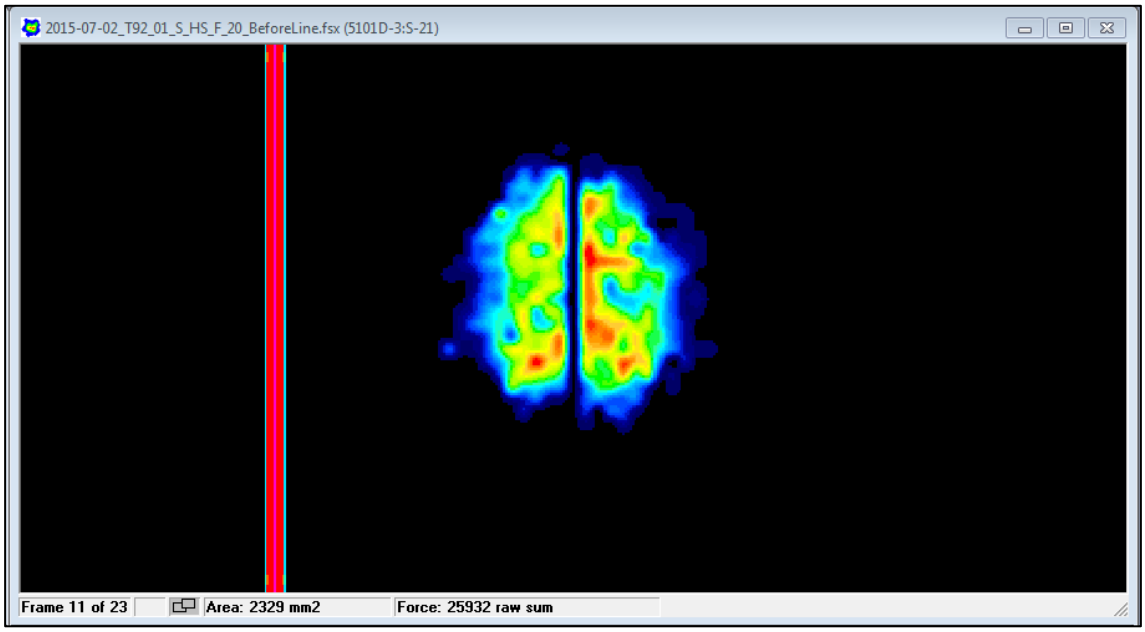

Figure 4.5: Image of a pressure pattern of submerged test S T92-01 at 100 mm/s with the flat indentation plate and with 20° ice cone angle (penetration depth approx. 11 mm). Left from the pink line is the damaged sensor section.

4.5 Microstructural Observations (Raw Samples, Ice Age)

The effect of different contact conditions was also assessed by examining the ice microstructure. After testing, some of the crushed ice specimens were stored in deep freezers at about -20°C for 1-6 weeks before they were further processed. In total, 31 ice specimens were kept for thin sectioning. An overview of the selected specimens is provided in the chapter covering each indenter and the observations are discussed.

Difficulties with the microtome introduced fractures and cracks into most of the thin sections and caused several samples to break. Those fractures are evident in the images (e.g. Figure 4.6, vertical thin sections), but do not reflect mechanisms of the ice crushing process. In many cases it was also not feasible to machine the ice samples down to the desired thickness of 1 mm or less to achieve the best visual observations. Samples of granular ice were especially fragile and inclined to break, mostly originating from a high crack density.

With respect to earlier comments on ice age, the thin sections of two raw samples are briefly discussed. Figure 4.6 displays thin section images of a 2-3 week “young” ice sample on the left, and of a 95 day “old” sample on the right. Left and right images show vertical and horizontal thin sections. The crystal structure of both samples is random and there are no obvious differences. Circular gray areas are air bubble inclusions in the ice specimens.

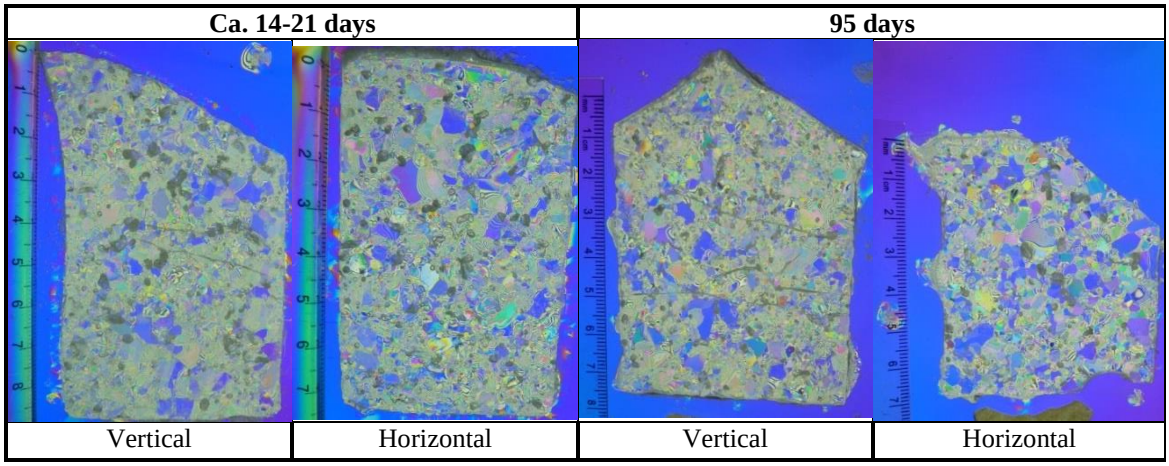

Figure 4.6: Images of vertical and horizontal thin sections between a cross-polarized filter of raw samples (Left) young: 2-3 weeks, (Right) old: 95 days. The images show the crystal structure of the parent (intact) ice. Cracks evident in the vertical thin sections were introduced during shaping with the microtome.

4.6 Multiple Regression Analysis

Regression analysis produces the most reliable results, when tests are carried out in a randomized order. Randomization reduces bias and averages out effects of uncontrollable and disregarded factors. In most physical experiments, practical restraints govern the test order. For this research, tests were performed in an order that was as randomized as feasible under the allowable circumstances. Factors such as ice cone angle and indentation rate were easily randomized in contrast to the contact conditions. On one test day, all anticipated runs for a surface contact condition were completed first before commencing tests in another environment. For example, if dry and submerged tests were scheduled for the same day, all dry tests were completed prior to the submerged tests.

Furthermore, full randomization was particularly constrained in tests that involved pressure sensors on the flat indentation plate or the wedge indenter. Priority was given to tests that were expected to bear the least risk of sensor damage and that were considered

to be more important to support the stated research objectives. The wedge shaped indenter was exclusively used in dry and submerged contact conditions. Therefore, only after all dry tests were completed, were the submerged scenarios undertaken. The flat plate was utilized with four different contact conditions. Dry tests were performed first, followed by snow tests. After those tests, the pressure sensors were exchanged to start with an intact sensor and watertight protection. Submerged tests were of higher priority and were completed before scenarios with granular ice as these last tests had the highest risk of sensor damage. Ultimately, the pressure sensors did not last over the entire test series.

A multiple regression analysis was then performed separately for each indenter using software package Minitab® 17. The analysis required the definition of responses that would characterize individual tests. Four values were identified. One was the mean force over the entire test length ("Force Mean Overall"). The other three responses comprised specific nominal contact area ranges, starting from 100 mm^2 for the spherical indenter, and from 1000 mm^2 for all other indenters, up to the end of the test. The responses were mean force, mean nominal pressure, and peak pressure ("Mean Force 1000", "Mean Pressure 1000", "Pressure Max 1000"). Common factors in all regression models were indentation rate and contact condition. The ice cone angle was an additional parameter considered only for the flat indentation plate.

In the case of the flat indentation plate, multiple regression analysis with a stepwise selection of terms was used to test the factors and their interactions with categorical predictor coding coefficients (-1, 0, +1) at a significance level $\alpha = 0.15$. That significance level was chosen in consideration of typically high variations in experimental ice

research, where 10 – 15 % deviation is common. The flat plate cases yielded statistically valid models that are more fully described in Section 5.1.5.

For all other indentation shapes, the selection of a specific method (stepwise, forward or backward) led to null models for some responses and a completely null model for the spherical indenter. This is attributed to the limited data for those shapes. Therefore, the multiple regression analysis was performed without any selection of model terms. The models include all factors and two factor interactions, but are insignificant in statistical terms. Still, they are useful to indicate trends of factor effects as it is one of the main objectives of this research.

The models' qualities are indicated in terms of the coefficient of determination. R^2 represents the percentage of total variability that is explained by the model, $R^2_{adjusted}$ denotes the model's capability to predict data points that were used to establish the model, and $R^2_{predicted}$ signifies its ability to predict new observations.

Chapter 5 Analytical Results and Interpretation

In this chapter, the results of the experiments are presented. The main discussion is distinguished by the four indentation shapes: flat plate, wedge shaped indenter, conical indenter and spherical indenter. Results include force-displacement histories, nominal average process pressure-area curves, measurements with tactile pressure sensors (flat plate and wedge only), as well as observations of the ice specimens after testing in general and on a microstructural basis. Furthermore, a linear regression analysis was separately carried out for each indenter.

Most tests were done for dry and submerged contact conditions with a large number of repeats. For clarity in comparing force-displacement histories and pressure-area plots, individual measurements are summarized and are displayed with shaded areas covering the range of results derived from the repeated tests. Green represents the dry contact condition and blue the submerged contact condition. Due to the limited number of tests with snow or granular ice on the indented surface, those are individually shown with dotted and dashed lines. Plots of all individual force histories or pressure-area curves are provided in the respective Appendix pertaining to the specific indenter.

For simplification, tests done for a certain contact condition are also named dry test, submerged test, snow test, and chips test (granular ice). This also applies to the specification of forces, pressures, and loads dependent on the respective contact condition.

5.1 Flat Indentation Plate

5.1.1 Test Overview

Table 5.1 summarizes the 71 tests performed with the flat indentation plate. Nominal indentation rate (Nom.) refers to the respective speed categorization (low, medium, high), whereas the average rate (Avg.) is the mean of the actual achieved speed. For submerged tests, information on water salinity and temperature is also provided. Superscript "*" indicates a test that was excluded from the analysis for later explained reasons. Superscript "P" denotes tests that involved tactile pressure sensor measurements and "T" where thin sections were completed. The test configuration for all contact conditions is displayed in Figure 5.1.

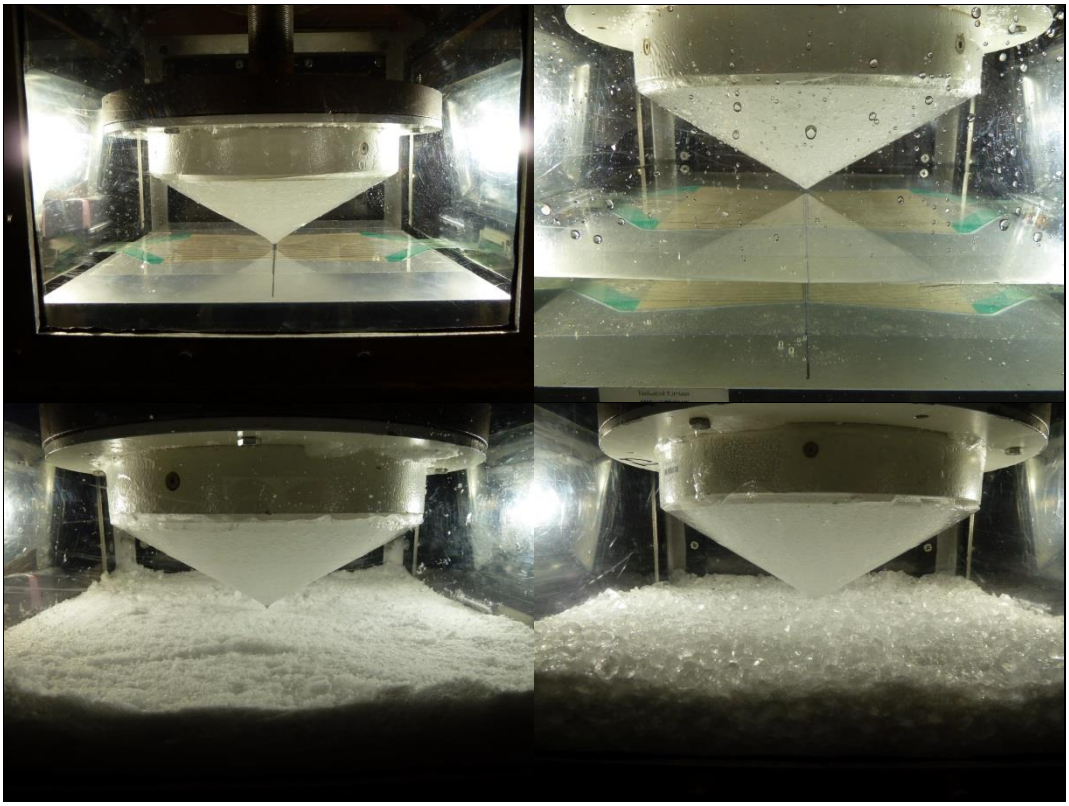

Figure 5.1: Still photos of the test setup for dry (top left), submerged (top right), snow (bottom left) and granular ice (bottom right) contact conditions with the flat indentation plate and 30° ice cone angle.

Table 5.1: Overview of 71 tests performed with the flat indentation plate.

Date	Test Number		Cone Angle [°]	Indentation Rate		Contact Condition	Water	
	Overall	Day		Nom. [mm/s]	Avg. [mm/s]		Salinity [ppt]	Temp. [°C]
03.11.2014	6	1	30	1	1.0	Dry	-	-
03.11.2014	7	2	30	100	92.2	Dry	-	-
03.11.2014	8	3	30	1	1.0	Dry	-	-
03.11.2014	9*	4	30	100	93.8	Dry	-	-
04.11.2014	10	1	20	1	1.0	Dry	-	-
04.11.2014	11	2	20	100	92.6	Dry	-	-
04.11.2014	12	3	20	1	1.0	Dry	-	-
04.11.2014	13	4	20	100	92.9	Dry	-	-
04.11.2014	14	5	20	10	10.0	Dry	-	-
05.11.2014	15	1	30	1	1.0	Submerged	30.3	+1.6
05.11.2014	16	2	30	100	90.8	Submerged	30.4	-1.1
07.11.2014	17	1	20	1	1.0	Submerged	28.9	+1.6
07.11.2014	18	2	20	100	90.3	Submerged	29.0	-0.9
07.11.2014	19	3	30	1	1.0	Submerged	31.8	+3.4
07.11.2014	20	4	30	100	93.2	Submerged	30.9	+0.1
10.11.2014	21	1	20	100	93.3	Dry	-	-
10.11.2014	22	2	30	100	93.4	Dry	-	-
12.11.2014	24	2	30	100	94.0	Dry	-	-
12.11.2014	25	3	20	1	1.0	Dry	-	-
12.11.2014	26	4	20	100	92.8	Dry	-	-
12.11.2014	27	5	30	100	91.2	Submerged	26.8	+1.8
12.11.2014	28	6	30	1	1.0	Submerged	26.6	-1.2
14.11.2014	29	1	20	10	10.0	Dry	-	-
14.11.2014	30	2	20	10	10.0	Dry	-	-
14.11.2014	31	3	30	100	88.8	Submerged	35.3	+1.9
14.11.2014	32	4	30	1	1.0	Submerged	36.8	-1.2
14.11.2014	33	5	20	1	1.0	Submerged	37.6	+1.3
14.11.2014	34	6	20	100	90.1	Submerged	36.9	-0.6
18.11.2014	35	1	20	1	1.0	Dry	-	-
18.11.2014	36	2	30	100	92.2	Dry	-	-
18.11.2014	37	3	20	100	91.8	Dry	-	-
18.11.2014	38	4	30	1	1.0	Dry	-	-
20.11.2014	39	1	30	1	1.0	Submerged	31.0	+1.2
20.11.2014	40	2	20	1	1.0	Submerged	32.4	-1.6
20.11.2014	41	3	20	100	88.9	Submerged	32.8	+3.6
20.11.2014	42	4	30	100	88.5	Submerged	31.9	+0.1
26.06.2015	73 [PT]	1	30	1	1.0	Dry	-	-
26.06.2015	74 [PT]	2	20	10	10.0	Dry	-	-

Date	Test Number		Cone Angle [°]	Indentation Rate		Contact Condition	Water	
	Overall	Day		Nom. [mm/s]	Avg. [mm/s]		Salinity [ppt]	Temp. [°C]
26.06.2015	75 [P T]	3	30	10	10.0	Dry	-	-
26.06.2015	76 [P T]	4	20	100	93.6	Dry	-	-
26.06.2015	77 [P T]	5	30	100	92.2	Dry	-	-
26.06.2015	78 [P T]	6	20	1	1.0	Dry	-	-
26.06.2015	79 [P]	7	30	10	10.0	Dry	-	-
26.06.2015	80 [P T]	8	30	1	1.0	Snow	-	-
26.06.2015	81 [P T]	9	30	100	92.1	Snow	-	-
29.06.2015	82 [P T]	1	20	100	88.4	Snow	-	-
29.06.2015	83 [P T]	2	20	1	1.0	Snow	-	-
29.06.2015	84 [P]	3	30	100	92.5	Snow	-	-
29.06.2015	85 [P]	4	20	100	91.9	Snow	-	-
29.06.2015	86 [P]	5	30	1	1.0	Snow	-	-
29.06.2015	87 [P]	6	20	1	1.0	Snow	-	-
30.06.2015	88	1	30	10	10.0	Submerged	28.9	-0.2
30.06.2015	89	2	20	10	10.0	Submerged	29.0	-1.5
30.06.2015	90 [T]	3	20	10	10.0	Submerged	29.5	-1.6
30.06.2015	91	4	30	10	10.0	Submerged	24.8	+1.1
02.07.2015	92 [P T]	1	20	100	87.4	Submerged	20.6	+2.0
02.07.2015	93 [P]	2	30	1	1.0	Submerged	21.7	+1.1
02.07.2015	94 [P]	3	20	1	1.0	Submerged	21.6	-0.2
02.07.2015	95 [P T]	4	30	100	92.1	Submerged	22.2	-0.9
02.07.2015	96 [P]	5	20	10	10.0	Submerged	21.4	+1.1
02.07.2015	97 [P]	6	30	10	10.0	Submerged	21.3	±0.0
03.07.2015	98 [P]	1	30	1	1.0	Chips	-	-
03.07.2015	99 [P T]	2	20	1	1.0	Chips	-	-
03.07.2015	100 [P]	3	30	100	94.0	Chips	-	-
03.07.2015	101 [P T]	4	20	100	92.6	Chips	-	-
03.07.2015	102	5	30	100	93.5	Chips	-	-
03.07.2015	103	6	20	1	1.0	Chips	-	-
03.07.2015	104	7	20	100	94.2	Chips	-	-
03.07.2015	105	8	30	1	1.0	Chips	-	-
03.07.2015	106 [T]	9	20	10	10.0	Chips	-	-
03.07.2015	107	10	30	10	10.0	Chips	-	-

* Test excluded from the analysis.

P Tactile pressure sensor measurements completed.

T Thin sections completed.

5.1.2 Measured Force and Nominal Process Pressure

For the flat indentation plate, force-displacement histories are displayed for 35 mm and 60 mm displacements on the x-axis, depending on 20° and 30° ice cone angles; the y-axis shows force up to 400 kN. Nominal process pressure-area relationships are plotted on a log-linear scale for a minimum nominal contact area of 1000 mm^2 on the x-axis and a maximum nominal pressure of 25 MPa on the y-axis. For clarity, the single tests of dry and submerged contact conditions are summarized in green and blue areas. Due to the limited test quantity with snow or granular ice, the results are individually displayed with dotted and dashed lines. Plots of all individual force-histories or nominal process pressure-area curves are provided in the Appendix (B2 – B4) pertaining to the respective indentation rate.

5.1.2.1 Indentation Rate: 1 mm/s

At 1 mm/s indentation rate with 20° ice specimens, a total of thirteen tests were performed: 5 dry, 4 submerged, and 2 each with snow and granular ice on the indenter's surface. Figure 5.2 shows forces vs. displacement. Forces during submerged tests (blue area) tend to be higher than those from dry tests (green area). Higher forces are recorded for snow or granular ice (chips). Low speed tests generally yield smooth force curves but more prevalent in the submergence case. For some reason, snow test T83-02 (yellow dotted line) has distinct load drops at 6.7 mm, 13.1 mm, and 19.2 mm. Another smaller drop is observed at a displacement of 24.3 mm. The deltas between first and last drop (6.7 s, 6.4 s, 6.1 s) follow some periodicity with an incremental decrease of 0.3 s. Similarity in behaviour is noticed only for dry test T35-01 with drops at 10.5 mm,

19.2 mm, and 24.2 mm displacements that are evident in the upper margin of the green shaded area. A single large drop also occurred during the chips test T103-06 (blue dashed line) at 26.6 mm.

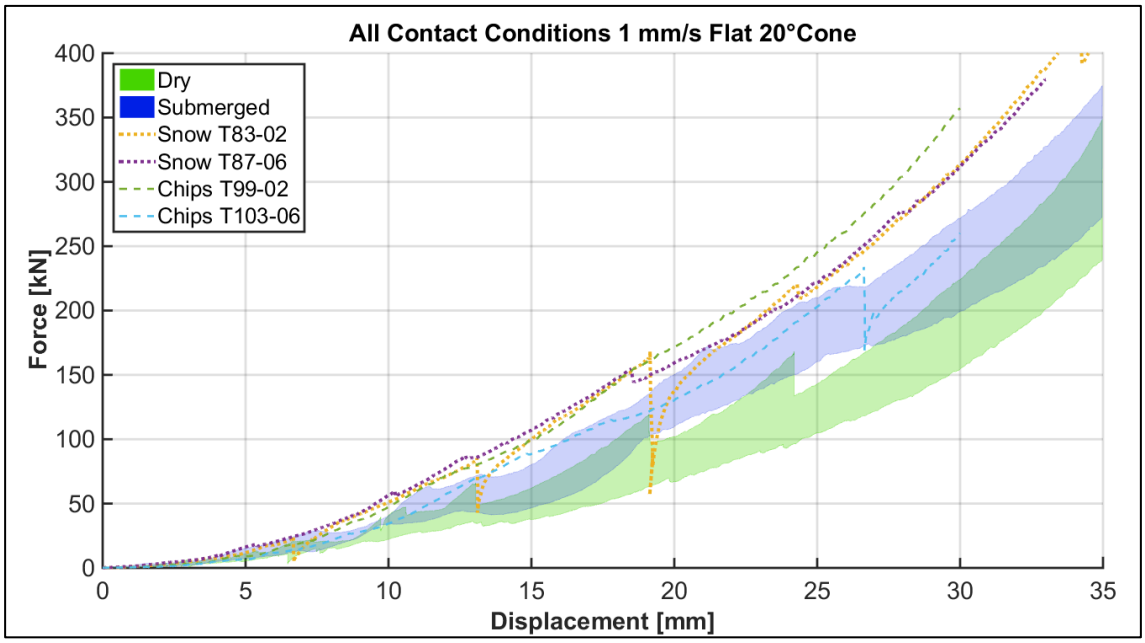

Figure 5.2: Flat plate, 1 mm/s, 20° ice specimens: force vs. displacement for all contact conditions. The shaded areas enclose all dry tests (5) in green and submerged tests (4) in blue.

Figure 5.3 displays nominal process pressures vs. nominal contact area. Nominal pressures tend to be higher in submergence (blue area) compared to the dry condition (green area), but there is also partial overlap. On the other hand, snow shows exceptionally high nominal pressures (dotted lines). High pressures can also be noticed for granular ice (dashed lines) that are lower compared to snow, but above those of dry and submerged conditions. Nominal pressures range from 4.9 MPa to 23.1 MPa at around 1000 mm^2, and between 8.2 MPa and 15.2 MPa at the end of the test. The highest pressure is 24.1 MPa at 2480 mm^2 area for snow test T87-06.

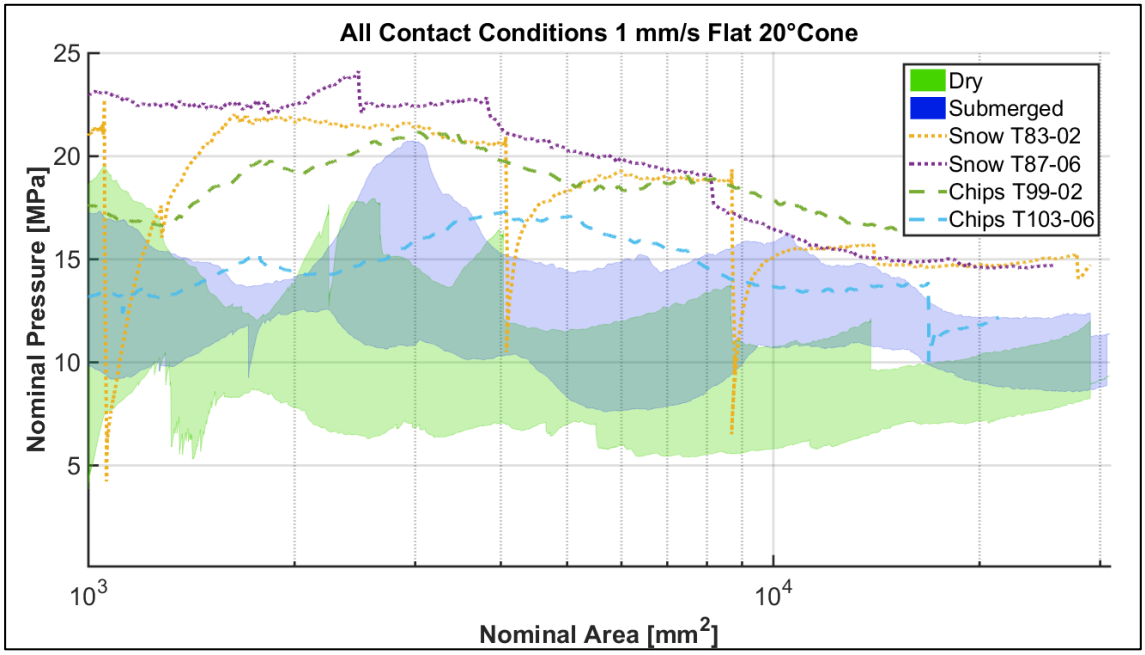

Figure 5.3: Flat plate, 1 mm/s, 20° ice specimens: nominal pressure-area curves for all contact conditions. The shaded areas enclose all dry tests (5) in green and submerged tests (4) in blue.

Fourteen tests were conducted with 30° ice cone angle: 4 dry, 6 submerged, and 2 each with snow and granular ice. Figure 5.4 displays the force histories for displacements up to 60 mm. The plot reveals very similar forces for dry and submerged conditions, but both forces are lower than those of the snow and granular ice tests. The results indicate that up to between 25 mm and 30 mm displacement, snow has slightly higher forces than chips. Beyond this point, the relation is reversed until no more information for granular ice tests was obtained.

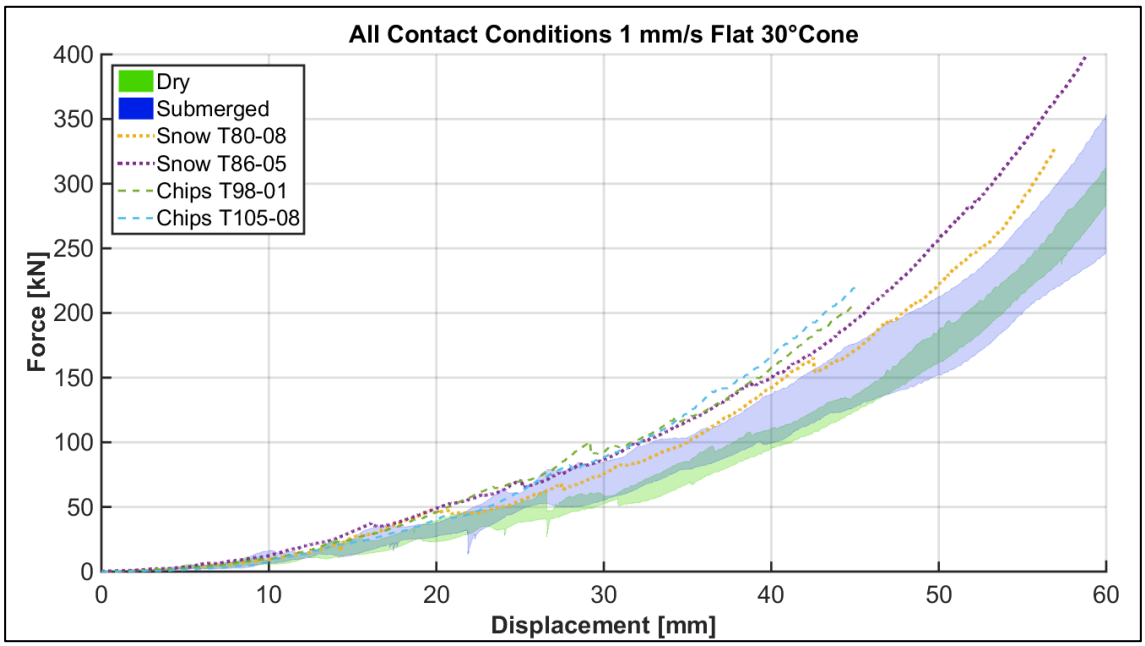

Figure 5.4: Flat plate, 1 mm/s, 30° ice specimens: force vs. displacement for all contact conditions. The shaded areas enclose all dry tests (4) in green and submerged tests (6) in blue.

The nominal pressures of dry and submerged tests in Figure 5.5 overlap, but almost throughout, the maximum pressures in submergence are higher. Snow and ice chips clearly have the highest pressures. In general, pressures range from approximately 6.6 MPa to 15.6 MPa at around 1000 mm^2, and at just over 31000 mm^2 between 7.2 MPa and 11.9 MPa.

Single curves for force-displacement histories and nominal pressure-area relationships of both ice specimen angles at 1 mm/s indentation rate are provided in Appendix B2.

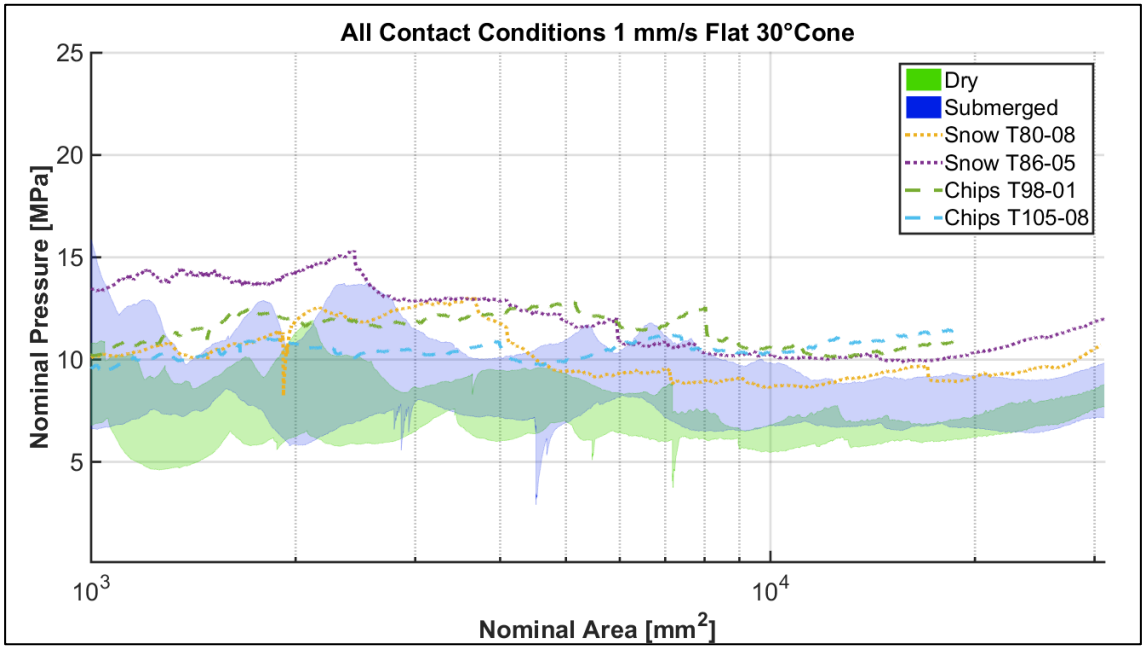

Figure 5.5: Flat plate, 1 mm/s, 30° ice specimens: nominal pressure-area curves for all contact conditions. The shaded areas enclose all dry tests (4) in green and submerged tests (6) in blue.

5.1.2.2 Indentation Rate: 10 mm/s

At the medium indentation rate, eight tests were carried out with 20° ice specimen: 4 in dry, 3 in submerged conditions, and 1 test with granular ice. The forces are displayed in Figure 5.6. The effect of submergence is relative. High forces were measured between a displacement of 17.5 mm and 26.5 mm, due to one individual test (S T96-05, Figure Appendix B3. 1), which may be an outlier. Other than that, the areas of both conditions mostly overlap. The force progress of the submerged tests is overall smooth. Dry tests, have a number of successive sudden force drops. The intensity increases above 28 mm displacement as it is indicated by the vertical incisions in the green area (better visible in Figure Appendix B3. 1). The force of the granular ice test T106-09 is comparable to the other two testing environments, and has only minor drops.

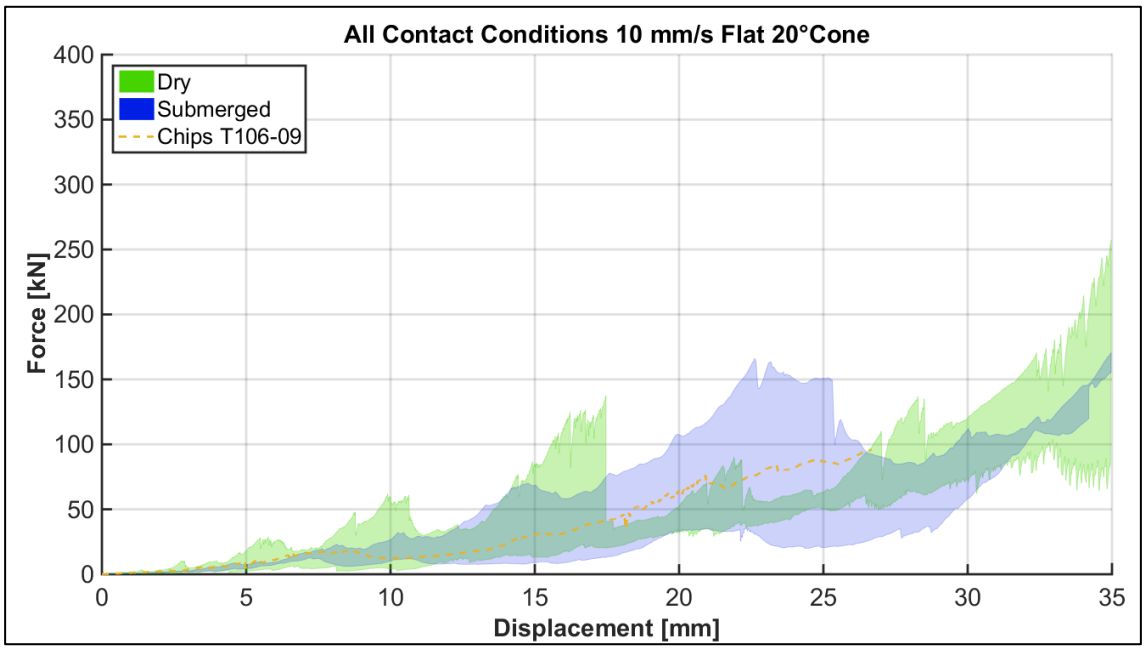

Figure 5.6: Flat plate, 10 mm/s, 20° ice specimens: force vs. displacement for all contact conditions. The shaded areas enclose all dry tests (4) in green and submerged tests (3) in blue.

The ambiguous picture continues in the average nominal pressures (Figure 5.7). In this scenario, the difference between dry and submerged conditions appears to be negligible. The nominal pressures spread from roughly 4.6 MPa to 14.2 MPa and between 2.5 MPa and 6.8 MPa at the end of the tests. The maximum pressure is 15.2 MPa at 1038 mm^2 for the chips test T106-09.

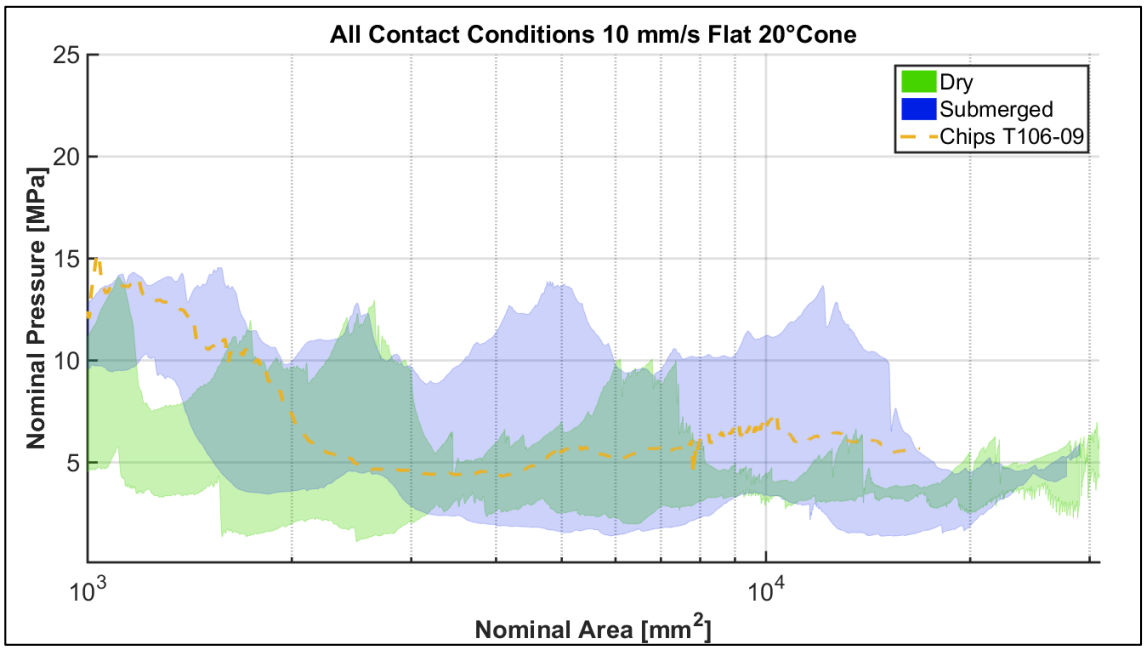

Figure 5.7: Flat plate, 10 mm/s, 20° ice specimens: nominal pressure-area curves for all contact conditions. The shaded areas enclose all dry tests (4) in green and submerged tests (3) in blue.

Six tests were done with 30° ice specimens: 2 dry, 3 submerged, and 1 with granular ice. In Figure 5.8 it is evident that starting from 31 mm displacement, submerged forces are clearly above those of the dry contact condition. The ice chips test (T107-10) has forces that are roughly in the middle of both other tested environments.

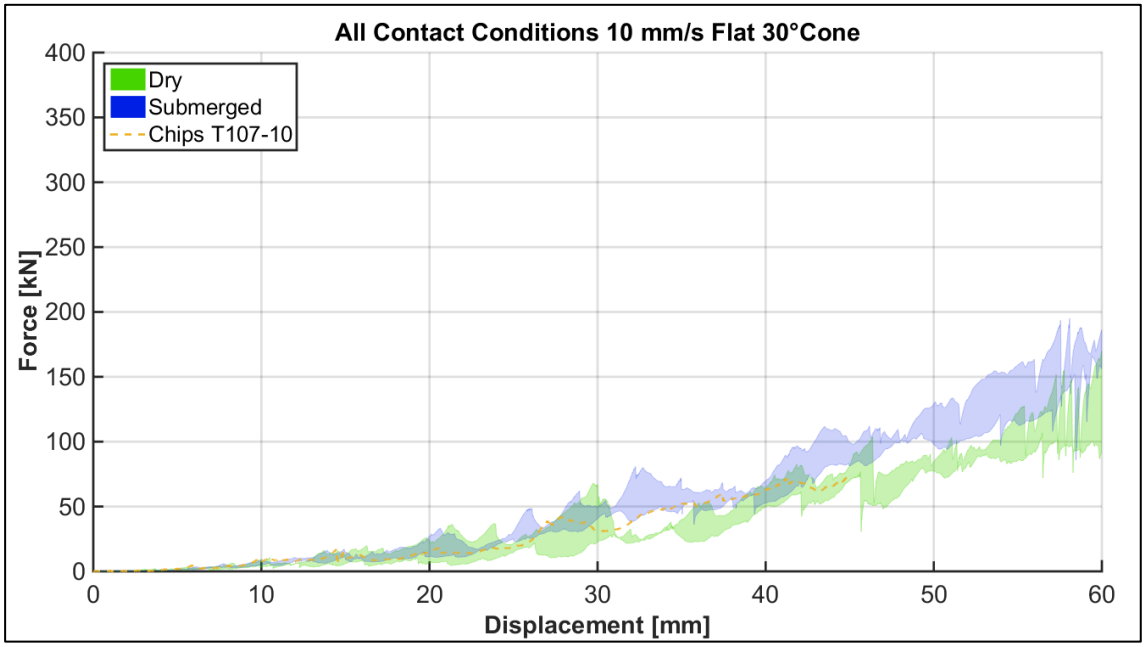

Figure 5.8: Flat plate, 10 mm/s, 30° ice specimens: force vs. displacement for all contact conditions. The shaded areas enclose all dry tests (2) in green and submerged tests (3) in blue.

Figure 5.9 shows the associated nominal pressures. For nominal areas below 9000 mm^2 (approximately 20 mm displacement) the nominal pressures are rather similar in dry and submerged conditions. At larger areas, pressures in submergence cases exceed those of the dry environment. The ice chips test initially has the highest pressures, but later settles in the mid-range of the two other environments. At 1000 mm^2, pressures for dry and submergence cases are between 3.9 MPa and 10.2 MPa and between 3.1 MPa and 5.7 MPa. Overall, pressures are above 1.0 MPa but below 9.1 MPa.

Force-displacement histories and nominal pressure-area relationships displaying each individual test are provided in Appendix B3.

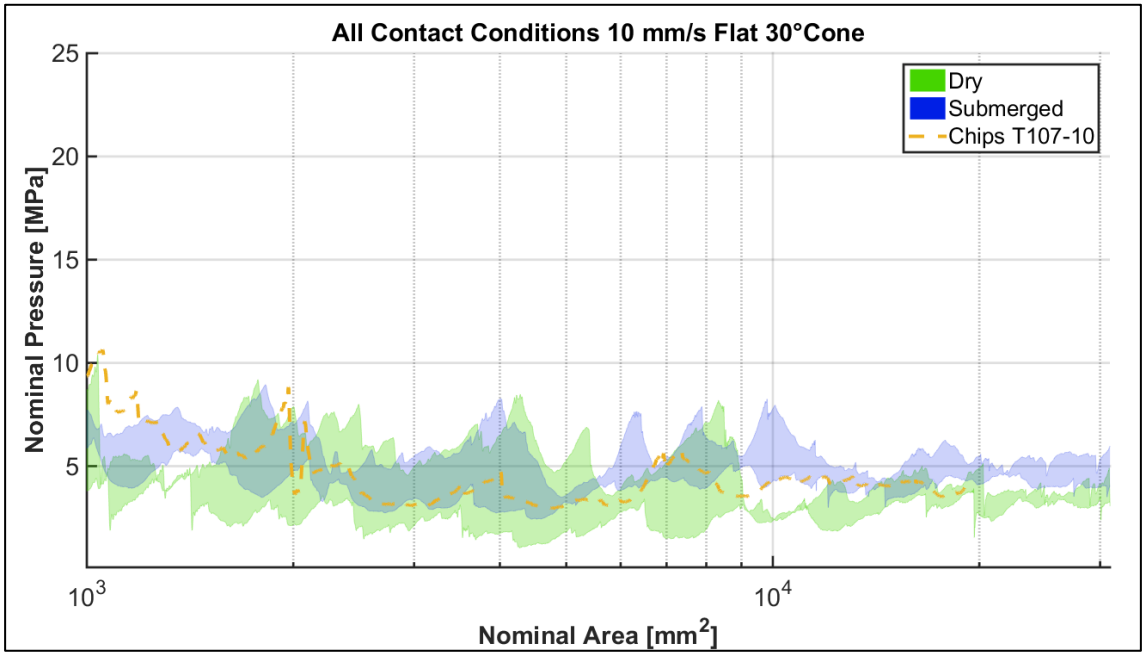

Figure 5.9: Flat plate, 10 mm/s, 30° ice specimens: nominal pressure-area curves for all contact conditions. The shaded areas enclose all dry tests (2) in green and submerged tests (3) in blue.

5.1.2.3 Indentation Rate: 100 mm/s

In total, fourteen tests with 20° ice cones were performed at 100 mm/s impact speed: 6 dry, 4 submerged, and 2 each with snow and granular ice on the indented surface. At this indentation rate, the effect of submergence is most evident. Figure 5.10 shows that, especially beginning from a displacement of 17 mm, submergence cases have higher forces than dry tests. Snow test T82-01 and chips test T101-04 are of similar magnitude to submergence cases. Snow test T85-04 remains fairly low up to a displacement of 30 mm. Beyond this point the forces converge to the value of other snow and submerged tests. Forces in the dry environment are consistently below those of the other contact conditions.

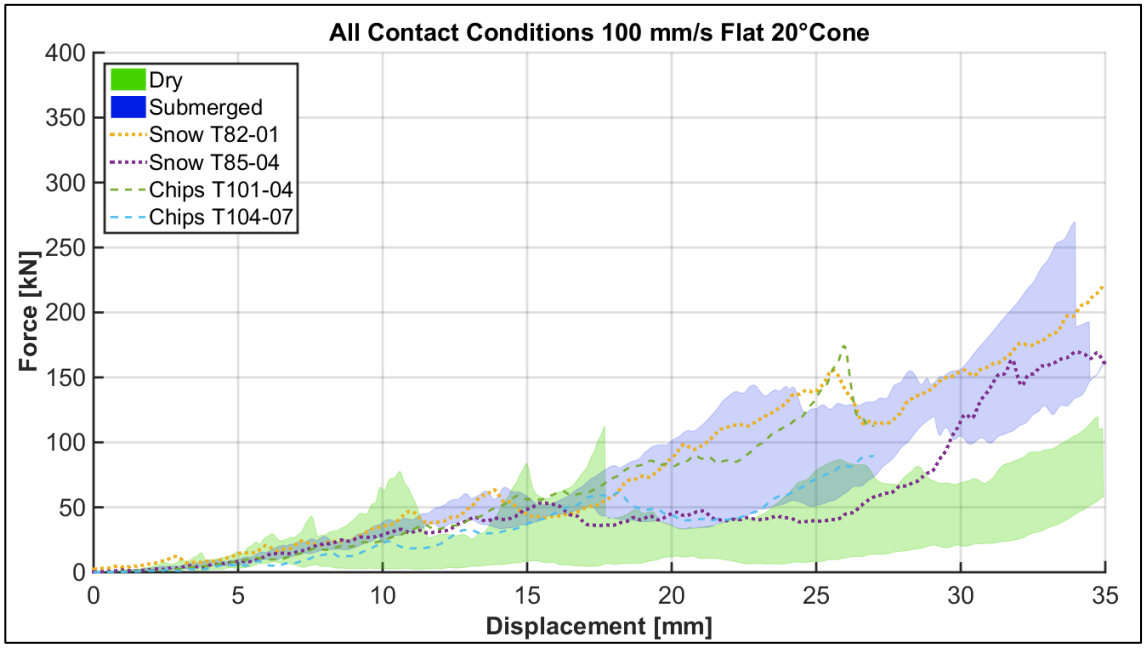

Figure 5.10: Flat plate, 100 mm/s, 20° ice specimens: force vs. displacement for all contact conditions. The shaded areas enclose all dry tests (6) in green and submerged tests (4) in blue.

Figure 5.11 shows constantly higher nominal pressures in submergence cases than in the dry condition, with very little overlap. Pressures in snow are comparable to those of submergence, and have a decreasing trend overall. Pressures for tests with granular ice, on the other hand, seem fairly constant; they are first lower than those of submergence and snow, but later become of similar magnitude. Dry pressures are consistently the lowest of all contact conditions, except for minor intersections. The overall nominal pressures decrease from between 5.7 MPa and 19.9 MPa at an area of 1000 mm^2, to between 2.0 MPa and 9.3 MPa at larger areas.

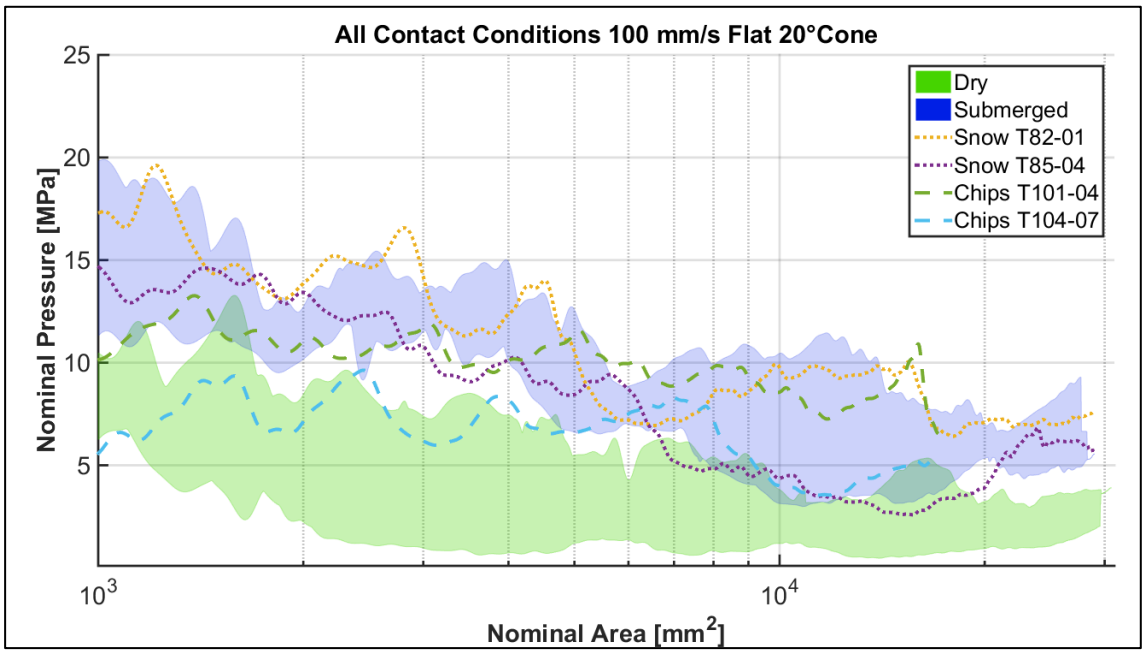

Figure 5.11: Flat plate, 100 mm/s, 20° ice specimens: nominal pressure-area curves for all contact conditions. The shaded areas enclose all dry tests (6) in green and submerged tests (4) in blue.

At 100 mm/s rate, sixteen tests were accomplished with 30° ice cones: 6 dry, 6 submerged, and 2 each with snow and granular ice. The analysis only comprises 5 dry tests since test D T09-04 was excluded as an outlier. It had exceptionally low forces for a displacement up to 26 mm, for unknown reason.

At 30° ice cone angle, the surface contact condition leads to evident force differences (Figure 5.12) similar to the 20° case. Overall, forces in submergence exceed those of a dry environment, although there is some overlap in early and late test stages. Tests involving snow and granular ice are similar to each other, as well as to the dry condition for displacement of up to approximately 36 mm. Later on in the test, the forces in the chips tests diverge and approach those of submerged tests. Snow tests remain similar to

dry tests, and for both contact conditions, the forces increase less with advancing displacement compared to submerged or granular ice conditions.

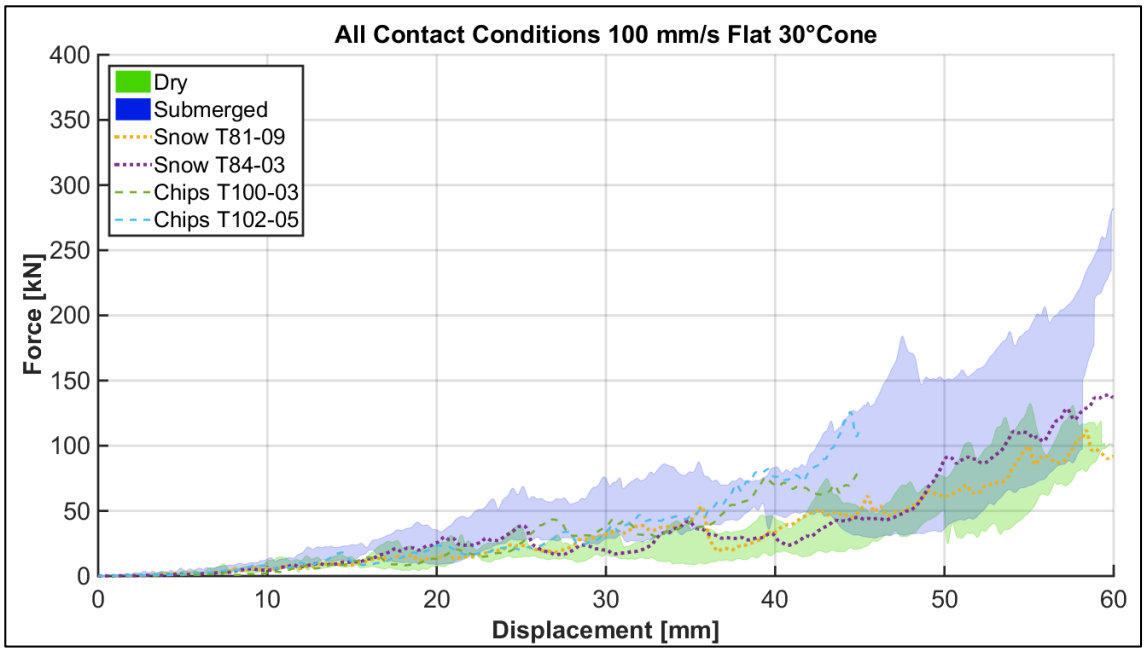

Figure 5.12: Flat plate, 100 mm/s, 30° ice specimens: force vs. displacement for all contact conditions. The shaded areas enclose all dry tests (5, excluding D T09-04) in green and submerged tests (6) in blue.

Figure 5.13 displays some overlap of nominal pressures for dry and submerged conditions, but generally higher pressures in submergence. Pressures for snow and granular ice are similar to the dry environment. Pressure in the case of granular ice is rather constant and at advanced displacements closer to submergence. Overall nominal pressures range between 3.1 MPa and 12.9 MPa at the beginning, and slightly decline to between 2.0 MPa and 6.4 MPa at the end of the range of displacement considered.

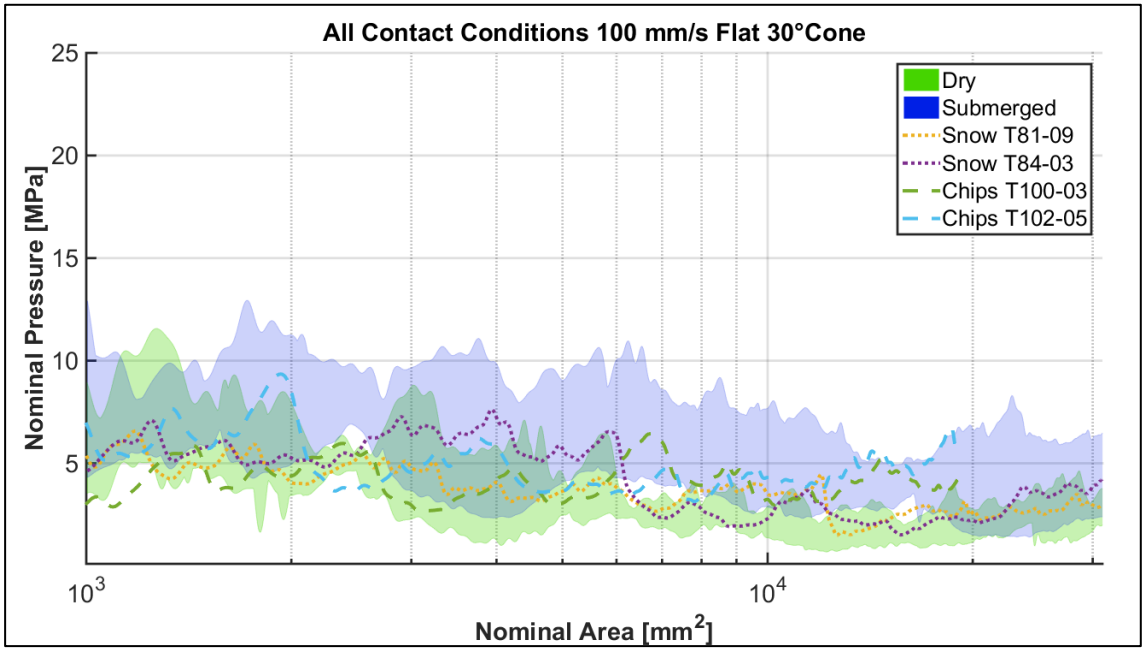

Figure 5.13: Flat plate, 100 mm/s, 30° ice specimens: nominal pressure-area curves for all contact conditions. The shaded areas enclose all dry tests (5, excluding D T09-04) in green and submerged tests (6) in blue.

Appendix B4 contains figures displaying single curves for force-displacement histories and pressure-area relationships for both ice specimen angles at 100 mm/s indentation rate. In order to provide a comprehensive picture, test D T09-04 is shown even though it is excluded from the analysis.

5.1.3 Local Pressure Pattern and Contact Area (Tactile Pressure Sensors)

Measurements with tactile pressure sensors were included in 25 out of the 71 test performed and are identified with superscript "P" in Table 5.1. Analyses of measured real contact area and pressure patterns are concentrated on low and high indentation rate tests only. Pressure patterns for the medium indentation rate are provided in Appendix B5, together with additional images for low and high indentation rates. All images are processed with a 5x5 interpolation and scaled to a maximum pressure of 110 in raw units

(see scale in Figure 5.14) to facilitate the comparison among different test scenarios. The red colors indicate the zones of high pressures (HPZs) and blue colors zones of low pressures (LPZs).

5.1.3.1 Indentation Rate: 1 mm/s

In the previous section 5.1.2.1, a trend of higher forces was observed in submergence compared to those for the dry environment at 1 mm/s indentation rate and for 20° ice cone angle. Even higher forces were noticed for snow and granular ice environments. Although the tendency was less pronounced at 30° ice cone angle, pressure sensor readings for that cone angle are displayed since the figures have better quality. Figure 5.14 shows one example for each condition at approximately 37.65 mm penetration depth: on the top left and right are dry and submerged environments, on the bottom left and right are snow and granular ice contact conditions.

This instance is selected as it is the last evaluable frame of the submerged test (Appendix B5 contains further examples at 10.30 mm, 23.98 mm, 45.98 mm and 54.31 mm). At this point, the dry test (top left) has one large continuous HPZ, and outwards diminishing pressures. In the other testing environments, the HPZs are less established and overall smaller. Granular ice (bottom right), has the least homogenous, but rather irregular pressure pattern with almost no HPZs. Figure 5.14 also reveals another important influence of the different contact conditions: the dry test has the smallest of all contact areas; submergence, snow, and granular ice have larger contact areas, in that ascending order, and valid for both ice cone angles.

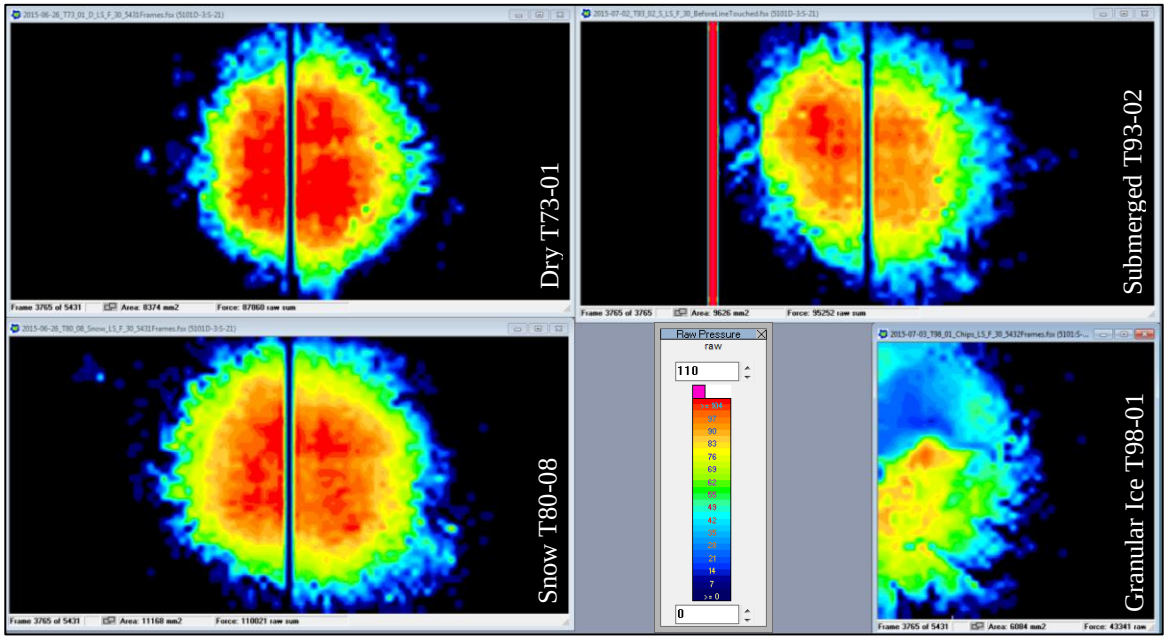

Figure 5.14: Flat plate, 1 mm/s, 30° ice cones: pressure patterns in approx. 37.65 mm penetration depth for all contact conditions. (Top) left: dry T73-01, right: submerged T93-02; (Bottom) left: snow T80-08, right: granular ice T98-01 (the granular ice case is for one sensor (half contact area) only).

Figure 5.15 and Figure 5.16 display measured contact areas vs. displacement for the flat indentation plate with 20° and 30° ice specimens at 1 mm/s in all conditions. For test in the granular ice condition, only one pressure sensor was available, thus only half the area compared to other tests. In order to be consistent, for all tests half the measurement is taken (right pressure sensor) and subsequently doubled. This is justified due to a symmetric contact area at this speed for the flat plate. It still introduces minor deviations from the complete contact area (consisting of measurements of two working sensors), as a comparison revealed.

From Figure 5.15 it can be noticed that for 20° ice cone angle the contact areas for snow (light blue, orange) are very similar. They are clearly above the nominal contact area (black), which they cross after 25.5 mm displacement. By viewing the pressure sensor

readings, it was observed that at this point and even earlier, the actual contact area began to exceed the area that was covered by the pressure sensors. The contact areas of granular ice (magenta) and submergence (dark blue) are also larger than the nominal area, but only up to approximately 19 mm displacement. The dry test (green), on the other hand, apart from the first 4 mm penetration depth is considerably below the nominal area.

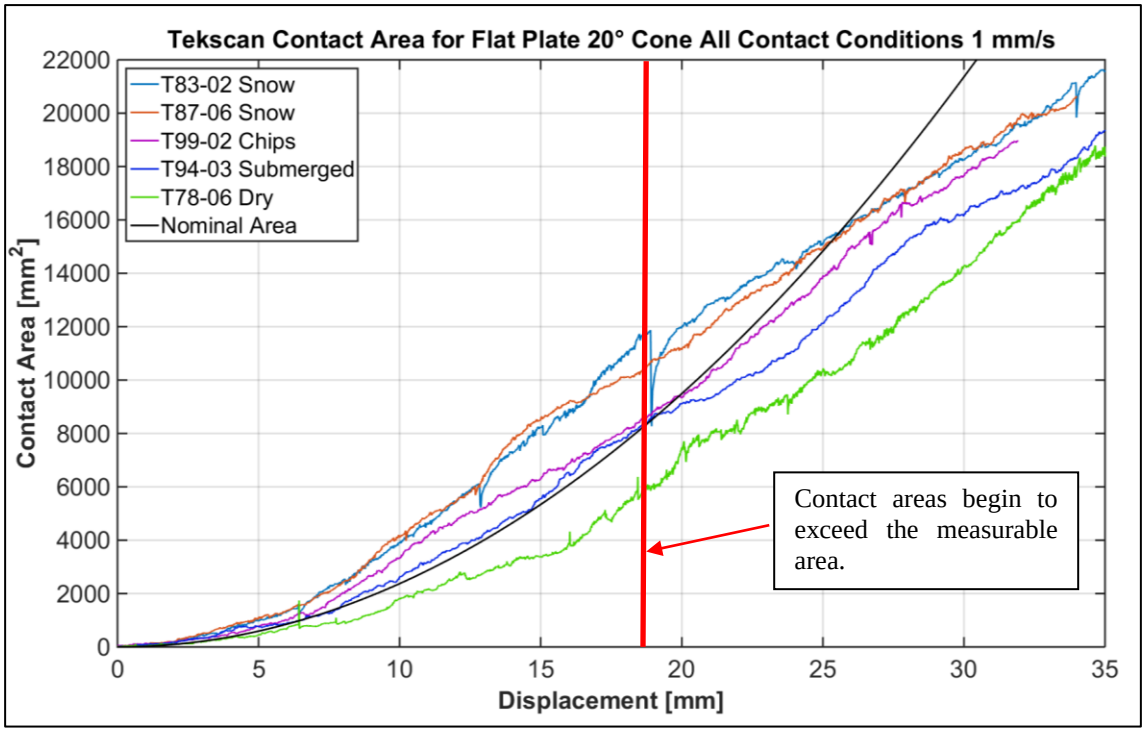

Figure 5.15: Flat plate, 1 mm/s, 20° ice specimen angle, all contact conditions: contact area vs. displacement from pressure sensor measurements. Note that all curves display the doubled contact area of one pressure sensor measurement.

Starting from this point, a distinction between two contact areas is made: the nominal area that expresses the calculated contact area at the ice-indenter interface as a function of displacement; and the (actual) contact area as it is derived from measurements with the tactile sensors.

Table 5.3 lists the ratios between nominal and actual contact areas for each environmental condition, averaged for displacements between 6.5 mm and 17.5 mm. This limitation is necessary to exclude parts of the data where the contact area exceeds the sensing area. For a standardized approach, applicable for both ice cone angles, the displacement range is defined with respect to the area range that is used for the nominal process pressure analysis, more precisely the corresponding displacement range (Table 4.2). The lower margin equals the minimum penetration (6.5 mm and 10.3 mm for 20° and 30°cone angles) and the upper margin is half the maximum considered displacement (35 mm and 60 mm). Within these limits, the contact areas for both ice cone angles remain within the sensing area. In Table 5.2 the values for nominal and measured contact areas are the sum of areas within the defined range.

Table 5.2 shows identical ratios for both snow tests. The actual contact areas are 35 % larger than the nominal area. The measured contact area of the granular ice (chips) test is 20 % larger, while it is only 6% for the submergence case. The actual contact area of the dry test, on the other hand, is only about half of the nominal area.

Table 5.2: Flat plate, 1 mm/s, 20° ice cones, all conditions: comparison of the nominal contact area with individual contact area measurements from the tactile pressure sensors.

Depth	**Condition**		**Dry**	**Submerged**	**Snow**		**Chips**
[mm]	**Test**	**Nominal**	**T78-06**	**T94-02**	**T83-02**	**T87-06**	**T99-02**
6.5 to 17.5	**Area [mm^2]**	4029850	2723864	4290602	6193520	6193520	5023608
	Ratio	1.00	1.48	0.94	0.65	0.65	0.80

Figure 5.16 shows the measured contact areas for 30° specimens. The actual contact areas of the snow (orange) and the granular ice (magenta) tests are very similar. Both exceed

the nominal area until a displacement of 35 mm. This is close to the point when the contact areas become larger than the measurable area. At that cone angle, the contact areas of the submerged and the dry tests are similar and both distinctly smaller than the nominal area.

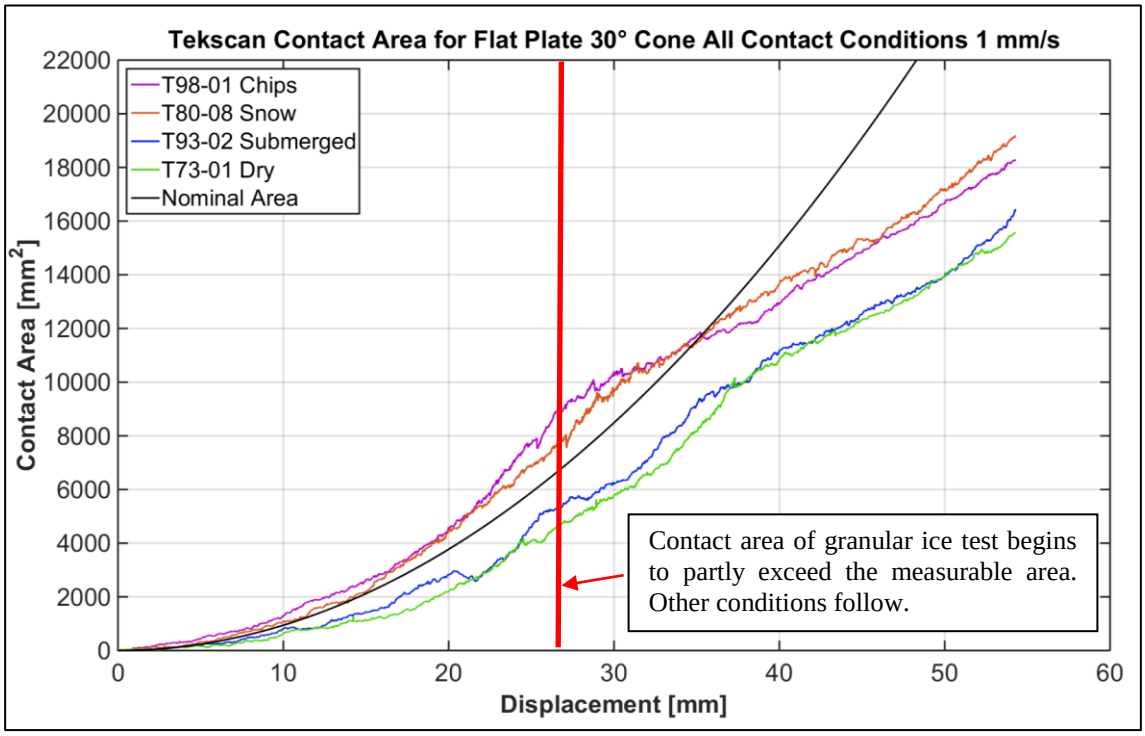

Figure 5.16: Flat plate, 1 mm/s, 30° ice specimen angle, all contact conditions: contact area vs. displacement from pressure sensor measurements. Note that all curves display the doubled contact area of one pressure sensor measurement.

Table 5.3 gives the ratios for contact areas between 10.3 mm and 30.0 mm displacement. Within this range, the contact areas from chips and snow were 21 % and 13 % larger than the nominal area respectively, but dry and submerged cases were smaller by 56 % and 37 %.

Table 5.3: Flat plate, 1 mm/s, 30° ice cones, all conditions: comparison of the nominal contact area with individual contact area measurements from the tactile pressure sensors.

Depth [mm]	**Condition**		**Dry**	**Submerged**	**Snow**	**Chips**
	Test	**Nominal**	**T73-01**	**T93-02**	**T80-08**	**T98-01**
10.3 to 30.0	**Area [mm^2]**	8159733	5216688	5962574	9406340	10280890
	Ratio	1.00	1.56	1.37	0.87	0.79

5.1.3.2 Indentation Rate: 100 mm/s

As previously discussed (section 5.1.2.3), the disparity between dry and submerged contact conditions was more evident at the high indentation rate. This is also clearly reflected in the pressure sensor readings. The pressure patterns of snow and granular ice, on the other hand, are only marginally different from the dry condition. Therefore, the analysis is concentrated on dry and submerged contact conditions. For a more comprehensive picture refer to Appendix B5 with the series of subsequent pressure pattern, as well as with two examples for snow and granular ice conditions (at penetration depths of 22 mm and 39 mm).

Figure 5.17 shows pressure patterns of 20° ice specimens at approximately 23 mm (last evaluable frame of the submerged test) for dry (left) and submerged (right) contact conditions. The difference between both contact areas is significantly large. For the dry test, the pressure map comprises of three narrow branches. The blue dots in the surroundings are small ice particles that are expelled at that time instant. In contrast, the contact area in the submergence case is one large circular area, encompassing a wide contiguous line-like HPZ plus several smaller ones. The overall shape in the submergence case is comparable to observations from slow speed tests (Figure 5.14)

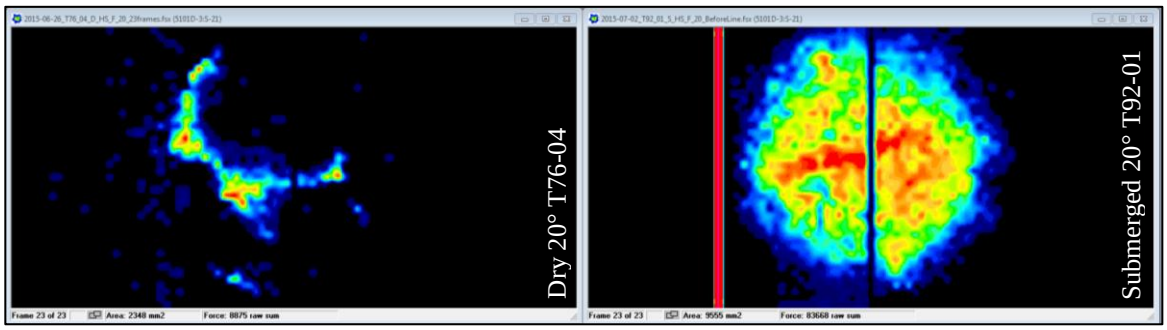

Figure 5.17: Flat plate, 100 mm/s, 20° ice cones: pressure patterns in approx. 23 mm penetration depth in dry (left, D T76-04) and submerged (right, S T92-01) contact conditions. The images show a clearly larger contact area in the case of submergence.

These findings are not as pronounced in the pressure patterns from the 30° ice specimens in Figure 5.18 (displacement of approximately 40 mm). Still, the contact area of the submerged test (right) is more compact and less stretched out than the one of the dry test (left). For the latter, the overall branch-like appearance, characterising this indentation rate, is more distinct, but local HPZs (red color) can be seen in both images.

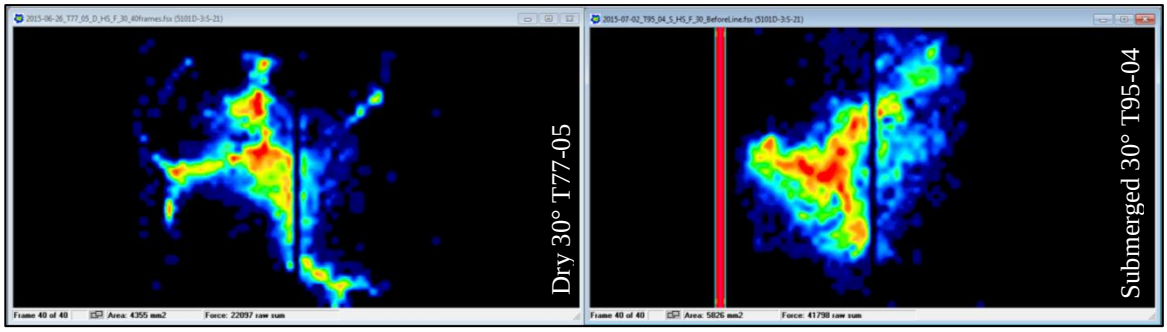

Figure 5.18: Flat indentation plate, 100 mm/s, 30° ice cones: pressure patterns in approx. 40 mm penetration depth in dry (left, D T77-05) and submerged (right, S T95-04) contact conditions.

The progress of contact area vs. displacement is plotted in Figure 5.19 and Figure 5.20. The curves are based on complete contact area measurements from two tactile pressure sensors. Some recordings of tests with granular ice are available, but in this case the contact area was not doubled as in the case of the low speed tests. The contact area at

100 mm/s indentation rate is usually asymmetrical and it is not believed that the same approach would be a reasonable representation. Consequently, only tests with complete measurements are evaluated.

Furthermore, there are two aspects worth mentioning in view of submerged tests: first, the contact area data is corrected by 284 mm^2, which was necessary due the offset caused by the defective sensel column (the red line in above figures). This offset was constant in all tests involving the Tekscan measurements after the damage occurred. Second, the contact area data does not comprise of the entire test length, since measurements were highly biased after the point when the contact area approached the trace of broken sensels and were neglected during the analysis.

The submerged contact area (blue) in Figure 5.19 is slightly smaller but fairly close to the nominal area (black). The dry contact area (green) is much smaller. This is also expressed in the contact area ratios in Table 5.4 for displacements between roughly 6.0 mm and 17.0 mm (the deviation to the range of 6.5 mm to 17.5 mm for low speed tests is due to the low data resolution that was limited by the maximum sampling rate with 100 Hz and prevented more precise determinations in high speed tests). Within that range, the contact area of the submerged test is 87 %, while the dry test is not even 39 % of the nominal area. This dry test is presumed to be somewhat abnormal, but it is the only available pressure sensor reading for that scenario.

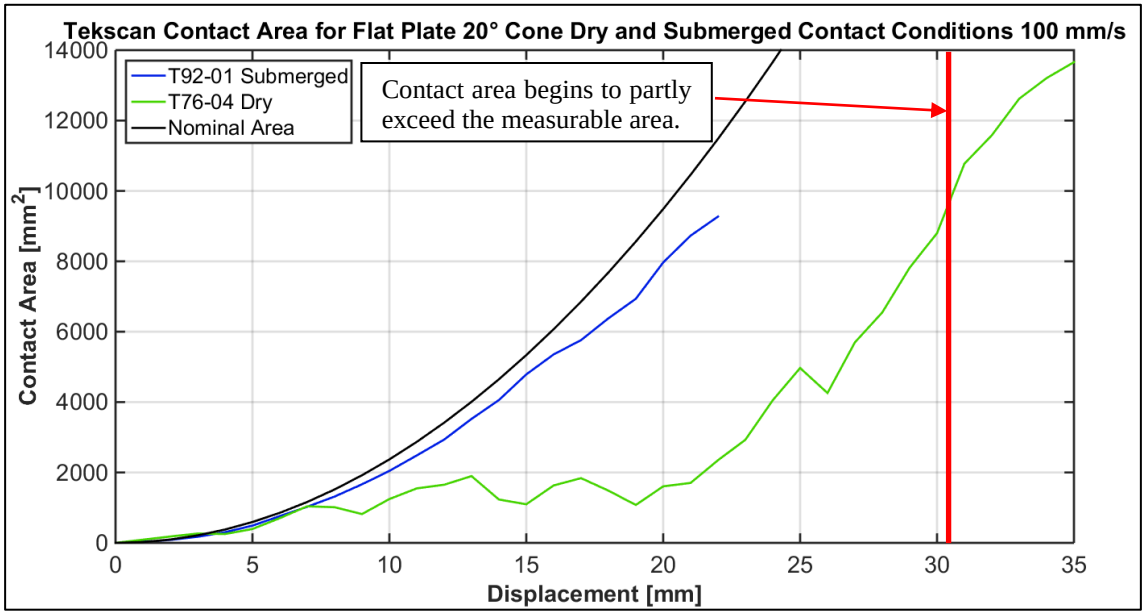

Figure 5.19: Flat plate, 100 mm/s, 20° ice specimen angle, dry and submerged contact conditions: contact area vs. displacement from pressure sensor measurements. Note that the contact area of the submerged test is corrected by 284 mm^2 to eliminate the offset that was caused by a defective sensor column.

Table 5.4: Flat plate, 100 mm/s, 20° ice cones, dry and submerged conditions: comparison of the nominal contact area with individual contact area measurements from the tactile pressure sensors.

Depth [mm]	**Condition**		**Dry**	**Submerged**
	Test	**Nominal**	**T78-06**	**T94-02**
6.0 to 17.0	**Area [mm^2]**	41619	16110	36204
	Ratio	1.00	2.58	1.15

In the experiments with the 30° ice specimen angle, the contact areas of the dry, submerged, and snow testing conditions are considerably below the nominal area. This is evident in Figure 5.20 and in the associated area ratios in Table 5.5. Interestingly, the conditions are very similar and are all roughly 2.2 times smaller compared to the nominal area (within the defined displacement range).

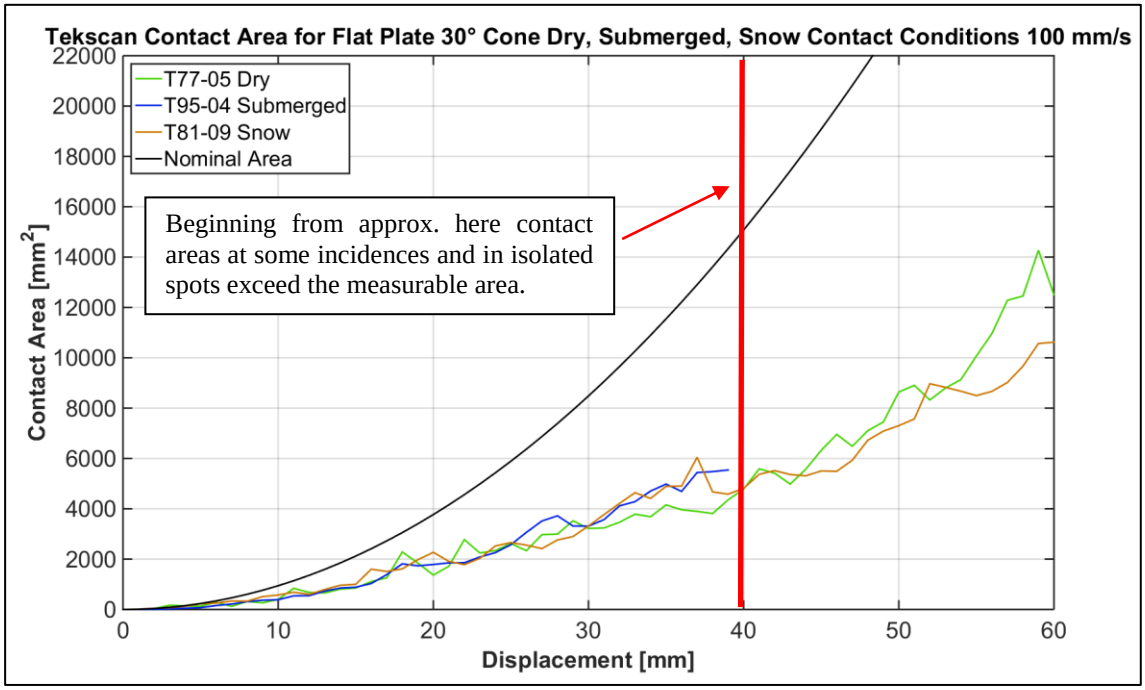

Figure 5.20: Flat plate, 100 mm/s, 30° ice specimen angle, three contact conditions: contact area vs. displacement from pressure sensor measurements. Note that the contact area of the submerged test was corrected by 284 mm2 to eliminate the offset that was caused by a broken sensor column.

Table 5.5: Flat plate, 100 mm/s, 30° ice cones, three contact conditions: comparison of the nominal contact area with individual contact area measurements from the tactile pressure sensors.

Depth [mm]	**Condition**		**Dry**	**Submerged**	**Snow**
	Test	**Nominal**	**T77-05**	**T95-04**	**T81-09**
10.0 to 30.0	**Area [mm^2]**	86425	38838	39248	38433
	Ratio	1.00	2.23	2.20	2.25

For a better understanding of the relationship between nominal and measured contact areas and the way the true contact area develops as a test proceeds, the proportion vs. displacement is plotted in Figure 5.21. There is a tendency of increasing ratios, implying an actual contact area that is progressively smaller than the nominal area with further penetration.

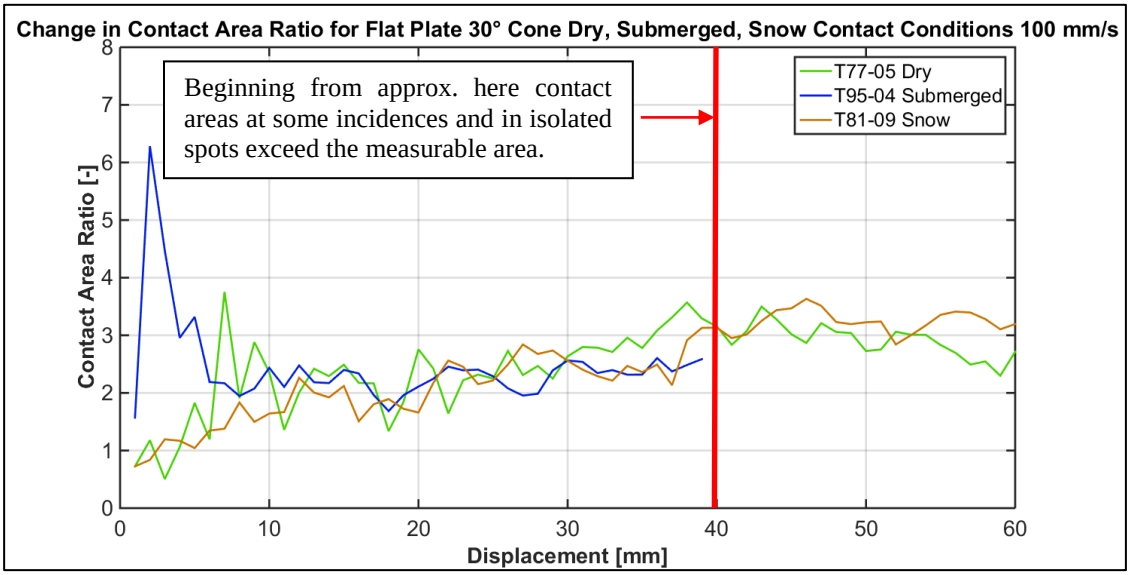

Figure 5.21: Flat plate, 100 mm/s, 30° ice specimen angle, three contact conditions: change in ratio between nominal and measured contact areas with displacement.

5.1.4 General and Microstructural Observations

The following paragraphs discuss visual observations focused on 1 mm/s and 100 mm/s indentation rates. The evaluated sources include high speed camera (HSC) footage, still photos of samples after test completion, and thin sections.

5.1.4.1 General Observations – During Testing: Ice Debris Formation, Ice Extrusion and Crack Propagation (HSC)

All tests were recorded with black and white high speed video camera (HSC). The footage is a valuable source to visually observe differences during ice crushing in dry and submerged conditions. Recordings of snow and granular ice tests could not be evaluated since the impact was entirely concealed by the material.

The images in Figure 5.22 are examples for 1 mm/s indentation rate and 20° cone angle at approximately 15.6 mm penetration depth. In the dry contact condition (left), the ice

specimen penetrating cracks, and broken off ice fragments are clearly visible. The ice debris was slowly pushed outwards and thereby further comminuted. In the submergence case (right), there are no evident cracks and single ice fragments are difficult to identify. In front (indicated in blue) are two detached ice pieces that only after some time floated to the water surface.

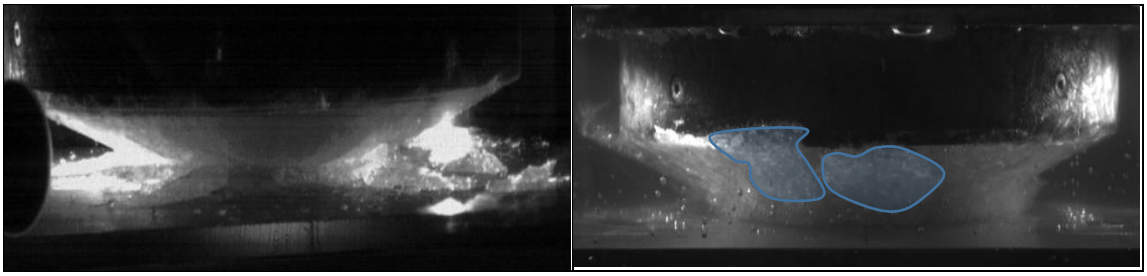

Figure 5.22: Flat plate, 1 mm/s, 20° ice specimens, dry (left, D T35-01) and submerged (right, S T94-03) contact conditions, approx. 15.6 mm penetration depth. Snap shots of HSC footage. Cracks and ice fragments are clearly visible in the dry environment. Ice debris is considerably less distinguishable in the submergence case.

Figure 5.23 shows two snap shots of a 30° ice specimen at displacements of approximately 18.9 mm and 35.1 mm, tested for a dry contact condition at 100 mm/s. In the top picture, cracks can be seen that penetrate the entire ice specimen and the ice debris that consists of small particles. The bottom image displays large ice fragments breaking off and unrestrictedly moving away from the contact zone.

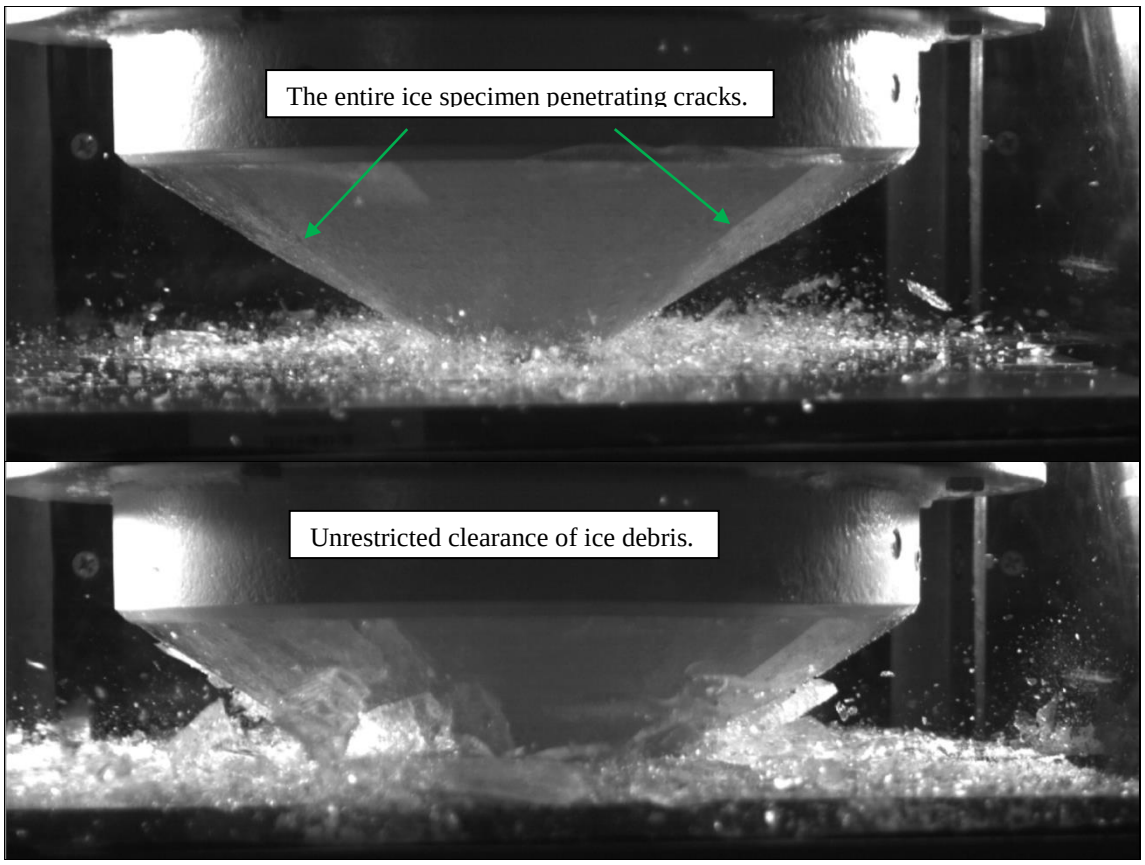

Figure 5.23: Flat plate, 100 mm/s, 30° ice specimen, dry D T77-05. HSC footage. (Top) approx. 18.9 mm penetration depth; cracks occurred and penetrated the entire ice specimen. (Bottom) approx. 35.1 mm; large ice fragments break off and are freely extruded.

In the submergence case, the appeareance of ice crushing is very different. Ice fracture seems to remain more localized in vicinity to the contact area as indicated in Figure 5.24 (top). The adjacent area is darker, which may be due to water infiltrating the crack. Generally, crack propagation seems reduced or decelerated. By comparing the middle of Figure 5.24 (submerged) and the top of Figure 5.23 (dry) (that show comparabe displacements), the difference in ice debris constitution and extrusion patterns are obvious. Although both samples are pervaded by cracks, there are less ice spalls in the submergence case and the ice specimen in itself appears to be more intact. The ice debris seems cloud-like and its extrusion is restrained in extent and ejection velocity. This is

more evident in the bottom image of Figure 5.24, where extruding ice debris is still within the 25 cm diameter of the ice cone base, while it is widely spread in the dry case (Figure 5.23, bottom). In the submergence case, ice fracture seems to be more sequential, stepswise penetrating the specimen but rarely entirely.

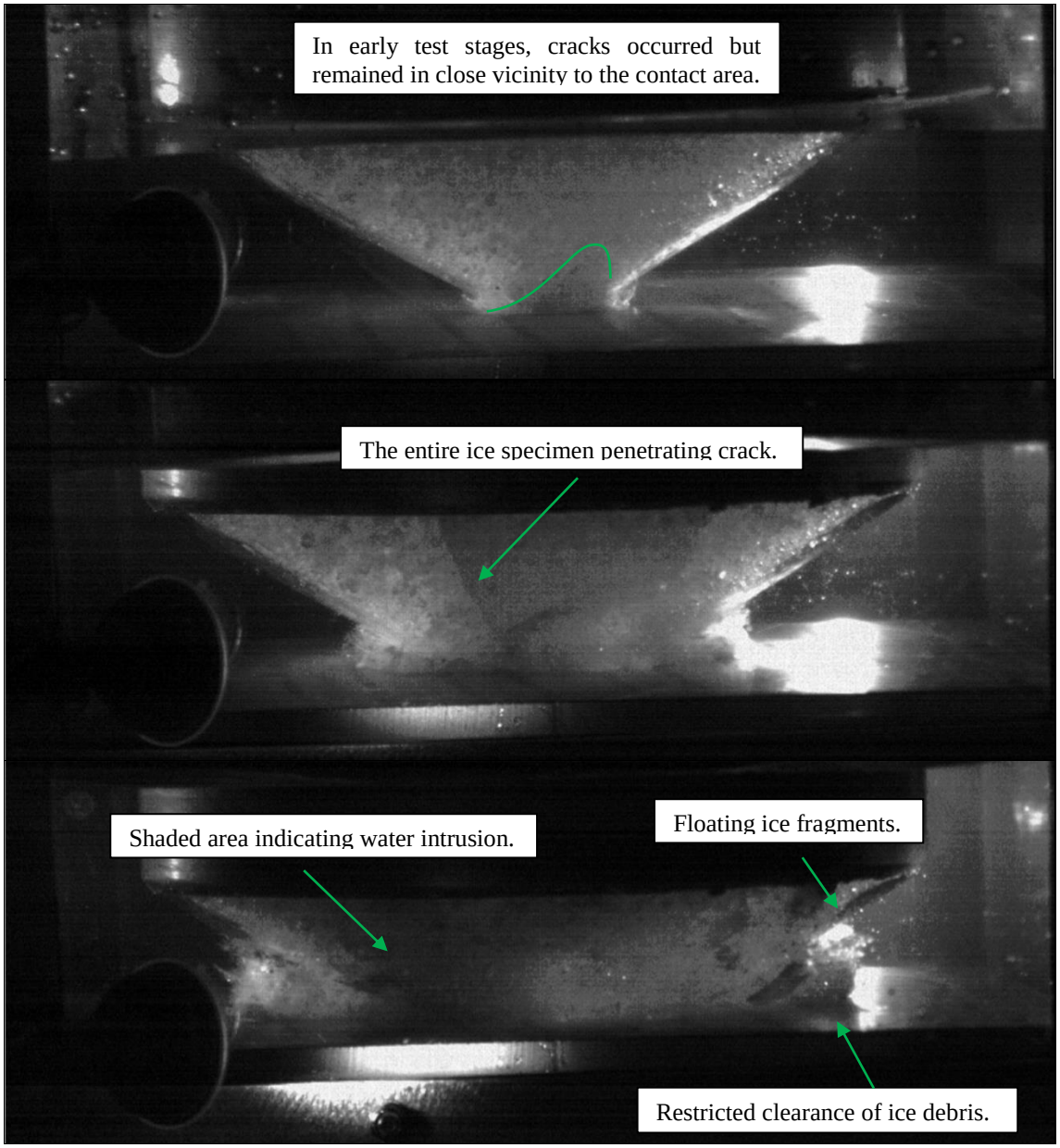

Figure 5.24: Flat plate, 100 mm/s, 30° ice specimen, submerged S T31-03. HSC footage. (Top) approx. 7.4 mm penetration depth; the impact affects the specimen localized at the cone tip. (Middle) approx. 20.4 mm; larger cracks occur, but the ice spalls remain in place. (Bottom) approx. 34.8 mm; cracks occurred and water intruded, visible in terms of the shaded areas.

5.1.4.2 General Observations – After Test Completion: Contact Area and Surface (Still Photos)

The effect of the different contact conditions is also evident in pictures taken of the ice samples after testing. In this section, only images for 20° ice cone angle tests at 1 mm/s and 100 mm/s indentation rate are discussed for all contact conditions. Photographs for 10 mm/s impact speed in dry, submerged, and granular ice contact conditions can be viewed in Appendix B6.

Figure 5.25 shows samples from low indentation rate (1 mm/s) tests. Displayed from the top to the bottom are dry, submerged, snow, and granular ice test cases. The final contact area is best visible in the photographs on the right hand side that are taken with back lighting. All samples have one large bright circular area in the centre. This is characteristic for low speed tests, where ductile and creep-like ice failure prevails. At the ice-indenter interface, the ice recrystallized from the middle, slowly expanding with progressive penetration. In the image of the dry sample (top), some large ice pieces are visible near the contact area. The transition between contact area and remaining ice material is marked by the distinct contrast of white and dark colors. In the photo of the submerged specimen, the transition zone is far less pronounced. There are fewer single ice pieces but the ice debris is slushy.

Dry **T78_06**	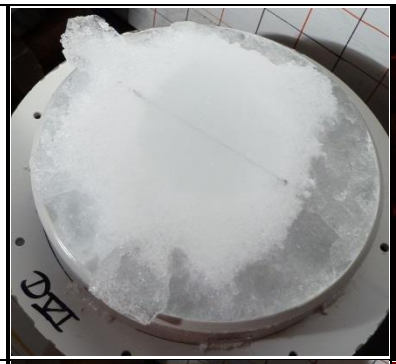	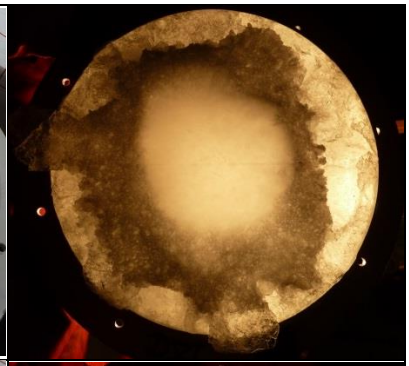
Submerged **T94_03**		
Snow **T83_02**		
Granular Ice **T99_02**		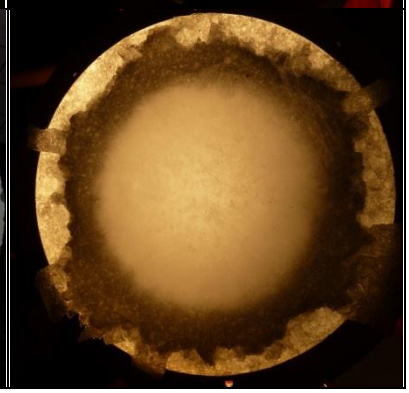

Figure 5.25: Flat plate, 1 mm/s, 20° ice specimens: images of samples after testing for each contact condition; on the left of indented surfaces, on the right with lighting applied from the back.

In Figure 5.25 (above), the images of snow and granular ice contact conditions appear similar at first with a fairly distinct transition between contact area and remnant ice. For granular ice, fragments near the contact area are better distinguishable. Despite the circumstance of often lower achieved penetration depths for snow and granular ice scenarios, the contact areas are larger than in the dry and submerged scenarios; the samples seem to have incorporated some of the adjacent material into their main body. At the low indentation rate, ice samples of dry and submerged tests that the tactile pressure sensors were used, generally displayed a defined imprint of the sensel array.

The images in Figure 5.26 are taken for 20° samples, crushed at 100 mm/s. As earlier discussed, this indentation rate is characterized by sudden fracture and spalling events causing branch-like pressure patterns. These are visible in the still photos of the sample surfaces in Figure 5.26. The bright colors indicate high pressure zones (HPZs), where most of the force was transmitted to the structure and that are sourrounded by low pressure zones (LPZs), darker in color. The pattern can be best recognized in the image from the granular ice test case (bottom right). The bottom left picture shows distinct fractures in the remaining ice body around the plateu-like contact area. Similar pronounced fractures are visible for snow and dry contact conditions. In the submergence case, fractures are less evident.

Dry **T76_04**	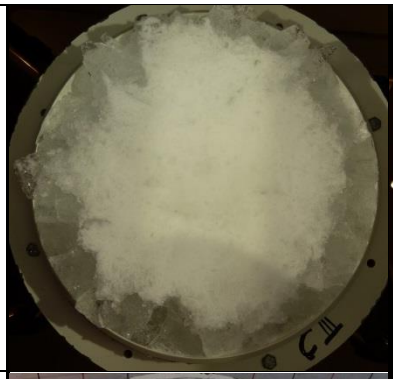	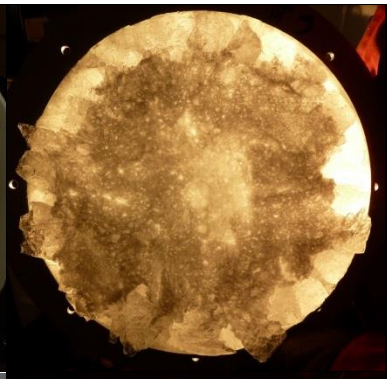
Submerged **T92_01**		
Snow **T82_01**		
Granular Ice **T101_04**	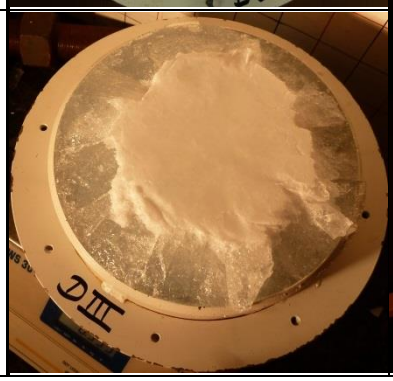	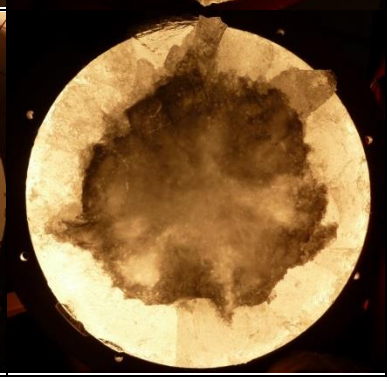

Figure 5.26: Flat plate, 100 mm/s, 20° ice specimens: images of samples after testing for each contact condition; on the left of indented surfaces, on the right with lighting applied from the back.

5.1.4.3 Microstructural Observations

The superscript “T” in Table 5.1 designates tests where thin sections were completed and that can be viewed in Appendix B7. Since the largest difference in ice loads due to dry and submerged contact conditions was observed at the high indentation rate (100 mm/s), only those results are discussed in this chapter.

Figure 5.27 shows examples for 20° ice cone angle, for dry (left) and submerged (right) contact conditions. At the top, where specimen and indentation plate were in contact, a layer of highly damaged ice was formed resulting in the white color due to light scattering. For the dry contact condition (left images) it is difficult to define a clear margin between the damaged ice and less affected ice. The region seems to extend to approximately 4 cm depth. In the submerged case (right images), the damaged region appears restricted to the top 2.0 cm to 2.5 cm.

The photographs taken with side lighting reveal cracks and fractures. It can be seen that the dry sample is deeply permeated by a significant number of micro-cracks and is more deeply affected than the submerged sample. A similar pattern is found for some of the ice samples tested with snow or granular ice (see Appendix B7). However, at the high indentation rate, variations or randomness in ice failure and force measurements can be substantial and only few thin sections are available. The observations made are somewhat specific for the two presented samples but may differ in other cases.

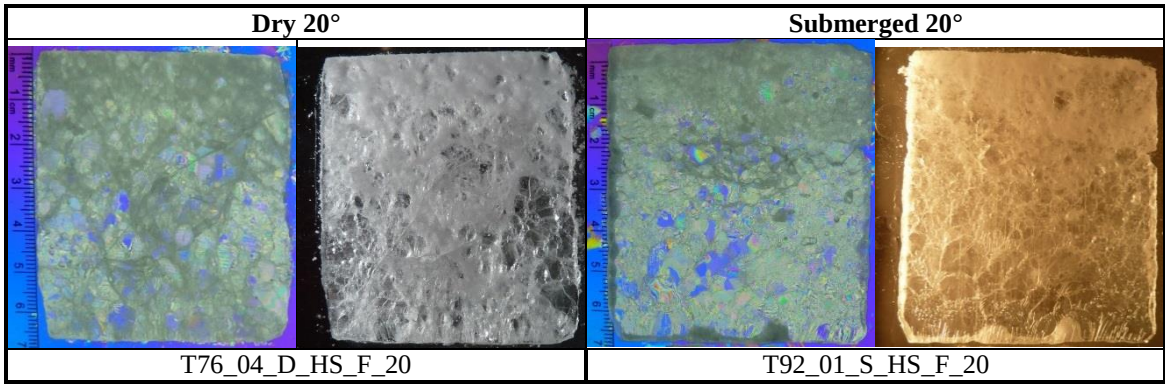

Figure 5.27: Flat plate, 100 mm/s, 20 ° ice samples: thin sections of dry (left) and submerged (right) conditions. The images show the sections between a cross-polarized filter on the left, and with side lighting applied on the right.

5.1.5 Multiple Regression Analysis

A multiple regression analysis was performed to indicate main factors and reveal important interactions of the varied parameters. In an initial analysis, the ice age was included as a factor to test its influence. The obtained models were less significant for the defined responses ("Force Mean Overall", "Mean Force 1000", "Mean Pressure 1000", "Pressure Max 1000") and thus ice age was precluded. Moreover, tests at 10 mm/s are left out of the analysis, because at this rate a small number of tests were performed and not all contact conditions were investigated. An analysis with this test speed was found not only to lead to poorer model qualities, but to produce misleading outcomes (i.e. the models ruled out an interaction of contact condition and indentation rate, which was counter to earlier findings). For these reasons, subsequently presented results are based on three factors (indentation rate, contact condition, and ice cone angle) and interactions between each pair of them. Three factor interactions are found to be insignificant.

For snow, and in particular for granular ice conditions, the maximum anticipated penetration stroke was often not accomplished. In these cases, the data lacks information

at advanced displacements, when the force is generally the highest, and this also prevents the determination of the nominal pressure. It is therefore likely that the importance of snow and granular ice conditions is underestimated in the regression models.

The residual plots (Appendix B8) do not indicate any deviations from the normal distribution, constant variance or independence of the data. Therefore no data transformation is required. All the main effects included in the models are highly significant (0 or 0.001), and also interactions generally are well below the significance level of α = 0.15 (Table 5.6). For all models, the lack of fit is insignificant and reasonable R^2 are obtained (Table 5.7), suggesting good model qualities.

Table 5.6: P-Values for factors and factor interactions of regression models at significance level α=0.15 for the flat indentation plate.

Response	**P-Value**					
	Factors and Interactions					
	Cone Angle	**Condition**	**Indentation Rate**	**Cone Angle x Condition**	**Cone Angle x Indentation Rate**	**Condition x Indentation Rate**
Force Mean Overall	0	0	0	0.016	0.123	0.013
Force Mean 1000	0	0	0	0.013	0.137	0.010
Pressure Max 1000	0	0.001	0	0.034	-	0.017
Pressure Mean 1000	0	0	0	0.001	0.062	0.000

Table 5.7: Model lack of fit, R^2, R^2 adjusted and R^2 predicted of linear regression models at significance level α=0.15 for the flat indentation plate

Response	Model Lack of Fit	R [%]		
		Square	Square Adjusted	Square Predicted
Force Mean Overall	0.74	89.91	87.10	82.13
Force Mean 1000	0.78	90.29	87.58	82.76
Pressure Max 1000	0.35	72.48	65.60	56.97
Pressure Mean 1000	0.83	91.55	89.19	74.72

The main effects for the response means are displayed in Figure 5.28, on the top for the forces and on the bottom for the pressures. Each graph shows the influence of ice cone angle (left), contact condition (middle), and indentation rate (right). The trends are fairly consistent. A steep ice cone angle of 30°, as well as the high indentation rate (100 mm/s) always causes lower force and pressure responses. Observing the contact conditions, submergence constantly yields higher force and pressure responses than the dry condition. For mean nominal pressure, granular ice (chips) results in a higher response compared with submergence, but responses are lower regarding forces (presumably due to the lower displacement that was achieved in the tests). Nevertheless, the highest results are always obtained for snow, while the dry condition generally has the lowest.

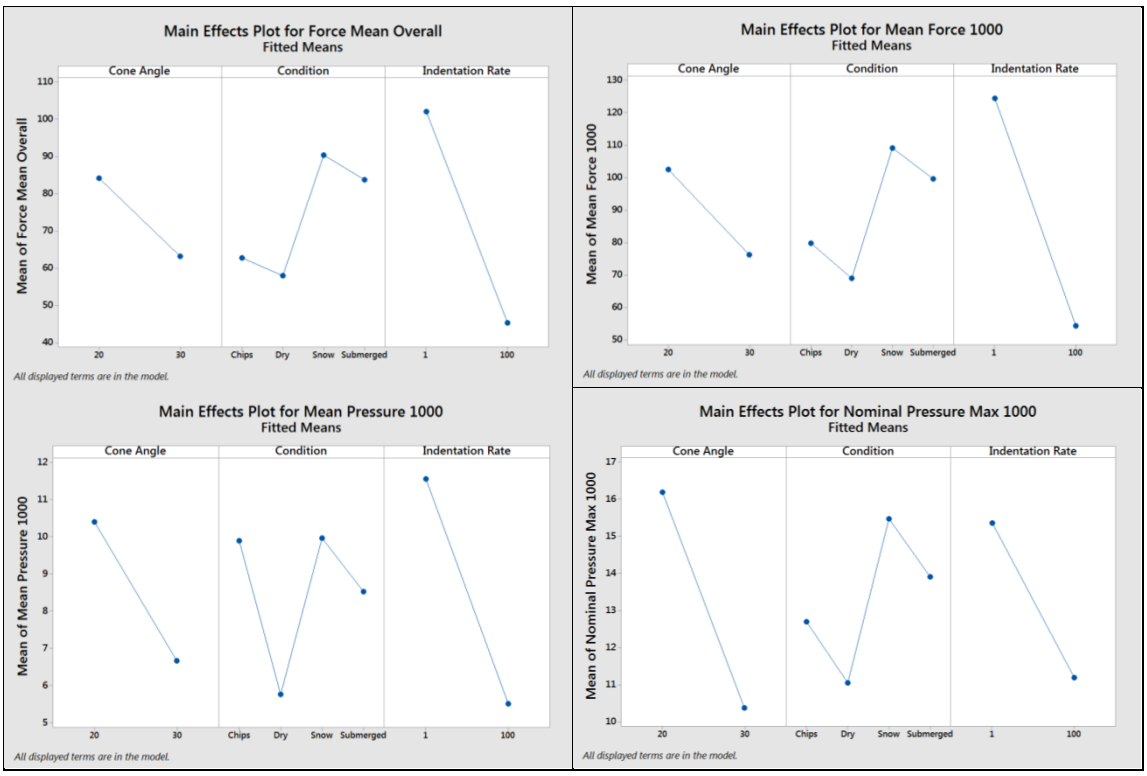

Figure 5.28: Overview of main effects on the means of the four responses for the flat indentation plate (α=0.15, stepwise selection of model terms, no data transformation).

Figure 5.29 shows two factor interaction plots, on the top left of cone angle and contact condition, on the bottom left of cone angle with indentation rate, and on the bottom right of contact condition and indentation rate.

Starting with the interaction of ice cone angle and contact condition, going from a 20° to 30° ice cone angle has the most effect on the nominal maximum pressure. It causes lower responses for all contact conditions, but especially for snow (green line). The interaction of cone angle and indentation rate is similar for all responses, but was irrelevant in terms of the nominal maximum pressure (a gray background indicates that this term was excluded from the model). In view of the interaction between contact condition and indentation rate, snow consistently has the highest responses at 1 mm/s indentation rate

(blue line). At this rate, submergence causes high responses as well, and this is also prevalent for granular ice (chips). In the granular ice tests the maximum anticipated displacement was not accomplished. Therefore, the responses for the granular ice condition are likely to be underestimated. In fact, it is reasonable to speculate that the presence of granular ice may be more important than submergence at the low indentation rate. The dry contact condition always has the lowest response. This is also true at 100 mm/s indentation rate (red line). At this speed, the submergence condition has the highest responses, followed by snow. Again, granular ice is presumably underestimated, but a tendency of higher responses (see mean pressure in Figure 5.29, bottom right) can be recognized, and responses are still above those of the dry condition.

For more detail refer to Appendix B8, which provides the full regression equations, as well as plots for residuals, main effects and interactions for each response, and listings of the coefficients for each factor and interaction.

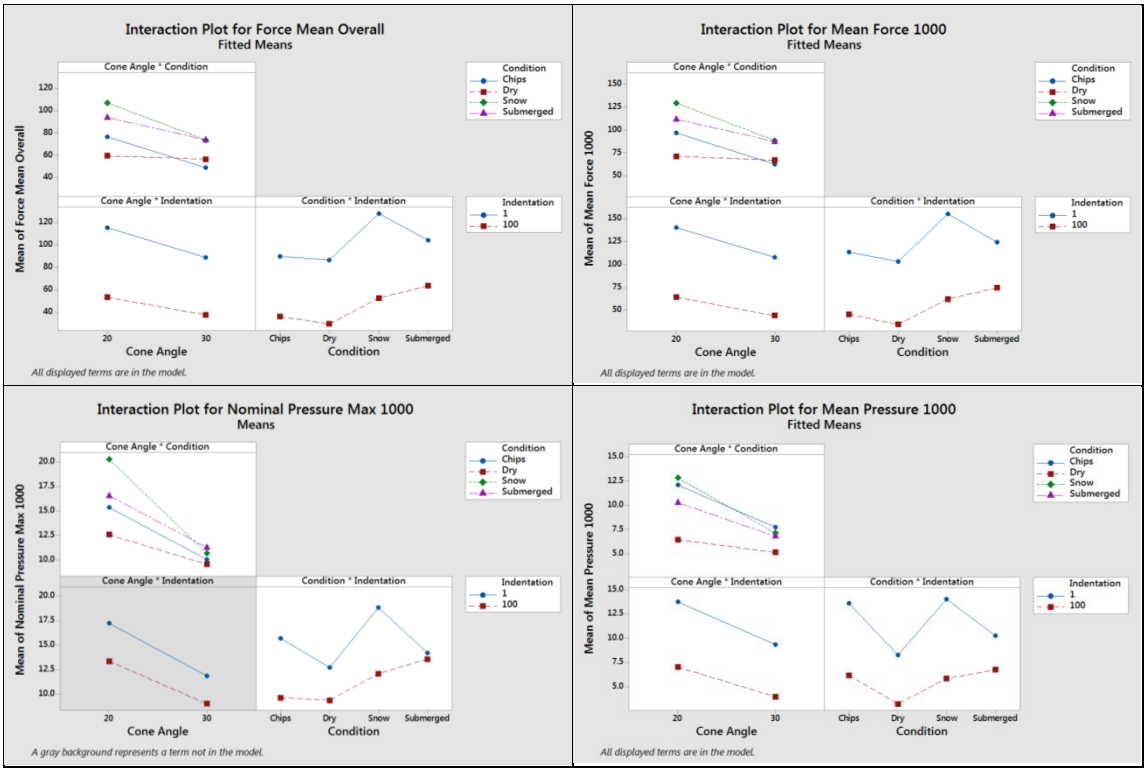

Figure 5.29: Overview of factor interactions for the four responses for the flat indentation plate (α=0.15, stepwise selection of model terms, no data transformation).

5.1.6 Summary and Discussion

5.1.6.1 Force

In low speed tests (1 mm/s), force measurements showed a trend of being higher in submergence cases compared to the dry contact condition. The difference was more pronounced at 20° than at 30° ice cone angle, where there was more overlap. For both ice cone angles, the forces obtained with snow or granular ice on the indenter surface, were as high as or even above those of the submergence cases.

Medium speed tests (10 mm/s) involved mainly dry and submerged conditions, and only one test with granular ice for each ice specimen angle was carried out. For 20° ice cones, dry and submerged forces considerably overlapped, and the granular ice test was in the

mid-range of the forces. For 30° cone angle, starting from about half of the maximum displacement (30 mm), forces in submergence cases clearly exceeded those in the dry environment. Again, the test with granular ice was in the medium range but had a tendency of being closer to the dry condition at advanced displacements.

In high speed tests (100 mm/s), the effect of submergence was by far the most evident. Typically, forces in submerged tests exceeded those of dry tests, and the difference increased with increasing penetration depth. The disparity was particularly pronounced at the 20° ice cone angle. In that case, also one snow and granular ice test produced forces that were at the high end of the submerged tests. The second snow and granular ice tests followed the pattern of the first ones, up to approximately half the maximum displacement (17.5 mm), but were subsequently low and at the upper end of the dry tests. Towards the end of the tests, forces picked up and approached the other measurements for these conditions. For 30° ice specimens, forces in dry and submerged tests were close, but those from the submerged condition generally higher. At advanced displacement (42 – 60 mm), there was more overlap. Forces in snow tests were at the high end of the dry forces. The behavior of the forces for granular ice was less consistent. Up to a displacement of approximately 25 mm, the forces were at the high end of the dry forces. As the experiments proceeded, the forces increased and converged to the mid-upper range of submerged forces.

5.1.6.2 Nominal Process Pressure

For each test, nominal average process pressure was determined based on the measured force and the nominal contact area, calculated as a function of the measured displacement. These nominal process pressures were substantially different depending on contact condition and indentation rate.

In low speed tests (1 mm/s), pressures had a tendency to be higher in submergence cases compared to the dry contact condition. Pressures were high in general at this rate, and differences due to contact condition were more pronounced for 20° than for 30° ice specimens. For the 20° ice cone angle, the nominal pressure covered a broad span from 5.0 MPa to 23.0 MPa. The maximum nominal pressures in submergence were above those of dry tests, but there was also distinct overlap. Snow and granular ice tests resulted in far higher nominal pressures, with the ones in snow exceeding all others. At the 30° ice cone angle, the bandwidth of nominal pressures was much narrower, mostly between 5.7 MPa and 14.3 MPa. Dry and submerged nominal pressures overlapped, but, overall, higher pressures were observed in submergence cases. High pressures were observed for granular ice and snow scenarios. Snow had the highest pressures up to about 4000 mm^2 area. At larger areas, pressures in tests with granular ice dominated.

Medium speed tests (10 mm/s) were characterized by considerable overlay of pressures for dry and submerged contact conditions. 20° ice specimens yielded higher pressures with a broad span from 1.2 MPa to 14.5 MPa. For 30° ice cones, pressures were lower and ranged from 1 MPa to 9 MPa. For larger contact areas, a slight trend of higher pressures in the submergence case was recorded. For both ice cone angles, one test each

with granular ice was evaluated. Both initially had the highest pressures, but later levelled in the median of dry and submerged pressures. Overall, the influence of the different contact conditions was rather ambiguous at the medium indentation rate.

In the high speed tests (100 mm/s), submergence typically caused pressures that exceeded those for a dry contact surface and this trend was particularly pronounced at the 20° ice cone angle. Tests with granular ice and snow resulted in pressures that were similar or lower than in submerged tests, but were higher than in the dry tests. Overall pressures started at 5.7 MPa to 19.9 MPa at 1000 mm^2, and subsequently decreased to between 2.0 MPa and 9.3 MPa at around 30000 mm^2. Tests with 30° ice specimens yielded lower pressures in general, declining from 3.1 MPa to 12.9 MPa to between 2.0 MPa and 6.4 MPa. Despite some overlap, submerged pressures were generally above dry pressures. Snow and granular ice produced nominal pressures mostly comparable to those of the dry condition. At advanced displacement, pressures of granular ice approached those of submergence.

5.1.6.3 Ice Failure and Local Pressure Pattern

In low speed tests, the pressure patterns were generally comprised of one continuously developing circular high pressure zone (HPZ) in the centre, and diminishing pressures on the outside. The exceptions were the granular ice cases with lower pressures over the entire contact area and only small isolated HPZs. The ice failure was in agreement with creep-like ice failure and ice recrystallization commonly reported for low test speeds. High speed camera footage (for dry and submerged contact conditions) showed the accumulation of ice debris in the vicinity to the contact area, where it was likely subject

to further comminution processes. In cases of submergence, the surrounding water impeded ice spalls from breaking off, and the ice specimens appeared to remain more intact.

High speed tests revealed the strongest influence of submergence. High speed camera footage indicated the restriction of ice debris extrusion; evident in the ice debris remaining close to the contact area and less ice spall development in general. Ice debris was mainly ejected in what was termed as a cloud-like manner. Tactile pressure sensor recordings were in support of these observations and displayed a contact area shape that was more comparable to slow speed tests, compact and uniformly round. Inside, though, the branch-like pattern of high pressure zones was still recognizable. Dry tests, on the other hand, had the high indentation rate characteristic branch-like pattern. Cracks formed and rapidly penetrated the ice specimens. Small ice particles were ejected and large ice fragments broke off, which were unrestrictedly expelled and quickly removed from the contact zone.

5.1.6.4 Contact Area

For the dry testing environment the measured contact area from the tactile pressure sensors, for both ice cone angles, at the low indentation rate was smaller than the nominal area and the smallest overall. The discrepancy with the nominal area was even more significant at the high indentation rate. This would be expected due to the higher occurrence of sudden fractures and an increased spalling activity.

In submergence cases, the actual contact area of a test with 20° ice cone angle at the low indentation rate was close to the nominal area. An increasing divergence at advanced

displacements was attributed to the fact that the sensing area was not sufficiently large to capture the entire contact area. The contact area for a submerged 30° ice specimen was distinctly smaller than the nominal area, but in good agreement with the dry one. At the high indentation rate, the actual contact area of a submerged 20° ice specimen was fairly close to the nominal area. The contact area of the dry test was considerably smaller. For a 30° ice specimen, on the other hand, there was more discrepancy between nominal and actual contact areas in the submerged case, but it was almost identical to the dry and snow test cases. To summarize for the submergence cases, the actual contact area of the 20° ice specimen was close to the nominal area, independent of impact speed. There was more disagreement for 30° ice specimens, but in those cases the difference between measured and nominal contact areas was nearly the same as in the dry testing environment – at both indentation rates.

The measured contact areas of two snow tests at the low indentation rate were larger than the nominal area and this was more distinct for the 20° ice specimens. Also the actual contact area for granular ice cases was larger than the nominal area. Compared to the contact areas in snow it was smaller at the 20° ice cone angle, but nearly identical at the 30° angle. During low speed tests, the ice samples incorporated some of the snow or granular ice and gained material at the ice-indenter interface.

Furthermore for snow, the contact area of a 30° ice cone at high indentation rate was smaller than the nominal contact area, but was roughly the same as that from the dry and submerged tests.

5.1.6.5 Contact Pressure (Adjusted Nominal Process Pressure)

Observations indicated an influence of the testing environment on the actual contact area size. This was visible in still photos taken after the tests, but especially evident in recordings of the tactile pressure sensors. The divergence of actual contact area from the nominal area for low and high indentation rates was discussed in section 5.1.3, based on the limited number of tests that involved the pressure sensors.

At the low indentation rate (1 mm/s), the (measured) contact area in submergence, but more importantly, in scenarios with snow and granular ice, was larger compared to the nominal area, and larger compared to the dry condition. This rate was associated with very high forces for snow and granular ice conditions that consequently resulted in the highest nominal average process pressures.

However, in view of the deviation between actual contact area and nominal area, the calculated pressure, based on nominal contact area, is not a realistic representation. The following plots display the adjusted process pressures for high and low indentation rates for both cone angles. Within this context the y-axis is designated as “contact pressure”, implying that this is the nominal process pressure of section 5.1.2 adjusted by factors established in section 5.1.3 for contact area ratios. The x-axis (nominal area) did not change. Two limitations are pointed out: first, the adjustment factors were determined by the ratio over the sum of the contact area within a certain displacement (as explained in section 5.1.3), but not for each individual data point. Second, the adjustment is done, based on very limited pressure sensor data. With one exception (1 mm/s, 20° ice cones,

snow), the factors were determined from one measurement and applied to all tests of the respective scenario.

The (modified) contact pressure vs. nominal area relationships for 1 mm/s indentation rate with 20° and 30° ice specimens are displayed in Figure 5.30 and Figure 5.31. Overall, the adjustment equalized the pressures. By comparing Figure 5.30 with Figure 5.3 (20° ice specimens), it can be observed that the previously very high nominal pressures for snow and granular ice conditions are now in the mid-range of the other two conditions. There is also more overlap of dry and submerged conditions, and dry contact pressures are at the top end. The repercussion for the 30° ice cone angle is similar (Figure 5.31). There was no significant difference between dry and submerged cases in the first place (see Figure 5.5), but after adjusting for the difference in contact area it is insignificant. Snow and granular ice cases, on the other hand, previously similar or even above submergence, now have the lowest contact pressures.

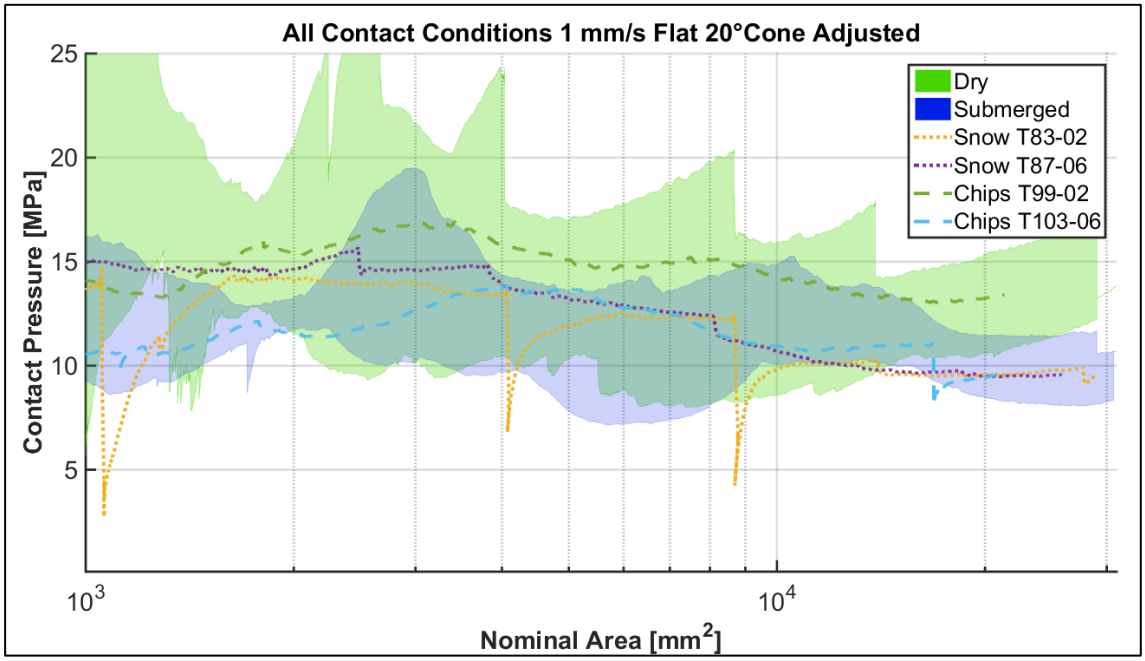

Figure 5.30: Flat plate, 1 mm/s, 20° ice specimens: contact pressure-area curves for all contact conditions. The adjustment (multiplication) factors were 1.48 for dry, 0.94 for submerged, 0.65 for snow and 0.80 for granular ice.

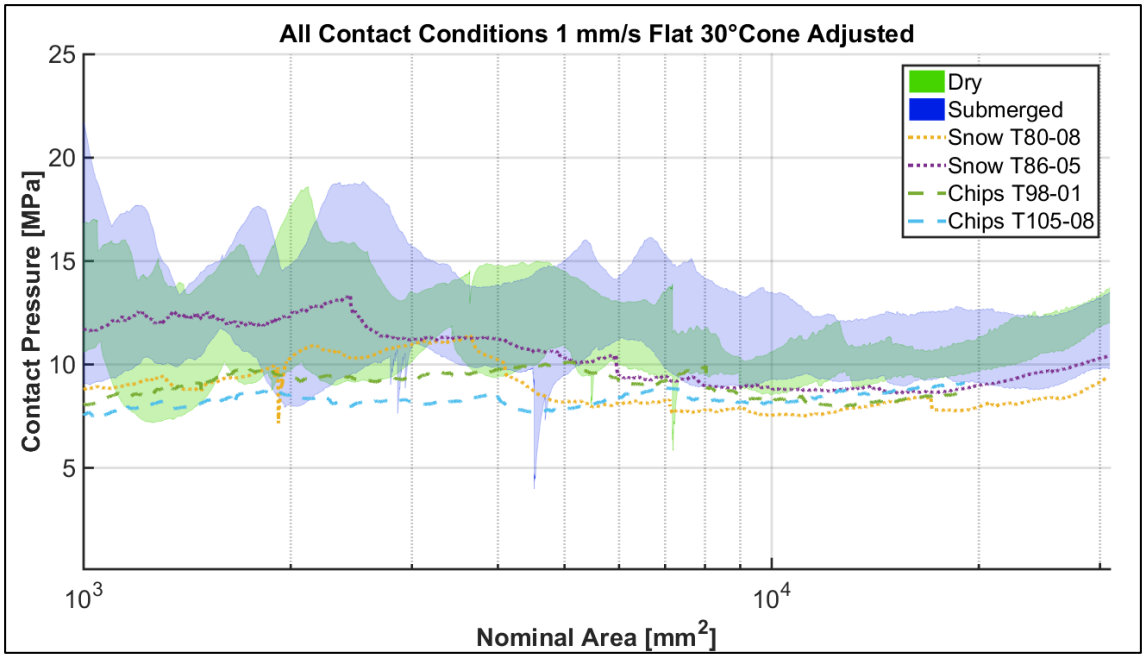

Figure 5.31: Flat plate, 1 mm/s, 30° ice specimens: contact pressure-area curves for all contact conditions. The adjustment (multiplication) factors were 1.56 for dry, 1.37 for submerged, 0.87 for snow and 0.79 for granular ice.

At 100 mm/s indentation rate, submergence was found earlier to have the most significant effect, with overall high nominal pressures - an impression that is significantly changed when the nominal pressures are adjusted by the contact area.

For the 20° ice cone angle, the contact pressures are presented in Figure 5.32. In this case, the curves of snow and granular ice are not included since the contact area measurements were not suitable. The figure shows that the adjustment for measured contact area essentially means that dry and submerged pressures are equal and there is practically no difference compared to the plot of nominal process pressure in Figure 5.11.

Unfortunately, for this case no conclusions can be drawn as to how the contact pressures of snow and granular ice would change.

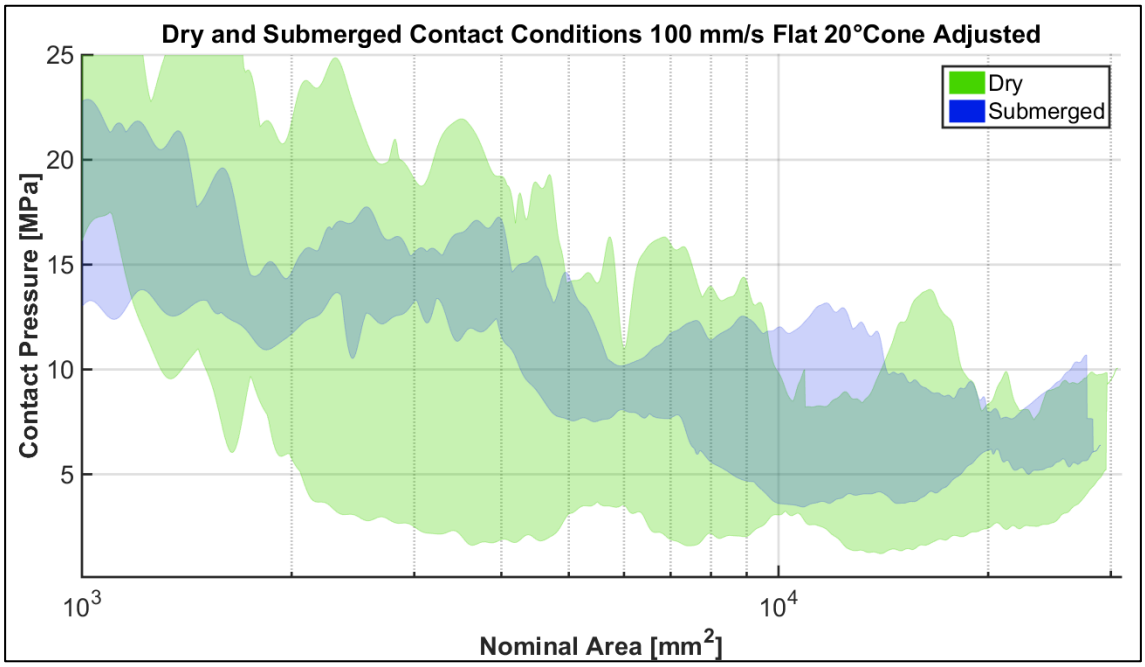

Figure 5.32: Flat plate, 100 mm/s, 20° ice specimens: contact pressure-area curves for dry and submerged contact conditions. The adjustment (multiplication) factors were 2.58 for dry, 1.15 for submerged. The curves of snow and the granular ice tests are left out because no adjustment factor could be established.

Figure 5.33 is the modified plot for 30° ice specimens. The pressures for granular ice are not included because of the lack of a suitable measurement. All other contact pressures for dry, submerged, and snow conditions are the results of roughly the same adjustment factor (2.2); therefore the overall trend did not change (compare Figure 5.13), except for more variation, overlap of dry and submerged pressures and higher contact pressures in general. Submergence has the tendency to cause higher contact pressures than the dry contact condition and contact pressure for snow are similar to the dry case.

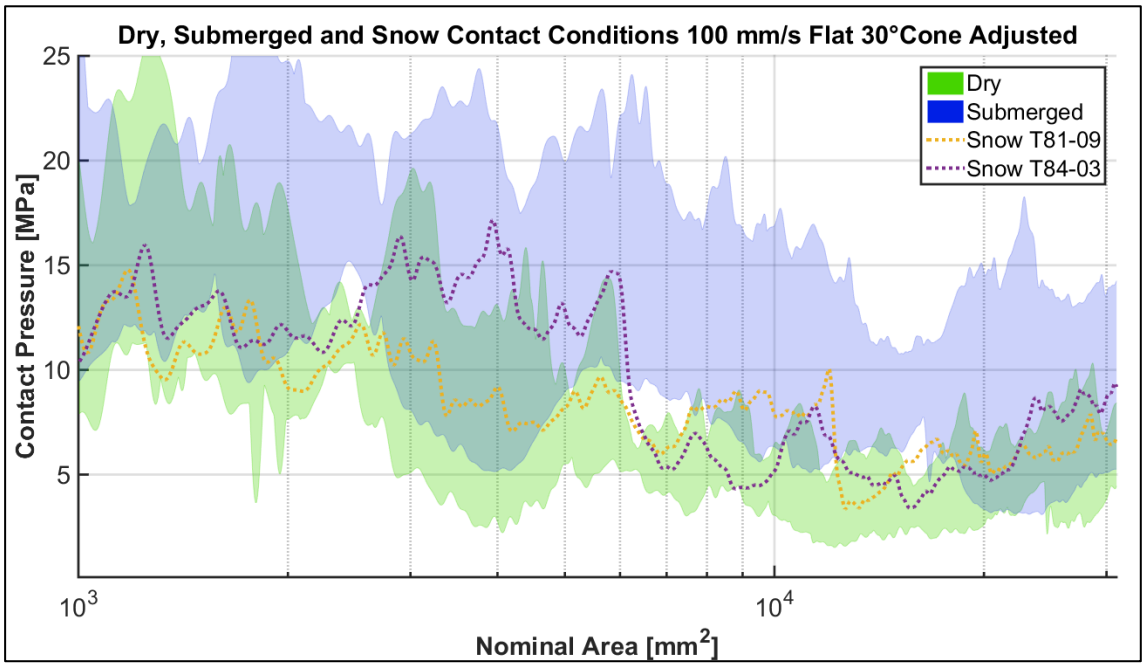

Figure 5.33: Flat plate, 100 mm/s, 30° ice specimens: contact pressure-area curves for dry, submerged and snow contact conditions. The adjustment (multiplication) factors were 2.23 for dry, 2.20 for submerged, 2.25 for snow. The curves of the granular ice tests are left out because no adjustment factor could be established.

5.1.6.6 Discussion

Overall significant differences in force magnitudes were measured depending on indentation rate and testing environment. These two parameters also dramatically influenced the contact area that was observed in the recordings with tactile pressure sensors. The discrepancy between measured and nominal contact area was assessed and served to re-evaluate earlier derived nominal process pressure-area relationship by means of the contact pressure. It is emphasized that the adjustments were done based on very limited data. In most cases, only one contact area measurement was available that was applied to all individual pressures of one scenario. The adjustment factors for 30° ice cone angle at high speed were rather uniform for dry, submerged, and snow contact conditions.

The adjustments were regarded to be essential in view of the observed contact area deviations and are believed to be a better representation of the true circumstances. The results prove that if a more realistic contact area is accounted for, the actual pressures at the low indentation rate would not change significantly, but the overall load would still vary due to the significant changes in contact area induced by the testing environment. At the high indentation rate, there would be some difference in real pressure due to submergence, but less due to snow, and presumably not significant for granular ice. The results indicate that the contact condition significantly affects the contact area and the change in contact area is what drives the general load transmission. The sequence of contact condition that led to higher or lower forces is reflected in the sequence of contact area sizes. For example, the snow tests at the low indentation rate produced the highest

forces, but also had the largest contact areas. Analogously, the lowest forces were obtained in the dry environment, associated with the smallest contact area. This implies a strong correlation between magnitude of transmitted force and size of contact area that is significantly influenced by the contact condition but may not necessarily affect the average process pressure.

5.2 Wedge Indenter

5.2.1 Test Overview

Table 5.8 summarizes 8 tests performed with the wedge shaped indenter, only involving dry and submerged contact conditions with the 30° ice specimens. Tactile pressure sensors were incorporated in all tests. The test setup is displayed in Figure 5.34 for both testing environments.

Table 5.8: Overview of 8 tests performed with the wedge shaped indenter.

Date	Test Number		Cone Angle [°]	Indentation Rate		Contact Condition	Water	
	Overall	Day		Nom. [mm/s]	Avg. [mm/s]		Salinity [ppt]	Temp. [°C]
24.06.2015	65	1	30	1	1.0	Dry	-	-
24.06.2015	66 [T]	2	30	100	94.7	Dry	-	-
25.06.2015	67	1	30	1	1.0	Dry	-	-
25.06.2015	68	2	30	100	94.4	Dry	-	-
25.06.2015	69 [T]	3	30	1	1.0	Submerged	25.0	-0.6
25.06.2015	70 [T]	4	30	100	93.7	Submerged	28.3	-1.8
25.06.2015	71	5	30	1	1.0	Submerged	29.7	-0.3
25.06.2015	72	6	30	100	94.9	Submerged	30.1	-1.7

T Thin sections completed.

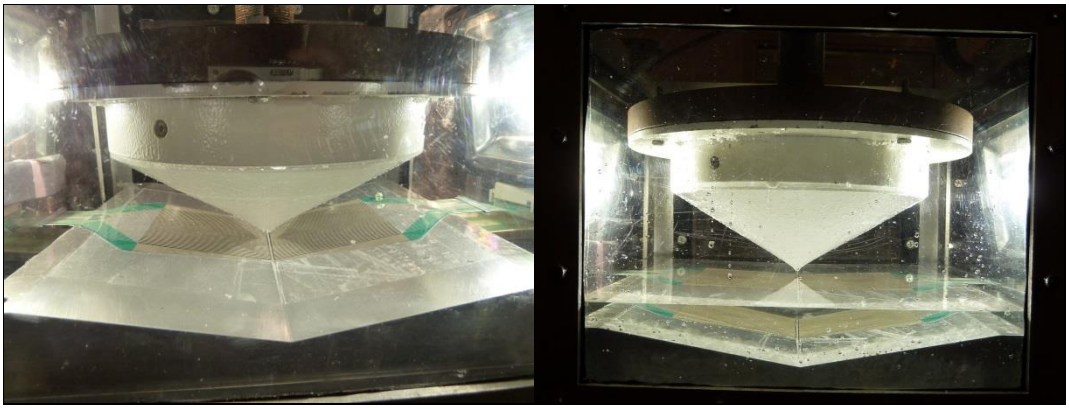

Figure 5.34: Still photos of the test setup for dry (left) and submerged (right) contact conditions with the wedge shaped indenter and 30° ice cone angle.

5.2.2 Measured Force and Nominal Process Pressure

In the following section, force-displacement histories are shown for up to 35 mm displacement on the x-axis, and for up to 200 kN force on the y-axis. Nominal process pressure-area relations are displayed on a log-linear scale for nominal areas above 1000 mm^2 and nominal pressures up to 25 MPa. The individual tests of dry and submerged contact conditions are summarized in green and blue areas. Single force vs. displacement and nominal pressure vs. nominal area curves can be viewed in Appendix C2 for 1 mm/s and in Appendix C3 for 100 mm/s.

5.2.2.1 Indentation Rate: 1 mm/s

At 1 mm/s indentation rate, four tests were carried out: 2 dry and 2 submerged. The force vs. displacement plot (Figure 5.35) reveals no apparent difference between the two conditions. In general, the force curves of submergence cases are fairly smooth and there is only one large load drop for submerged test S T71-05, close to 32 mm displacement. The forces of both tests vary considerably as is implied by the extensive blue shaded area. Forces from the higher test are fairly close to the upper range of the dry tests (green area), but the second one has the lowest forces of all four tests. For dry tests, several sudden force drops are visible, mainly in the region up to 21 mm displacement.

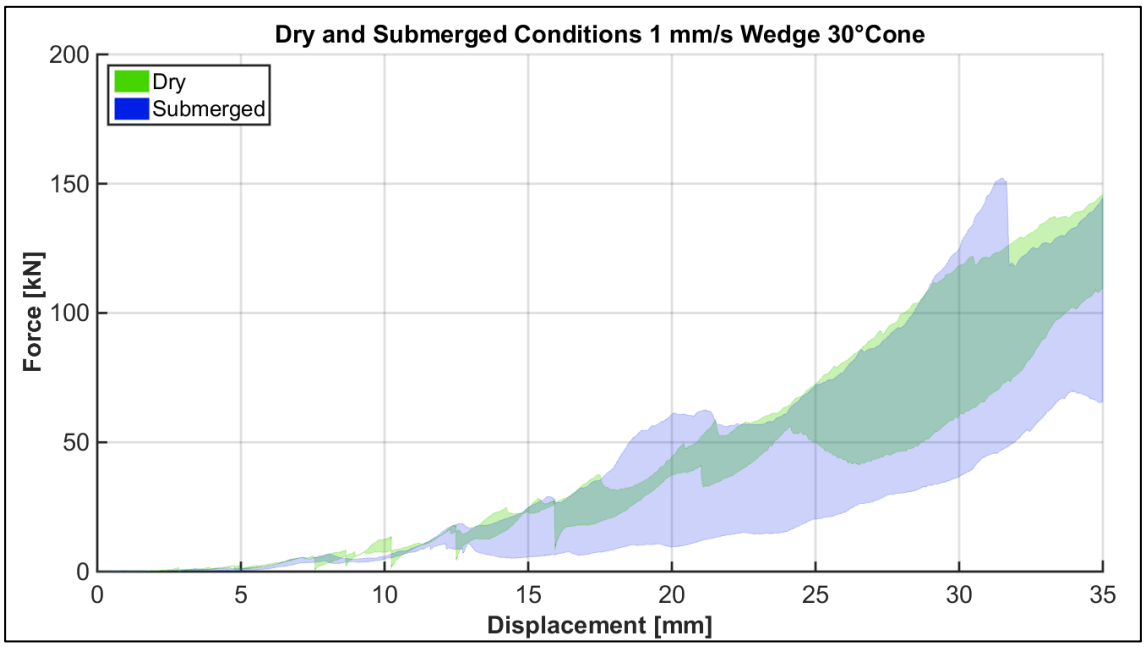

Figure 5.35: Wedge, 1 mm/s, 30° ice specimens: force vs. displacement for dry and submerged contact conditions. The shaded areas enclose all dry tests (2) in green and submerged tests (2) in blue.

The sudden load drops are reflected in the nominal process pressure-area relationships in Figure 5.36. For areas up to almost 4000 mm^2, the green area of the dry tests has distinct incisions. Nominal pressures of submerged tests are similar up to 2000 mm^2, but diverge at larger areas. Overall, the nominal pressures are fairly constant or slightly increase, while mostly remain below 8.5 MPa.

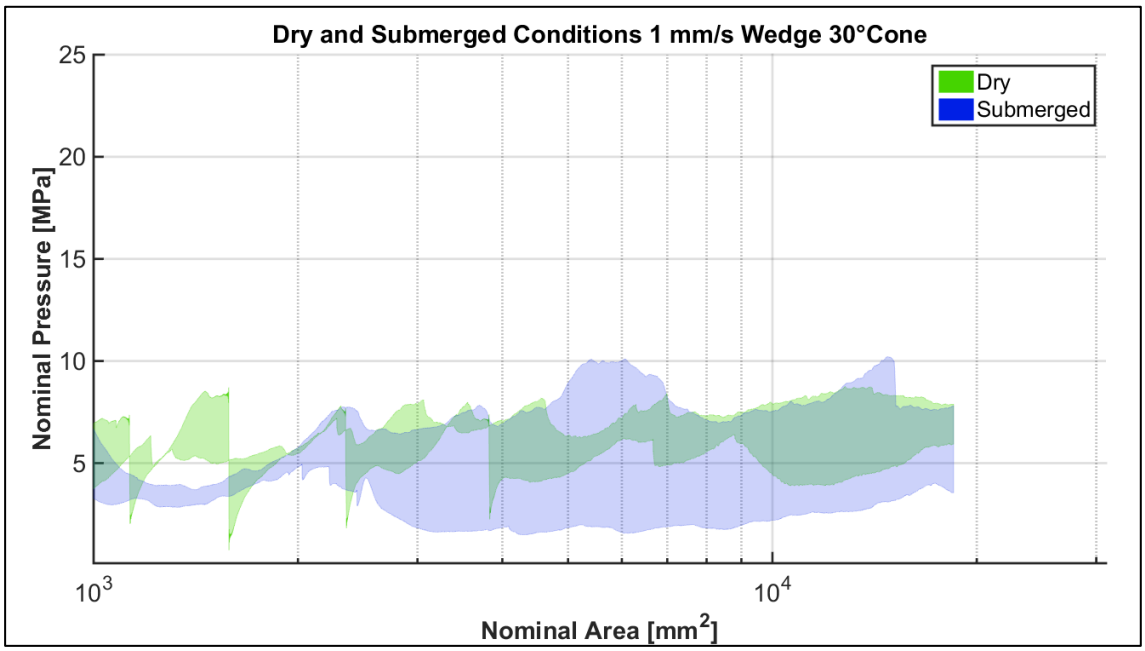

Figure 5.36: Wedge, 1 mm/s, 30° ice specimens: nominal pressure-area curves for all contact conditions. The shaded areas enclose all dry tests (2) in green and submerged tests (2) in blue.

5.2.2.2 Indentation Rate: 100 mm/s

At the high indentation rate, four tests were performed, 2 each in dry and submerged conditions. For up to 18 mm displacement, Figure 5.37 shows a trend of submerged forces being distinctly above dry forces. Up to that point, the forces of the two tests in either condition are very similar (narrow areas). For advanced displacements, the difference between contact conditions diminishes, as well as both areas spread out indicating more variations within the test scenarios.

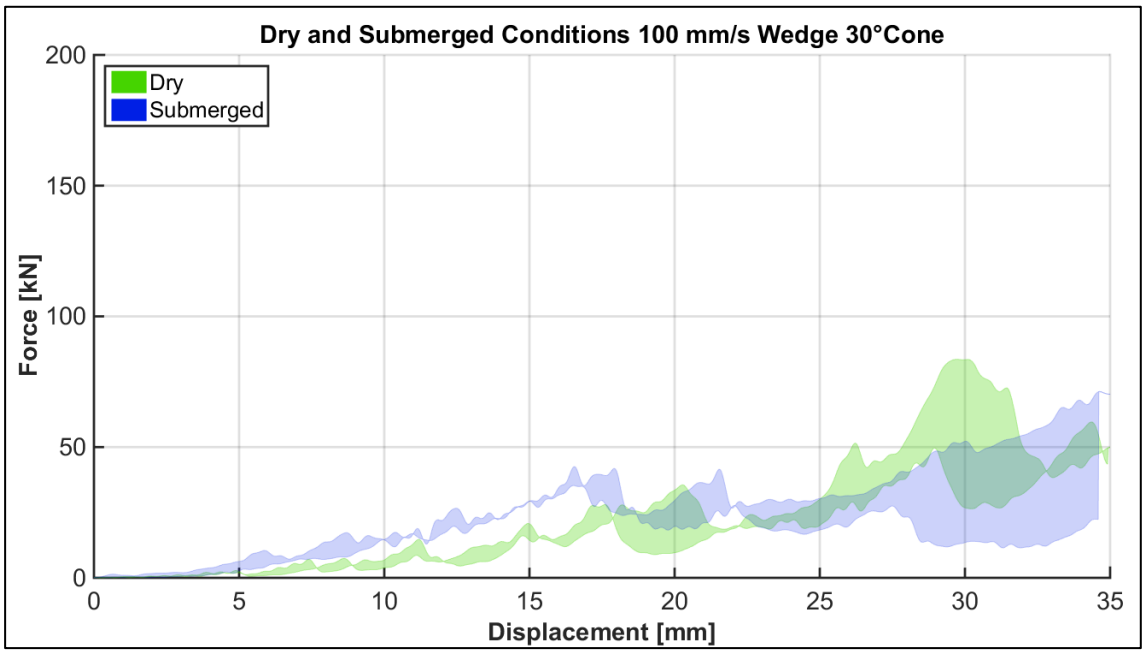

Figure 5.37: Wedge, 100 mm/s, 30° ice specimens: force vs. displacement for dry and submerged contact conditions. The shaded areas enclose all dry tests (2) in green and submerged tests (2) in blue.

The nominal pressure-area relationships are given in Figure 5.38. At 1000 mm^2 area (8.1 mm displacement), nominal pressures for submergence range from 7.3 MPa to 13.9 MPa; dry pressures, on the other hand, are between 2.4 MPa and 5.6 MPa. Up to an area of 5070 mm^2 (18.3 mm displacement), submerged pressures clearly exceed dry pressures. Subsequently, pressures in submergence decrease; pressures for both contact conditions overlap and are below 3.8 MPa. Overall, Figure 5.38 shows a reduction in pressures with increasing contact area in submergence, while dry pressures remain rather constant.

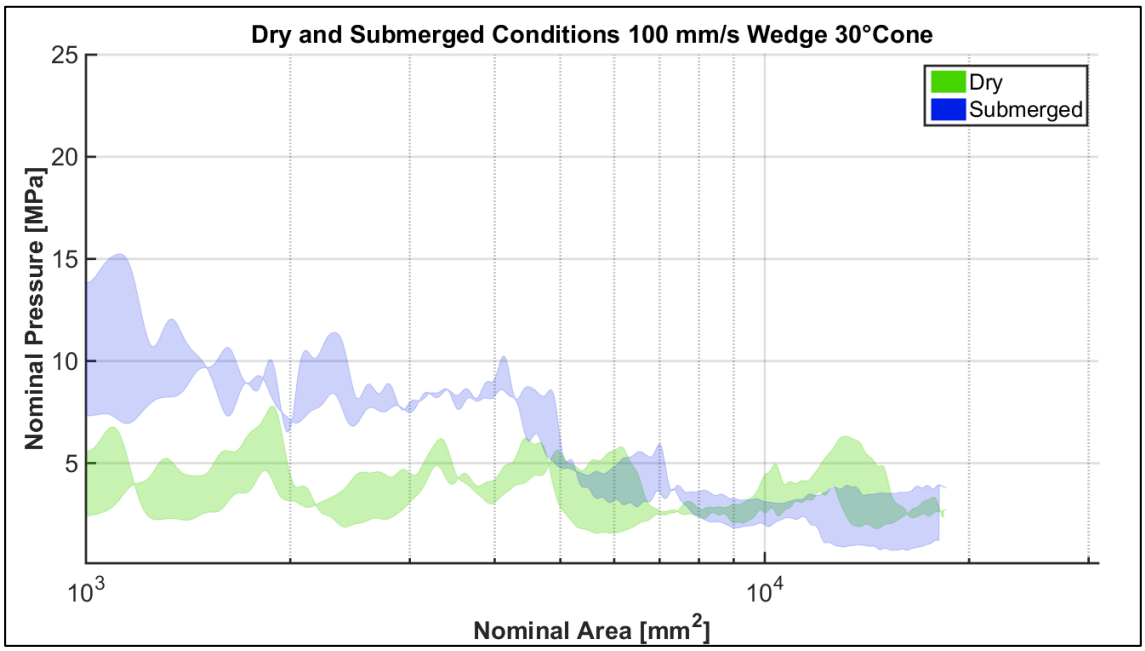

Figure 5.38: Wedge, 100 mm/s, 30° ice specimens: nominal pressure-area curves for all contact conditions. The shaded areas enclose all dry tests (2) in green and submerged tests (2) in blue.

5.2.3 Local Pressure Pattern and Contact Area (Tactile Pressure Sensors)

5.2.3.1 Indentation Rate: 1 mm/s

Analysis in section 5.2.2.1 revealed no significant submergence effect at the low indentation rate. This is also reflected in the tactile pressure sensor readings with examples provided in Figure 5.39, left and right for dry and submerged conditions. In general, the contact area is of an ellipsoidal shape, with a stretched zone of higher pressure in the middle that is declining outwards. The two tests on the top are fairly similar and so are the two at the bottom. Test S T69-03 (top right) with a high occurrence of ice spalls throughout the crushing event is somewhat deviating with respect to the effect of submergence. This is associated with a smaller contact area and correlates well with the low force history measured by the MTS machine (Figure Appendix C2. 1). It is likely due to common random variation in high speed tests. Both submerged ice samples

were crushed at similar water temperatures of -0.6°C and -0.3°C and were 16 days old at the time the experiment were conducted.

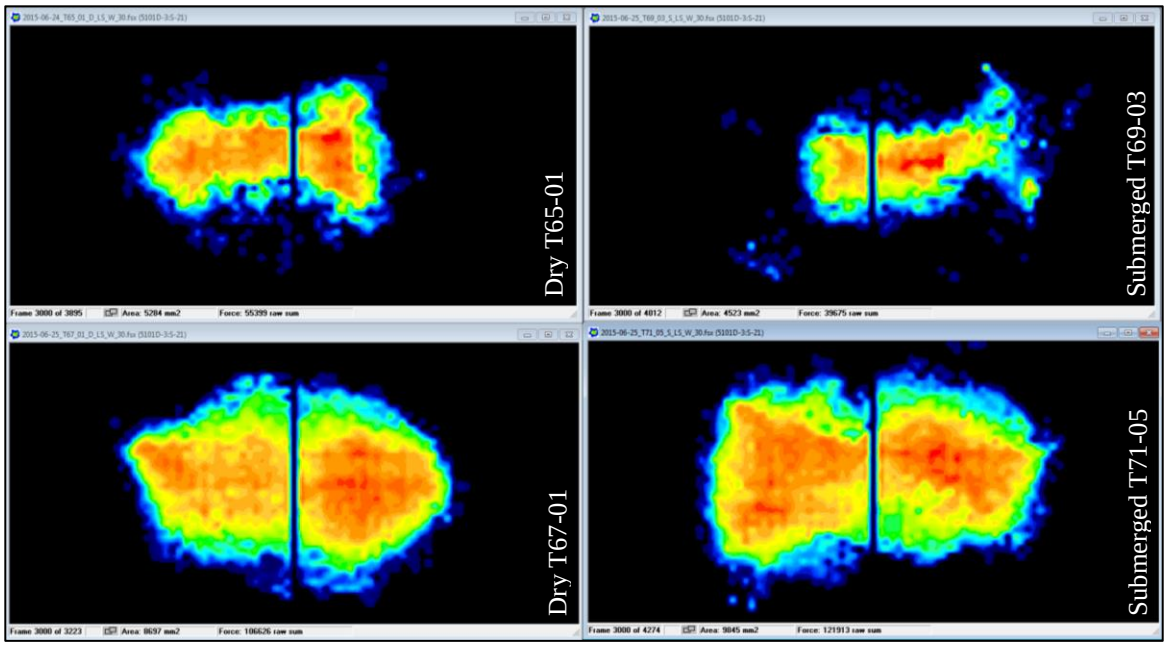

Figure 5.39: Wedge, 1 mm/s, 30° ice cones: pressure patterns in approx. 30 mm penetration depth for dry (left) and submerged (right) contact conditions. (Left) dry tests D T65-01 (top) and D T67-01 (bottom); (Right) submerged tests S T69-03 (top) and S T71-05 (bottom).

Figure 5.40 presents measured contact area vs. displacement for all four tests. For the wedge indenter, the contact area never exceeded the sensing area and the curves show the complete contact area progresses throughout the tests. All measured contact areas are well below the nominal contact area (black curve). Furthermore, the curves reflect the observation made in the pressure patterns in Figure 5.39 with the tests being very similar to each other. Upper and lower curves each represent one dry and one submerged test. Despite the high occurrence of ice spalls and the deviating behavior of S T69-03 (blue curve), the spikes at 10.3 mm, 10.5 mm, 11.2 mm, and 11.7 mm displacements are attributed to electrical signal noise. These spikes are apparent in the pressure sensor

readings in form of suddenly activated areas at considerable distance from the contact area in the centre. HSC footage does not provide any evidence of fracture or spalling events that could explain these incidences. At the low indentation rate, ice pieces break off rather slowly and in submergence float to the water surface. It is highly unlikely that any ice piece of such size would have hit the indenter at that distance to the contact area.

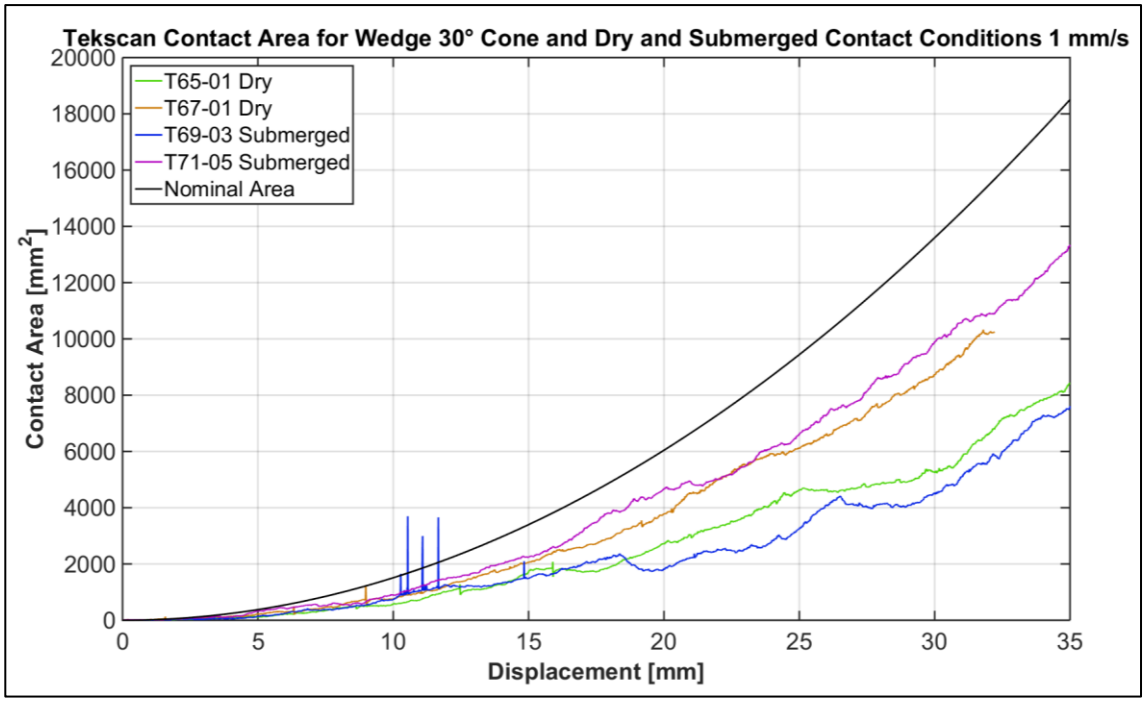

Figure 5.40: Wedge, 1 mm/s, 30° ice specimen angle, dry and submerged contact conditions: contact area vs. displacement from pressure sensor measurements.

The progress of the ratio between nominal and measured contact area over displacement is shown in Figure 5.41. For up to 7 mm displacement, the relationship is fairly variable and the actual contact area is up to 5 times smaller than the nominal contact area. Beyond that point, the relationship stabilizes and is almost constant. An exception is submerged test S T69-03 with a sudden rise at a displacement of about 18 mm and also subsequently more variation compared to the other tests.

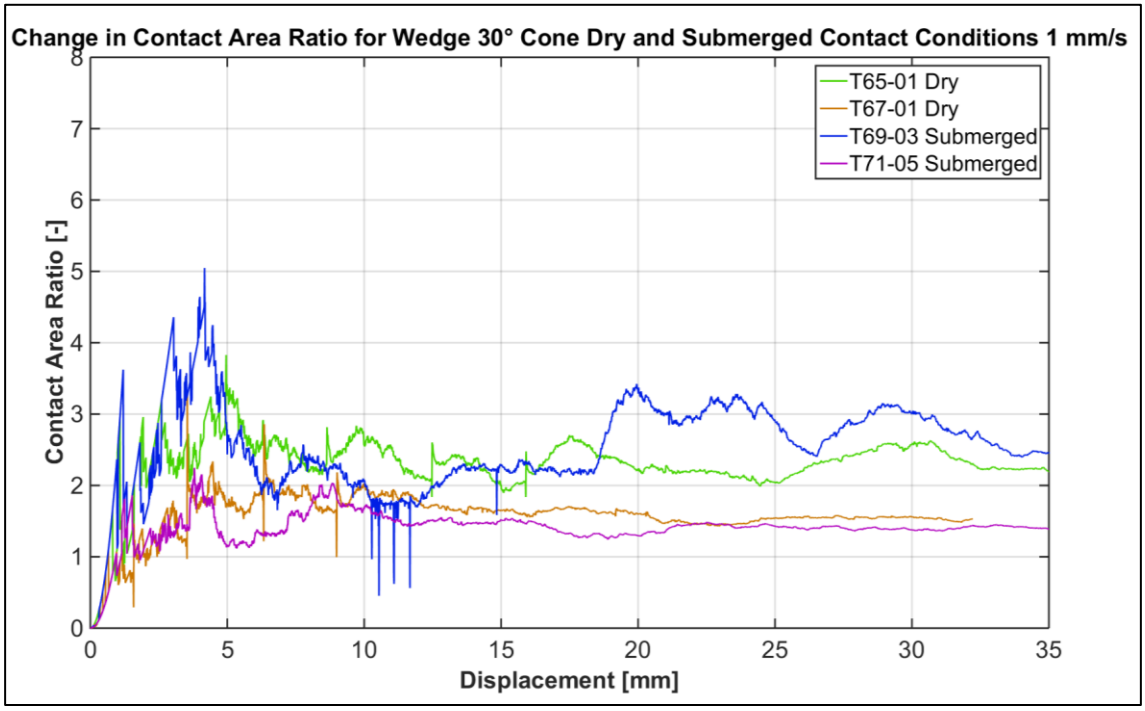

Figure 5.41: Wedge, 1 mm/s, 30° ice specimen angle, dry and submerged contact conditions: change in ratio between nominal and measured contact areas with displacement.

The average ratios between nominal and real contact areas are summarized in Table 5.9. The values for area express the sum of areas within the defined displacement range between 8.1 mm and 17.5 mm. This range is defined with respect to the limits that were used in earlier discussed nominal process pressure plots (Table 4.2) and the upper boundary is half the maximum displacement (analogous to the methodology used for flat indentation plate). Within these limits, the measured contact areas are between 1.5 and 2.28 times smaller than the nominal area and are close to the level that the curves in Figure 5.41 settle into.

Table 5.9: Wedge, 1 mm/s, 30° ice cones, dry and submerged conditions: comparison of the nominal contact area with individual contact area measurements from the tactile pressure sensors.

Depth [mm]	**Condition**		**Dry**		**Submerged**	
	Test	**Nominal**	**T65-01**	**T67-01**	**T69-03**	**T71-05**
8.1 to 17.5	**Area [mm^2]**	2431834	1064755	1435776	1161767	1626244
	Ratio	1.00	2.28	1.69	2.09	1.50

5.2.3.2 Indentation Rate: 100 mm/s

At the high indentation rate, dry and submerged contact conditions differed distinctly. This was most evident for displacement up to approximately 18 mm in the MTS data (see Figure 5.37) and is reflected in the pressure sensor data. Up to this point, the dry tests have the typical branch-like pressure patterns (Figure 5.42, left). The submerged tests have a more compact shape (Figure 5.42, right), similar to the pressure pattern observed in the low speed tests (Figure 5.39). Later, the submerged tests began to branch out as well. The onset is visible in the top right image (S T70-04), in terms of an area loss in the upper middle that interrupts the former contiuous perimeter. At this point, the pressure distribution shape of test S T72-06 (bottom right) is still fairly compact. This difference diminishes with increasing penetration and the pressure patterns of dry and submerged tests become more comparable. Additional images of pressure patterns and information on contact area for both indentation rates can be found in Appendix C4.

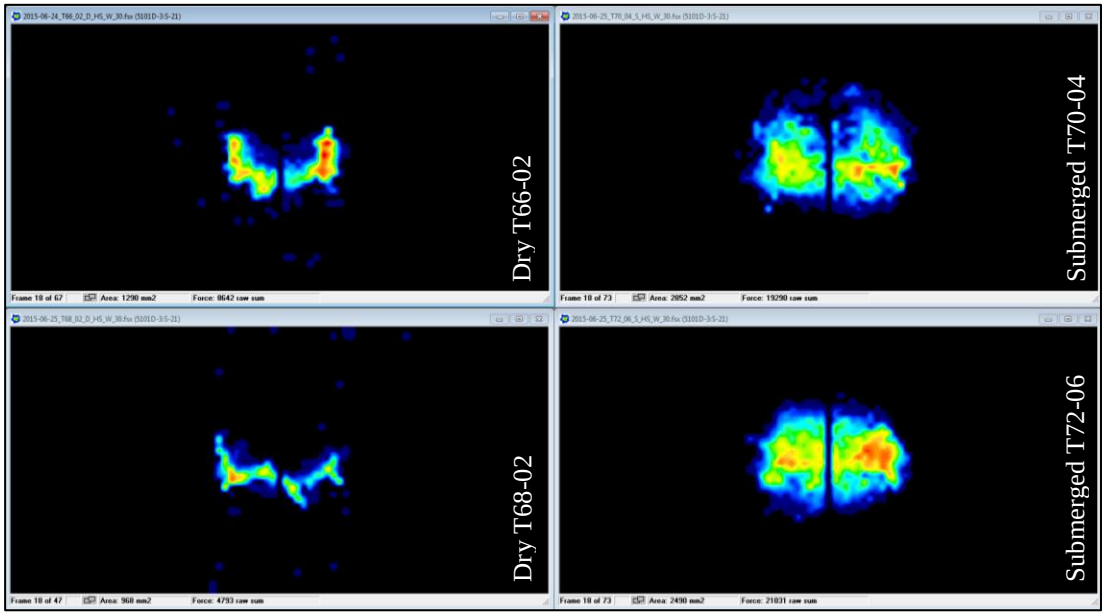

Figure 5.42: Wedge, 100 mm/s, 30° ice cones: pressure patterns in approx. 18 mm penetration depth for dry (left) and submerged (right) contact conditions. (Left) dry tests D T66-02 (top) and D T68-02 (bottom); (Right) submerged tests S T70-04 (top) and S T72-06 (bottom).

The progress of the measured contact areas in comparison to the nominal area is displayed in Figure 5.43. At 100 mm/s indentation rate, the discrepancy is pronounced. The contact areas of submerged tests are consistently above those of the dry tests and closer to the nominal contact area up to a displacement of 22 mm. This is around the time when the pressure patterns for both testing environments start to become similar (as discussed above). At higher displacements, the initial distinction is substantially reduced.

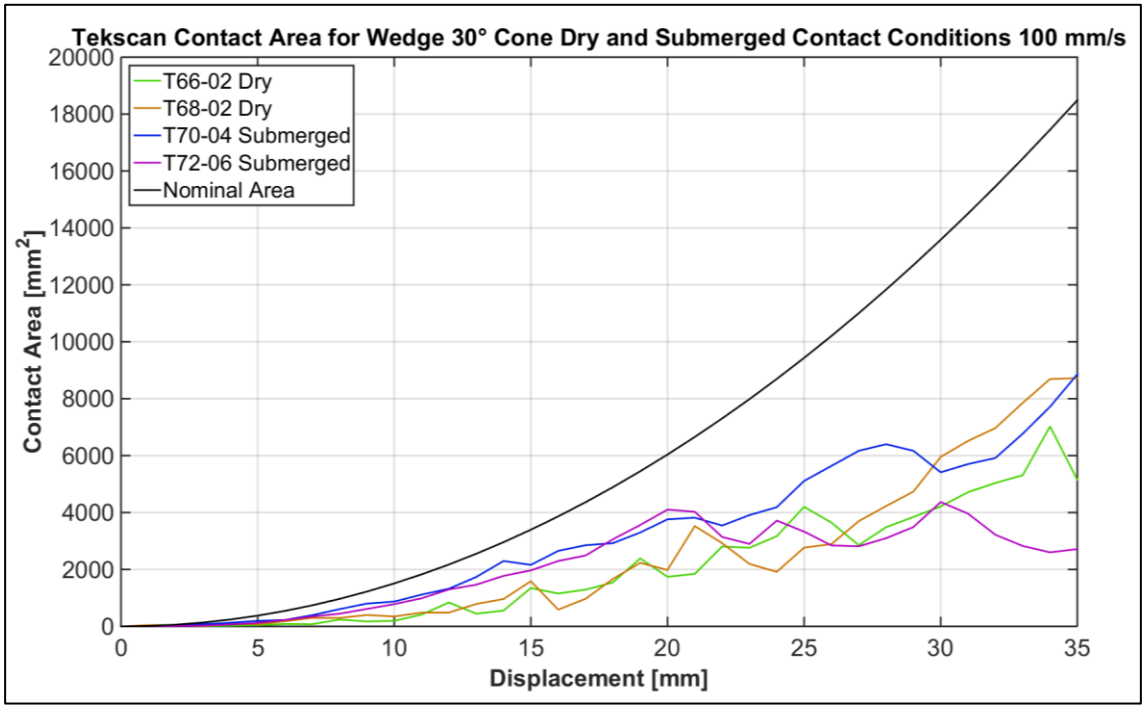

Figure 5.43: Wedge, 100 mm/s, 30° ice specimen angle, dry and submerged contact conditions: contact area vs. displacement from pressure sensor measurements.

Figure 5.44 shows the ratios of nominal and measured contact area over penetration depth. Distinct variation can be observed for the dry tests (green, orange), in particular at about a displacement of 3 mm, where both tests are off by a factor of 22. This occurs at the early test stages, when large discrepancies between the theoretical and actual contact are expected. Viewing the recordings of the pressure sensors, both tests are similar and characterized by a high amount of ice spalls from the beginning of the test. In the submergence cases (blue, magenta), few ice spalls are visible and the contact areas continuously increase from the beginning as is reflected in the smooth and almost constant ratios in Figure 5.44.

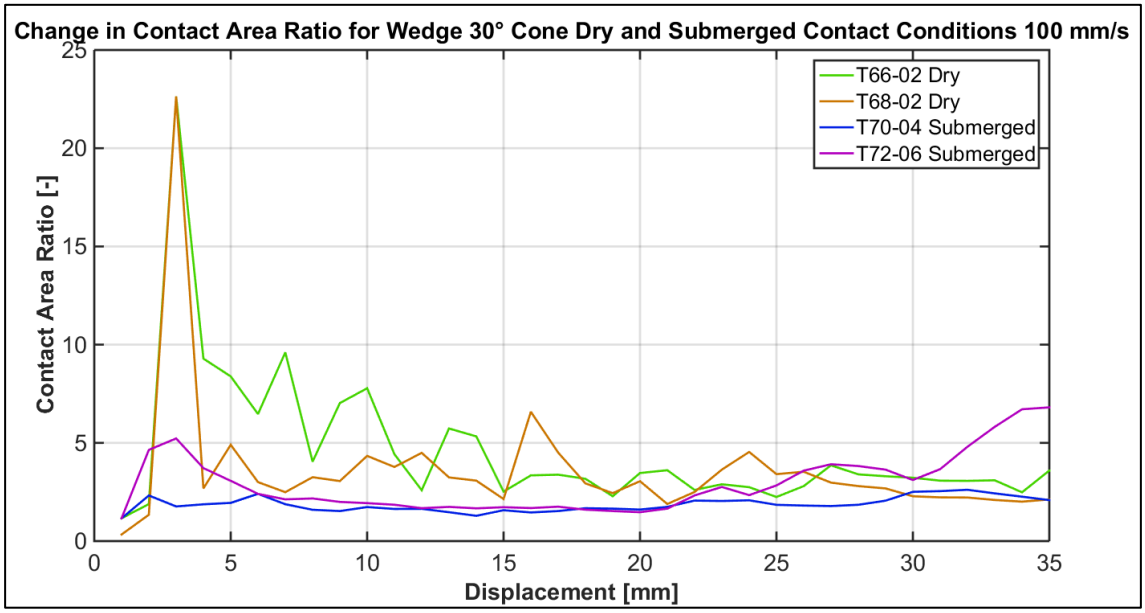

Figure 5.44: Wedge, 100 mm/s, 30° ice specimen angle, dry and submerged contact conditions: change in ratio between nominal and measured contact areas with displacement.

The mean ratios between approximately 8.10 mm and 17.5 mm displacement are listed in Table 5.10. In the given range, both dry tests have considerable offsets of 3.73 and 3.60. The contact areas in submergence deviate less with 1.51 and 1.76.

Table 5.10: Wedge, 100 mm/s, 30° ice cones, dry and submerged conditions: comparison of the nominal contact area with individual contact area measurements from the tactile pressure sensors.

Depth [mm]	**Condition**		**Dry**		**Submerged**	
	Test	**Nominal**	**T66-02**	**T68-02**	**T70-04**	**T72-06**
8.0 to 17.0	**Area [mm^2]**	24829	6652	6903	16413	14117
	Ratio	1.00	3.73	3.60	1.51	1.76

5.2.4 General and Microstructural Observations

The following paragraphs discuss visual observations for some tests in the context of high speed camera (HSC) footage, still photos of samples after test completion, and thin sections.

5.2.4.1 General Observations – During Testing: Ice Debris Formation, Ice Extrusion and Crack Propagation (HSC)

The snap shots in Figure 5.45 show two low speed tests at roughly 15 mm displacement. In the dry condition (left), ice spalls and smaller ice fragments are clearly visible. In the submergence case (right), although the water introduced some obscurity, less ice spalls and ice debris are noticeable.

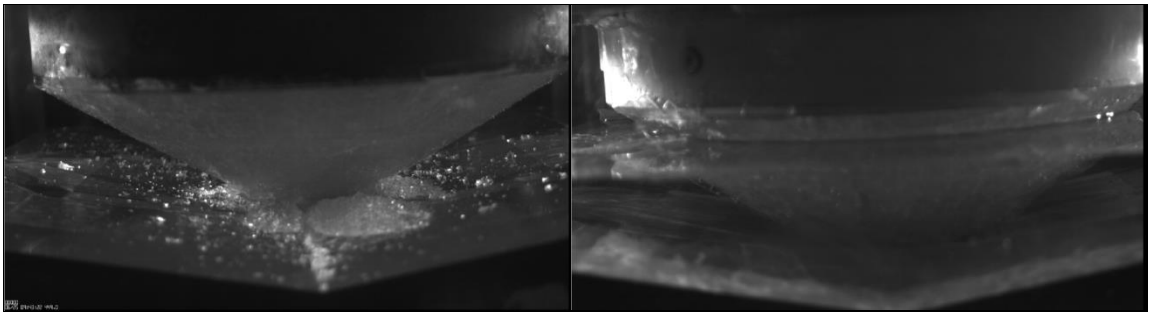

Figure 5.45: Wedge, 1 mm/s, 30° ice specimen, dry (left, T67-01) and submerged (right, T 69-03) contact conditions, approx. 14.9 mm penetration depth. Still photos of HSC footage showing the different ice debris development in dry and submerged environments.

The images in Figure 5.46 are at a similar displacement (14.9 mm) but for 100 mm/s indentation rate. Fine grained ice material is extruded in the dry condition (left), while under water (right) hardly any ice debris is visible as the ice extrusion is mitigated and restricted close to the contact area. At this displacement, all four samples have no large fractures.

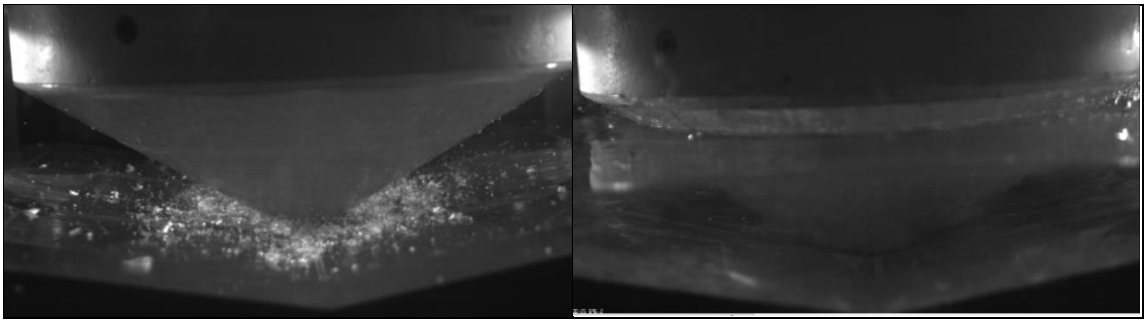

Figure 5.46: Wedge, 100 mm/s, 30° ice specimen, dry (left, T66-02) and submerged (right, T 70-04) contact conditions, approx. 14.9 mm penetration depth. Snap shots of HSC footage.

5.2.4.2 General Observations - After Test Completion: Contact Area and Surface (Still Photos)

Figure 5.47 displays photos of two sample surfaces after being tested at the low indentation rate (1 mm/s). For this test speed, the contact area is one large region. It is slightly ellipsoidal as it is the contact area between an ice cone and a (reverse) wedge shaped indenter. In the dry case (top), the contact area is a plateau on the remaining ice sample's body that is clearly separated from the surrounding ice. This is considerably less distinct for the submerged sample (bottom), where the transition from the contact area to the residual ice is much smoother. The contact area is darker in color instead of the usually white color.

Dry **T65_01**		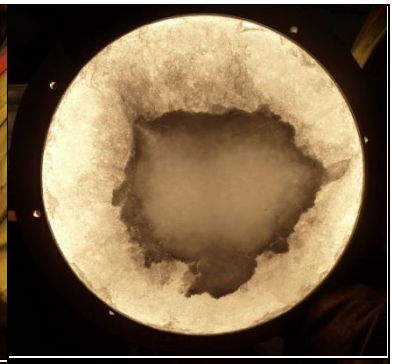
Submerged **T69_03**	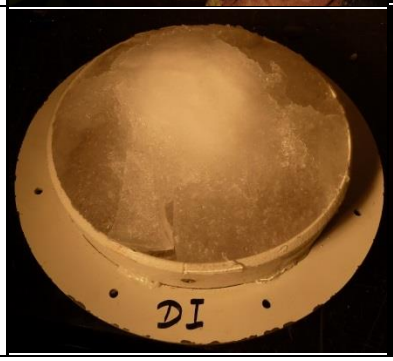	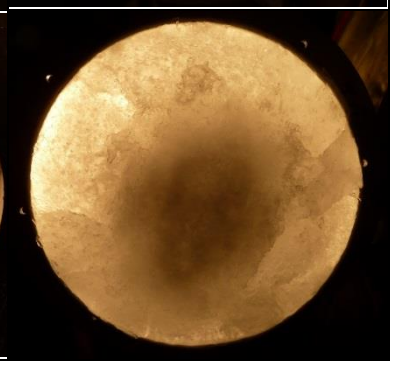

Figure 5.47: Wedge, 1 mm/s, 30° ice specimens: images of ice samples after testing in dry (top) and submerged (bottom) contact conditions; on the left of indented surfaces, on the right with lighting applied from the back.

Images for high speed test are displayed in Figure 5.48. The dry sample (top) displays the branch-like pattern, typical for high indentation rates. The bright, almost Y-shaped area indicates zones of high pressures, surrounded by darker areas, where lower pressures prevailed. In the submergence case(bottom right), there is only one rather homogeneous shaded area in the centre, where the sample was crushed into the indenter. Two ice spalls stick to the sample's remnants.

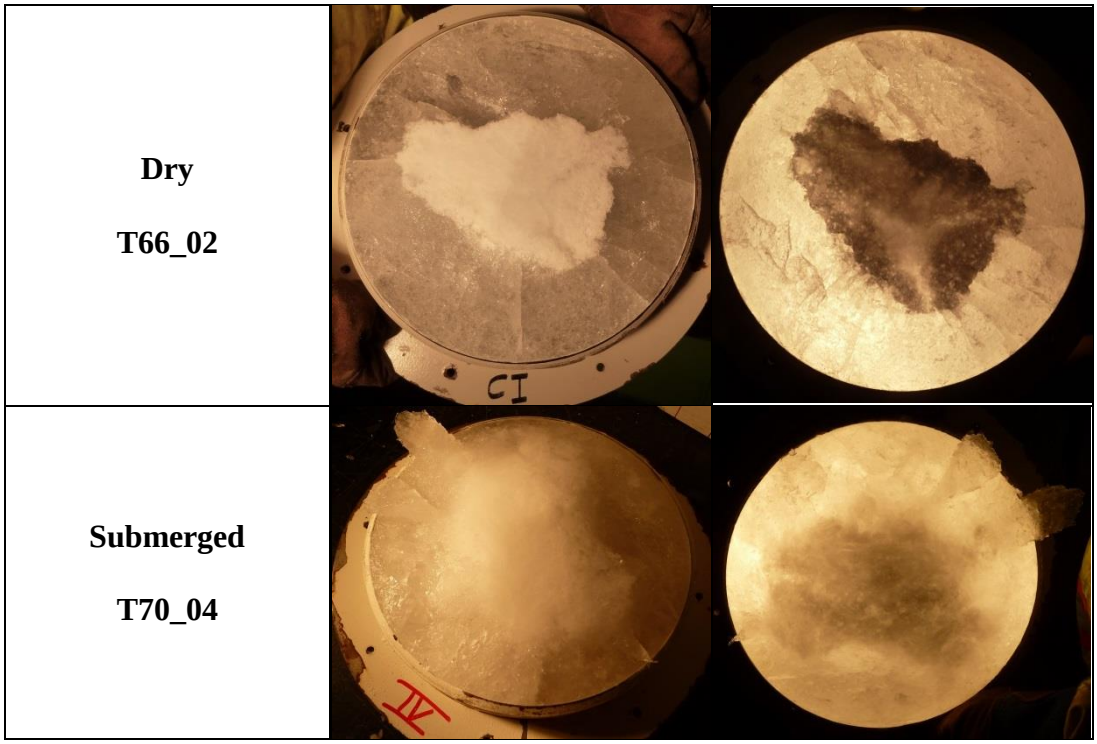

Figure 5.48: Wedge, 100 mm/s, 30° ice specimens: images of ice samples after testing in dry (top) and submerged (bottom) contact conditions; on the left of indented surfaces, on the right with lighting applied from the back.

The influence of contact condition is also visible in the vertical cross-sections (7-8 mm thick) in Figure 5.49. At both rates and for both testing environments the ice specimens' remnants show a well-defined V-shape on the top, reflecting the indenter profile. Samples of the dry condition have a distinct horizontal margin. At 1 mm/s indentation rate, it is one straight line near the height where the steel ring of the ice holder ends. At 100 mm/s, the margin is somewhat curved with additional inclined fractures expanding with increasing depth. These observations possibly imply some effect of the ice holder setup. In images of submerged tests at low and high indentation rates these features are not evident. The ice was damaged during the impact but mainly at the very top and independent of indentation rate. It is not penetrated by fractures or cracks.

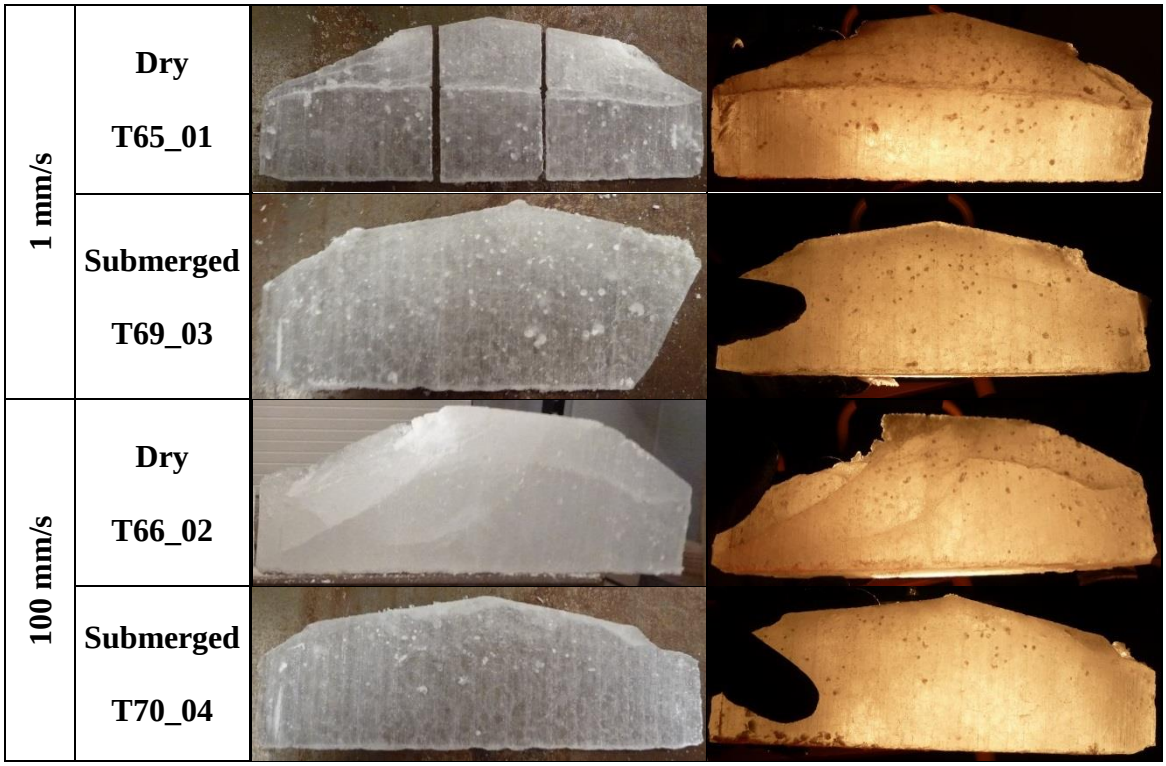

Figure 5.49: Wedge, 1 mm/s and 100 mm/s, 30° ice specimens: images of vertical cross-sections showing the effect of indentation rate (1 mm/s, 100 mm/s) and contact condition (dry, submerged). In the dry condition, the samples are penetrated by cracks. In submergence cases, the samples were affected in less depth and have no cracks and fractures.

5.2.4.3 Microstructural Observations

Samples where thin sections were completed are denoted with superscript “T” in Table 5.8. The dry high speed test (D T66-02) caused severe problems in the preparation and resulted in a thin section of poor quality. For another dry high speed test, all attempts failed. The high tendency to fracture is not surprising in view of the severe fractures that were noticed in the vertical cross-sections of these samples (see Figure 5.49 above).

For the wedge shaped indenter, submergence only influenced ice loads at the high indentation rate. Thin sections of related ice specimens for both contact conditions are displayed in Figure 5.50. Most of the cracks in the sample of the dry test (D T66-02) were

induced during the shaping process, but the crystal structure constitution remained unaffected. The layer of highly damaged ice extends to about 1-1.5 cm, and the crystal size of the ice below is noticeably smaller than the parent ice (Figure 4.6). The damaged layer of the submerged sample (Figure 5.50, right images) has a similar thickness but the ice underneath is unchanged; crystal size and orientation are predominantly the composition of the parent ice. Apparently, submergence reduced the effect on the ice microstructure and preserved more of the original (parent) ice crystals. An example of a submerged low speed test is included in Appendix C5 (in that case the damaged layer seems to reach deeper and the overall crystal size tends to be reduced).

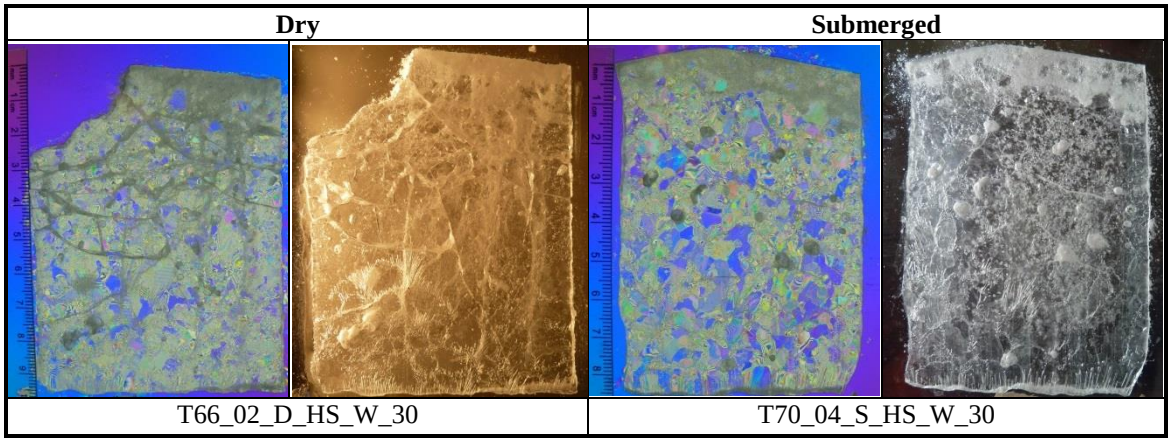

Figure 5.50: Wedge, 100 mm/s, 30° ice cones: Thin sections of tests in dry (left) and submerged (right) conditions. The images show the sections between a cross-polarized filter on the left and with side lighting applied on the right.

5.2.5 Multiple Regression Analysis

With the wedge shaped indenter, a total of 8 tests were performed (Table 5.8). In view of the limited data, the regression analysis does not allow the definition of a (reasonable) significance level, or any method for selecting the model terms, and thus no statistically significant model is obtained. Moreover, different data transformations (lambda optimal,

log normal, square root) are not found to improve the models or to affect overall trends. Consequently, no transformation is applied and the models include all terms. For these reasons the following results need to be seen as qualitative trend indicators, but not as quantitative conclusive statements. The models are based on two categorical factors, indentation rate and contact condition, and their interaction.

Figure 5.51 displays the main effects for the four defined responses. Except for Nominal Pressure Max 1000 (bottom right), the high indentation rate always has a lower response. Submergence has opposite effects: responses for forces are slightly lower, but those for pressures are higher, especially of Nominal Pressure Max 1000.

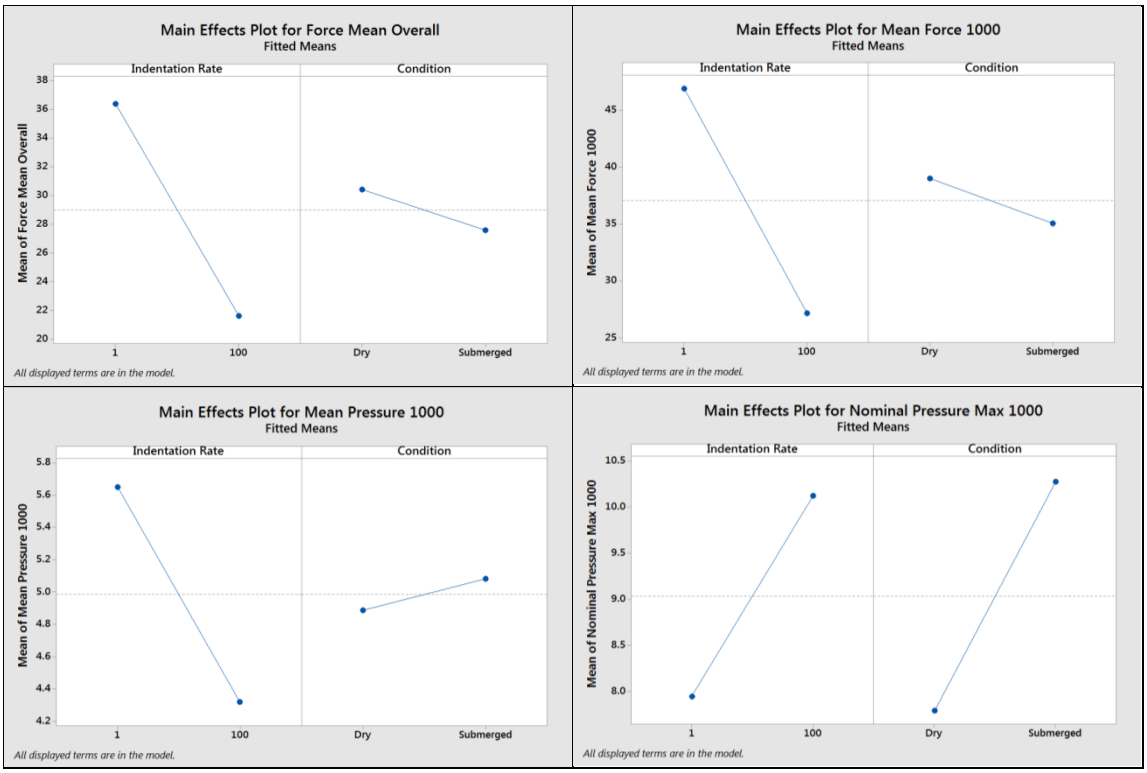

Figure 5.51: Overview of main effects on the means of the four responses for the wedge shaped indenter.

The interaction plots in Figure 5.52 offer consistent tendencies, although different in peculiarity. In view of forces, submergence lowers the response at 1 mm/s indentation rate, but slightly increases it at 100 mm/s. The same trend is apparent regarding pressures, where submergence causes a distinct higher response at 100 mm/s, but a reduced response at 1 mm/s.

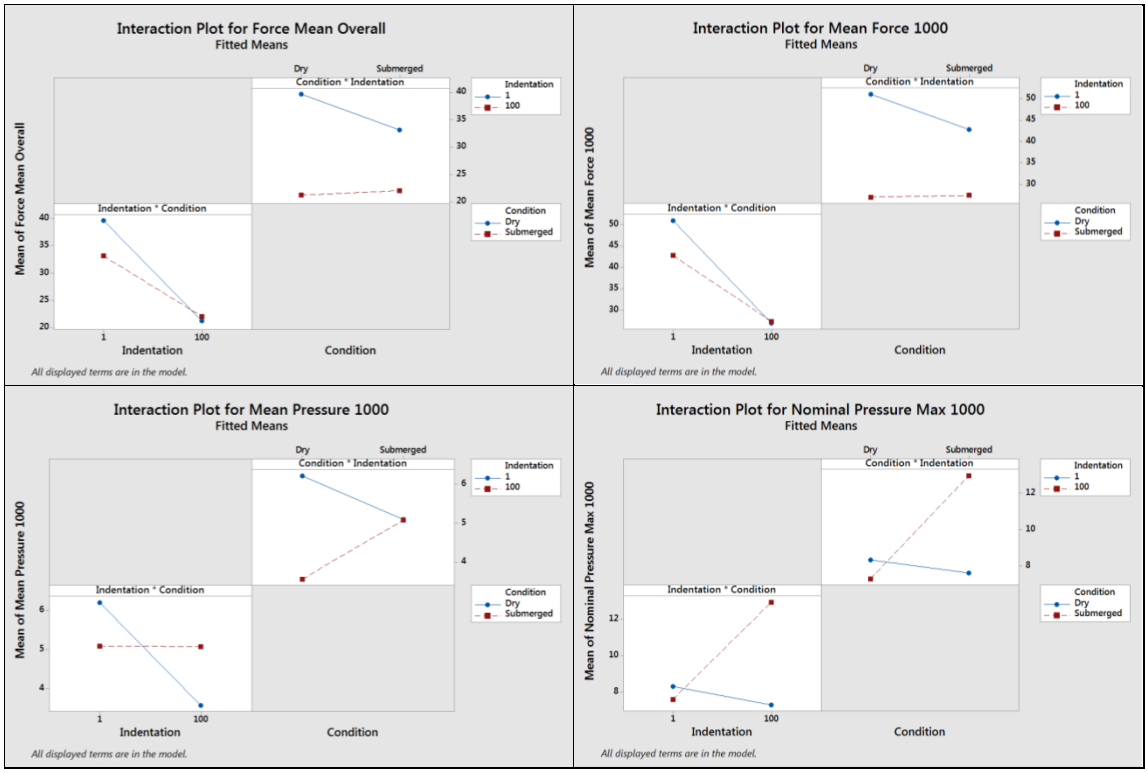

Figure 5.52: Overview of the effect of indentation rate and contact condition interaction on the means of the four responses of the wedge shaped indenter.

In summary, the results reflect the strong cross-correlation of submergence with indentation rate. Reponses in submergence are lower at the low indentation rate, but generally increased at the high indentation rate compared to the dry test environment. For more details relating to the regression analysis, refer to Appendix C6 that provides plots of residuals, interactions as well as the regression equations.

5.2.6 Summary and Discussion

5.2.6.1 Force

For 1 mm/s indentation rate, no difference in force magnitude dependent on testing condition was observed. At high indentation rates, forces in submergence were higher up to a displacement of about 18 mm, but the difference subsequently diminished. Overall, forces at 1 mm/s indentation rate were higher compared to 100 mm/s.

5.2.6.2 Nominal Process Pressure

At the low indentation rate (1 mm/s), no difference between dry and submerged contact condition was found. The two submerged tests largely differed from each other in both pressure magnitudes and the pressure patterns recorded with the tactile pressure sensors. The results suggest that this deviation was due to general random variation. Nominal pressures were constant overall or slightly increasing, generally remaining below 10 MPa.

The high indentation rate (100 mm/s) resulted in initially high nominal pressures in submergence (up to approximately 15 MPa). Later, the pressures decreased to magnitudes comparable to dry tests. Dry tests produced low (below 5 MPa) and mostly constant pressures throughout.

5.2.6.3 Local Pressure Pattern and Contact Area

The contact area for low speed tests in both dry and submerged testing environments followed the characteristic appearance for this indentation rate: the pattern comprised a large continuous zone of high pressures in the centre and pressures decreasing outwards.

At the high indentation rate, the contact area of dry tests quickly changed and showed the typical high-rate branch-like pattern. In submerged tests, the branch-like pattern was mitigated in early stages, but more apparent later. The contact area was more continuous and uniformly increasing with proceeding penetration. Only starting from advanced displacements (about 22 mm), larger spalling events took place, resulting in contact areas that were similar to those of the dry test condition. This occurred about the time when the difference in forces between both test environments diminished.

5.2.6.4 Contact Pressure (Adjusted Nominal Process Pressure)

For the wedge shaped indenter, the tactile pressure sensors were included in all tests. The measurements revealed a consistently smaller contact area than nominal area for all tests. In section 5.2.3, a factor for each test was established that expresses the ratio between the nominal and actual contact areas. To account for the smaller contact area, the nominal pressure of each test was multiplied by its specific adjustment factor resulting in a modified pressure, termed contact pressure.

In low speed tests, there was previously not much difference between the two contact conditions. The nominal pressure (Figure 5.36) was below 10 MPa, but mostly around 5 MPa. With the adjustment, the contact pressure (Figure 5.53) ranges between 5 MPa to 15 MPa and the tendency is a higher contact pressure for the dry testing environment.

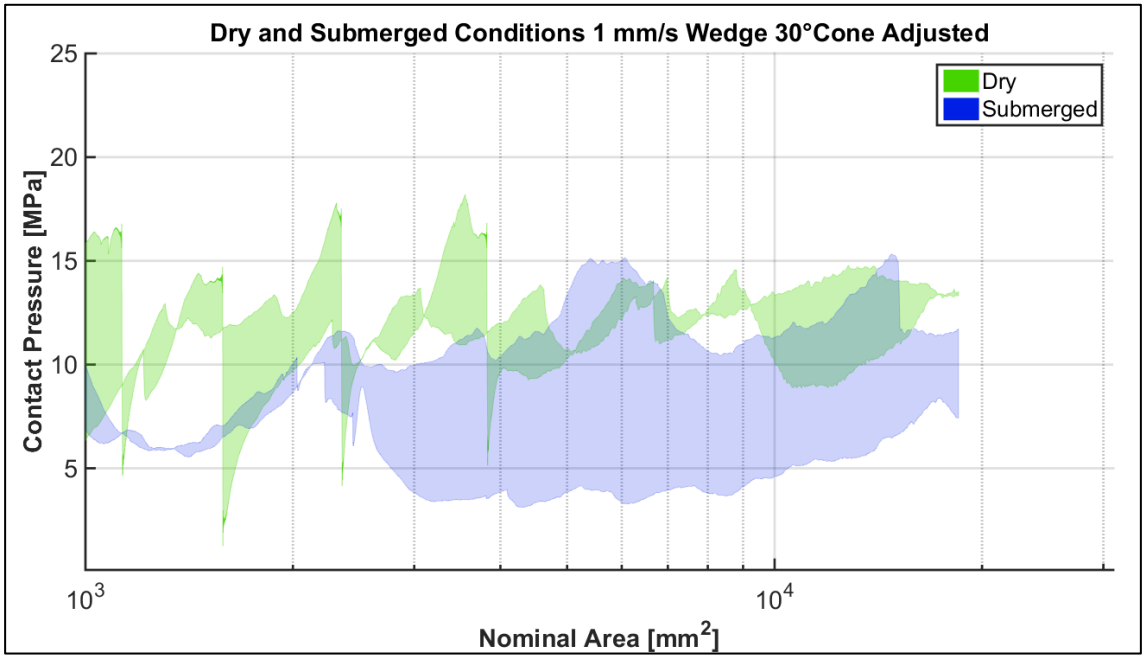

Figure 5.53: Wedge, 1 mm/s, 30° ice specimens: contact pressure-area curves for all contact conditions. The adjustment factors were 2.28 and 1.69 for the dry, and 2.09 and 1.50 for the submerged tests.

A similar shift is observed for the high speed tests. Formerly, for contact areas up to about 5000 mm^2 the nominal pressures in submergence were distinctly above those of the dry contact cases (Figure 5.38) and were subsequently similar. In contrast, the contact pressures (Figure 5.54) for both testing environments overlap in the first section, and for larger areas the dry contact pressures exceed those in submergence. Each adjustment factor was determined for between 8.0 and 17.0 mm displacement. It does not account for the increased discrepancy between actual and nominal contact areas that can be observed in Figure 5.44, for the submerged tests in particular (especially S T72-06). This would bring contact pressures in submergence closer to those of the dry condition. Due to the adjustment, the overall pressure range was increased. Based on the theoretical area, the nominal pressures were maximum at about 15 MPa, but mostly clearly lower. The contact

pressures in Figure 5.54, on the other hand, vary around 15 MPa and sporadically exceed 25 MPa.

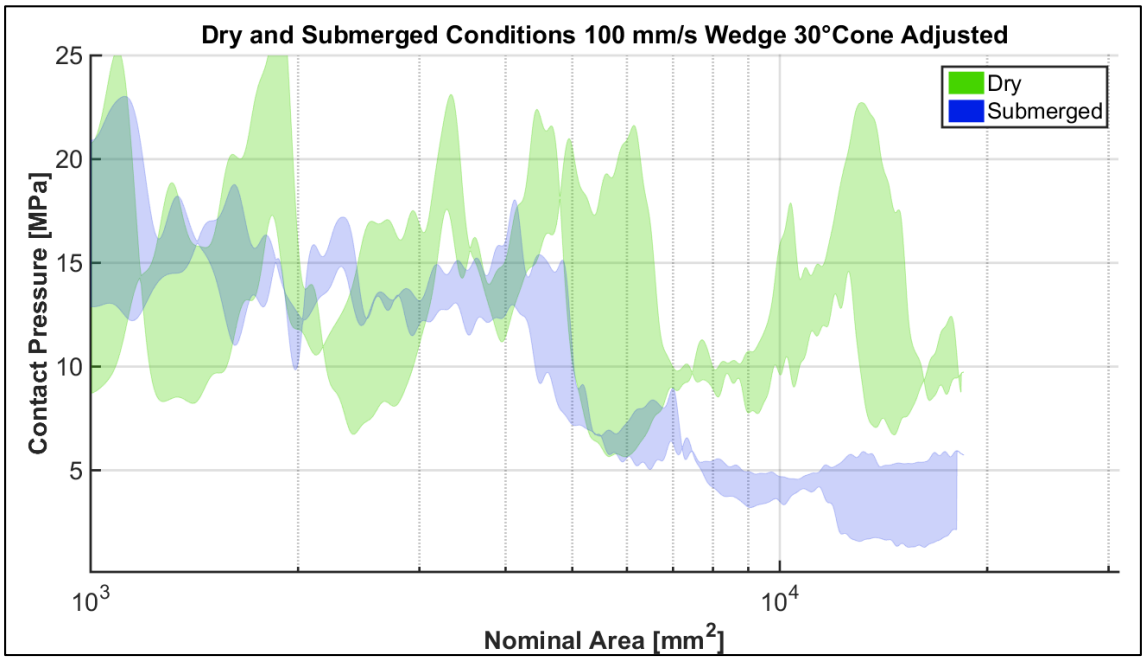

Figure 5.54: Wedge, 100 mm/s, 30° ice specimens: contact pressure-area curves for all contact conditions. The adjustment factors were 3.73 and 3.60 for the dry, and 1.51 and 1.76 for the submerged tests.

5.2.6.5 Discussion

The force measurements at the low indentation rate did not indicate a difference between the dry and submerged testing conditions; consequently, the nominal pressures did not differ. At the high indentation rate, higher forces were measured in submergence for a displacement of up to 18 mm compared to the dry tests, resulting in higher nominal pressures for the submerged tests. Independent of the indentation rate, the actual contact area was generally smaller than the theoretical nominal area, and the degree of difference was significantly affected by the contact condition. This was taken into account by adjusting the nominal pressure-area relationships with a factor established for each test

(section 5.2.6.4). This caused a change of earlier noted trends. Contact pressures were distinctly higher than nominal pressures and the ratio between pressure magnitudes dependent on testing condition was reversed: dry contact pressures had a tendency of being higher than submerged contact pressures.

The adjustment factors were determined for a defined displacement range, but not for each individual displacement instant. The latter approach was impeded due to the low sampling rate of the pressures sensors (100 Hz) compared to the MTS machine (4096 Hz in high speed tests); because it is not possible to match precisely two unsynchronized data acquisition systems. The attempt to synchronize the two data acquisition systems failed due to technical issues with the synchronization device that influenced the displacement control of the piston of the MTS machine. The matching of both sources in the analysis would induce significant errors, in particular at the high indentation rate, where the size of contact area changes rapidly. Even though the contact pressures are derived based on a simplified approach, they are believed to be a better representation of the true pressures.

The outcome suggests that the contact area drives the load magnitude (force) that can be transmitted to a structure. At the low indentation rate, the measured contact areas and forces of comparable dry and submerged cases were very similar. At the high indentation rate, the forces in submerged tests were first above those of the dry tests, but later on converged to the dry forces. A similar behavior was reflected in the measured contact areas. The curves of both submerged tests were first higher, but later tended towards the dry ones. These correlations indicate that the water affects the development of the contact area that controls the transmittable force. The submergence effect was more evident in the

high speed tests, implying a speed dependency. High speed camera footage showed fewer ice spalls and tactile pressure sensor recordings revealed a more compact contact area compared to the dry contact condition. In submergence, the overall shape of the contact area had a trend to be more similar to low speed tests, but it still preserved the characteristically localized zones of high pressures at high test speeds. The water apparently restricts ice debris extrusion, and effectively increases the contact area. The presence of water also impeded development and progression of ice fracture. This was reflected in the ice cross-sections (Figure 5.49) and in the thin sections (Figure 5.50). The ice seemed to be affected in less depth underneath the ice- indenter interface, where those areas had no cracks evident.

5.3 Conical Indenter

5.3.1 Test Overview

Table 5.11 lists 12 tests performed with the conical indenter in dry and submerged contact conditions, at 1 mm/s and 100 mm/s indentation rates, and with 30° ice cone angle. The test setup is displayed in Figure 5.55 for both testing environments.

Table 5.11: Overview of 12 tests performed with the conical indenter.

Date	Test Number		Cone Angle [°]	Indentation Rate		Contact Condition	Water	
	Overall	Day		Nom. [mm/s]	Avg. [mm/s]		Salinity [ppt]	Temp. [°C]
26.2.2015	43*	1	30	1	1.0	Dry	-	-
26.2.2015	44	2	30	1	1.0	Dry	-	-
26.2.2015	45	3	30	100	91.1	Dry	-	-
26.2.2015	46	4	30	1	1.0	Dry	-	-
26.2.2015	47	5	30	100	93.5	Dry	-	-
03.03.2015	56 [T]	1	30	1	1.0	Submerged	45.2	+0.7
03.03.2015	57	2	30	100	92.5	Submerged	46.3	-1.2
03.03.2015	58 [T]	3	30	1	1.0	Submerged	47.2	-2.2
25.03.2015	61 [T]	3	30	100	92.5	Dry	-	-
25.03.2015	62 [T]	4	30	1	1.0	Dry	-	-
25.03.2015	63 [T]	5	30	100	92.6	Submerged	28.6	+1.7
25.03.2015	64 [T]	6	30	1	1.0	Submerged	28.5	-0.2

* Test excluded from the analysis.
T Thin sections completed.

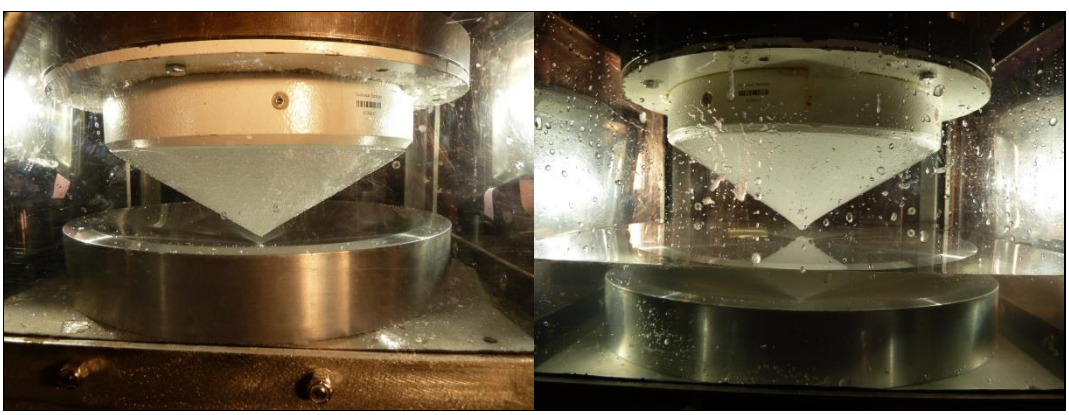

Figure 5.55: Still photos of the test setup for dry (left) and submerged (right) contact conditions with the conical indenter and 30° ice cone angle.

5.3.2 Measured Force and Nominal Process Pressure

The following force-displacement histories show displacements up to 35 mm on the x-axis, and forces up to 400 kN on the y-axis. Nominal process pressure-area relationships are plotted on a log-linear scale for a minimum nominal contact area of 1000 mm^2, and a maximum nominal pressure of 25 MPa. Green and blue areas enclose all dry and submerged tests, respectively. Figures displaying single curves for force vs. displacement and nominal pressure vs. area are provided in Appendix D2 for 1 mm/s and in Appendix D3 for 100 mm/s.

5.3.2.1 Indentation Rate: 1 mm/s

In total, seven tests were conducted with the conical indenter at 1 mm/s penetration rate: 4 dry and 3 submerged. Only 3 dry tests are analyzed in the following discussion. Test D T43-01 is excluded due to its atypical behavior (see Appendix D2). This is attributed to the sample's properties: a malfunction of the deepfreeze during the production had caused it to melt after it has already been frozen solid.

Figure 5.56 shows mostly overlapping forces, there is no difference between dry and submerged testing environments. The narrowness of each area implies fairly similar forces of the tests in either contact condition.

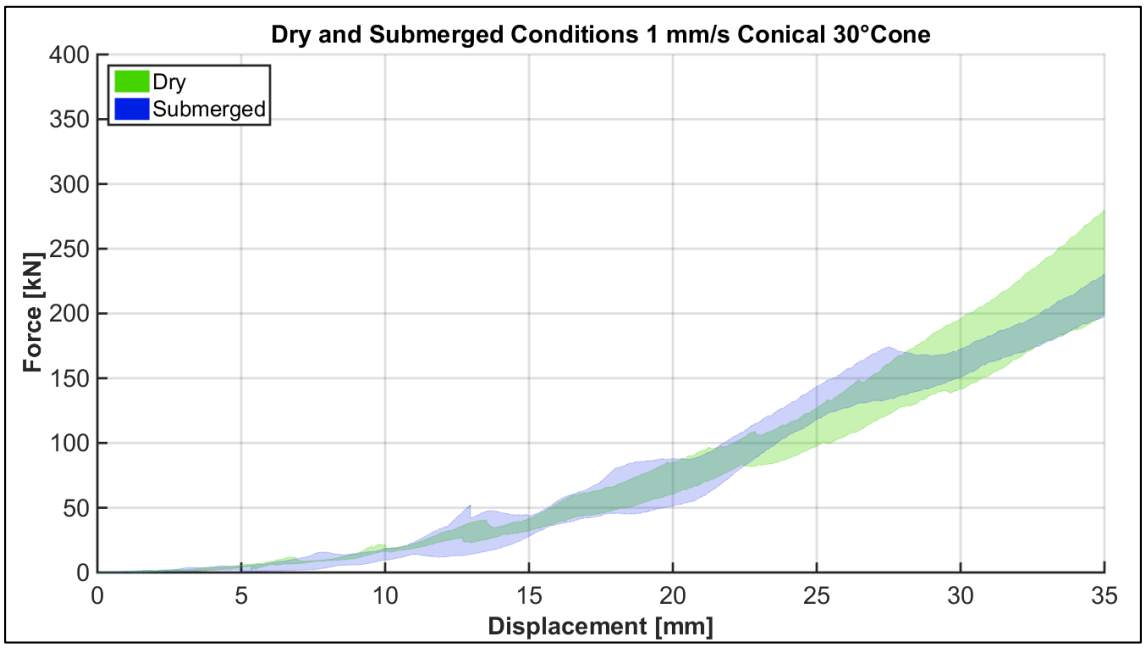

Figure 5.56: Conical indenter, 1 mm/s, 30° ice specimens: force vs. displacement for dry and submerged contact conditions. The shaded areas enclose all dry tests (3, excluding D T43-01) in green and submerged tests (3) in blue.

The nominal process pressures of submerged tests (blue) are varying at 1000 mm^2 area but assimilate for larger areas (Figure 5.57). The dry nominal pressures (green) are more alike all throughout. The nominal pressures barely exceed 13.4 MPa, and only at one incident reach 15.7 MPa. The pressures tend to slightly rise with increasing nominal area.

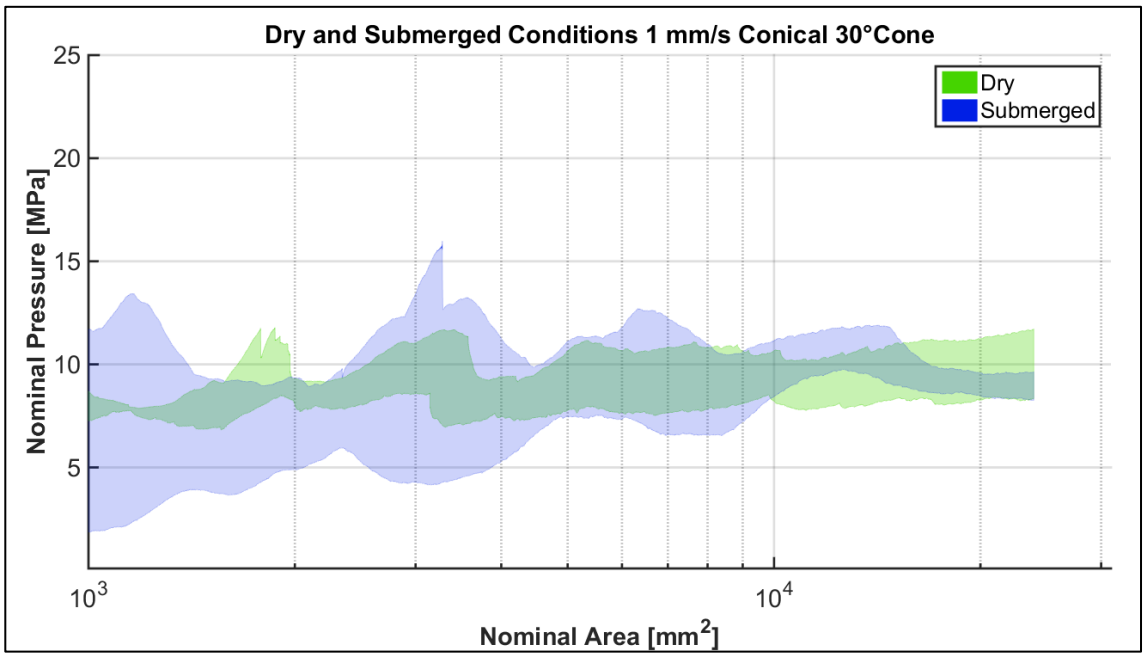

Figure 5.57: Conical indenter, 1 mm/s, 30° ice specimens: nominal pressure-area curves for all contact conditions. The shaded areas enclose all dry tests (3, excluding D T43-01) in green and submerged tests (3) in blue.

5.3.2.2 Indentation Rate: 100 mm/s

Five tests were accomplished with the conical indenter at the high impact speed: 3 dry and 2 submerged. Figure 5.58 does not display a significant difference in forces depending on the respective contact condition. Forces are low and remain under 150 kN.

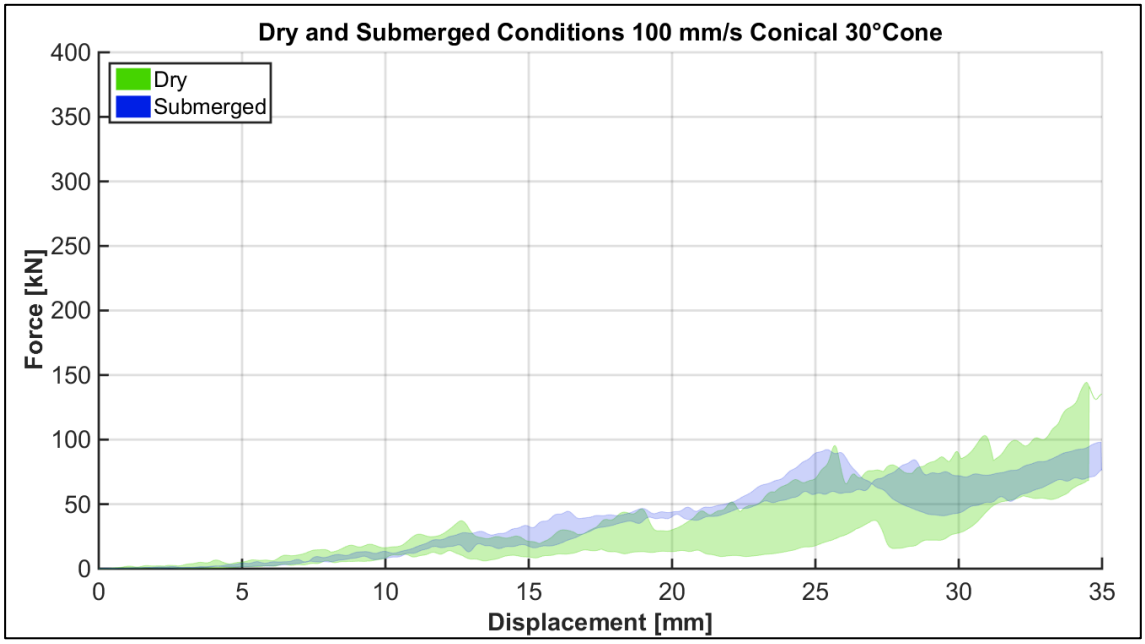

Figure 5.58: Conical indenter, 100 mm/s, 30° ice specimens: force vs. displacement for dry and submerged contact conditions. The shaded areas enclose all dry tests (3) in green and submerged tests (2) in blue.

The nominal pressures in Figure 5.59 mostly overlap. There is a slight trend of higher submerged nominal pressures (blue) for areas between 3300 mm^2 and 13000 mm^2, but the difference subsequently diminishes. The nominal pressures of both contact conditions are within 3.0 MPa to 13 MPa at 1000 mm^2 and between 2.9 MPa and 6.2 MPa at the end of the test.

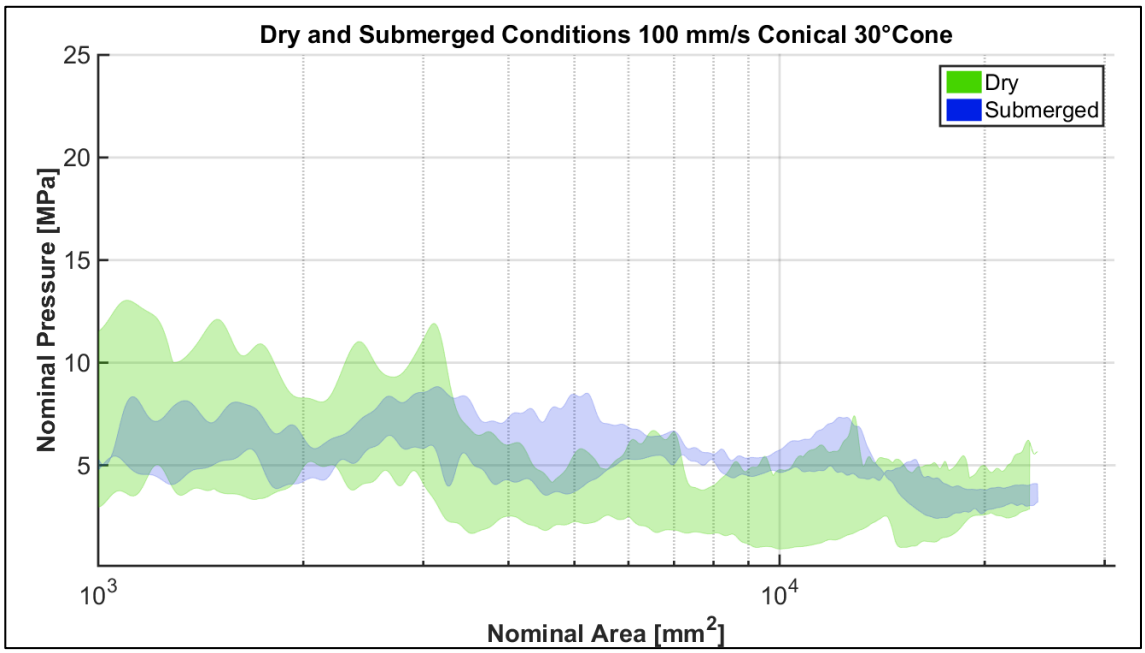

Figure 5.59: Conical indenter, 100 mm/s, 30° ice specimens: nominal pressure-area curves for all contact conditions. The shaded areas enclose all dry tests (3) in green and submerged tests (2) in blue.

5.3.3 General and Microstructural Observations

Subsequent paragraphs address visual observations based on high speed camera (HSC) footage, still photos of sample surfaces after test completion, and thin sections.

5.3.3.1 General Observations – During Testing: Ice Debris Formation, Ice Extrusion and Crack Propagation (HSC)

Figure 5.60 shows two examples of 1 mm/s rate tests at a displacement of approximately 19.3 mm. The dry sample (left) has distinct fractures and many ice spalls are breaking off. In contrast, the submerged sample (right) seems far less affected and is more intact.

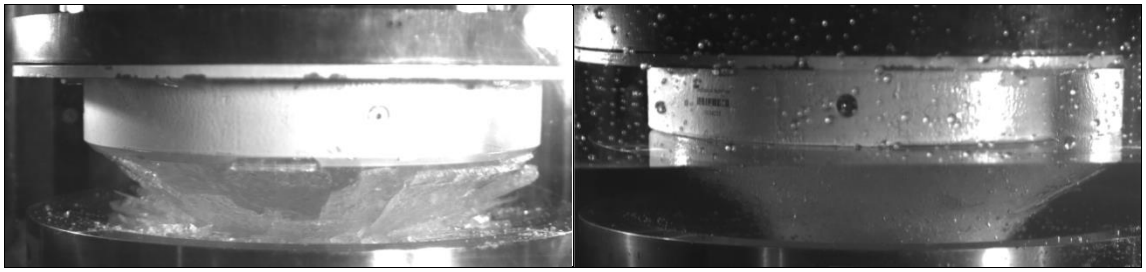

Figure 5.60: Conical indenter, 1 mm/s, 30° ice specimens, dry (left, D T46-04) and submerged (right, S T56-01) contact conditions, approx. 19.3 mm penetration depth. Still photos of HSC footage showing distinct fractures and ice spalls in the dry environment. The submerged sample seems to be fairly intact.

Also at the high indentation rate, the formation of ice debris and its extrusion are distinctly different for the two contact conditions (Figure 5.61). In the dry scenario (left), ice debris is expelled and widely extruded. In the submergence case (right), the ice debris seems cloud-like, and remains fairly concentrated around the contact area.

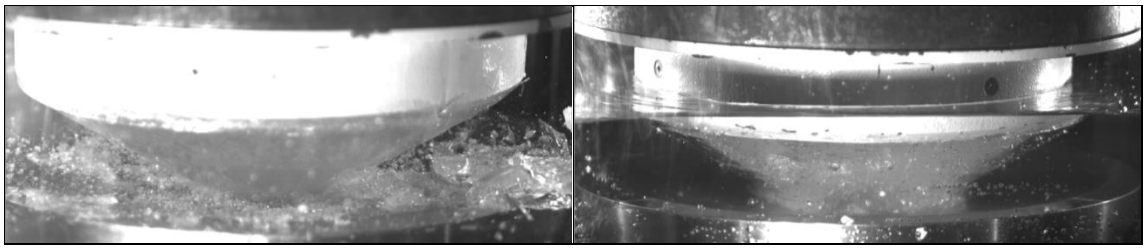

Figure 5.61: Conical indenter, 100 mm/s, 30° ice specimens, dry (left, D T61-03) and submerged (right, S T63-05) contact conditions, approx. 19.4 mm penetration depth. Still photos of HSC footage showing significant ice debris formation in the dry testing environment, but considerably less in submergence.

5.3.3.2 General Observations - After Test Completion: Contact Area and Surface (Still Photos)

Samples tested with the conical indenter at low speed have the typical low-rate contiguous circular contact area, comparable for dry and submerged conditions (Figure 5.62). In the dry condition (top), the contact area is distinctly separated from the remaining ice body. In the submerged condition (bottom), the perimeter of the contact area is less well differentiated but the transition to the remnant ice is smooth.

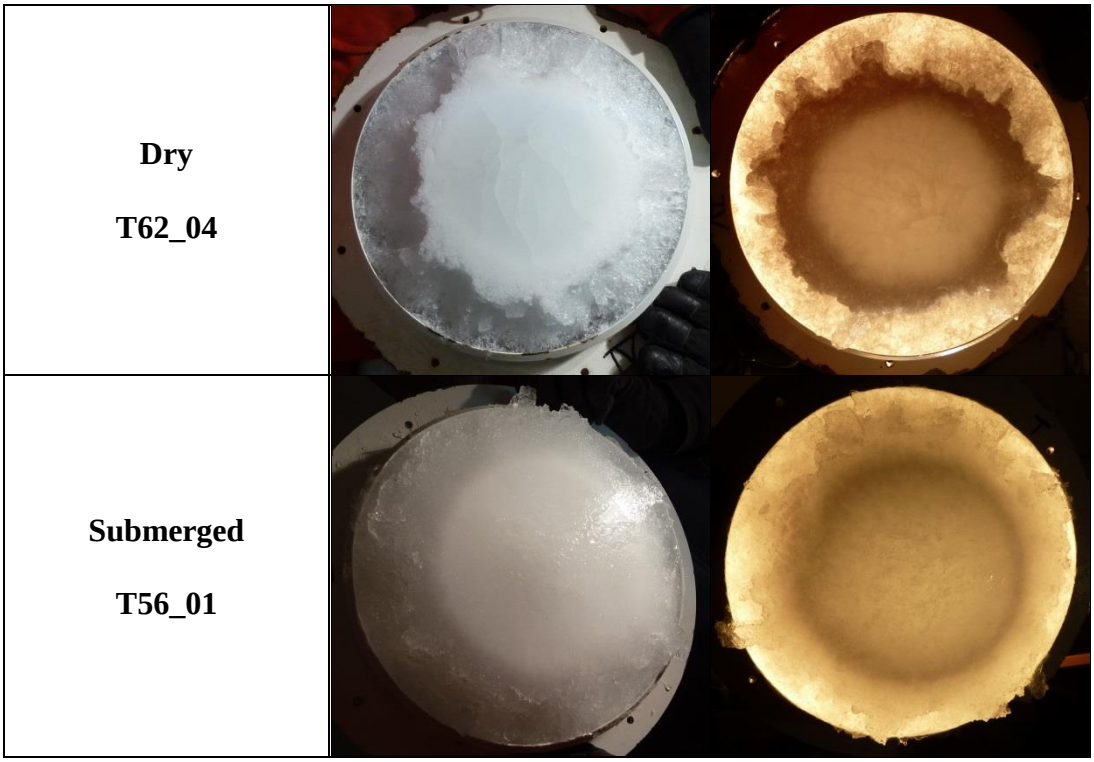

Figure 5.62: Conical indenter, 1 mm/s, 30° ice specimens: images of ice samples after testing in dry (top) and submerged (bottom) contact conditions; on the left of indented surfaces, on the right with lighting applied from the back.

Dry samples at the high indentation rate have the typical high-speed branch-like pattern consisting of high and low pressures zones (Figure 5.63, top). For submerged samples, on the other hand, there is no recognizable HPZ pattern (Figure 5.63, bottom). A large fragment in the middle is missing. For further examples refer to Appendix D4.

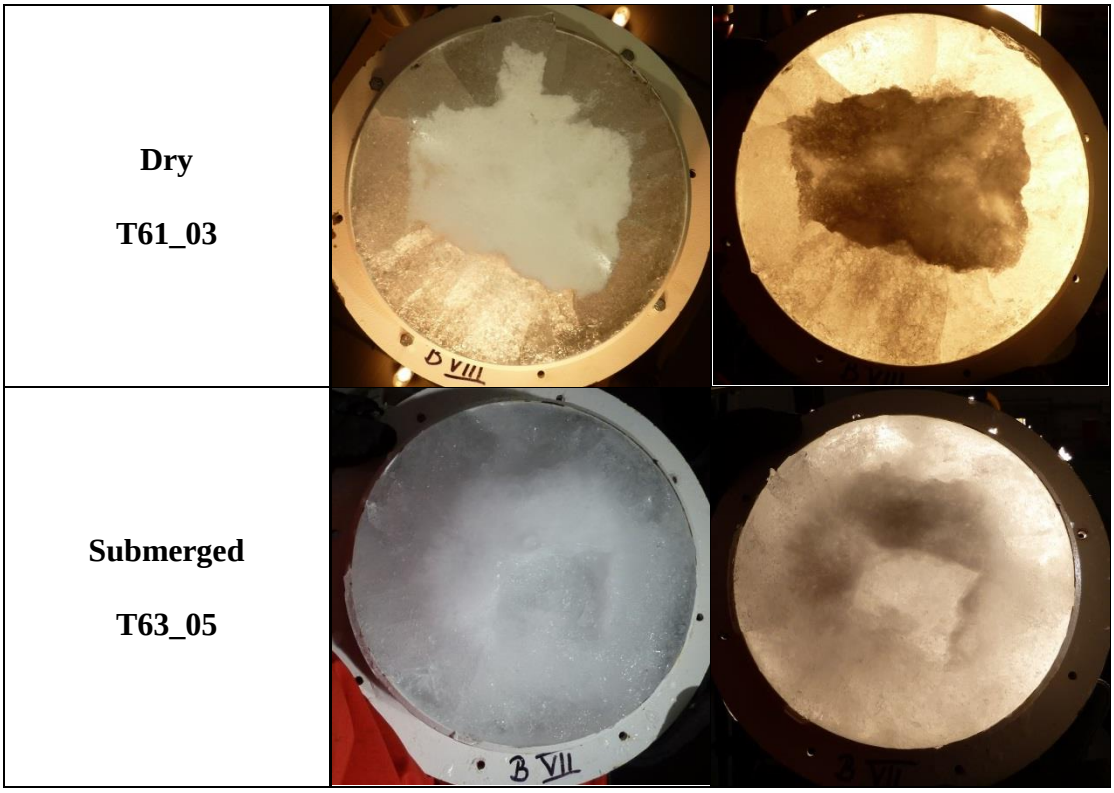

Figure 5.63: Conical indenter, 100 mm/s, 30° ice specimens: images of ice samples after testing in dry (top) and submerged (bottom) contact conditions; on the left of indented surfaces, on the right with lighting applied from the back.

5.3.3.3 Microstructural Observations

Tests where thins sections were taken are indicated with superscript "T" in Table 5.11. Some of them are discussed in the following paragraph but all photos are included in Appendix D5.

For the conical indenter, no difference in ice loads due to the contact condition at either indentation rate was observed. Also, the microstructures of two high speed tests in Figure 5.64 (dry: left, submerged: right) have no obvious dissimilarities. In both cases, the crushed ice layer is approximately 1 cm. The submerged sample (right), may have slightly reduced ice crystal sizes.

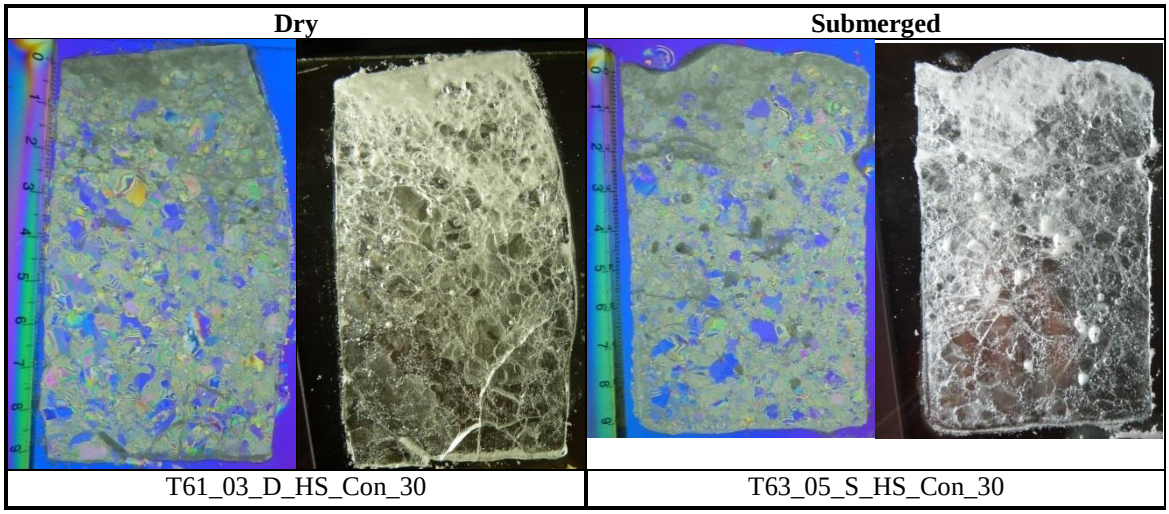

Figure 5.64: Conical indenter, 100 mm/s, 30° ice cones: thin sections tests in dry (left) and submerged (right) conditions. The images show the sections between a cross-polarized filter on the left and with side lighting applied on the right.

5.3.4 Multiple Regression Analysis

Twelve tests were completed with the conical indenter (Table 5.11). The limited data did not allow significant regression models to be established. Therefore, the trends can be considered a qualitative analysis of the results. The models are not based on any significance level and the data is not transformed. Two categorical factors are considered, indentation rate and contact condition, as well as their interaction.

Figure 5.65 reveals that indentation rate is more important than contact condition. Going from 1 mm/s to 100 mm/s entails a distinct decrease in every response. Submergence, on the other hand, only slightly increases three out of four responses and mitigates the response of Nominal Pressure Max 1000.

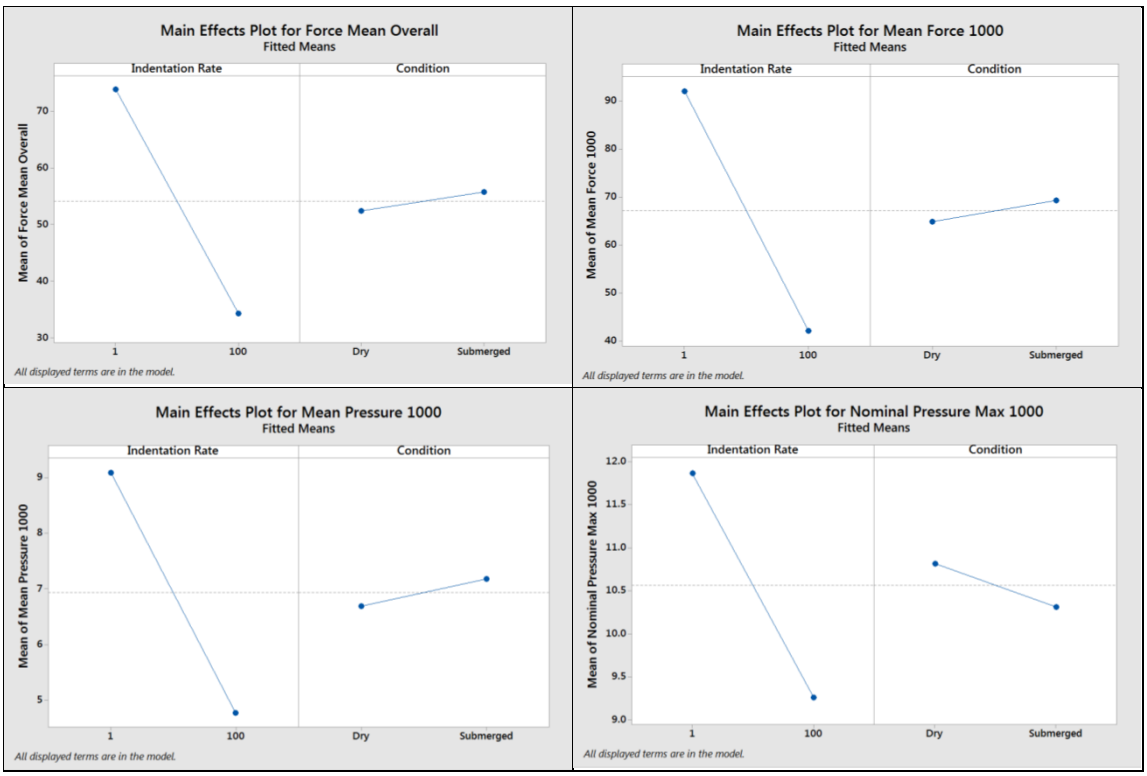

Figure 5.65: Overview of main effects on the means of the four responses for the conical indenter.

The interaction trends (Figure 5.66) are fairly consistent. The responses in both conditions at 1 mm/s are usually higher than those at 100 mm/s. Generally, submergence has higher responses at both rates with one exception, Nominal Pressure Max 1000.

More information (plots of residuals and interactions, regression models) can be viewed in Appendix D6.

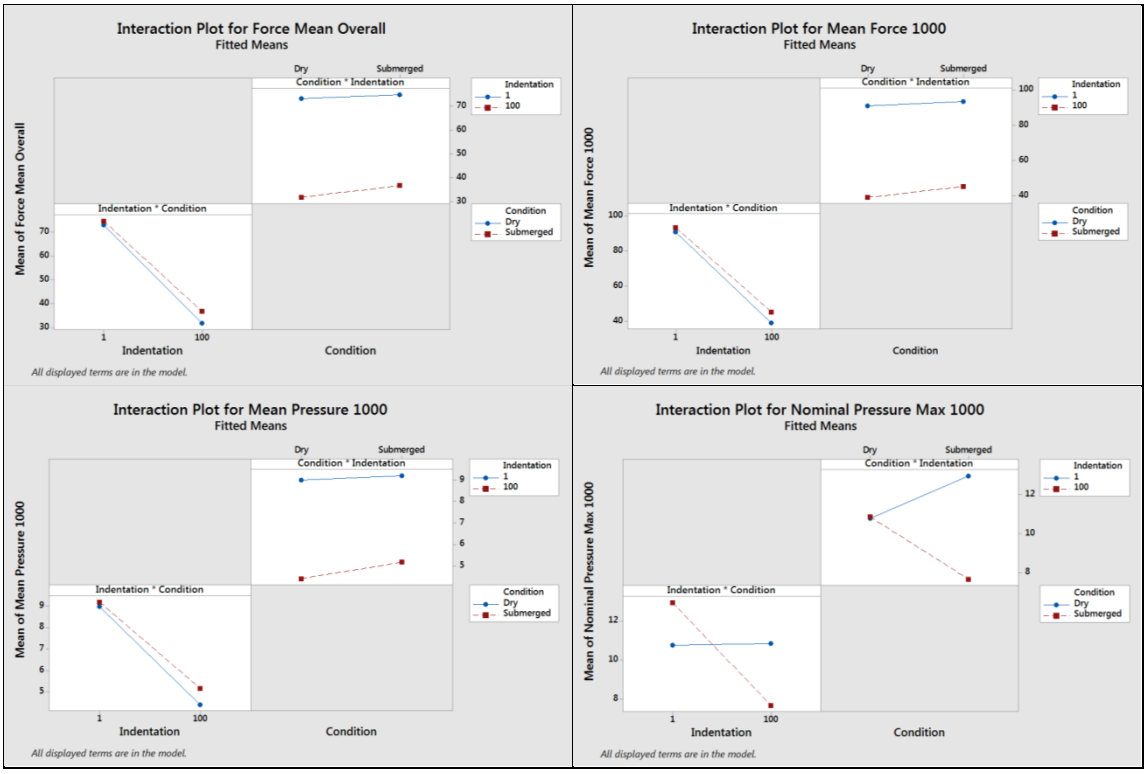

Figure 5.66: Overview of the effect of indentation rate and contact condition interaction on the means of the four responses of the conical indenter.

5.3.5 Summary and Discussion

At 1 mm/s indentation rate, both contact conditions resulted in similar nominal process pressures that slightly increased with advancing displacement. Nominal pressures of submerged tests varied more first but this diminished for contact areas above 10000 mm^2. Also, still photos of contact surfaces after the tests and thin section images of the ice crystal structure did not indicate a difference between dry and submerged testing environments.

At 100 mm/s indentation rate there was no difference between the contact conditions. Nominal pressures decreased overall. In view of contact area, dry tests showed a distinct

branch-like pattern, whereas no pattern was identifiable in the submerged tests. Thin sections of samples for both contact conditions were similar.

In summary, for the conical indenter, submergence did not have an effect at either indentation rate. At 1 mm/s, the nominal pressures seemed to increase with increasing area, but to decrease at 100 mm/s.

5.4 Spherical Indenter

5.4.1 Test Overview

Table 5.12 summarizes the 10 tests carried out with the spherical indenter. The tests were done with 20° ice specimen angle, at low and high indentation rates, and in dry and submerged environments. Figure 5.67 displays the test setup for both contact conditions.

Table 5.12: Overview of 10 tests performed with the spherical indenter.

Date	Test Number		Cone Angle [°]	Indentation Rate		Contact Condition	Water	
	Overall	Day		Nom. [mm/s]	Avg. [mm/s]		Salinity [ppt]	Temp. [°C]
27.02.2015	48	1	20	1	1.0	Dry	-	-
27.02.2015	49	2	20	100	94.8	Dry	-	-
27.02.2015	50 [T]	3	20	1	1.0	Dry	-	-
27.02.2015	51 [T]	4	20	100	94.7	Dry	-	-
02.03.2015	52 [T]	1	20	1	1.0	Submerged	44.5	+4.4
02.03.2015	53 [T]	2	20	100	94.4	Submerged	45.7	+2.9
02.03.2015	54	3	20	1	1.0	Submerged	45.8	+1.9
02.03.2015	55	4	20	100	95.1	Submerged	45.6	+0.8
25.03.2015	59	1	20	1	1.0	Dry	-	-
25.03.2015	60	2	20	100	95.0	Dry	-	-

T Thin sections completed.

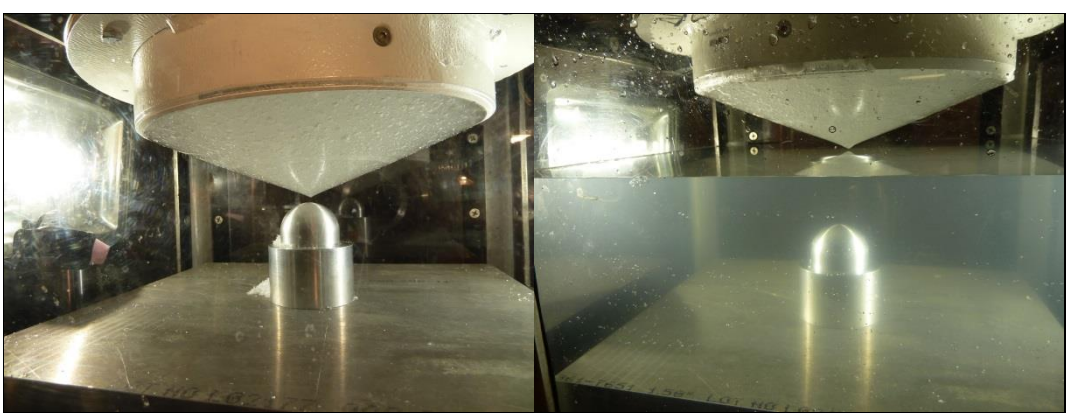

Figure 5.67: Still photos of the test setup for dry (left) and submerged (right) contact conditions with the spherical indenter and 20° ice cone angle.

5.4.2 Measured Force and Nominal Process Pressure

The force-displacement histories in the following sections are shown for displacements up to 30 mm on the x-axis, and for forces up to 25 kN on the y-axis. The nominal process pressure-area relationships are on log-linear scales up to 25 MPa, and for areas between 100 mm^2 and 1914 mm^2 (2.7 mm to 30.0 mm displacement). All tests of dry and submerged contact conditions are summarized in green and blue areas. Individual test curves are provided in Appendix E2 and in Appendix E3 for 1 mm/s and 100 mm/s indentation rates.

5.4.2.1 Indentation Rate: 1 mm/s

In total, five tests were performed at the low indentation rate: 3 dry and 2 submerged. Figure 5.68 displays very similar forces in the dry and submerged contact conditions. Forces steadily increase up to a displacement of approximately 25 mm, and flatten subsequently; near the point where the sphere is almost entirely enclosed by the ice specimen and the nominal contact area only marginally grows (Figure 4.3). In general, forces are low and remain below 16.6 kN.

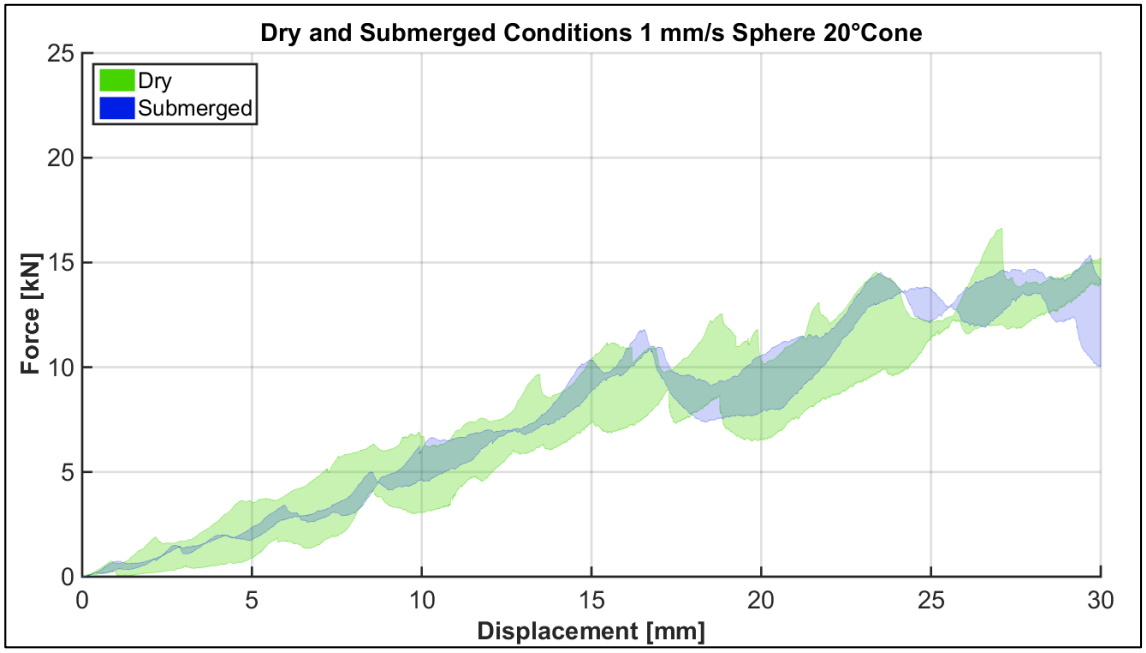

Figure 5.68: Sphere, 1 mm/s, 20° ice specimens: force vs. displacement for dry and submerged contact conditions. The shaded areas enclose all dry tests (3) in green and submerged tests (2) in blue.

Figure 5.69 shows that the nominal pressures in the submergence cases (blue) are in the mean of the dry pressures (green) overall. Dry pressures vary more first, but later assimilate. Pressures of both contact conditions end in a narrow bandwidth from 5.5 MPa to 7.9 MPa.

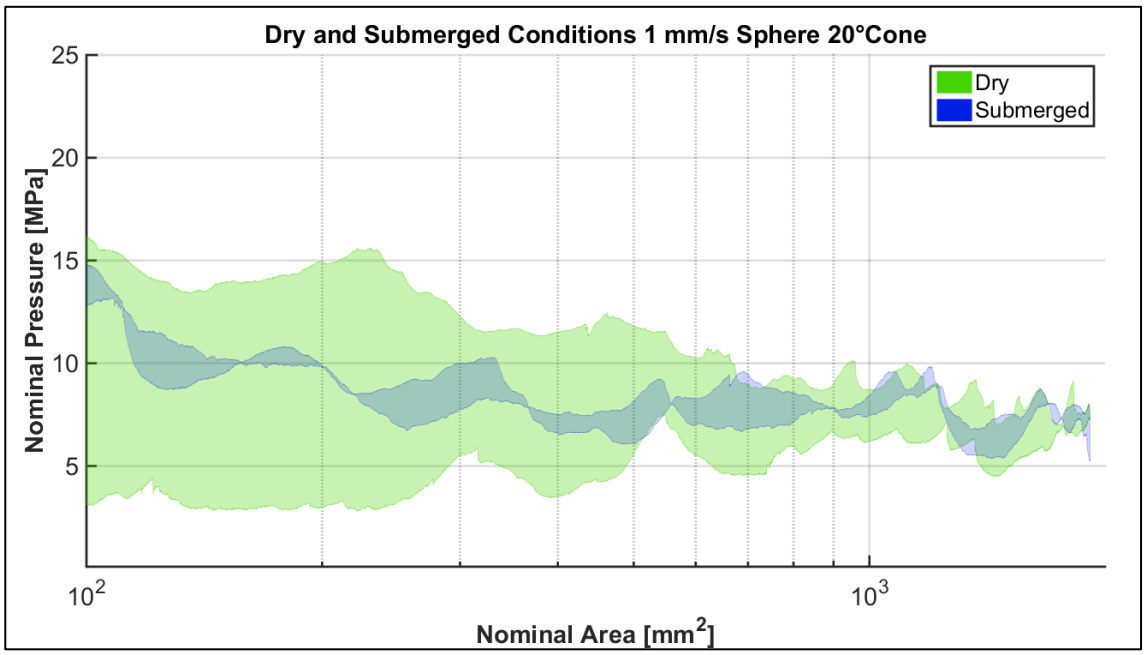

Figure 5.69: Sphere, 1 mm/s, 20° ice specimens: nominal pressure-area curves for all contact conditions. The shaded areas enclose all dry tests (3) in green and submerged tests (2) in blue.

5.4.2.2 Indentation Rate: 100 mm/s

Five tests were carried out at 100 mm/s impact speed: 3 dry and 2 submerged. Figure 5.70 shows that for up to a displacement of 16.6 mm, submerged forces exceed dry forces. Beyond this point (17-21 mm), submerged forces distinctly vary, and overlap with dry forces. Between displacements of 21.3 mm and 25.4 mm, submerged forces are similar to each other and are below the dry forces. Close to the maximum displacement, submerged forces are above dry forces. Eventually, all forces are within 5.5 kN and 10.4 kN. Overall, in Figure 5.70 the forces slowly but steadily incline up to approximately 16.4 mm (submerged) and 18.6 mm (dry) displacements. Subsequently, both areas flatten but fluctuate. This is about the displacement where the nominal contact area only marginally increases further. The earlier data might vary more at the high indentation rate due to the more dynamic ice crushing and spalling in the beginning stages of the indentation.

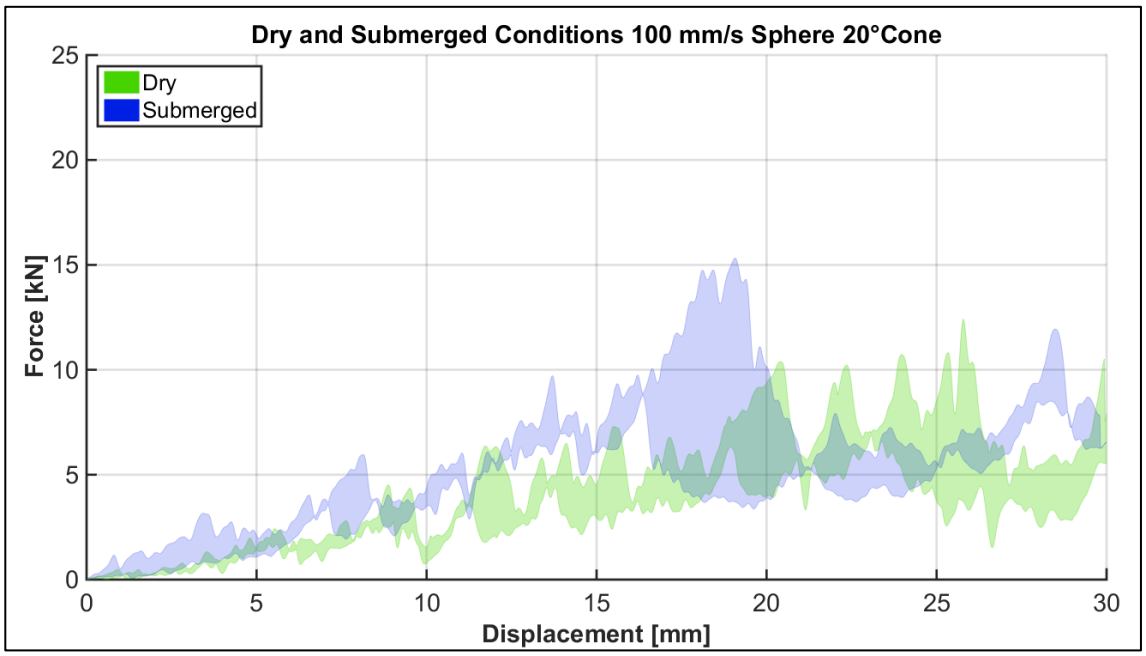

Figure 5.70: Sphere, 100 mm/s, 20° ice specimens: force vs. displacement for dry and submerged contact conditions. The shaded areas enclose all dry tests (3) in green and submerged tests (2) in blue.

The nominal pressure-area relationships are given in Figure 5.71. At small contact areas the variation among the two submerged tests is significant. Although the pressures of both contact conditions overlap in some parts, the pressures in the submergence cases tend to be higher. The proportion changes for nominal contact areas between 1200 mm^2 and 1800 mm^2 where there is substantial overlap and the ratio is reversed. For areas above 1800 mm^2 submerged pressures are higher, but eventually terminate in the mid-range of dry pressures (2.9 MPa to 5.4 MPa).

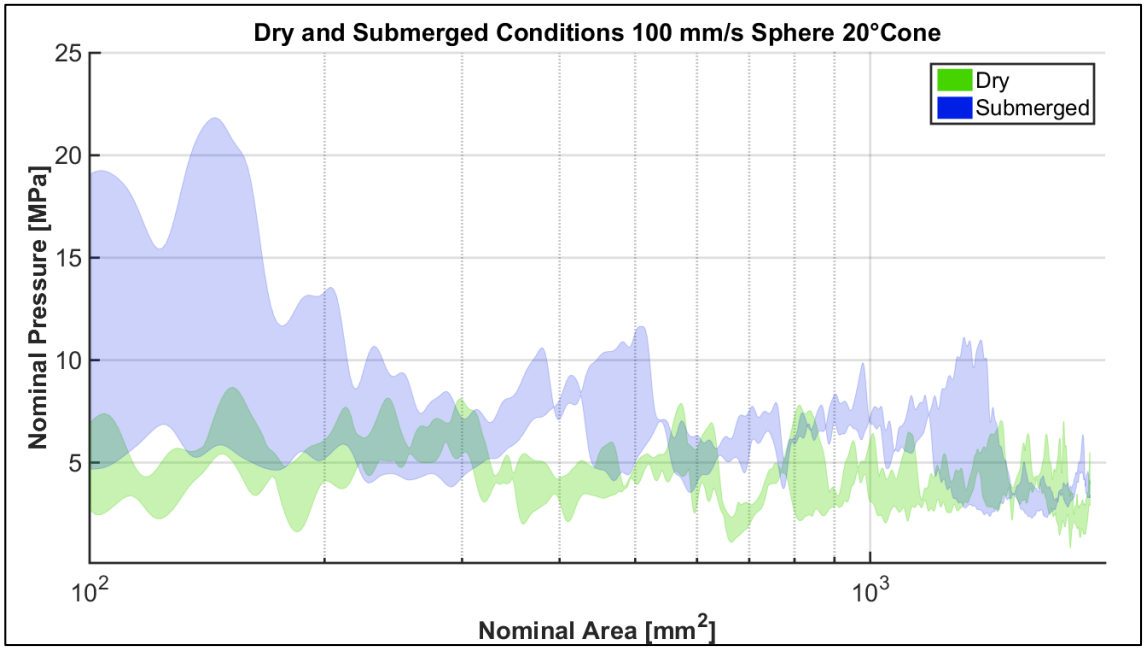

Figure 5.71: Sphere, 100 mm/s, 20° ice specimens: nominal pressure-area curves for all contact conditions. The shaded areas enclose the dry tests (3) in green and submerged tests (2) in blue.

5.4.3 General and Microstructural Observations

The following subsections discuss visual observations by means of high speed camera (HSC) footage, still photos of sample surfaces after test completion, and thin sections.

5.4.3.1 General Observations – During Testing: Ice Debris Formation, Ice Extrusion and Crack Propagation (HSC)

At the low indentation rate in the dry testing environment the extruding ice debris consisted of ice spalls and crushed ice, where the latter prevailed at small displacements. The first visible large crack (Figure 5.72, left) formed between a displacement of approximately 8.2 mm and 8.7 mm, but the spall only started to break off after another 17.6 mm was exceeded. Meanwhile ice spalls at other locations had already broken off.

In submergence cases (e.g. Figure 5.72, right), mainly ice flakes were observed. These formed locally, at about 1 cm to 1.5 cm distance from the contact zone. When a flake was detached from its initial position, it slowly floated alongside the ice cone surface. After a short distance travelled it stopped and presumably re-bonded with the ice specimen. Larger ice spalls were formed only at advanced displacement and slowly floated to the water surface.

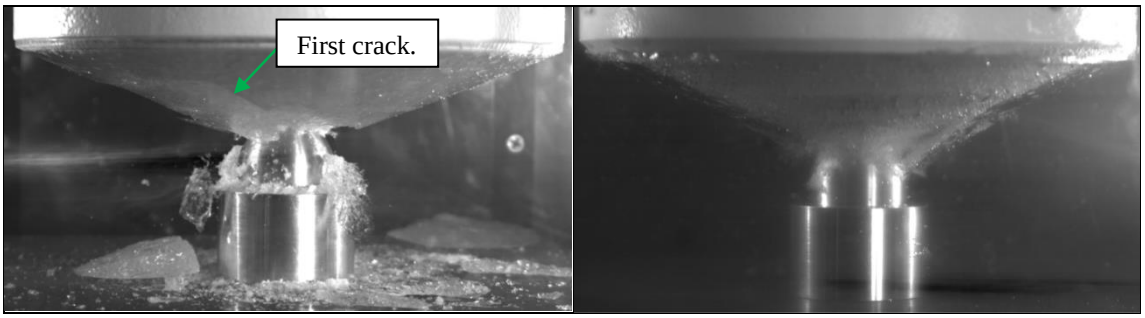

Figure 5.72: Sphere, 1 mm/s, 20° ice specimens, dry (left, D T50-03) and submerged (right, S T52-01) contact conditions, approx. 19.3 mm penetration depth. Still photos of HSC footage. In the dry contact condition (left), crushed ice is extruded and ice spalls break off. In submergence, the ice debris mostly consists of ice flakes and only later ice spalls are formed that float to the water surface.

In the dry environment at the high indentation rate, ice debris was expelled in a waterfall-like manner (Figure 5.73, left). This extruded material mostly consisted of fine grained ice and occasional ice flakes. Large ice pieces only broke off at very advanced displacements.

For up to approximately 16 mm penetration, the failure of the submerged sample was similar to the one at the low indentation rate, mainly affected near the ice-indenter interface. A cloud of ice debris, mostly consisting of crushed ice, was pushed forward and enveloped the sphere's cap (Figure 5.73, right). Within a fraction of a second (67th of a second, displacement of 1.5 mm) significant cracking occurred, but no ice pieces fell off

during the entire test. At this time, the ice cloud seemed to be comprised of mainly fine grained material with some ice fragments. The water reduced the formation of spalls and kept those that formed in place.

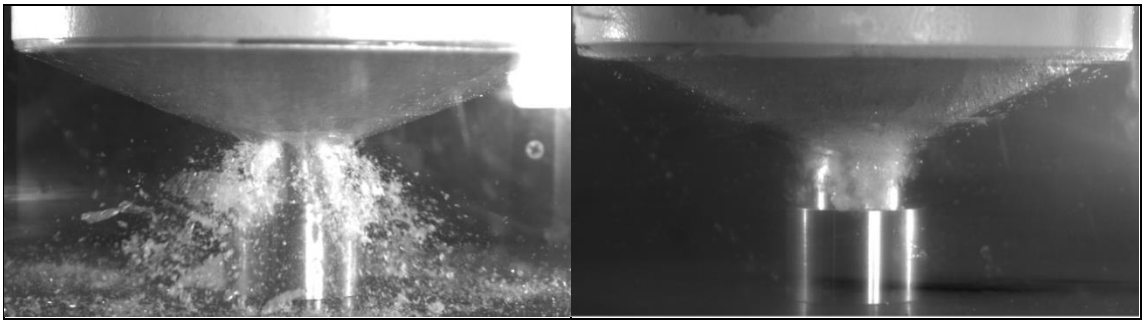

Figure 5.73: Sphere, 100 mm/s, 20° ice specimens, dry (left, D T51-04) and submerged (right, S T53-02) contact conditions, approx. 19.3 mm penetration depth. Snap shots of HSC footage. In the dry contact condition (left), crushed ice is waterfall-like extruded. In submergence, ice spall formation is reduced and the ice debris appears cloud-like.

5.4.3.2 General Observations - After Test Completion: Contact Area and Surface (Still Photos)

For the spherical indenter, submergence only affected ice loads at the 100 mm/s indentation rate and the following discussion is concentrated on those tests. The sphere left a clear imprint in the centre of the ice remnants, especially in the dry environment (Figure 5.74, top). Four large fractures radially extend from the centre to the ice holder, approximately 90° apart from another. Such fractures were common in the tests with the spherical indenter, although not in this specific spacing array. In submerged tests, the sphere's mark is less pronounced and there are fewer radial cracks (Figure 5.74, bottom).

Figure 5.74: Sphere, 100 mm/s, 20° ice specimens: images of ice samples after testing in dry (top) and submerged (bottom) contact conditions; on the left of indented surfaces, on the right with lighting applied from the back.

The overall appearance of samples tested at 1 mm/s was similar (see Appendix E4). In the dry contact condition, the relatively small and curved surface of the sphere produced indentation rate typical patterns, i.e. a circular area at 1 mm/s, and a branch-like pattern at 100 mm/s (Figure 5.75, left and right).

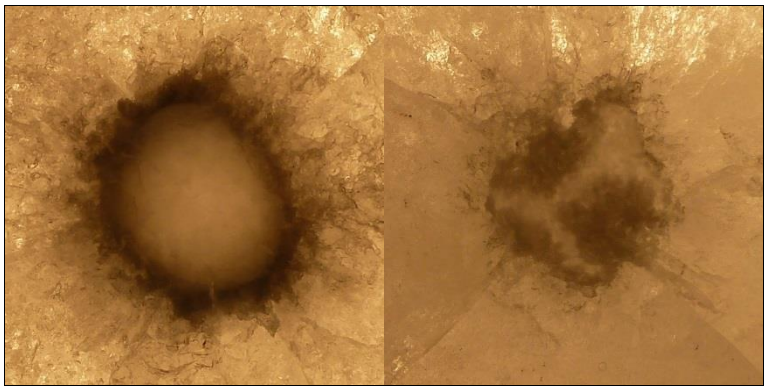

Figure 5.75: Close-ups of surface contact areas of dry tests with the spherical indenter at 1 mm/s (left, D T59-01) and 100 mm/s (right, D T49-02) indentation rates. The images display rate-typical contact areas, i.e. a circular shape for low speed tests, and a branch-like pattern for high speed tests.

5.4.3.3 Microstructural Observations

Tests where thin sections were taken are indicated with superscript “T” in Table 5.12. All results are provided in Appendix E5.

Samples of (dry) high speed tests were particularly prone to breaking. Processing with the microtome caused severe fractures as is evident in Figure 5.76. The figure shows thin sections of 100 mm/s tests. The dry test (left) has an approximately 5 mm thin layer of damaged ice and the ice microstructure beneath has significantly reduced ice crystals. In contrast, submergence (right) has preserved larger ice crystals. The sample is mainly affected within the maximal 5 mm small layer at the contact interface but the microstructure below seems fairly unchanged (compared to the parent ice).

Thin sections of low speed tests are included in Appendix E5. Both contact conditions do not essentially differ from one another. The crystal structure is similarly affected with generally smaller crystal sizes and the layer of damaged ice extends into more depth compared to the examples shown below.

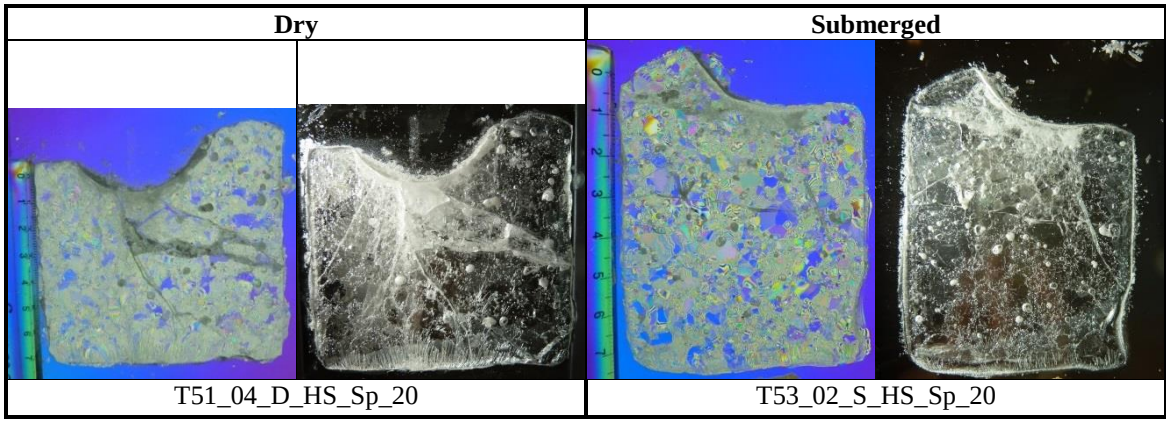

Figure 5.76: Sphere, 100 mm/s, 20° ice cones: thin sections of tests in dry (left) and submerged (right) conditions. The figure shows the sections of the specimens between a cross-polarized filter on the left and with side lighting on the right.

5.4.4 Multiple Regression Analysis

The limited quantity of 10 performed tests (Table 5.12) does not permit the determination of a significance level in the regression analysis. Furthermore, no data transformation is applied. The outcome will be briefly discussed, but it should be pointed out that the results mainly serve as general trend indicators. Considered factors are indentation rate, contact condition, and their interaction. Responses are the same as were earlier indicated; but in the present case, maximum pressure, mean pressure, and mean force refer to nominal areas above 100 mm^2 rather than the 1000 mm^2 used for the larger indenters.

The main effects in Figure 5.77 provide an almost uniform picture. Responses at 1 mm/s are above those at 100 mm/s. In all cases, submergence causes higher responses compared to the dry contact condition.

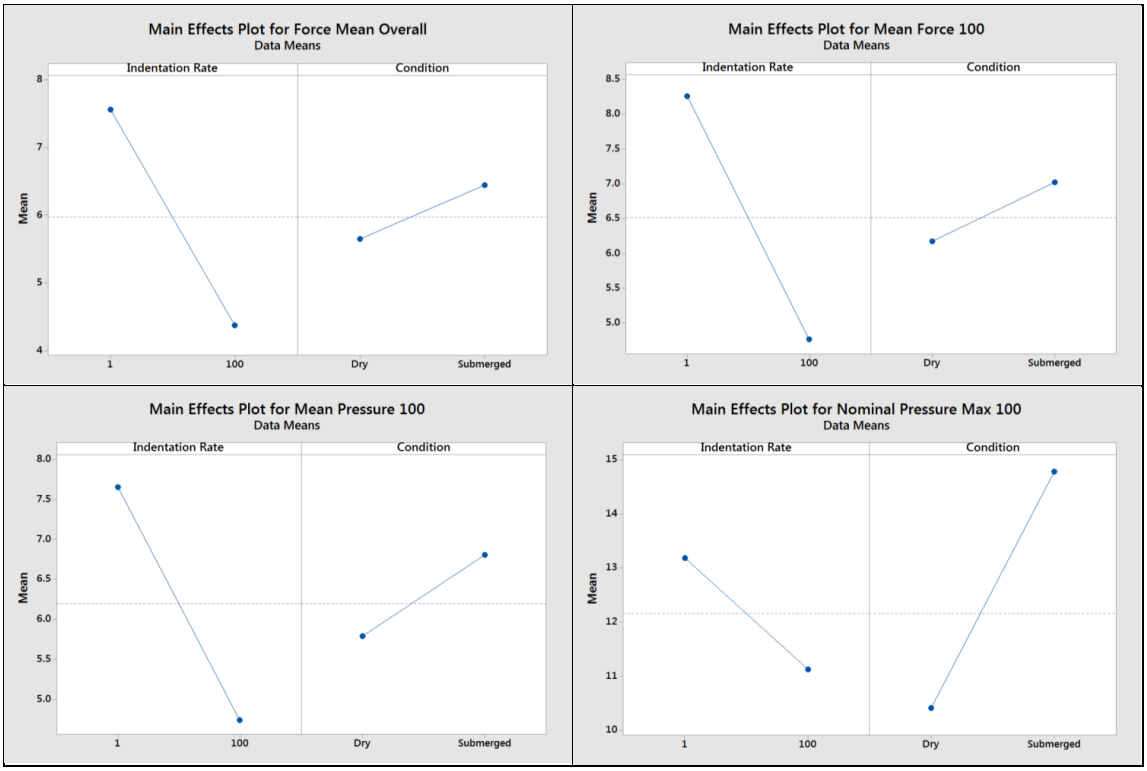

Figure 5.77: Overview of main effects on the means of the four responses for the spherical indenter.

The interaction plots in Figure 5.78 reveal overall higher responses in submergence in combination with the high indentation rate.

Supplementary information regarding residuals and the regression models is provided in Appendix E6.

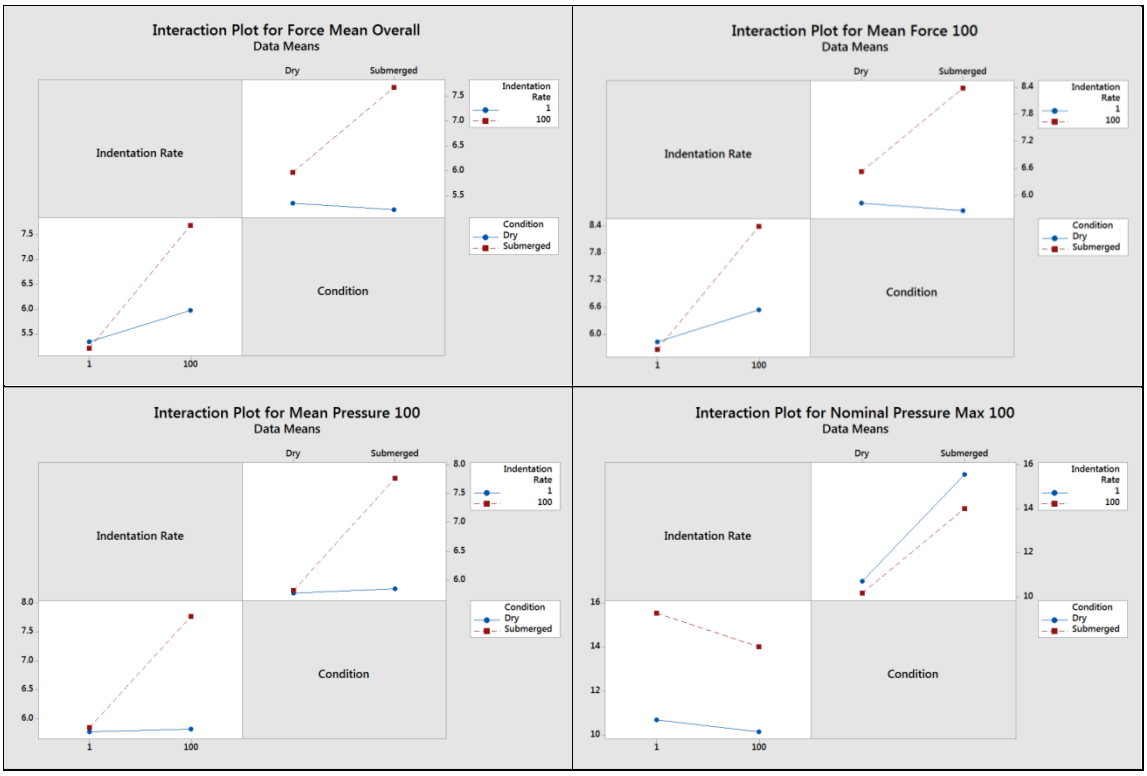

Figure 5.78: Overview of the effect of indentation rate and contact condition interaction on the means of the four responses of the spherical indenter.

5.4.5 Summary and Discussion

The analysis of low indentation rate tests with the spherical indenter did not reveal any difference between dry and submerged contact conditions. Submerged loads were similar to each other, and in the mid-range of dry loads. Also the ice microstructure did not exhibit a visible difference. In both cases, subjacent to the layer of damaged ice, the crystal size was reduced throughout. The high speed camera (HSC) recordings allowed for the observation of a distinct difference in the ice debris formation and extrusion. Fine grained material and ice spalls were expelled in the dry environment. In the submergence cases, ice failure resulted in a slowly downward moving cloud of ice debris; the surrounding water likely bonded fine grained material and ice flakes so far it developed. Ice spall formation was reduced and only observed at late stages of the tests.

Ice loads at the high indentation rate showed stronger evidence of a submergence effect. Loads in submergence were higher, but in some parts also varied more than dry loads. By comparing the ice microstructure of two samples, the submerged sample seemed less affected by the impact and had larger grain sizes than the dry sample. This supports observations made from HSC footage, where ice failure in submergence appeared to remain more localized at the contact zone. The ice debris was found to mainly consist of fine grained material. Some ice fragments were formed but barely left the initial position. Overall, the surrounding water kept ice flakes and spalls in place, presumably promoted by a combination of buoyancy and re-bonding between ice fragments and specimen. HSC recordings of dry tests showed a constant waterfall-like extrusion of fine grained material with occasional ice flakes, and with ice spalls only at advanced displacement.

In general, ice loads at the high indentation rate were below those at the low indentation rate. In both cases, the forces flattened on approaching the final displacement. This was explained by the slow increase in nominal (projected) contact area near the end of the test that limited to the structure transmittable loads. It also maintains the idea of a predominantly perpendicular force transmission to the structure and the initial assumption of the projected contact being a better representation than the tangent contact area. While the growth of the projected contact area decelerates, the tangent contact area still distinctly increases (Figure 4.3), and would likely have facilitated higher forces. In reality, it can be expected that the true contact area differs significantly from the (idealized) nominal area.

Chapter 6 Theoretical Implications

This chapter elaborates on the observed influences in the obtained results and theoretical implications of the observed phenomena.

6.1 Effect of Indentation Rate and Contact Condition

The indentation rate was of significant influence on the measured force magnitudes. In each figure presented below the colors characterize: the low indentation rate (1 mm/s) in green, medium (10 mm/s) in blue, and high (100 mm/s) in red. The numbers in brackets in figure capitations signify the test quantity at the individual rate.

6.1.1 Flat Plate

Tests with the flat indentation plate involved 20° and 30° ice specimens, and are discussed separately.

6.1.1.1 20° Ice Specimens

Figure 6.1 illustrates the typical effect of indentation rate in test with conical ice specimens in dry cases. The low indentation rate (1 mm/s) yields the highest loads, followed by medium rate (10 mm/s), and high indentation rate (100 mm/s). The explicitness of the sequence increases with advancing penetration.

From Figure 6.2 it can be inferred that this categorization does not apply to the submerged testing environment. While the water only slightly increases forces at the low indentation rate, it causes a significant rise at the high rate that is now above the medium indentation rate, which is less affected by submergence.

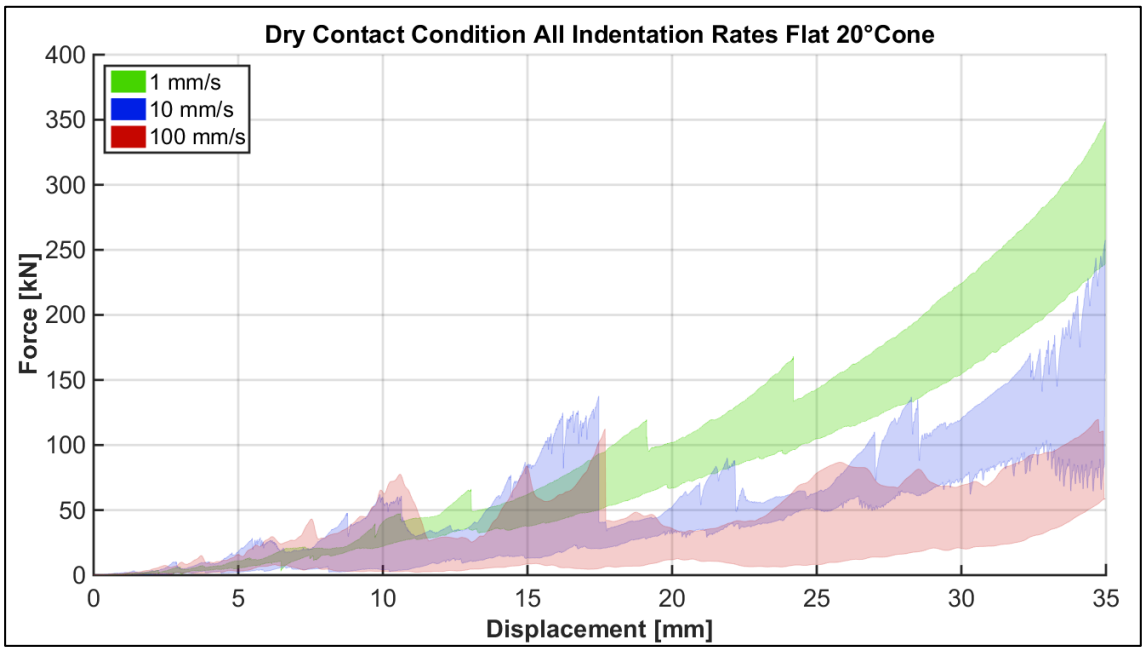

Figure 6.1: Flat plate, 20° ice specimens, dry: force vs. displacement for 1 mm/s (5), 10 mm/s (4) and 100 mm/s (6).

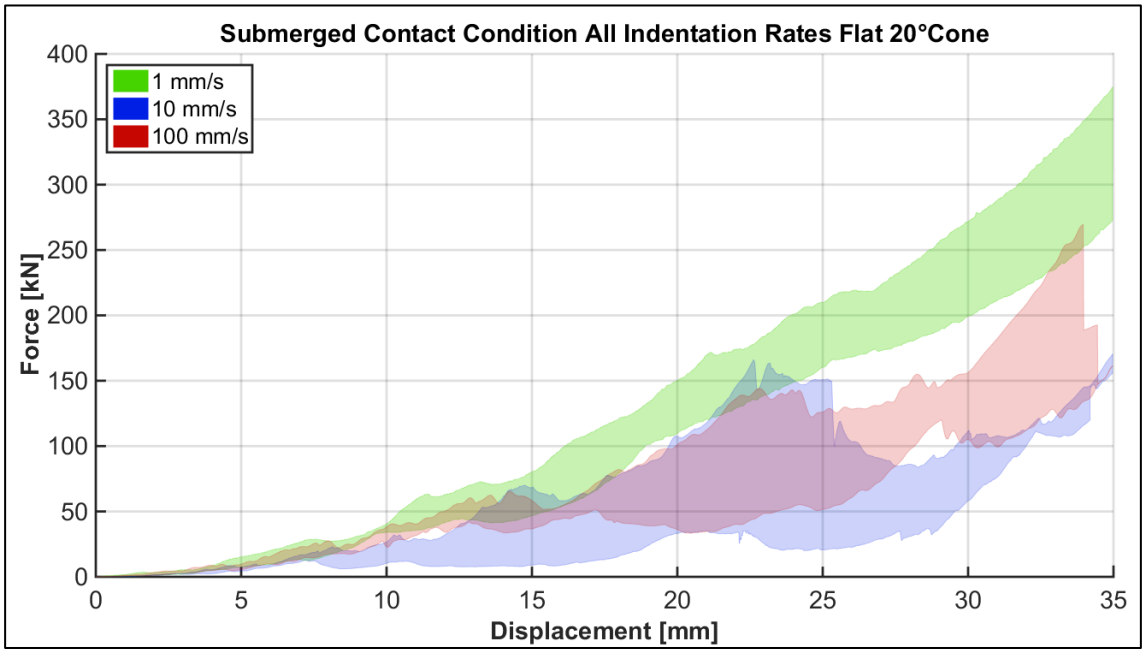

Figure 6.2: Flat plate, 20° ice specimens, submergence: force vs. displacement for 1 mm/s (4), 10 mm/s (3) and 100 mm/s (4).

Snow (Figure 6.3) and granular ice (Figure 6.4) cases are similar in a sense that the low indentation rate produces higher forces, than the high indentation rate. Forces are also higher compared to the dry contact condition. Furthermore, the effects of granular ice (Figure 6.4) and submergence (Figure 6.2) are comparable with respect to the changed ratio between medium and high indentation rates: both environments raised forces of the high indentation rate to an equal or higher level than the medium indentation rate.

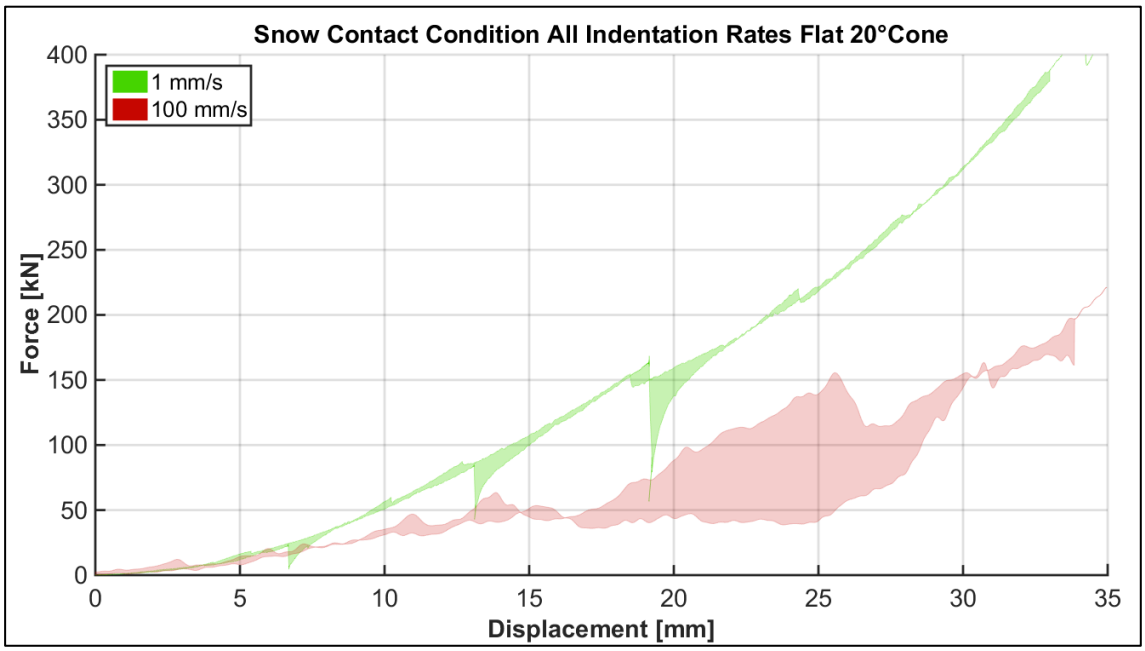

Figure 6.3: Flat plate, 20° ice specimens, snow: force vs. displacement for 1 mm/s (2) and 100 mm/s (2).

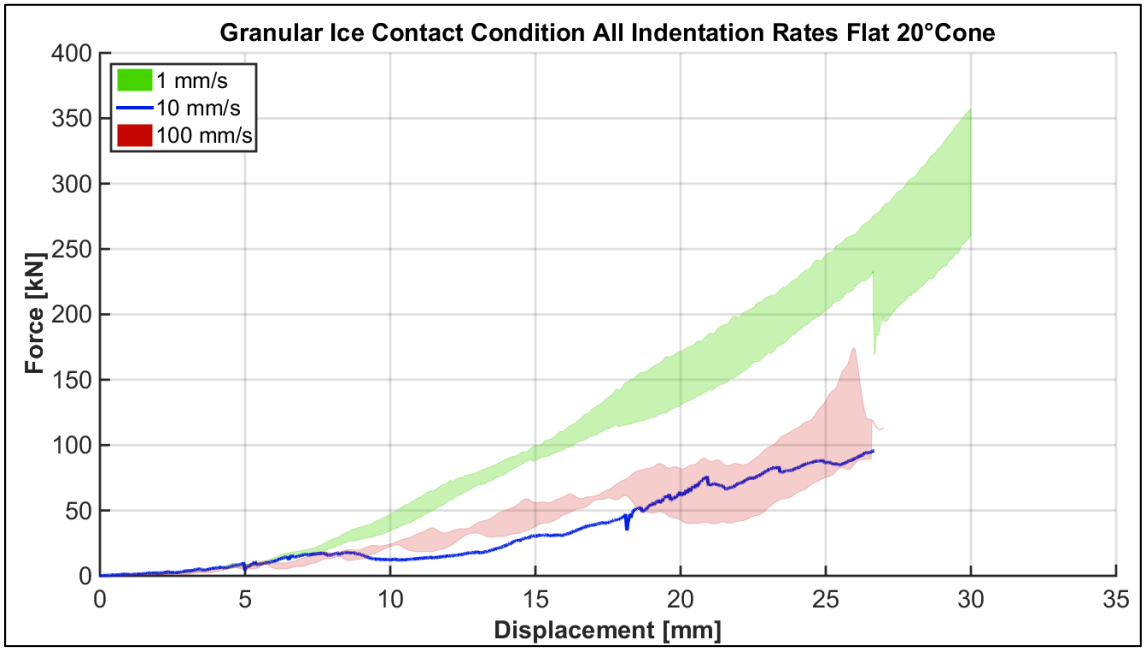

Figure 6.4: Flat plate, 20° ice specimens, granular ice: force vs. displacement for 1 mm/s (2), 10 mm/s (1) and 100 mm/s (2).

6.1.1.2 30° Ice Specimens

For 30° ice specimens in a dry testing environment, the overall sequence is the same as that of the lower ice cone angle: the low indentation rate results in the highest forces (Figure 6.5). At the 30° cone angle, medium and high indentation rate results are fairly close to each other, and there is less variation amongst the test (compare Figure 6.1).

The variation among tests is also less for the submergence cases (Figure 6.6), but for medium and high velocities the forces are higher, compared to the dry case in Figure 6.5. Submergence affects the higher indentation rates and causes forces to approach those at lower speeds.

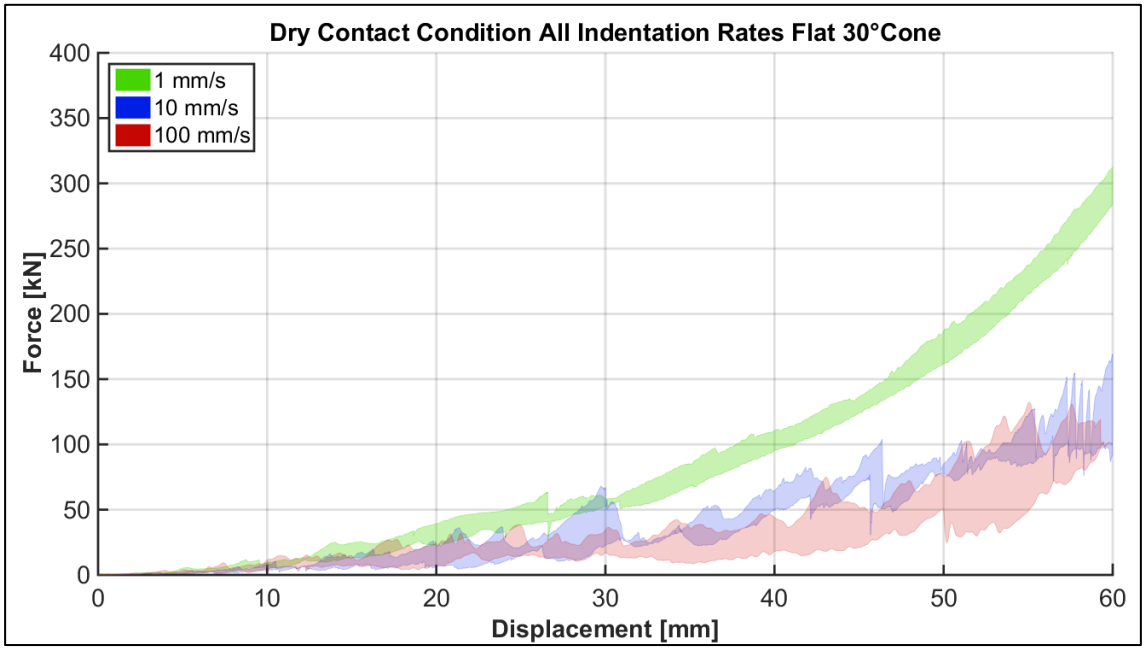

Figure 6.5: Flat plate, 30° ice specimens, dry: force vs. displacement for 1 mm/s (4), 10 mm/s (2) and 100 mm/s (5).

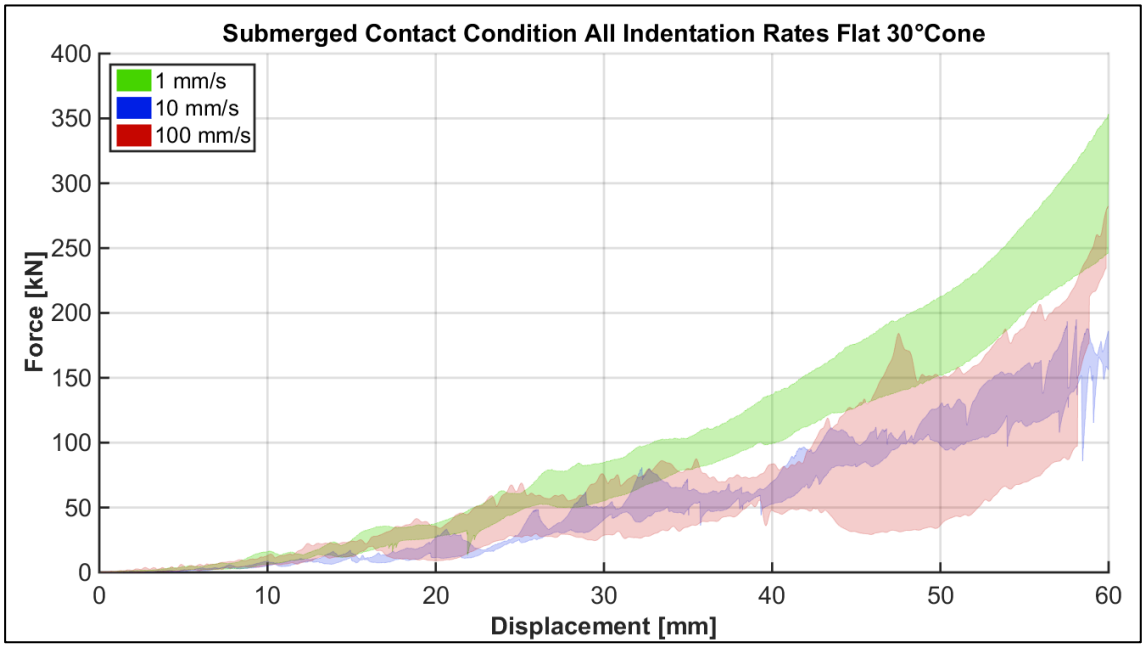

Figure 6.6: Flat plate, 30° ice specimens, submergence: force vs. displacement for 1 mm/s (6), 10 mm/s (3) and 100 mm/s (6).

At the low indentation rate, the forces arising from the presence of snow (Figure 6.7) and granular ice (Figure 6.8) are in a similar range and distinctly higher compared to the high indentation rate and the dry environment (Figure 6.5). For granular ice, forces at medium and high indentation rates are similar, with a tendency of a steeper increase compared to forces in snow cases at the same impact speed.

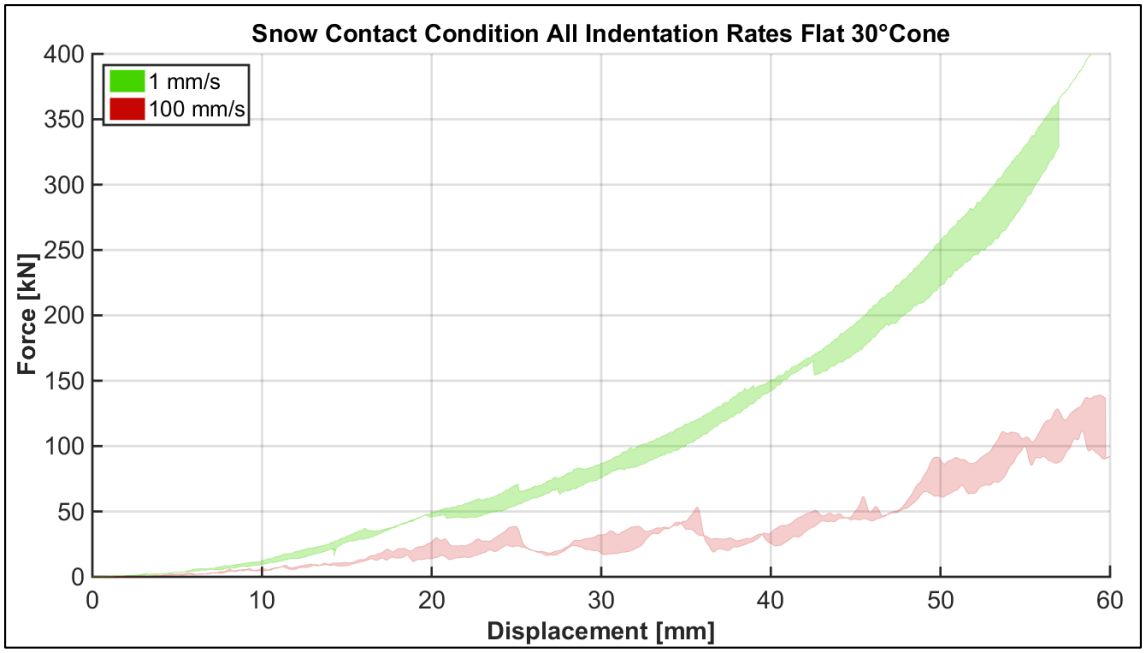

Figure 6.7: Flat plate, 30° ice specimens, snow: force vs. displacement for 1 mm/s (2) and 100 mm/s (2).

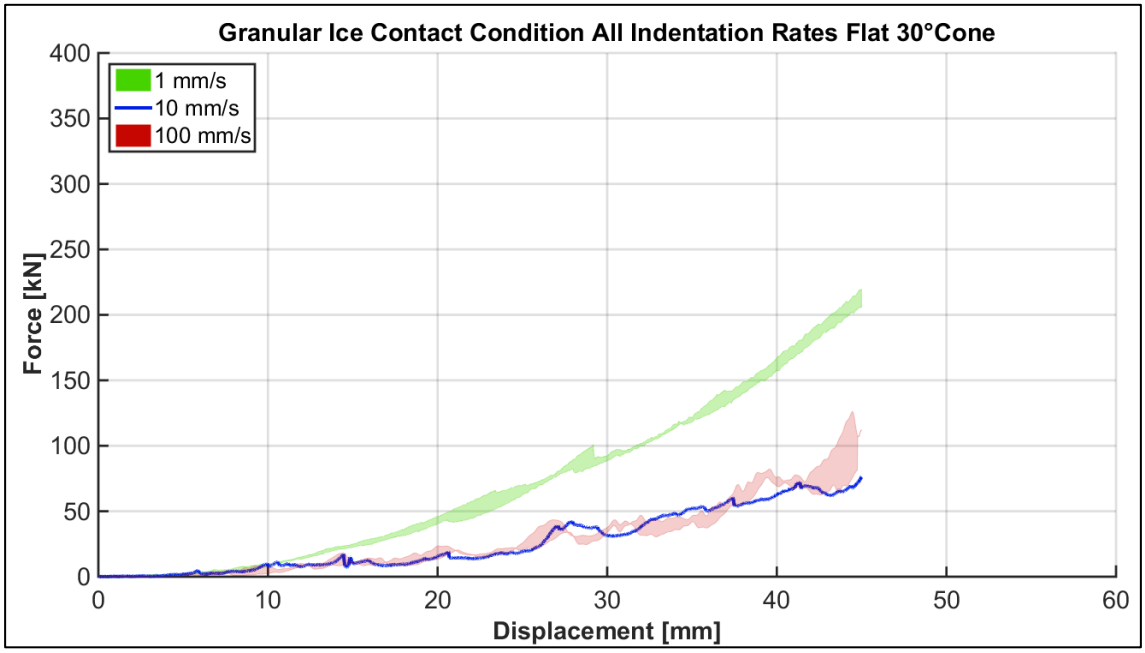

Figure 6.8: Flat plate, 30° ice specimens, granular ice: force vs. displacement for 1 mm/s (2), 10 mm/s (1) and 100 mm/s (2).

6.1.2 Wedge

Wedge tests were performed at low and high indentation rates with 30° ice specimens, and for dry and submerged contact conditions. Two tests for each test scenario were done.

Figure 6.9 displays the typical outcome with high forces at low indentation rate and considerably lower forces at high indentation rate. This relation is somewhat changed in submergence cases (Figure 6.10), where forces at the high indentation rate are first above, but later below those of the low impact speed.

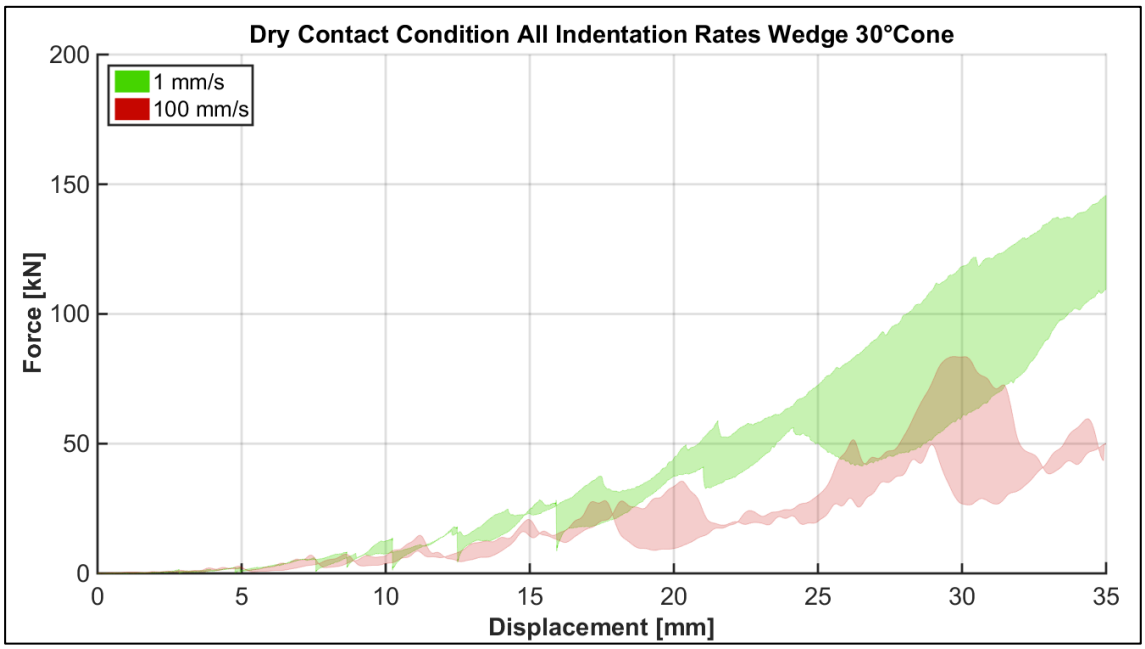

Figure 6.9: Wedge, 30° ice specimens, dry: force vs. displacement for 1 mm/s (2) and 100 mm/s (2).

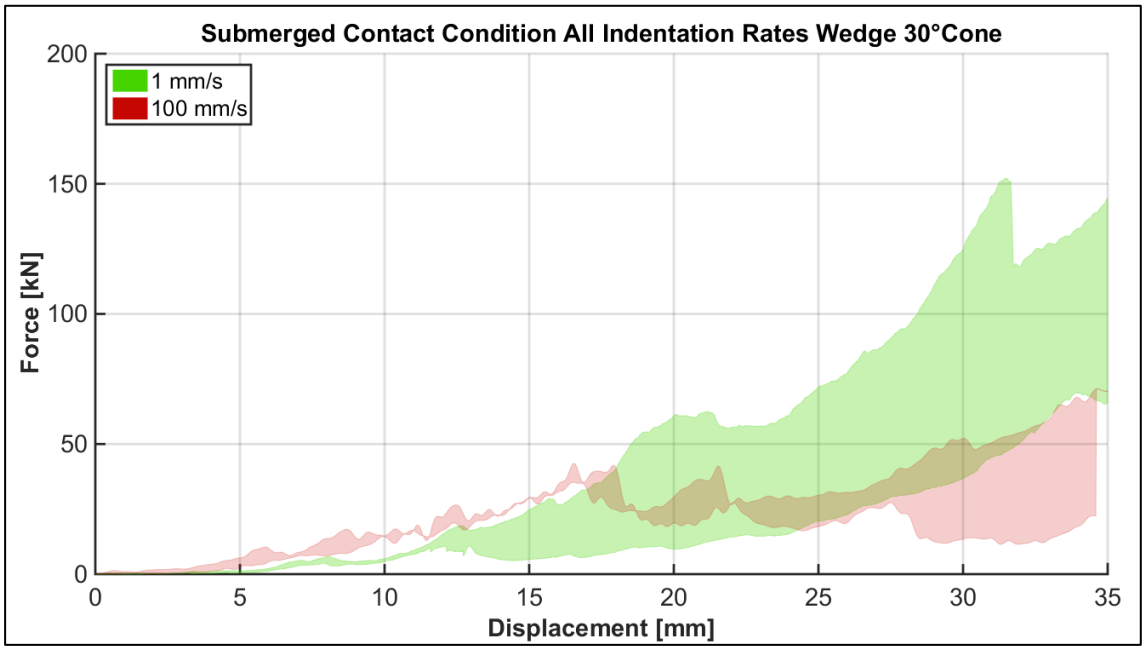

Figure 6.10: Wedge, 30° ice specimens, submerged: force vs. displacement for 1 mm/s (2) and 100 mm/s (2).

6.1.3 Conical indenter

The force sequence for the conical indenter showed higher forces at the low indentation rate and the trend is the same for both dry and submerged testing environments. It was earlier mentioned that for this indenter shape, no evidence for a submergence effect was found. Also the related speed plots (Appendix D7) do not offer any additional information and are therefore not provided at this point.

6.1.4 Spherical Indenter

Tests with the spherical indenter were conducted at low and high indentation rates with 20° ice specimens, and for dry and submerged contact conditions. Forces in the dry testing environment (Figure 6.11) are in agreement with the rate-typical findings: high forces at the low indentation rate and lower forces at the high indentation rate. In submergence (Figure 6.12), forces at low and high indentation rates are similar up to a displacement of about 16 mm, but subsequently deviate distinctly. Submergence raised the forces at the high indentation rate closer to the level of the low indentation rate. Forces tend to flatten at the low indentation rate for both testing environments at displacements of around 25 mm, and at the high indentation rate at approximately 16.4 mm (submerged) and 18.6 mm (dry). This was attributed to the sphere approaching the point where it is entirely enveloped in the ice and the only slight increase in contact area simultaneously.

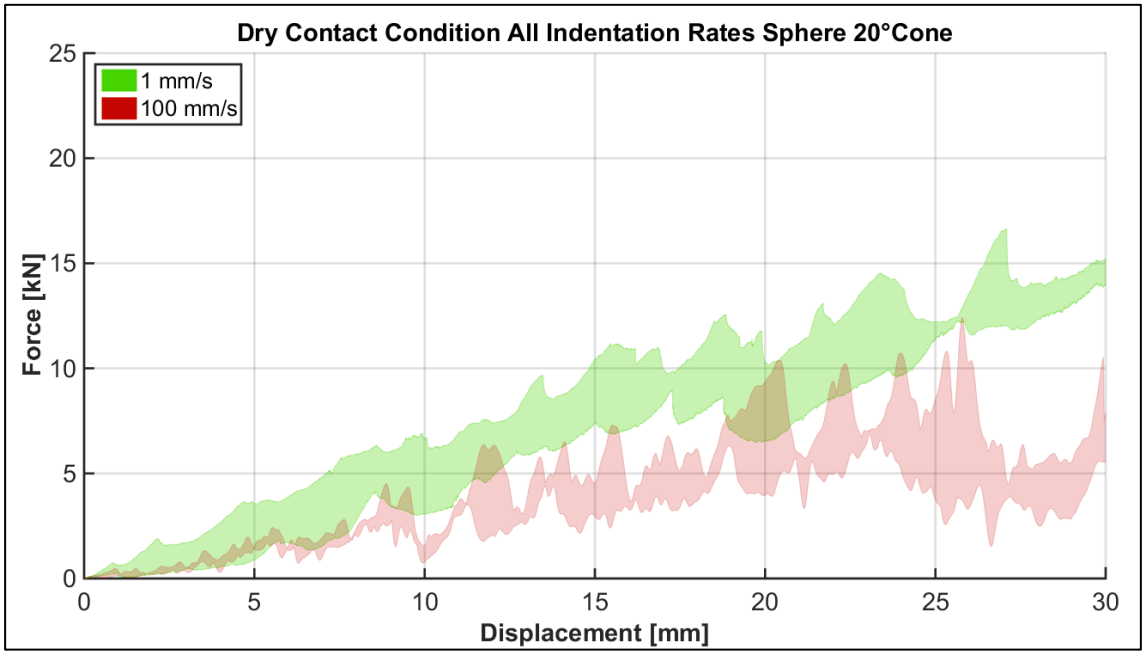

Figure 6.11: Sphere, 20° ice specimens, dry: force vs. displacement for 1 mm/s (3) and 100 mm/s (3).

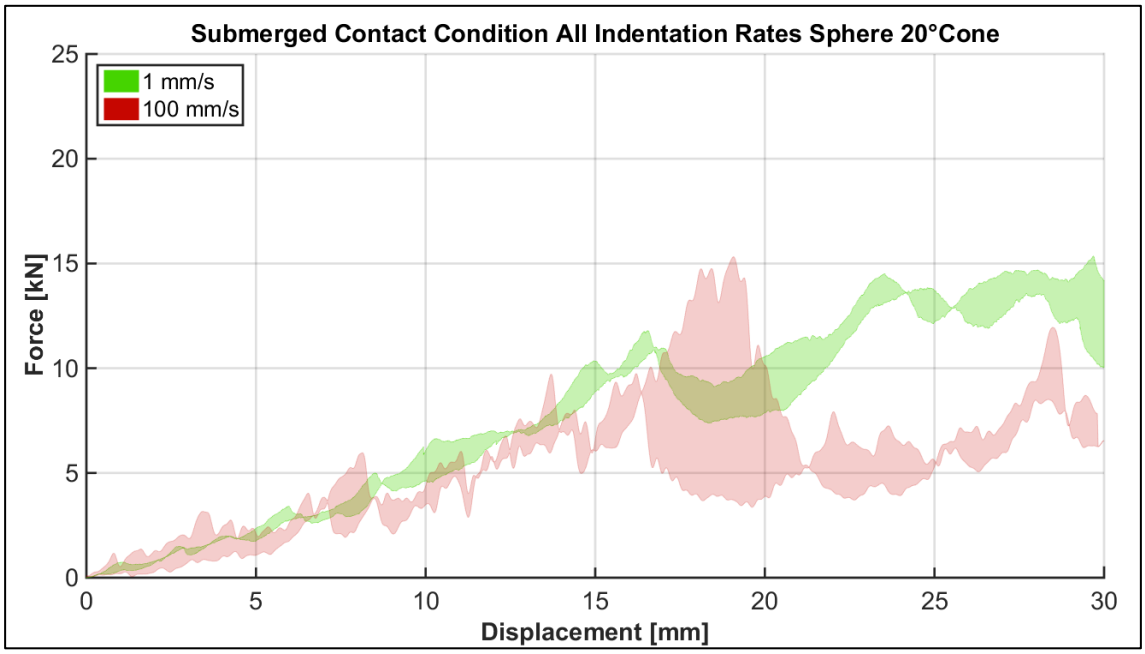

Figure 6.12: Sphere, 20° ice specimens, submerged: force vs. displacement for 1 mm/s (2) and 100 mm/s (2).

6.1.5 Summary

Independent of indenter geometry or contact condition, generally the highest forces were obtained for the low indentation rate (1 mm/s). For the dry contact condition, the impact speed (100 mm/s) generally resulted in considerably lower loads. Except for the conical indenter, this relationship was reduced in the other testing environments (submerged, snow, ice chips), where loads were usually shifted towards those at the low indentation rate.

6.2 Effect of Indenter Shape

Four different indenter shapes were used in the experiments: a flat plate, wedge shaped indenter, conical indenter and sphere. The overall magnitude of measured force at each indentation rate varied with indenter shape. Depending on its geometry, each indenter supplied a different level of confinement, leaving more or less space for ice extrusion, and varying degrees of further ice comminution enhancement. Ice debris accumulation further restricts extrusion processes. In addition, it can carry a part of the load and create a back pressure, requiring more load to induce subsequent ice failure. Even if these processes were neglected, the nominal contact area for the conical indenter, for instance, develops more quickly, than for the wedge shaped indenter or the flat indentation plate (Figure 4.4); not to mention the spherical indenter. In earlier analysis, it was noticed that the force was mainly controlled by contact area, and thus the conical indenter would inevitably produce higher forces at earlier displacements compared to other indenter geometries. With respect to the actual (measured) contact area, significant discrepancies with the nominal contact areas were observed in tests with the flat indentation plate and the wedge

shaped indenter, where the tactile pressure sensor measurements were employed. How this would affect the average process pressure was shown in the adjusted contact pressure-area relationships, where previous ratios between contact conditions were changed or even reversed. It is therefore believed that a true comparison of indenter shapes by means of pressures would require better information on the actual contact area. Within the scope of this test series, only a relatively limited number of tests involved the technology to measure the actual contact area, and therefore this approach does not seem applicable at this point. In addition, a force comparison based on displacement seems inappropriate due to the differences in contact area.

To facilitate some idea on how the force is controlled by contact area a simplified comparison of measured force vs. nominal area is carried out for two fundamentally opposing indenter geometries. So far, the spherical indenter has not been used in drawing parallels to other indenters due to its small contact area, and because of the range that was chosen for examining the data. Tests with the sphere provided the least degree of confinement and restriction in the extrusion of ice, and achieved just above 1900 mm^2 of contact area at the maximum penetration (Figure 6.13). With this indenter only 20° ice specimens were employed. Out of all other indenter shapes, the flat plate supplied the next lowest geometrical restrictions. The comparison is focused on results for 30° ice cones and for nominal contact areas up to 2000 mm^2 (Figure 6.14) in analogy to the spherical case. Against this background, for both indenters in a dry environment, force development and magnitude are actually fairly similar, and roughly 5 – 15 kN at 1800 mm^2 (equals displacements of 26.5 mm for the sphere, and 13.8 mm for the flat

plate with 30° specimens). In submergence (Figure 6.15 and Figure 6.16), forces are comparable up to 1200 mm^2 or 1400 mm^2, but are higher for the flat plate at larger areas. For the latter, the surrounding water likely affected the contact area development to a greater extent due to the higher pre-existing restriction originating from the indenter and ice geometry combination. At about that time, the nominal (projected) contact area only marginally continued to increase (Figure 4.3). These observations indicate that the indenter geometry mainly influences the force due to the surface it provides for establishing the contact between ice-indenter and, equally important, through the space it leaves for ice extrusion. If compared based on the nominal contact area, the distinct curvature of the sphere does not lead to significantly different forces. It also maintains the same continuous contact area in low speed tests, and the branch-like pattern in high speed tests (see section 5.4.3.2) that was noticed for other indenter shapes. Forces from tests with the flat indentation plate and 20° ice specimens (no figure provided) do not compare with the cases discussed above.

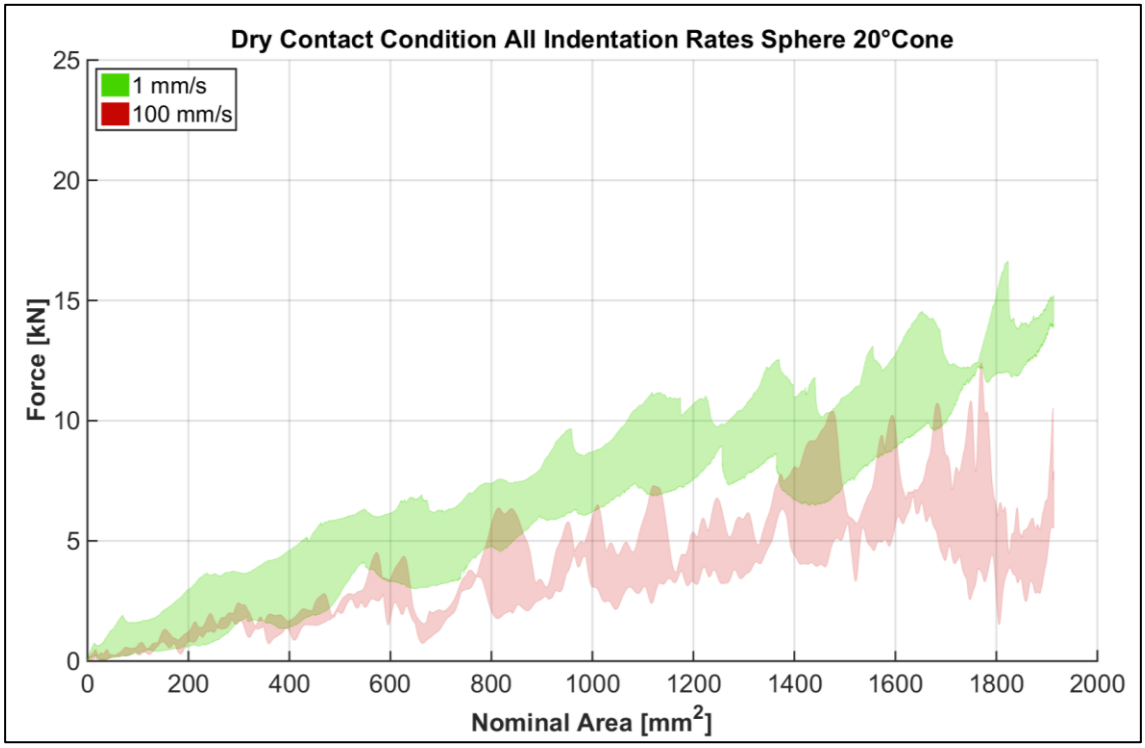

Figure 6.13: Sphere, 20° ice specimens, dry: force vs. nominal area for 1 mm/s (3) and 100 mm/s (3).

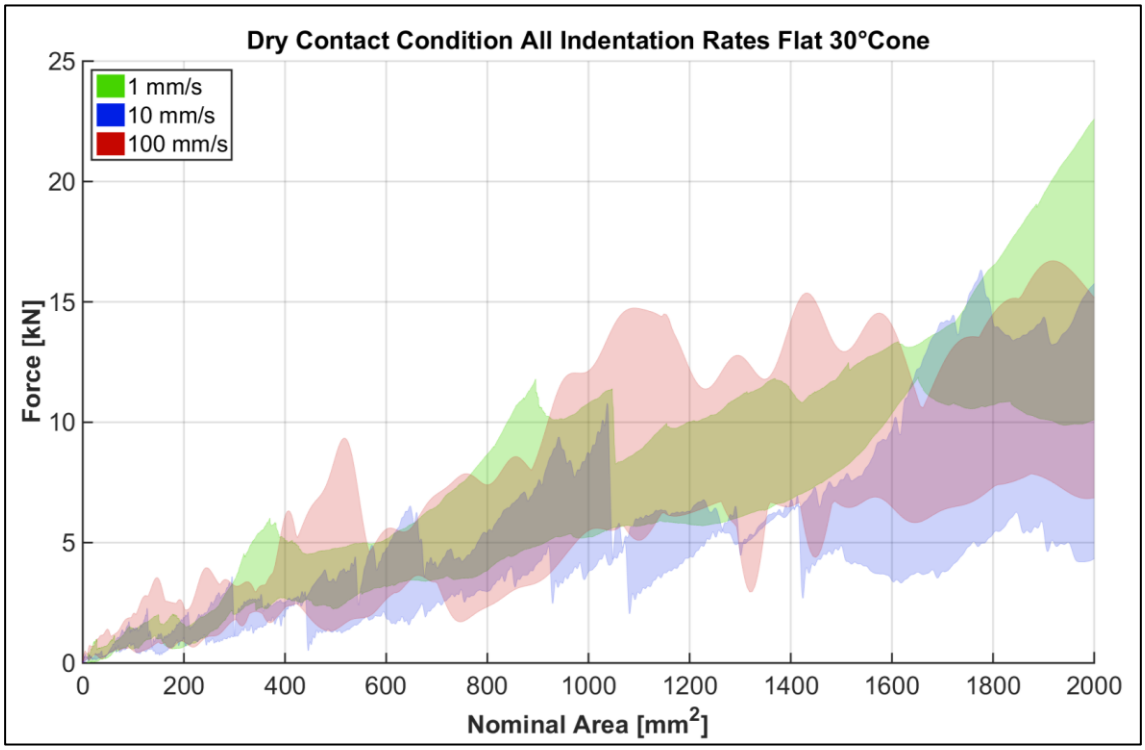

Figure 6.14: Flat plate, 30° ice specimens, dry: force vs. nominal contact area up to 2000 mm^2 for 1 mm/s (4), 10 mm/s (2) and 100 mm/s (5).

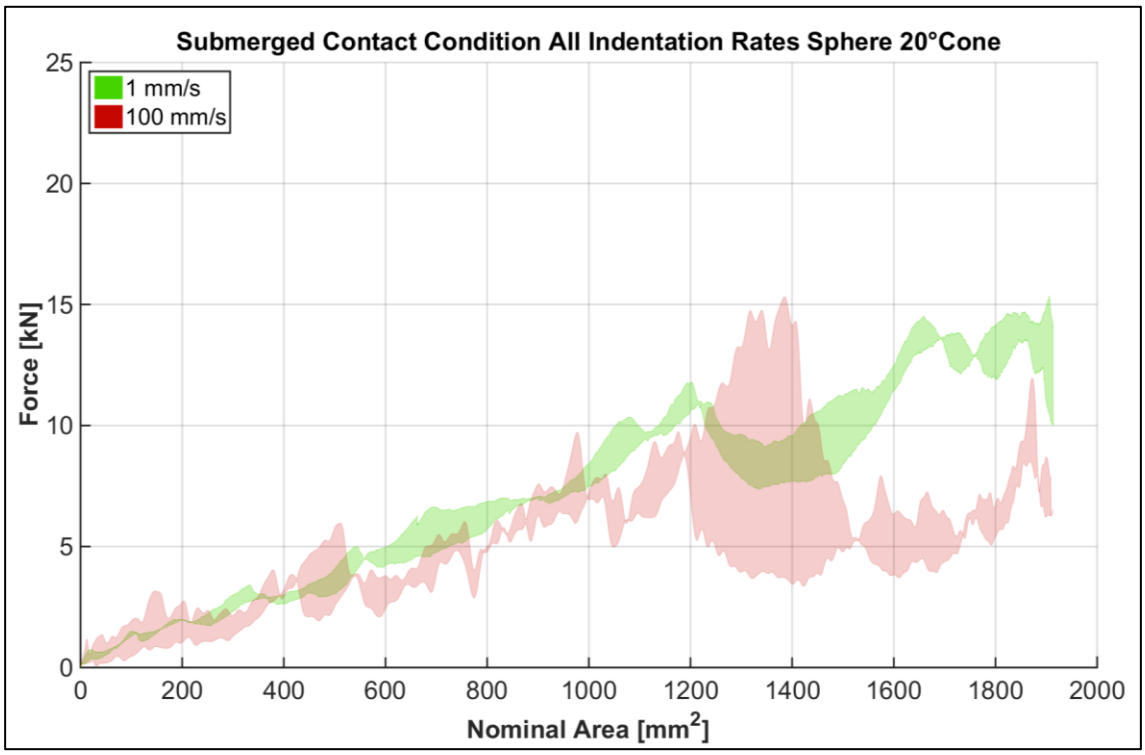

Figure 6.15: Sphere, 20° ice specimen, submerged: force vs. nominal area for 1 mm/s (3) and 100 mm/s (3).

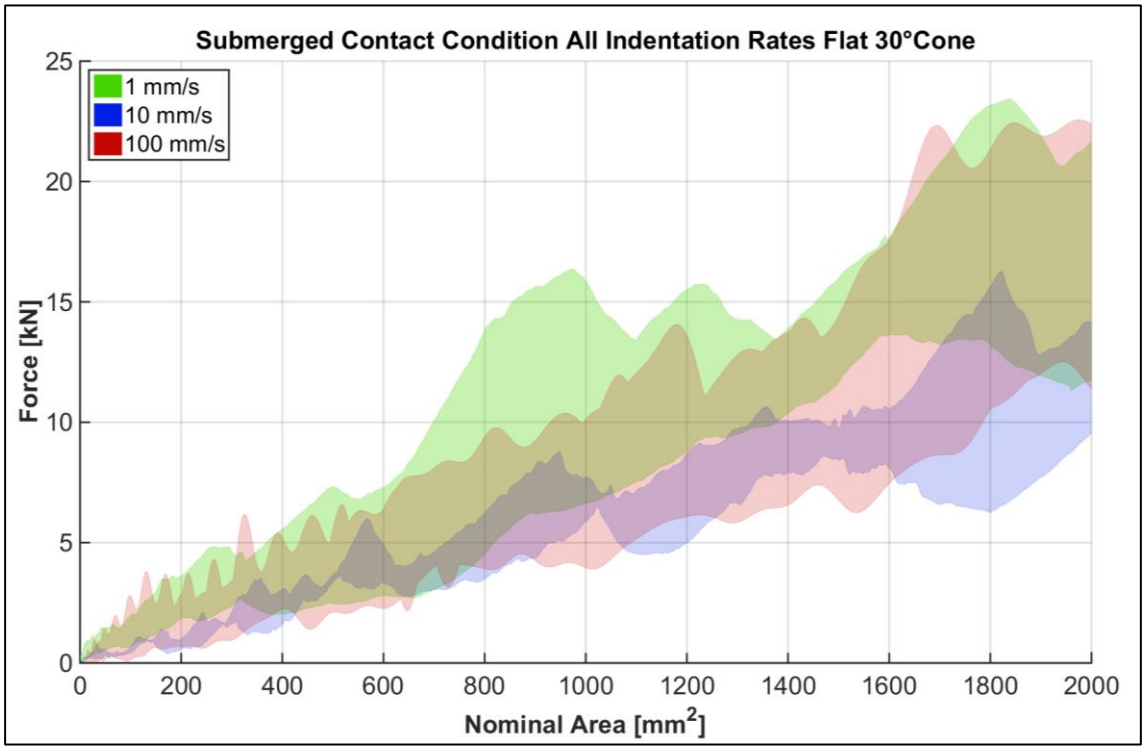

Figure 6.16: Flat plate, 30° ice specimens, submerged: force vs. nominal contact area up to 2000 mm^2 for 1 mm/s (4), 10 mm/s (2) and 100 mm/s (5).

This can be explained by evaluating the relationship of indenter geometry and the level of confinement, or the available space for ice extrusion, respectively. The images in Figure 6.17 on the left visualize this circumstance for the flat plate for a 20° (top figure) and for a 30° (bottom figure) ice specimen. The photo on the right shows the spherical indenter with a 20° ice cone. The angle between specimen surface and indenter surface is named extrusion angle theta θ and this provides a measure of the space or aperture available for ice extrusion. In flat plate scenarios theta equals the respective ice cone angle. In the sphere case, the extrusion space is similar to the space a 30° ice specimen in combination with the flat indentation plate. This provides another part of the explanation for the similar force magnitudes.

Altogether, the influence of indenter shape is comprised of two aspects: the pace of the growing contact area and the available space for ice extrusion. Generally, a more compact ice geometry can, to some degree, compensate for less confinement resulting from the indenter.

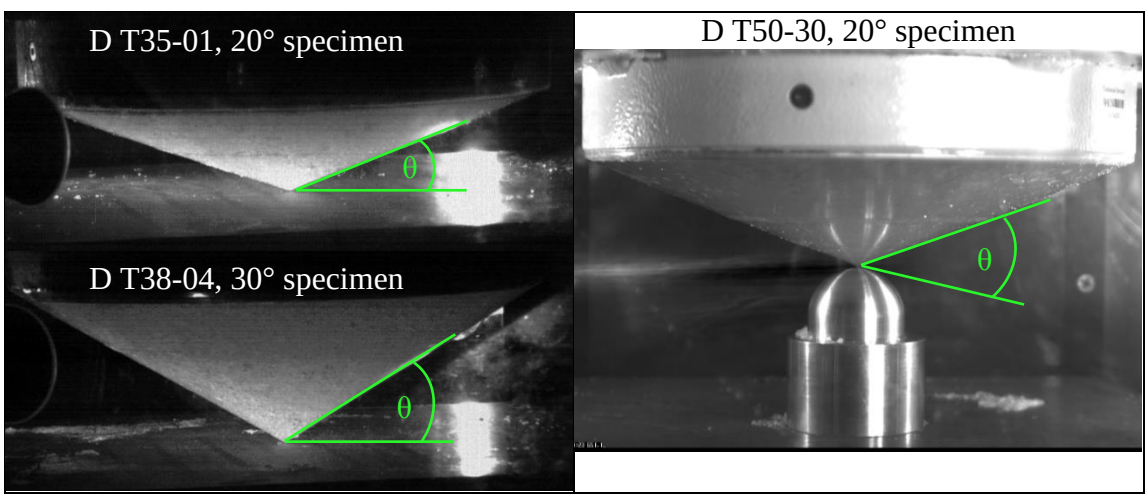

Figure 6.17: Extrusion angle θ dependend on indenter-ice geometry combination. On the left, for the flat indentation plate and 20° (top) and 30° (bottom) ice specimen angle. On the right for the spherical indenter and a 20° ice cone.

6.3 Effect of Contact Condition

The significance of the dry or submerged contact condition has proven to strongly correlate with indentation rate. For the indentation rates considered in this research, submergence was more influential at the high impact speed, but was of minor or negligible effect at lower velocities, dependent on indenter geometry (Table 6.1). The medium indentation rate was only used in combination with the flat indentation plate, with the least number of experiments performed. At this rate, the influence of contact condition was rather ambiguous.

Table 6.1: Identification of the submergence effect depending on indenter geometry and indentation rate.

Indenter	**Indentation Rate [mm/s]**		
	1	**10**	**100**
Flat Plate	significant	weak	significant
Wedge	insignificant	-	significant
Conical	insignificant	-	insignificant
Sphere	insignificant	-	significant

Snow and granular ice were only employed with the flat indentation plate, and at low and high indentation rates. Table 6.2 shows that the effect of these contact conditions was mainly important at the low indentation rate, especially at 20° ice cone angle.

Table 6.2: Identification of the influence of snow and granular ice on the flat indentation plate depending on indentation rate and ice cone angle.

Condition	**Ice Cone Angle [°]**	**Indentation Rate [mm/s]**		
		1	**10**	**100**
Snow	**20**	strong	-	significant
	30	significant	-	insignificant
Granular Ice	**20**	strong	-	significant
	30	significant	-	weak

Evidently, the influence of contact condition is speed dependent. Therefore, the following paragraphs discuss the respective most influencing environment on ice loads separately for high and low indentation rates.

6.3.1 Submergence at High Indentation Rate

Submergence has various repercussions and affects a number of ice crushing processes. Generally, tactile pressure sensor readings as well as still photos of the samples surfaces after test completion indicated larger real contact areas in submerged cases compared to the dry testing environment.

Figure 6.18 helps to visualize different aspects that may contribute to the submergence effect. Each is in the following paragraphs addressed in more detail. It is proposed, although introduced in separate subchapters, that the submergence effect is comprised of the interplay of some or all of these aspects, which prevail under different circumstances.

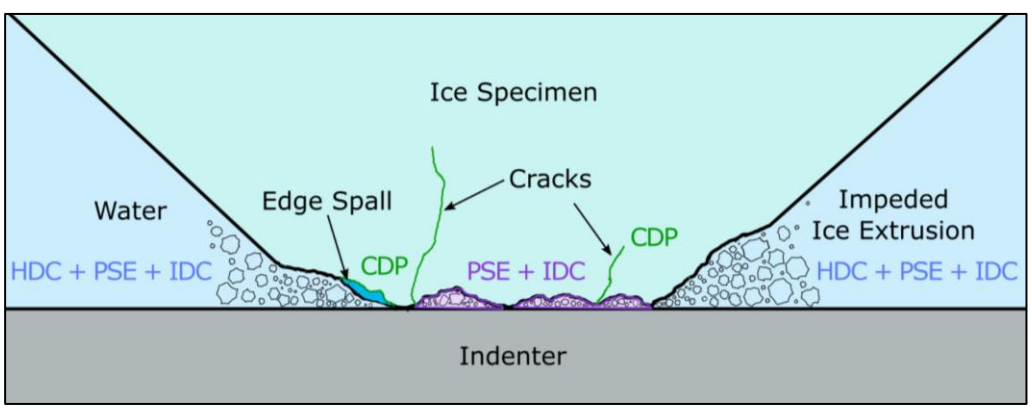

Figure 6.18: Concept sketch indicating processes and components at the ice-structure interface during ice crushing. The blue areas represent three different effects of the water: hydrodynamic confinement (HDC), effect on ice debris constitution (IDC), and pressure spreading effect (PSE). The purple area is mostly affected by PSE and IDC. Green color indicates the influence on crack development and propagation (CDP).

6.3.1.1 Influence of Indenter and Ice Geometry

The submergence effect was found to be nonlinear, and to vary dependent on geometry, and with penetration depth. In this context, geometry refers to the geometry of the indenter, as well as of the impacting ice feature, both contributing different degrees of confinement. The influence of ice and/ or indenter shape has been the focus of many studies in field tests (e.g. Frederking et al., 1990; Masterson et al., 1993), as well as in laboratory tests (Kennedy et al., 1994; Kim et al., 2012; Kim, 2014), but none of these studies addressed submergence as a possible source of additional or modified confinement.

The correlation of submergence with indenter geometry is displayed in Table 6.1. Only for the conical indenter, water does not seem to be of consequence. In this case, ice failure and associated ice loads must be entirely dominated by the indenter's shape. For all other indenters, submergence leads to increased ice loads. As all these cases provide less geometrical confinement than the conical indenter, the water apparently assumes some of the confining function, except in cases where the geometry is so restrictive that the effects of the water are not significant.

The implication of ice cone angle was shown in section 5.1.2.3, for the flat indentation plate at 100 mm/s test speed and 20° and 30° ice cone angles. Ice loads were higher for the blunter ice specimen in general, but especially in submergence cases (Figure 5.10). For the 30° ice cone angle, the difference in ice loads due to dry and submerged contact conditions was less pronounced, but still evident (Figure 5.12). Higher loads for dry tests at a smaller ice cone angle were also found by Kim (2014). The load disparity may be

explained by the opening angle θ (Figure 6.19 bottom) between ice specimen and indentation surface. θ is smaller for 20° ice specimens, leaving less space for ice extrusion. Ice debris is more easily trapped and further comminuted. This contributes to a fast growth in contact area that allows the transmission of higher loads; an effect that appears amplified in submergence.

6.3.1.2 Effect on Ice Debris Constitution (IDC)

At high indentation rates, (dry) ice failure is very dynamic, resulting in fine grained ice material and ice spalls (Figure 6.19, top). The ice is generally only affected to a small depth underneath the indenter and ice spalls form in a zone fairly localized in its vicinity. This is a commonly reported phenomenon (e.g. Frederking et al, 1990; Jordaan and Xiao, 1992) and was also observed in these experiments. In submergence cases, the constitution of ice debris was significantly changed. Its appearance was more cloud-like, presumably because of the water leading to a conglomeration of small ice particles (Figure 6.19, bottom). At fast indentation rates, quickly shifting high pressure zones, associated with spalling ice, likely facilitate the development of voids at the ice-structure interface. In Figure 6.18 this would be the void space between two contact zones between the ice feature and the structure. In such cavities, trapped fine grained ice material is more probable to be formed into ice slush by the water, and to be re-compacted to fairly solid ice. In that case, ice sintering may play a role as well. In ice related experiments, ice sintering is often referred to in conjunction with ice that was stuck to the indented surface. This was also noticed in these tests. Szabo and Schneebeli (2007) found that ice sintering (in air) can take place within milliseconds and is accelerated for ice close to its melting

temperature. Blackford (2007) reported enhanced ice sintering in the presence of fluids, demonstrated for solid ice crystals and a brine solution (salt water). In the submerged tests, salt water was present due to the testing environment and presumably promoted ice sintering. In addition, the water temperature being around the ice melting point may have accelerated the process even further.

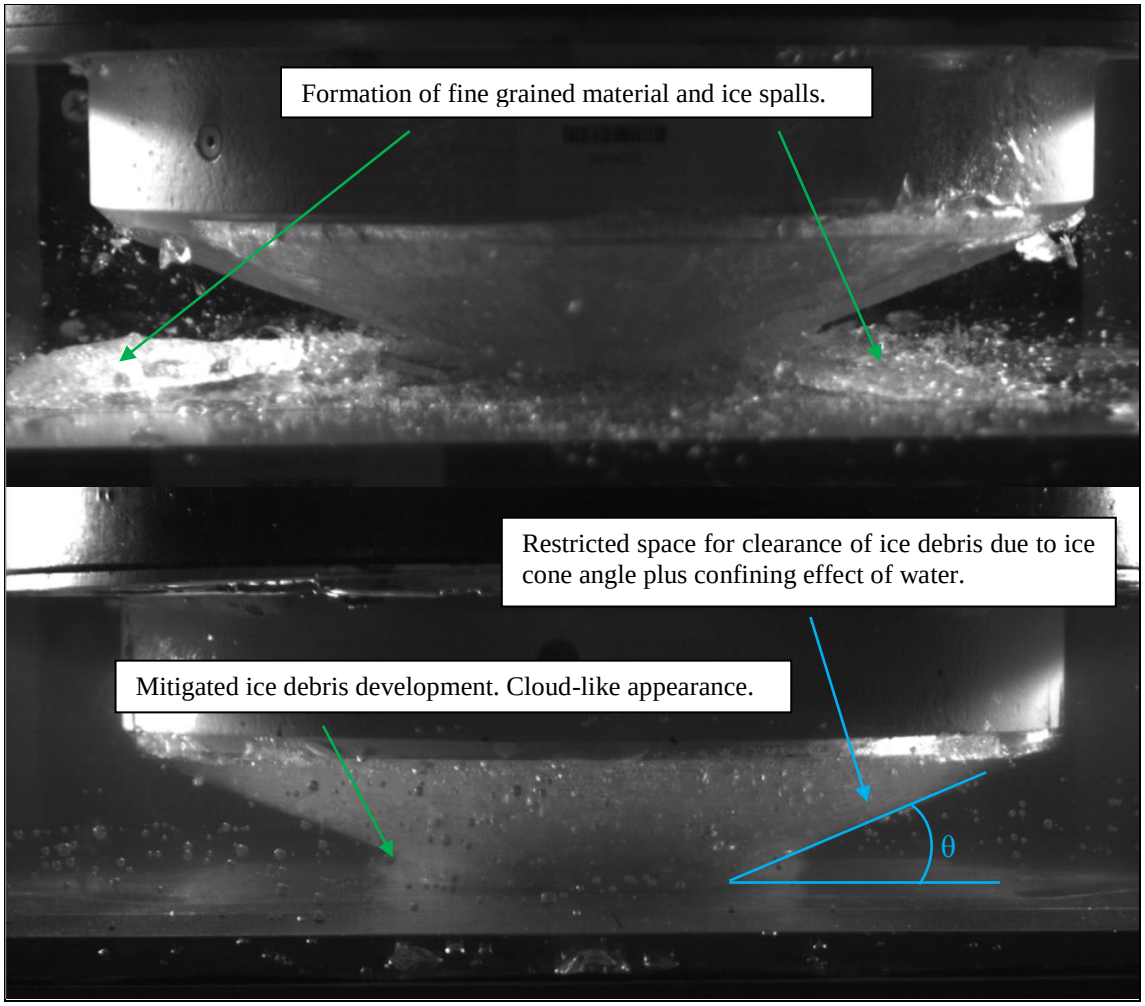

Figure 6.19: Flat plate, 100 mm/s, 20° ice specimens, dry (top, D T76-04) and submerged (bottom, S T92-01), approx. 14.4 mm penetration depth. HSC footage. The photos show the different development and extrusion of ice debris due to contact conditions. Compared to the dry condition (top), both are clearly altered by the surrounding water (bottom). Also clearance angle θ between ice specimen and indentation plate is indicated.

6.3.1.3 Effect on Crack Development and Propagation (CDP)

Hydrostatic pressure has been recognized for its ability to alter ice behavior during crushing events and its ability to lead to higher ice strength at low confining pressures, even for pre-damaged ice (e.g. Singh and Jordaan, 1996). In triaxial test, it is commonly observed that crack development and propagation are impeded, and recrystallization is enhanced (Stone et al., 1997; Melanson et al., 1999; Meglis et al., 1999). In this study, submergence was noticed to have a similar effect. Although insufficient thin section data was collected to support this finding on a microstructural level, the entirety of observations leads to the conclusion that submergence is somewhat comparable to a triaxial stress state. Restricted crack development was very evident in the vertical cross-sections from the wedge shaped indenter samples (Figure 5.49). At both indentation rates submergence samples had no cracks but the dry samples had significant fractures.

Observations from the HSC footage showed fewer ice spalls and suggested an impaired crack evolution in submergence cases. The water appears to restrict ice failure closer to the indenter surface. This action is probably a combination of cohesion, capillarity, and re-freezing processes. When an ice spall forms, a small gap between the spall and the parent ice sample body is generated. In this gap, cohesion forces likely act against the separation of the two ice features. Cracks seem to be quickly filled by the surrounding water, possibly due to capillary effects. It is suggested that the thermal capacity of the ice would be sufficient to quickly freeze the infiltrating water and establish a new bond between ice specimen and ice spall. This would lead to the closure of small gaps and

decelerate crack propagation, promoting a “healing-effect” in the early stages of ice damage.

6.3.1.4 Hydrodynamic Confinement Zone (HDC)

In an earlier paragraph, it was referred to as confinement based on ice and indenter geometries. This relationship has been the subject of many studies (e.g. Frederking et al., 1990; Masterson et al., 1993; Tukhuri, 1995). For example, Kim (2014) found significantly increased ice loads for a conical indenter, compared to a flat indentation plate. Another observation relating to confinement, for instance, is the reduced ice splitting activity for lateral confined ice blocks in sphere tests done by Kim et al. (2012).

In this study, a trend of higher forces in the case of submergence was found at the 100 mm/s indentation rate in particular, concurrently with a significantly altered ice crushing appearance that was characterized by fewer ice spalls. This was especially evident in HSC recordings from the spherical indentation tests. Furthermore, the clearance of ice flakes and spalls was impeded and this likely promoted the accumulation of ice debris nearby the contact zone. An example is given with the snap shots from HSC footage in Figure 6.19, where the expansion of the extruding ice debris in the submergence case (bottom) is noticeably smaller compared to the dry testing environment (top). The observations altogether suggest that submergence can apply similar restrictions to geometric confinement, but it depends on the degree of pre-existing geometric confinement. The influence of water is greatest when the geometric influence is lower and the water influence is reduced when the geometric influence is higher.

The pre-existing confinement due to indenter geometry distinctly affects the development of the submergence effect. In the tests with the conical indenter, that provided the most confinement in itself, submergence did not have any effect. In that case, the geometrical constraints governed the crushing process and the resulting loads. For all other indenter shapes implying less geometrical restriction, submergence increased ice loads - at least in some parts. For the wedge shaped indenter (Figure 5.37) and for the sphere (Figure 5.70), dry and submerged forces assimilated towards the end of the test. Pertaining to the wedge, this occurred at approximately half of the maximum displacement. It may indicate that up to that point, the surrounding water carried the confining function that was successively resumed by the indenter. In view of the sphere, it was mentioned earlier that forces flattened when approaching the point where the indenter was entirely enveloped by the ice, but this phenomenon was independent of the testing environment.

It is concluded that the submergence effect depends on the space that is available for the water to act, and on the contact area. The simplified sketches in Figure 6.20 (top views) may help explain this relation by means of contact area *C* and a hydrodynamic confinement zone *HDC*. C is the nominal contact area between ice specimen and indenter that increases with ice cone penetration δ. The HDC encloses the equidistant adjacent space from the perimeter of C. Its extent depends on parameters such as fluid viscosity, pre-existing confinement (or available space for ice extrusion), and on ice spall size that relates to parameters such as crystal size and indentation rate. Figure 6.20 (left) shows the situation for small δ, where the water has a large working surface compared to the contact area and thus is of the most influence. Figure 6.20 (right) pictures the situation at

advanced penetration depths with large contact areas. The HDC can only act at the contact area perimeter and in its vicinity that is some distance from the inside of the critical area where the load determining ice crushing processes take place. At this penetration stage, it is likely that the ice debris has accumulated, and would contribute to confinement and contact area. The ice debris possibly shields the active crushing region against the surrounding water and promotes the process to "dry-out". Hence, at advanced displacements the submergence effect would be mitigated due to an insulation of the critical crushing zone from the surrounding water.

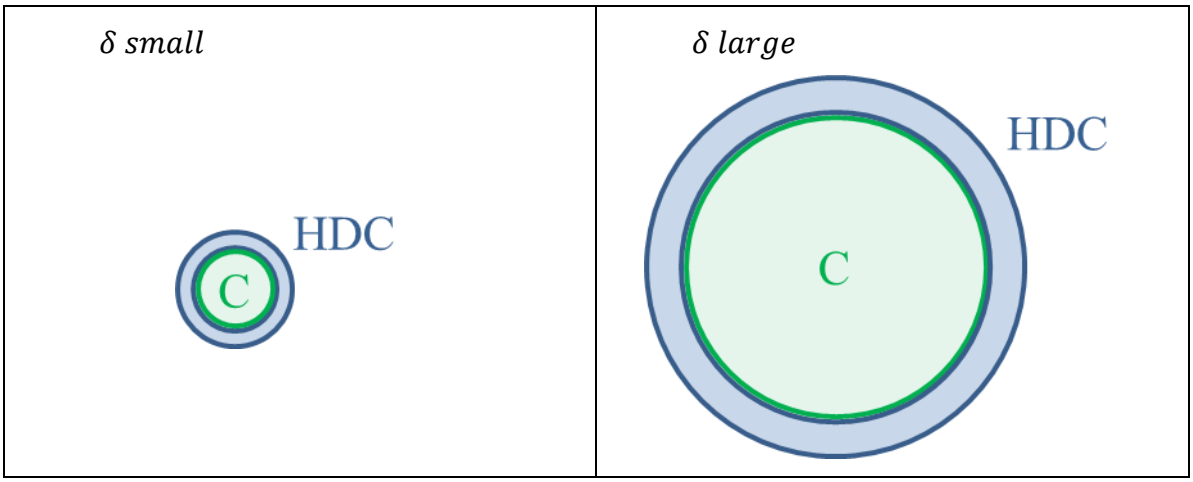

Figure 6.20: Visualization of contact area (C) and hydrodynamic confinement zone (HDC) ratios to explain the varying importance of the submergence effect depending on ice specimen penetration depth (δ).

6.3.1.5 Pressure Spreading Effect (PSE) – at Grain Boundaries

Another likely effect of water during ice impacts is a pressure spreading effect (PSE) at the ice-indenter interface, more specifically at the grain boundaries. This would be a similar situation to the hydrodynamic friction mentioned earlier (section 2.2.5), where the water takes over the load transmission to the strcuture (Kietzig et al., 2010). The sketch in Figure 6.18 shows how ice asperities and larger irregularities are embedded in water.

Voids between ice and the structure are filled with water leading to a compensation of pressure peaks at ice grain boundaries. Pressures are more evenly distributed and fractures are delayed because it requires more load to exceed the localized critical pressures and to induce subsequent ice failure. Furthermore, the water would restrict the separation of spalls from the parent ice feature.

It is emphasized that the pressure spreading effect in this context is proposed to mostly concern peak pressures at grain boundaries. From Figure 5.17, Figure 5.18, and Appendix B5 it can be seen, that the pressure pattern in submergence with respect to high pressure zones is similar to the dry condition. However, submergence seems to yield larger continuous high pressure zones, probably faciliated through a back pressure applied by the accumulating ice debris.

6.3.1.6 Ice Friction

Ice friction is supposed to have played only a subordinate role in the submerged tests. Internal ice friction between individual ice grains along grain boundaries likely contributed to slowing down the separation of ice flakes and spalls from the parent ice, and possibly affected the clearance of ice debris. Nevertheless, the factors explained above may have been of greater importance. In view of external friction between ice specimen and indenter, the abundance of water would have compensated for small asperities on the indentation surface (as well as in the ice) overall. The state would be comparable to the hydrodynamic friction (see section 2.2.5) with a water layer thickness well above the elevation of surface asperities.

6.3.1.7 Implications for Ice-Structure Interactions with other Geometries

The explanations above are based on interpretations of the effects of geometries and mechanisms that would be relevant for an iceberg impact, with blunt or rounded ice features. The essential role of aspect ratio was addressed in Masterson and Frederking (1993).

The subject of aspect ratio was brought forward earlier in the context of the hydrodynamic confinement zone (HDC). The aspect ratio determines the working surface that is available for the water to act. For that reason it can be speculated that the hydrodynamic confinement phenomenon would be more significant in ice floe–structure interactions. Here, the ratio of contact area and perimeter (Figure 6.21) would change linearly with ice penetration (instead of a quadratic change as in the case of the conical ice penetration). The working surface for the water would not decrease as significantly with increasing contact area. This is provided the assumption of fairly uniform ice failure, which in turn requires essentially consistent ice floe thickness and properties, as well as overall constant boundary conditions.

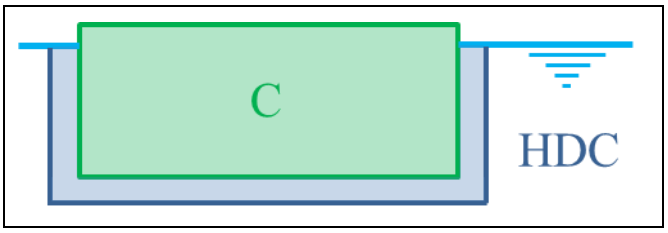

Figure 6.21: Visualization of contact area (C) and hydrodynamic confinement zone (HDC) for an ice floe. The working surface of the water (submergence effect) would linearly change in an ice-structure interaction that would cause the ice floe to expand sideways.

6.3.1.8 Summary of Submergence Effects at High Indentation Rate

In the experimental work, it was noticed that submergence led to increased ice loads. In the analysis, a correlation with larger contact areas was found (compared to the dry testing environment) and the larger contact area allows the transmission of more load to the structure. The difference in contact area was visible in still photos of samples surfaces after test completion, but it was especially evident in tactile pressure sensor recordings of scenarios with the flat indentation plate and the wedge shaped indenter.

Discussed above are a number of physical mechanisms that are suggested to have contributed to the effect of submergence to cause increased ice loads or larger contact areas. Based on the established data it is difficult to determine the relative importance of each factor. This requires more experimental work with the objective to separate single processes and deduce their specific importance, and is beyond the scope of this thesis. What has been achieved here is to identify and provide evidence of a number of plausible effects that emanate from the presence of water in an ice-structure interaction. These effects contribute to the understanding of the process of ice failure, which starts with the ice material properties and continues with a process of ice deformation and removal. This is shown to strongly influence the apparent ice strength, which is influenced by the boundary conditions of the impact.

6.3.2 Snow and Granular Ice at Low Indentation Rate

At the outset of this study, tests with snow and granular ice on the indented surface were anticipated to be mainly secondary scenarios. The objective was to roughly explore the effect of these materials on ice loads, and their importance in comparison to

submergence. However, during the analysis of the results, these environments increasingly gained importance.

Scenarios with snow and granular ice are principally very similar to tests on ice extrusion. Most studies on ice extrusion approach the subject from either one of the two directions: when granular ice material is just developing and is extruded during a crushing event; or, when the ice debris is already generated and the objective is to determine its material and flow properties (e.g. Tuhkuri and Riska, 1990). In the experiments carried out in the present study, it was a combination of both. Ice material was provided in the first place, and further ice debris was generated during the impact, while both circumstances interacted with each other.

It was proven that snow and granular ice material are capable of causing loads similar to the submergence cases at high indentation rates (100 mm/s). At the low indentation rates (1 mm/s) where submergence was of minor influence, snow and granular ice significantly increased the ice loads (Table 6.2), which were attributed to an increased contact area. Analogously to submergence, it is thought that this effect originates from the interplay of multiple factors. The following discussion is primarily focused on the low indentation rate and the processes involved.

6.3.2.1 Confinement Effect – Impeded Ice Extrusion

The presence of snow or granular ice on the indenter surface restricts the sideways extrusion of ice debris. This causes a significantly fast increase in contact area due to the accumulation of ice debris. Furthermore, it causes a back pressure that impedes

subsequent ice extrusion and ice failure, and consequently more load is required to overcome the ice strength, and to initiate crack development and propagation.

6.3.2.2 Recrystallization

The confinement caused by the added material, likely enhances processes like recrystallization and ice sintering. As these processes are more prominent at low indentation rates, snow or granular ice provide supplementary material sources that are partly incorporated into the ice specimens, leading to enlarged contact areas.

6.3.2.3 Local Pressure Spreading Effect

Ice debris itself can carry a part of the load and change the overall pressure distribution (Daley et al., 1996). In the present case, the added material also transmitted some load. It altered the pressure pattern that was evident in the pressure sensor readings for granular material in particular. Due to equipment failure during experimentation, only one pressure sensor reading was available. Figure 6.22 shows two separate measurements for 20° (left) and 30° (right) ice specimens (see also Figure 5.14 and Appendix B5). It can be recognized that the local pressures are generally low, and isolated high pressure zones (red colours) are smaller and more localized compared to the other conditions in Figure 6.23. On the other hand, snow (Figure 6.23, bottom right) only differs slightly from the dry (left) and submerged (top right) testing environments.

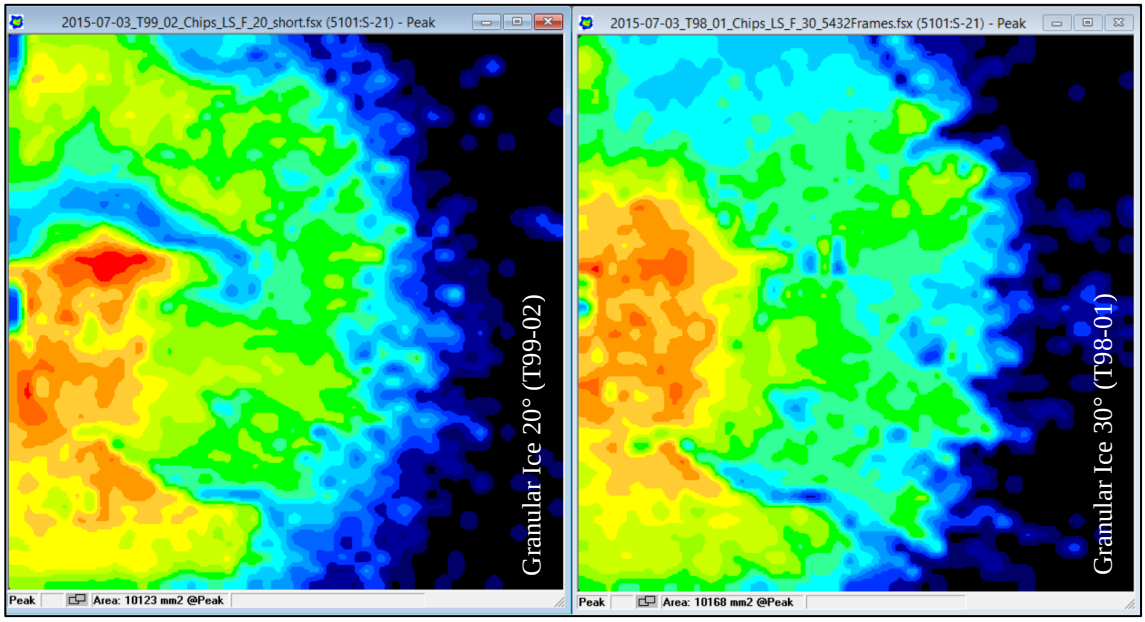

Figure 6.22: Flat plate, 1 mm/s, ice specimen angles 20° (left) and 30° (right), granular ice condition: pressure distribution at peak pressure. Only small isolated high pressure zones can be recognized. Pressures are locally low but the overall load is increased, as is the contact area.

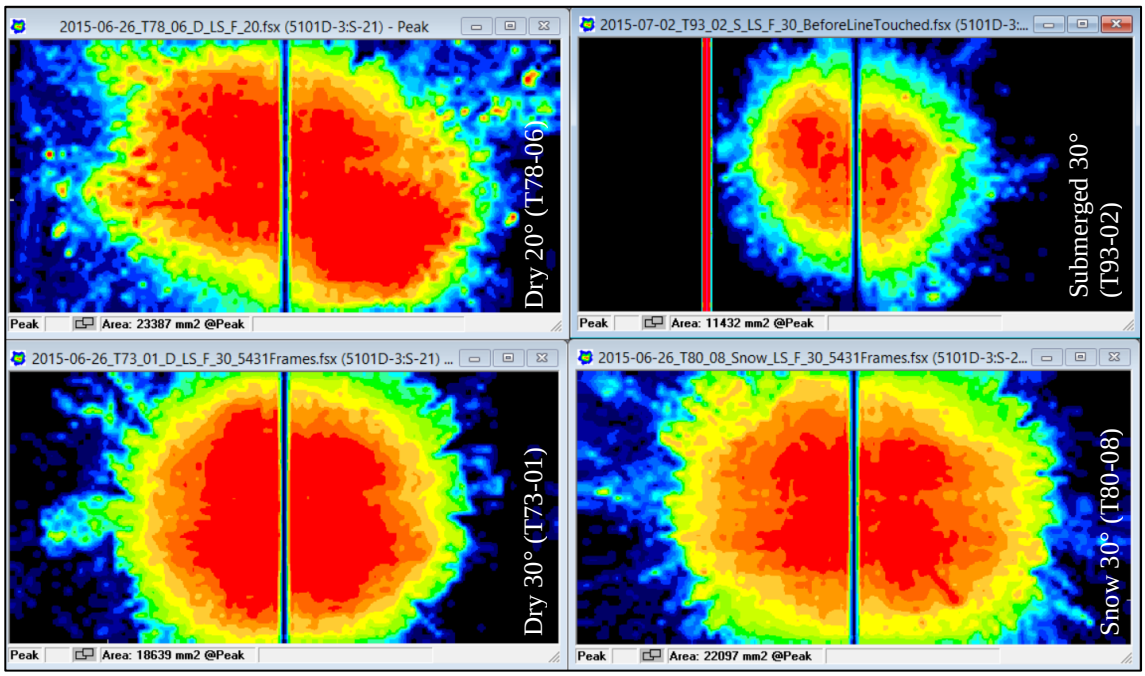

Figure 6.23: Flat plate, 1 mm/s, both ice specimen angles: peak pressures in (Left) the dry contact condition for 20° (top) and 30° (bottom) ice specimens. (Right) pressure patterns for 30° specimens in submergence (top) and with snow (bottom). Images consistently show large areas of local high pressures that dinminish with distance to the center contact area.

6.3.2.4 Summary of Snow and Granular Ice at Low Indentation Rate

The increased forces in tests at the low indentation rate (flat plate) in the presence of snow and granular ice are more pronounced than the effects of submergence at the high indentation rate. This was related to a considerably enlarged contact area that was visible in still photos of sample surfaces, as well as in recordings of the tactile pressure sensors. The preceding discussion addressed the processes that are suggested to have contributed to the contact area increase.

Scenarios with snow and granular ice were initially only added as exploratory investigations. However, the exceptionally high forces that were measured for these contact conditions drew more attention to these cases. In this study, experiments were only performed with loose and dry material; it was not consolidated, combined with water, or allowed to cure – common processes in nature, where snow and granular ice on ice floes, for instance, are exposed to precipitation, salt-water spray, but also to sun that can cause partial melting. These influences may augment the observed force trends and would be worth investigating further.

6.4 Pressure-Area Effect

In section 2.4, the relationship between process pressure and area was addressed. The pressure trend with increasing penetration or area is still a debated subject. Some researchers found decreasing nominal pressure with increasing penetration (Varsta, 1983) or with progressively larger areas (Sanderson, 1988). Others pointed out that this premise may not be as easily generalized due to the lack of independent measurements (Daley, 2007) or that the interplay of a variety of factors needed to be taken into account (Timco

and Sudom, 2013). It was also important to distinguish between an area that controls the force and the region over where it is measured (Palmer, 2009). In experiments with confined ice blocks (Kim et al., 2012) it was found that a larger indenter would lead to higher vertical forces, but the indenter size did not actually affect the average pressure.

With respect to discussions on the progress of the average process pressure during a crushing event, some of the nominal pressure-area plots derived in the context of the present study indicated a decreasing trend with progressive displacement or area increase (e.g. Figure 5.11, Figure 5.38); others were rather constant (e.g. Figure 5.5, Figure 5.9) or had a slight increasing tendency (e.g. Figure 5.36, Figure 5.57). Some nominal average pressures first decreased, and flattened or slightly increased later. The character of the average nominal pressure also varied with testing environment, but was not necessarily consistent for a specific indenter-indentation rate combination.

The influence of different contact area assumptions on the average process pressure was demonstrated. Based on the nominal contact area, exceptionally high nominal process pressures were found for snow and granular ice environments at 1 mm/s indentation rate (for the flat indentation plate), and generally increased nominal pressures in submergence at 100 mm/s impact speed. This was subsequently put into perspective by adjusting the average nominal pressure with a factor that was established by comparing the nominal area with the actual contact area that was measured. The approximation was not exact because information on the actual contact area was only available for a limited test quantity and for two indenter shapes. It is still believed that the adjustment resulted in a more realistic contact pressure estimate. These investigations further revealed that the

ratio between nominal and actual contact area was not constant throughout a crushing event, and an ascending ratio would counteract a previously decreasing process pressure trend. Particularly for high impact speeds it can be noticed that the ratio rose as the event proceeded; this was fairly evident in Figure 5.21 for the flat indentation plate and 30° ice specimen; it was less pronounced in Figure 5.44 for the wedge shaped indenter, except for one submerged test (S T72-06), where the ratio increased for displacements above 22 mm. This may imply two aspects: first, in cases of ice-structure interactions, the deviation between true and nominal contact areas likely becomes larger with advancing penetration. Secondly, if the wedge would represent a deformed structure, or an intersection of two structural components, the discrepancy between both contact areas would still be significant, but it may not necessarily further increase and be mitigated due to the pre-existing confinement.

Furthermore, in the submergence cases at the high indentation rate, ice loads were increased. This was always associated with a larger contact area as the measurements revealed. The pattern of local high pressure zones (HPZs) was similar in shape to dry tests (branch-like), but seemed augmented in size and magnitude (e.g. Figure 5.17, Appendix B5). The larger contact area appeared to have facilitated the build-up of higher local pressures over larger regions. Consequently, if the increased contact area was associated with more pronounced local HPZs, the average process pressure would not necessarily decrease with further penetration. This circumstance was already addressed by Palmer (2009), who speculated that the pressure-area effect would be mitigated for a higher quantity of HPZs at larger areas.

The results from the present work support findings of previous researchers that suggest that the average process pressure does not inevitably decrease with increasing area; its development depends on the boundary conditions and the interplay of several factors, but there is no generally applicable approach for all scenarios of ice-structure interactions. The observed deviations between nominal and actual contact area question generalizations of a decreasing average process pressure trend with increasing area that may simply originate from a lack of information on the true contact area.

6.5 Other Influences

The following paragraphs address some aspects that may have influenced the experimental results.

6.5.1 Water Level

For the flat indentation plate, the submergence effect was more pronounced at the blunter ice cone angle of 20° that showed higher pressures in general. The more compact ice specimen geometry is likely to have restricted and limited the space for ice debris extrusion. Another circumstance that possibly contributed to the variable submergence effect due to ice cone angle, is the different degrees of submergence when first impact occurred (20° ice cones: 100 %; 30° ice specimens: 83 %). This also applies to tests with the wedge shaped indenter. At the time the tests were performed, this was not expected to be of concern. Subsequently viewing the high speed camera recordings suggested that the water influenced the extent and velocity of crack propagation. Consequently, that different initial boundary condition may have had some effect. On the other hand, cracks that pervaded the entire ice specimens usually did not develop within the first 15-20 mm

of penetration, but at a time when the ice specimens were typically entirely submerged. Therefore, the influence of the different initial boundaries is thought to have been mitigated.

6.5.2 Water Temperature

The measured water temperature, before the samples were positioned, varied between + 4.4 and - 2.2°C over the entire test series. At the time testing took place, it was somewhat lower. Temperature fluctuation was inevitable since it was merely regulated by adding and removing water to and from the aluminum container to stay within reasonable limits. In the analysis process, the force-histories of submerged tests were also examined against the background of water temperature, but no evidence was found that indicated an influence.

6.5.3 Mounting Steel Plate

Due to the mounting of the ice specimen to a steel plate, thermodynamic heat transfer may have occurred. Its effect on the test results is unknown, but it was consistent throughout all tests, and is supposed to have affected all results to a similar extent.

6.5.4 Ice Age

As mentioned earlier, due to a breakdown of the testing equipment, several samples were stored for a longer period than others until testing was resumed. The examined thin sections did not exhibit any disparity that would indicate that the ice crystal structure had changed. Also no evidence was found in the data of the MTS machine or the tactile pressure sensors. For verification, a regression analysis was performed taking ice age into

account as a separate factor. The outcome was in support of above statements. The inclusion of ice age in the regression analysis yielded less significant models.

6.5.5 Indentation Rate Variations

Ice failure at high impact speeds is random and characterized by high variability in load measurements. Ice fractures cause very sudden changing displacements that the material testing system (MTS) tries to compensate for. As the maximum capacity of the MTS machine was 100 mm/s, the actual attained average speeds was generally lower, but most of the time deviated by less than 10 %. Still, speed control variations induced some variability in the data since the MTS machine was over- and undershooting the anticipated indentation rate. The extent to that this may have affected the results is unknown and was not further investigated. At lower velocities, where ice fails in a more ductile mode, there was almost no deviation between anticipated and achieved average indentation rate.

6.5.6 Malfunction of Tactile Pressure Sensors

The tactile pressure sensors overall functioned reliably and produced reasonable measurements. The measures taken to mitigate the sensors' exposure to shear forces, water and puncture provided sufficient protection to employ the sensors in all anticipated testing conditions. Nevertheless, the crushing ice caused substantial wear on the protecting Mylar sheet, as well as on the sensors themselves eventually. In more than one case, intruding water led to a defective sensel column. This caused a constant error that was easily removed from the data. Granular ice presented the highest risk for damage. Those tests were performed last, and as expected the sensors did not last very long. It is

noted, though, that the software that processed the information from the pressure sensors, did not indicate any broken sensels and the sensor was still functioning although parts of a sensor were already missing (granular ice tests). This raises the question of the reliability with which the damage is reported by the software and if the sensors were entirely intact in other tests. It is believed that the presented data is unbiased and exempt from significant measurement errors. Recordings with evident sensor damage were not evaluated.

6.6 Implications for Numerical Simulations

In these experiments, the load magnitude was mainly driven by the contact area. Structures could be safer and more economically designed if the increase or decrease in contact area due to the environment and other boundary conditions was taken into account. Based on the available data, in the dry contact condition the actual contact area was consistently smaller than the theoretical nominal area. In other testing environments, the contact area was enlarged. This is an important aspect in an ice crushing event and leads to significantly changed pressures, particularly average pressures that are used for the global design of ship structures. Submergence and snow on the indenter surface did not seem to significantly influence the principal appearance of the local pressure patterns. Both appeared to promote larger continuous high pressure zones, likely due to the confinement and extrusion back pressure that these environments cause. On the other hand, the change in the pressure pattern caused by granular ice was very evident, characterized by generally lower local pressures. To date, numerical simulations of ice-structure interactions are still a major challenge. Meanwhile some models produce

promising results regarding the replication of ice breaking behavior and processes involved. Others are reasonably successful in determining the overall load that a structure would experience when impacted by ice. In both cases, less attention is paid to the environmental or boundary conditions where the impact takes place. The objective of the present study was to reveal differences in ice loads depending on contact condition and indenter geometry. The results indicate that the environment where an impact takes place can significantly alter the contact area and with it the load transmission. The results also showed that the influence on the contact condition is not necessarily linear, but changes during the impact. With regard to submergence, it was proven that its effect varied with geometrical boundaries. The information gathered within the scope of this thesis is not sufficient to allow the full quantification of the submergence effect, or of any of the other tested environments, by the means of a representative factor or relationship. It will require substantially more experimental work to establish such relations before these aspects can be implemented in numerical simulations. This study would be a good starting point for future research.

Chapter 7 Summary, Conclusions and Recommendations

7.1 Summary

The motivation of this study was to enhance the knowledge on external circumstances influencing ice loads, in order to facilitate further advances in Arctic ship and offshore structure design. Specifically, the objective was to explore the interrelated effects of submergence, and contact geometry with some additional consideration of the presence of snow and granular ice. In total, 101 laboratory ice crushing tests were performed with four indenter geometries. These were impacted with artificially produced conical ice specimens.

Data acquisition comprised time, vertical force, and displacement as it was obtained from the material testing system (MTS). In some tests with the flat plate and the wedge shaped indenter, information on local pressure patterns and contact area was derived from measurements with tactile pressure sensors. Furthermore, all tests were recorded with high speed camera, and still photos were taken before and after each test; of some specimens thin sections were taken as well.

The objectives of this study were to investigate, how submergence, and other contact conditions, influence ice load magnitude and how it varied with impact velocity or indenter geometry. Furthermore, the purpose was to identify primary underlying physical processes that would cause a difference in observed load, and whether this difference was as significant as to require its consideration in ice design load determinations. All the originally stated research objectives were achieved. It was proven that submergence, as

well as snow and granular ice, yielded higher forces compared to the dry contact condition. The distinctness depended on impact velocity as well as on indenter geometry. Within the range of utilized impact speeds, an effect of submergence was particularly noticed at the high indentation rate (100 mm/s); this was most evident for the flat indentation plate and the spherical indenter, and with restrictions for the wedge shaped indenter. No evidence was found for the conical indenter. It is suggested that submergence is capable of applying a level of confinement similar in effect to that provided by indenter geometry. Its influence is nonlinear and dependent on a variety of interrelated processes and circumstances, such as the pre-existing confinement originating from indenter and ice geometry. In addition, the ice debris constitution is significantly affected by the presence of water. Some factors and mechanisms that likely contributed to the effect were discussed.

Independent of contact condition, higher forces were always found to correlate with enlarged contact areas, where contact area measurements were available. Measured and nominal contact area significantly differed. At high indentation rates, dry and submerged contact areas were distinctly smaller than the theoretical nominal contact area by a variable offset. In some cases, the difference seemed to increase with the proceeding crushing event and would imply that there is no premise for the true average process pressure, measured over the real contact area, to decrease with advancing penetration.

In tests with the flat indentation plate at low indentation rates (1 mm/s), submergence yielded higher forces as well. More importantly, with snow and granular ice on the

indenter's surface the highest forces out of all contact conditions were measured. This was attributed to a gain in contact area and presumed processes involved were discussed.

The established data does not offer sufficient information for developing a relationship or a factor to express the submergence effect, or the effect of one of the other contact conditions or parameter. The findings do indicate some distinct trends and interrelations. This leads to a conclusion that realistic ice load definitions may require a more scenario based design instead of a generalized approach.

7.2 Conclusions

It was noticed in earlier studies that water influences ice loads, but it had not been investigated in detail. This work makes some fundamental contributions to elucidate the effect of submergence and it has been proven that a submergence effect exists. The measured forces for ice impacts under water exceeded those of a dry contact surface. Furthermore, high forces were obtained with snow and granular ice on the indenter surface. In all cases, the increased forces were correlated with larger contact areas. The overall outcome suggests the following conclusions:

- The (environmental) boundary condition, in an ice crushing event, significantly controls the true contact area and the contact area controls the transmittable force;
- Submergence causes higher ice loads compared to a dry contact surface;
    - The effect of submergence depends on a variety of interrelated processes, pre-existing confinement, aspect-ratio (or the ratio of internal crushing vs. external crushing), and its influence is most pronounced at high rates;

    - At high indentation rates, submergence tends to make the contact area look more like those observed at the low rates (more compact);
    - The presence of bulk water leads to a reduced propensity of cracks to form and a reduced propagation of cracks;
    - The presence of water at the immediate ice-structure interface causes a pressure spreading effect (PSE) at the grain boundaries and in continued event more load is required to overcome the ice strength and induce subsequent ice failure;
- The increased force observed as ice penetration proceeds and nominal contact area grows is not necessarily associated with an increased or decreased average process pressure. The average process pressure may not significantly change but may in fact be most significantly influenced by changes in the true contact area within the nominal contact patch;
    - Boundary conditions limit forces and pressures;
    - The mechanism of ice extrusion has a strong influence on the supported pressure and ice extrusion is influenced by the geometry and the presence of water. The two mechanisms also interact and the fluid effect dominates when the geometry effect is low and vice-versa;
- In case of low geometrical confinement, the water resumes a confining function, creating a hydrodynamic confinement zone (HDC) around the ice crushing region, where fluid drag restricts ice spall ejection. This leads to the accumulation of ice debris and promotes an increased contact area;

- At low indentation rates, snow and granular ice material at the ice-indenter interface are incorporated into the impacting ice feature, likely due to ice recrystallization and ice sintering.

The results of this study emphasize the need to employ suitable technologies in future ice impact tests to allow better insight into the contact area during the event. In the current work, the contact area measurements showed that actual and nominal contact areas differed significantly, and that this considerably changed the estimation of average process pressure relations between contact conditions, as well as between indentation rates.

As the pressures for ice design loads are generally based on nominal contact area assumptions, this study may reflect the need to pay closer attention to the actual contact area and the boundary conditions. In addition, present ice design loads are mostly extrapolated from dry impact tests, but these most often do not consider the boundary condition, or the geometry of the contact scenario. The current work indicates that both factors influence the effective load and the nature of the contact pressure distribution. With reference to discussed contact area measurements, especially at high rates, the contact area for a dry contact condition had a distinct tendency to be smaller than anticipated. Furthermore, it may not be reasonable to expect average or localized pressures to decrease with increasing penetration or interaction area, depending on boundary conditions. Regarding other contact conditions and submergence, in particular, the increased area allows more force to be transmitted to the structure. Here, global loads

may be higher than expected. Further research is needed to investigate the influences and effects, and especially the repercussions on local and global loads in more detail.

The findings of this study indicate a strong dependency of ice loads on boundary conditions. This suggests that an optimized design for ships operating in the Arctic and Arctic offshore structures would require a more scenario based approach to estimating ice loads, where different factors (e.g. contact condition, geometries,…) are taken into account.

7.3 Recommendations

The effect of different surface contact conditions was reflected in increased force measurements, associated mainly with enlarged contact areas, which are in turn influenced by post failure extrusion or other processes. It is recommended to adapt new technologies in ice impact tests to gather information on contact area and local pressures during ice crushing events. In the best case, the development of the contact area would be measured throughout the entire event, as it represented some limitations for the analysis of the tests that were carried out for this study. In many tests, the employed pressure sensing system did not cover sufficient area to capture the contact area until the end of the test. This fact was known beforehand and was accepted due to space and financial constraints. A custom-made system would have cost many times more than the system used, which was the most feasible setup under given circumstances and with the available equipment.

Such measurements would also allow more explicit statements on the effect of environmental conditions on local pressures, as it was not done in this study. The preparation of the tactile pressure sensors used, is a crucial matter and fairly complex. Many thoughts were given to this issue and knowledgeable people were consulted to develop an appropriate procedure and preparation setup. However, the confidence in the preparation procedure was not sufficient to state pressure values. Furthermore, the map that was used for combining two sensors to one connected area generally requires preparing both sensors together in the anticipated position. This error was realized only later and technical support was sought to resolve the problem. A method to correct the issue exists but was not implemented within this thesis.

The objective of this study was to examine differences in ice loads depending on testing environment, but not ice material properties. Ice specimens had consistent properties, grain size was not varied, and this would likely change spall size and ice debris. Considering the facts that the surrounding water to a great extent influenced the constitution of the extruding ice, and significantly impeded the ejection of ice spalls, it would be interesting to see how these processes would be affected for other ice constitutions. If the proposed hydrodynamic confinement zone exists, and if it was dependent on ice spall size, it is probably of more importance for larger ice spalls. This would indicate that the submergence effect is also related to ice properties. On the other hand, it may not make a difference implying that it is less a hydrodynamic confinement that is governing, but rather ice “internal” processes, such as re-freezing - which leads to the next recommendation.

Tests with other materials that facilitate the separation of material effects and physical processes would further elucidate interrelations and would help identifying the dominating parameters involved.

As the maximum indentation rate used in this research was limited to a velocity of 100 mm/s by the testing equipment, investigation at higher indentation rates would facilitate further clarification of the hierarchy of factors and processes involved. More importantly, it would be closer to impact speeds as they occur in real ice-structure collisions.

Furthermore, other ice and indenter geometries and combinations should be employed. The effect of submergence was found to depend on pre-existing confinement and was supposed to be interrelated with aspect ratio. This would be worth further investigation, especially with respect to extrapolating the submergence effect to larger scales.

In this regard, the effect of submergence, as well other contact conditions should be examined at larger scales. Small scale experiments as they were conducted for this study are a feasible and cost efficient method to explore fundamental relations and create a general understanding. How these results compare to events as they occur in nature needs to be assessed. It is believed that the outcome would not substantially differ because the basic underlying processes do not change.

References

ACIA. 2005. Arctic climate impact assessment. ACIA Overview report. Cambridge University Press.

Blackford, J. R. 2007. Sintering and microstructure of ice: A review. Journal of Physics D: Applied Physics 40 (21): R355.

Browne, T., R. Taylor, I. Jordaan, and A. Guertner. 2013. Small-scale ice indentation tests with variable structural compliance. Cold Regions Science and Technology 88 (Apr 2013): 2-9.

Bruneau, S. E., A. K. Dillenburg, and S. Ritter. 2012. Ice sample production techniques and indentation tests for laboratory experiments simulating ship collisions with ice. Paper presented at International Offshore and Polar Engineering Conference, ISOPE2012.

Cole, D. M. 2001. The microstructure of ice and its influence on mechanical properties. Engineering Fracture Mechanics 68 (17): 1797-822.

Daley, C., J. Tuhkuri, and K. Riska. 1996. Discrete chaotic ice failure model incorporating extrusion effects. National Energy Board.

Daley, C. 2004. A study of the process-spatial link in ice pressure-area relationships. St. John's, N.L.: PERD, Memorial University of Newfoundland, 7-108.

Daley, C., J. Tuhkuri, and K. Riska. 1998. The role of discrete failures in local ice loads. Cold Regions Science and Technology 27 (3) (6): 197-211.

Daley, C. G. 2007. Reanalysis of ice pressure-area relationships. Marine Technology 44 (4): 234-44.

Daley, C. G. 1991. Ice edge contact a brittle failure process model. Acta Polytechnica Scandinavica, Mechanical Engineering Series no.100: 1-92.

Daley, C. 1992. Ice edge contact and failure. Cold Regions Science and Technology 21 (1) (9): 1-23.

Dillenburg, A. K. 2012. Rate dependency in conical ice indenter failure. Master Thesis., University of Duisburg-Essen. Institute of Ship Technology, Ocean Engineering and Transport Systems. Germany.

Dragt, R. C. 2013. The collison of cone-shape ice samples against steel plates of varying surface roughness. Master Thesis., Delft University of Technology, Department of Structural Dynamics. Netherlands.

Frederking, R. 1998. Pressure area relation in the definition of ice forces. Paper presented at Proceedings of the Eighth (1998) International Offshore and Polar Engineering Conference, Montreal, Canada.

Frederking, R., I. J. Jordaan, and J. S. McCallum. 1990. Field tests of ice indentation at medium scale hobsons's choice ice island, 1989. Paper presented at Proceedings International Association for Hydraulic Research, IAHR '90, Espoo, Finland.

Gagnon, R., A. Bugden, and R. Ritch. 2009. Preliminary testing of a new ice impact panel gagnon. Paper presented at Proceedings of the 20th International Conference on Port and Ocean Engineering under Arctic Conditions (POAC'09), Luleå, Sweden.

Gagnon, R. 2008. Analysis of data from bergy bit impacts using a novel hull-mounted external impact panel. Cold Regions Science and Technology 52 (1): 50-66.

Gautier, D. L., K. J. Bird, R. R. Charpentier , A. Grantz, D. W. Houseknecht, T. R. Klett, T. E. Moore. 2009. Assessment of undiscovered oil and gas in the arctic. Science 324 (5931): 1175-9.

Gudimetla, P. S. R., B. Colbourne, C. Daley, S. E. Bruneau, and R. Gagnon. 2012. Strength and pressure profiles from conical ice crushing experiments. In , 167-174. Banff, Alberta, Canada.

Hill, B. T. 2000. Database of ship collisions with icebergs. St. John's, Newfoundland: National Research Council Canada, Institute for Marine Dynamics.

Houseknecht, D. W., K. J. Bird, and C. P. Garrity. 2012. Assessment of undiscovered petroleum resources of the arctic alaska petroleum province. U.S. Geological Survey, Reston, Virginia: 2012: U.S. Department of the Interior, U.S. Geological Survey, 5147.

Izumiyama, K., T. Takimoto, and S. Uto. 2007. Length of ice load patch on a ship bow in level ice. In . Vol. 2, 1287-1294.

Johnston, M. E., and G. W. Timco. 2008. Understanding and identifying old ice in summer. Ottawa: National Research Council Canada, Canadian Hydraulics Centre, CHC-TR-055.

Jones, S. J. 2007. A review of the strength of iceberg and other freshwater ice and the effect of temperature. Cold Regions Science and Technology 47 (3) (3): 256-62.

Jones,S. J. 1997. High strain-rate compression tests on ice. The Journal of Physical Chemistry B 101 (32): 6099-101.

Jones, SJ, R. E. Gagnon, A. Derradji, and A. Bugden. 2003. Compressive strength of iceberg ice. Canadian Journal of Physics 81 (1-2): 191-200.

Jordaan, I. J. 2001. Mechanics of ice-structure interaction. 68 (Engineering Fracture Mechanics): 1923-60.

Jordaan, I. J., and J. Xiao. 1992. Interplay between damage and fracture in ice-structure interaction. Paper presented at Proceedings International Association for Hydraulic Research, IAHR '92, Banff, Alberta, Canada.

Jordaan, I. J., M. A. Maes, and J. P. Nadreau. 1988. The crushing and clearing of ice in fast spherical indentation tests. Paper presented at 7th International Conference on Offshore Mechanics and Arctic Engineering (OMAE), Houston, Texas, USA.

Kennedy, K. P., I. J. Jordaan, M. A. Maes, and A. Prodanovic. 1994. Dynamic activity in medium-scale ice indentation tests. Cold Regions Science and Technology 22 (3): 253-67.

Kietzig, A. -M, S. Hatzikiriakos, and P. Englezos. 2010. Physics of ice friction. Journal of Applied Physics 107 (8): 081101,081101-15.

Kim, E., N. Golding, E. M. Schulson, S. Løset, and C. E. Renshaw. 2012. Mechanisms governing failure of ice beneath a spherically- shaped indenter. Cold Regions Science and Technology 78 : 46-63.

Kim, H. 2014. Ice crushing pressure on non-planar surface. Doctoral Thesis, Memorial University of Newfoundland, Canada.

Kim, H., and C. Daley. 2013. Reanalysis of pressure patterns and pressure-area curves considering resolution of pressure measurement film. Paper presented at Proceedings of the 22nd International Conference on Port and Ocean Engineering under Arctic Conditions, POAC' 13, Espoo, Finland.

Kim, H., C. Daley, and C. Ulan-Kvitberg. 2012. Reappraisal of pressure distribution induced by ice- structure interaction using high-precision pressure measurement film. Paper presented at International Conference and Exhibition on Performance of Ships and Structures in Ice (ICETECH 2012), Banff, Alberta, Canada.

Kim,H.;Daley,C. and C. Ulan-Kvitberg. 2011. Crushing characteristics of dry, wetted and submerged ice. Paper presented at 21st International Offshore and Polar Engineering Conference, Maui, Hawaii, USA.

Kubat, I., and G. W. Timco. 2003. Vessel damage in the canadian arctic. Paper presented at Proceedings of the 17th International Conference on Port and Ocean Engineering under Arctic Conditions, POAC'03, Trondheim, Norway.

Kubat, I., A. Collins, B. Gorman, and G. Timco. 2006. Impact of climate change on arctic shipping: Vessel damage and regulations. Ottawa, Ontario: National Research Council Canada, CHC-TR-038.

Kujala, P. 1994. Modelling of the ice-edge failure process with curved failure surfaces. Annals of Glaciology 19: 158-64.

Kujala, P., and S. Arughadhoss. 2012. Statistical analysis of ice crushing pressures on a ship's hull during hull-ice interaction. Cold Regions Science and Technology 70: 1-11.

Masterson, D. M., R. M. W. Frederking, I. J. Jordaan, and P. A. Spencer. 1993. Description of multi-year ice indentation tests at Hobsons's choice ice island - 1990. Paper presented at Proceedings of the 12th International Conference on Offshore Mechanics and Arctic Engineering, Glasgow, Scotland.

Masterson, D. M., and R. M. W. Frederking. 1993. Local contact pressures in ship/ice and structure/ice interactions. Cold Regions Science and Technology 21 (2) (1): 169-85.

Masterson, D. M., R. M. W. Frederking, B. Wright, T. Karna, and W. P. Maddock. 2007. A revised ice pressure-area curve. Proceedings of the International Conference on Port and Ocean Engineering Under Arctic Conditions, POAC: 305-14.

Meglis, I. L., P. M. Melanson, and I. J. Jordaan. 1999. Microstructural change in ice: II. creep behavior under triaxial stress conditions. Journal of Glaciology 45 (151): 438-48.

Melanson, P. M., I. L. Meglis, I. J. Jordaan, and B. M. Stone. 1999. Microstructural change in ice: I. constant-deformation-rate tests under triaxial stress conditions. Journal of Glaciology 45 (151): 417-37.

Michel, B. 1978. Ice mechanics. Québec: Les Presses de l'Université Laval.

Muggeridge, K. J., and I. J. Jordaan. 1999. Microstructural change in ice: III. observations from an iceberg impact zone. Journal of Glaciology 45 (151): 449-55.

NSIDC. 2014. Arctic sea ice continues low; antarctic ice hits a new high. National Snow and Ice Data Center (NSIDC). Available at www.nsidc.org. Accessed February 04, 2015.

Palmer, A. C., and K. Croasdale. 2013. Arctic offshore engineering. Singapore, SGP: World Scientific Publishing Co.

Parsons, B. L. 1993. An estimate of the size of the damage zone beneath an indenter on ice. Cold Regions Science and Technology 21 (4) (7): 371-80.

Pizzolato, L., S. E. L. Howell, C. Derksen, J. Dawson, and L. Copland. 2014. Changing sea ice conditions and marine transportation activity in Canadian Arctic waters between 1990 and 2012. Climate Change(123): 161-73.

Pritchard, R. S., G. S. Knoke, and D. C. Echert. 2012. Sliding friction of sea ice blocks. Cold Regions Science and Technology 76–77 (0) (6): 8-16.

Ralph, F., R., R. McKenna, and R. Gagnon. 2008. Iceberg characterization for the bergy bit impact study. Cold Regions Science and Technology 52 (1) (3): 7-28.

Ritch, R., R. Frederking, F. Johnston, F. Browne, and F. Ralph. 2008. Local ice pressures measured on a strain gauge panel during the CCGS terry fox bergy bit impact study. Cold Regions Science and Technology 52 (1): 29-49.

Sanderson, T. J. O. 1988. Ice mechanics: Risks to offshore structures. London, UK; Boston: Graham & Trotman.

Scott, J. 2005. Drag of Cylinders and Cones. Retrieved September 21. 2015, from http://www.aerospaceweb.org/question/aerodynamics/q0231.shtml.

Schulson, E., M. 2001. Brittle failure of ice. Engineering Fracture Mechanics 68 (17–18) (12): 1839-87.

Schulson, E. M., and A. L. Fortt. 2012. Friction of ice on ice. Journal of Geophysical Research B: Solid Earth 117 (12).

Shazly, M., V. Prakash, and B. Lerch A. 2009. High strain-rate behavior of ice under uniaxial compression. International Journal of Solids and Structures 46 (6) (3/15): 1499-515.

Singh, S. K., and I. J. Jordaan. 1996. Triaxial tests on crushed ice. Cold Regions Science and Technology 24 (2): 153-65.

Singh, S. K., I. J. Jordaan, J. Xiao, and P. A. Spencer. 1995. The flow properties of crushed ice. Journal of Offshore Mechanics and Arctic Engineering 117 (4) (11/01): 276-82, http://dx.doi.org/10.1115/1.2827234.

Smith, L. C., and S. R. Stephenson. 2013. New trans-arctic shipping routes navigable by midcentury. Pnas(Proceedings of the National Academy of Sciences Plus): 1191-5.

Sopper, R., C. Daley, and B. Colbourne. 2015a. Ice loads in dry and submerged conditions. Paper presented at Proceedings of the 34th International Conference on Ocean, Offshore and Arctic Engineering (OMAE), St. John's, Newfoundland, Canada.

Sopper, R., R. Gagnon, C. Daley, and B. Colbourne. 2015b. Measurements of spatial and temporal variations in ice impact pressures. Paper presented at Proceedings of the 23rd International Conference on Port and Ocean Engineering under Arctic Conditions (POAC), Trondheim, Norway.

Spencer, P. A., D. M. Masterson, J. Lucas, and I. J. Jordaan. 1992. The flow properties of crushed ice: Experimental observation and apparatus. Paper presented at Proceedings International Association for Hydraulic Research, IAHR '92, Banff, Alberta, Canada.

Stone, B. M., I. J. Jordaan, J. Xiao, and S. J. Jones. 1997. Experiments on the damage process in ice under compressive states of stress. Journal of Glaciology 43 (143): 11-25.

Sumiya, T., Y. Suzuki, T. Kasahara, and H. Ogata. 1998. Sensing stability and dynamic response of the F-scan in-shoe sensing system: A technical note. Journal of Rehabilitation Research and Development 35 (2): 192-200.

Szabo, D., and M. Schneebeli. 2007. Subsecond sintering of ice. Applied Physics Letters 90 (15): 151916.

Tekscan, Inc. 2003. I-scan equilibration and calibration practical suggestions rev. A. South Boston, MA: Company Publication.

The Mariport Group Ltd. 2007. Canadian arctic shipping assessment. Transport Canada.

Timco, G. W., and K. R. Croasdale. 2006. How well can we predict ice loads? Paper presented at Proceedings on the 18th IAHR International Symposium on Ice, Sapporo, Japan.

Timco, G. W., and D. Sudom. 2013. Revisiting the sanderson pressure-area curve: Defining parameters that influence ice pressure. Cold Regions Science and Technology 95 : 53-66.

Timco, G. W., and W. F. Weeks. 2010. A review of the engineering properties of sea ice. Cold Regions Science and Technology 60 (2) (2): 107-29.

Tuhkuri, J., and K. Riska . 1990. Results from tests on ice extrusion of crushed ice. Otaniemi: Helsinki University of Technology, Faculty of Mechanical Engineering, Laboratory of Naval Architecture and Marine Engineering, M-98.

Tuhkuri, J. 1995. Experimental observations of the brittle failure process of ice and ice-structure contact. Cold Regions Science and Technology 23 (3) (5): 265-78.

U.S.G.S., 2009. Circum-arctic resource appraisal (north of the arctic circle) assessment units GIS data. U.S. geological survey. Available from http://energy.usgs.gov/arctic/.

Ulan-Kvitberg, C. A. 2012. Adapting pressure films to measure pressure patterns in ice-steel interaction experiments. Master Thesis, Memorial University of Newfoundland.

United States ArmyCorps of Engineers. 2006. Engineering and design: Ice engineering. Vol. 1110-2-1612.; 1110-2-1612. Washington, D.C: U.S. Army Corps of Engineers.

Varsta, P. 1983. On the mechanics of ice load on ships in level ice in the baltic sea. Publications 11 ed. Espoo: Technical Research Centre of Finland.

Wells, J., I. Jordaan, A. Derradji-Aouat, and R. Taylor. 2011. Small-scale laboratory experiments on the indentation failure of polycrystalline ice in compression: Main results and pressure distribution. Cold Regions Science and Technology 65 (3) (Mar 2011): 314-25.

Yen, Y., F. Odar, and L. R. Bracy. 10/1970. Impact of spheres on ice. Journal of the Engineering Mechanics Division 96 (5): 641 - 652.

Appendices

Appendix A : Projected and Tangent Contact Area Derivations

Appendix A1 : Wedge Shaped Indenter

The following presented general derivation and illustrations are the result of private correspondence with Prof. Dr. Glyn George. They were developed by Dr. George in August 2015 and are provided by his courtesy.

Parameter definitions:

α semi-opening-angle of the conical ice specimen

θ half the angle between the intersecting planes of the indenter, with $\theta > \alpha$

L length of the contact between ice and indenter in the *x*-*z* plane

C vertical distance between the actual tip of the ice and where the tip of the cone would be in the absence of the indenter.

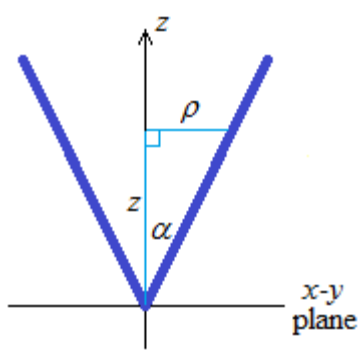

$$\rho = \sqrt{x^2 + y^2} \quad \text{(distance from } z \text{ axis)}$$

$$\tan\alpha = \frac{\rho}{z} \quad \Rightarrow \quad z = \frac{\rho}{\tan\alpha}$$

The equation of the ice cone is

$$\boxed{z^2 = \left(x^2 + y^2\right)\cot^2\alpha}$$

More relationships:

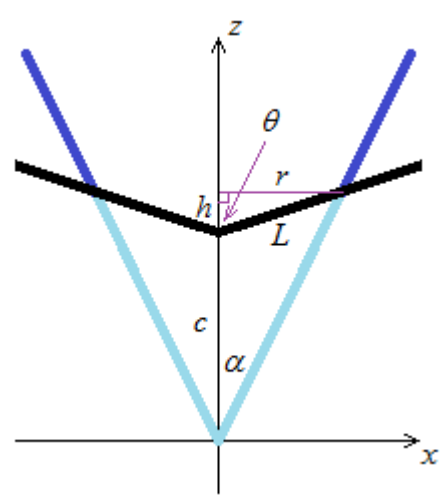

$$\tan\alpha = \frac{r}{c+h} \quad \Rightarrow \quad c + h = r\cot\alpha$$

$$\tan\theta = \frac{r}{h} \quad \Rightarrow \quad h = r\cot\theta$$

$$\Rightarrow \quad c = r\left(\cot\alpha - \cot\theta\right)$$

$$r = L\sin\theta \quad \Rightarrow \quad c = L\left(\cot\alpha \cdot \sin\theta - \cos\theta\right)$$

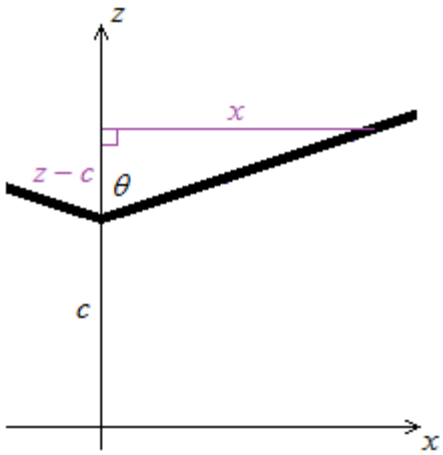

The equation of the right half-plane of the indenter is

$$\frac{x}{z-c} = \tan\theta \quad \Rightarrow \quad \boxed{z = c + x\cot\theta}$$

(and the left half-plane is $z = c - x\cot\theta$)

The curve of intersection between ice and indenter is found by equating the two expressions for z^2. For the right half of the indenter we have:

$$z^2 = \left(x^2 + y^2\right)\cot^2\alpha = \left(c + x\cot\theta\right)^2$$

$$\Rightarrow \quad x^2 + y^2 = \left(c + x\cot\theta\right)^2 \tan^2\alpha$$

$$\Rightarrow \quad \boxed{y^2 = \left(c + x\cot\theta\right)^2 \tan^2\alpha - x^2}$$

and on the other half of the indenter (where $x < 0$) the curve has the equation

$$y^2 = \left(c - x\cot\theta\right)^2 \tan^2\alpha - x^2$$

where $c = L\left(\cot\alpha \cdot \sin\theta - \cos\theta\right)$

For $x > 0$ and $y > 0$ the parametric form for the boundary curve where the conical ice specimen meets the indenter wedge is

$$\vec{\mathbf{r}} = \begin{bmatrix} x \\ y \\ z \end{bmatrix} = \begin{bmatrix} x \\ +\sqrt{\left(c + x\cot\theta\right)^2 \tan^2\alpha - x^2} \\ c + x\cot\theta \end{bmatrix}, \qquad \left(0 \le x \le r\right)$$

$$\left(\text{where} \quad r = \frac{c}{\cot\alpha - \cot\theta}\right)$$

The contact area is the area enclosed by this curve on the inclined plane of the indenter.

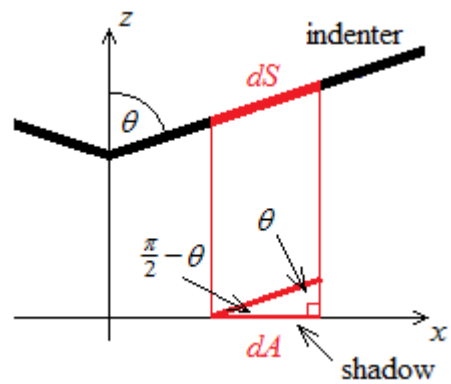

The relationship between the required area and the area enclosed by the shadow of the curve on the *x-y* plane is easy to obtain:

The right half of this curve lies entirely on a plane inclined at a constant angle θ to the vertical and therefore an angle $\left(\frac{\pi}{2}-\theta\right)$ to the *x-y* plane. An area S on the indenter is related to the area D of its shadow on the *x-y* plane by the projection $D = S\cos\left(\frac{\pi}{2}-\theta\right) = S\sin\theta \quad \Rightarrow \quad S = \dfrac{D}{\sin\theta}$

The total contact area, by symmetry, is four times the part of the area in the first quadrant $(x>0 \text{ and } y>0)$. Therefore the contact area A is

$$\boxed{A = \frac{4}{\sin\theta}\int_0^r \int_0^{\sqrt{(c+x\cot\theta)^2\tan^2\alpha - x^2}} 1\,dy\,dx = \frac{4}{\sin\theta}\int_0^r \sqrt{(c+x\cot\theta)^2\tan^2\alpha - x^2}\,dx}$$

where $c = L(\cot\alpha\cdot\sin\theta - \cos\theta)$ and $r = L\sin\theta = \dfrac{c}{\cot\alpha - \cot\theta}$

This can be expressed in terms of α, θ and L only as

$$A = \frac{4}{\sin\theta}\int_0^{L\sin\theta} \sqrt{(L\sin\theta - L\cos\theta\tan\alpha + x\cot\theta\tan\alpha)^2 - x^2}\,dx$$

or, in terms of α, θ and c only as

$$\boxed{A = \frac{4}{\sin\theta}\int_0^{c/(\cot\alpha-\cot\theta)} \sqrt{(c+x\cot\theta)^2\tan^2\alpha - x^2}\,dx}$$

GHG

2015 August 06

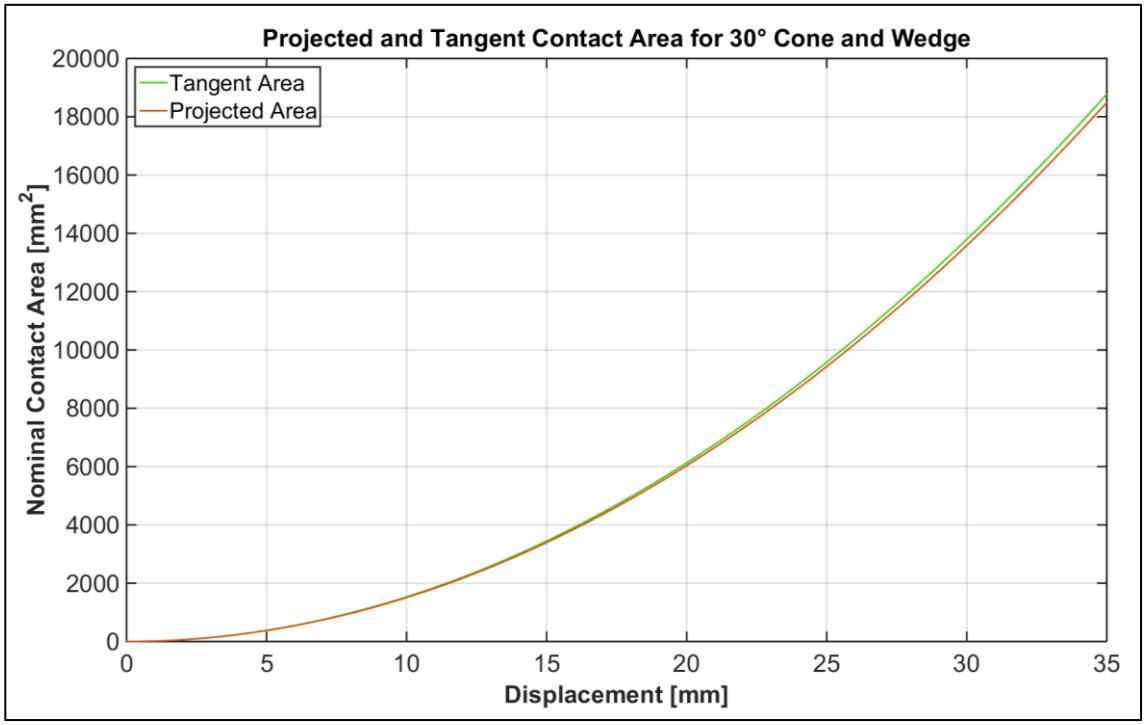

Figure Appendix A1. 1: Comparison of projected and tangent contact area for a 30° cone and the 10° wedge indenter.

Appendix A2 : Conical Indenter

For the interaction of a conical specimen and a wedge shaped indenter, tangent and a projected area are displayed in Figure Appendix A2. 1. The tangent area (green) refers to the contact area that develops on the indenter surface. The projected area (red) corresponds to the contact area projected on a horizontal that is defined by the ice cone-indenter intersection.

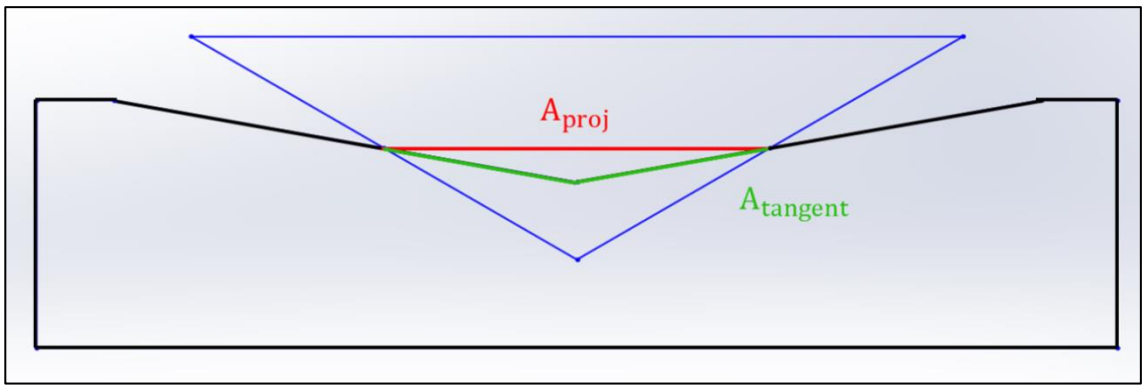

Figure Appendix A2. 1: Overview of projected and tangent area of a cone intersecting with a conical or wedge shaped indenter.

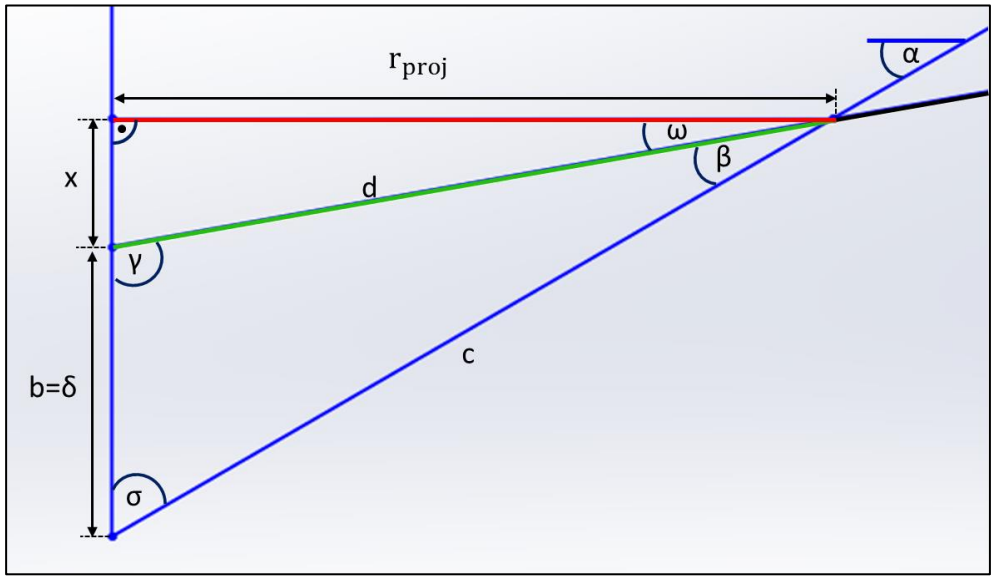

Figure Appendix A2. 2: Detail drawing of geometric relations for the determination of projected and tangent area of a cone impacting a conical shaped indenter.

The following equations express the derivation of both contact areas based on the parameter definitions in above Figure Appendix A2. 2.

$$\frac{d}{\sin\sigma} = \frac{b}{\sin\beta} = \frac{c}{\sin\gamma}$$

$$d = \sin\sigma * \frac{b}{\sin\beta}$$

$$\sin\omega = \frac{x}{d}$$

$$x = d * \sin\omega$$

$$\tan\sigma = \frac{r_{proj}}{(\delta + x)}$$

$$r_{proj} = (\delta + x)\tan\sigma$$

$$A_{proj} = \pi * {r_{proj}}^2$$

$$A_{tangent} = \pi * r_{proj} * d$$

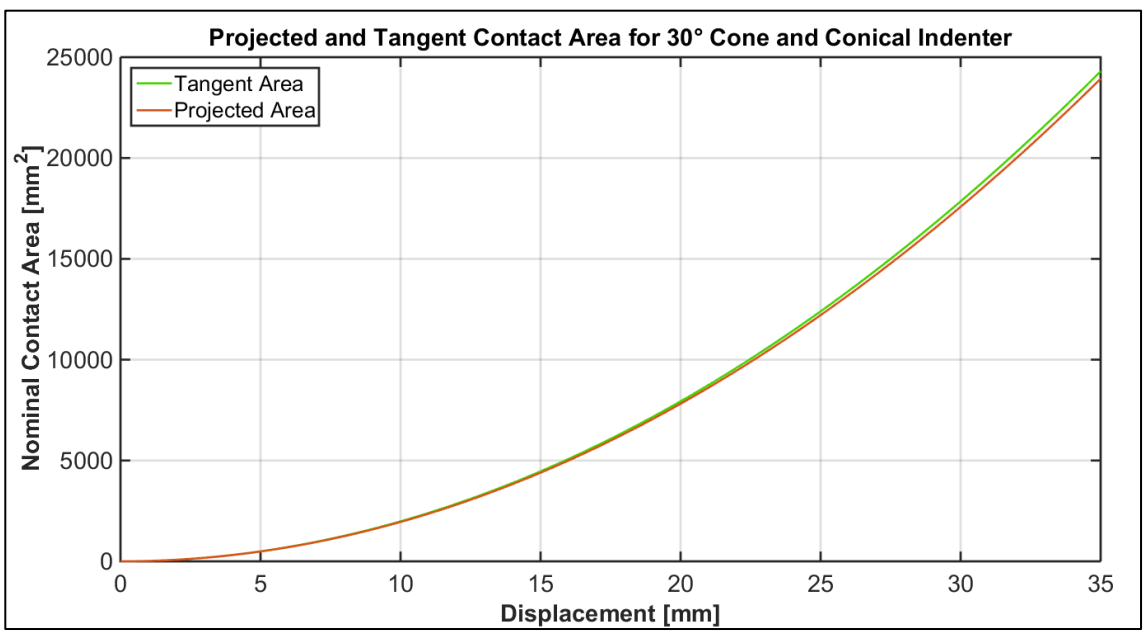

Figure Appendix A2. 3: Comparison of projected and tangent contact area a 30° cone and the 10° conical indenter.

Appendix A3 : Spherical Indenter

Figure Appendix A3. 1 sketches the projected (red) and the tangent (green) contact areas for a conical ice specimen and a spherical indenter.

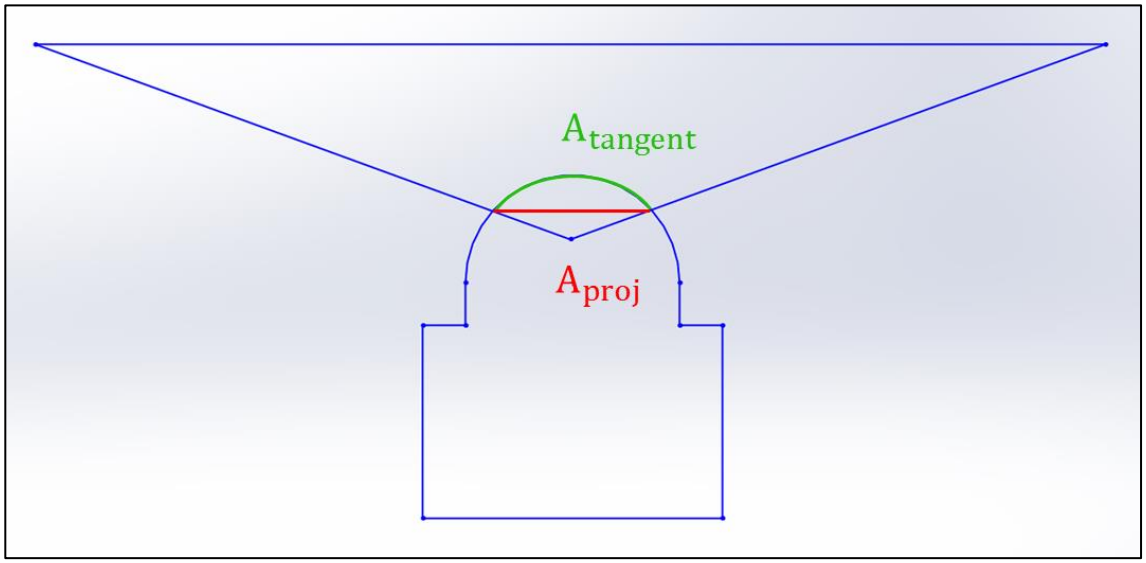

Figure Appendix A3. 1: Overview of projected and tangent contact area of a cone intersecting with a spherical indenter.

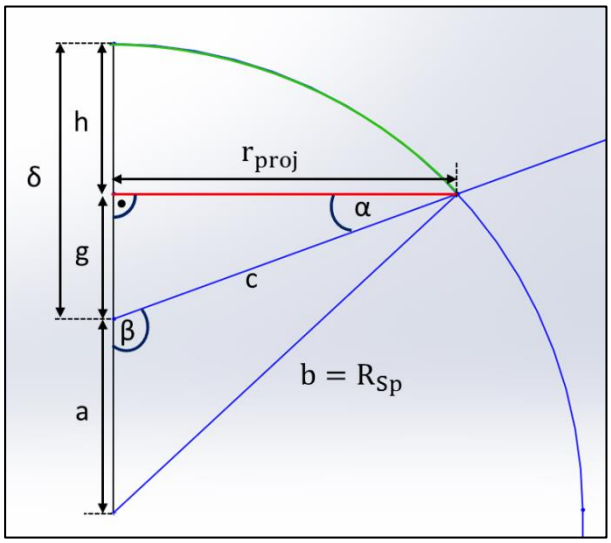

Figure Appendix A3. 2: Detail drawing of geometric relations for the determination of projected and nominal area of a cone-sphere impact.

In the equations below, r_{proj} is the radius of the (circular) projection of ice-indenter interface on a horizontal plane. b is the radius of the spherical indenter (25 mm). h is the height of the sphere's cap that is the length of a vertical from the tip of the sphere to the horizontal plane (A_{proj}) where the two shapes intersect. A visual definition of the parameters is given in above Figure Appendix A3. 2.

$$b = R_{Sp}$$

$$a = b - \delta$$

$$\cos\beta = \frac{c^2 + a^2 - b^2}{2ca}$$

$$2ca * \cos\beta + b^2 - a^2 - c^2 = 0$$

$$c^2 - 2ca * \cos\beta - b^2 + a^2 = 0$$

$$p = 2ca * \cos\beta$$

$$q = -b^2 + a^2$$

$$c_{1/2} = \frac{-p \pm \sqrt{p^2 - 4 * 1 * q}}{2 * 1}$$

$$c_{1/2} = \frac{2a\cos\beta}{2} \pm \frac{\sqrt{4a^2(\cos\beta)^2 - 4(-b^2 + a^2)}}{2}$$

$$c_{1/2} = a\cos\beta \pm \sqrt{a^2(\cos\beta)^2 + b^2 - a^2}$$

$$c_{1/2} = a\cos\beta \pm \sqrt{a^2((\cos\beta)^2 - 1) + b^2}$$

$$c \geq 0$$

$$\cos\alpha = \frac{r_{proj}}{c}$$

$$r_{proj} = c * \cos\alpha$$

$$A_{proj} = \pi * r_{proj}^2$$

Determination of *h* for the tangent area

$$\sin\alpha = \frac{g}{c}$$

$$g = c * \sin\alpha$$

$$h = \delta - g = \delta - c * \sin\alpha$$

$$A_{tangent} = 2\pi bh$$

Sphere is entirely enveloped in ice when

$$r_{proj} = r = \frac{D}{2} = 25\ mm$$

$$x = g + a$$

$$\tan\alpha = \frac{x}{r}$$

$$x = r * \tan\alpha = 25 * \tan 20 = 9.099\ mm$$

$$\delta = 25 + 9.099 = 34.099\ mm$$

Therefore the maximal considered displacement was limited to 30 mm.

Appendix B : Flat Indentation Plate

Appendix B1 : Spectral Analysis (FFT)

Overall, at the high indentation rate (100 mm/s), distinct differences in the Fourier spectra are observed dependent on the respective contact condition. Figure Appendix B1. 1 shows eight selected Fourier spectra for all contact conditions (top to bottom: dry, submerged, snow, granular ice) and for both ice cone angles (left: 20° cones; right: 30° cones). Frequencies up to 1000 Hz are displayed along the x-axis.

In the dry contact condition (top row), the curves are unsteady with high fluctuations as it is characterizing for this scenario. In most cases, the frequencies die off at or slightly higher than 400 Hz; this margin is closer to 500 Hz for test D T11-02. This test also shows a distinct drop at 251 Hz and a spike at 349 Hz. Within the same frequency range, other Fourier spectra have similar spikes and drops as well as accumulations of both (besides the general high variations).

For the submerged condition (second row) the Fourier spectra are similar to the dry spectra in their overall progress but the amplitudes are smaller and have fewer spikes. Amplitudes taper off at around 400 Hz or higher. Also a layer of snow or granular ice at the contact surface yields lower amplitudes when compared to dry tests. Submergence, snow and granular ice (chips) apparently dampen the frequency amplitudes; the curves of tests with granular ice are more ambiguous compared to other scenarios as observed in the two spectra on the bottom of Figure Appendix B1. 1. For the high indentation rate, a different ice cone angle does not significantly influence the Fourier spectra. At this rate the spectra are typically unsteady and highly variable.

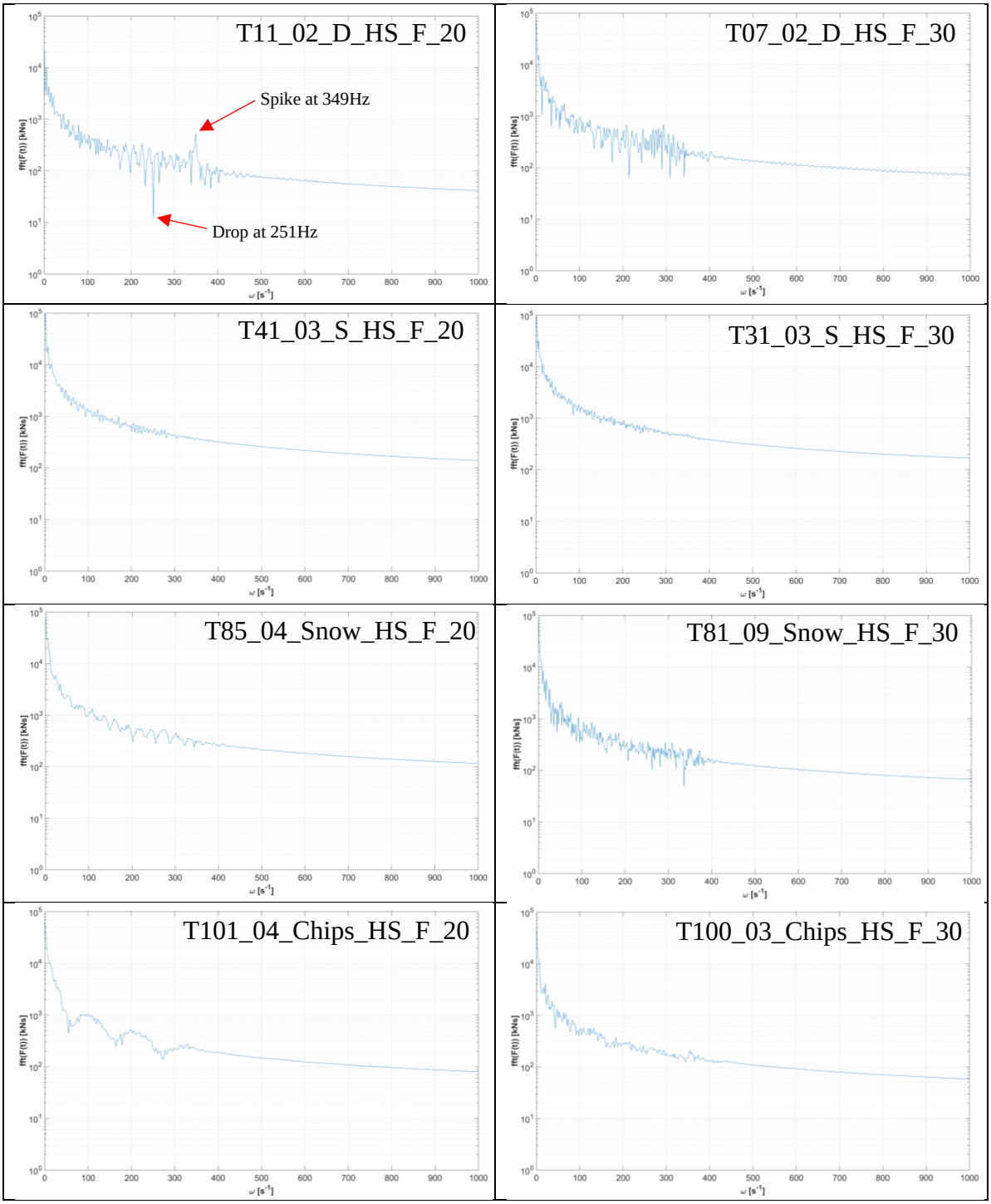

Figure Appendix B1. 1: Fourier spectra (FFT) for high speed tests with the flat plate for frequencies up to 1000 Hz. From the top to the bottom displayed are spectra for the dry, submerged, snow and chips contact conditions. The left column shows results for 20° cones, the right column for 30° cones

Flaws in the data acquisition system, such as a loose wire, or a compliant test setup may have introduced noise into the signal. Such noise is apparent in the spectra of high speed tests D T11-02 and D T07-02 (Figure Appendix B1. 1). To remove the noise, a low pass filter was applied at different frequencies (170 Hz, 200 Hz, 300 Hz) dependent on spectra distortions. Examples of the effect of a 200 Hz low pass filter on the force – displacement histories of tests D T11-02 and D T07-02 are given in Figure Appendix B1. 2 and Figure Appendix B1. 3. The displacements range to 35 mm and 60 mm for the respective cone angles of 20° and 30°. Unfiltered data are displayed in blue and the filtered data in red. Steady oscillations in some parts of the unfiltered forces are removed and cleaner signals are obtained. Overall, the low pass filter at 200 Hz proved to be sufficient to remove most distortions while preserving the original force history. In order to guarantee consistency, all test data of the flat indentation plate is processed with a low pass filter at 200 Hz.

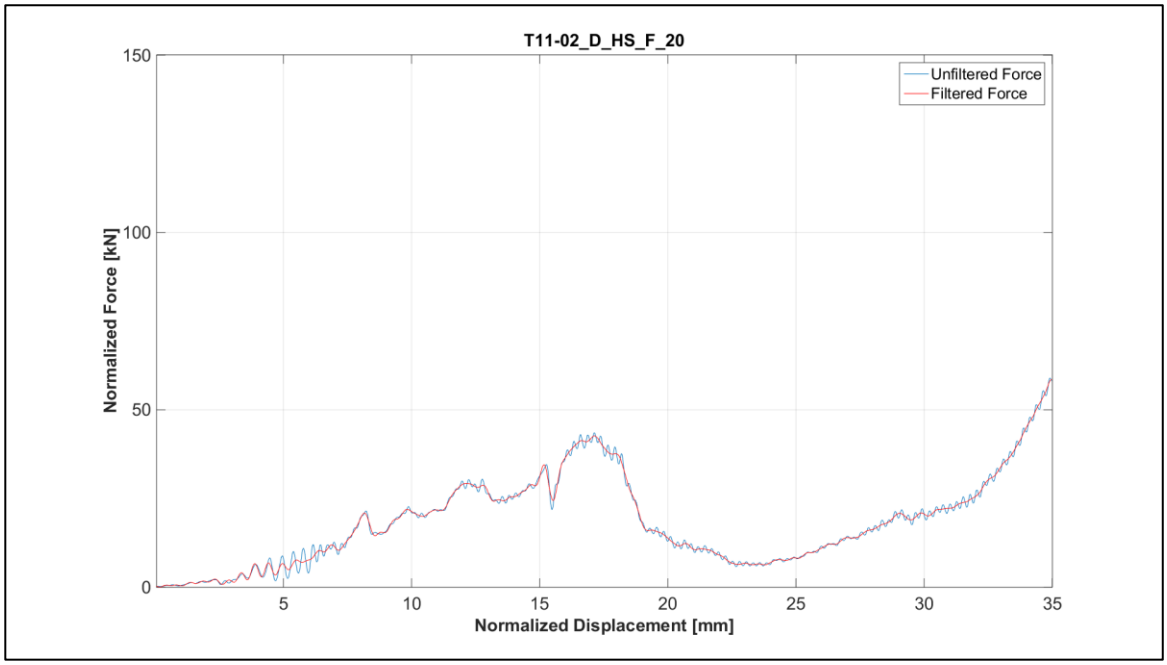

Figure Appendix B1. 2: Unfiltered (blue) and with 200 Hz low pass filtered (red) force - displacement history of test T11-02_D_HS_F_20.

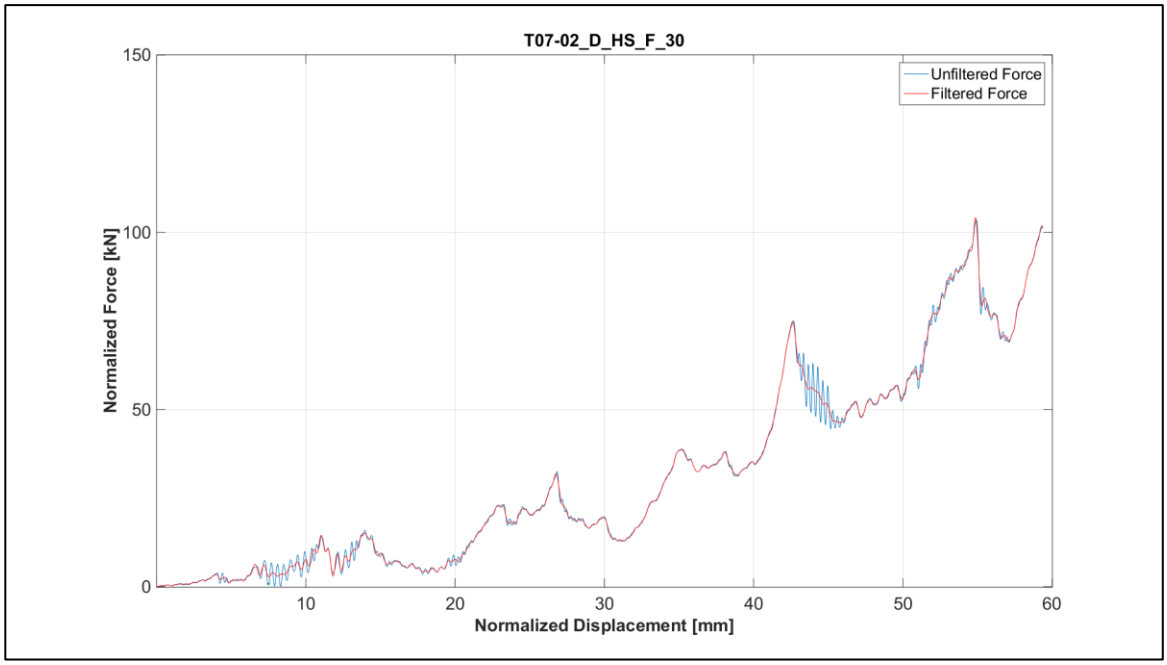

Figure Appendix B1. 3: Unfiltered (blue) and with 200 Hz low pass filtered (red) force - displacement history of test T07-02_D_HS_F_30.

The difference in the structural response in frequency domain is examined for medium and low indentation rates. Tests at the medium indentation rate were performed only for dry, submerged and granular ice contact conditions. Similar to the high speed tests, a different ice cone angle in medium speed tests (10 mm/s) in dry environment and granular ice did not produce an apparent difference in the Fourier spectra but the contact condition did. Typical curves are shown in Figure Appendix B1. 4. Test D T29-01, on the left, represents the dry contact condition with large frequency amplitudes. In contrast, the amplitudes are smaller for the granular ice condition (Chips T107-10).

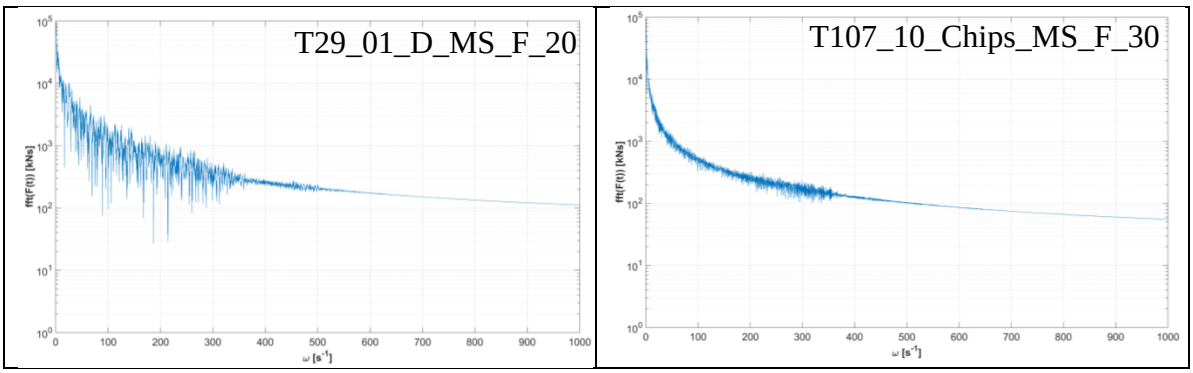

Figure Appendix B1. 4: Fourier spectra (FFT) for medium speed tests with the flat plate for frequencies up to 1000 Hz. Displayed are typical curves in dry condition on the left (20° cone) and with granular ice on the indented surface on the right (30° cone).

The filtered (low pass at 200 Hz, red) and unfiltered (blue) force of test D T29-01 are displayed in Figure Appendix B1. 5. This example shows the negligible effect of a low pass filter at the medium indentation rate.

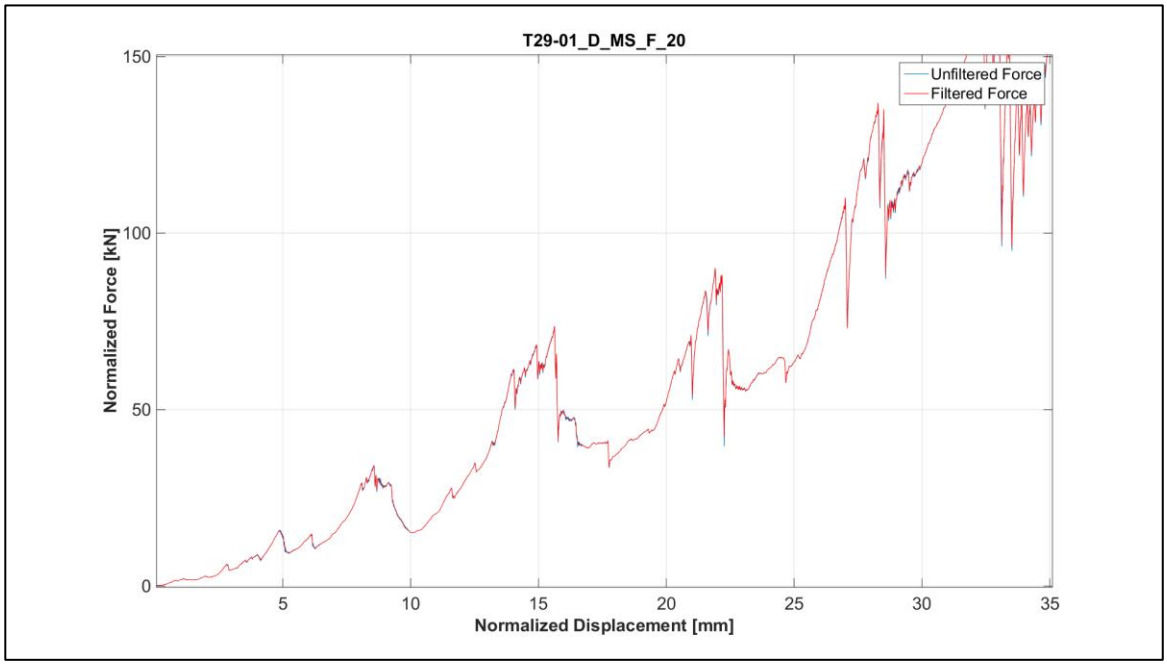

Figure Appendix B1. 5: Unfiltered (blue) and with 200 Hz low pass filtered (red) force - displacement history of test T29-01_D_MS_F_20.

In contrast to the high speed tests, in the medium speed tests submergence resulted in distinct different spectra for both cone angles as well as among tests with 20° cones. The spectra in Figure Appendix B1. 6 are derived for submerged tests. The spectra of the three tests with 20° cones (S T89-02, S T90-03, S T96-05) and one for 30° cones characterizing example (S T88-01) are displayed. The difference between 20° and 30° cone angle indicates a strong influence of the ice geometry at the medium indentation rate. The variance within the 20° cones may be the result of common randomness.

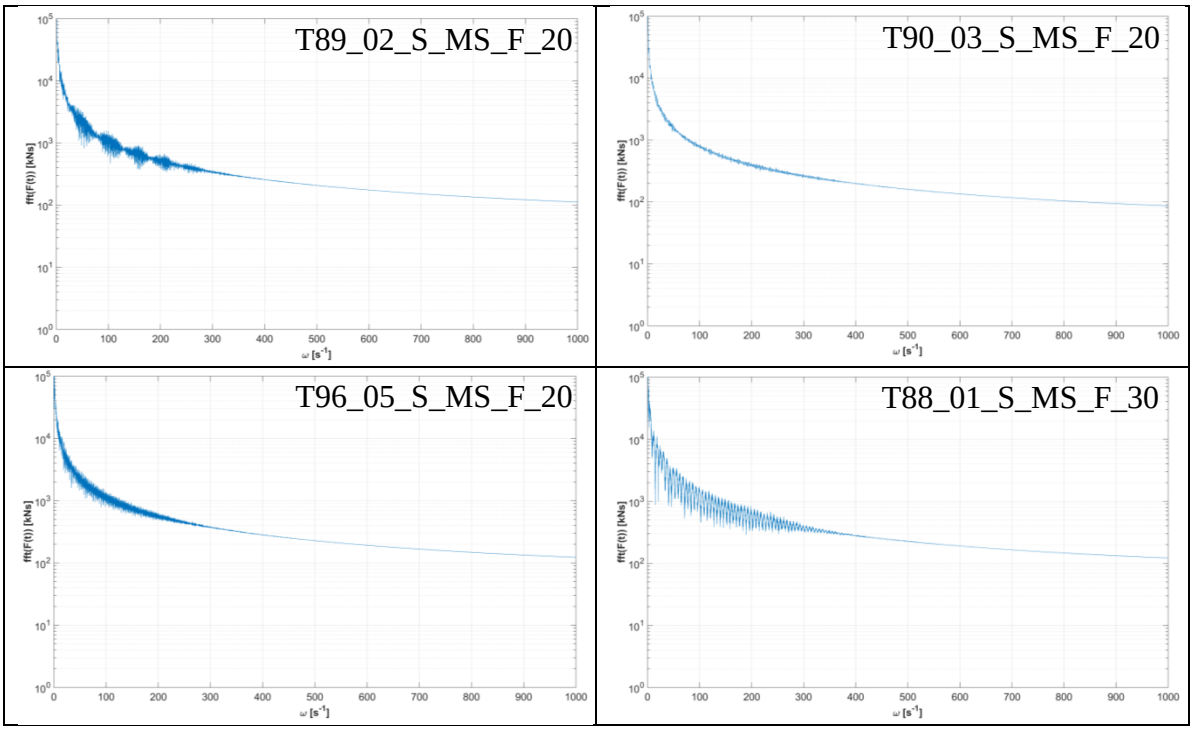

Figure Appendix B1. 6: Fourier spectra (FFT) for medium speed tests with the flat plate in submerged condition and for frequencies up to 1000 Hz. The spectra of tests with 20° cones (T89-02, T90-03, T96-05) revealed distinct differences. The spectrum of T88-01 (bottom right) shows a typical curve for tests with 30° cones.

In low speed tests (1 mm/s) the Fourier spectra consistently have a band-like or line-like nature mainly differing in width (Figure Appendix B1. 7). This is true for all contact conditions and for both cone angles. Only test D T08-03 (Figure Appendix B1. 7, right)

shows a small accumulation at around 200 Hz. Still, at the low indentation rate the structural response does not seem to be affected by the cone angle or by the respective contact condition.

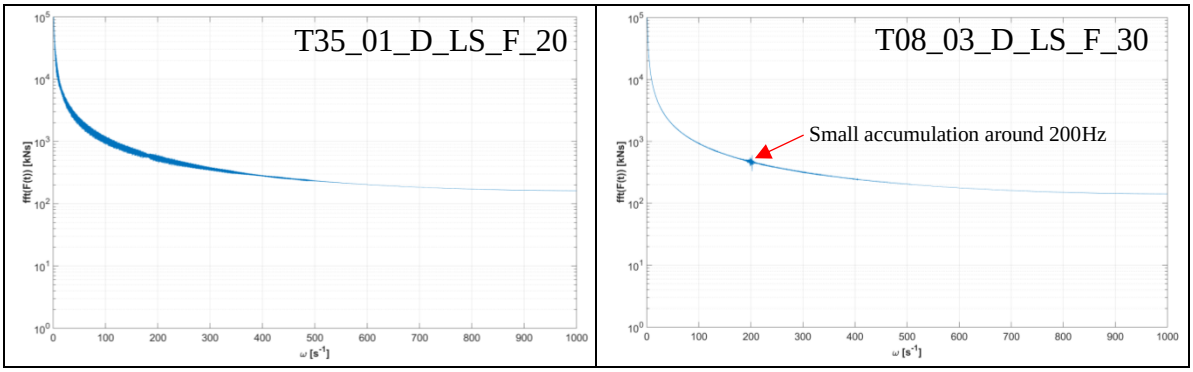

Figure Appendix B1. 7: Fourier spectra (FFT) for low speed tests with the flat plate in dry condition for both ice cone angles and for frequencies up to 1000 Hz.

The filtered and unfiltered forces for low speed tests are not displayed because the graphs would consist of a single curve which would not contribute useful information.

Appendix B2 : Plots for 1 mm/s Indentation Rate

20° Ice Cone Angle

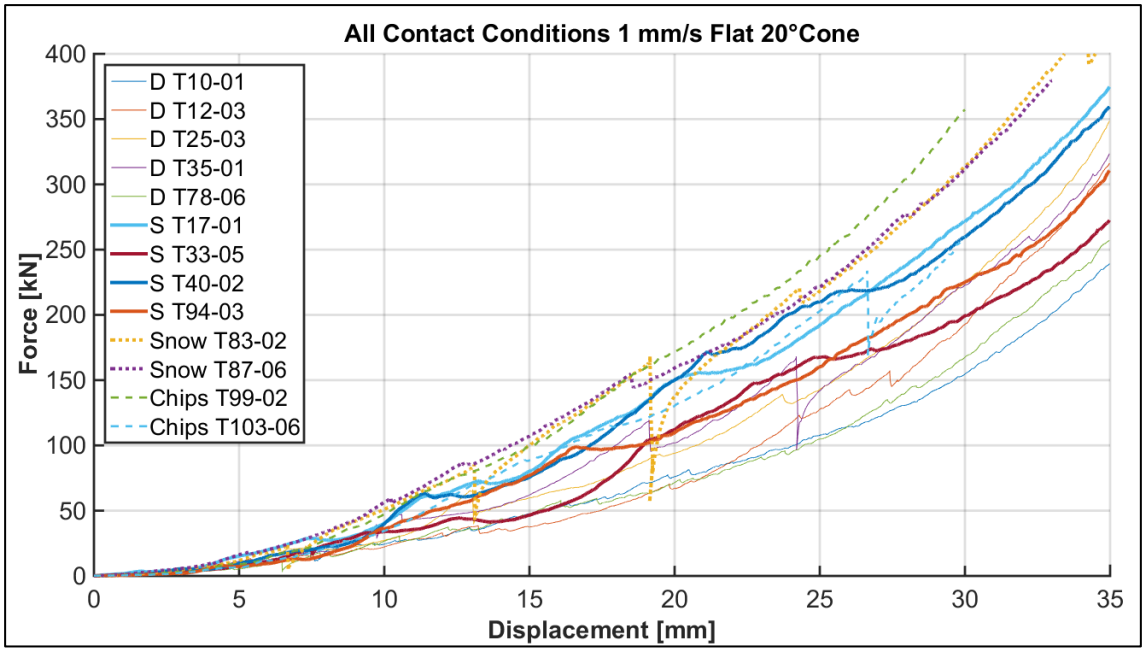

Figure Appendix B2. 1: Flat plate, 1 mm/s, 20° ice specimens: force vs. displacement for individual tests and for all contact conditions.

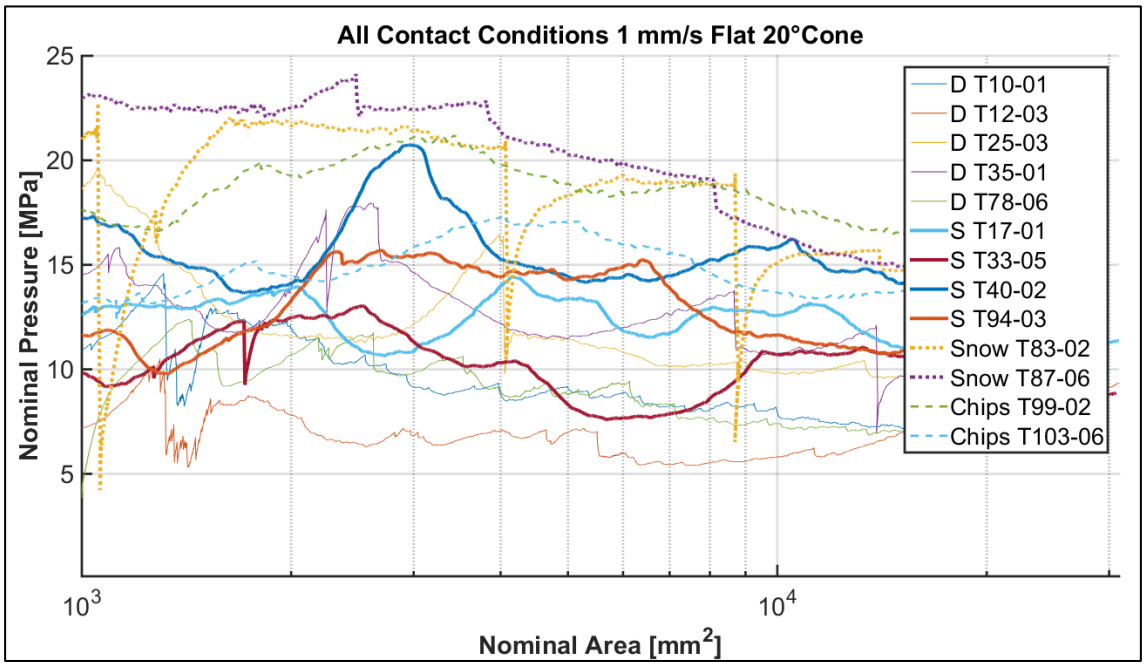

Figure Appendix B2. 2: Flat plate, 1 mm/s, 20° ice specimens: nominal pressure vs. area curves for individual tests and for all contact conditions.

30° Ice Cone Angle

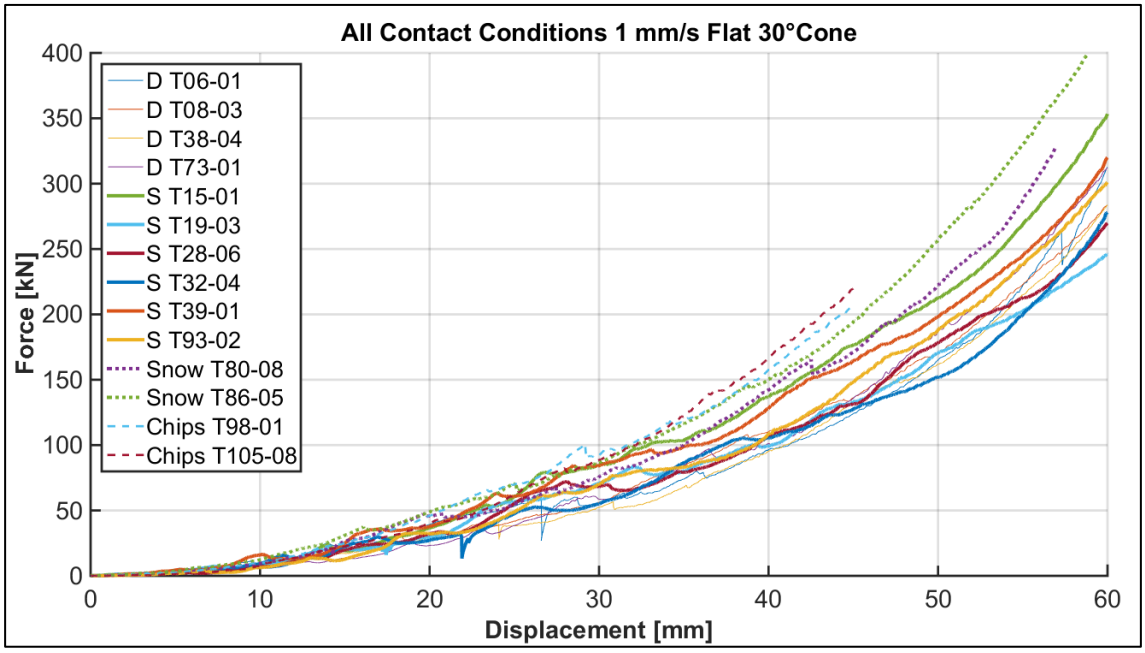

Figure Appendix B2. 3: Flat plate, 1 mm/s, 30° ice specimens: force vs. displacement for individual tests and for all contact conditions.

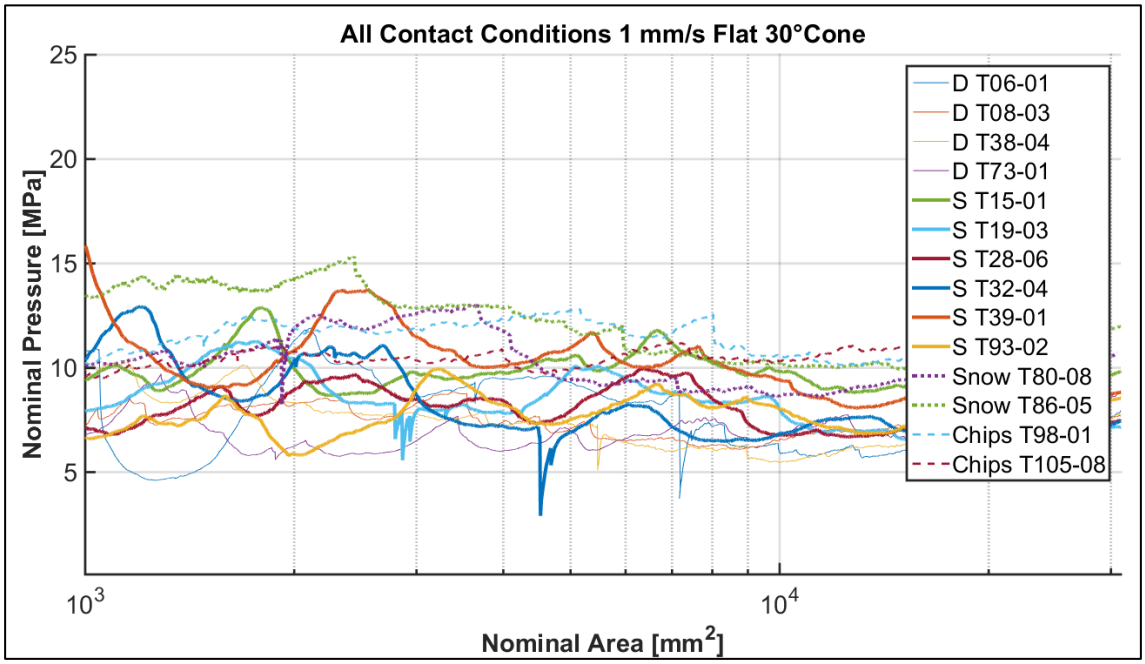

Figure Appendix B2. 4: Flat plate, 1 mm/s, 30° ice specimens: nominal pressure vs. area curves for individual tests and for all contact conditions.

Appendix B3 : Plots for 10 mm/s Indentation Rate

20° Ice Cone Angle

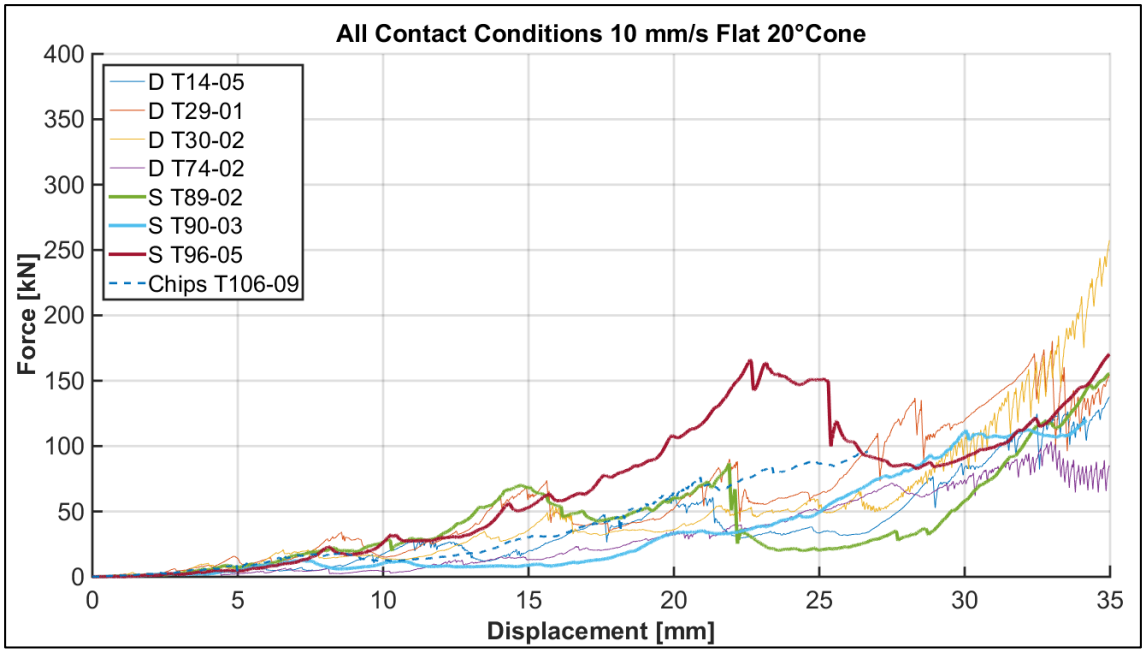

Figure Appendix B3. 1: Flat plate, 10 mm/s, 20° ice specimens: force vs. displacement for individual tests and for all contact conditions.

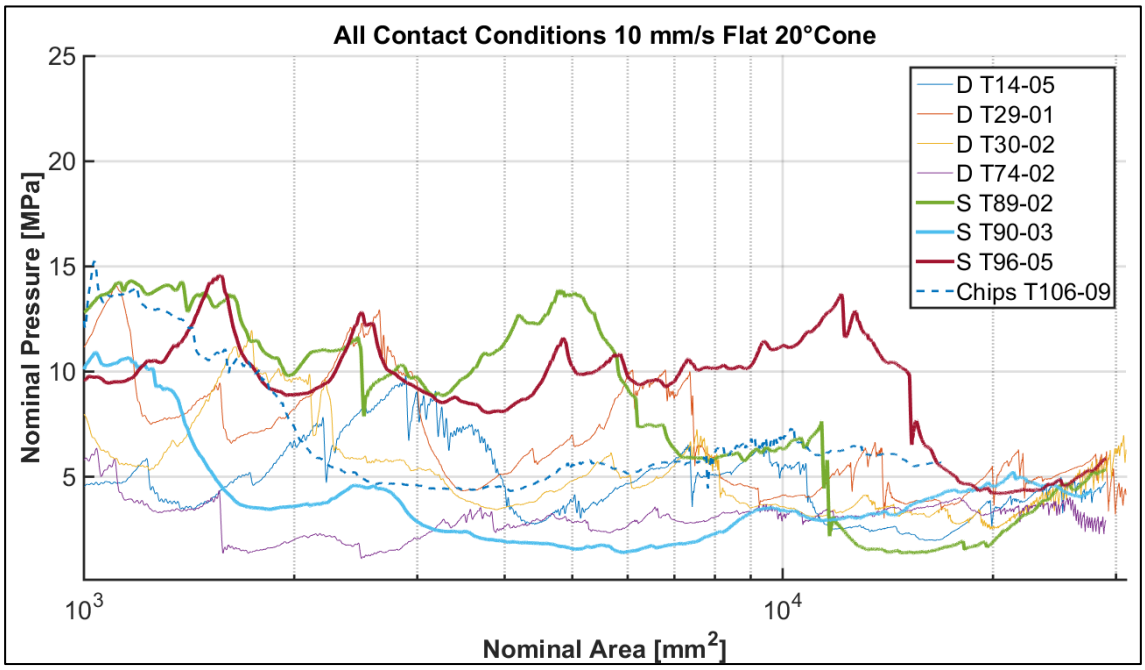

Figure Appendix B3. 2: Flat plate, 10 mm/s, 20° ice specimens: nominal pressure vs. area curves for individual tests and for all contact conditions.

30° Ice Cone Angle

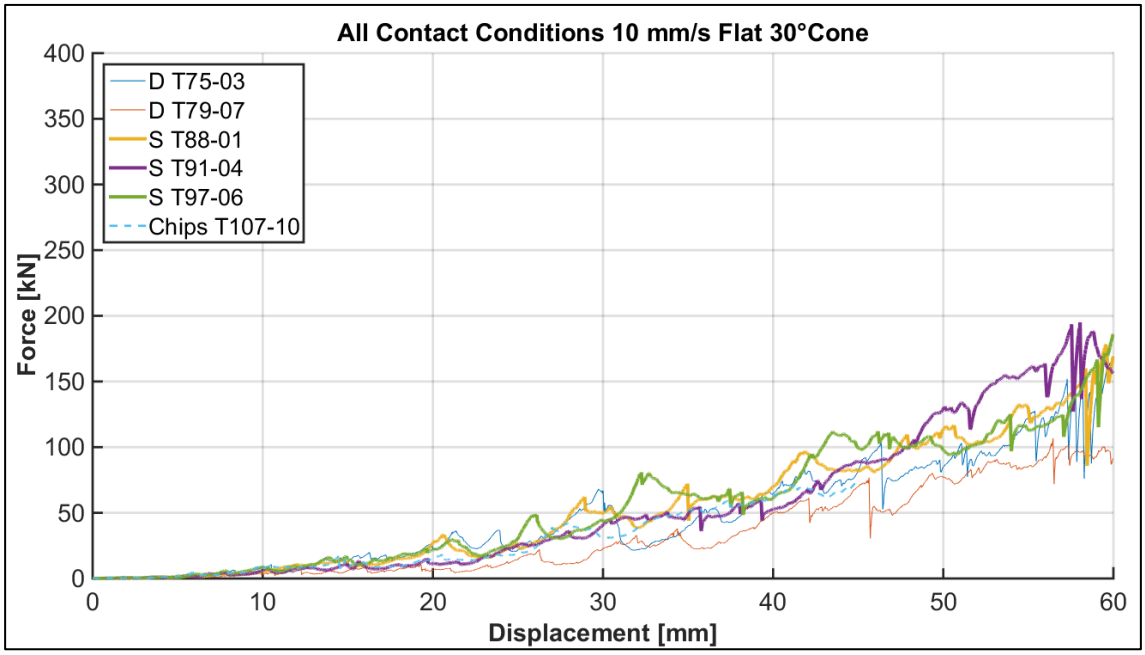

Figure Appendix B3. 3: Flat plate, 10 mm/s, 30° ice specimens: force vs. displacement for individual tests and for all contact conditions.

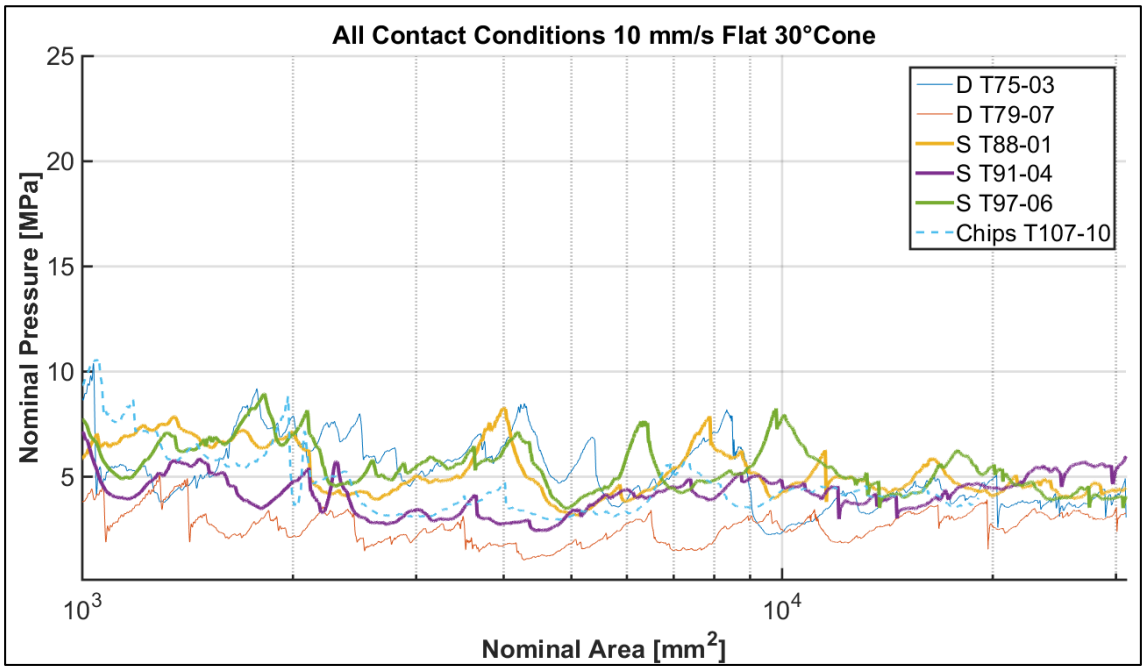

Figure Appendix B3. 4: Flat plate, 10 mm/s, 30° ice specimens: nominal pressure vs. area curves for individual tests and for all contact conditions.

Appendix B4 : Plots for 100 mm/s Indentation Rate

20° Ice Cone Angle

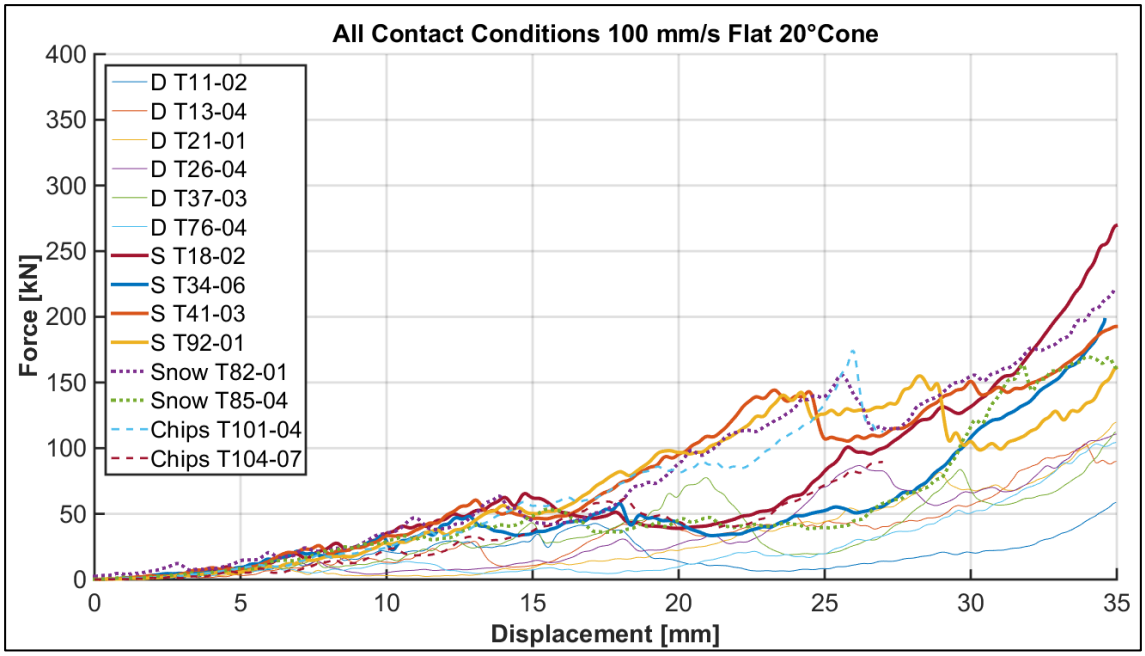

Figure Appendix B4. 1: Flat plate, 100 mm/s, 20° ice specimens: force vs. displacement for individual tests and for all contact conditions.

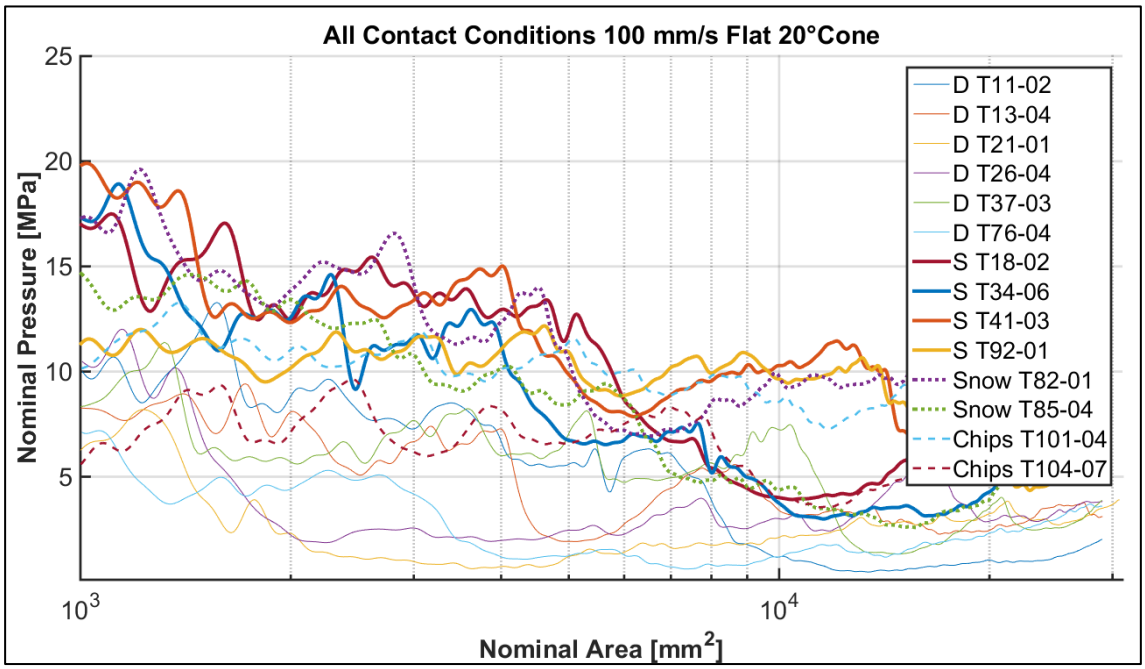

Figure Appendix B4. 2: Flat plate, 100 mm/s, 20° ice specimens: nominal pressure vs. area curves for individual tests and for all contact conditions.

30° Ice Cone Angle

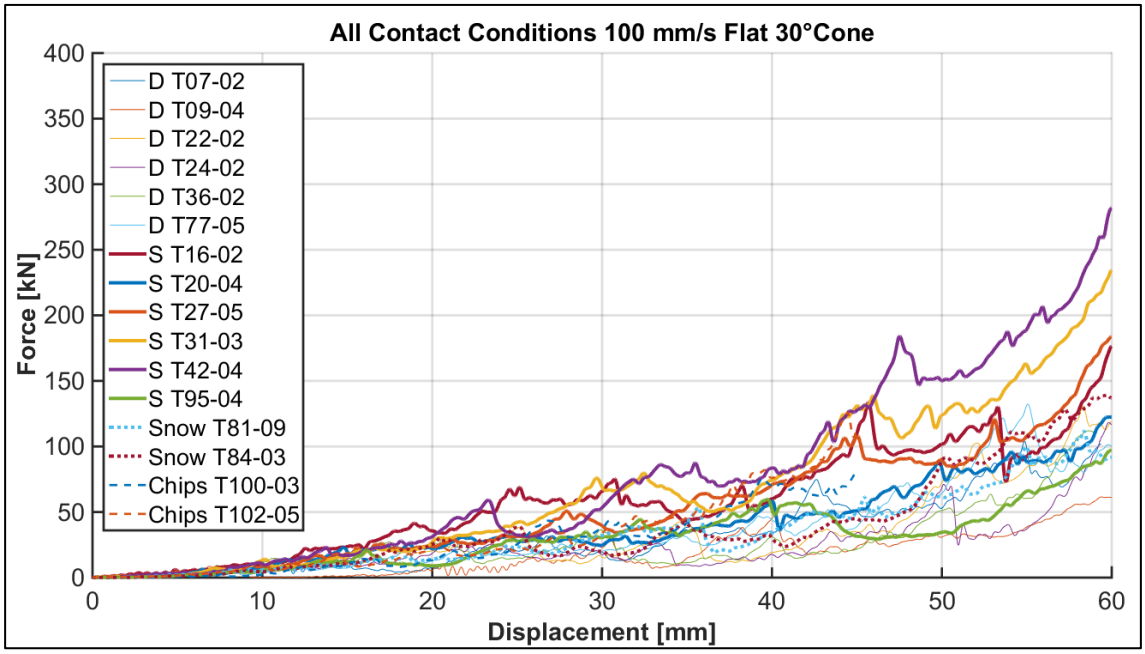

Figure Appendix B4. 3: Flat plate, 100 mm/s, 30° ice specimens: force vs. displacement for individual tests and for all contact conditions.

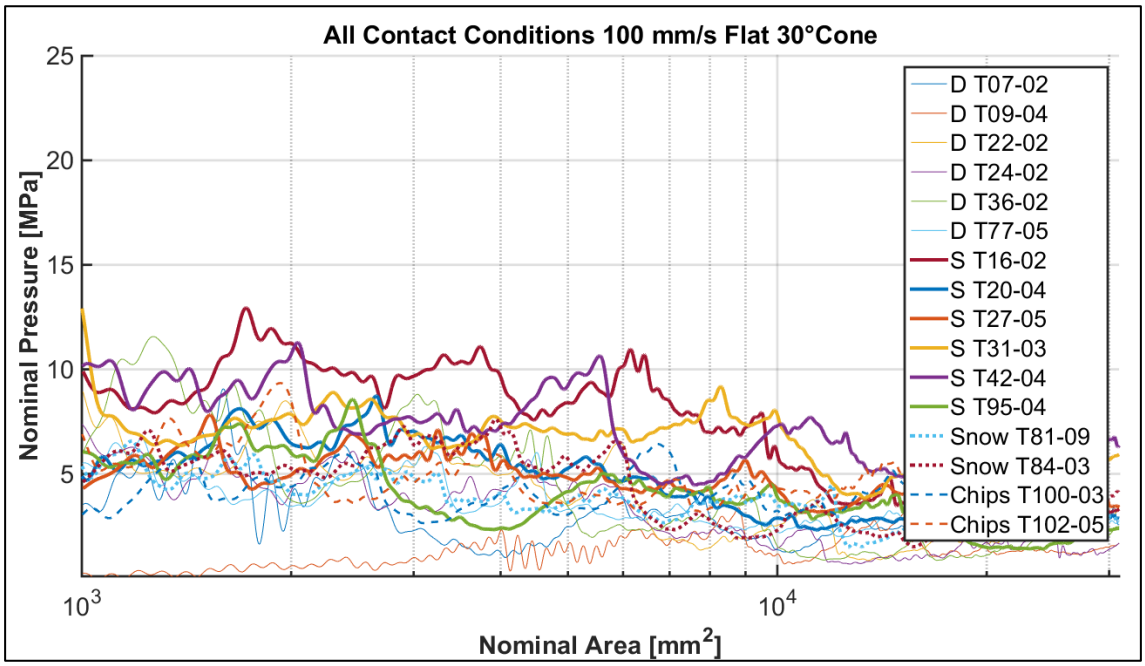

Figure Appendix B4. 4: Flat plate, 100 mm/s, 30° ice specimens: nominal pressure vs. area curves for individual tests and for all contact conditions.

Appendix B5 : Pressure Patterns (Tactile Pressure Sensors)

1 mm/s – All Conditions - 30° Ice Cone Angle (Sampling Rate 100 Hz)

The following figures show pressure patterns for 30° ice cone specimens for all four external boundary conditions. The respective tests are:

Top left:	Dry	T73_01_D_LS_F_30
Top right:	Submerged	T93_02_S_LS_F_30
Bottom left:	Snow	T80_08_Snow_LS_F_30
Bottom right:	Chips	T98_01_Chips_LS_F_30

The dark vertical line in the centre of each reading is a small gap between the two facing sensors. The pink vertical line in the readings of the submerged test indicates that that sensel column was damaged and saturated. The damage began in frames 1256 and 1257 and led to sudden jumps in area and raw force. Measurements are unreliable beyond frame 3766, as at this frame the contact area of the ice specimen in submergence exceeded the broken pressure sensor sensel column. Data prior to frame 3766 are unbiased. The offsets in contact area and raw force, based on the damaged sensel column, are constant values (Area: 284 mm^2, Raw Force: 11220). These values are determined in the frame before first impact occurred and are identical for both tests. The measurements of area and raw force are corrected by subtracting these offsets. For the granular ice condition, only the pressure sensor on the right hand side is available.

In the following, five selected instances are provided. The first displayed frame (1030) was captured at approximately 10.30 mm penetration. At that depth, the calculated nominal contact area is 1000 mm^2 which is the minimum margin for ice pressure comparisons that were derived from the material testing system (MTS). The last suitable

frame of the submerged test is number 3765, the last suitable frame of the granular ice test is number 5431. Frames 2398 and 4598 are selected as intermediate points.

Penetration depth approximately 10.3 mm (nominal area 1000 mm^2)

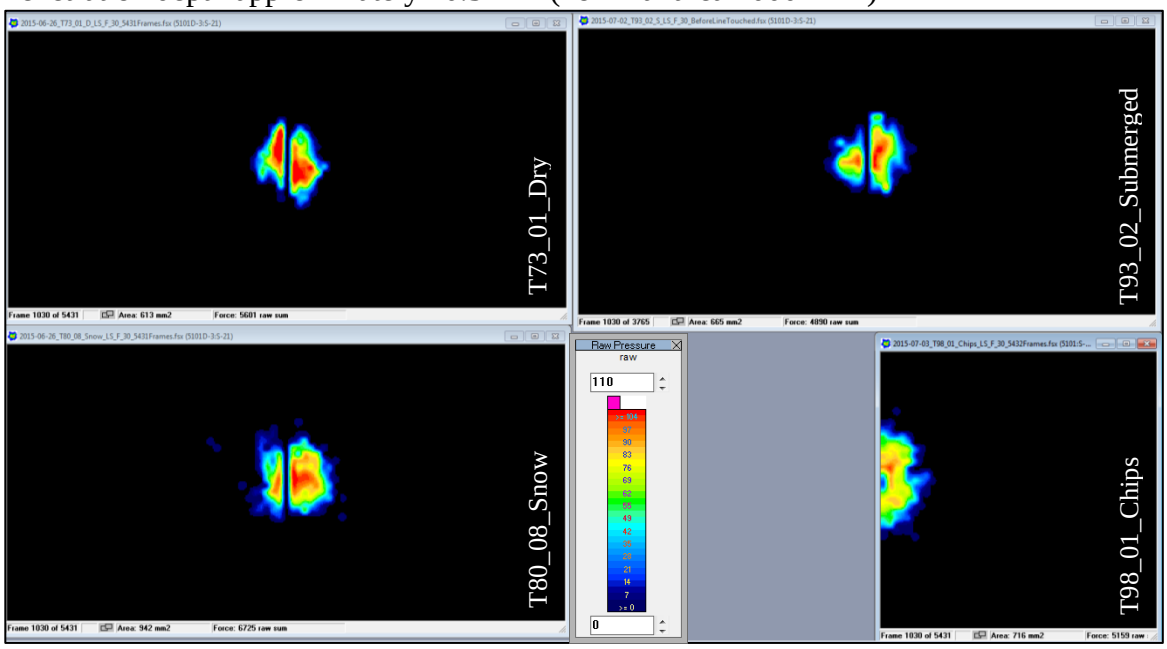

Penetration depth approximately 23.98 mm

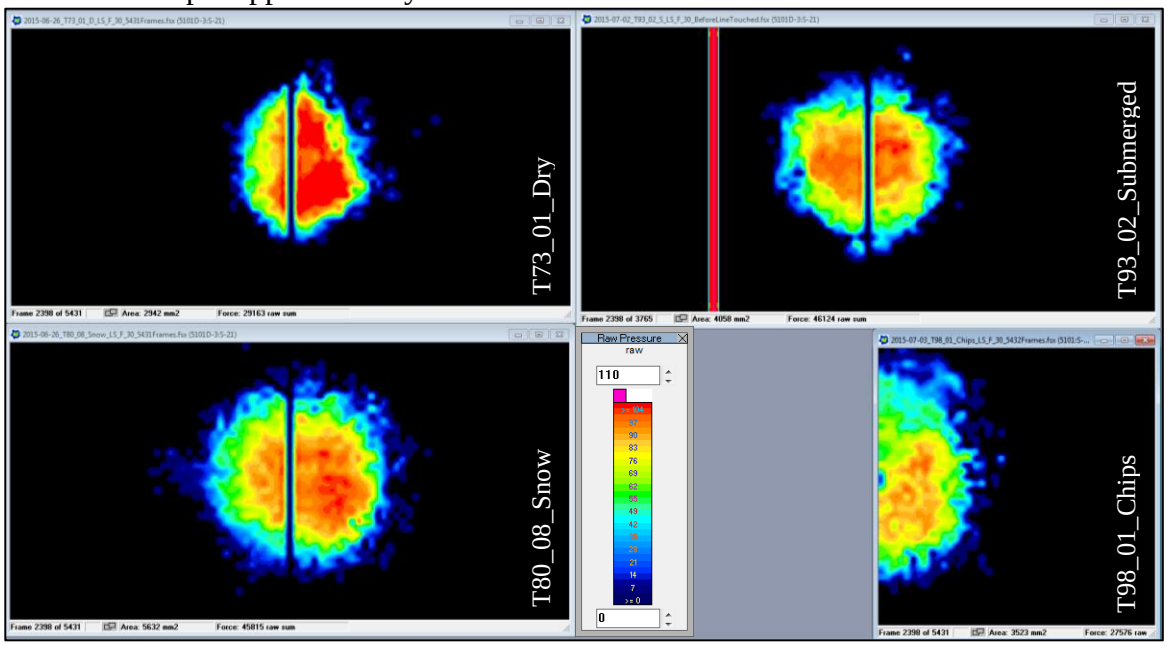

Last submerged frame at penetration depth approximately 37.65 mm

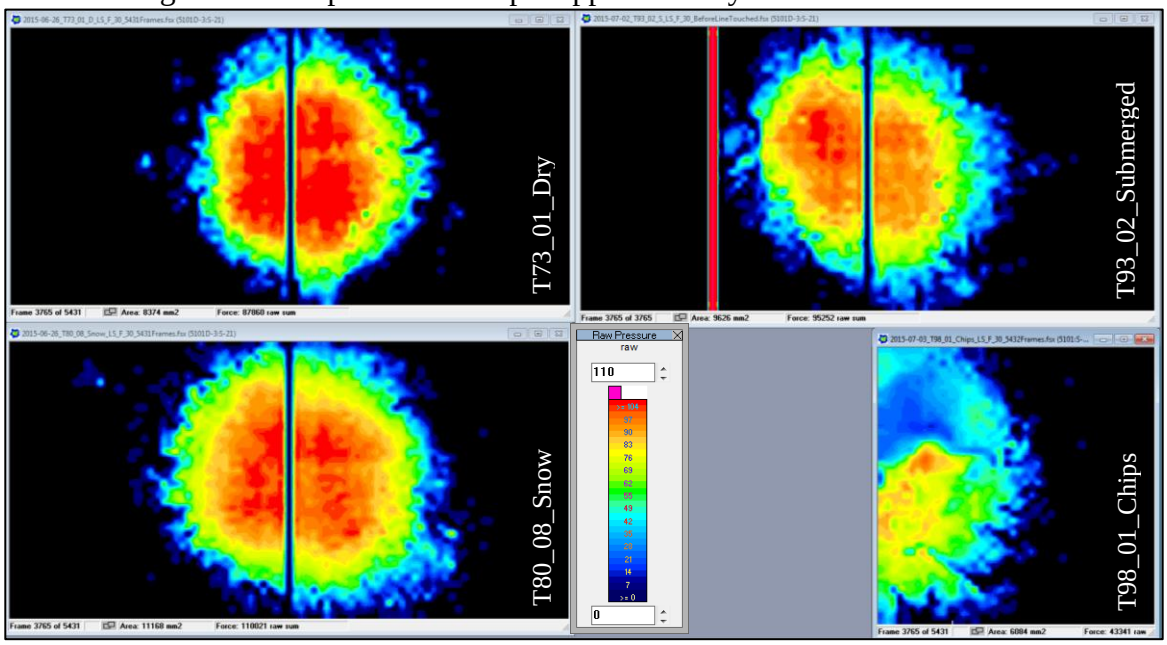

Penetration depth approximately 45.98 mm

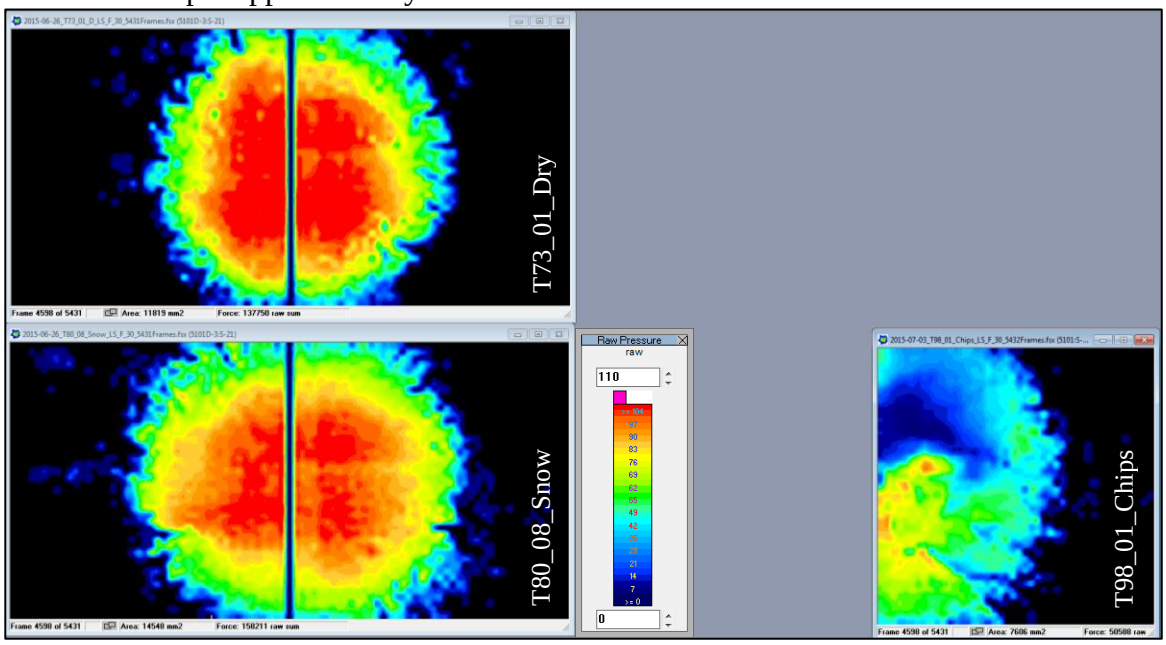

Penetration depth approximately 54.31 mm

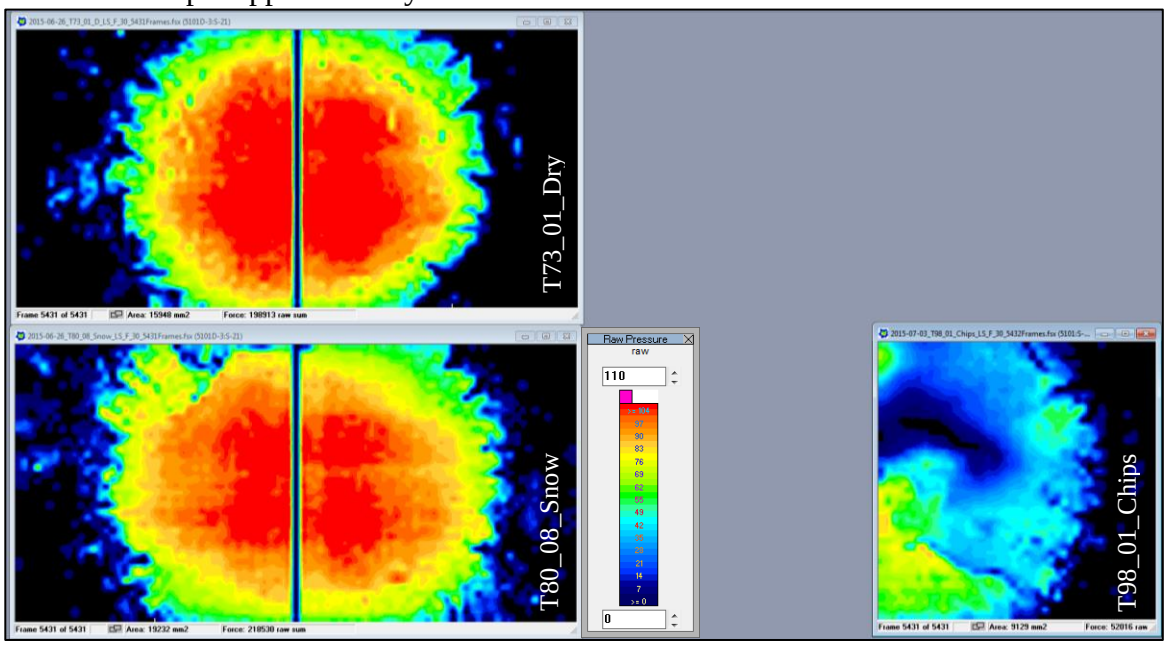

Below table lists the numbers for area in mm^2 and for raw force as it was derived from the tactile pressure sensors.

Depth [mm]	Condition Test	Dry T73-01	Submerged T93-02	Snow T80-08	Chips (Doubled) T98-01	Nominal Area
10.30	Area [mm^2]	613	665	942	1432	1000
	Raw Force	5601	4890	6725	10318	-
23.98	Area [mm^2]	2942	3774	5632	7046	5420
	Raw Force	29163	34889	45815	55152	-
37.65	Area [mm^2]	8374	9342	11168	12168	13360
	Raw Force	87860	84017	110021	86682	-
45.98	Area [mm^2]	11819	-	14548	15212	19926
	Raw Force	137750	-	158211	101176	-
54.31	Area[mm^2]	15948	-	19232	18258	27799
	Raw Force	198913	-	218530	104032	-

Remarks:

Only one sensor was available for granular ice tests. Stated values are the double of the measured values and are so somewhat inaccurate.

The Nominal Area is the area, calculated based on penetration depth and 30° ice cone angle. Generally, the area derived from the pressure sensors is likely to slightly underestimate the true contact area, due to the gap in the middle of the two facing sensors and because the contact area exceeded the measurable area at advanced test stages.

10 mm/s – Dry and Submerged Conditions – 20° and 30° Ice Cone Angles

(Sampling Rate 100 Hz)

The following figures show pressure patterns on the top and bottom for 20° and 30° ice cone specimens in dry and submerged contact conditions. The respective tests are:

Top Left:	Dry	20°	T74_02_D_MS_F_20
Top Right:	Submerged	20°	T96_05_S_MS_F_20
Bottom Left:	Dry	30°	T75_03_D_MS_F_30
Bottom Middle:	Dry	30°	T79_07_D_MS_F_30
Bottom Right:	Submerged	30°	T97_06_S_MS_F_30

Penetration depth approximately 6.5 mm (nominal area 20° cone: 1000 mm^2)

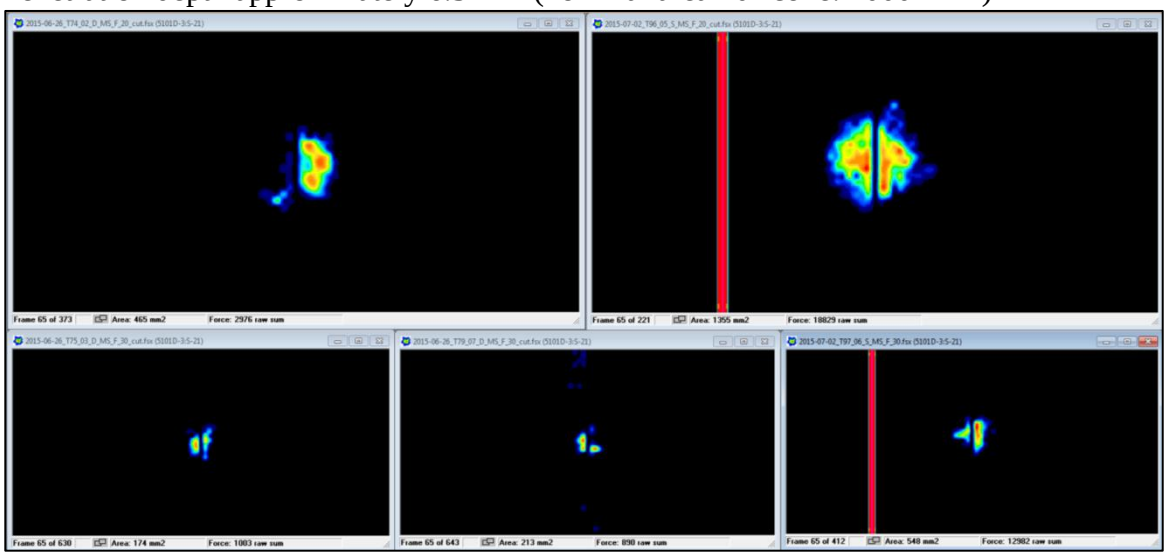

Penetration depth approximately 10.3 mm (nominal area 30° Cone: 1000 mm^2)

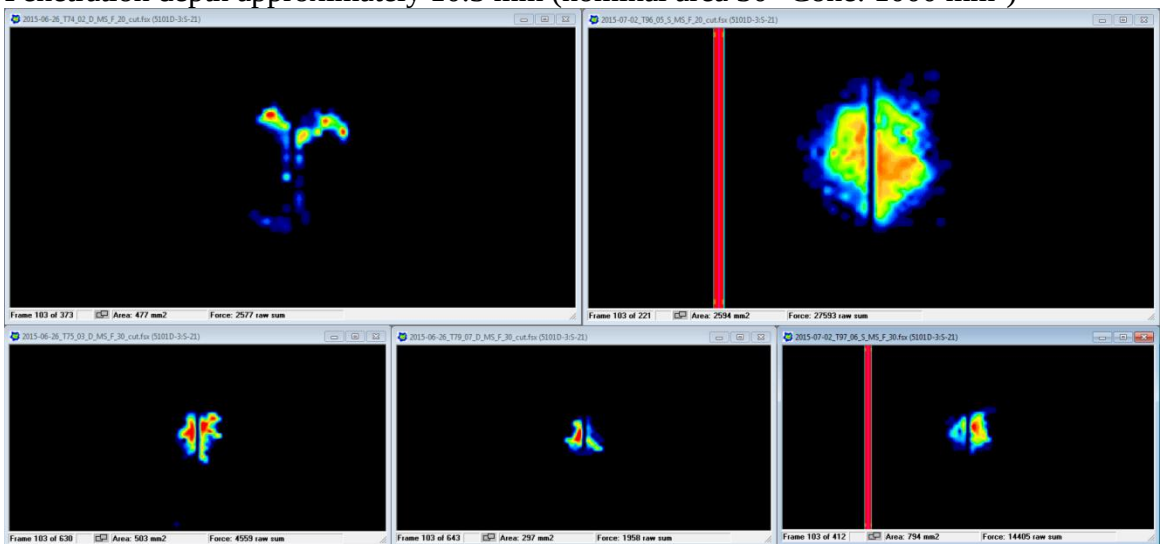

Penetration depth approximately 16 mm

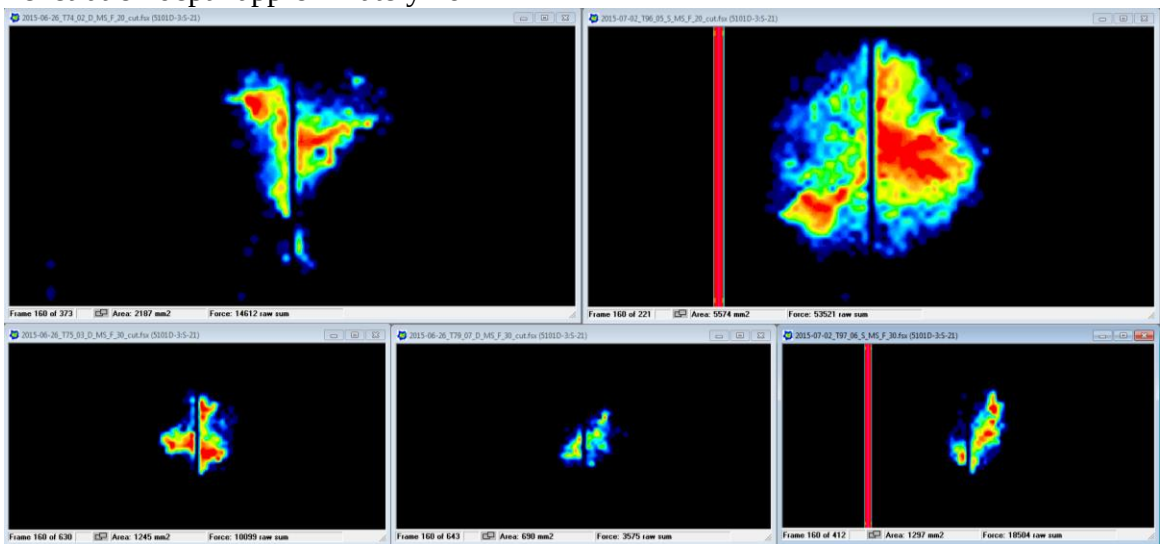

Penetration depth approximately 22.1 mm

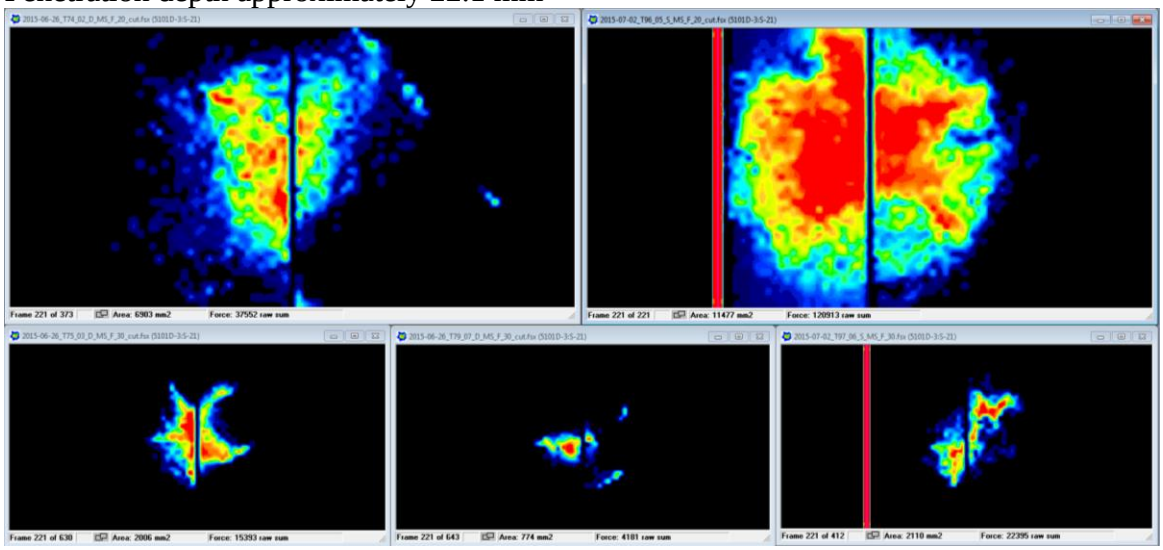

Penetration depth approximately 41.2 mm

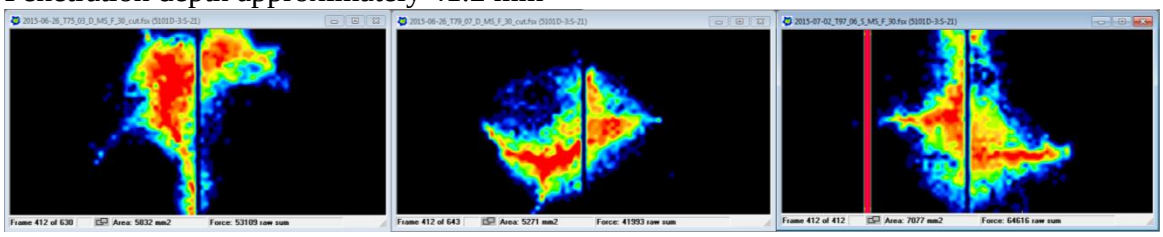

The tables below list the values for area in mm^2 and for raw force as it was derived from the tactile pressure sensors separate for each ice cone angle.

Ice Cone Angle		**20**		
Depth [mm]	**Condition Test**	**Dry T74-02**	**Submerged T96-05**	**Nom. Area**
6.5	Area [mm^2]	465	1071	1002
	Raw Force	2976	7609	-
10.3	Area[mm^2]	477	2310	2516
	Raw Force	2577	16373	-
16.0	Area [mm^2]	2187	5290	6071
	Raw Force	14612	42301	-
22.1	Area [mm^2]	6903	11193	11583
	Raw Force	37552	109693	-

Ice Cone Angle		30			
Depth [mm]	Condition	Dry		Submerged	Nom. Area
	Test	T75-03	T79-07	T97-06	
6.5	Area [mm^2]	174	213	264	398
	Raw Force	1003	890	1762	-
10.3	Area[mm^2]	503	297	510	1000
	Raw Force	4559	1958	3185	-
16.0	Area [mm^2]	1245	690	1013	2413
	Raw Force	10099	3575	7284	-
22.1	Area [mm^2]	2006	774	1826	4603
	Raw Force	15393	4181	11175	-
41.2	Area [mm^2]	5832	5271	6793	15998
	Raw Force	53109	41933	53396	-

100 mm/s – Dry and Submerged Conditions – 20° and 30° Ice Cone Angles

(Sampling Rate 100 Hz)

The following figures show pressure patterns on the top and bottom for 20° and 30° ice cone specimens in dry and submerged contact conditions. The respective tests are:

Top left:	Dry	20°	T76_04_D_HS_F_20
Top right:	Submerged	20°	T92_01_S_HS_F_20
Bottom left:	Dry	30°	T77_05_D_HS_F_30
Bottom right:	Submerged	30°	T95_04_S_HS_F_30

The dark vertical line in the centre of each reading is a small gap between the two facing sensors. The red vertical lines in the readings of the submerged tests indicate that that sensel column was damaged and saturated.

For the 100 mm/s indentation rate, all continuous frames up to 23 are displayed. Frame 23 is the last frame before the contact area of the submerged 20° ice specimen (top right) crosses the damaged sensel column (red vertical line). Subsequent readings are not reliable. The offsets in contact area and raw force, based on the damaged sensel column, are constant values (Area: 284 mm^2, Raw Force: 11220). They are determined in the frame before first impact occurred and are identical for both tests. The area and raw force measurements are corrected by subtracting these offsets.

Beyond frame 23, figures merely show measurements of 30° ice cone angle (former bottom images). Because the contact area increases at a slower rate at this ice cone angle, the damaged sensel column was first reached at frame 40.

In addition, for frames 23 and 40, pressure patterns for one snow test (T81_09_Snow_HS_F_30) and one test with granular ice (T100_03_Chips_HS_F_30) are displayed. Both tests were performed with 30° ice cones. For the granular ice condition, only the pressure sensor on the right hand side is available.

Penetration depth approximately 1 mm (frame 02: first frames that showed signs of impact)

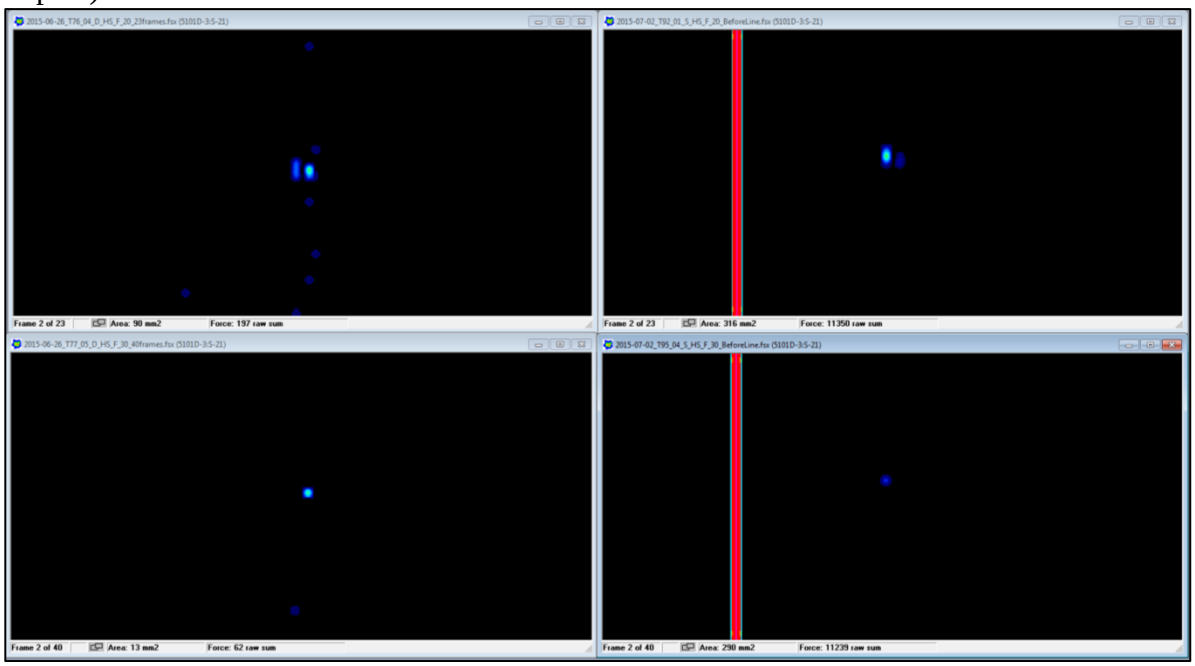

Penetration depth approximately 2 mm

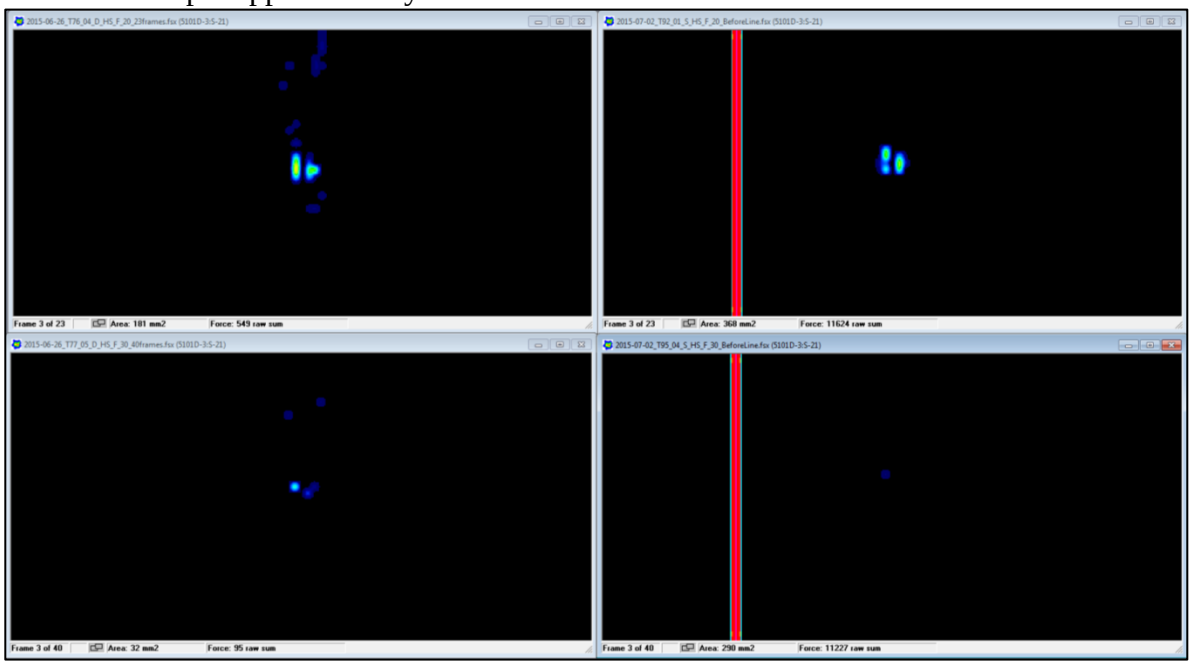

Penetration depth approximately 3 mm

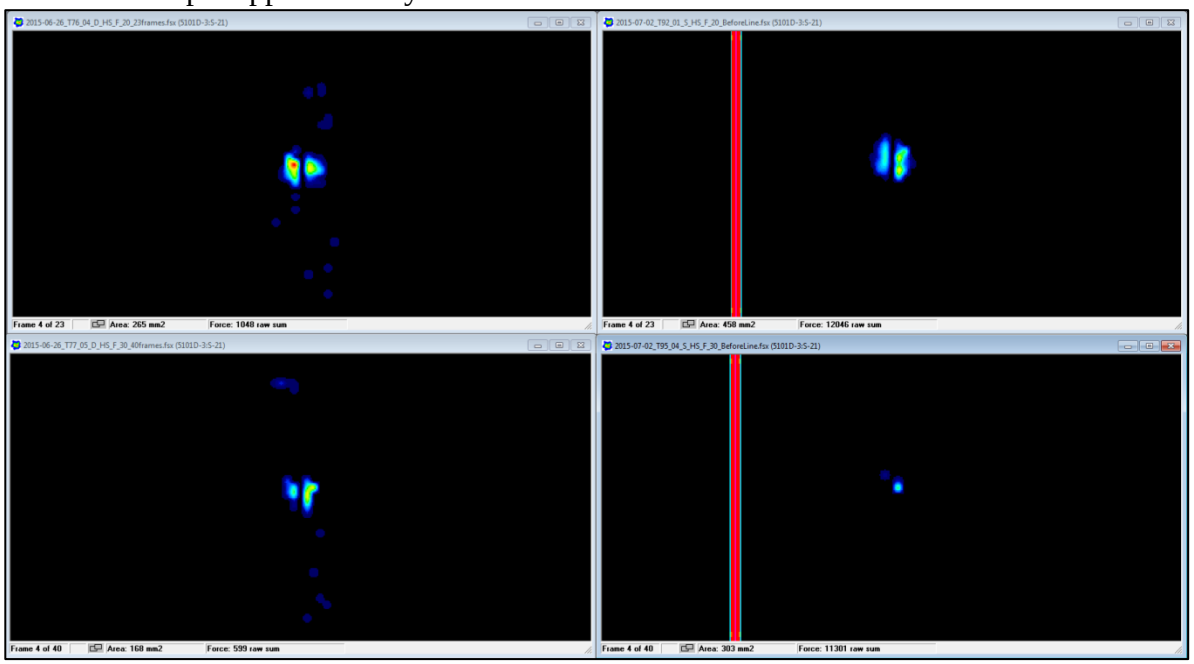

Penetration depth approximately 4 mm

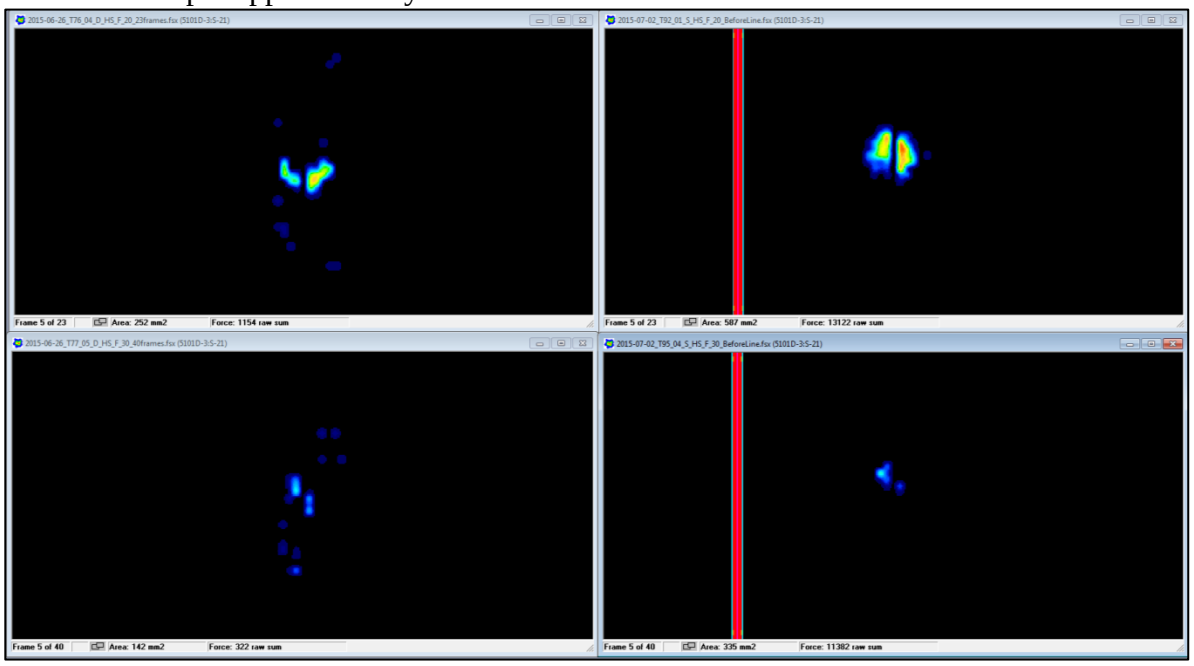

Penetration depth approximately 5 mm

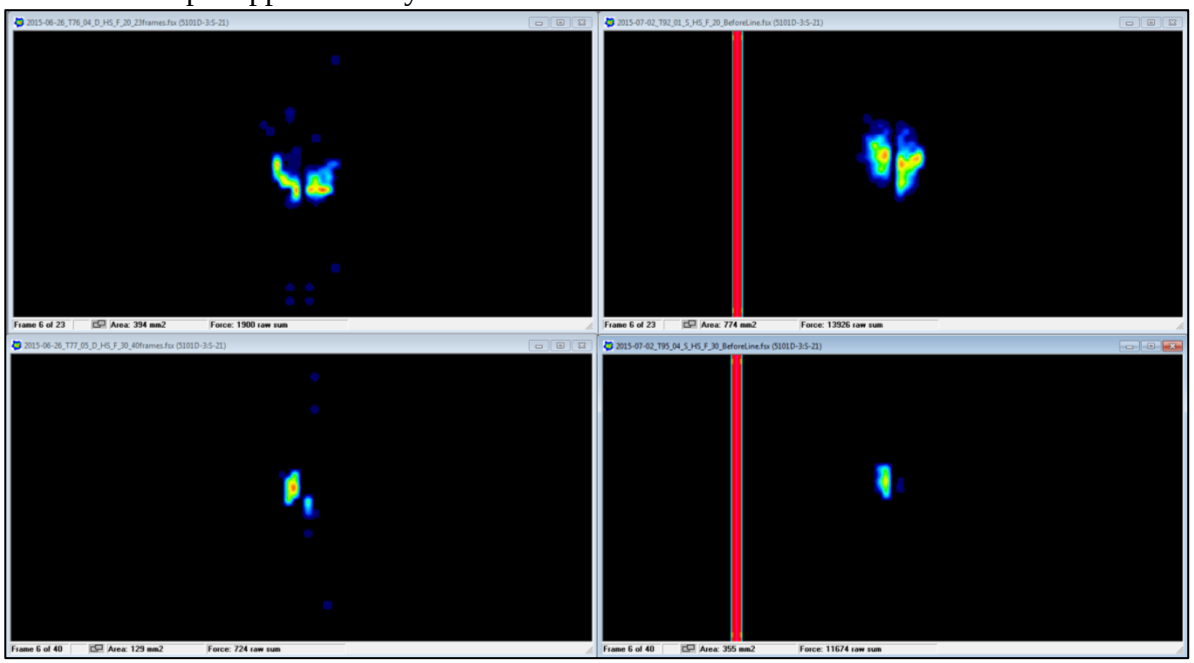

Penetration depth approximately 6 mm

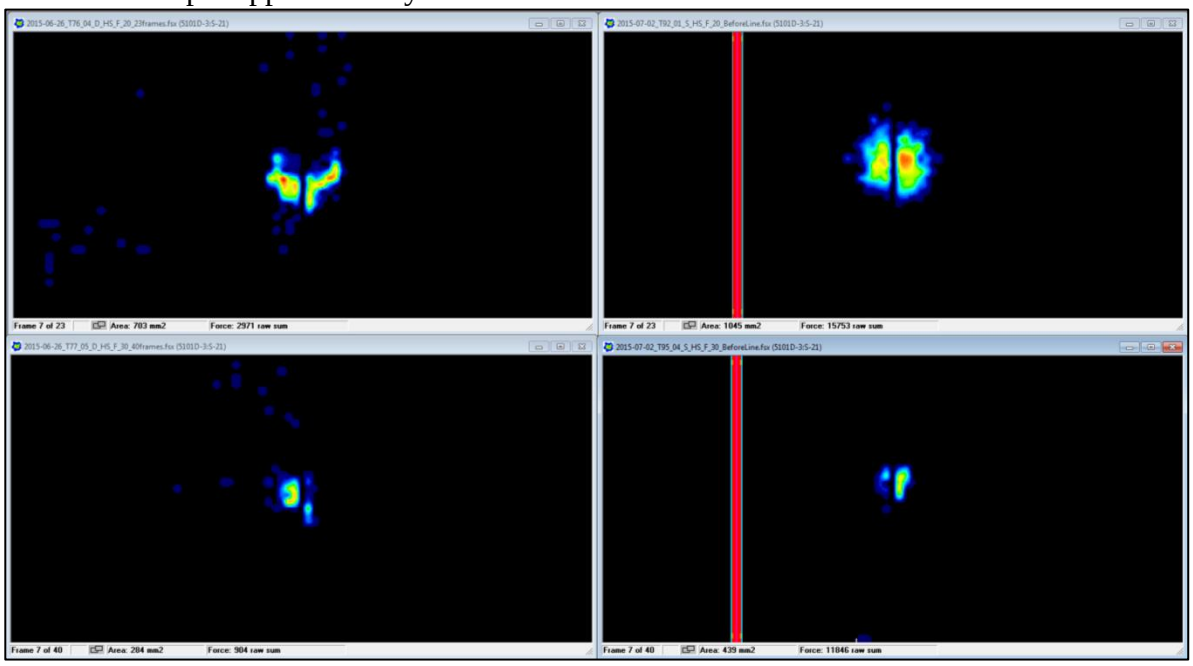

Penetration depth approximately 7 mm

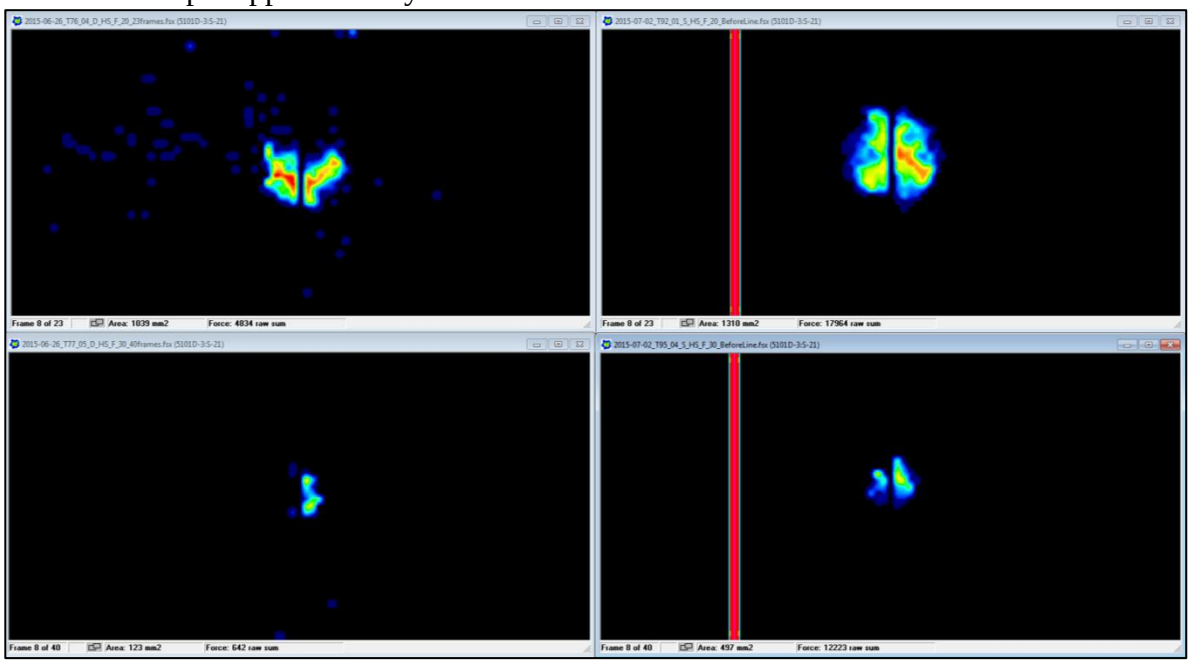

Penetration depth approximately 8 mm

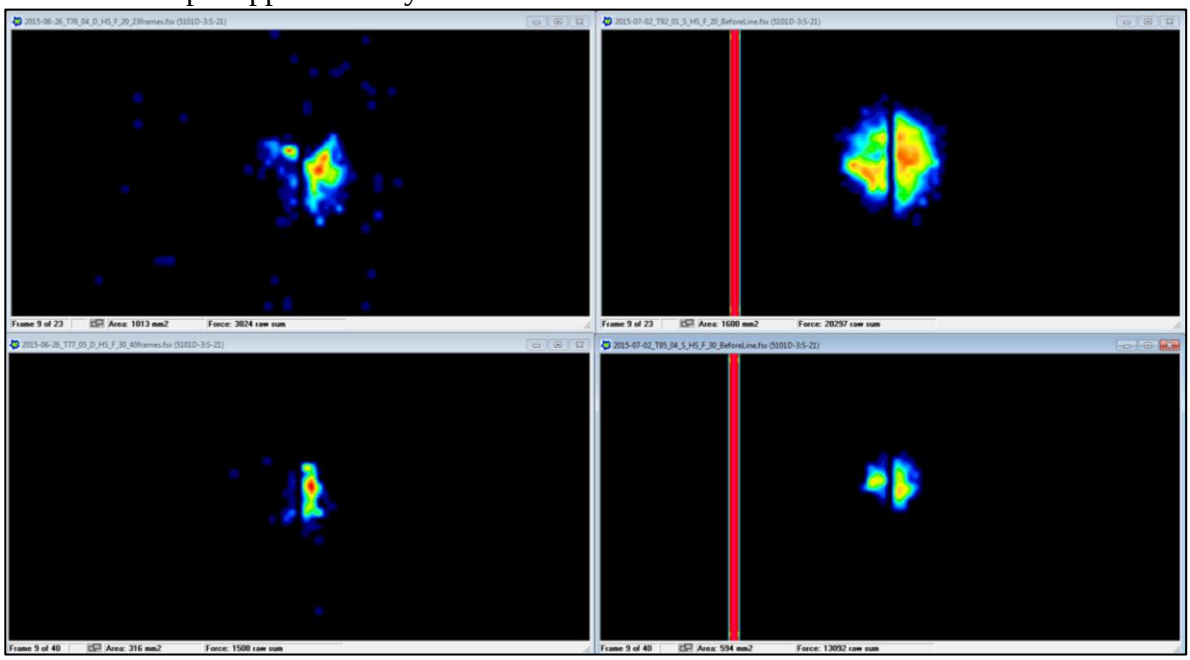

Penetration depth approximately 9 mm

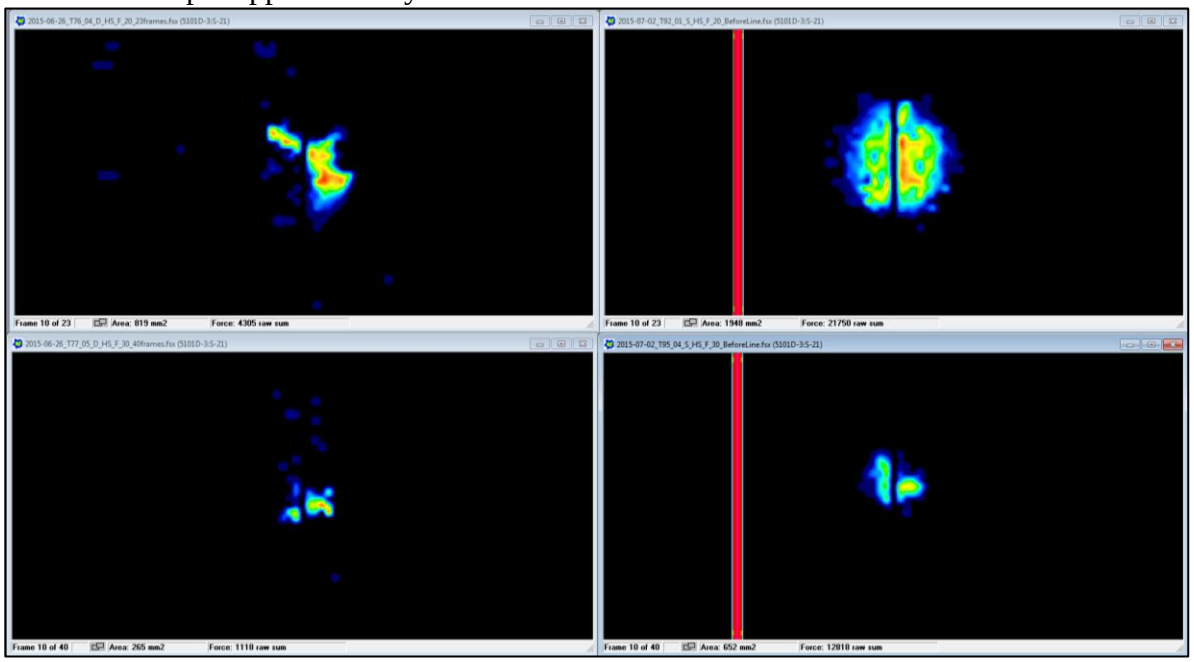

Penetration depth approximately 10 mm

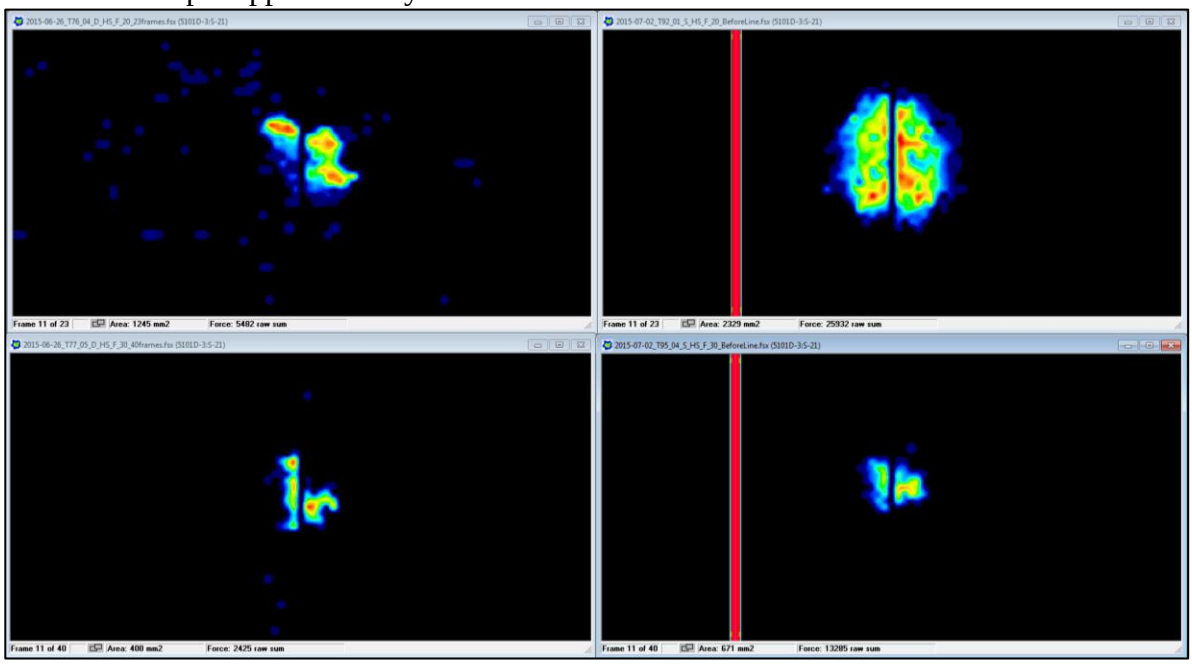

Penetration depth approximately 11 mm

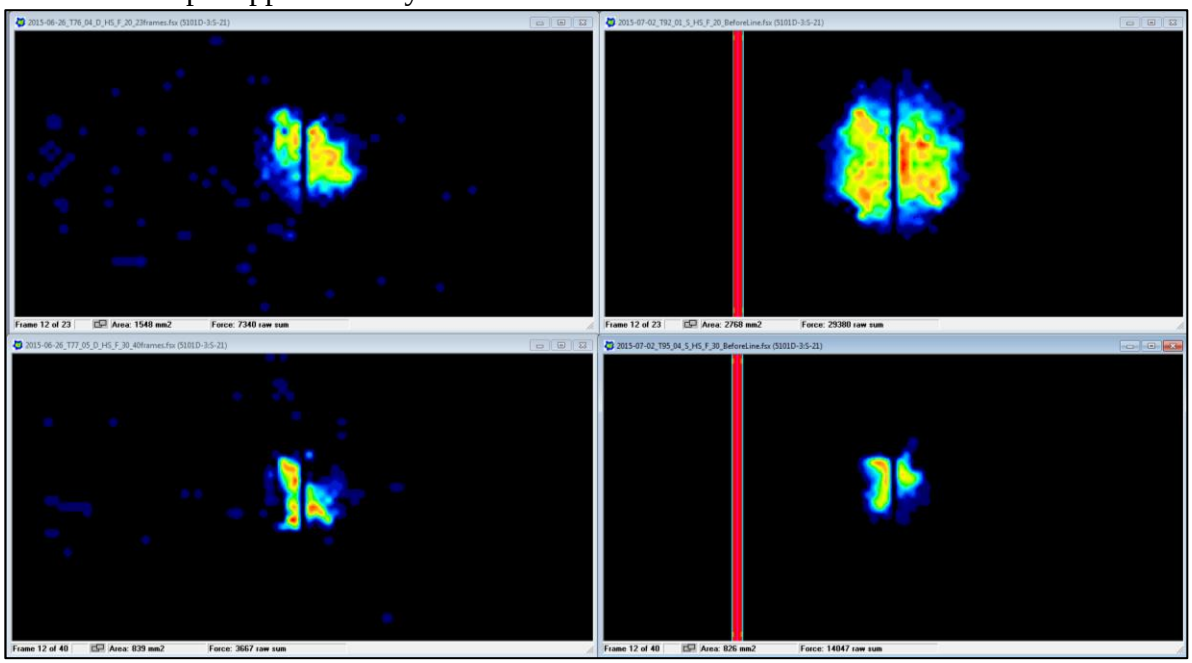

Penetration depth approximately 12 mm

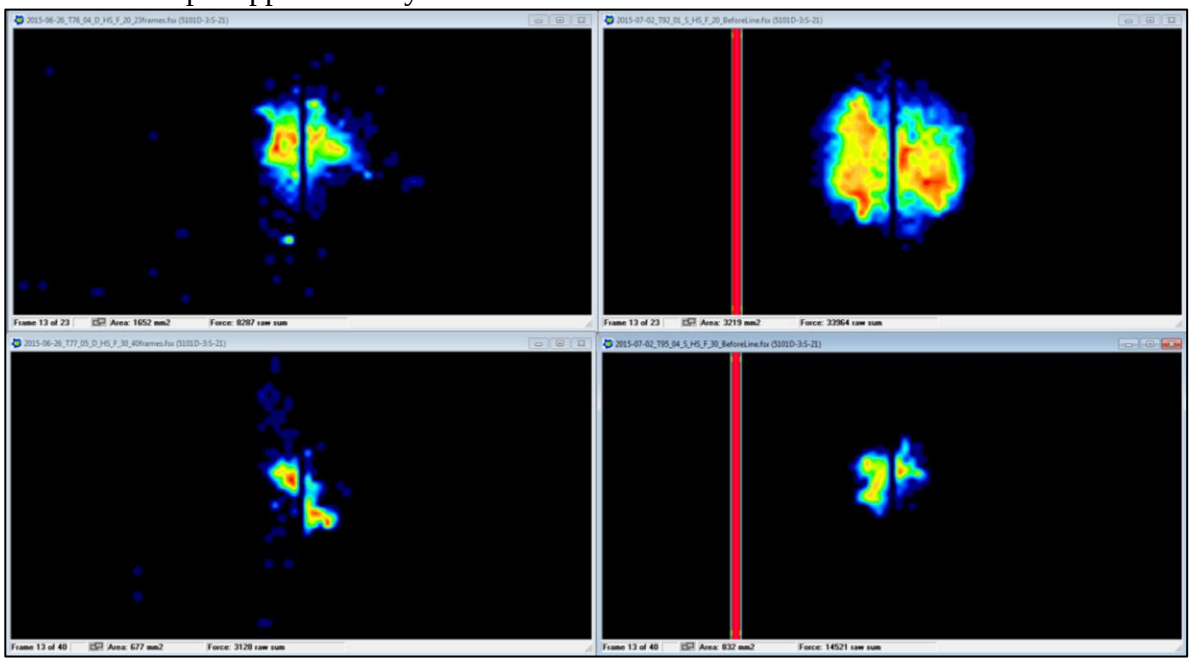

Penetration depth approximately 13 mm

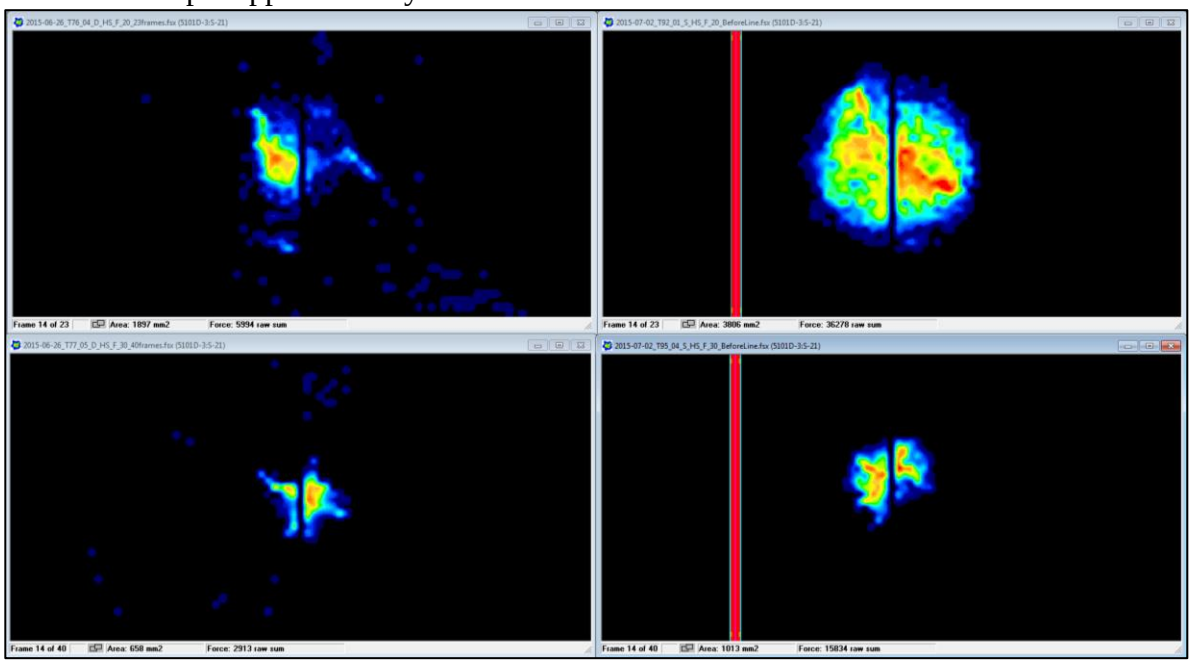

Penetration depth approximately 14 mm

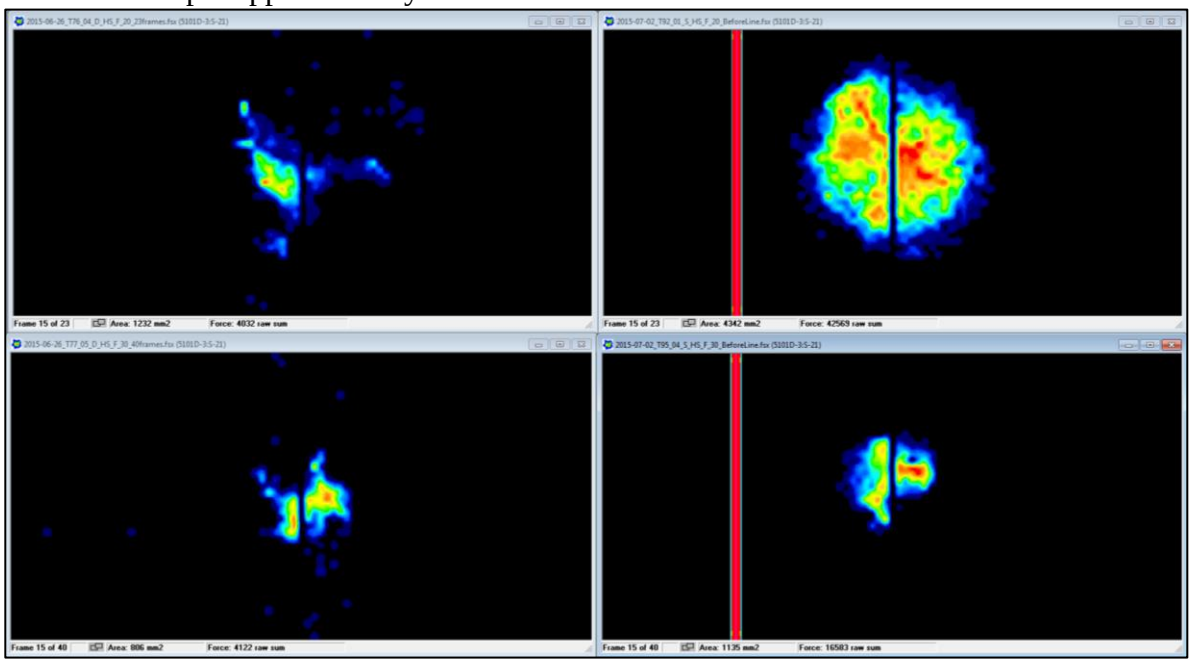

Penetration depth approximately 15 mm

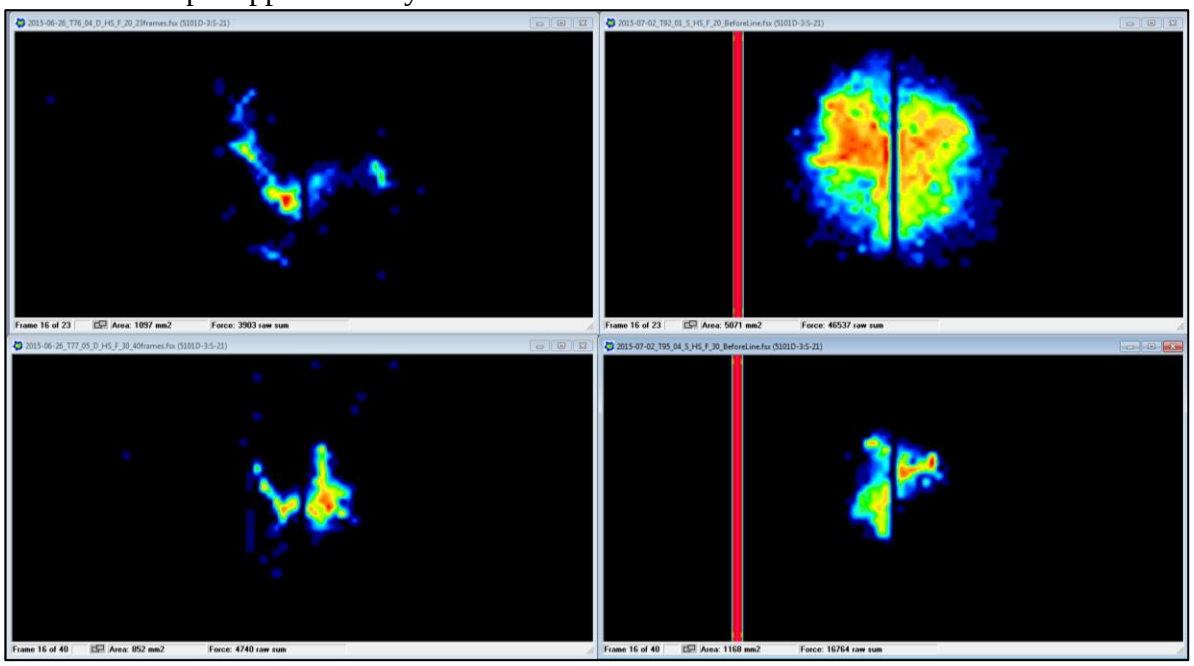

Penetration depth approximately 16 mm

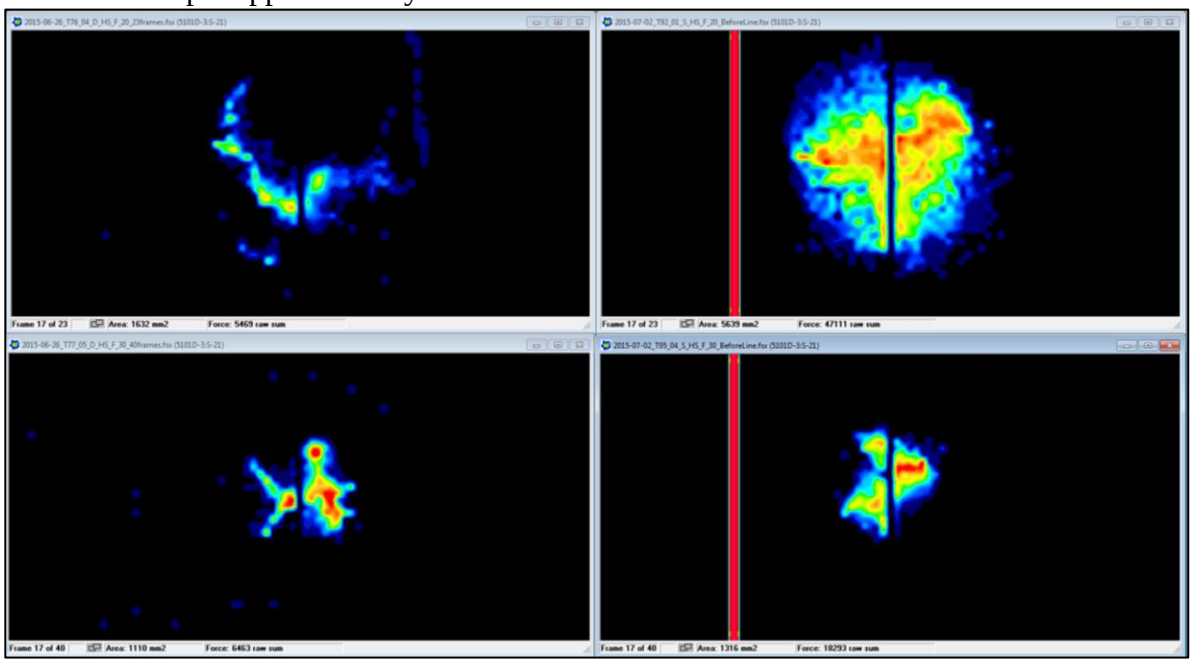

Penetration depth approximately 17 mm

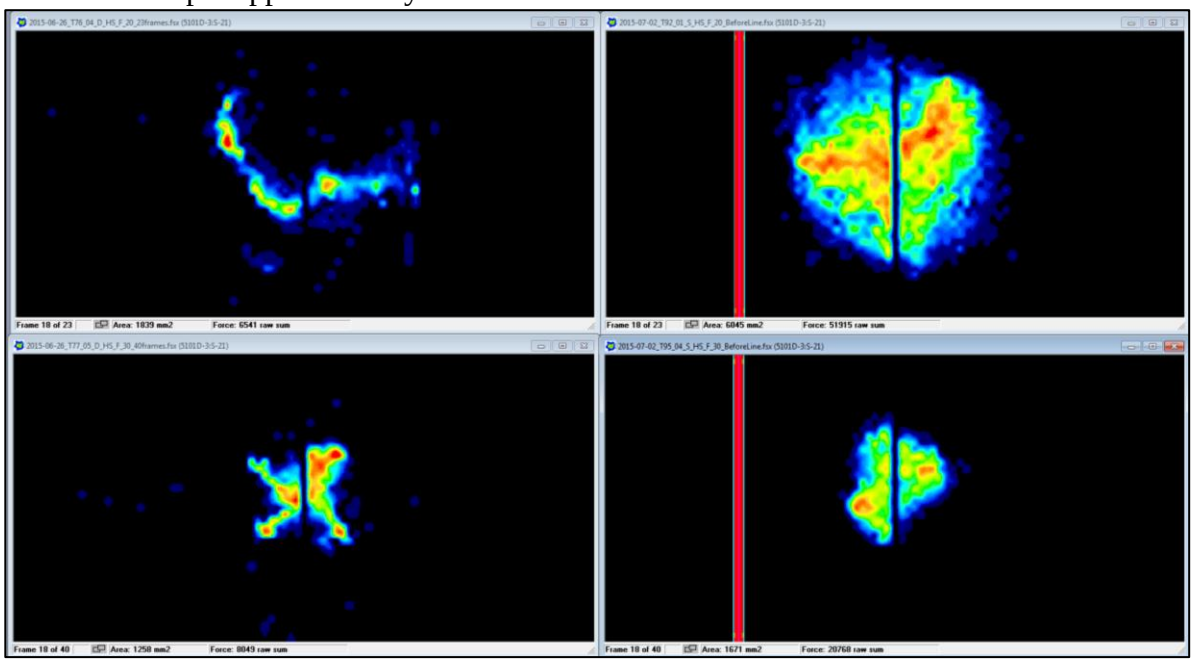

Penetration depth approximately 18 mm

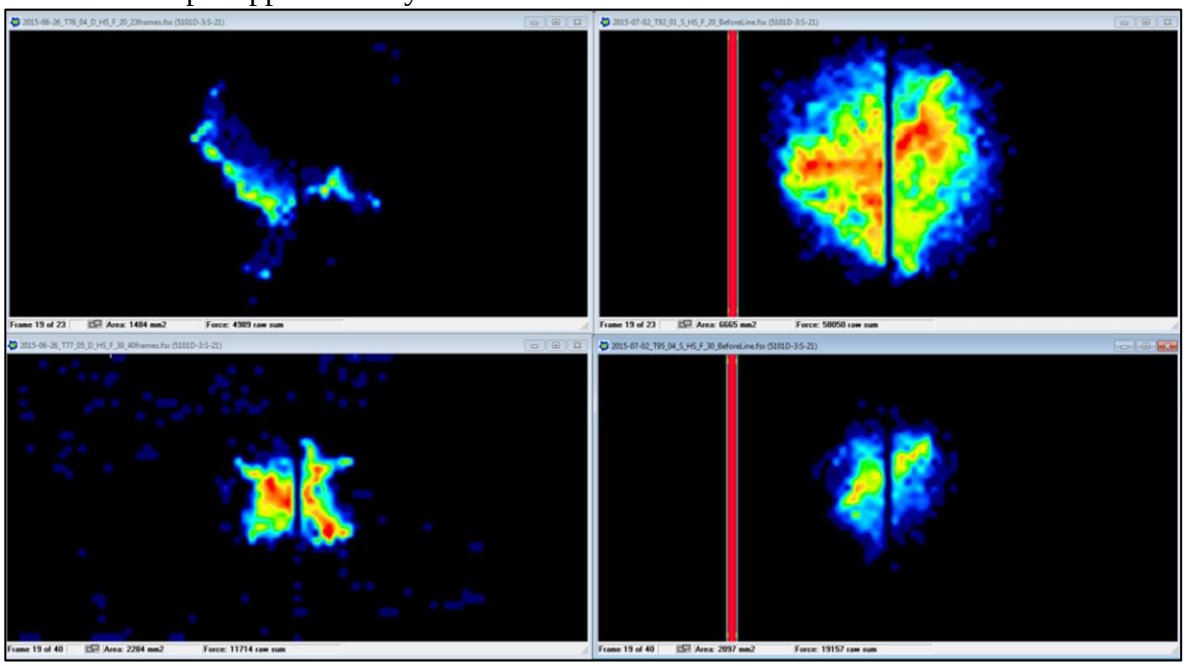

Penetration depth approximately 19 mm

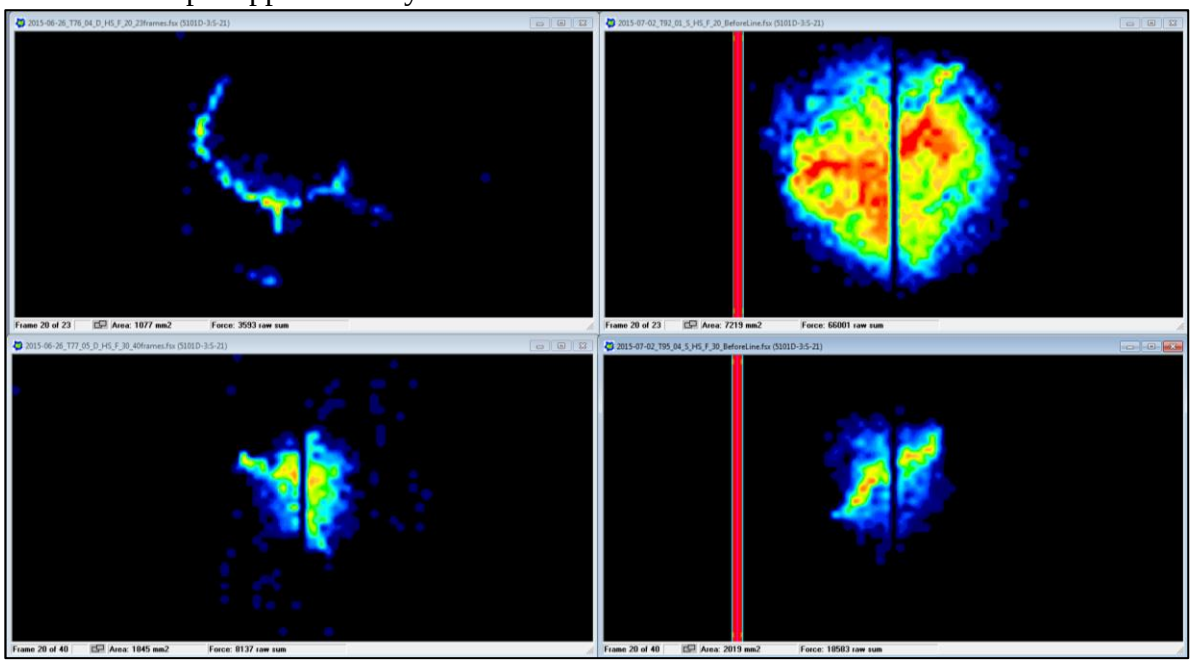

Penetration depth approximately 20 mm

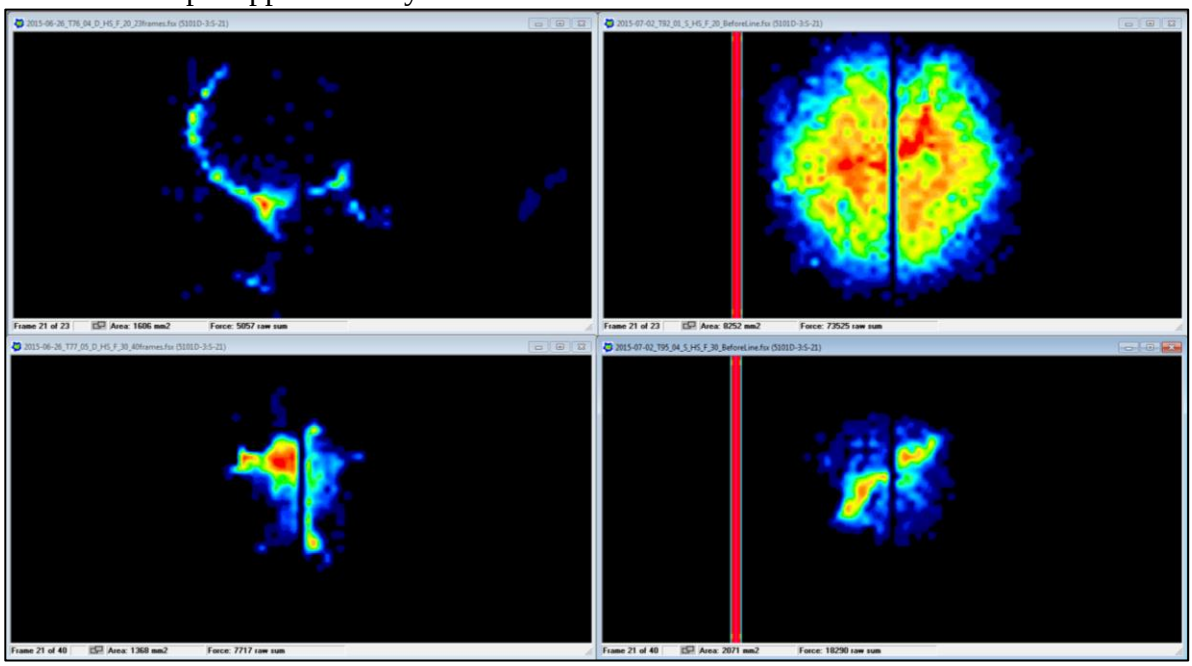

Penetration depth approximately 21 mm

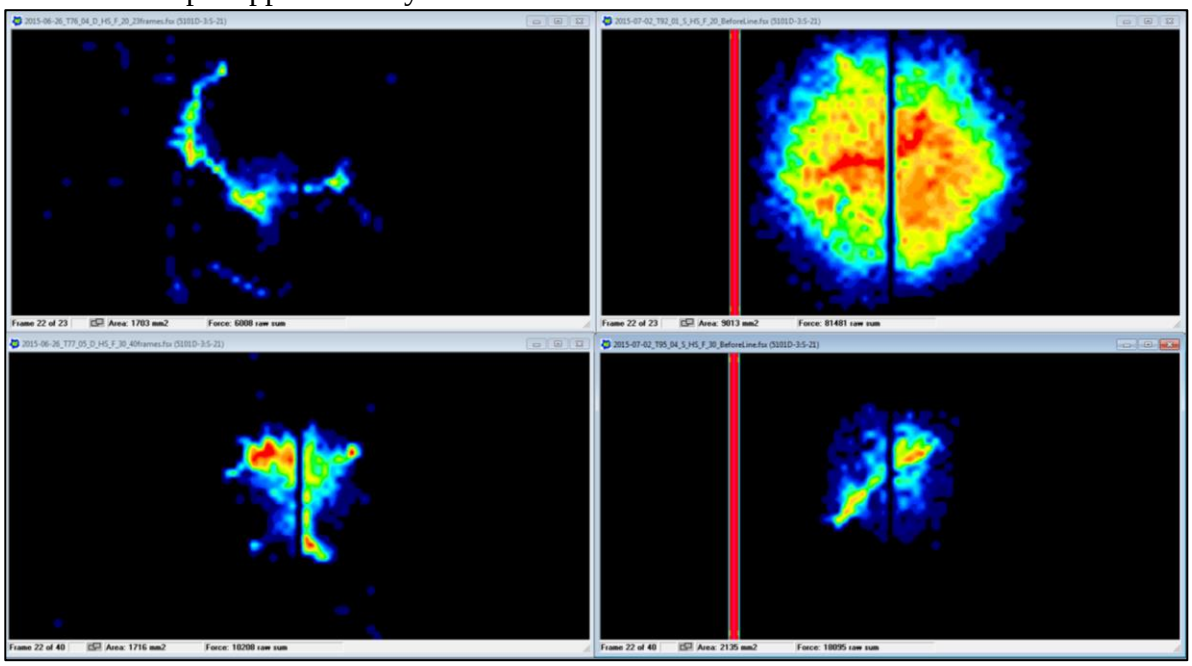

Penetration depth approximately 22 mm

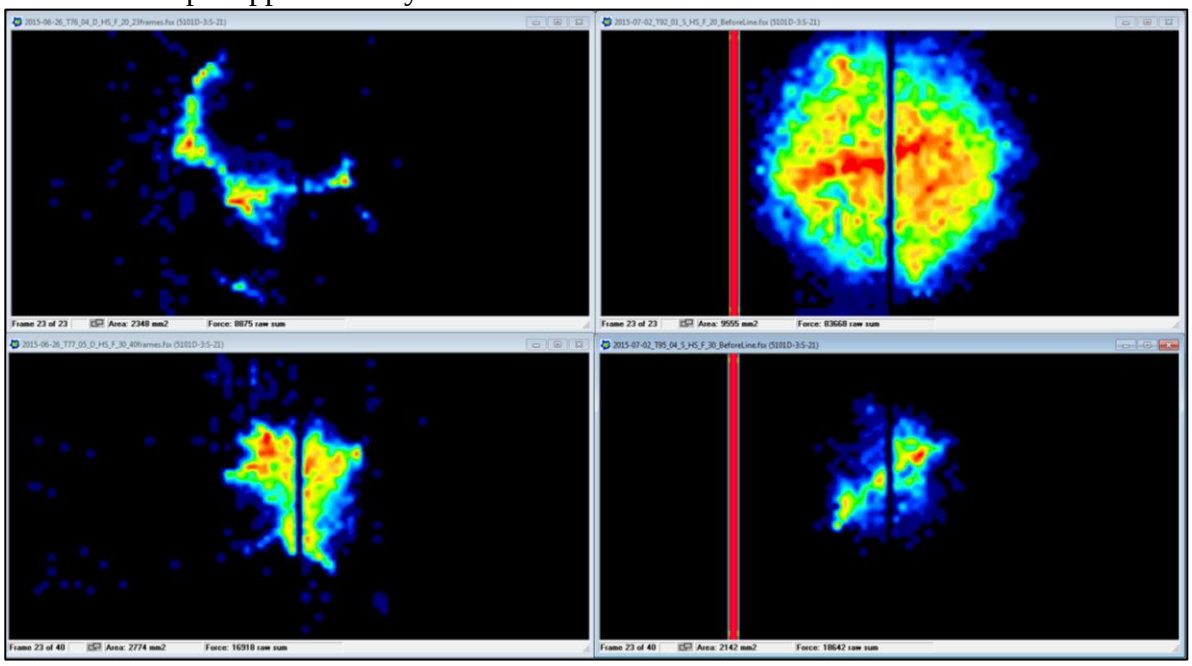

Dry test D T76-04 (top left in above images) at penetration depth approximately 40 mm

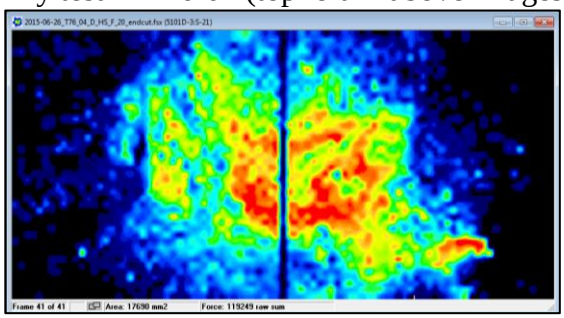

Penetration depth approximately 22 mm

Left: T81_09_Snow_HS_F_30 Right: T100_03_Chips_HS_F_30

Starting from here only 30° ice cone angle is displayed

Penetration depth approximately 23 mm

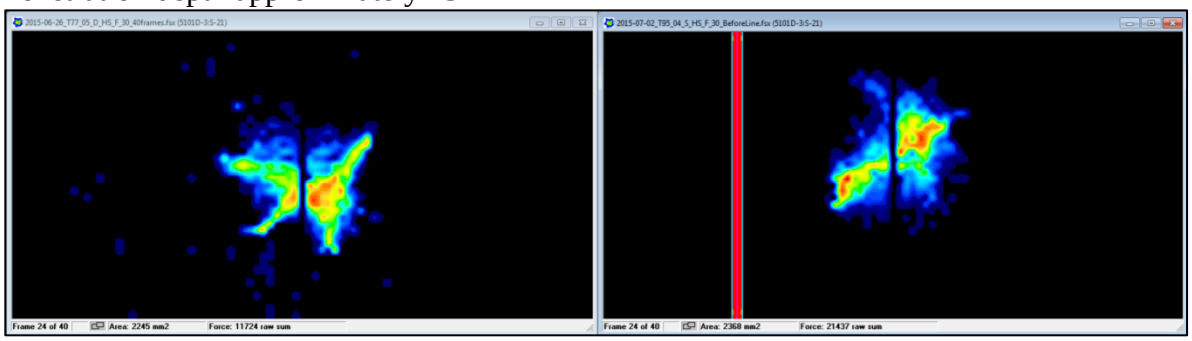

Penetration depth approximately 24 mm

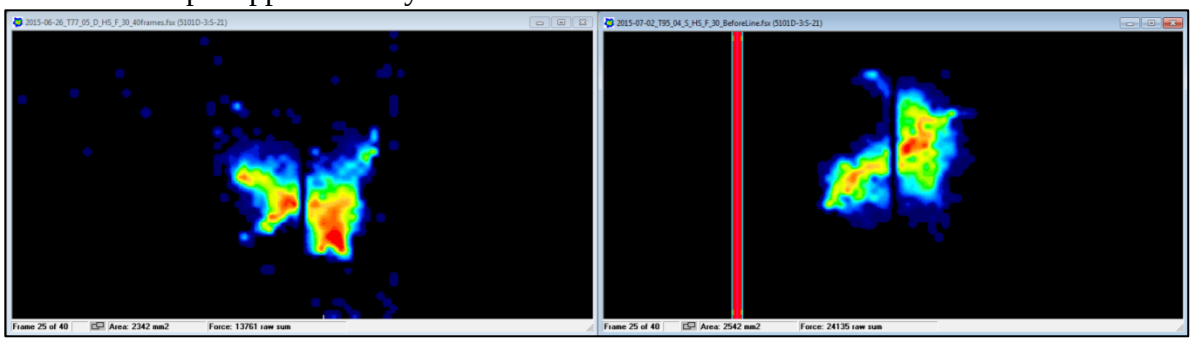

Penetration depth approximately 25 mm

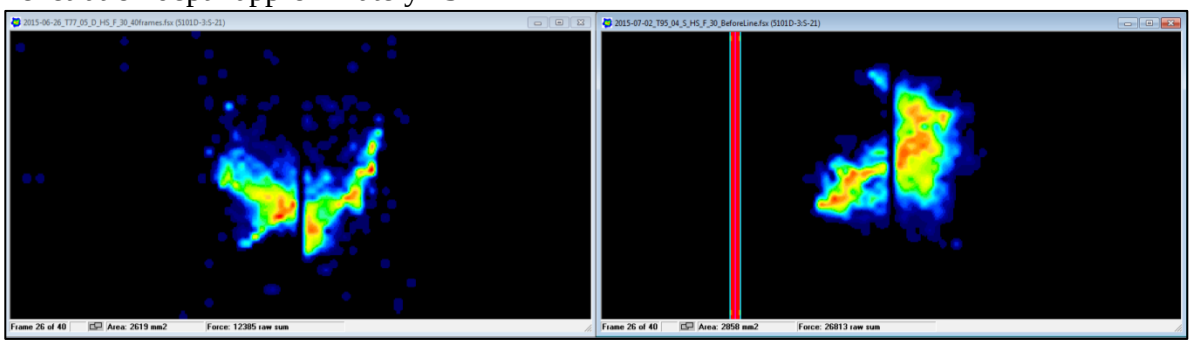

Penetration depth approximately 26 mm

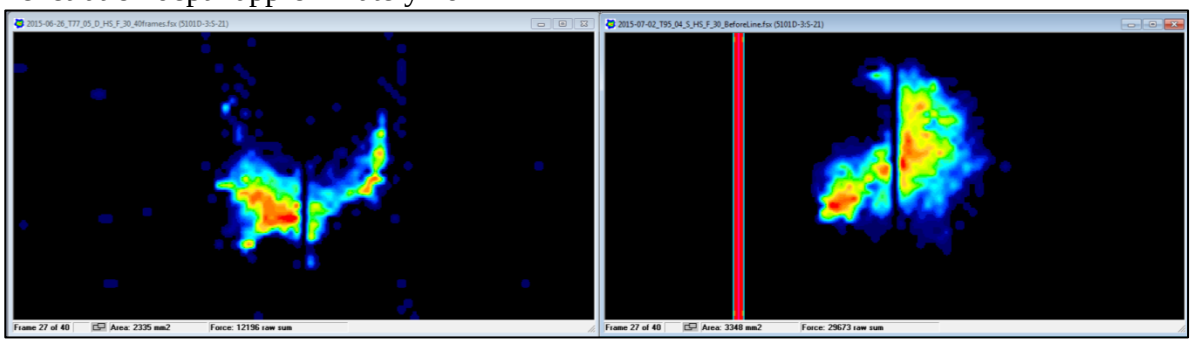

Penetration depth approximately 27 mm

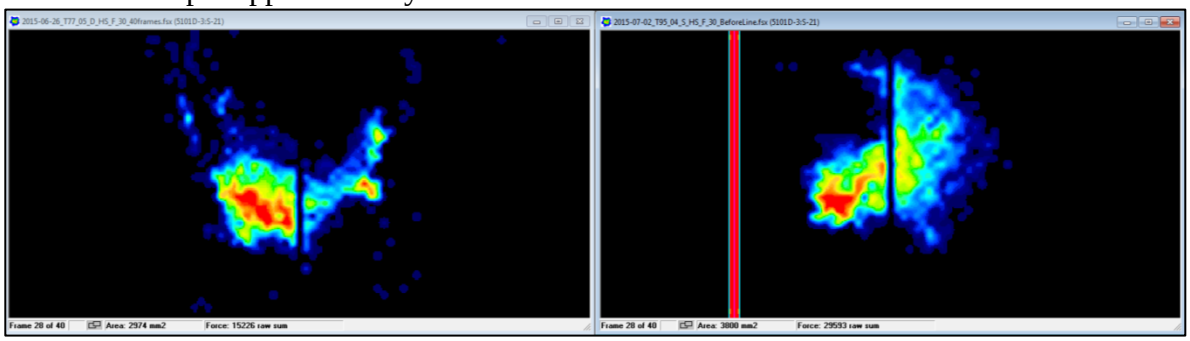

Penetration depth approximately 28 mm

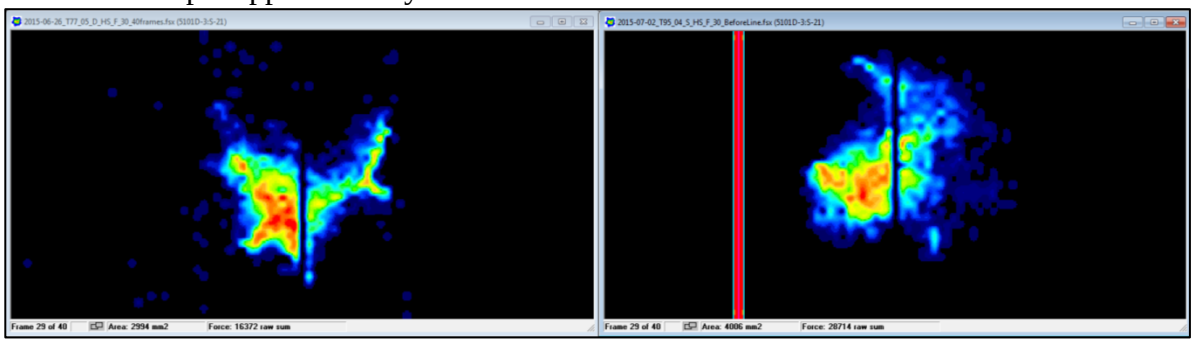

Penetration depth approximately 29 mm

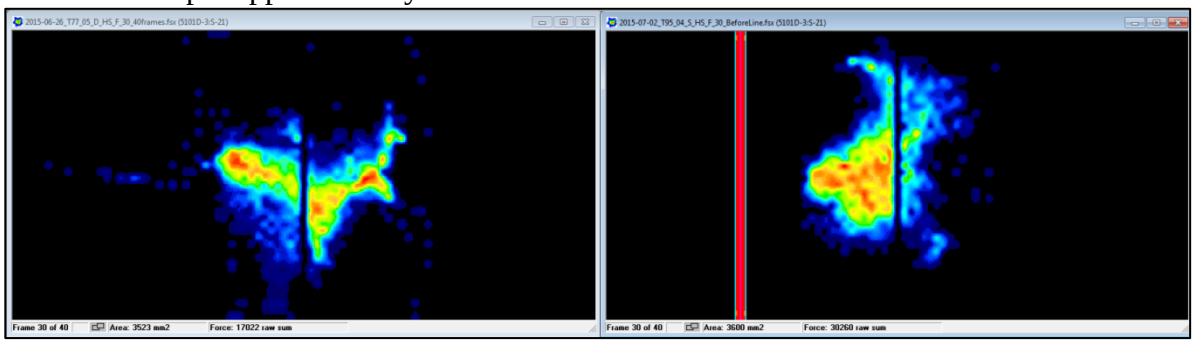

Penetration depth approximately 30 mm

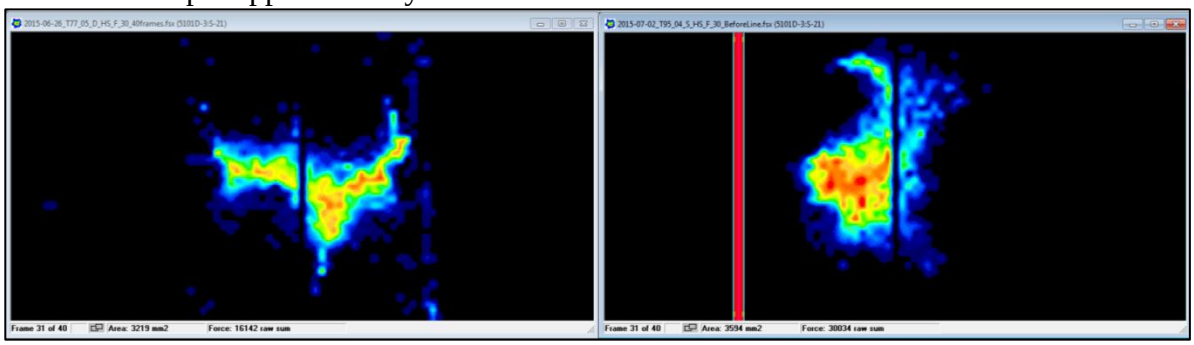

Penetration depth approximately 31 mm

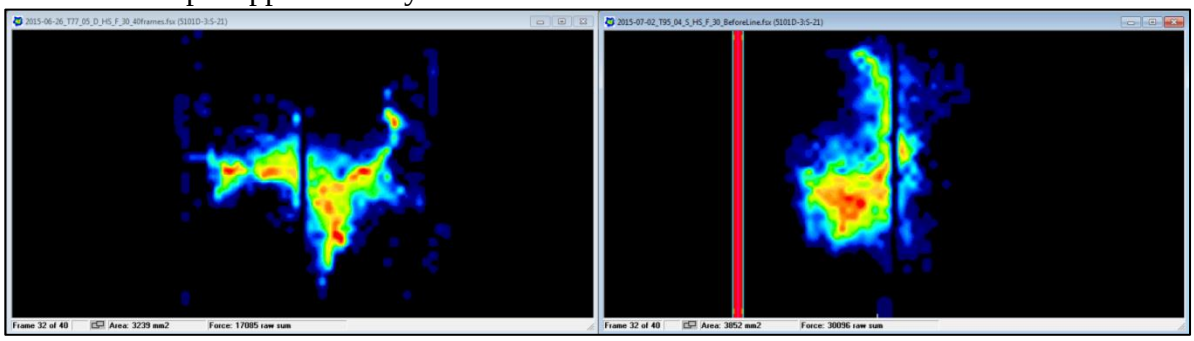

Penetration depth approximately 32 mm

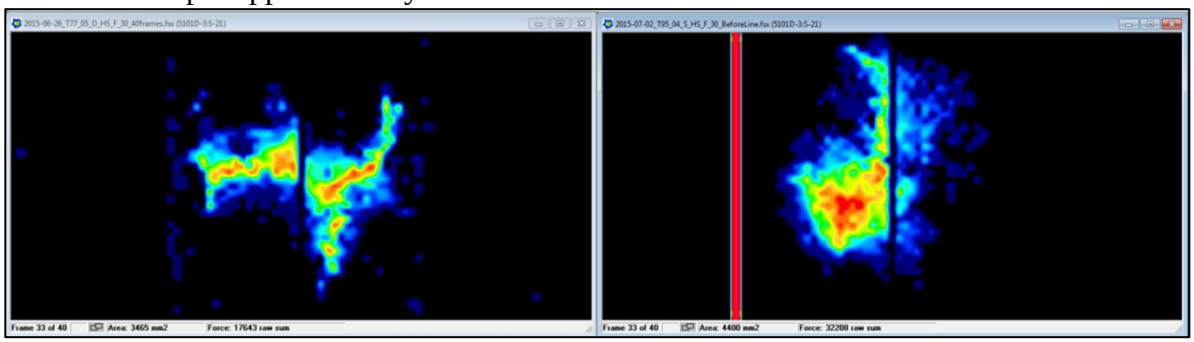

Penetration depth approximately 33 mm

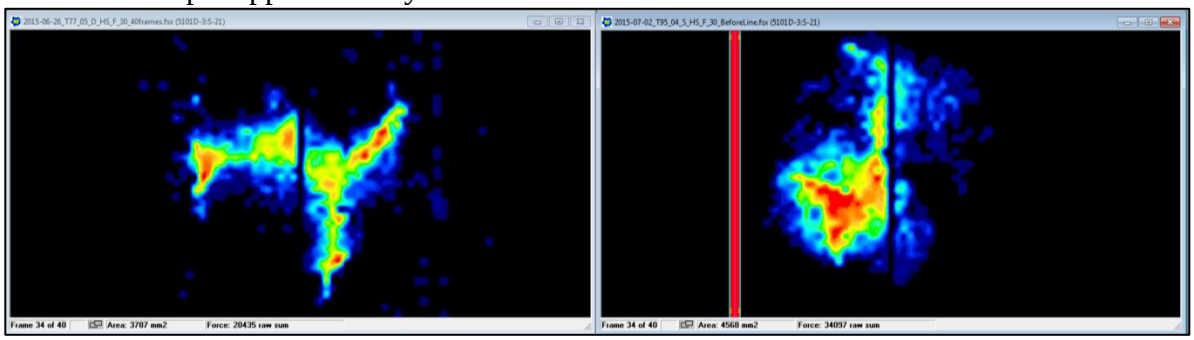

Penetration depth approximately 34 mm

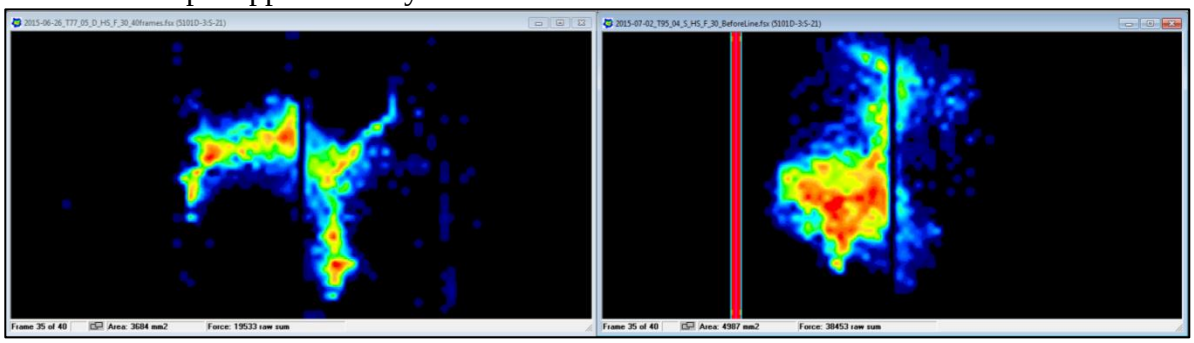

Penetration depth approximately 35 mm

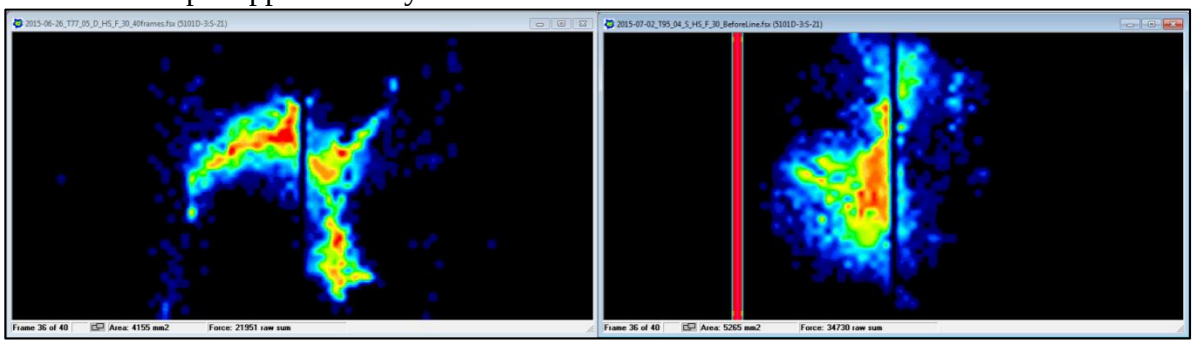

Penetration depth approximately 36 mm

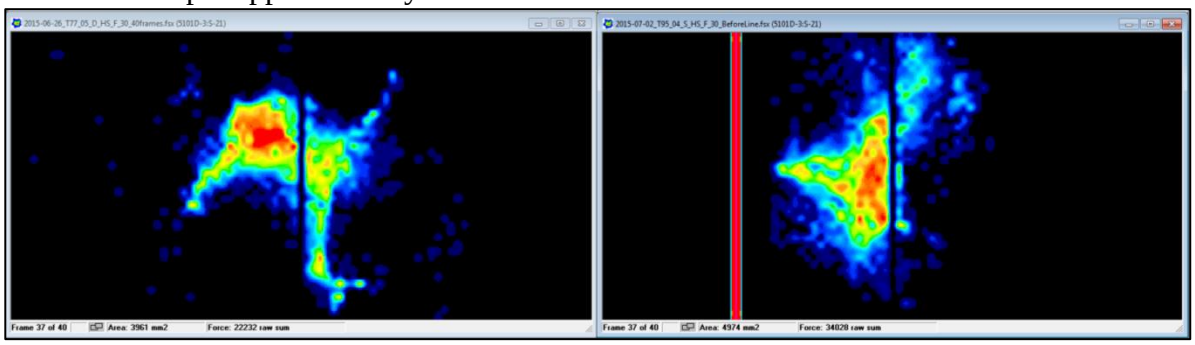

Penetration depth approximately 37 mm

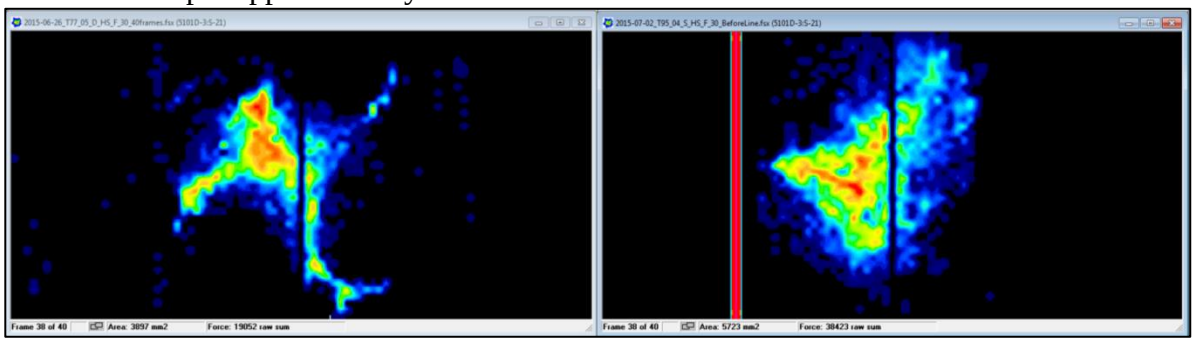

Penetration depth approximately 38 mm

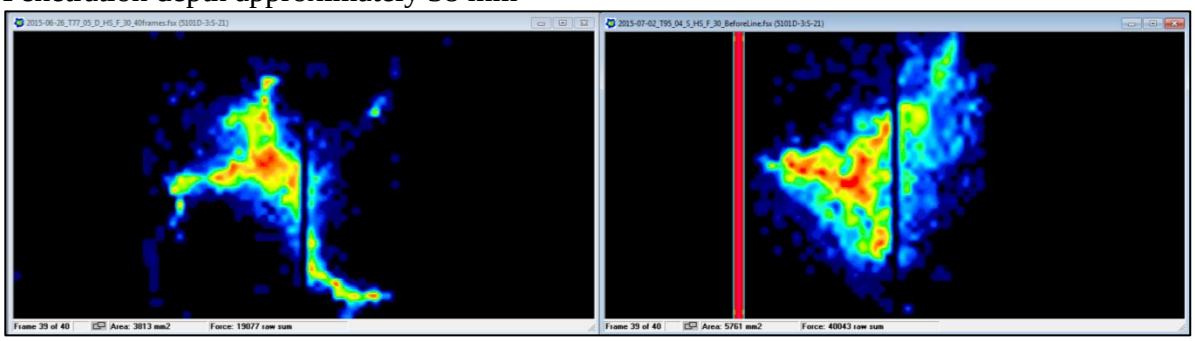

Penetration depth approximately 39 mm

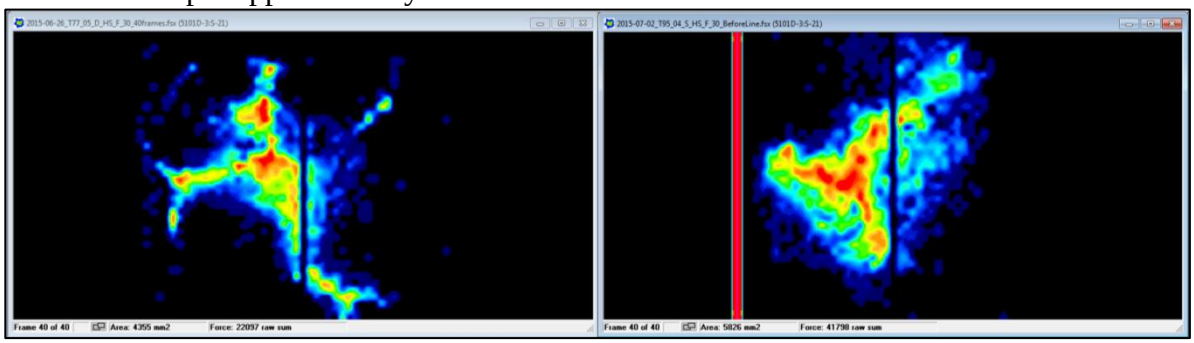

Penetration depth approximately 39 mm

Left: T81_09_Snow_HS_F_30 Right: T100_03_Chips_HS_F_30

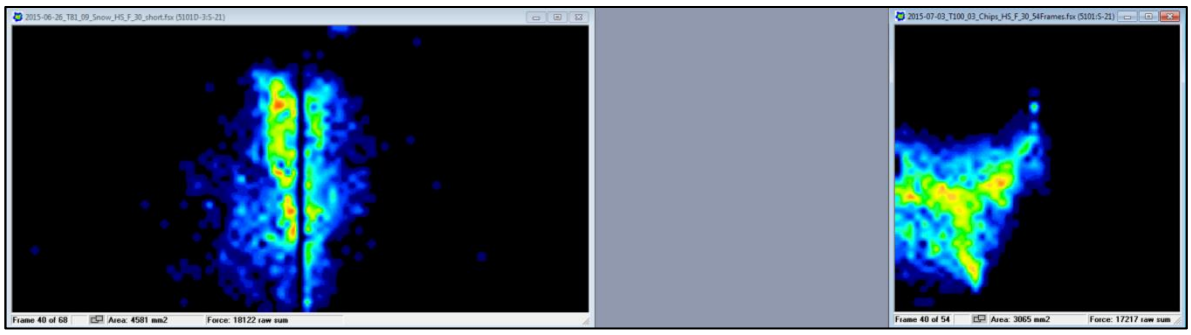

The table below lists contact area and for raw force as they were derived from the tactile pressure sensors for approximately every other frame. The values of the submerged tests are corrected by the constant offset values (Area: 284 mm^2, Raw Force: 11220) that originated from the damaged sensel column.

.

Ice Cone Angle		20			30		
Depth [mm]	**Condition Test**	**Dry T76-04**	**Submerged T92-01**	**Nom. Area**	**Dry T77-05**	**Submerged T95-04**	**Nom. Area**
2	Area [mm^2]	181	84	95	32	6	38
	Raw Force	549	404	-	95	7	-
4	Area [mm^2]	252	303	379	142	51	151
	Raw Force	1154	1902	-	322	162	-
6	Area [mm^2]	703	761	854	284	155	339
	Raw Force	2971	4533	-	904	626	-
8	Area [mm^2]	1013	1316	1518	316	310	603
	Raw Force	3824	9077	-	1508	1872	-
10	Area[mm^2]	1245	2045	2372	400	387	943
	Raw Force	5482	14712	-	2425	2065	-
12	Area [mm^2]	1652	2935	3415	677	548	1357
	Raw Force	8287	22744	-	3128	3301	-
14	Area [mm^2]	1232	4058	4648	806	851	1847
	Raw Force	4032	31349	-	4122	5363	-
16	Area [mm^2]	1632	5355	6071	1110	1032	2413
	Raw Force	5469	35891	-	6463	7073	-
18	Area [mm^2]	1484	6381	7684	2284	1813	3054
	Raw Force	4989	46830	-	11714	7937	-
20	Area[mm^2]	1606	7968	9486	1368	1787	3770
	Raw Force	5057	62305	-	7717	7070	-
22	Area [mm^2]	2348	9271	11478	2774	1858	4562
	Raw Force	8875	72448	-	16918	7422	-
24	Area [mm^2]	-	-	-	2342	2258	5429
	Raw Force	-	-	-	13761	12915	-
26	Area [mm^2]	-	-	-	2335	3064	6371
	Raw Force	-	-	-	12196	18453	-
28	Area [mm^2]	-	-	-	2994	3722	7389
	Raw Force	-	-	-	16372	17494	-
30	Area[mm^2]	-	-	-	3219	2310	8482
	Raw Force	-	-	-	16142	18814	-
32	Area [mm^2]	-	-	-	3465	4116	9651
	Raw Force	-	-	-	17643	20988	-
34	Area [mm^2]	-	-	-	3684	4703	10895
	Raw Force	-	-	-	19533	27233	-
35	Area [mm^2]	-	-	-	3961	4690	12215
	Raw Force	-	-	-	22232	22808	-
38	Area [mm^2]	-	-	-	3813	5477	13609
	Raw Force	-	-	-	19077	28823	-
39	Area[mm^2]	-	-	-	4355	5542	14335
	Raw Force	-	-	-	22097	30578	-

Appendix B6 : General Observations: 10 mm/s, 20° Ice Cone Angle

Dry **T74_02**		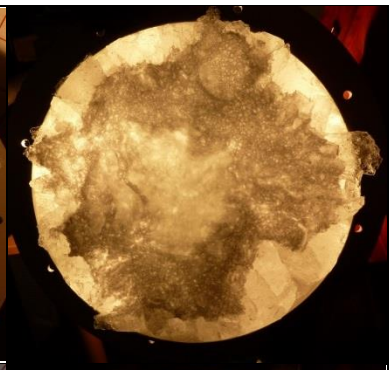
Submerged **T94_03**		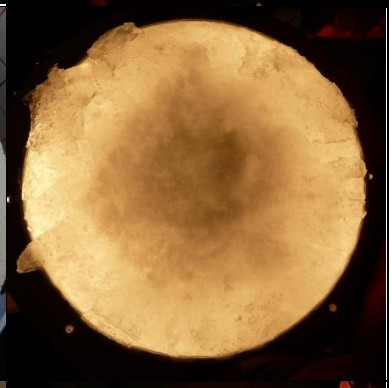
Granular Ice **T106_09**		

Appendix B7 : Microstructural Observations (Thin Sections)

1 mm/s

Dry 20°	Dry 30°
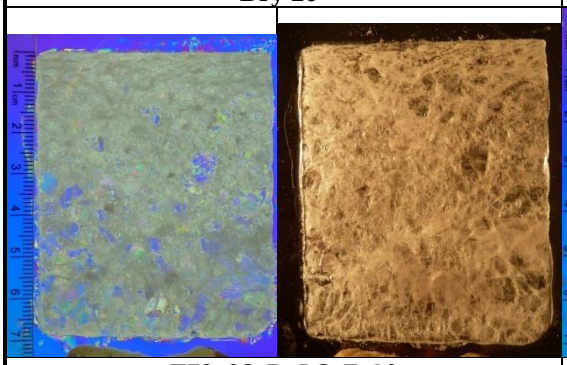	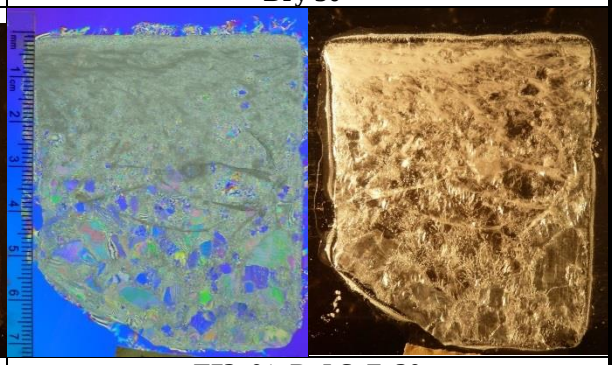
T78_06_D_LS_F_20	T73_01_D_LS_F_30
Snow 20°	**Snow 30°**
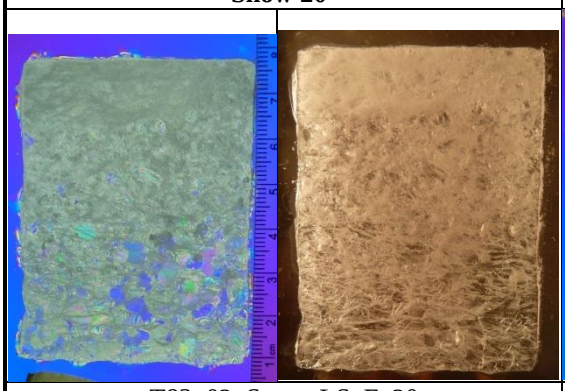	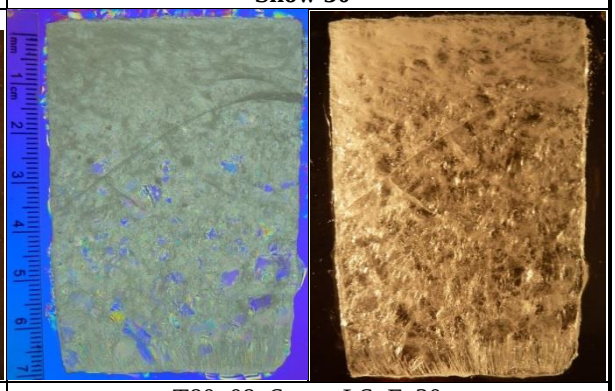
T83_02_Snow_LS_F_20	T80_08_Snow_LS_F_30
Granular Ice 20°	n/a
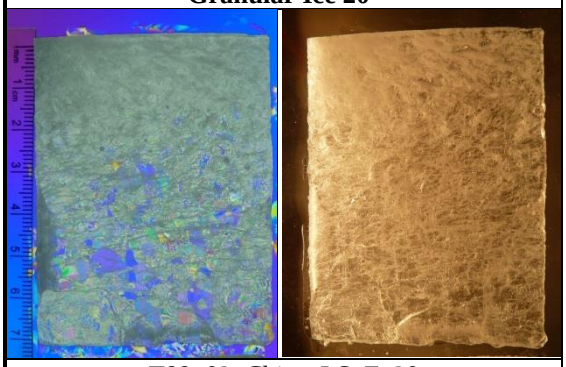	
T99_02_Chips_LS_F_20	

10 mm/s

Dry 20°	Dry 30°
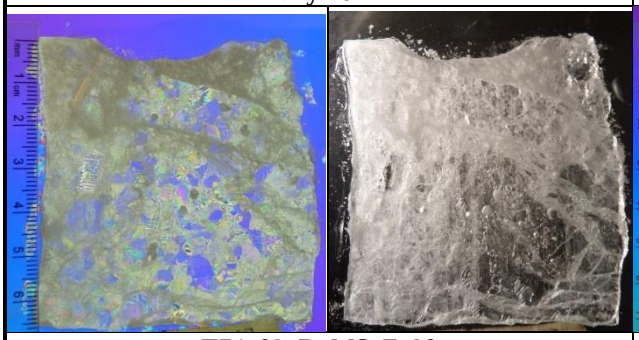	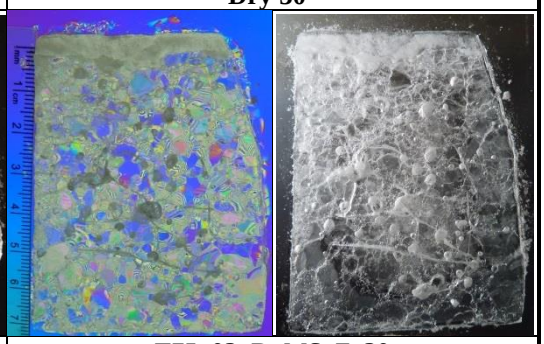
T74_02_D_MS_F_20	T75_03_D_MS_F_30
Submerged 20° - vertical	**Submerged 20° - horizontal**
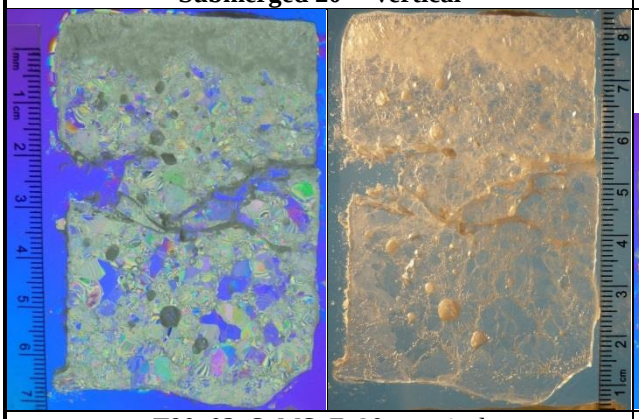	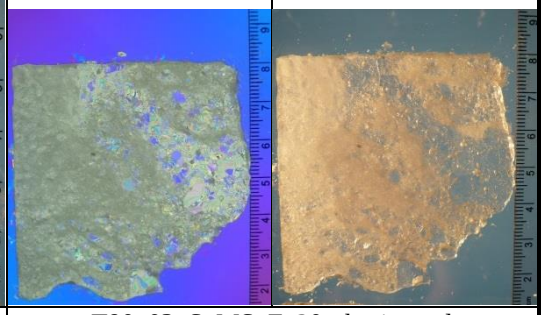
T90_03_S_MS_F_20 - vertical	T90_03_S_MS_F_20 - horizontal
Granular Ice 20°	
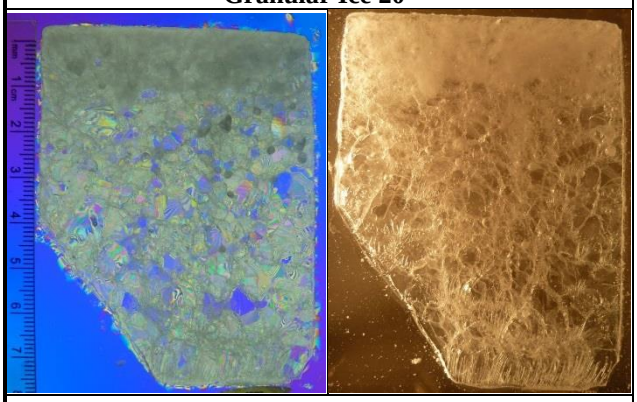	n/a
T106_09_Chips_MS_F_20	

100 mm/s

Dry 20°	Dry 30°
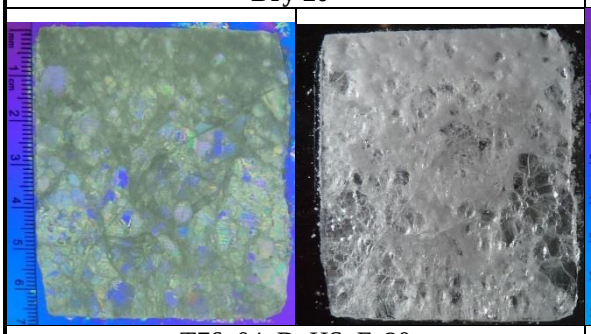	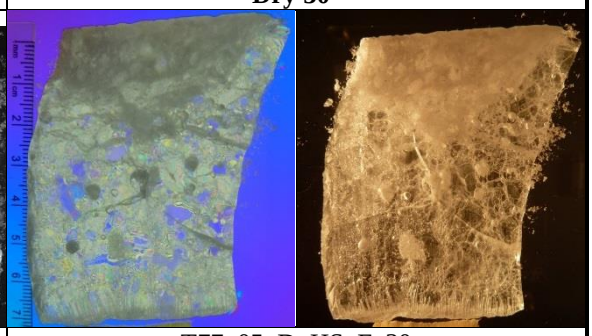
T76_04_D_HS_F_20	T77_05_D_HS_F_30
Submerged 20°	**Submerged 30°**
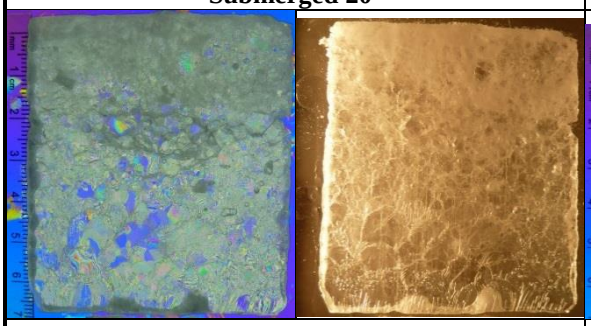	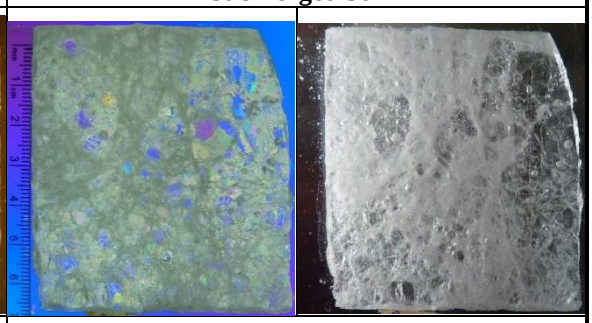
T92_01_S_HS_F_20	T95_04_S_HS_F_30
Snow 20°	**Snow 30°**
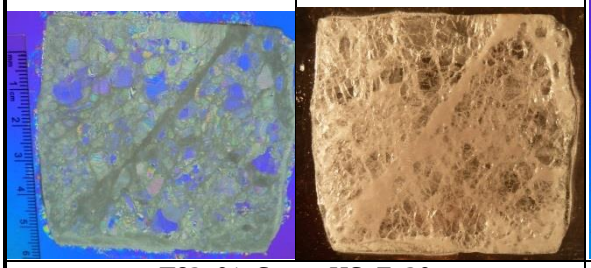	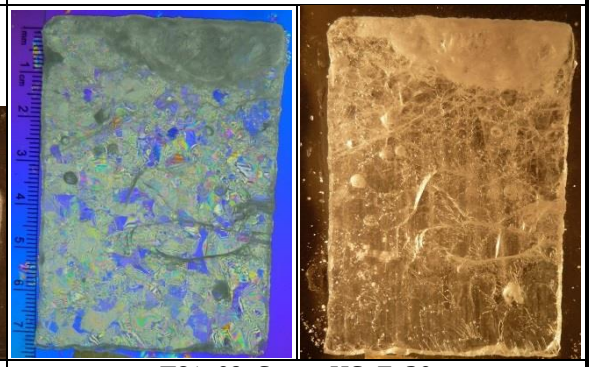
T82_01_Snow_HS_F_20	T81_09_Snow_HS_F_30
Granular Ice 20°	
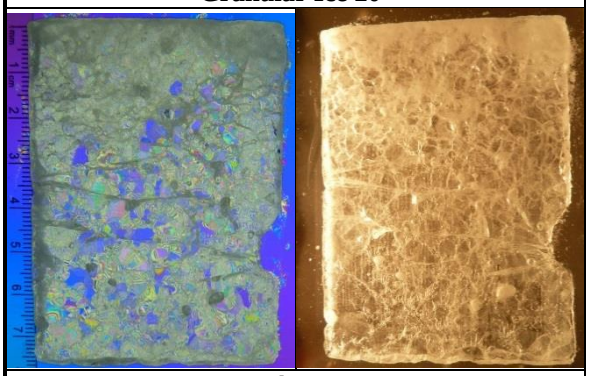	n/a
T101_04_Chips_HS_F_20	

Appendix B8 : Multiple Regression Analysis

Mean Force Overall

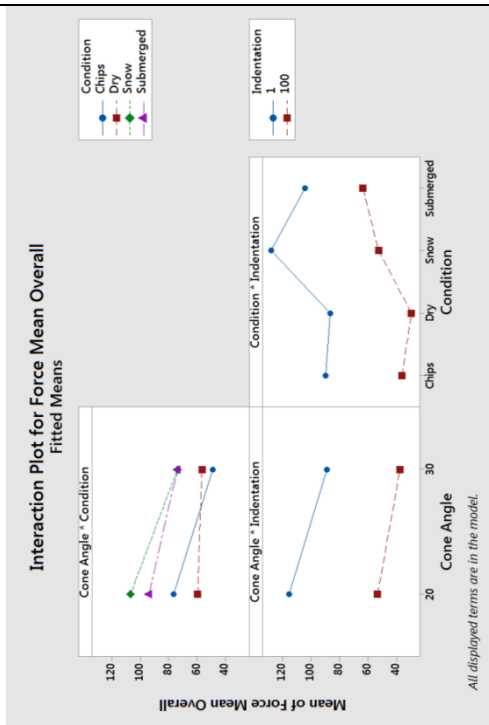

Regression Equation
Force Mean Overall =
73.73 + 10.50 Cone Angle_20 - 10.50 Cone Angle_30
- 10.95 Condition_Chips - 15.72 Condition_Dry + 16.58 Condition_Snow
+ 10.09 Condition_Submerged + 28.33 Indentation Rate_1
- 28.33 Indentation Rate_100 + 3.33 Cone Angle*Condition_20 Chips
- 9.00 Cone Angle*Condition_20 Dry + 6.03 Cone Angle*Condition_20 Snow
- 0.36 Cone Angle*Condition_20 Submerged
- 3.33 Cone Angle*Condition_30 Chips
+ 9.00 Cone Angle*Condition_30 Dry - 6.03 Cone Angle*Condition_30 Snow
+ 0.36 Cone Angle*Condition_30 Submerged
+ 2.62 Cone Angle*Indentation Rate_20 1
- 2.62 Cone Angle*Indentation Rate_20 100
- 2.62 Cone Angle*Indentation Rate_30 1
+ 2.62 Cone Angle*Indentation Rate_30 100
- 1.59 Condition*Indentation Rate_Chips 1
+ 1.59 Condition*Indentation Rate_Chips 100
+ 0.16 Condition*Indentation Rate_Dry 1
- 0.16 Condition*Indentation Rate_Dry 100
+ 9.42 Condition*Indentation Rate_Snow 1
- 9.42 Condition*Indentation Rate_Snow 100
- 8.00 Condition*Indentation Rate_Submerged 1
+ 8.00 Condition*Indentation Rate_Submerged 100

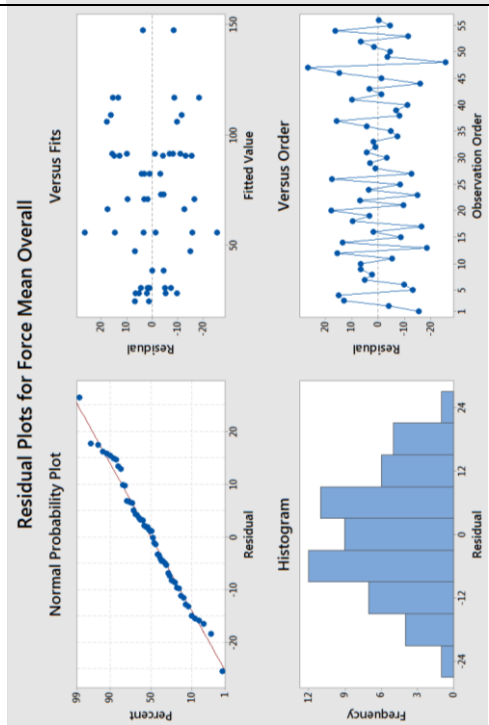

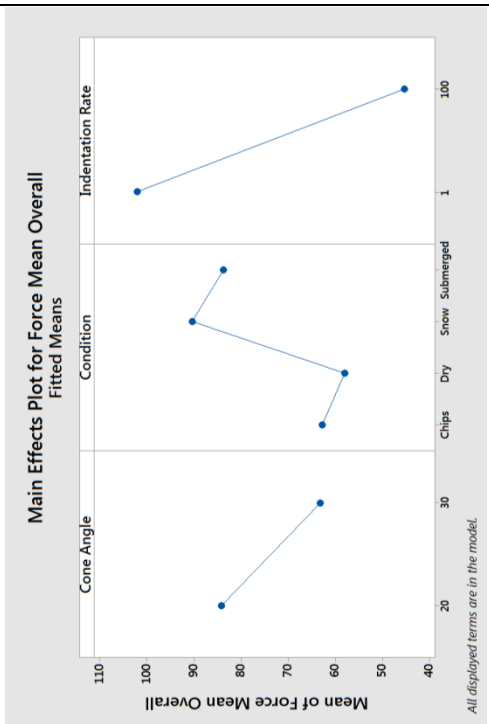

Mean Force Above 1000 mm^2

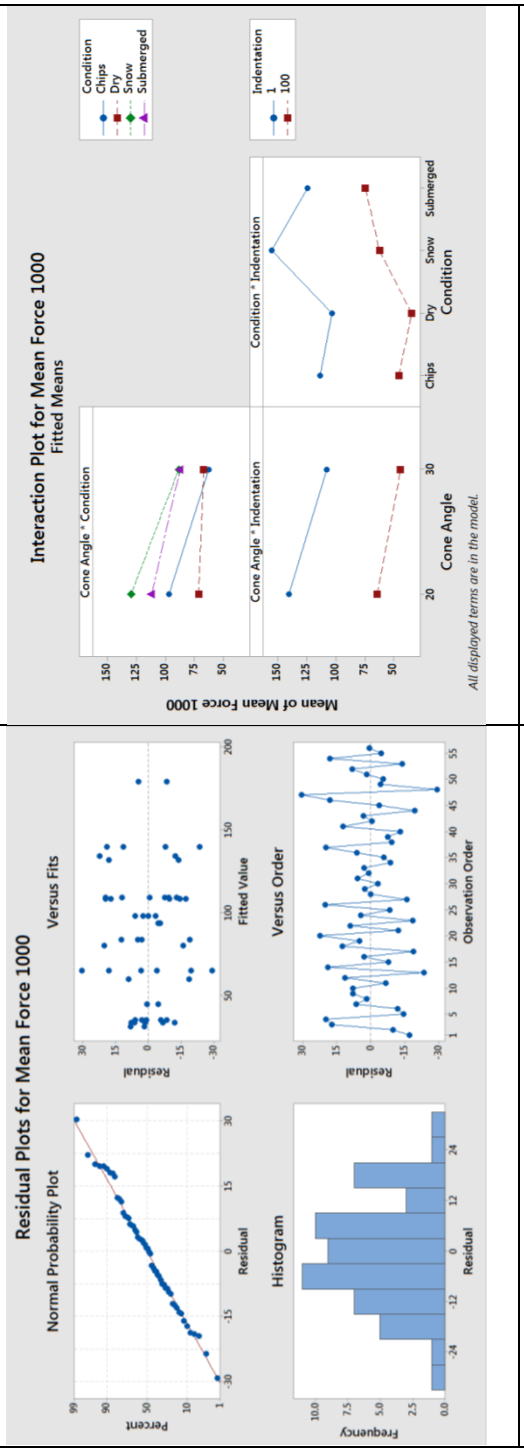

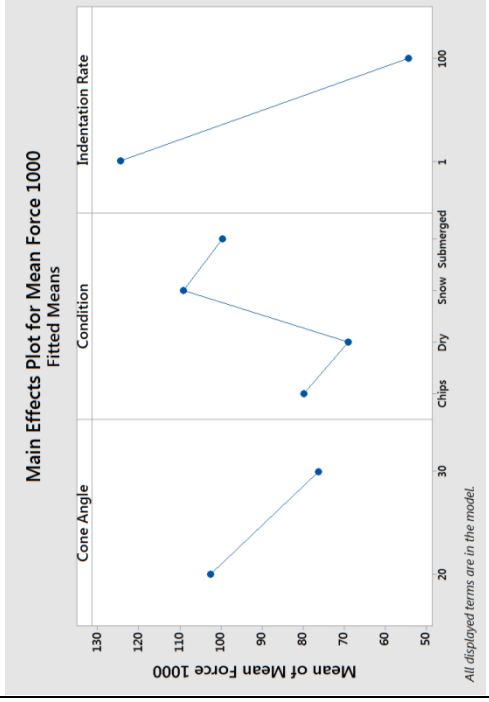

Regression Equation
Mean Force 1000 =
89.40 + 13.08 Cone Angle_20 - 13.08 Cone Angle_30 - 9.55 Condition_Chips
- 20.32 Condition_Dry +19.70 Condition_Snow + 10.17 Condition_Submerged
+ 34.93 Indentation Rate_1 - 34.93 Indentation Rate_100
+ 4.17 Cone Angle*Condition_20 Chips
- 10.88 Cone Angle*Condition_20 Dry
+ 7.48 Cone Angle*Condition_20 Snow
- 0.76 Cone Angle*Condition_20 Submerged
- 4.17 Cone Angle*Condition_30 Chips
+ 10.88 Cone Angle*Condition_30 Dry
- 7.48 Cone Angle*Condition_30 Snow
+ 0.76 Cone Angle*Condition_30 Submerged
+ 3.01 Cone Angle*Indentation Rate_20 1
- 3.01 Cone Angle*Indentation Rate_20 100
- 3.01 Cone Angle*Indentation Rate_30 1
+ 3.01 Cone Angle*Indentation Rate_30 100
- 0.92 Condition*Indentation Rate_Chips 1
+ 0.92 Condition*Indentation Rate_Chips 100
- 0.61 Condition*Indentation Rate_Dry 1
+ 0.61 Condition*Indentation Rate_Dry 100
+ 11.57 Condition*Indentation Rate_Snow 1
- 11.57 Condition*Indentation Rate_Snow 100
- 10.04 Condition*Indentation Rate_Submerged 1
+ 10.04 Condition*Indentation Rate_Submerged 100

Mean Pressure Above 1000 mm^2

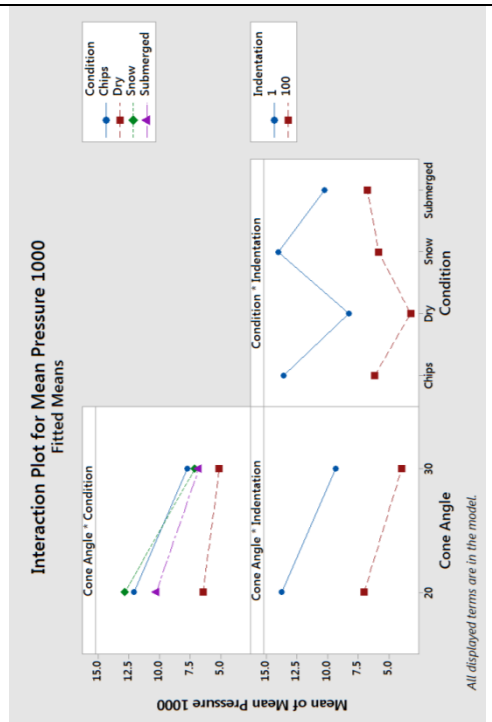

Regression Equation
Mean Pressure 1000 =
8.533 + 1.864 Cone Angle_20 - 1.864 Cone Angle_30
+ 1.362 Condition_Chips - 2.772 Condition_Dry + 1.423 Condition_Snow
- 0.013 Condition_Submerged + 3.018 Indentation Rate_1
- 3.018 Indentation Rate_100 + 0.323 Cone Angle*Condition_20 Chips
- 1.203 Cone Angle*Condition_20 Dry
+ 0.998 Cone Angle*Condition_20 Snow
- 0.118 Cone Angle*Condition_20 Submerged
- 0.323 Cone Angle*Condition_30 Chips
+ 1.203 Cone Angle*Condition_30 Dry
- 0.998 Cone Angle*Condition_30 Snow
+ 0.118 Cone Angle*Condition_30 Submerged
+ 0.335 Cone Angle*Indentation Rate_20 1
- 0.335 Cone Angle*Indentation Rate_20 100
- 0.335 Cone Angle*Indentation Rate_30 1
+ 0.335 Cone Angle*Indentation Rate_30 100
+ 0.676 Condition*Indentation Rate_Chips 1
- 0.676 Condition*Indentation Rate_Chips 100
- 0.490 Condition*Indentation Rate_Dry 1
+ 0.490 Condition*Indentation Rate_Dry 100
+ 1.073 Condition*Indentation Rate_Snow 1
- 1.073 Condition*Indentation Rate_Snow 100
- 1.259 Condition*Indentation Rate_Submerged 1
+ 1.259 Condition*Indentation Rate_Submerged 100

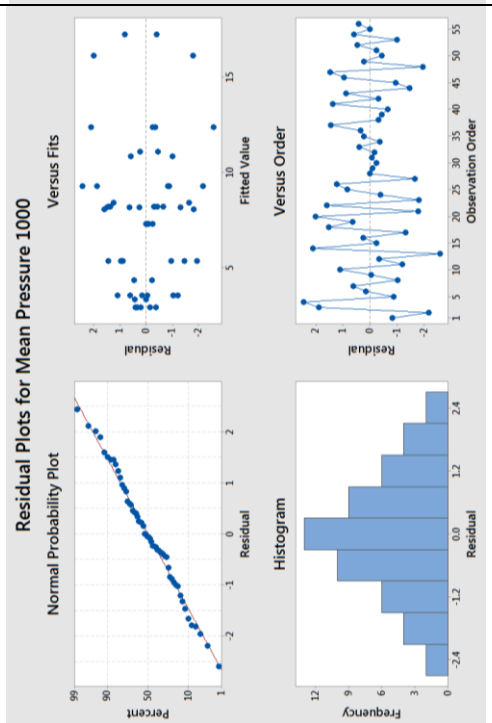

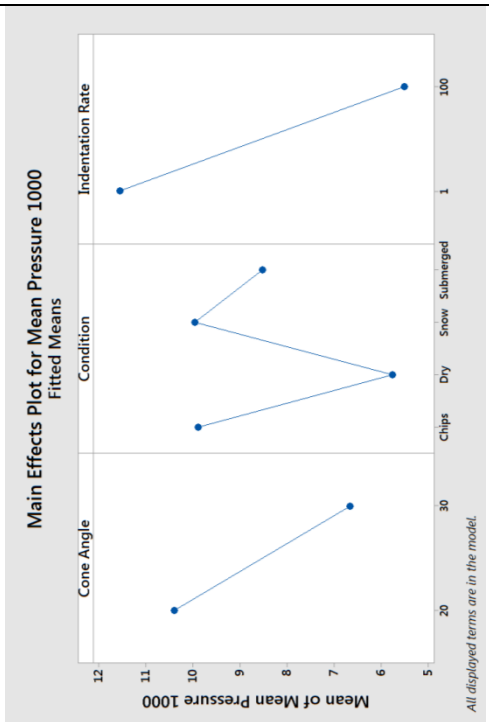

Maximal Nominal Pressure Above 1000 mm^2

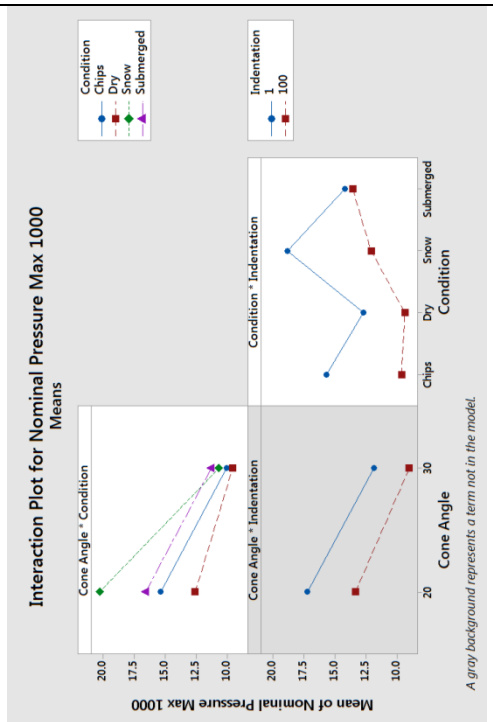

Regression Equation
Nominal Pressure Max 1000 =
13.283 + 2.910 Cone Angle_20 - 2.910 Cone Angle_30
- 0.585 Condition_Chips - 2.228 Condition_Dry
+ 2.190 Condition_Snow + 0.623 Condition_Submerged
+ 2.083 Indentation Rate_1 - 2.083 Indentation Rate_100
- 0.246 Cone Angle*Condition_20 Chips
- 1.397 Cone Angle*Condition_20 Dry
+ 1.907 Cone Angle*Condition_20 Snow
- 0.264 Cone Angle*Condition_20 Submerged
+ 0.246 Cone Angle*Condition_30 Chips
+ 1.397 Cone Angle*Condition_30 Dry
- 1.907 Cone Angle*Condition_30 Snow
+ 0.264 Cone Angle*Condition_30 Submerged
+ 0.944 Condition*Indentation Rate_Chips 1
- 0.944 Condition*Indentation Rate_Chips 100
- 0.434 Condition*Indentation Rate_Dry 1
+ 0.434 Condition*Indentation Rate_Dry 100
+ 1.273 Condition*Indentation Rate_Snow 1
- 1.273 Condition*Indentation Rate_Snow 100
- 1.783 Condition*Indentation Rate_Submerged 1
+ 1.783 Condition*Indentation Rate_Submerged 100

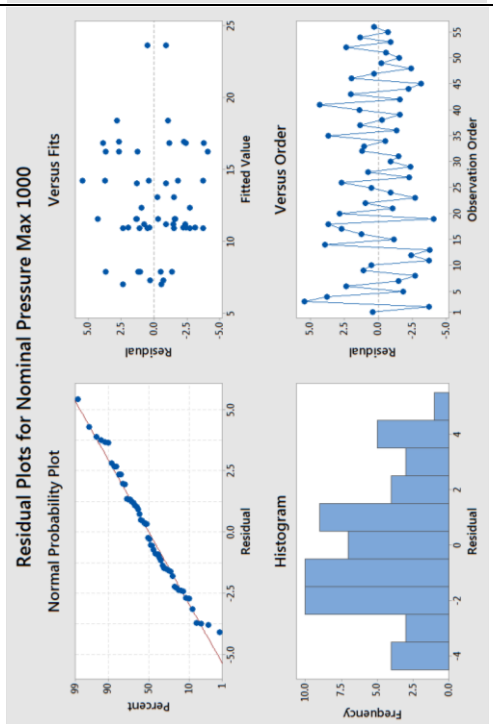

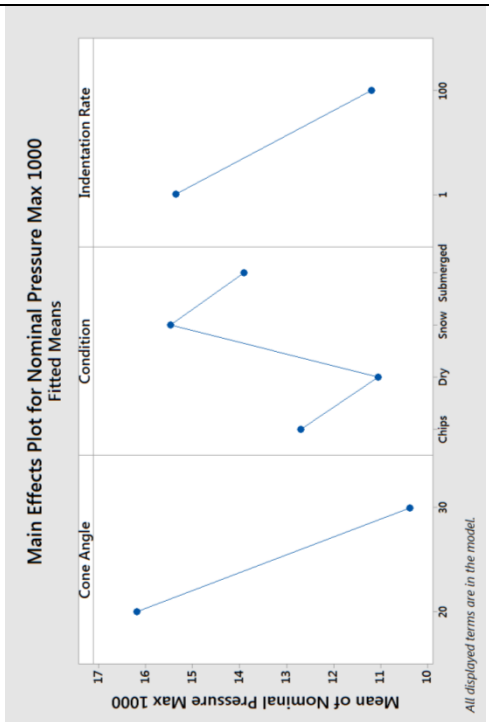

The coefficients for the obtained linear regression models (α = 0.15) are listed in Table Appendix B8. 1 for constants and factors, and in Table Appendix B8. 2 for factor interactions. All signs refer to 20° ice cone angle and are the opposite for 30° ice cone angle.

Table Appendix B8. 1: Coefficients for constants and factors of linear regression models at significance level α=0.15 for the flat indentation plate. Signs refer to 20° ice cone angle.

Response	Coefficient						
	Constant	Cone Angle 20°	Ind. Rate [mm/s]	Contact Condition			
			1	Chips	Dry	Snow	Sub
Force Mean Overall	73.73	10.50	28.33	-10.95	-15.72	16.58	10.09
Force Mean 1000	89.40	13.08	34.93	-9.55	-20.32	19.70	10.17
Pressure Max 1000	13.28	2.91	2.08	-0.59	-2.23	2.19	0.62
Pressure Mean 1000	8.53	1.86	3.02	1.36	-2.77	1.42	-0.01

Table Appendix B8. 2: Coefficients for factor interactions of linear regression models at significance level α=0.15 for the flat indentation plate. Signs refer to 20° ice cone angle.

Response	Factor Interaction Coefficient								
	20° Cone Angle x 1 mm/s Ind. Rate	20° Cone Angle x Contact Condition				20° Cone Angle x 1 mm/s Indentation Rate			
		Chips	Dry	Snow	Sub	Chips	Dry	Snow	Sub
Force Mean Overall	2.62	3.33	-9.00	6.03	-0.36	-1.59	0.16	9.42	-8.00
Force Mean 1000	3.01	4.17	-10.88	7.48	-0.76	-0.92	-0.61	11.57	10.04
Pressure Max 1000	-	-0.25	-1.40	1.91	-0.26	0.94	-0.43	1.27	-1.78
Pressure Mean 1000	0.34	0.32	-1.20	1.00	-0.12	0.68	-0.49	1.07	-1.26

Reversed signs for 30° ice cone angle, as well as for 100 mm/s.

Appendix C : Wedge Indenter

Appendix C1 : Spectral Analysis (FFT)

Tests with the wedge shaped indenter involved 30° ice cones, dry and submerged conditions and two indentation rates (1 mm/s, 100 mm/s). Each test was replicated once. Figure Appendix C1. 1 displays the spectra of two high speed tests, on the left in dry condition (D T68-02) and on the right for the submerged condition (S T70-04). Both curves have similar variations, but dry test D T68-02 has some large fluctuations between 275 Hz and 367 Hz. The same is true for the second dry test (not displayed; D T66-02) at higher frequencies (327 – 389 Hz). None of the submerged tests yielded similar results.

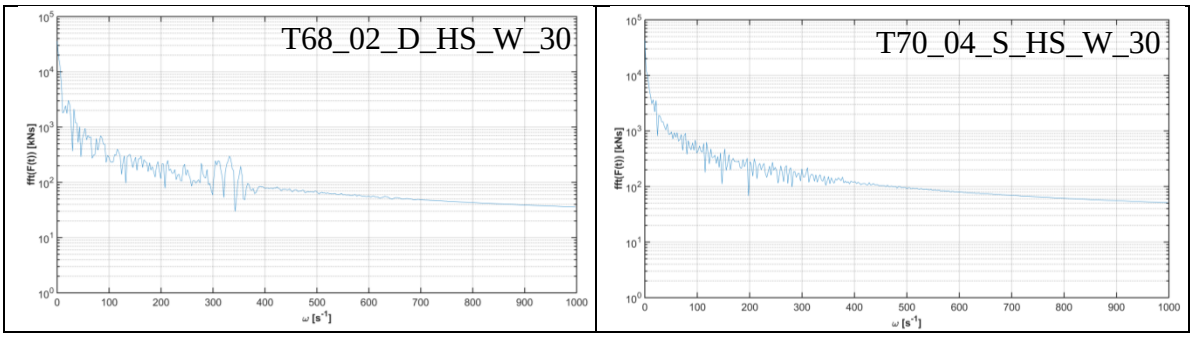

Figure Appendix C1. 1: Fourier spectra (FFT) for high speed tests with the wedge indenter and for frequencies up to 1000 Hz. Displayed are representative curves for the dry condition (T68-02) on the left and for the submerged condition (T70-04) on the right.

The slow speed tests produced band-like or line-like Fourier spectra, comparable to those of 1 mm/s tests with the flat indentation plate. The curves of dry and submerged conditions differ from one another mainly in breadth (Figure Appendix C1. 2). The spectra of both submerged tests have small spikes at 60 Hz and/or multiples (180 Hz, 300 Hz, 420 Hz), possibly indicating structural compliance or an effect of submergence on the ice failure behavior.

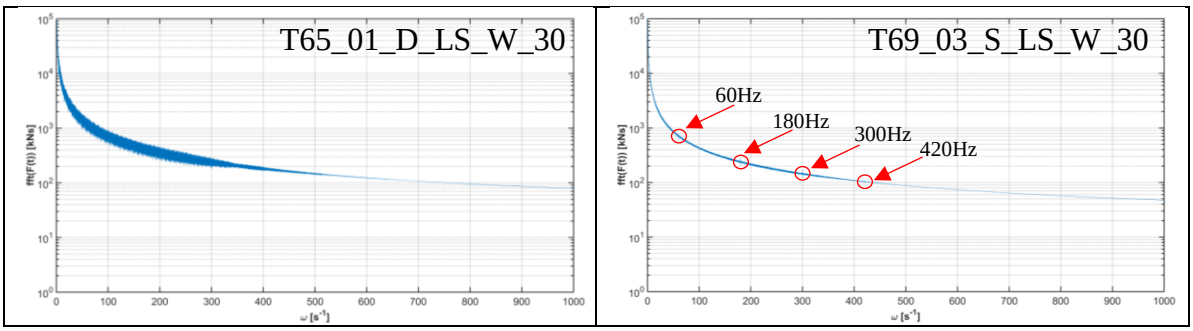

Figure Appendix C1. 2: Fourier spectra (FFT) for low speed tests with the wedge indenter and for frequencies up to 1000 Hz. Displayed are representative curves for the dry condition (D T65-01) on the left and for the submerged condition (S T69-03) on the right.

Due to the fluctuations at higher frequencies that were noticed in the dry high indentation rate tests, and for consistency (analogous to the flat indentation plate), all wedge data are filtered with a low pass filter at 200 Hz. Graphs below show two examples of high speed tests with the unfiltered (blue) and filtered (red) forces up to 150 kN. Figure Appendix C1. 3 (D T68-02) demonstrates that the low pass filter removes oscillations in the force history. The distortions are evident in terms of the large variations in the spectrum in Figure Appendix C1. 1 (left). By comparison, the effect of the low pass filter on the submerged test S T70-04 (Figure Appendix C1. 4) are minor. For data derived at low test speed, the application of the low pass filter is of negligible effect and so examples are not provided.

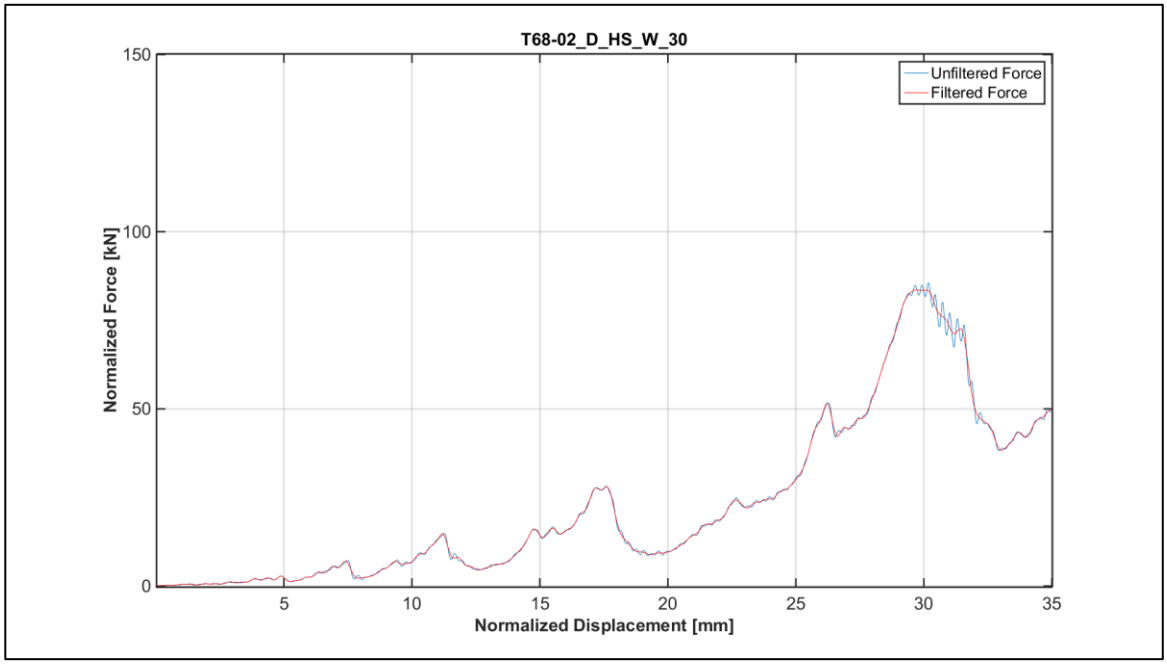

Figure Appendix C1. 3: Unfiltered (blue) and with 200 Hz low pass filtered (red) force - displacement history of test T68-02_D_HS_W_30.

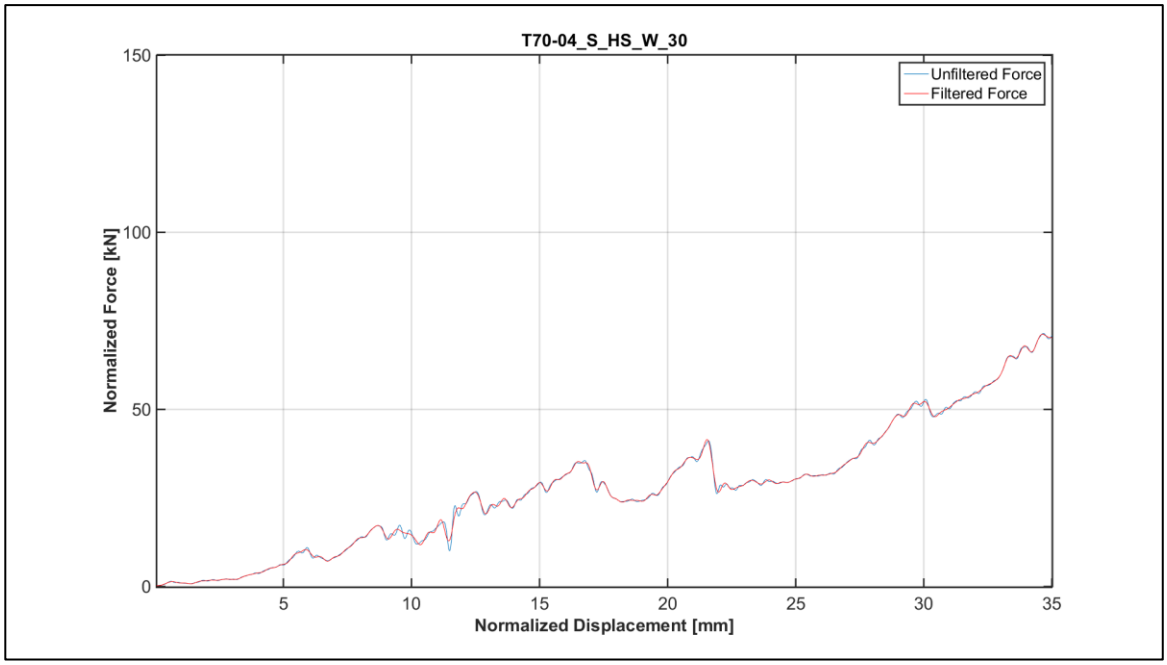

Figure Appendix C1. 4: Unfiltered (blue) and with 200 Hz low pass filtered (red) force - displacement history of test T70-04_S_HS_W_30.

Appendix C2 : Plots for 1 mm/s Indentation Rate

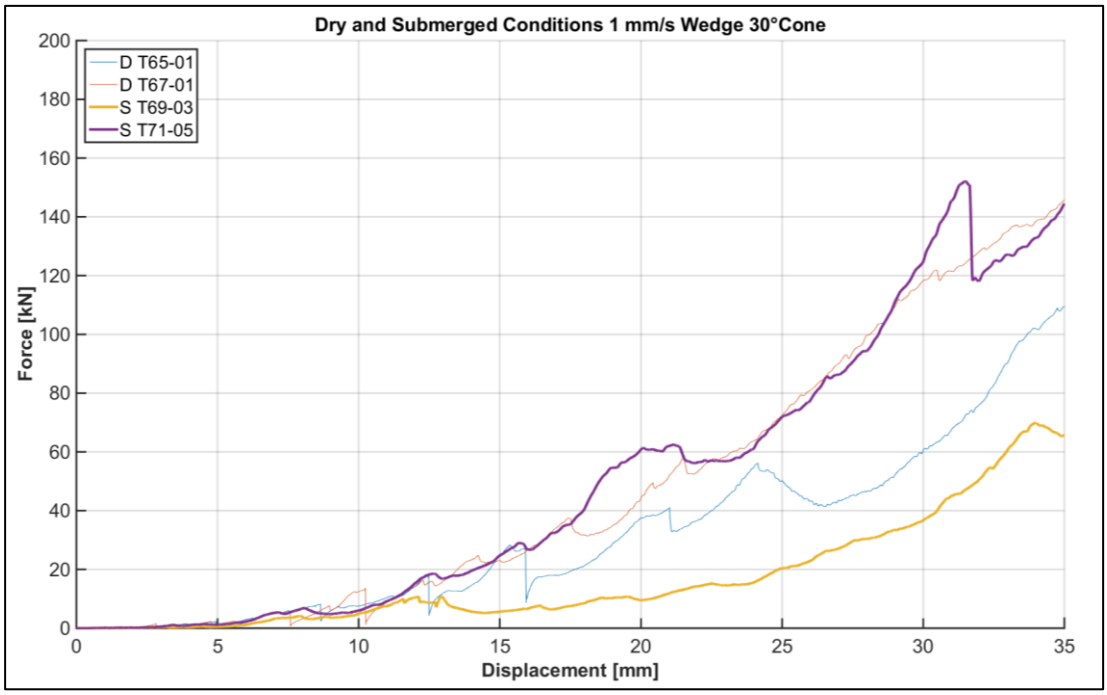

Figure Appendix C2. 1: Wedge, 1 mm/s, 30° ice specimens: force vs. displacement for individual tests in dry and submerged contact conditions.

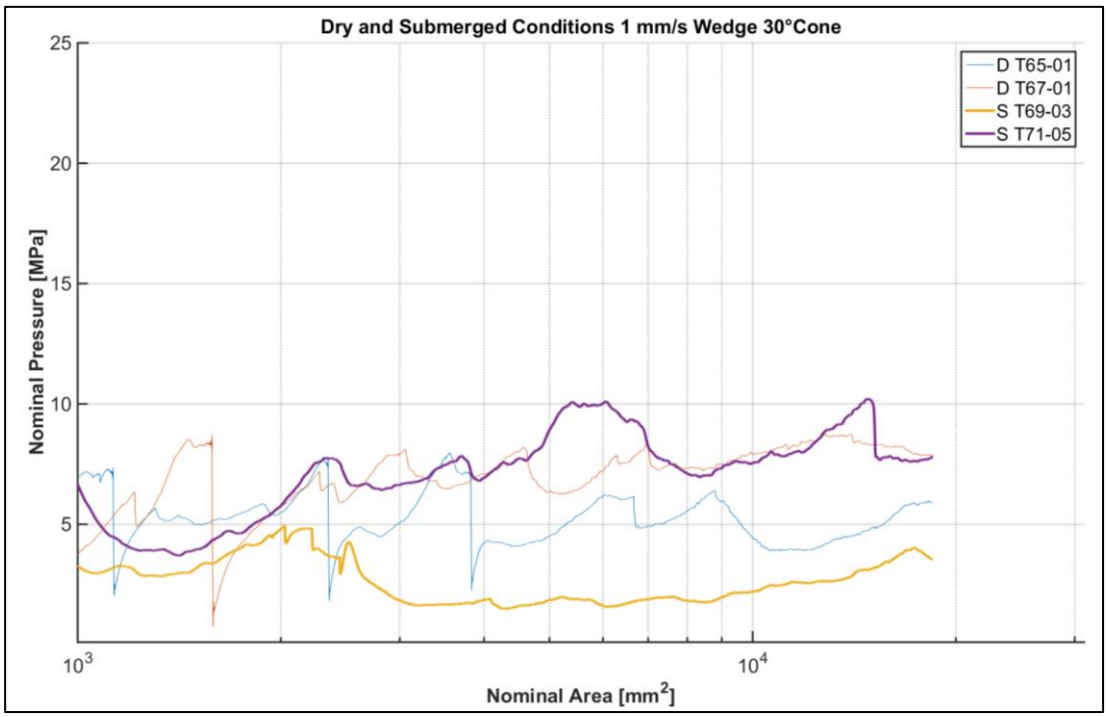

Figure Appendix C2. 2: Wedge, 1 mm/s, 30° ice specimens: nominal pressure vs. area curves for individual tests in dry and submerged contact conditions.

Appendix C3 : Plots for 100 mm/s Indentation Rate

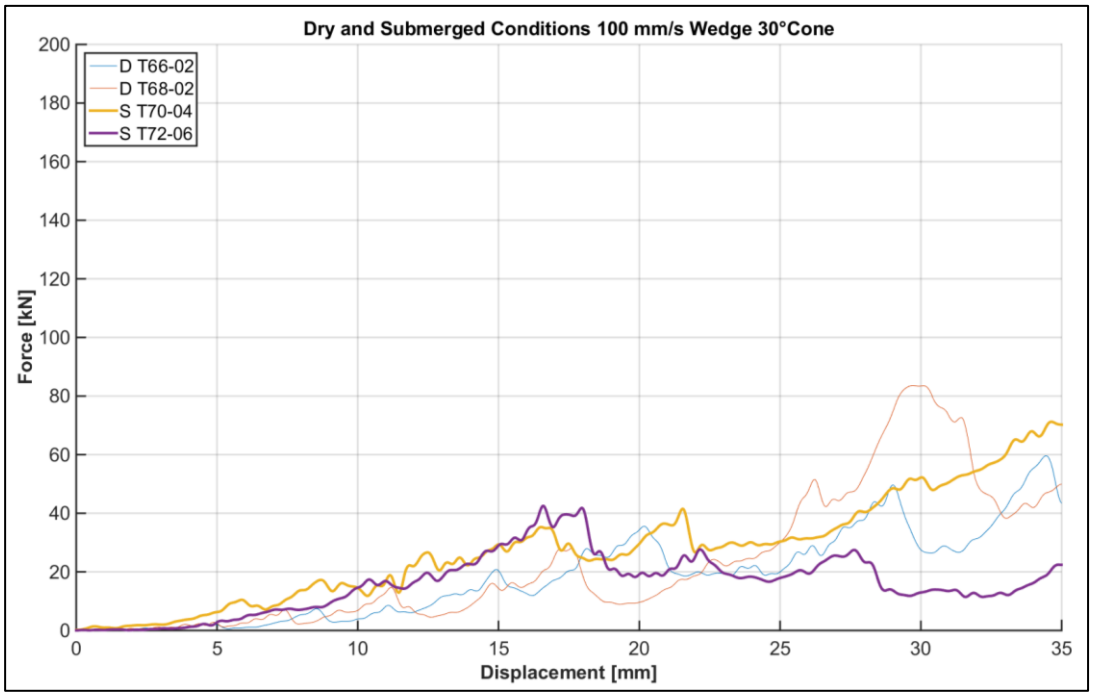

Figure Appendix C3. 1: Wedge, 100 mm/s, 30° ice specimens: force vs. displacement for individual tests in dry and submerged contact conditions.

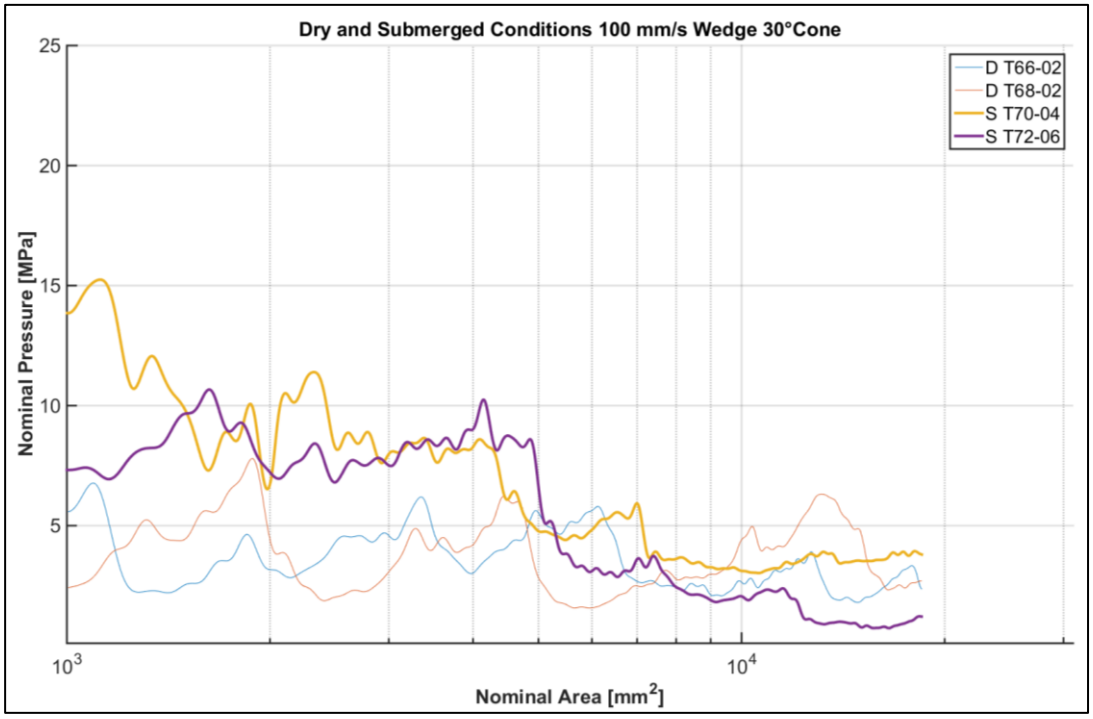

Figure Appendix C3. 2: Wedge, 100 mm/s, 30° ice specimens: nominal pressure vs. area curves for individual tests in dry and submerged contact conditions.

Appendix C4 : Pressure Patterns (Tactile Pressure Sensors)

1 mm/s – Dry and Submerged Conditions - 30° Ice Cone Angle

(Sampling Rate 100 Hz)

The following figures show the results of tests with 30° ice specimens at 1 mm/s. Dry tests are listed on the left and submerged tests on the right. The displayed tests are:

Top left:	Dry	T65_01_D_LS_W_30
Top right:	Submerged	T69_03_S_LS_W_30
Bottom left:	Dry	T67_01_D_LS_W_30
Bottom right:	Submerged	T71_05_S_LS_W_30

Penetration depth approximately 8.14 mm

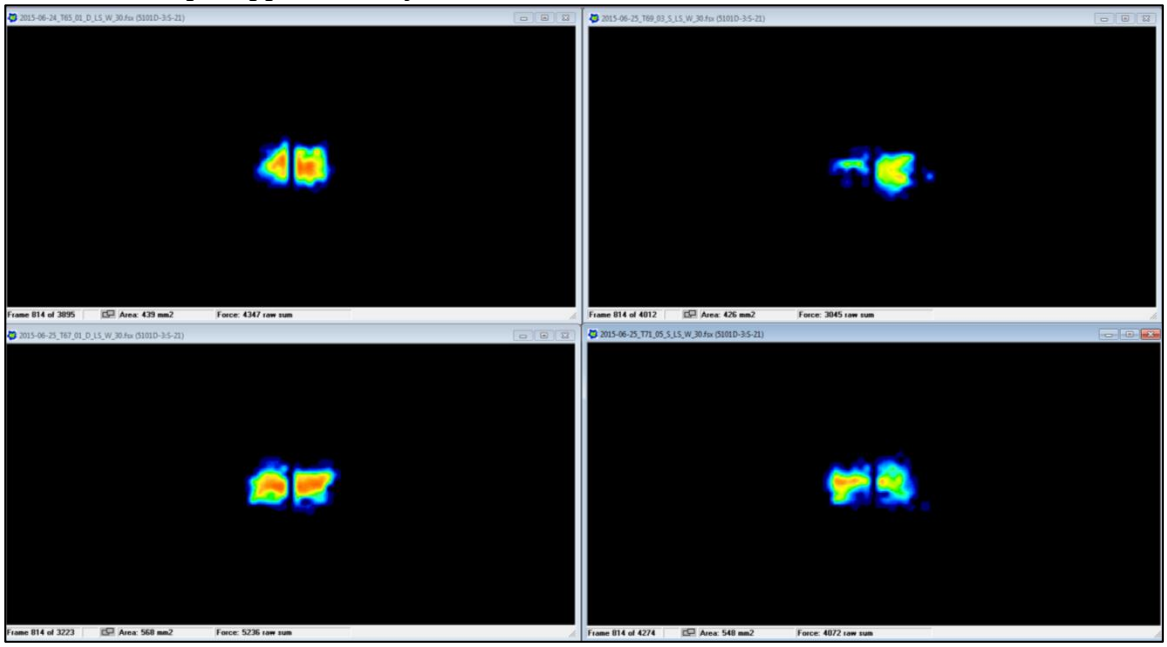

Penetration depth approximately 15 mm

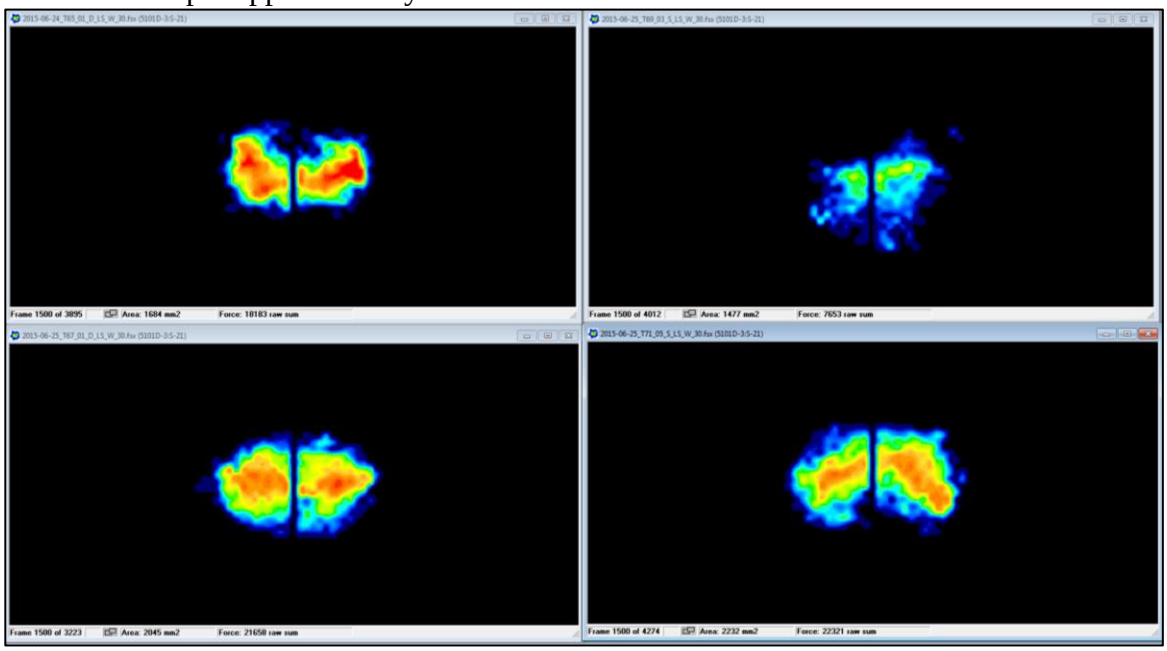

Penetration depth approximately 25 mm

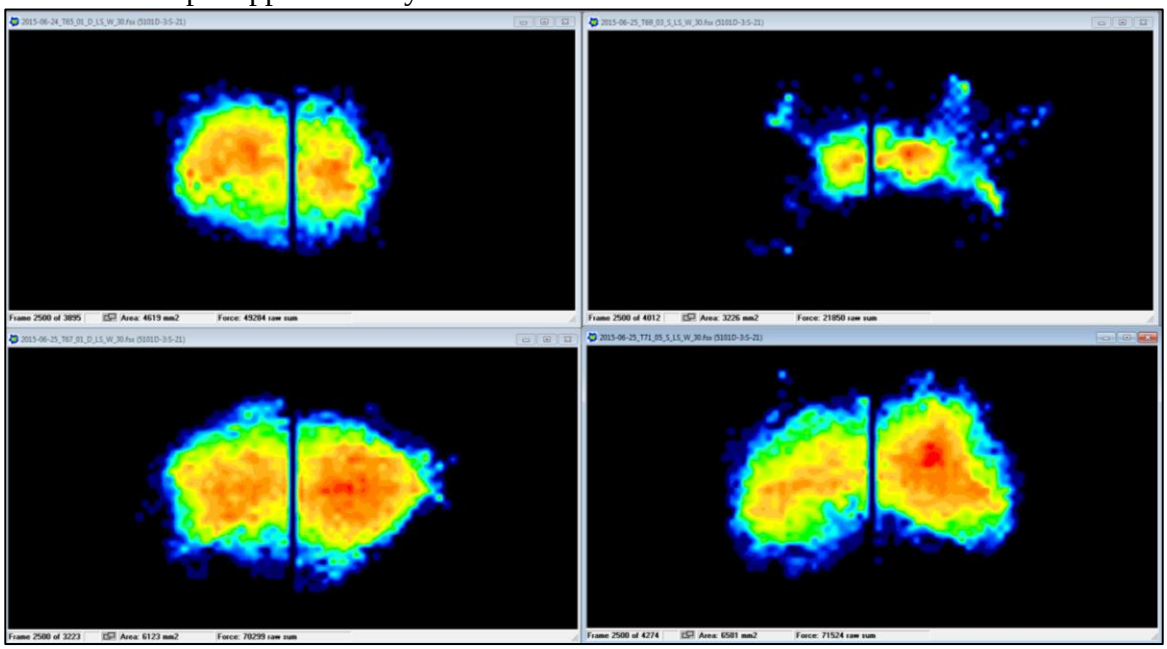

Penetration depth approximately 35 mm

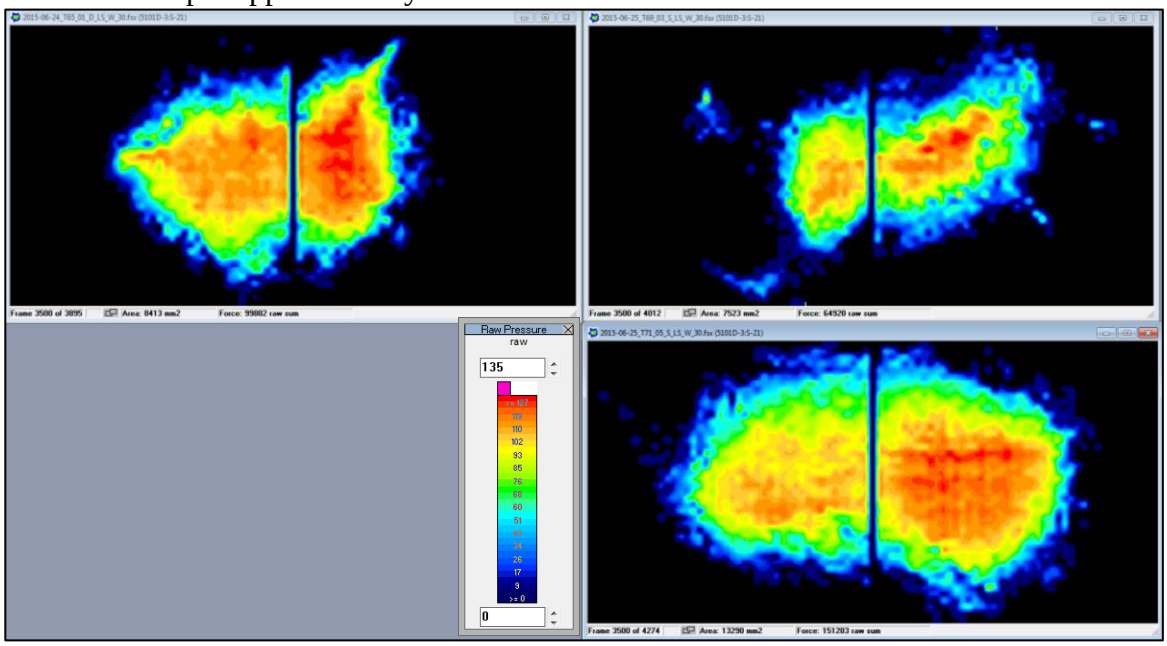

The table below lists contact area and for raw force as it was obtained from the tactile pressure sensors.

Depth [mm]	Condition	Dry		Submerged		Nominal Area
	Test	T65-01	T67-01	T69-03	T71-05	
5.0	Area [mm^2]	110	219	135	329	377
	Raw Force	599	1644	761	2013	-
8.1	Area [mm^2]	439	568	426	548	1000
	Raw Force	4347	5236	3045	4072	-
10.0	Area [mm^2]	587	748	735	890	1509
	Raw Force	5622	7034	6140	7321	-
15.0	Area [mm^2]	1684	2045	1477	2232	3396
	Raw Force	18183	21658	7653	22321	-
20.0	Area[mm^2]	2710	3774	1800	4658	6037
	Raw Force	30915	42381	11104	49743	-
25.0	Area [mm^2]	4619	6123	3226	6581	9434
	Raw Force	49284	70299	21850	71524	-
30.0	Area[mm^2]	5284	8697	4523	9845	13584
	Raw Force	55399	106626	39675	121913	-
35.0	Area[mm^2]	8413	-	7523	13290	18490
	Raw Force	99802	-	64920	151283	-

100 mm/s – Dry and Submerged Conditions –30° Ice Cone Angles

(Sampling Rate 100 Hz)

The following figures show the results of tests with 30° ice specimens at 100 mm/s. Dry tests are lists on the left and submerged tests on the right. The displayed tests are:

Top left:	Dry	T66_02_D_HS_W_30
Top right:	Submerged	T70_04_S_HS_W_30
Bottom left:	Dry	T68_02_D_HS_W_30
Bottom right:	Submerged	T72_06_S_HS_W_30

Penetration depth approximately 5 mm

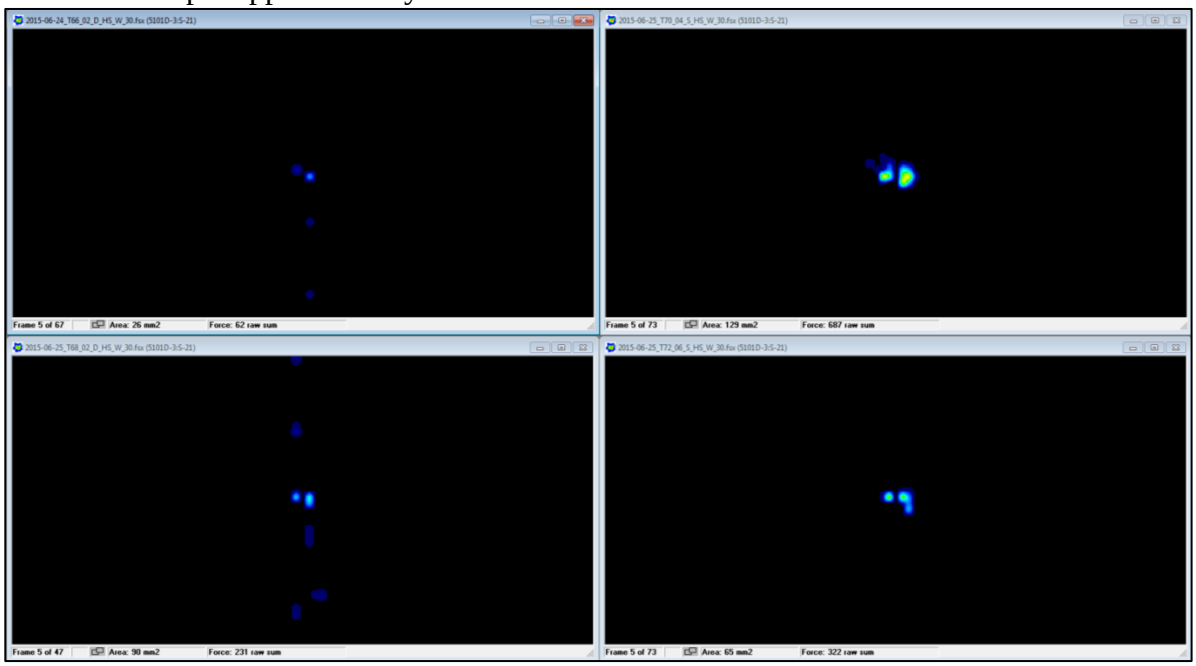

Penetration depth approximately 8 mm (nominal contact area 1000 mm^2)

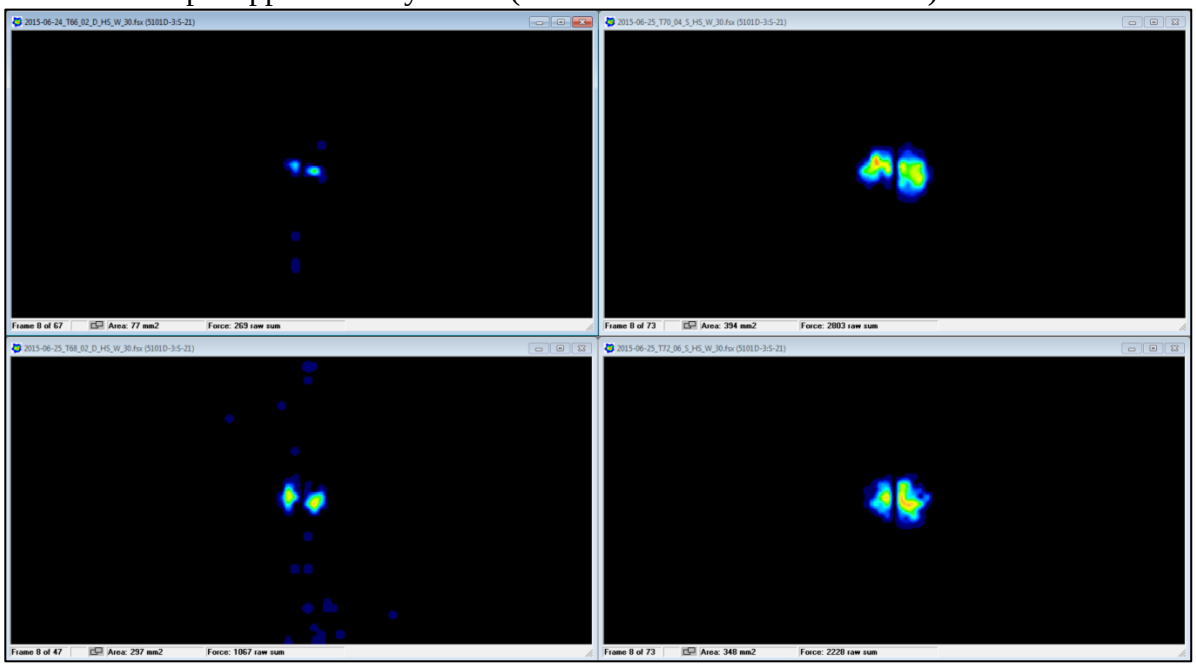

Penetration depth approximately 10 mm

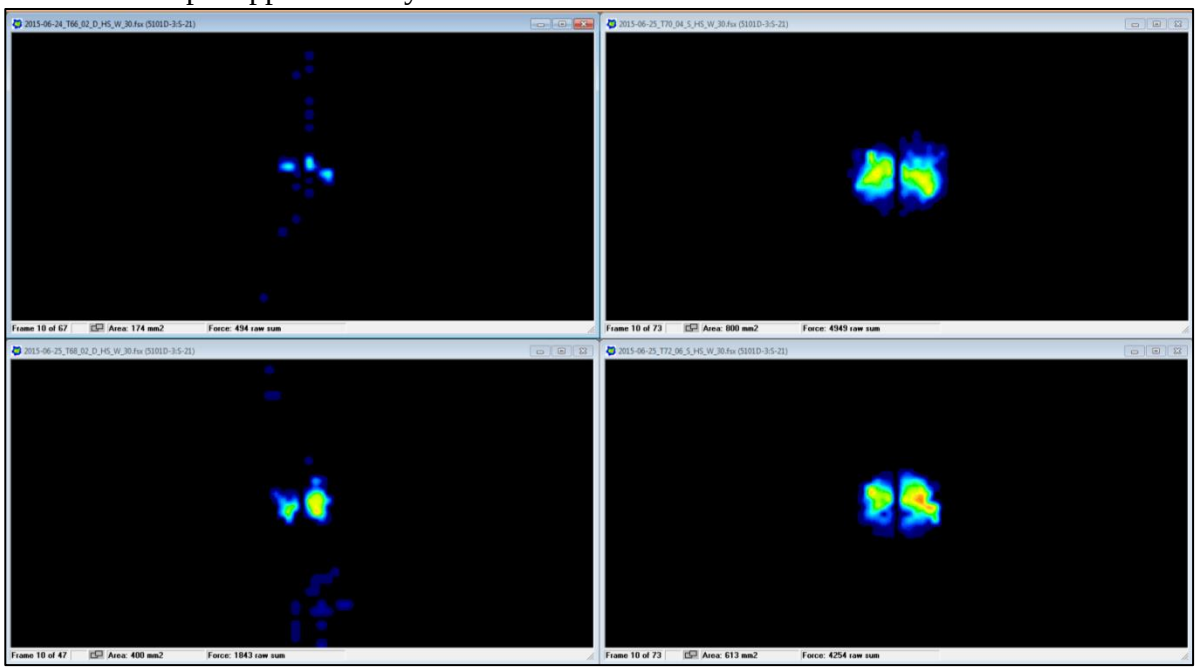

Penetration depth approximately 15 mm

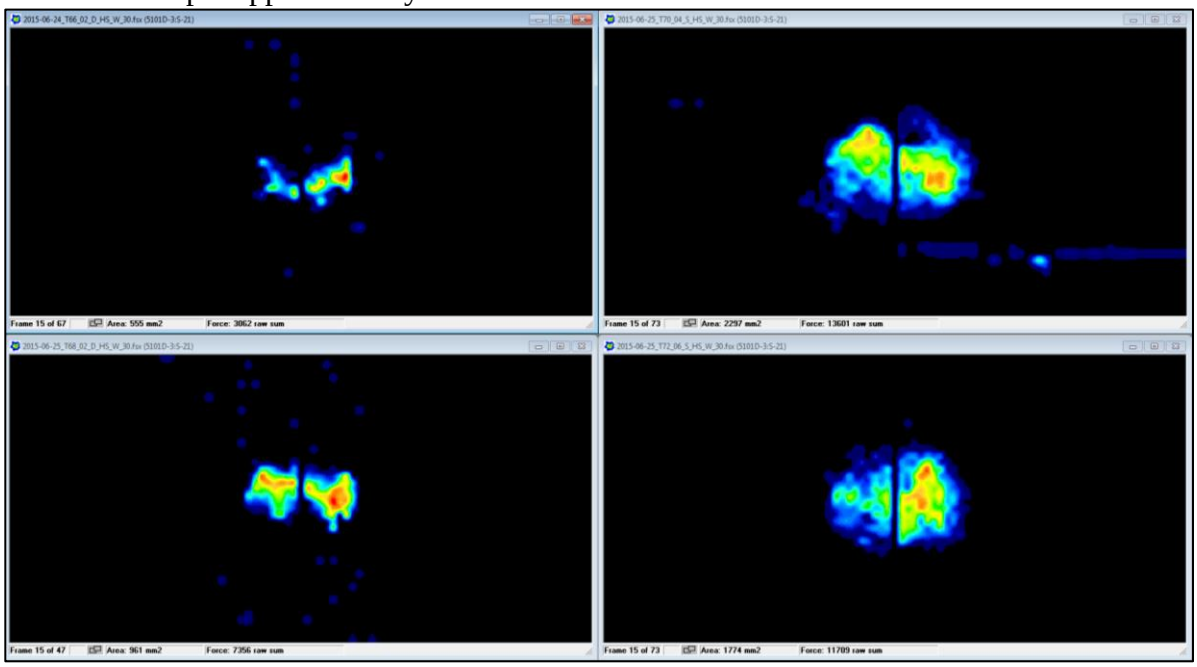

Penetration depth approximately 20 mm

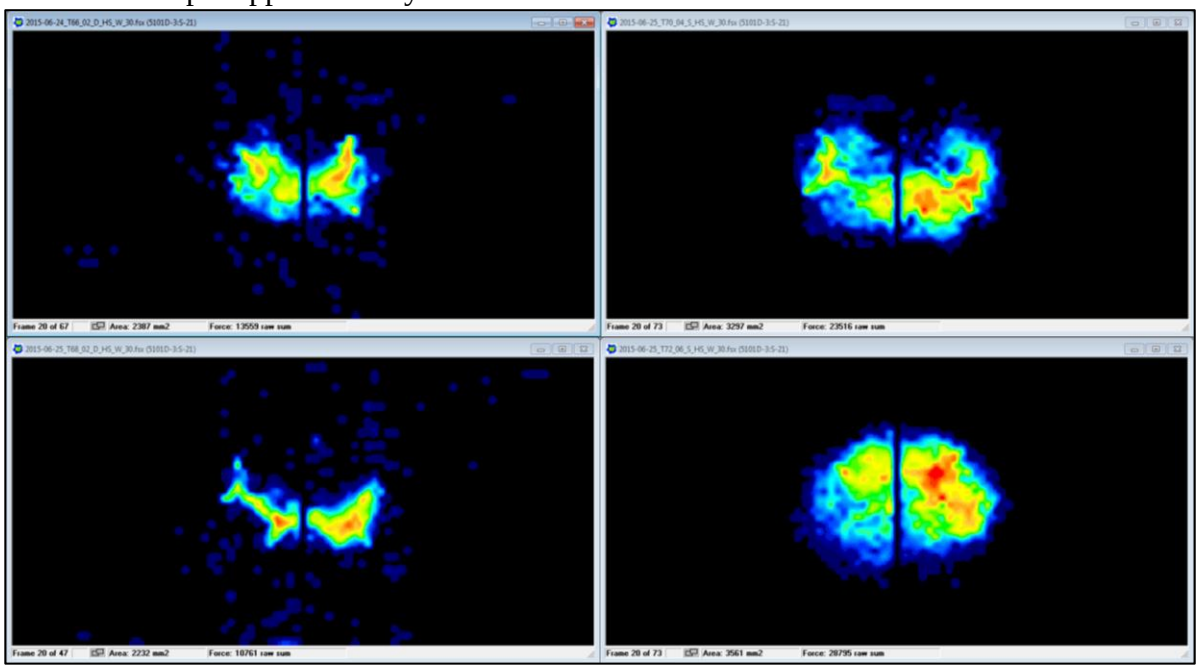

Penetration depth approximately 25 mm

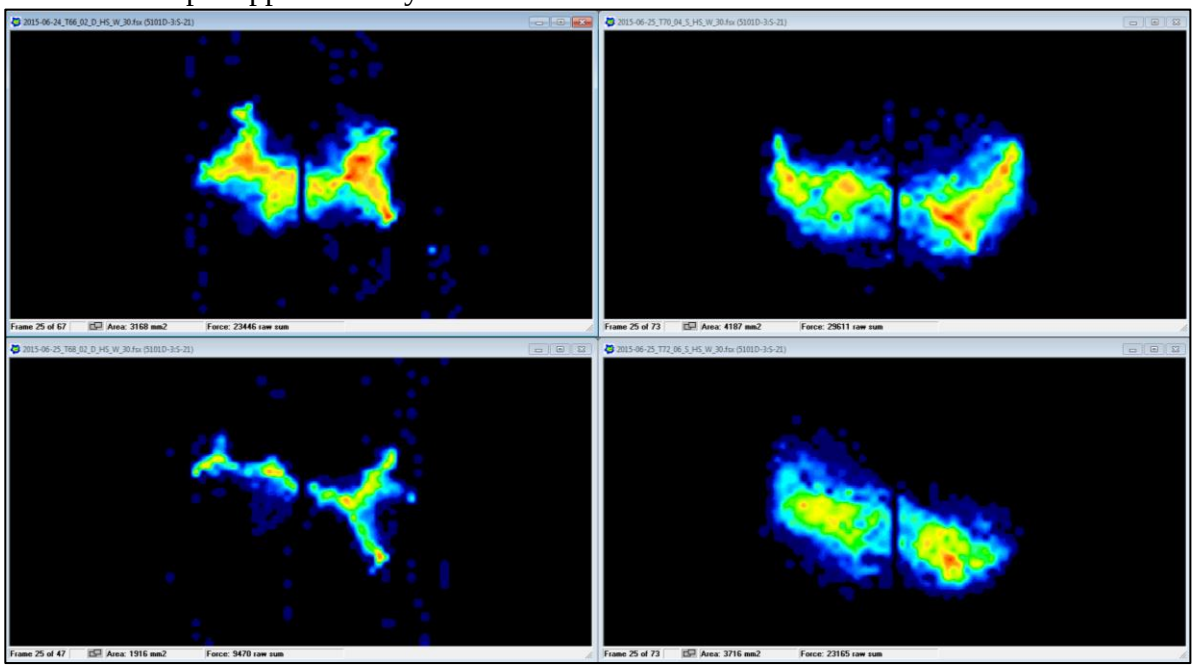

Penetration depth approximately 30 mm

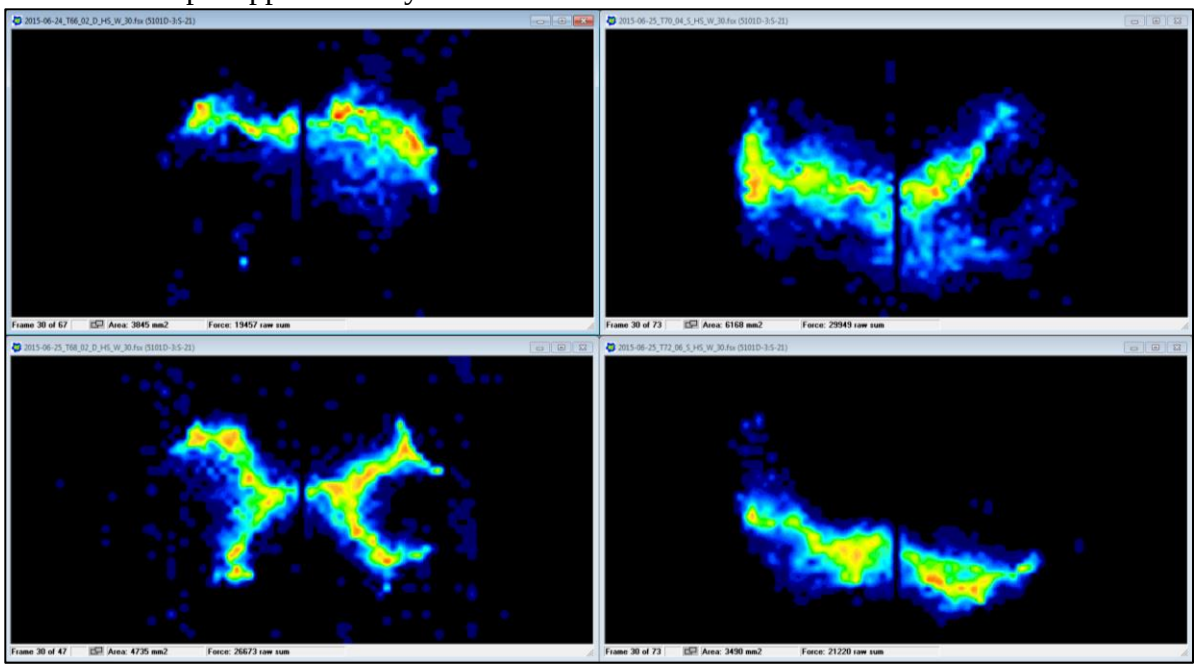

Penetration depth approximately 35 mm

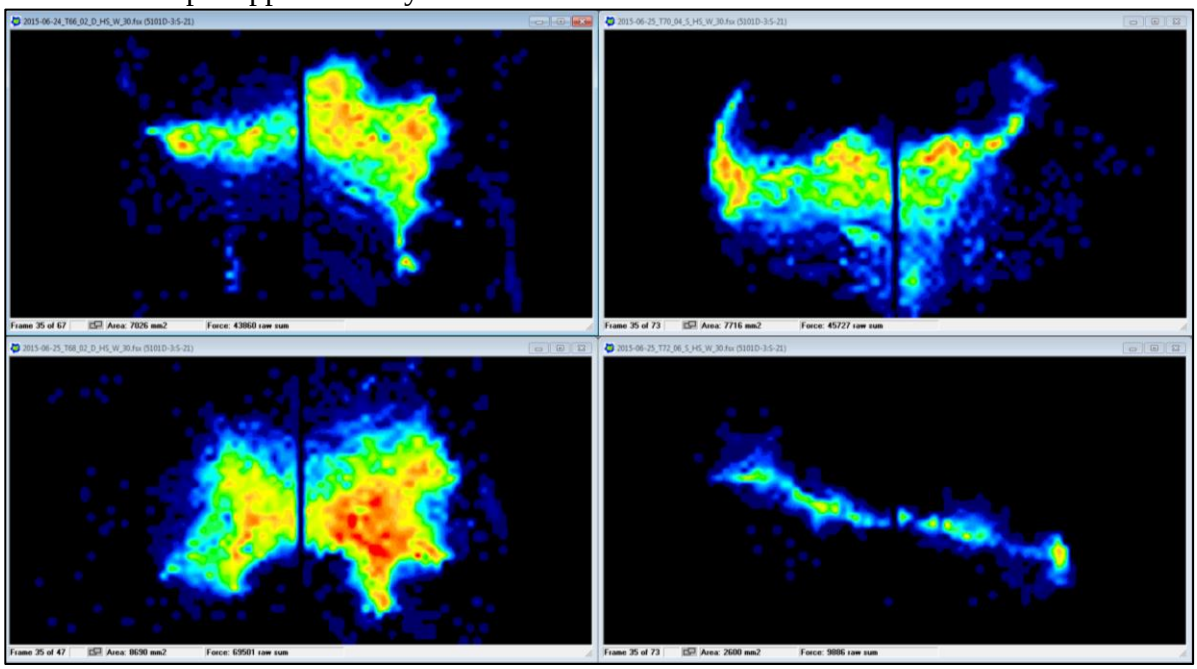

Penetration depth approximately 40 mm

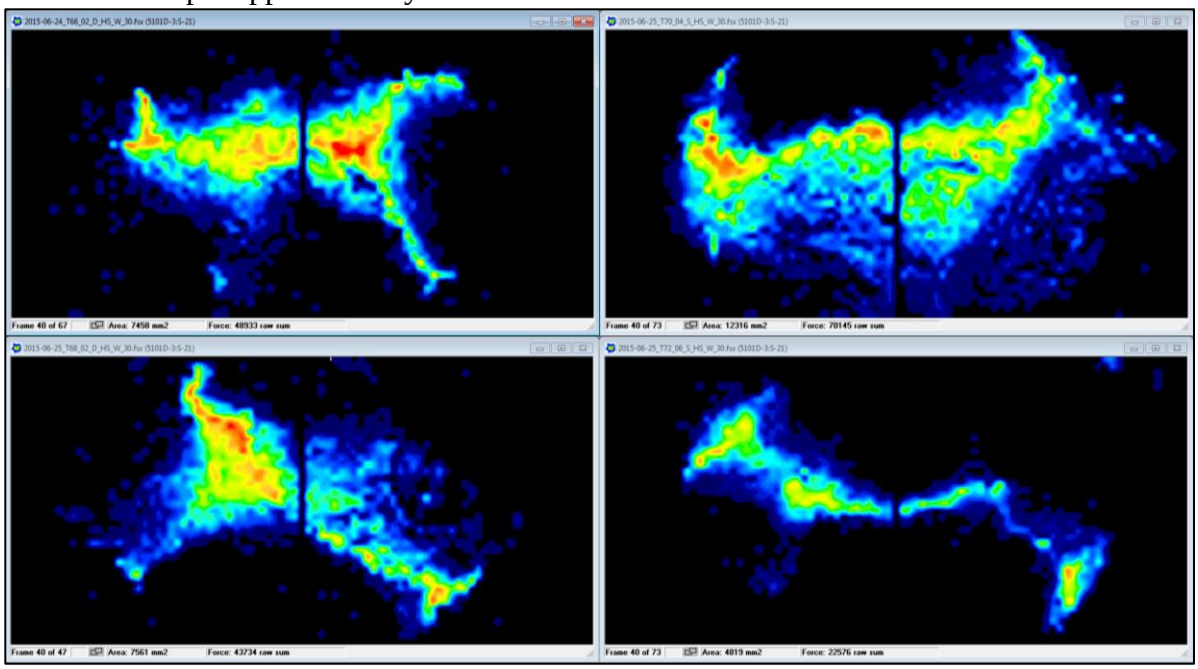

Penetration depth approximately 45 mm

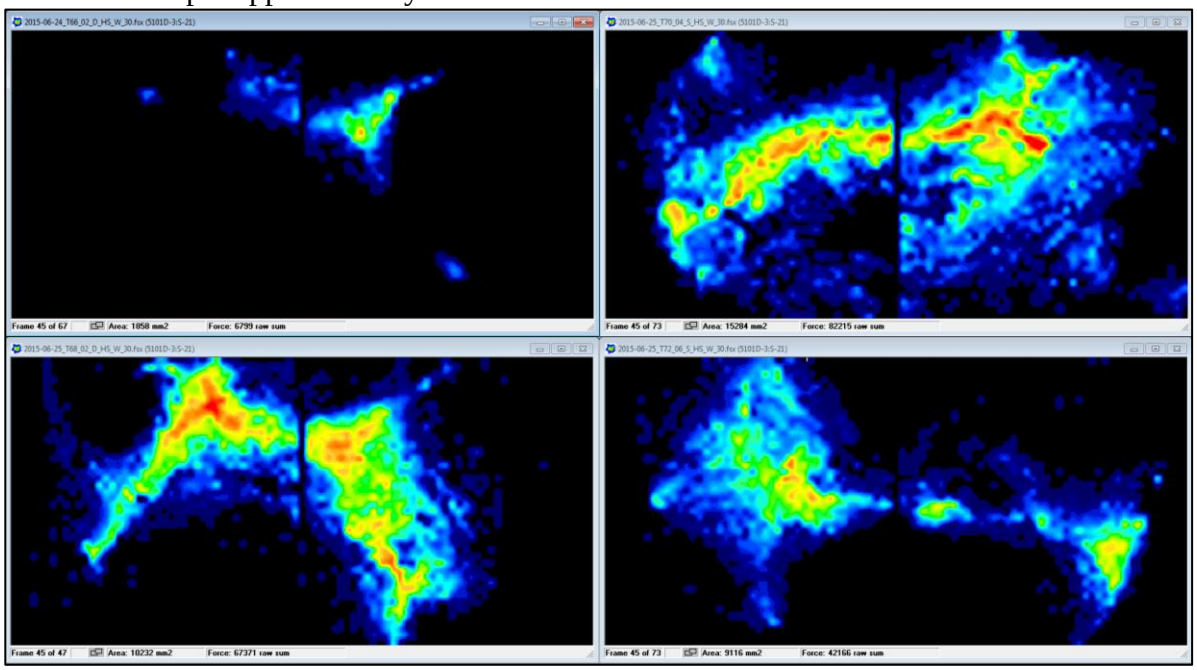

Depth [mm]	Condition	Dry		Submerged		Nominal Area
	Test	T66-02	T68-02	T70-04	T72-06	
5.0	Area [mm^2]	26	90	129	65	377
	Raw Force	62	231	687	322	-
8.0	Area [mm^2]	77	297	394	348	1000
	Raw Force	269	1067	2803	2228	-
10.0	Area [mm^2]	174	400	800	613	1509
	Raw Force	494	1843	4949	4254	-
15.0	Area [mm^2]	555	961	2297	1774	3396
	Raw Force	3062	7356	13601	11709	-
18.0	Area [mm^2]	1290	968	2852	2490	4890
	Raw Force	8642	4793	19290	21031	-
20.0	Area[mm^2]	2387	2232	3297	3561	6037
	Raw Force	13559	10761	23516	28795	-
25.0	Area [mm^2]	3168	1916	4187	3716	9434
	Raw Force	23446	9470	29611	23165	-
30.0	Area[mm^2]	3845	4735	6168	3490	13584
	Raw Force	19457	26673	29949	21220	-
35.0	Area[mm^2]	7026	8690	7716	2600	18490
	Raw Force	43860	69501	45727	9886	-
40.0	Area[mm^2]	7458	7561	12316	4819	24150
	Raw Force	48933	43734	70145	22576	-
45.0	Area[mm^2]	1858	10232	15284	9116	30565
	Raw Force	6799	67371	82215	42166	-

Appendix C5 : Microstructural Observations

1 mm/s

Dry	Submerged
n/a	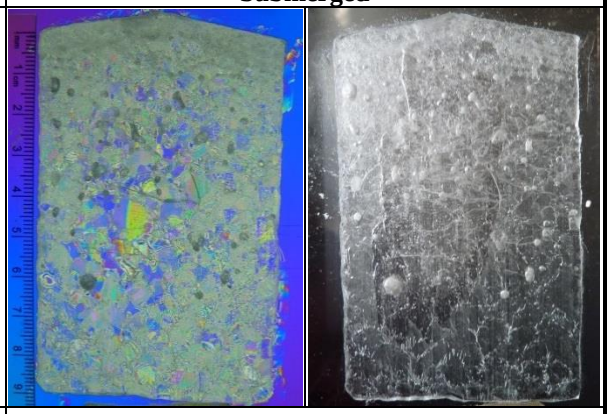
T65_01_D_LS_W_30	T69_03_S_LS_W_30

100 mm/s

Dry	Submerged
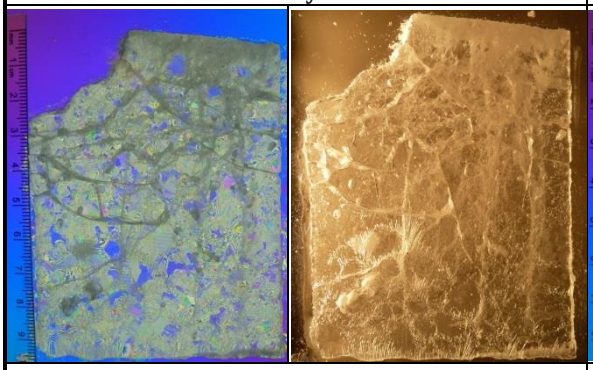	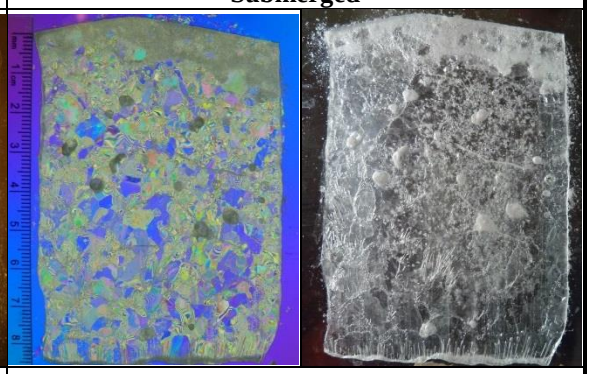
T66_02_D_HS_W_30	T70_04_S_HS_W_30

Remark:

T66-02: The large visible fractures are the result of the shaping process with the microtome.

Appendix C6 : Multiple Regression Analysis

Mean Force Overall

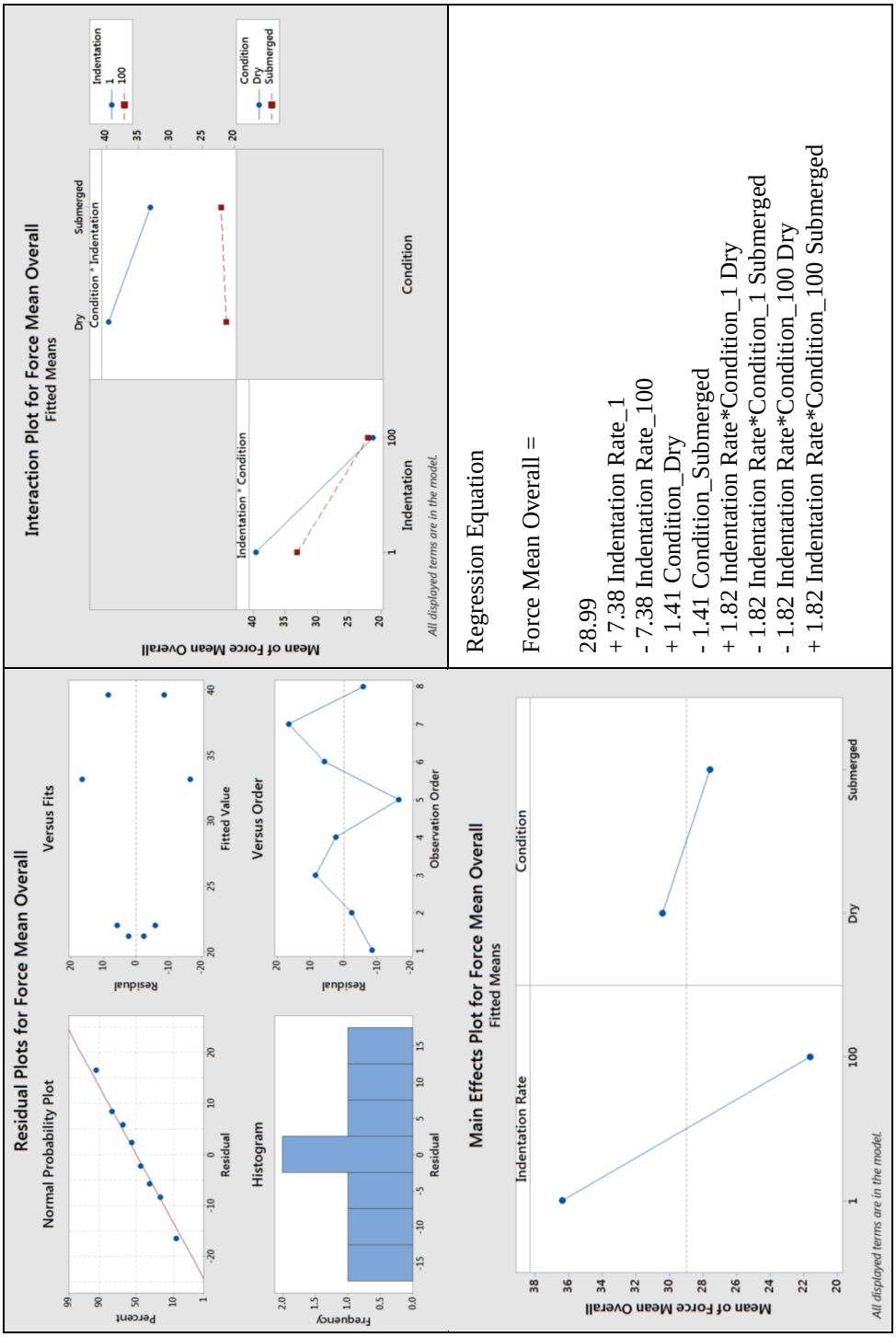

Regression Equation

Force Mean Overall =

28.99
+ 7.38 Indentation Rate_1
- 7.38 Indentation Rate_100
+ 1.41 Condition_Dry
- 1.41 Condition_Submerged
+ 1.82 Indentation Rate*Condition_1 Dry
- 1.82 Indentation Rate*Condition_1 Submerged
- 1.82 Indentation Rate*Condition_100 Dry
+ 1.82 Indentation Rate*Condition_100 Submerged

Mean Force Above 1000 mm^2

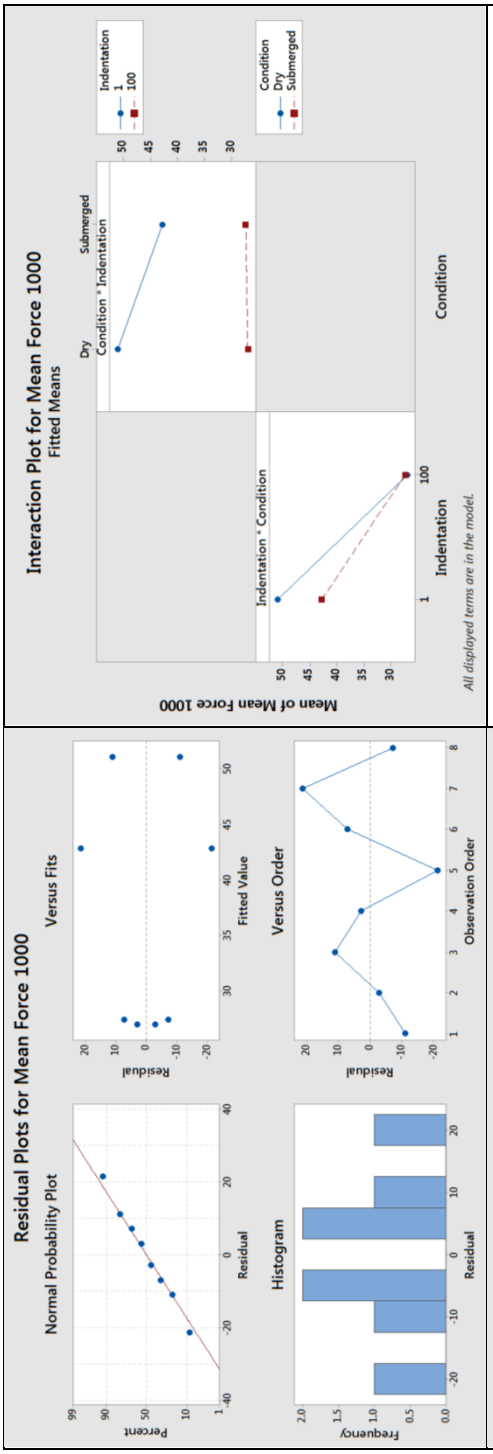

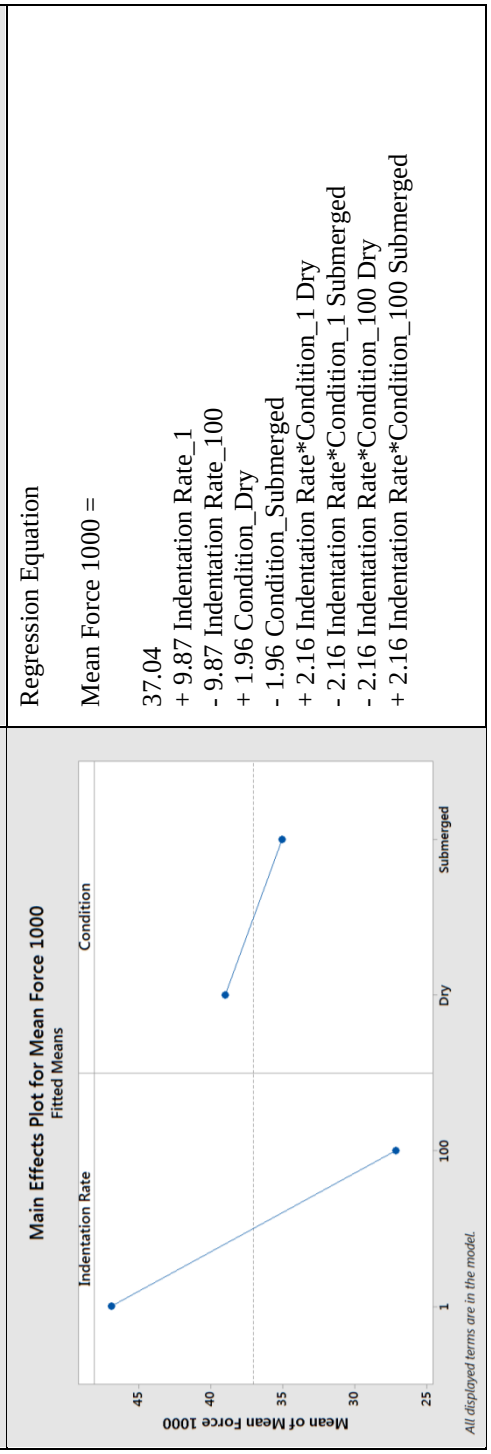

Regression Equation

Mean Force 1000 =

37.04
+ 9.87 Indentation Rate_1
- 9.87 Indentation Rate_100
+ 1.96 Condition_Dry
- 1.96 Condition_Submerged
+ 2.16 Indentation Rate*Condition_1 Dry
- 2.16 Indentation Rate*Condition_1 Submerged
- 2.16 Indentation Rate*Condition_100 Dry
+ 2.16 Indentation Rate*Condition_100 Submerged

Mean Pressure Above 1000 mm^2

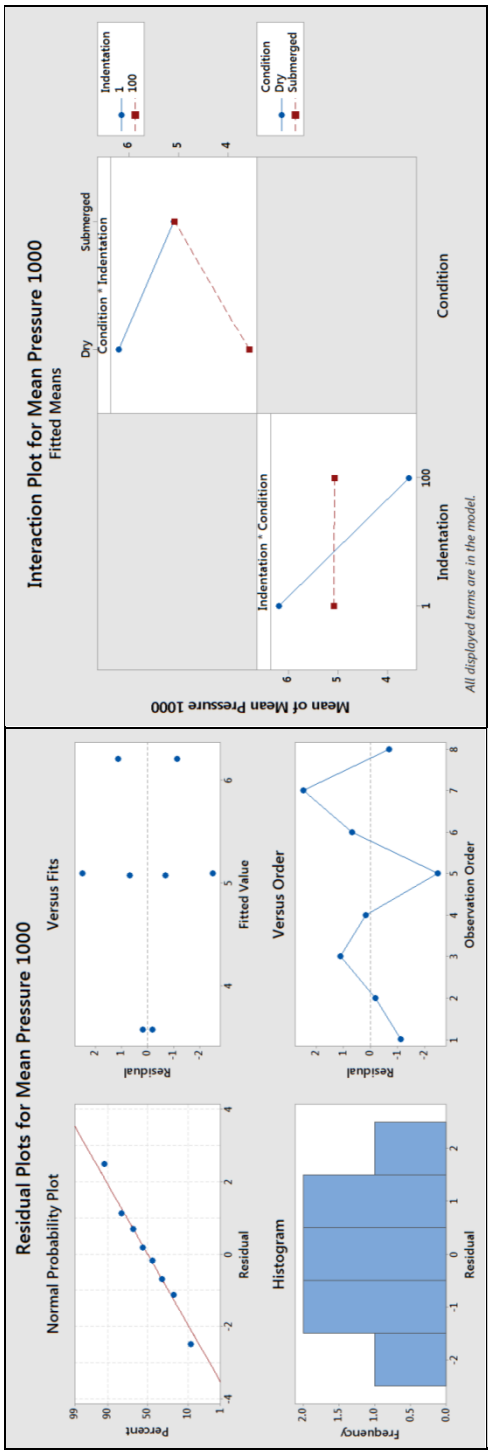

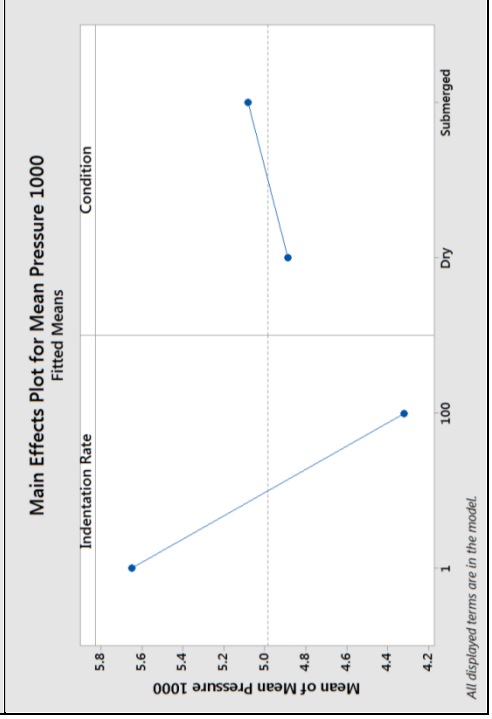

Regression Equation

Mean Pressure 1000 =

4.984
+ 0.665 Indentation Rate_1
- 0.665 Indentation Rate_100
- 0.097 Condition_Dry
+ 0.097 Condition_Submerged
+ 0.655 Indentation Rate*Condition_1 Dry
- 0.655 Indentation Rate*Condition_1 Submerged
- 0.655 Indentation Rate*Condition_100 Dry
+ 0.655 Indentation Rate*Condition_100 Submerged

Maximal Nominal Pressure Above 1000 mm^2

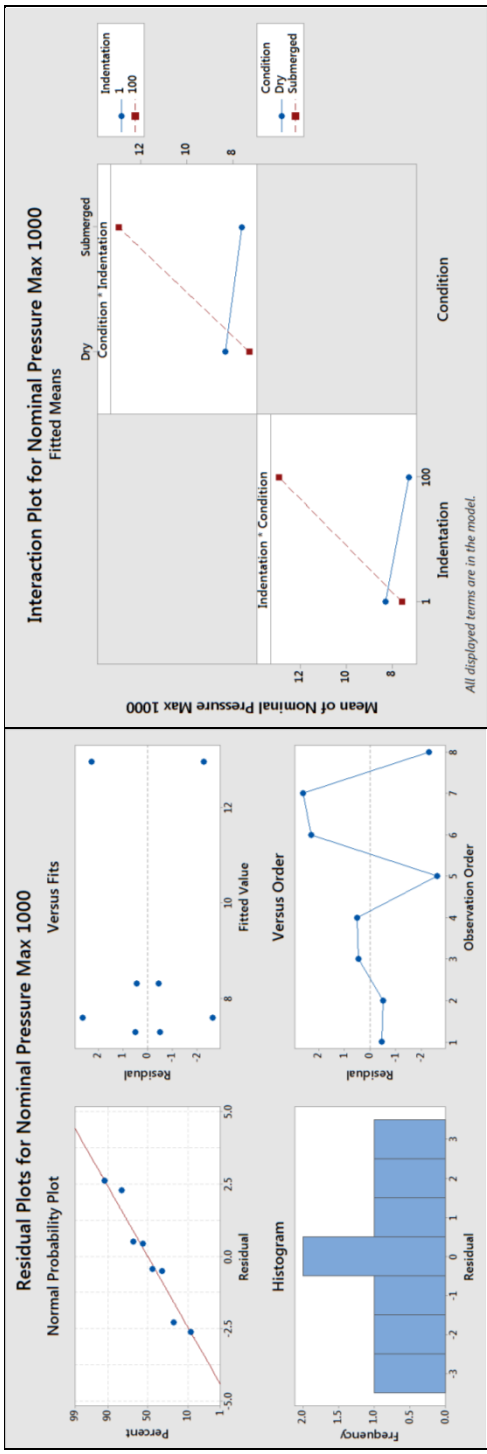

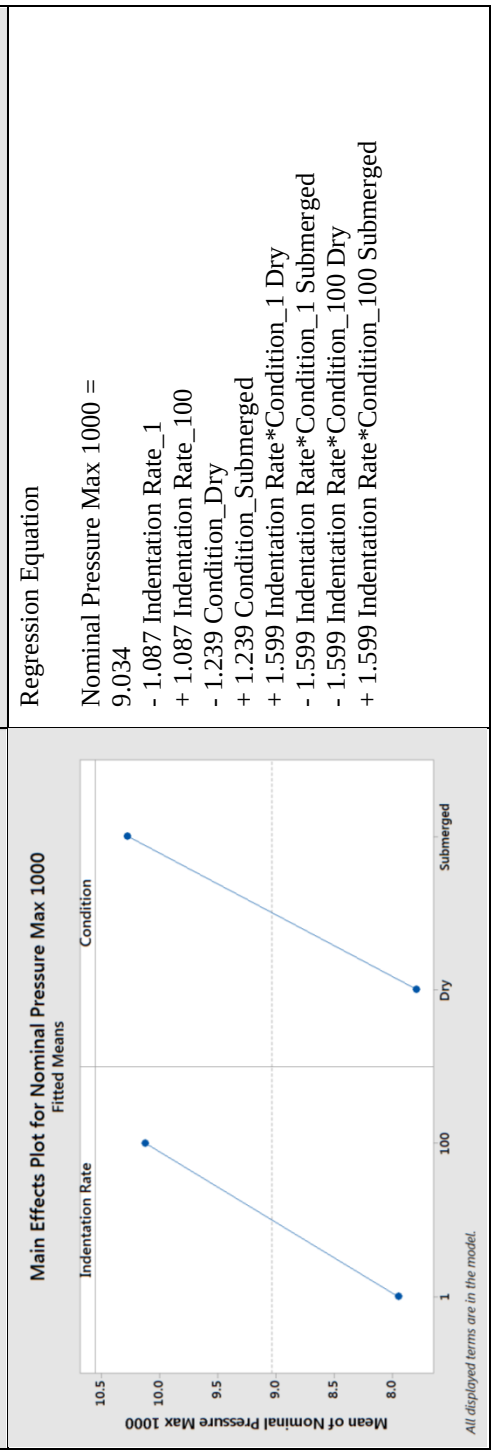

Regression Equation

Nominal Pressure Max 1000 =
9.034
- 1.087 Indentation Rate_1
+ 1.087 Indentation Rate_100
- 1.239 Condition_Dry
+ 1.239 Condition_Submerged
+ 1.599 Indentation Rate*Condition_1 Dry
- 1.599 Indentation Rate*Condition_1 Submerged
- 1.599 Indentation Rate*Condition_100 Dry
+ 1.599 Indentation Rate*Condition_100 Submerged

Appendix D : Conical Indenter

Appendix D1 : Spectral Analysis (FFT)

Tests with the conical indenter involved 30° ice cones in dry and submerged conditions at 1 mm/s and 100 mm/s. Figure Appendix D1. 1 shows Fourier spectra of high speed tests, for a dry test (D T45-03) on the left, and for a submerged test (S T57-02) on the right. For test D T45-03 a significant drop at 278 Hz is visible that is followed by large fluctuations up to about 351 Hz. A similar result was also observed in spectra of the other two dry high speed tests (not displayed). In contrast, amplitudes of submerged tests are somewhat smaller and have no drops, suggesting a dampening effect of water during the impact (Figure Appendix D1. 1, right).

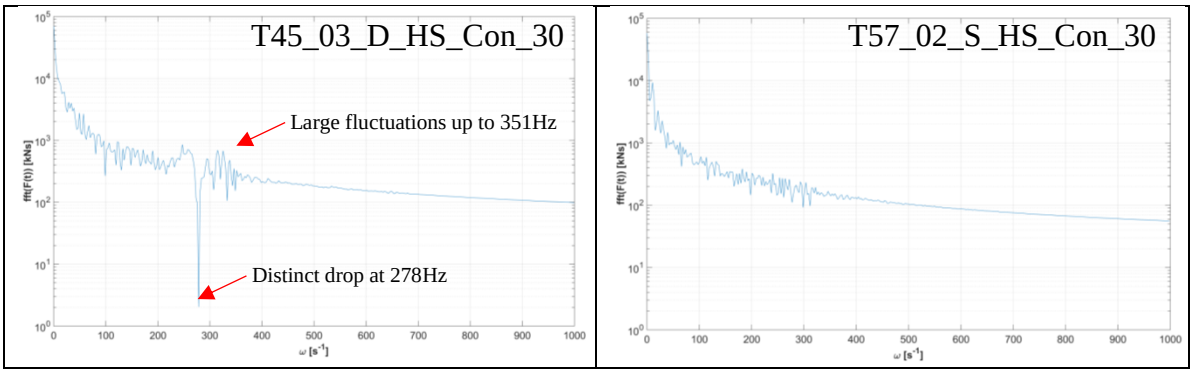

Figure Appendix D1. 1: Fourier spectra (FFT) for high speed tests with the conical indenter and for frequencies up to 1000 Hz. Displayed are curves for the dry condition (T45-03) on the left and for the submerged condition (T57-02) on the right.

Because of the distinct drops at high frequencies in two out of three high speed tests and the subsequent large deviations, the data are processed with a low pass filter at 200 Hz. Figure Appendix D1. 2 and Figure Appendix D1. 3 display the unfiltered (blue) and filtered (red) force histories of the aforementioned tests. In the filtered curves, the oscillations are removed.

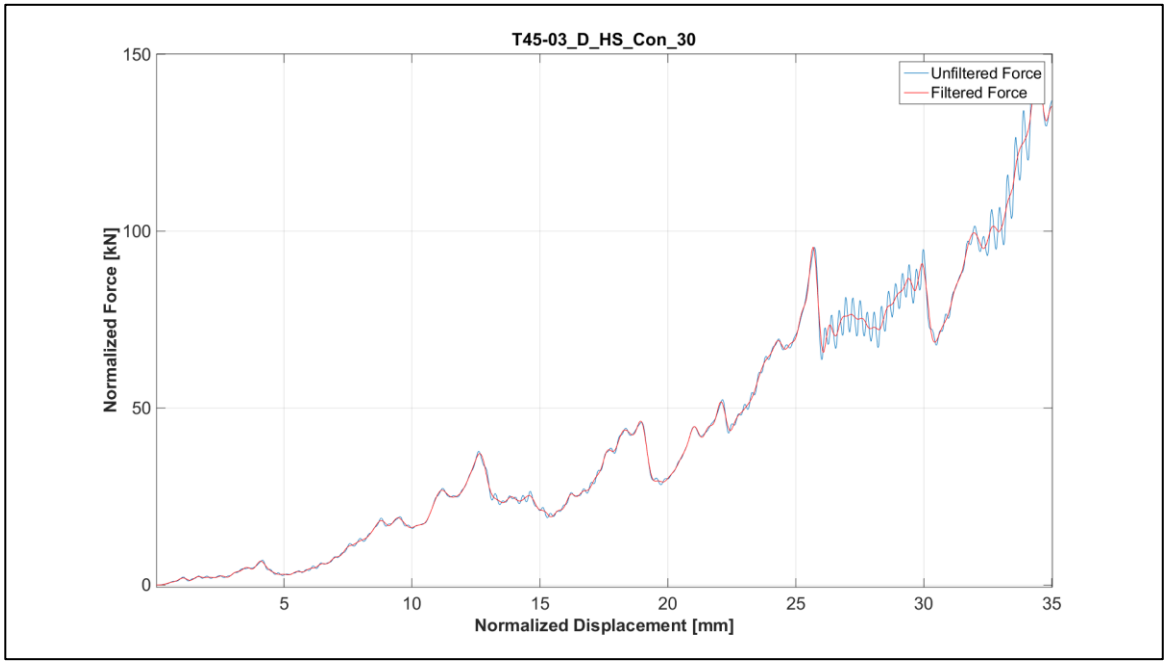

Figure Appendix D1. 2: Unfiltered (blue) and with 200 Hz low pass filtered (red) force - displacement history of test T45-03_D_HS_Con_30.

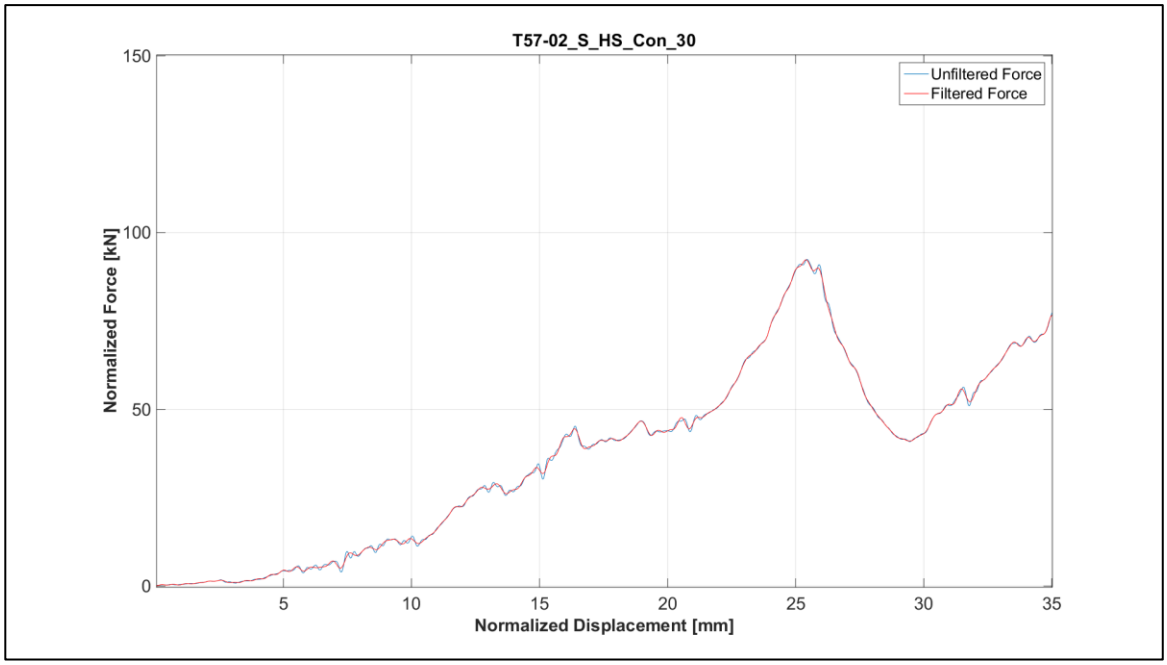

Figure Appendix D1. 3: Unfiltered (blue) and with 200 Hz low pass filtered (red) force - displacement history of test T57-02_S_HS_Con_30.

At 1 mm/s indentation rate, a smaller difference between the spectra for dry and submerged condition emerges. The shapes typically have a band-like appearance that only differs slightly in breadth (Figure Appendix D1. 4). It indicates that the contact condition does not affect the crushing event at the low indentation rate as significantly as it does at the high indentation rate.

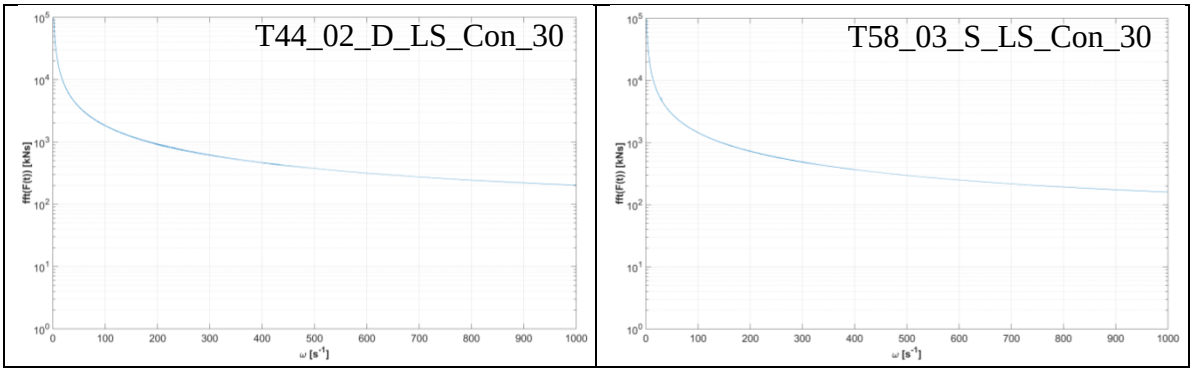

Figure Appendix D1. 4: Fourier spectra (FFT) for low speed tests with the wedge indenter and for frequencies up to 1000 Hz. Displayed are representative curves for the dry condition (T44-02) on the left and for the submerged condition (T58-03) on the right.

Because two out of three high speed tests have distinct drops in high frequencies that are followed by large deviations, all data of the conical indenter are processed with a low pass filter at 200 Hz, consistent with the procedures used for the flat indentation plate and the wedge shaped indenter. As in other tests, filtering the data of low speed tests does not lead to any significant change and thus no figures are provided.

Appendix D2 : Plots for 1 mm/s Indentation Rate

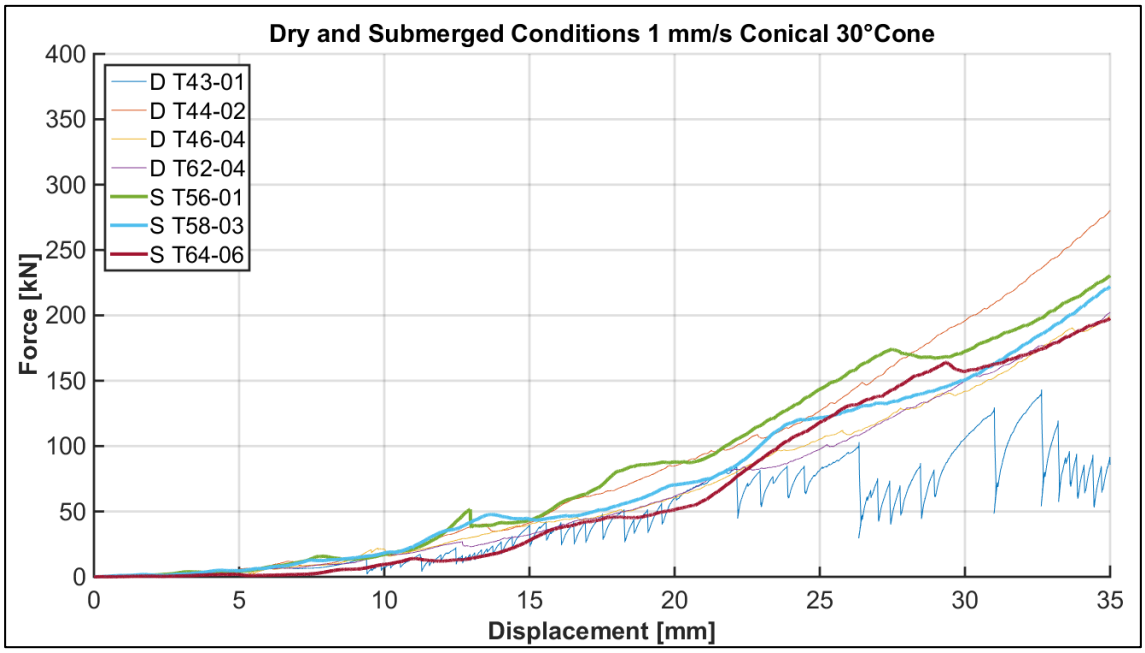

Figure Appendix D2. 1: Conical indenter, 1 mm/s, 30° ice specimens: force vs. displacement for individual tests in dry and submerged contact conditions.

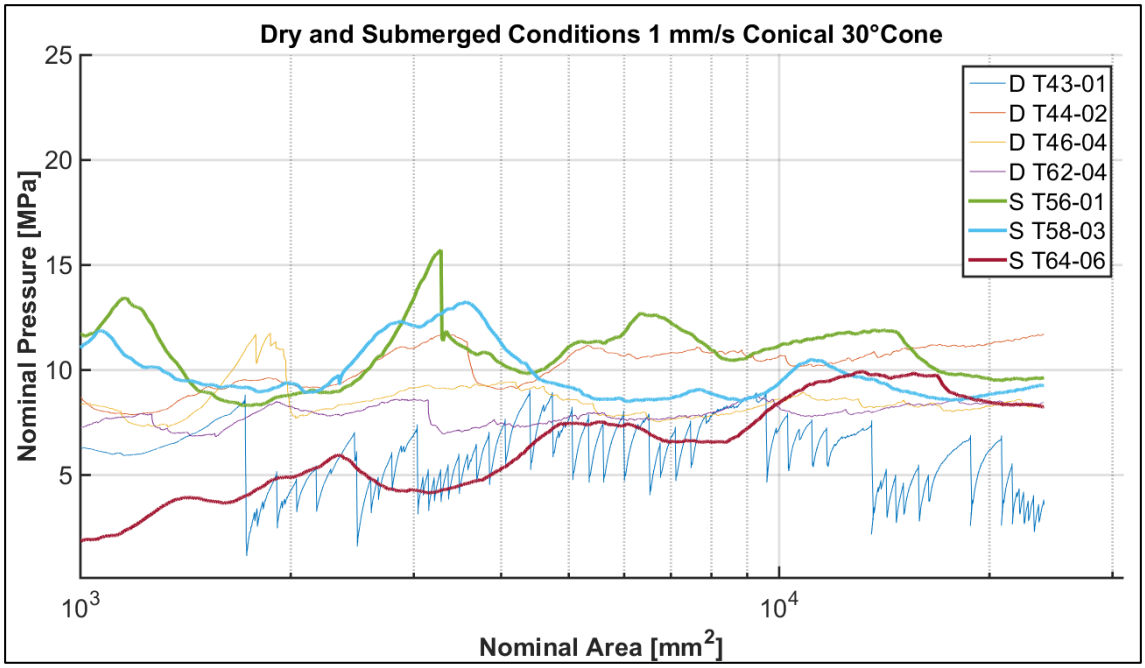

Figure Appendix D2. 2: Conical indenter, 1 mm/s, 30° ice specimens: nominal pressure vs. area curves for individual tests in dry and submerged contact conditions.

Appendix D3 : Plots for 100 mm/s Indentation Rate

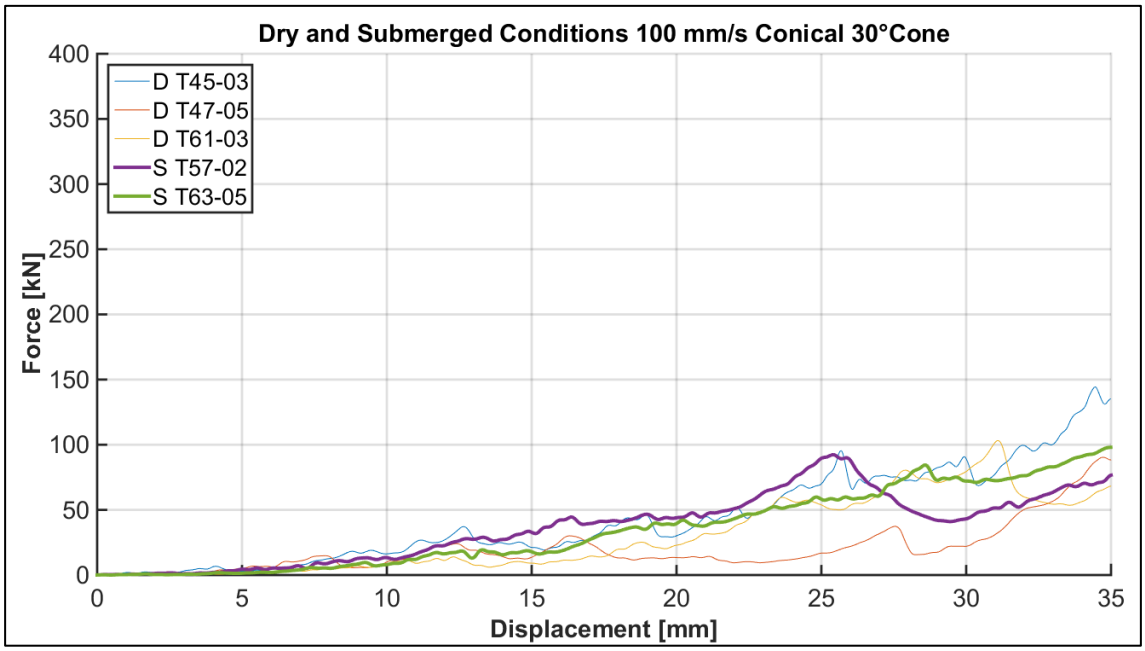

Figure Appendix D3. 1: Conical indenter, 100 mm/s, 30° ice specimens: force vs. displacement for individual tests in dry and submerged contact conditions.

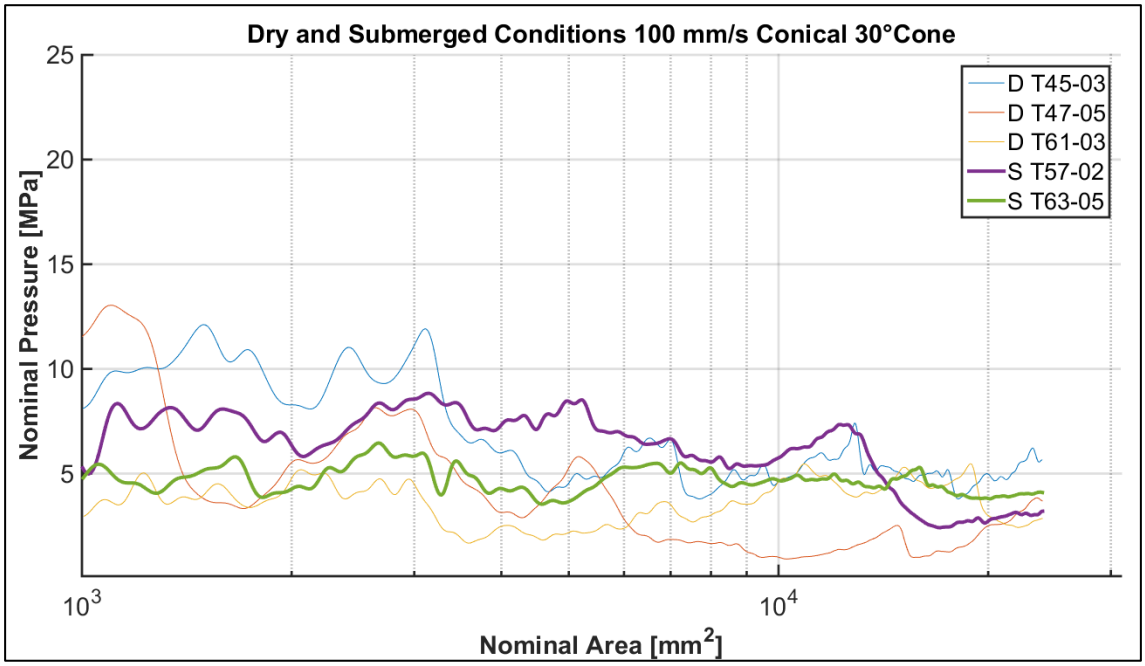

Figure Appendix D3. 2: Conical indenter, 100 mm/s, 30° ice specimens: nominal pressure vs. area curves for individual tests in dry and submerged contact conditions.

Appendix D4 : General Observations

1 mm/s

Dry **T62_04**		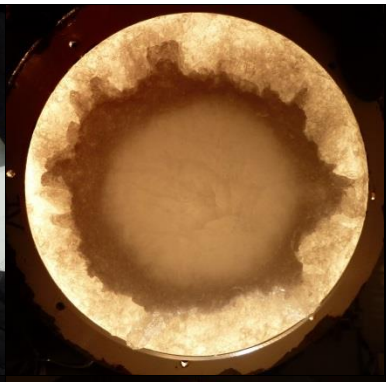
Submerged **T56_01**		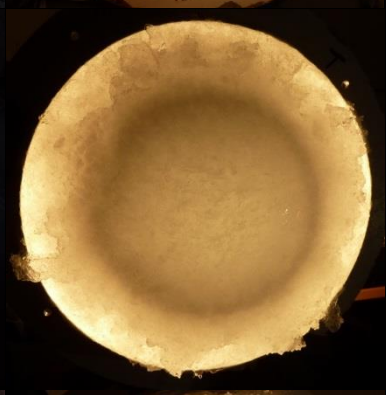
Submerged **T58_03**		
Submerged **T64_06**		

100 mm/s

Dry **T45_03**		
Dry **T61_03**		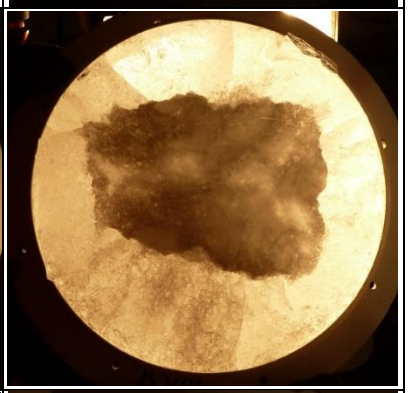
Submerged **T57_02**		
Submerged **T63_05**		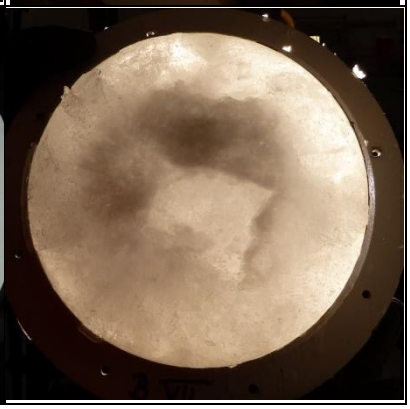

The following images display ice slabs of tests with the conical indenter at 1 mm/s and 100 mm/s for dry and submerged contact conditions. The photos show the depth to which the samples are affected depending on indentation rates and contact conditions.

1 m/s	**Dry** **T62_04**	
	Submerged **T64_06**	
100 mm/s	**Dry** **T61_03**	
	Submerged **T61_03**	n/a

Appendix D5 : Microstructural Observations

1 mm/s

Dry Vertical	Dry Horizontal (Top)
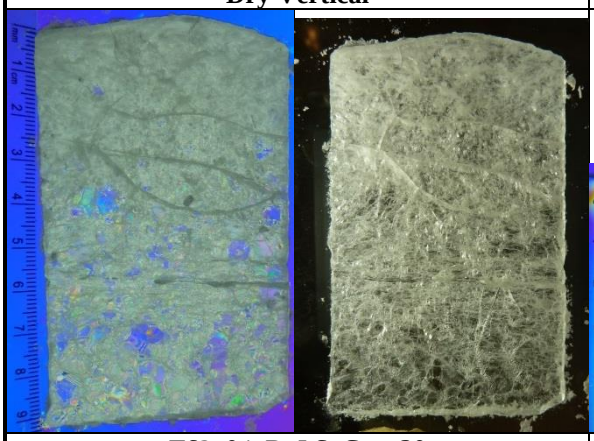	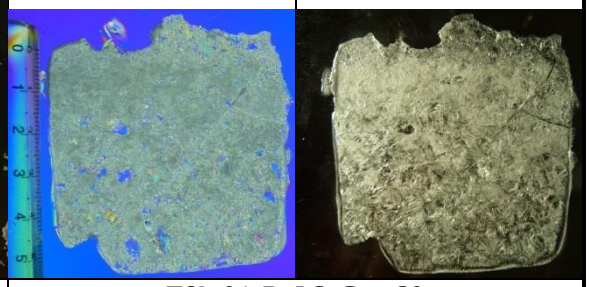
T62_04_D_LS_Con_30	T62_04_D_LS_Con_30
Submerged Vertical	**Submerged Horizontal (Top)**
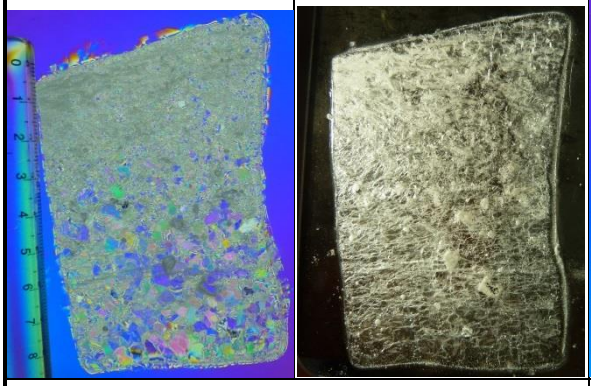	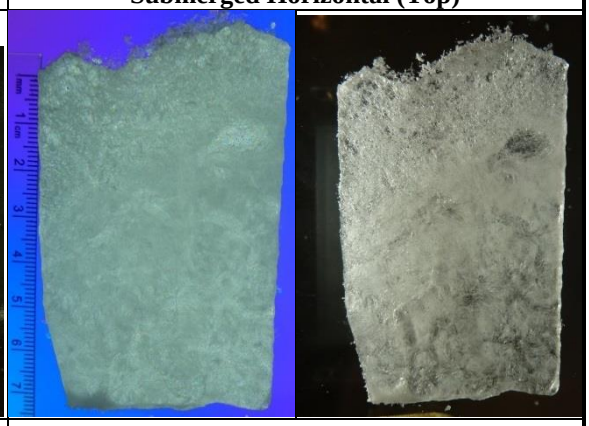
T56_01_S_LS_Con_30	**Submerged Horizontal (Bottom)**
	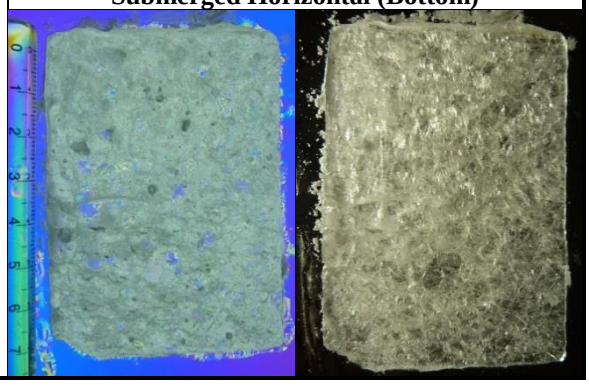

1 mm/s - continued

Submerged Vertical			
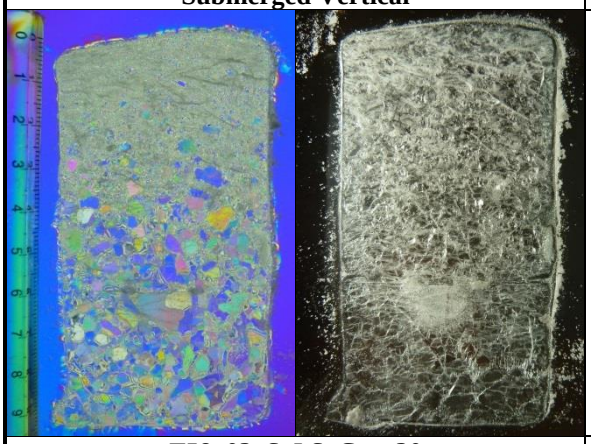			
T58_03_S_LS_Con_30			
Submerged Vertical		**Submerged Horizontal (Top)**	
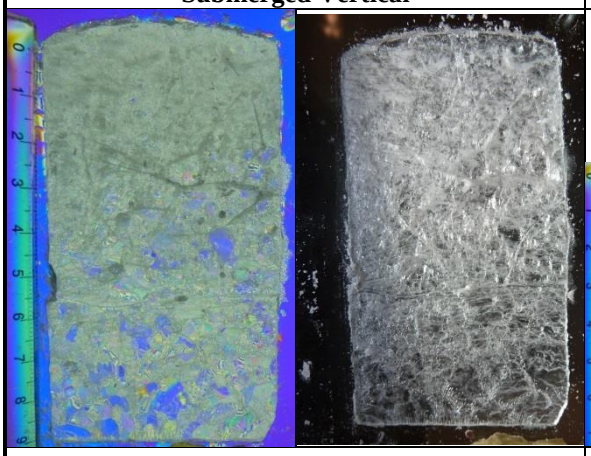		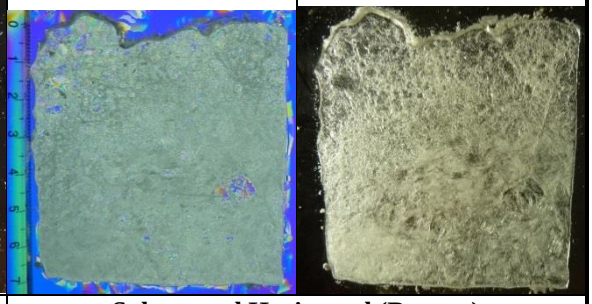	
T64_06_S_LS_Con_30		**Submerged Horizontal (Bottom)**	
		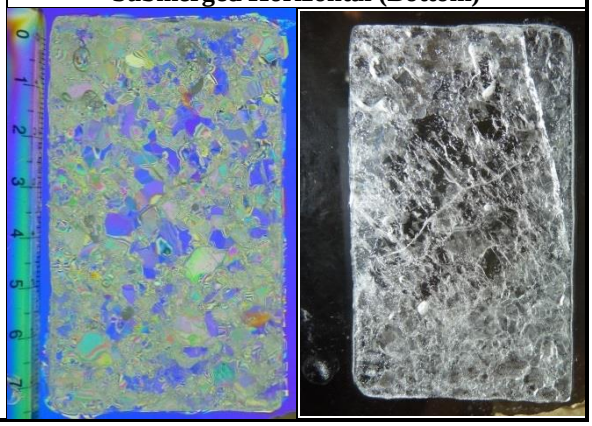	

100 mm/s

Dry Vertical	Dry Horizontal (Bottom)
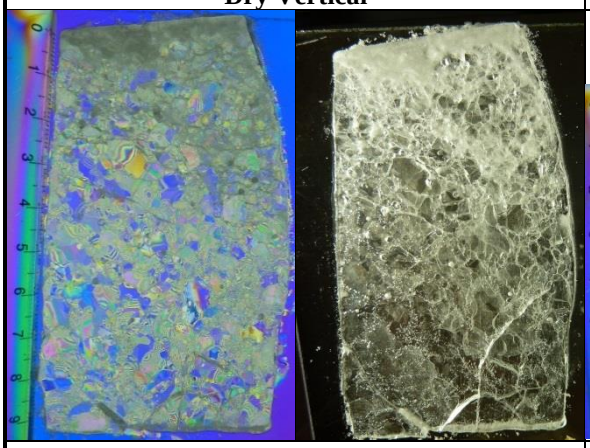	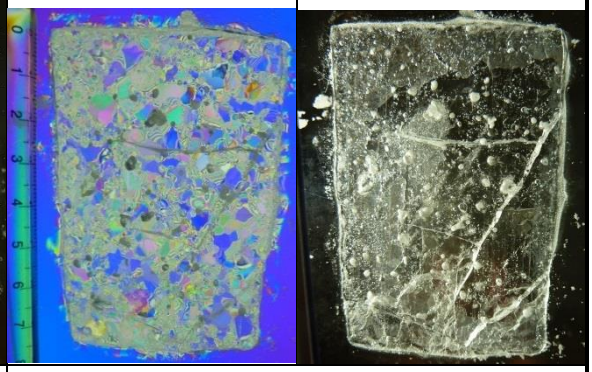
T61_03_D_HS_Con_30	T61_03_D_HS_Con_30
Submerged Vertical	**Submerged Horizontal (Bottom)**
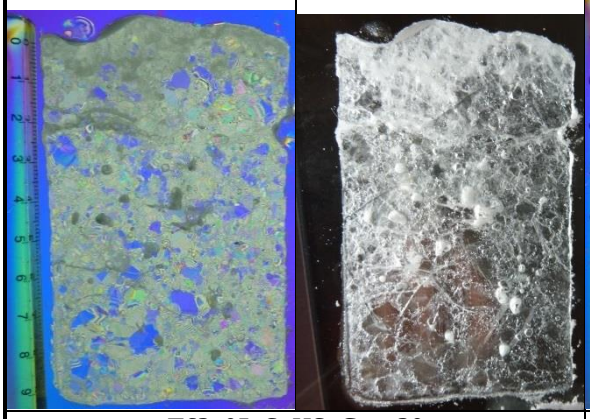	
T63_05_S_HS_Con_30	T63_05_S_HS_Con_30

Remarks:

- Large fractures in above images mostly originate from the thin sectioning process. This especially applies to tests:
    - 1 mm/s: D T62_04
    - 100 mm/s: D T61_03, S T63_05
- Horizontal thin sections refer to:
    - Top: right below the impacted surface where the ice is highly damaged and fairly soft.
    - Bottom: several centimetres below the impacted surface. The remaining large ice crystals n some of these sections indicate that the ice microstructure was affected in less depth.

Appendix D6 : Multiple Regression Analysis

Mean Force Overall

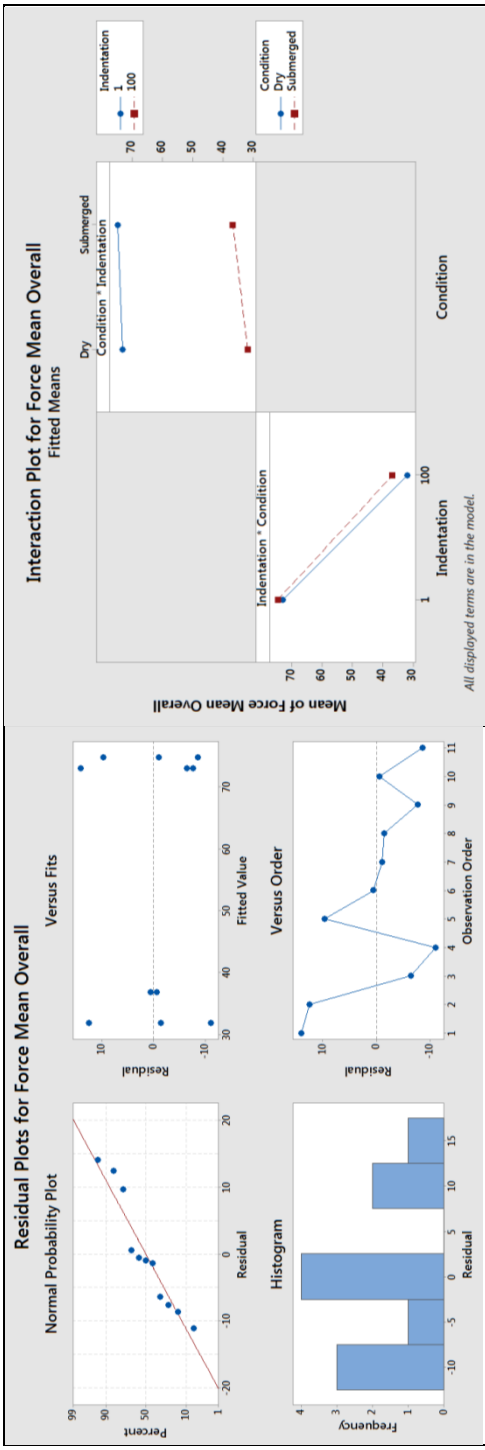

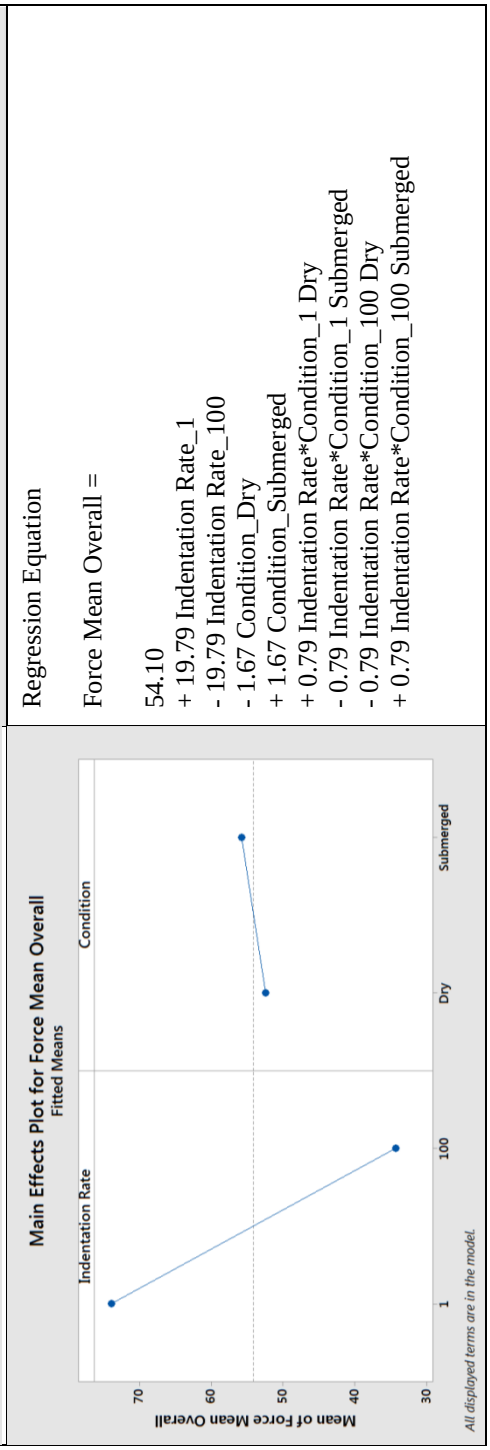

Regression Equation

Force Mean Overall =

54.10
+ 19.79 Indentation Rate_1
- 19.79 Indentation Rate_100
- 1.67 Condition_Dry
+ 1.67 Condition_Submerged
+ 0.79 Indentation Rate*Condition_1 Dry
- 0.79 Indentation Rate*Condition_1 Submerged
- 0.79 Indentation Rate*Condition_100 Dry
+ 0.79 Indentation Rate*Condition_100 Submerged

Mean Force Above 1000 mm^2

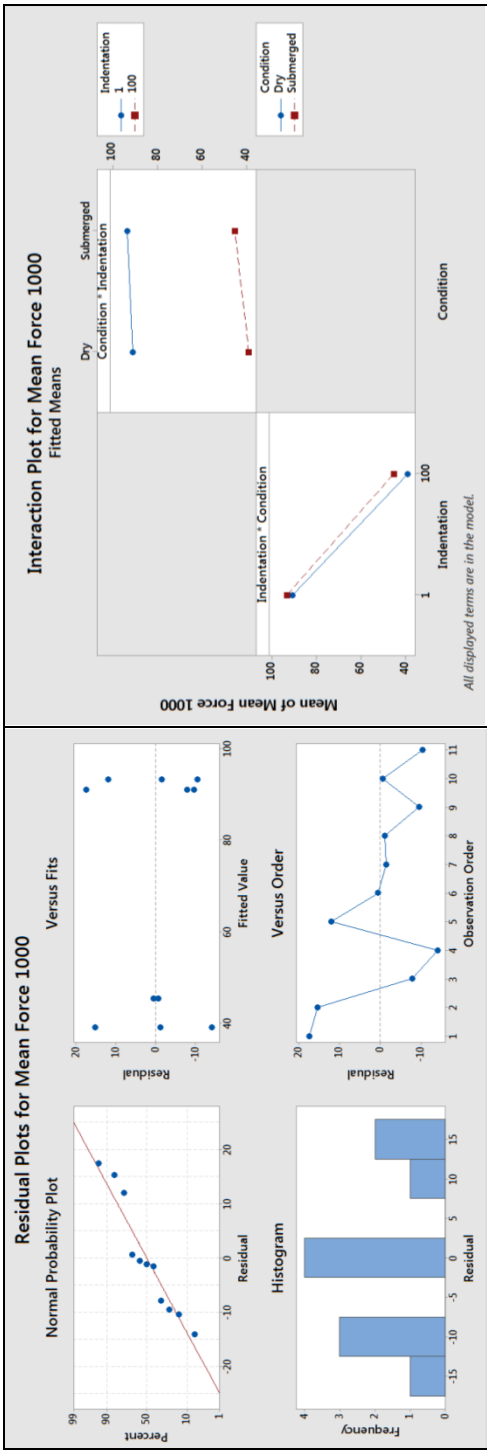

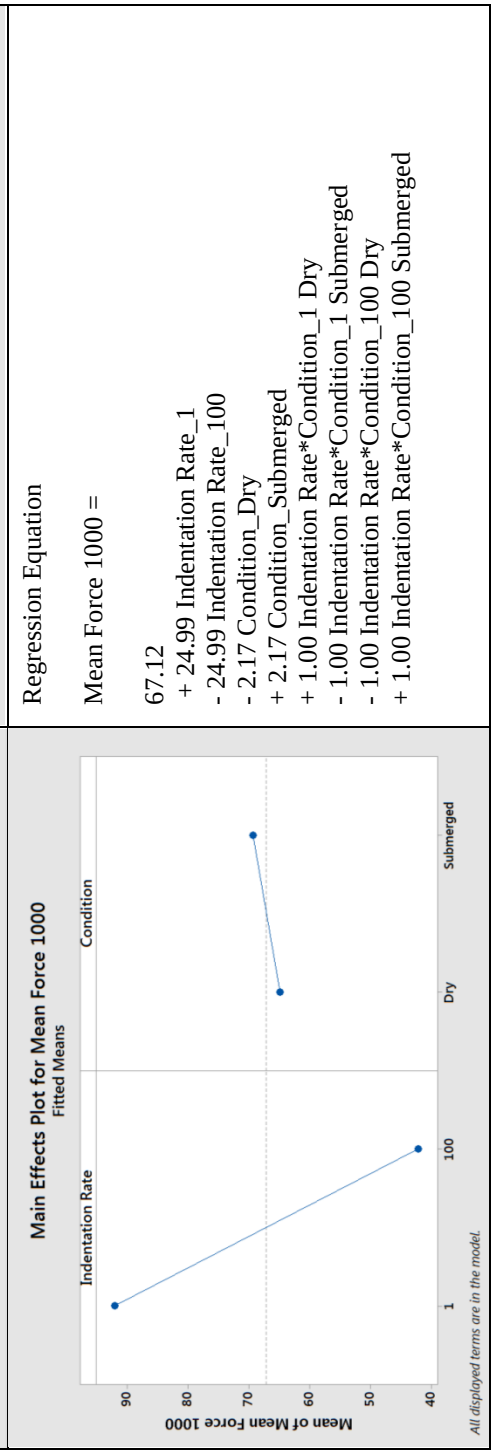

Regression Equation

Mean Force 1000 =

67.12
+ 24.99 Indentation Rate_1
- 24.99 Indentation Rate_100
- 2.17 Condition_Dry
+ 2.17 Condition_Submerged
+ 1.00 Indentation Rate*Condition_1 Dry
- 1.00 Indentation Rate*Condition_1 Submerged
- 1.00 Indentation Rate*Condition_100 Dry
+ 1.00 Indentation Rate*Condition_100 Submerged

Mean Pressure Above 1000 mm^2

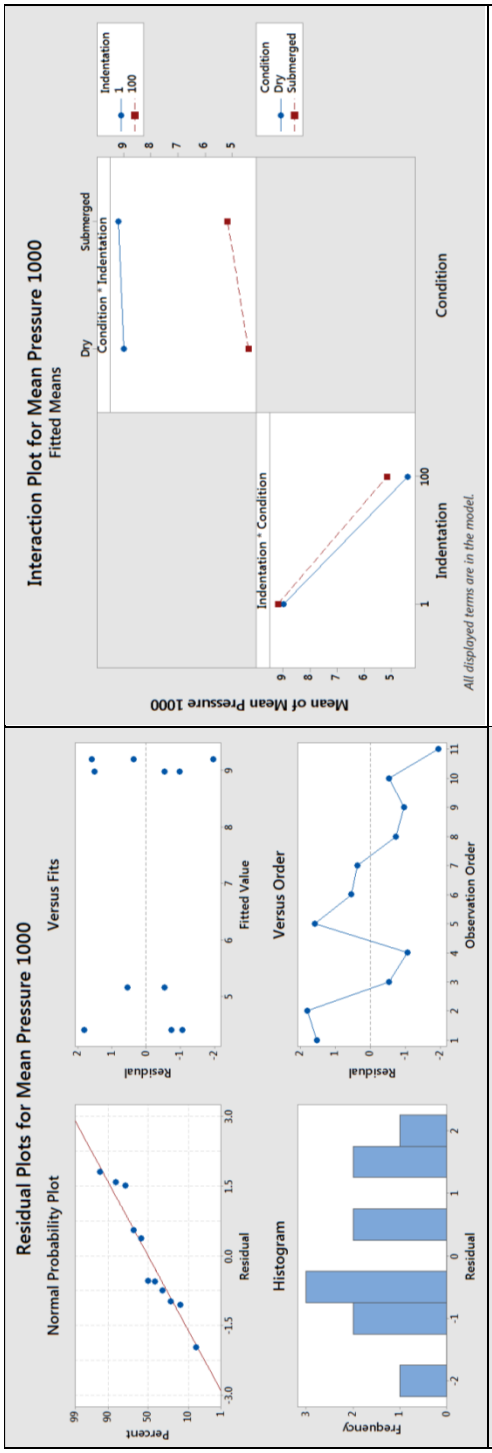

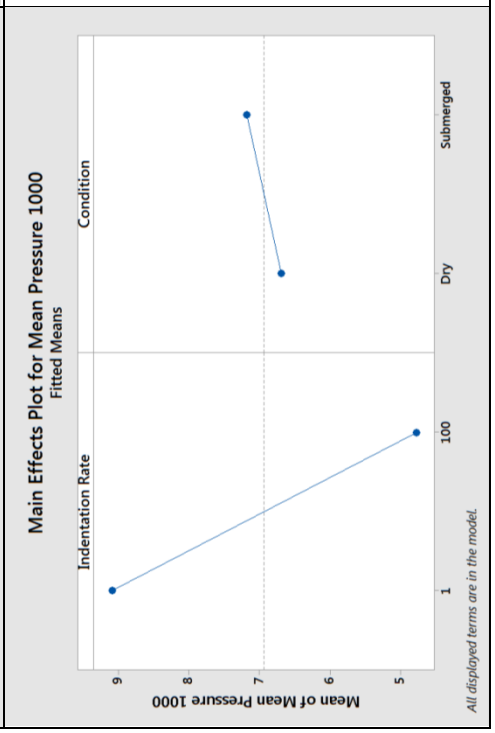

Regression Equation

Mean Pressure 1000 =

6.938
+ 2.153 Indentation Rate_1
- 2.153 Indentation Rate_100
- 0.244 Condition_Dry
+ 0.244 Condition_Submerged
+ 0.136 Indentation Rate*Condition_1 Dry
- 0.136 Indentation Rate*Condition_1 Submerged
- 0.136 Indentation Rate*Condition_100 Dry
+ 0.136 Indentation Rate*Condition_100 Submerged

Maximal Nominal Pressure Above 1000 mm^2

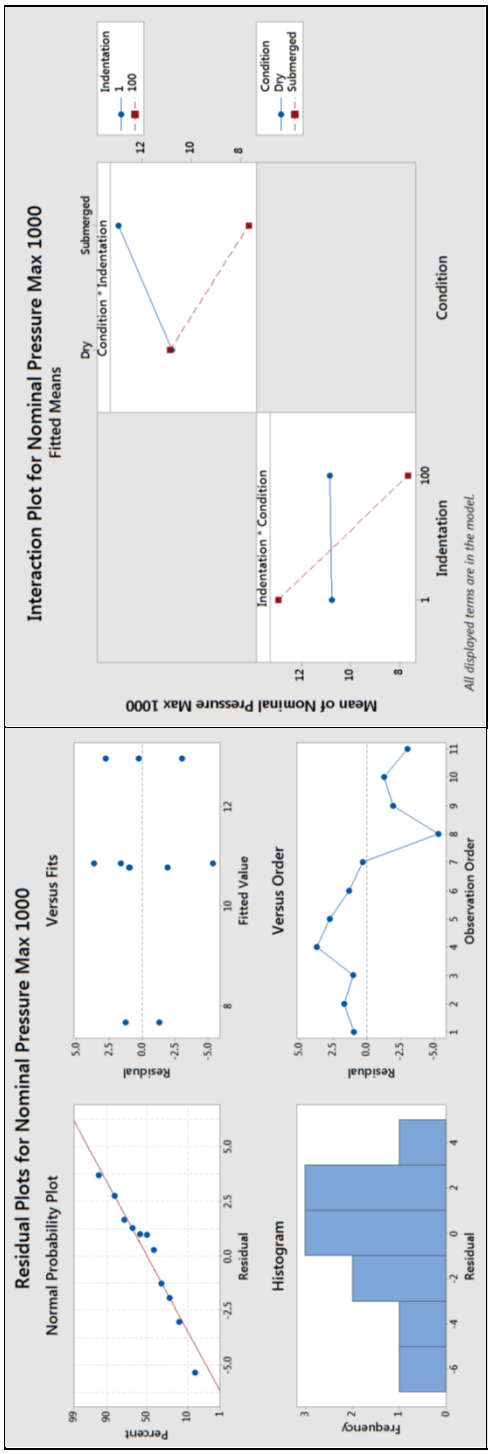

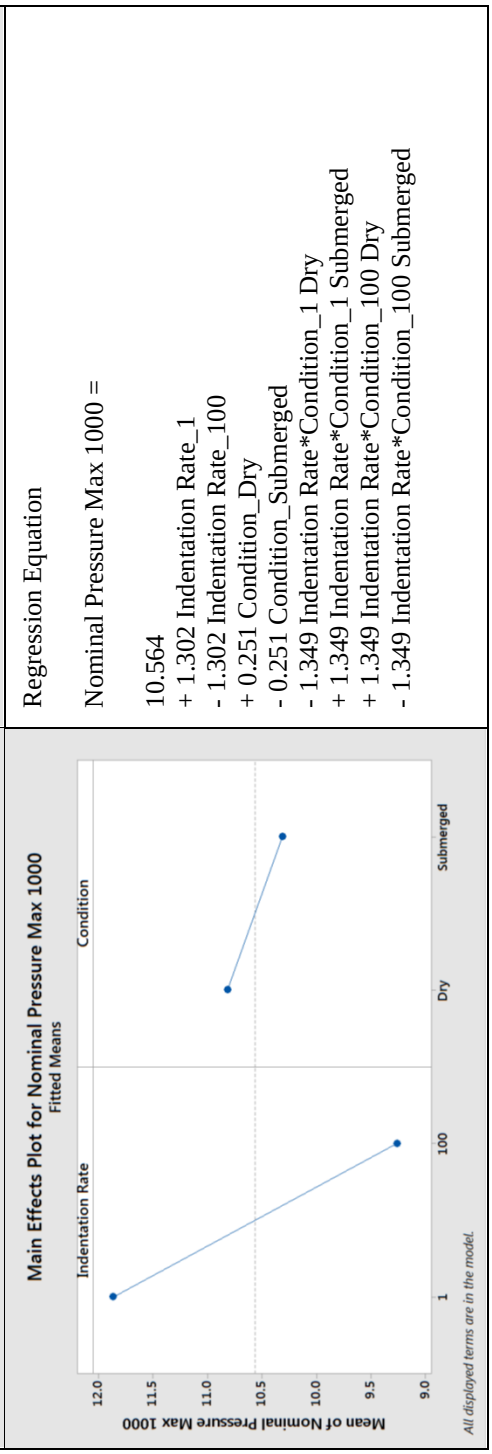

Regression Equation

Nominal Pressure Max 1000 =

10.564
+ 1.302 Indentation Rate_1
- 1.302 Indentation Rate_100
+ 0.251 Condition_Dry
- 0.251 Condition_Submerged
- 1.349 Indentation Rate*Condition_1 Dry
+ 1.349 Indentation Rate*Condition_1 Submerged
+ 1.349 Indentation Rate*Condition_100 Dry
- 1.349 Indentation Rate*Condition_100 Submerged

Appendix D7 : Effect of Indentation Rate

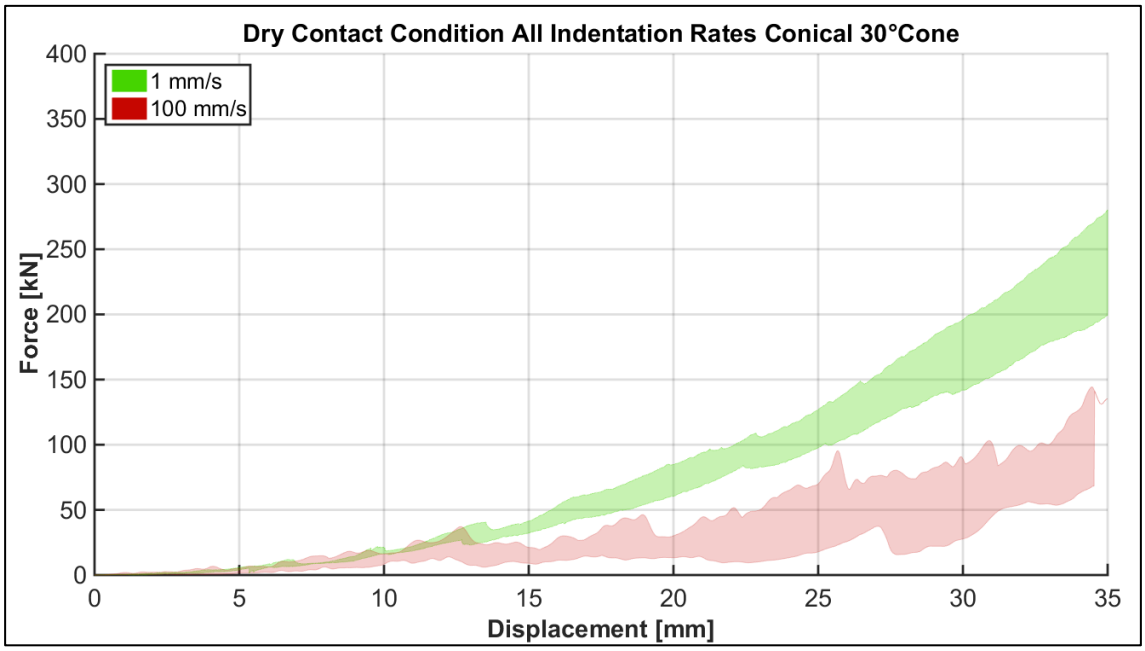

Figure Appendix D7. 1: Conical indenter, 30° ice specimens, dry: force vs. displacement for 1 mm/s (4) and 100 mm/s (3).

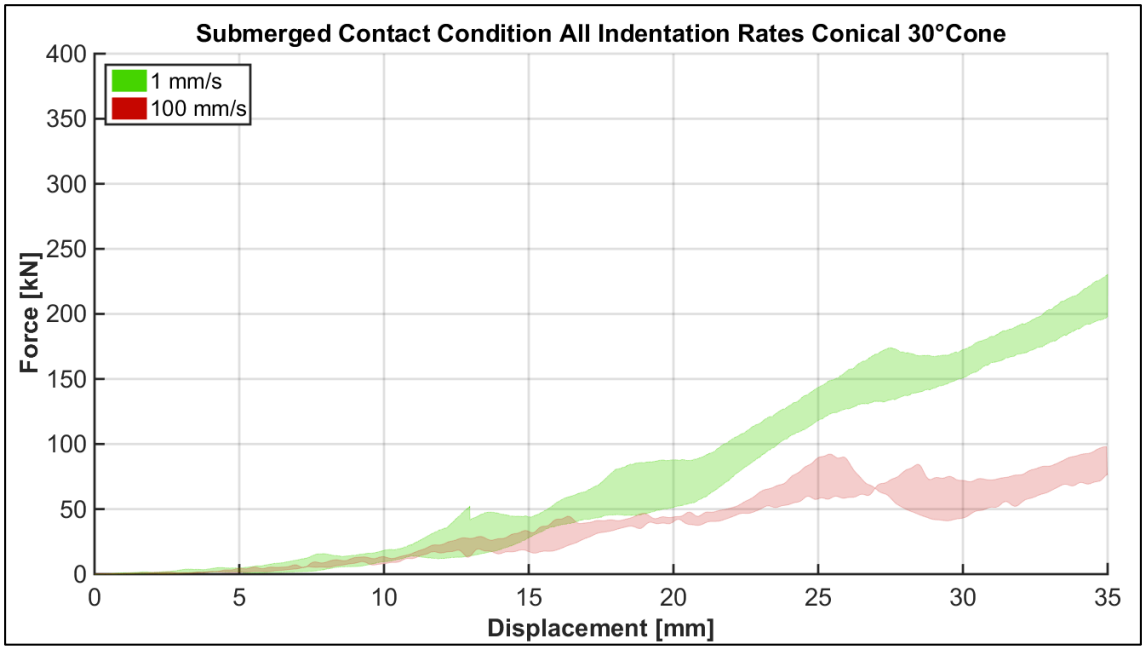

Figure Appendix D7. 2: Conical indenter, 30° ice specimens, submerged: force vs. displacement for 1 mm/s (3) and 100 mm/s (2).

Appendix E : Spherical Indenter

Appendix E1 : Spectral Analysis (FFT)

The Fourier spectra of tests with the spherical indenter are similar regardless of indentation rate. The examples of high speed tests in Figure Appendix E1. 1 show no significant difference between the dry (left) and the submerged condition (right). At this indentation rate in particular, a pronounced structural response was expected due to the compliance of the experimental setup. The spectra do not reveal spikes or other abnormalities and therefore the data was not filtered, preserving the original force history.

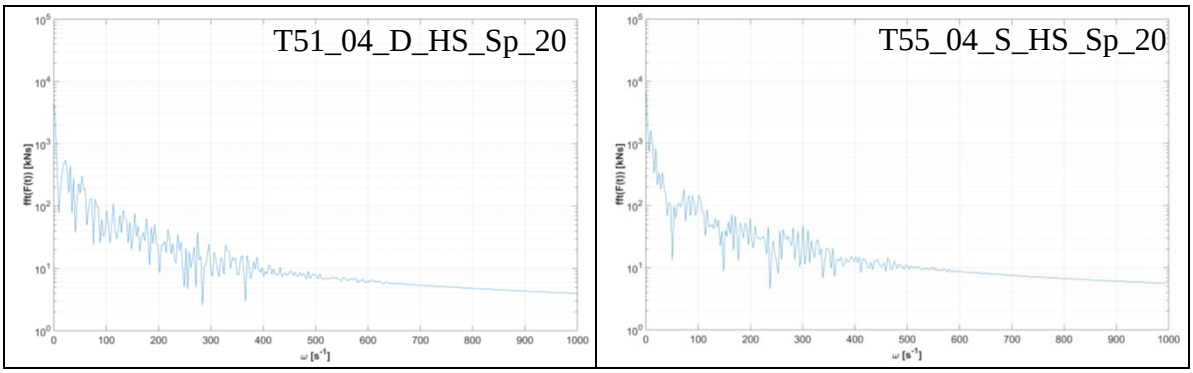

Figure Appendix E1. 1: Fourier spectra (FFT) of high speed tests with the spherical indenter and for frequencies up to 1000 Hz. Displayed are curves (Left) for the dry condition (D T51-04) and (Right) for the submerged condition (S T55-04).

The low speed tests produced band-like spectra. The two examples of both conditions in Figure Appendix E1. 2 have spikes at 29.7 Hz. Test D T59-01 has a small spike at 180 Hz. Furthermore, only test S T54-03 (not displayed) has generated a very small spike at 29.7 Hz. The three other tests performed at this speed produced no spikes

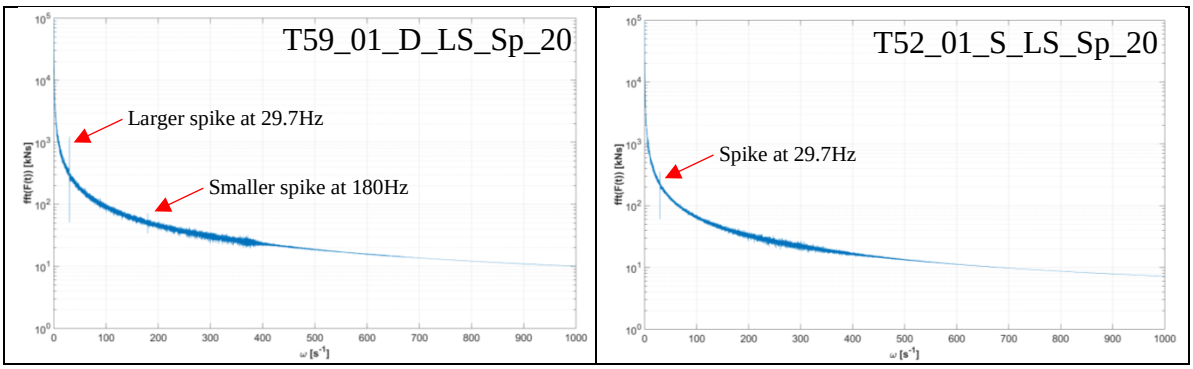

Figure Appendix E1. 2: Fourier spectra (FFT) for low speed tests with the spherical indenter and for frequencies up to 1000 Hz. Displayed are curves for the dry condition (T59-01) on the left and for the submerged condition (T52-01) on the right.

The Fourier spectra do not reveal extraordinary deviations that would indicate external influences on the data. Consequently, and in order to preserve the original force histories, the data of the spherical indenter are not filtered.

Appendix E2 : Plots for 1 mm/s Indentation Rate

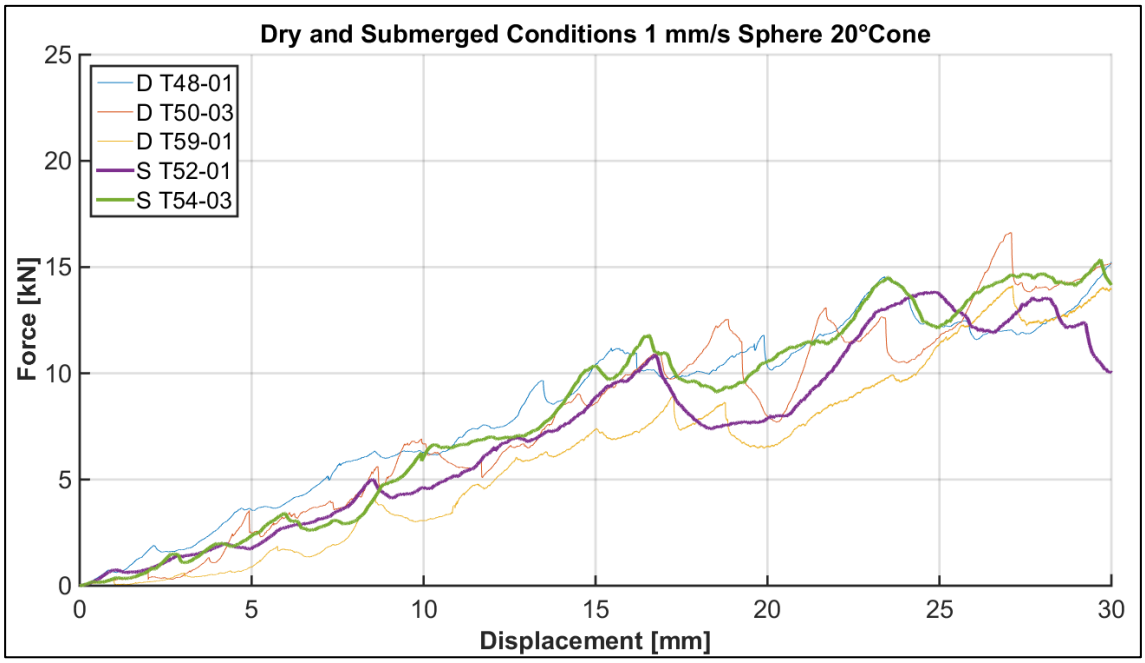

Figure Appendix E2. 1: Sphere, 1 mm/s, 20° ice specimens: force vs. displacement for individual tests in dry and submerged contact conditions.

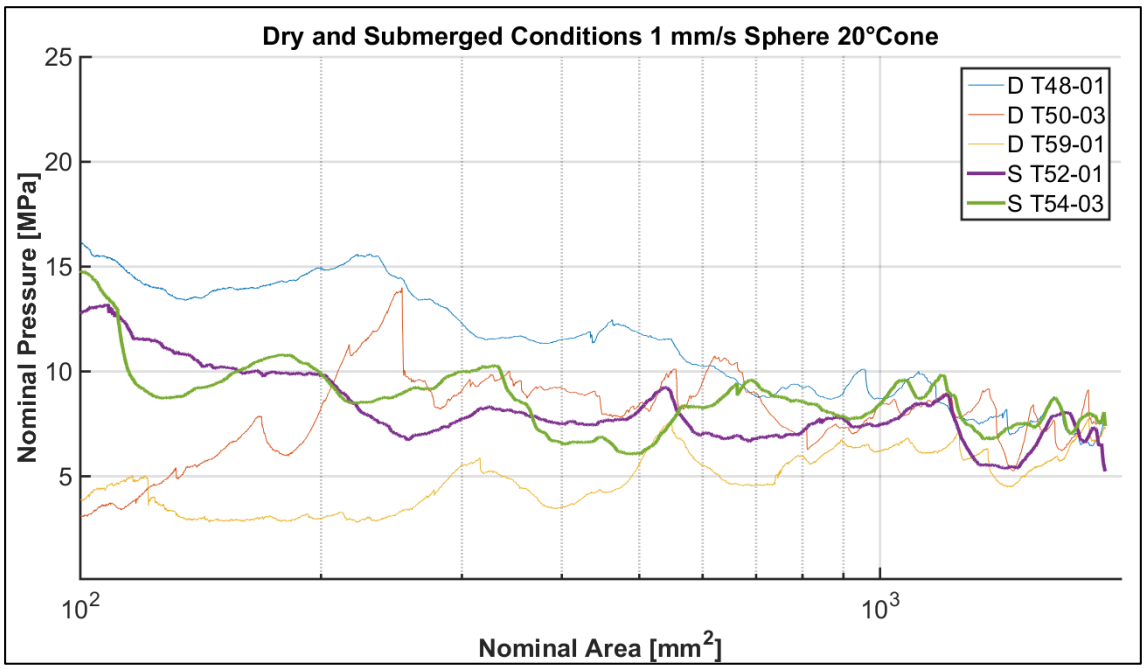

Figure Appendix E2. 2: Sphere, 1 mm/s, 20° ice specimens: nominal pressure vs. area curves for individual tests in dry and submerged contact conditions.

Appendix E3 : Plots for 100 mm/s Indentation Rate

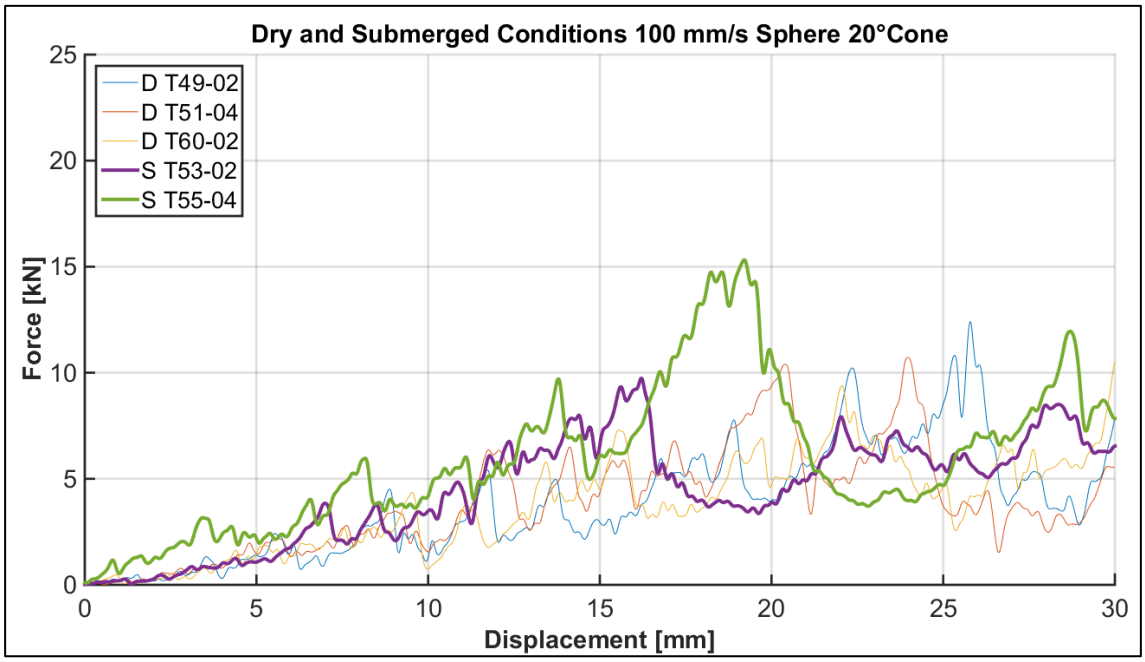

Figure Appendix E3. 1: Sphere, 100 mm/s, 20° ice specimens: force vs. displacement for individual tests in dry and submerged contact conditions.

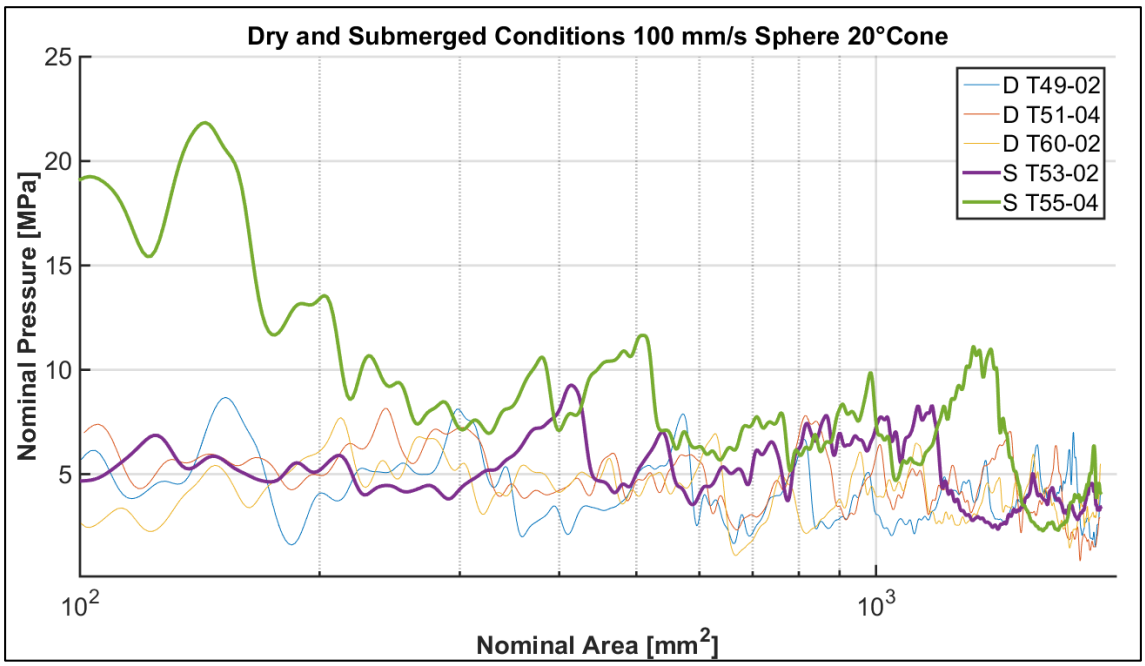

Figure Appendix E3. 2: Sphere, 100 mm/s, 20° ice specimens: nominal pressure vs. area curves for individual tests in dry and submerged contact conditions.

Appendix E4 : General Observations

1 mm/s

Dry **T50_03**		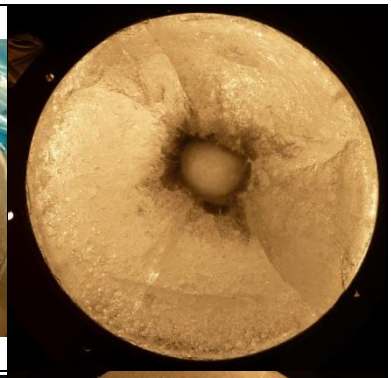
Submerged **T52_01**		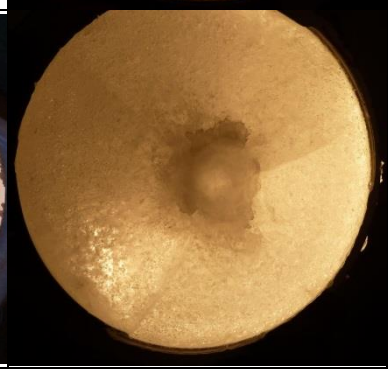

100 mm/s

Dry **T51_04**		
Submerged **T53_02**	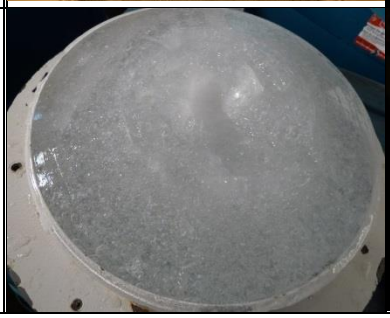	

Appendix E5 : Microstructural Observations

1 mm/s

Dry Vertical	Dry Horizontal
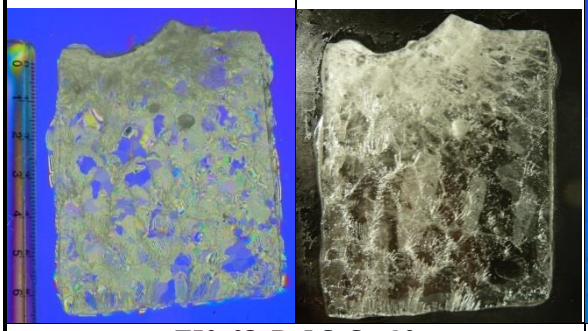	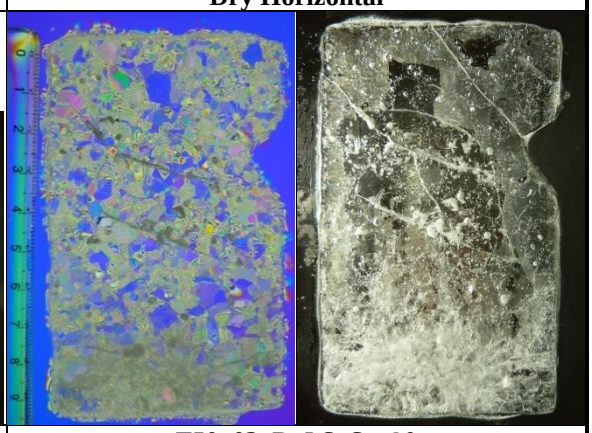
T50_03_D_LS_Sp_20	T50_03_D_LS_Sp_20
Submerged Vertical	**Submerged Horizontal**
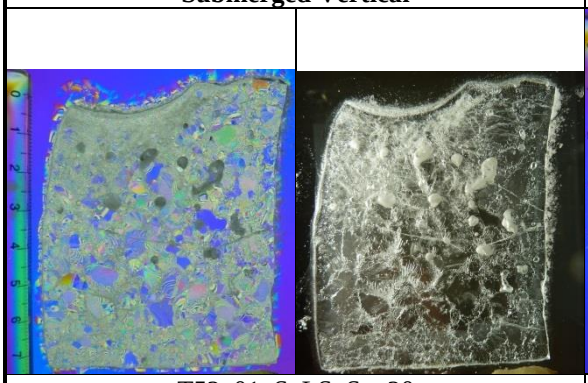	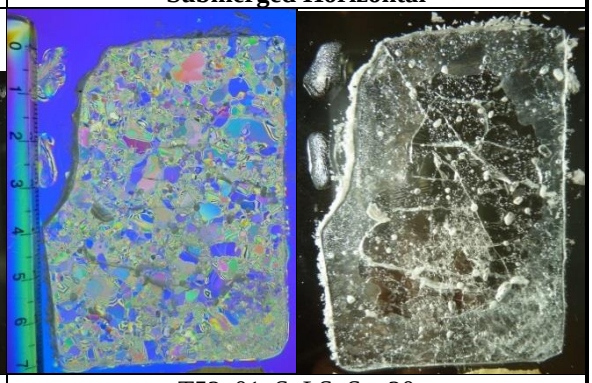
T52_01_S_LS_Sp_20	T52_01_S_LS_Sp_20

100 mm/s

Dry Vertical		Dry Horizontal	
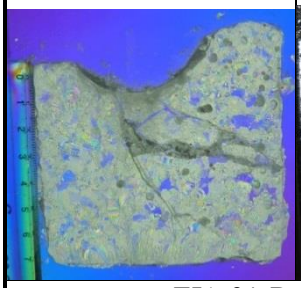		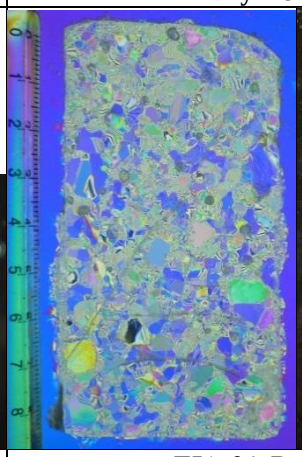	
T51_04_D_HS_Sp_20		T51_04_D_HS_Sp_20	
Submerged Vertical		**Submerged Horizontal**	
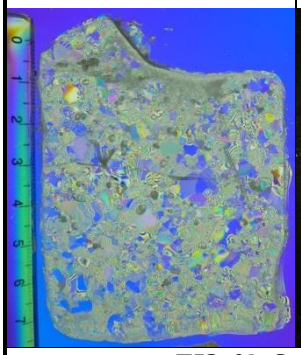		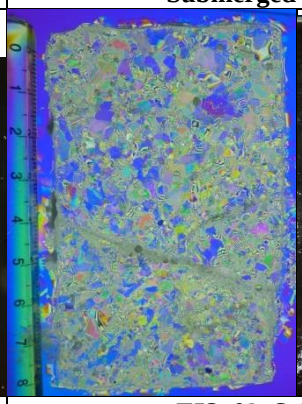	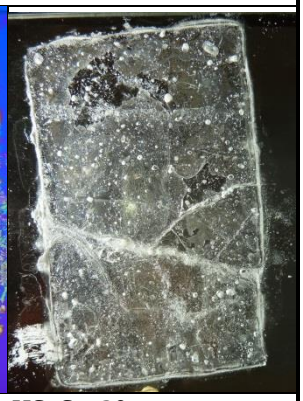
T53_02_S_HS_Sp_20		T53_02_S_HS_Sp_20	

Remarks:

These samples were especially prone to fracture in the thin section preparation process. The most distinct large fractures (e.g. inclined horizontal cut in S T53-02) originated from either the shaping with the microtome or from the attempt to remove and turn the sample to machine the second side.

Appendix E6 : Multiple Regression Analysis

Mean Force Overall

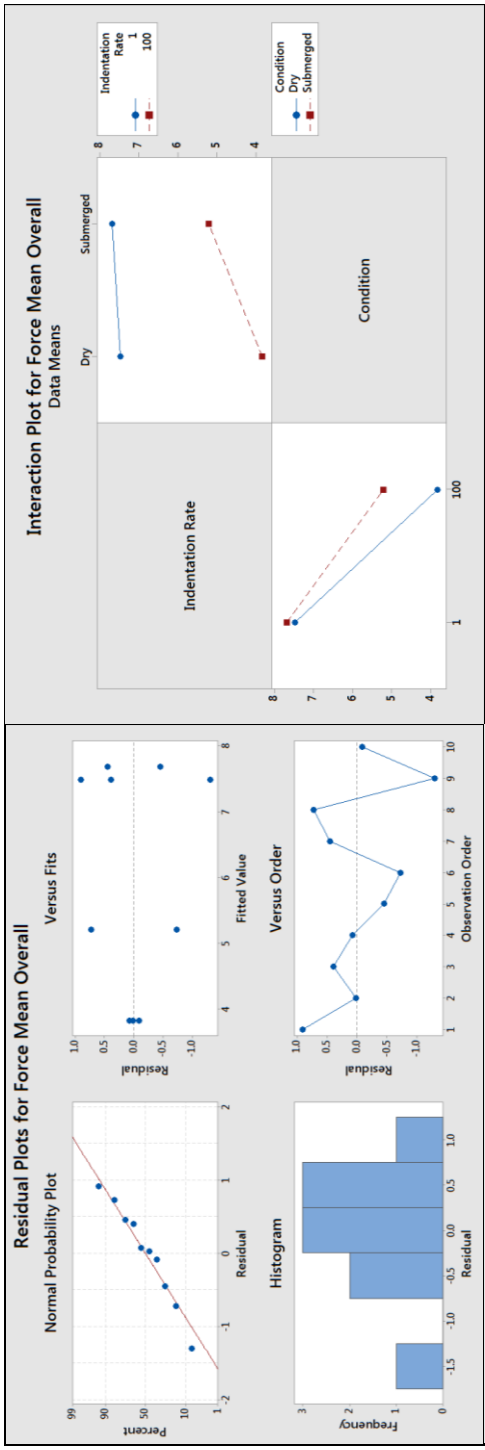

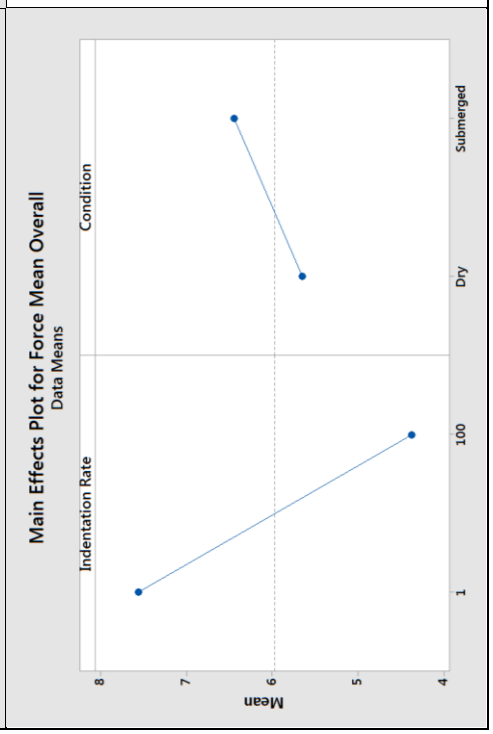

Regression Equation

Force Mean Overall =

6.051
+ 1.534 Indentation Rate_1
- 1.534 Indentation Rate_100
- 0.395 Condition_Dry
+ 0.395 Condition_Submerged
- 0.293 Indentation Rate*Condition_1 Dry
+ 0.293 Indentation Rate*Condition_1 Submerged
- 0.293 Indentation Rate*Condition_100 Dry
+ 0.293 Indentation Rate*Condition_100 Submerged

Mean Force Above 100 mm^2

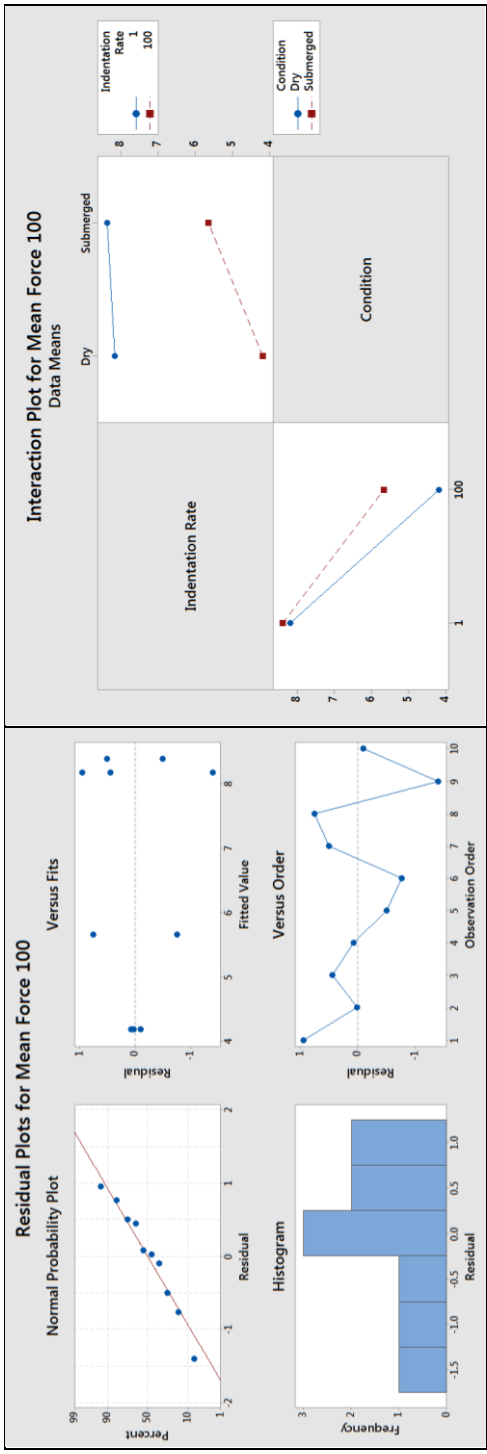

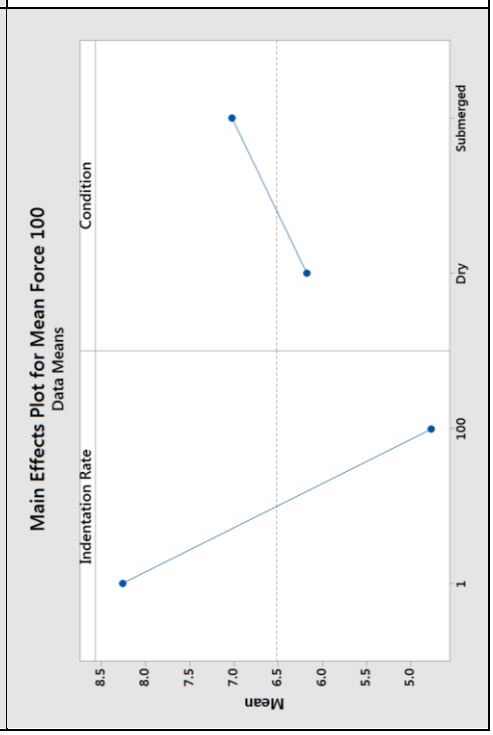

Regression Equation

Mean Force 100 =

6.600
+ 1.683 Indentation Rate_1
- 4.683 Indentation Rate_100
- 0.423 Condition_Dry
+ 0.423 Condition_Submerged
+ 0.315 Indentation Rate*Condition_1 Dry
- 0.315 Indentation Rate*Condition_1 Submerged
- 0.315 Indentation Rate*Condition_100 Dry
+ 0.315 Indentation Rate*Condition_100 Submerged

Mean Pressure Above 100 mm^2

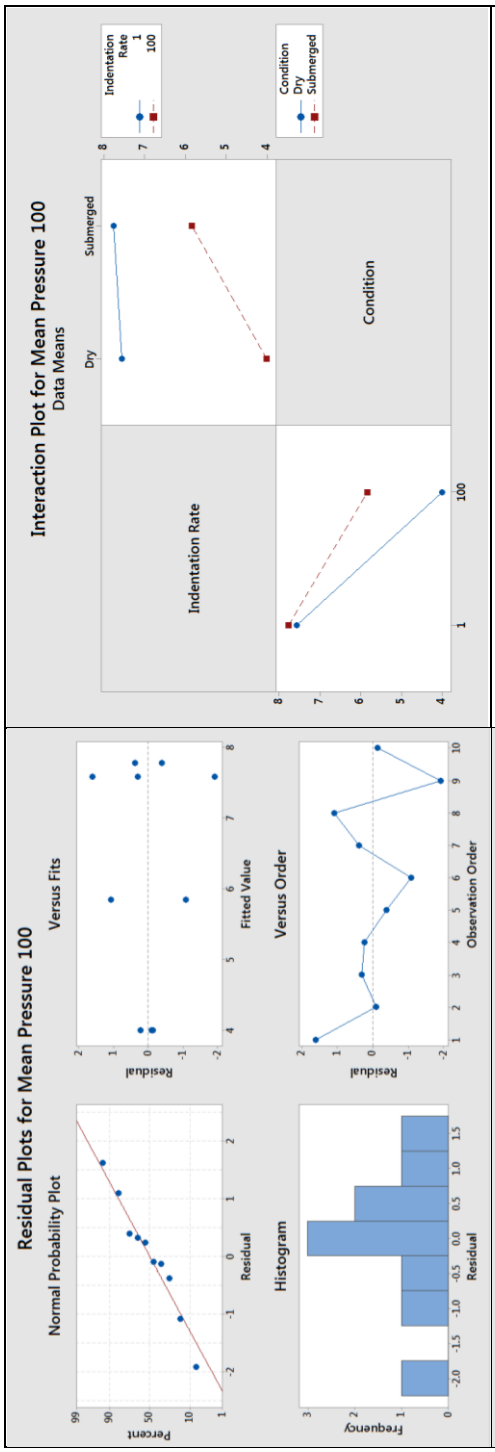

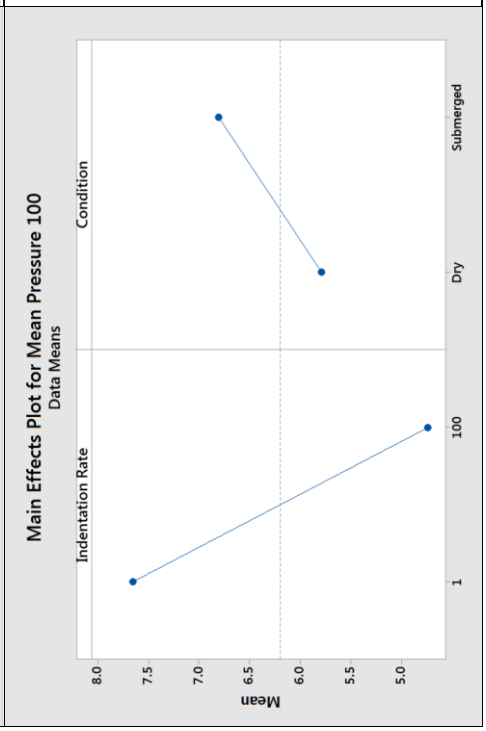

Regression Equation

Mean Pressure 100 =

6.298
+ 1.375 Indentation Rate_1
- 1.375 Indentation Rate_100
- 0.508 Condition_Dry
+ 0.508 Condition_Submerged
- 0.411 Indentation Rate*Condition_1 Dry
+ 0.411 Indentation Rate*Condition_1 Submerged
- 0.411 Indentation Rate*Condition_100 Dry
+ 0.411 Indentation Rate*Condition_100 Submerged

Maximal Nominal Pressure Above 100 mm^2

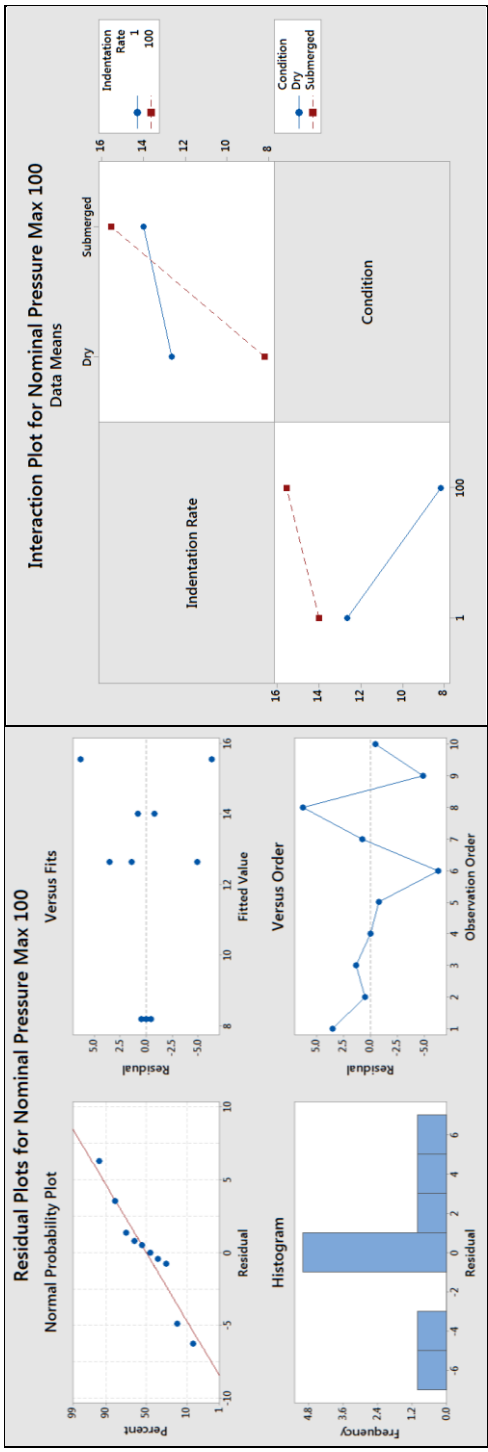

Regression Equation

Nominal Pressure Max 100 =

12.59
+ 0.73 Indentation Rate_1
- 0.73 Indentation Rate_100
- 2.18 Condition_Dry
+ 2.18 Condition_Submerged
+ 1.50 Indentation Rate*Condition_1 Dry
- 1.50 Indentation Rate*Condition_1 Submerged
- 1.50 Indentation Rate*Condition_100 Dry
+ 1.50 Indentation Rate*Condition_100 Submerged

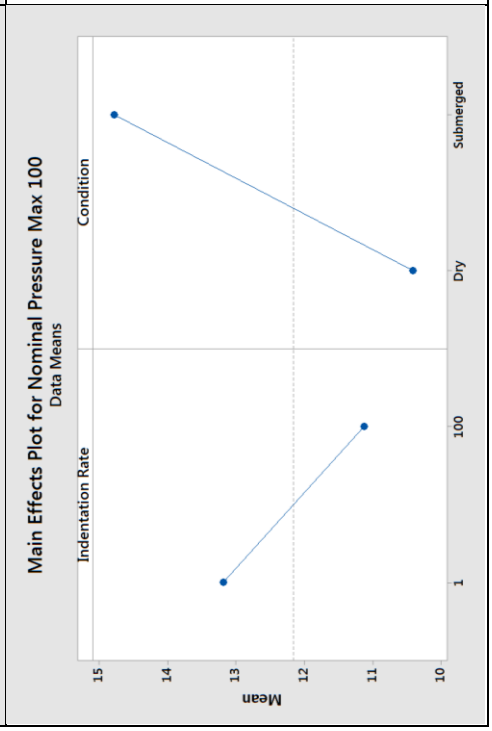

Appendix F : Tactile Pressure Sensors

General Considerations

Tactile pressure sensors were used in various studies to measure contact pressures and contact areas. The proper installation and application requires the consideration of several factors.

The operating temperature is specified with -40°C to 60°C and the sensors are sensitive to temperature changes. Errors can be as high as 0.25 % for every °F that calibration and testing temperature differ (Tekscan, Inc., 2003). Furthermore, the handles that transmit the information from the sensors to the data acquisition system are only rated for 0°C to 50°C. It is generally desirable to use the same materials for the calibration that are components of the later test. For the sensors used in the present tests, the preparation took place at testing temperature but it did not involve materials that were part of the experiments (ice). During the actual tests, the sensors were inevitably subject to temperature changes by the contact with ice, water, snow and ice chips. The sensors are also known to be susceptible to unevenness and to be shear-sensitive. In the present test series, shear forces originating from extruding ice were expect, a circumstance that would be amplified when the sensors were installed at the inclined surface of the wedge shaped indenter. The different testing environments posed severe risks for ripping or puncturing the sensors, adding a final significant concern.

Sensor Conditioning, Equilibration and Calibration Procedure

ensor preparation took place inside the cold room at the testing temperature of -7°C using the material testing system (MTS) that was employed for the tests. To condition, equilibrate and calibrate them, the sensors were placed in a sandwich-like setup consisting of several components. A flat steel plate was attached to the piston of the MTS machine. A thin (1.587 mm) rectangular (152.4 mm x 152.4 mm) sheet of Ultra-Strength Neoprene Rubber, similar in size to the sensor area (entire sensing area plus surrounding material), was placed in the centre of the steel plate to compensate for slight surface unevenness. The next layer was of similar size and consisted of brass shim stock (Alloy 260) with 0.0508 mm thickness to reduce plastic deformation of the sensors originating from the compliant Neoprene. The sensor was then positioned on the brass shim stock. The top layers were of the same materials in reverse order, and slightly smaller than the 111.8 mm x 111.8 mm sensel area (Figure Appendix F 1, left). This was to ensure the force application to precisely the matrix area and therewith the pressure was known. For the compensation of slight inclinations, the top was an adjustable steel plate, attached to the crosshead of the MTS machine (Figure Appendix F 1, right).

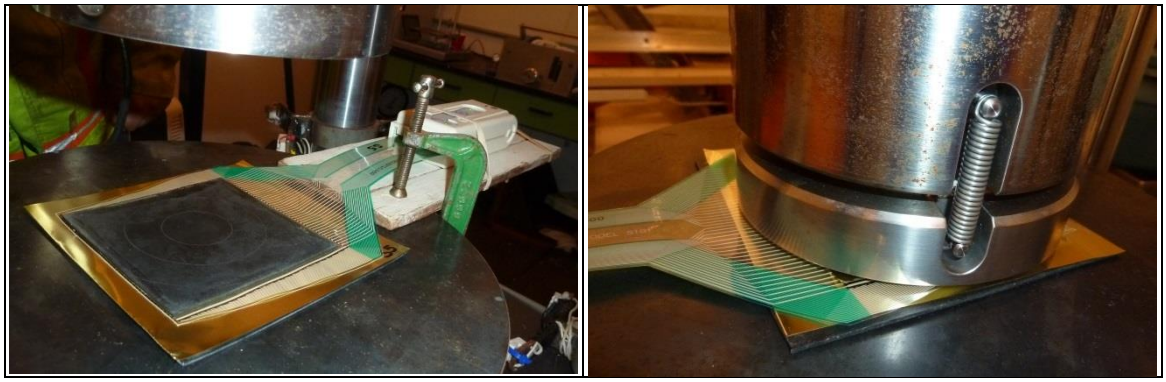

Figure Appendix F 1: (Left) Sensor preparation setup with Neoprene for the bottom layer, followed by brass shim stock and the sensor. The top layers were the same materials in reverse order. (Right) Sensor preparation setup with the adjustable steel plate in position to perform the preparation steps.

The preparation arrangement was prone to shifting and thus all required preparation steps were consecutively performed without interruption. The piston of the MTS machine was manually raised to minimize the gap between the adjustable steel plate and the top Neoprene layer. Then the sensor preparation commenced using force control. First the sensors were conditioned and equilibrated by applying a constant load over some time. Conditioning ensures that in the sensor enclosed air is pushed out. During the equilibration the software determines small differences in the sensitivity of the sensels and balances those by establishing a gain factor for each sensel. For performing these steps, first at a rate of 5000 N/s the piston of the MTS machine was ramped up to 320 kN where it remained for 15 seconds. The load was then reduced to the first target load of a four point calibration: 75 kN, 150 kN, 225 kN and 300 kN. Each level was held for 7 seconds. These loads generated pressures of approx. 6 MPa, 12 MPa, 18 MPa and 24 MPa. Each sensor was individually prepared and separate sensor specific equilibration and calibration files were saved.

Sensor Protection and Installation

Pressure sensors are sensitive to shear forces and prone to puncture. To protect the sensors in the different testing environments and against shear they were covered with a thin layer (0.05 mm) of clear Moisture-Resistant Polyester (Mylar), the same material that the sensors are made of. The Mylar had an adhesive back and was certified for temperatures between -45°C to 135°C. The Mylar was not included in the sensor preparation and likely dampened or smoothened the measurements which was not further investigated. The application also entailed the risk of trapping air and small particles that could influence in the sensor recordings.

Using the Mylar, two facing sensors were fixed to the indenter surface. The indenter and attached sensors were placed inside the aluminum container. The sensor tabs were then guided outside of the container through thin slots that were previously cut out of two opposing acrylic windows (Figure Appendix F 2, left). The remaining gaps were sealed with silicone (Dow Corning®, 700 industrial grade silicone sealant) as displayed in the right image of Figure Appendix F 2. The sensor tabs were wrapped with transparent 3M® 471 Vinyl tape to protect them, especially against the exposure to water.

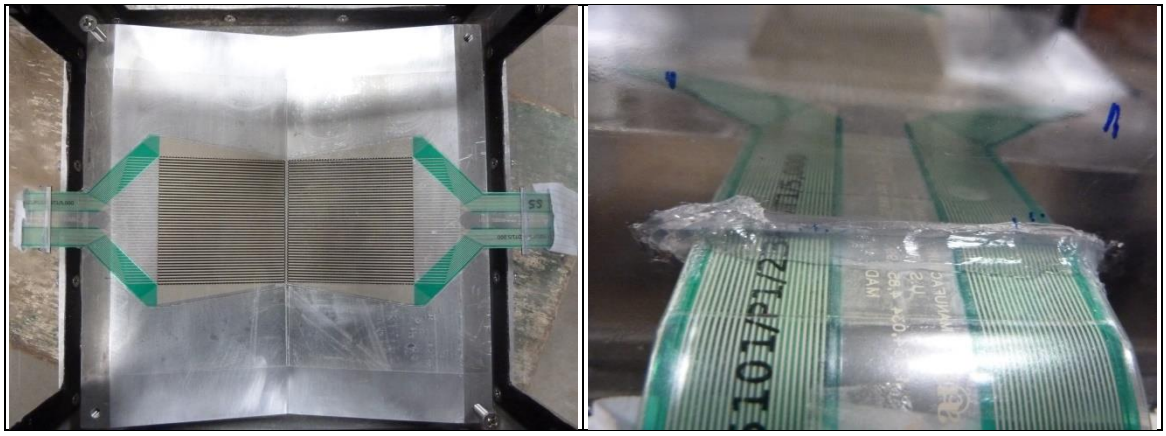

Figure Appendix F 2: (Left) Photo showing two pressure sensors attached to the wedge shaped indenter inside the container. (Right) Close up of a pressure sensor tab guided through a cut in the acrylic window and sealed with silicone.

Outside of the container the tabs were inserted into the handles that were attached to clamps below halogen lights on both sides of the container and moved with the testing setup. Those handles received the information from the sensors and transmitted it to the data acquisition system outside of the cold room.

Data Limitations and Encountered Challenges

Several points regarding the sensor preparation and the quality of the obtained data are worthy of note.

Although many thoughts were given to the establishment of a suitable preparation setup, a more comprehensive pre-study would be required to receive quantitative evaluable results. With the preparation setup described above, higher loads in the equilibration and calibration steps generally caused the pressure sensors to be considerably and permanently deformed. For those reason, the loads were limited to the earlier stated values. This prohibited a sensors calibration with approximately 20 % exceedance of the

maximum that was expected during the test and as it is recommended by the manufacturer to capture all peak pressures. The brass shim stock had been permanently deformed and had to be replaced for every sensor; the deformation matched the array of the pressure sensels exactly (which was also observed on the sample surfaces in low speed tests).

Furthermore, it was only later realized that the use of Map 5101D that connects two individual sensors to one sensing area, requires performing the preparation procedure in the anticipated arrangement but the preparation procedure was executed for single sensors. This error complicated the evaluation of the pressure data but did not affect contact area measurements or the general appearance of pressure patterns.

Although precautions were taken to prevent sensor damage and to establish a watertight setup, several problems were encountered during the experimentation. For instance, leakage through the silicone seals occurred. If the gap was sufficiently small water froze and closed it, otherwise the hole had to be sealed with silicone.

In two cases the wrapping of Vinyl tape around the sensor tabs created a small conduct from the container inside to the outside. Water drained out between the sensor tab and the Vinyl tape. This damaged one handle and only one sensor could be used thereafter.

In submerged tests, one sensel column was damaged and saturated. This resulted in the vertical pink line that is apparent in most of the in the (submerged) recordings. The manufacturer confirmed that measurements up to that column are unbiased. Sensels before the broken column are unaffected, but the physical turn on threshold for everything beyond goes to infinity.

Although the Mylar sheet provided some protection, especially tests in granular ice environment were highly abrasive and resulted in broken sensors after only a few tests.

Appendix G : Effect of Cone Tip Offset

For a perfectly pointed ice cone tip the area at zero displacement ($\delta_0 = 0$; just before the impact occurs) equals zero ($A_{\delta_0} = 0$). This ideal case was not always realized. Sometimes the cone tip is slightly blunt or truncated generating an initial area. To examine how this affects the average nominal pressure, four different initial areas at zero displacement δ_0 are assumed and the forces related to the modified areas. This is done for four randomly selected tests (Table Appendix G 1), two for both cone angles, each for 1 mm/s and 100 mm/s indentation rates in dry condition with the flat indentation plate.

Table Appendix G 1: Overview of four tests used for analysis of a cone tip offset.

Test Date	Test Number	Cone Angle [°]	Indenter	Indentation Rate [mm/s]	Condition
2014-11-04	T10-01	20	Flat	1	Dry
2014-11-12	T26-04	20	Flat	100	Dry
2014-11-18	T38-04	30	Flat	1	Dry
2014-11-03	T09-04	30	Flat	100	Dry

For simplicity, the initial offset area A_Δ is assumed with a whole number from 50 mm^2 up to 125 mm^2 in steps of 25 mm^2. Each area is associated with an initial radius r_Δ (Figure Appendix G 1 that is calculated with Eq. (G.1)

$$r_\Delta = \sqrt{A_\Delta/\pi} \tag{G.1}$$

The radius delta is added to the initial radius and a new nominal contact area over the entire test length is determined. The radius delta correlates with an initial displacement $\Delta\delta$ as it is expressed in Eq. (G.2), and represents the cone tip offset that differs depending on ice cone angle $\propto$.

$$\Delta\delta_{\propto,A\Delta} = r_\Delta * \tan \propto \tag{G.2}$$

Furthermore, R_T in Figure Appendix G 1 is the distance from a point on the vertical symmetry axis of the cone to the transition point where a rounded cone tip would intersect with the inclined surface of a perfectly pointed cone. In the present case, R_T is supposed with 20 mm. $\propto_\Delta$ is the angle between R_T and the vertical and is determined with Eq. (G.3).

$$\propto_\Delta = \sin^{-1}\left(\frac{r_\Delta}{R_T}\right) \tag{G.3}$$

With this and $\varphi_\Delta = 2 * \propto_\Delta$, arc length b_Δ can be calculated according to Eq. (G.4).

$$b_\Delta = \frac{\varphi_\Delta}{180°} * R_T * \pi \tag{G.4}$$

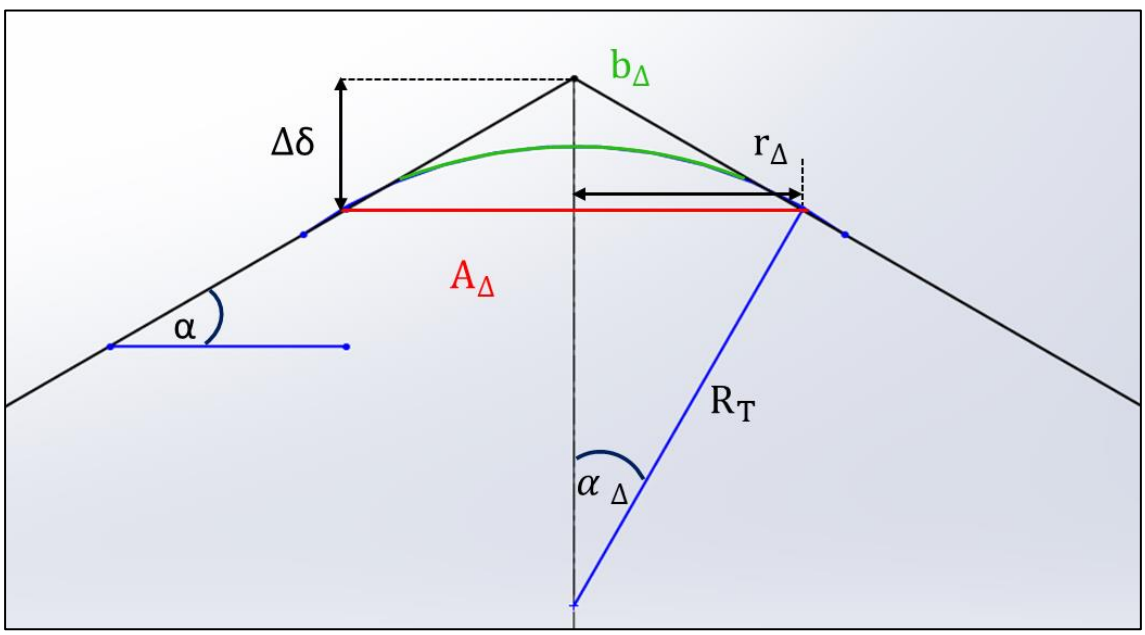

Figure Appendix G 1: Geometric relations and parameter definitions for a blunt or truncated cone tip.

Table Appendix G 2 lists the results for the four selected tests. For example, an initial area of 75 mm^2 would exist if a 20° or 30° cone was short by 1.78 mm or 2.82 mm, respectively. This would lead to a rounded cone tip of approximately 9.87 mm length (presuming $R_T = 20\,mm$). Overall, the cone tip offset is at least $\Delta\delta_{20,50} = 1.45\,mm$ for a 20° cone and an initial area $A_\Delta = 50\,mm^2$ and at most $\Delta\delta_{30,125} = 3.64\,mm$ with $A_\Delta = 125\,mm^2$ for a 30° cone; this encompasses the range of offsets that was noticed in the tests which was maximal 3 mm for a 30° cone.

Table Appendix G 2: Overview of initial areas and associated radii, displacements, angles and arc lengths.

$\boldsymbol{A_\Delta}$	[mm^2]	**50**	**75**	**100**	**125**
$\boldsymbol{r_\Delta}$	[mm]	3.99	4.89	5.64	6.31
$\boldsymbol{\Delta\delta_{20,A\Delta}}$	[mm]	1.45	1.78	2.05	2.30
$\boldsymbol{\Delta\delta_{30,A\Delta}}$	[mm]	2.30	2.82	2.26	3.64
$\boldsymbol{\alpha_\Delta}$	[°]	11.51	14.14	16.39	18.38
$\boldsymbol{\varphi_\Delta}$	[°]	23.02	28.28	32.77	36.77
$\boldsymbol{b_\Delta}$	[mm]	8.03	9.87	11.44	12.83

Subsequently a modified nominal area is determined based on the sum of original radius (derived from the measured displacement) and r_Δ. The force measured at each sampling point is related to the modified area to receive a modified average nominal pressure. In order to compare the effect of the four initial areas, pressure averages and standard deviations are calculated over three different considered ("cons.") area ranges: first over the entire data series, starting from 0 mm^2 area and then for areas above 100 mm^2 and 1000 mm^2 (determined from the original data series). The results of the average pressures are provided in Table Appendix G 3 and the corresponding standard deviations in Table Appendix G 4. The effect of an initial area (due to a cone tip offset) on the average

nominal pressure over the entire tests length is significant. It causes pressures infinity for infinitesimal small areas at the small penetration depths (initial area 0 mm^2). The agreement is less than 30 % and for test T09-04 it is as low as 0.1 % (note: this test seemed to be an outlier and was excluded from the analysis for explained reasons). The higher the minimum area margin, the less becomes the difference in average pressures. The agreement ranges from 76.9 % for the worst offset (125 mm^2, 20° cone) to 87.5 % (50 mm^2, 30°cone) for the least offset. For a better comparability of the results and to mitigate the effect of a cone tip offset on nominal average pressures, a lower margin of 1000 mm^2 was chosen in the data analysis to evaluate the average nominal pressures.

Table Appendix G 3: Average nominal pressures for selected tests with an without a presumed cone tip offset (expressed by means of an intitial area). The pressures refer to the entire data series, and to areas above 100 mm^2 and 1000 mm^2.

	Area [mm^2]	**Average Pressures [MPa]**				
	Initial / Cons.	**0**	**50**	**75**	**100**	**125**
T10_01 D_LS_F_20	**Entire Test**	22.82	6.81 29.8 %	6.48 28.4 %	6.24 27.3 %	6.04 26.5 %
	> 100	9.00	7.07 78.5 %	6.75 75.0 %	6.51 72.3 %	6.32 70.1 %
	> 1000	8.45	7.11 84.2 %	6.86 81.3 %	6.66 78.9 %	6.50 76.9 %
T26_04 D_HS_F_20	**Entire Test**	16.82	3.56 21.2 %	3.31 19.7 %	3.14 18.7 %	3.00 17.9 %
	> 100	4.55	3.37 74.0 %	3.20 70.2 %	3.06 67.3 %	2.96 65.0 %
	> 1000	3.51	2.96 84.3 %	2.86 81.5 %	2.78 79.2 %	2.71 77.3 %
T38_04 D_LS_F_30	**Entire Test**	82.48	5.72 6.9 %	5.46 6.6 %	5.27 6.4 %	5.12 6.2 %
	> 100	7.31	5.88 80.4 %	5.64 77.2 %	5.46 74.7 %	5.31 72.7 %
	> 1000	7.04	6.01 85.4 %	5.81 82.6 %	5.66 80.4 %	5.53 78.6 %

T09_04 D_HS_F_30	**Entire Test**	1234.61	1.65 0.1 %	1.52 0.1 %	1.44 0.1 %	1.37 0.1 %
	> 100	2.21	1.57 71.1 %	1.48 67.1 %	1.42 64.0 %	1.36 61.6 %
	> 1000	1.28	1.12 87.5 %	1.09 85.1 %	1.07 83.1 %	1.04 81.5 %

Table Appendix G 4: Standard deviations of average pressures for selected tests. The numbers refer to the entire data series, and areas to above 100 mm^2 and 1000 mm^2.

	Area [mm^2]	**Standard Deviations [MPa]**				
	Initial / Cons.	**0**	**50**	**75**	**100**	**125**
T10_01 D_LS_F_20	**Entire Test**	1820.35	1.35	1.36	1.37	1.37
	> 100	2.09	0.84	0.79	0.78	0.79
	> 1000	1.51	0.70	0.59	0.52	0.47
T26_04 D_HS_F_20	**Entire Test**	211.25	1.80	1.52	1.35	1.24
	> 100	3.25	1.60	1.43	1.31	1.22
	> 1000	1.73	1.23	1.15	1.10	1.06
T38_04 D_LS_F_30	**Entire Test**	18779.67	1.13	1.18	1.22	1.25
	> 100	1.29	0.82	0.86	0.90	0.94
	> 1000	0.98	0.68	0.68	0.68	0.69
T09_04 D_HS_F_30	**Entire Test**	43160.36	1.50	1.33	1.21	1.12
	> 100	2.80	1.49	1.33	1.22	1.14
	> 1000	0.62	0.56	0.54	0.53	0.53

The reasonability of 1000 mm^2 as the lower margin was further examined by comparing the pressure-area curves that are derived according to Eq. (2.2) with $P = C \cdot A^{ex}$. Table Appendix G 5 lists coefficients *C*, *ex* and the coefficient of determination R^2. The assumption of an initial area A_Δ has a severe effect on *C* (pressure per 1 m^2 unit), but is of little effect on coefficient *ex*.

Table Appendix G 5: Coefficients *C*, *ex* and coefficient of determination R^2 of pressure-area relationship depending on initial area.

	A_Δ [mm^2]	C [MPa]	ex [-]	R^2 [-]
T10_01 D_LS_F_20	**0**	34.02	-0.156	0.780
	50	13.41	-0.071	0.476
	75	11.12	-0.054	0.352
	100	9.54	-0.040	0.236
	125	8.37	-0.028	0.136
T26_04 D_HS_F_20	**0**	3.68	-0.014	0.0012
	50	1.46	0.0704	0.0312
	75	1.21	0.0872	0.0475
	100	1.04	0.101	0.0630
	125	0.91	0.113	0.0777
T38_04 D_LS_F_30	**0**	11.73	-0.0570	0.158
	50	4.75	0.0250	0.0436
	75	3.96	0.0413	0.115
	100	3.41	0.190	0.190
	125	3.01	0.0659	0.026
T09_04 D_HS_F_30	**0**	0.017	0.451	0.385
	50	0.0070	0.533	0.457
	75	0.0059	0.549	0.470
	100	0.0050	0.562	0.480
	125	0.0044	0.574	0.490

These data show the influence of the initial cone tip constitution on the average nominal pressures. In order to account for cone tip offsets, that were noticed during the experimentation an offset value $\Delta\delta$ is included in the analysis. For further mitigation, only areas above 1000 mm^2 (3.2 cm x 3.2 cm) are used in the analysis of the average nominal pressure for the flat indentation plate, for the conical indenter, and for the wedge.

For tests prior to April 2015, $\Delta\delta$ was determined by onscreen measurements of pictures taken of the specimens before the tests. As this was not the initial purpose of the photographs, most of the images were taken at angles and reference lengths were difficult

to identify. Therefore, these values are approximations but not exact measurements. In later tests the cone tips were more precisely monitored and notes of deviations were taken at the time tested.